Heinrich Heine Universität Düsseldorf

1965–2025

Theoretical Modeling of Vibronic Transitions in OLED Emitters: From Method Development to Application

Inaugural-Dissertation

zur Erlangung des Doktorgrades der Mathematisch-Naturwissenschaftlichen Fakultät der Heinrich-Heine-Universität Düsseldorf

vorgelegt von

Tobias Böhmer

aus Grevenbroich

Düsseldorf, Feb. 2025

aus dem Institut für Theoretische Chemie und Computerchemie der Heinrich-Heine-Universität Düsseldorf

Gedruckt mit der Genehmigung der
Mathematisch-Naturwissenschaftlichen Fakultät der
Heinrich-Heine-Universität Düsseldorf

Berichterstatter:

1. Prof. Dr. Christel M. Marian
2. Dr. Martin Kleinschmidt
3. Prof. Dr. Horst Köppel

Tag der mündlichen Prüfung: 23.06.2025

Eidestattliche Erklärung

Ich versichere an Eides statt, dass die Dissertation von mir selbstständig und ohne unzulässige fremde Hilfe unter Beachtung der "Grundsätze zur Sicherung guter wissenschaftlicher Praxis an der Heinrich-Heine-Universität Düsseldorf" erstellt worden ist. Die Dissertation wurde weder in dieser, noch in ähnlicher Form bei anderen Prüfungsbehörden vorgelegt. Es wurden keine früheren erfolglosen Promotionsversuche unternommen.

Düsseldorf, den 10.02.2025

„There could be a 100 people in the room and 99 don't believe in you.
And just one does and that's him."

Lady Gaga

Danksagung

Ich möchte diese Gelegenheit nutzen, um mich bei den Personen zu bedanken, die mich während meiner Promotion stets unterstützt haben.

Zuallererst möchte ich mich bei meiner Doktormutter, Prof. Dr. Christel M. Marian, bedanken. Ich kann mich noch gut an den Tag erinnern, an dem es hieß, man suche jemanden, der sich um das VIBES kümmert. Erst viel später wurde mir bewusst, worauf ich mich da eigentlich eingelassen hatte. Meine Entscheidung bereue ich jedoch nicht, denn in den vergangenen Jahren durfte ich so viel Neues lernen, neue Orte sehen und so viele Menschen kennenlernen, die ich sonst nie getroffen hätte. Und heute weiß ich, dass es nicht selbstverständlich ist, seine Doktoranden und Doktorandinnen mit so viel Zeit und Hingabe zu betreuen – und dafür bin ich dankbar.

Ich danke Martin Kleinschmidt für die Übernahme des Zweitgutachtens und ganz besonders dafür, sich jedes technischen Problems anzunehmen.

Den Initiatoren und Initiatorinnen sowie meinen Kollegen und Kolleginnen des Graduiertenkollegs ModISC danke ich für die zahlreichen Kooperationen. Insbesondere möchte ich mich bei Matthias Jantz, Lennart Bunnemann, sowie Dragana Sretenović für die gelungene Zusammenarbeit bedanken. Für die finanzielle Unterstützung meiner Promotion möchte ich mich bei der Deutschen Forschungsgemeinschaft (DFG) – GRK 2482 / Projektnummer 396890929 – bedanken.

Ich danke meinen Kollegen und Kolleginnen aus dem Arbeitskreis, die mich lange Zeit begleitet haben und ohne die diese Arbeit gar nicht erst möglich gewesen wäre. Ich danke Dennis und Fabian dafür, dass ihr mir bei jedem Problem rund um das Programmieren beigestanden habt. Ich hätte noch so viel von euch lernen können. Ohne deine Expertise, Jeremy, wäre ich bei den Rechnungen schlichtweg verzweifelt. Ich danke Simon für den verantwortungsvollen Umgang mit dem Feuer beim Aufguss der Feuerzangenbowle und Hannah für ihre Aufzeichnungen in MPESP. Ich danke euch, Jasper und Markus, dafür, dass es in unserem Büro einfach nie langweilig geworden ist und dass wir jede noch so kleine Kleinigkeit zusammen ausdiskutieren konnten. Gracias a ti, Johny, he vuelto a aprender español. Gracias por el tándem y por escucharme siempre con paciencia.

Nicht zuletzt danke ich meiner Familie. Auch wenn ihr mir fachlich mittlerweile nicht mehr helfen konntet, habt ihr mir stets aufmerksam zugehört, wenn ich mal wieder klugscheißen musste. Von Anfang an habt ihr an mich geglaubt und dieses verrückte Projekt niemals in Frage gestellt – dafür danke ich euch.

Summary

Vibronic spectroscopy is an essential tool for studying emitter molecules and their behavior following electronic excitation. By employing experimental and quantum chemical methods, the energetic positions of electronic states, their vibrational levels, and the rate constants of nonradiative processes between them can be determined. Simulating vibronic transitions enables the identification of molecular vibrations that significantly influence the decay processes. This insight allows for targeted adjustments to emitter systems to achieve desired photophysical properties. However, conventional adiabatic approaches often fail to yield meaningful results for promising OLED emitters and TADF systems that undergo substantial geometric changes upon electronic excitation.

This work focuses on the implementation and application of an alternative approach to simulate vibronic transitions, the so-called Vertical Hessian (VH) method. Based on the work of Ferrer *et al.*, this method has been integrated into the in-house VIBES program. The VH method utilizes the Hessian matrix and gradients of the final state of a vibronic transition at the Franck-Condon (FC) point to extrapolate the potential energy surface and normal modes of this state. This enables a more accurate description of the potential energy surface at the FC point and promises improved simulation of vibronic transitions. Benchmark results demonstrate that vertical approaches significantly enhance the validity of the linear Duschinsky transformation compared to adiabatic methods. This is reflected in an increase in the determinant of the Duschinsky rotation matrix, substantially reduced Duschinsky mixing, and smaller spatial displacements of the potential energy surfaces. These factors lead to greater overlap of vibrational wavefunctions and a more accurate description of vibronic transitions, particularly for systems with significant geometric changes.

This thesis presents results from collaborations within the research training group ModISC, showcasing the versatility of the VH method: (I) For the well-known TADF emitter DMAC-TRZ, previously unreported absorption bands and the phenomenon of dual emission in rigid matrix materials were attributed to the coexistence of two conformers. (II) For another spiro-bridged donor–acceptor system, calculations of the triplet absorption spectrum demonstrated the need to correct a previously published decay mechanism. (III) A study of donor–acceptor emitters exhibiting sterically divers substituents revealed how the orientation of donor and acceptor influences the TADF properties. (IV) Additionally, the impact of hydrogen bonding on the fluorescence properties and decay processes of efficient fluorophores was modeled. These findings emphasize that the VH method not only enables a meaningful simulation of vibronic transitions but also possesses broad applicability in quantum chemical research.

Kurzzusammenfassung

Die vibronische Spektroskopie ist ein essenzielles Werkzeug zur Untersuchung von Emittermolekülen und deren Verhalten nach elektronischer Anregung. Mithilfe experimenteller und quantenchemischer Methoden lassen sich beispielsweise die energetische Lage elektronischer Zustände, deren Schwingungsniveaus sowie die Geschwindigkeiten nichtradiativer Prozesse bestimmen. Die Simulation vibronischer Übergänge ermöglicht es, molekulare Schwingungen zu identifizieren, die Zerfallsprozesse maßgeblich beeinflussen können. Dies erlaubt Rückschlüsse darauf, wie Emittersysteme gezielt angepasst werden können, um gewünschte photophysikalische Eigenschaften zu erzielen. Gerade für vielversprechende OLED Emitter und TADF Systeme, die nach elektronicher Anregung große geometrische Veränderungen erfahren, liefern herkömmliche adiabatische Ansätze jedoch keine sinnvollen Ergebnisse.

Diese Arbeit fokussiert sich auf die Implementierung und Anwendung eines alternativen Ansatzes zur Simulation vibronischer Übergänge, der sogenannten Vertical Hessian (VH) Methode. Basierend auf den Arbeiten von Ferrer *et al.* wurde die Methode in das hauseigene VIBES Programm integriert. Im Kern nutzt die VH Methode die Hesse-Matrix und Gradienten des finalen Zustands eines vibronischen Übergangs am Franck-Condon (FC) Punkt, um die Potentialfläche und Normalmoden dieses Zustands zu extrapolieren. Dies ermöglicht eine präzisere Beschreibung der Potentialfläche am FC Punkt und verspricht eine verbesserte Simulation vibronischer Übergänge. Die Ergebnisse eines Benchmarks zeigen, dass vertikale Ansätze die Gültigkeit der linearen Duschinsky-Transformation im Vergleich zu adiabatischen Methoden erheblich verbessern. Dies äußert sich in einem Anstieg der Determinante der Duschinsky-Rotationsmatrix, einem deutlich reduzierten Duschinsky-Mixing sowie kleineren räumlichen Verschiebungen der Potentialflächen. Diese Faktoren führen zu einem größeren Überlapp der Schwingungswellenfunktionen und einer genaueren Beschreibung vibronischer Übergänge, insbesondere bei Systemen mit großen geometrischen Veränderungen.

Im Rahmen dieser Arbeit werden Ergebnisse aus Kooperationen des Graduiertenkollegs ModISC vorgestellt, die die Vielseitigkeit der VH Methode demonstrieren: (I) Für den literaturbekannten TADF-Emitter DMAC-TRZ konnten bisher unbeschriebene Absorptionsbanden sowie das Phänomen der dualen Emission in rigiden Matrixmaterialien auf die Koexistenz zweier Konformere zurückgeführt werden. (II) Für ein weiteres spiroverbrücktes Donor–Akzeptor-System beweisen die Berechnungen des Triplet-Absorptionsspektrums, dass ein in der Literatur publizierter Zerfallsmechanismus korrigiert werden muss. (III) Eine Untersuchung sterisch unterschiedlicher Donor–Akzeptor-Emitter zeigte, wie die Orientierung von Donor und Akzeptor zueinander die TADF-Eigenschaften beeinflusst. (IV) Darüber hinaus wurde der Einfluss von Wasserstoffbrückenbindungen auf die Fluoreszenzeigenschaften und Zerfallsprozesse effizienter Fluorophore modelliert. All diese Ergebnisse verdeutlichen, dass die VH Methode nicht nur eine präzisere Simulation vibronischer Übergänge ermöglicht, sondern auch eine breite Anwendbarkeit in der quantenchemischen Forschung besitzt.

List of Publications

1. Toward the improvement of vibronic spectra and non-radiative rate constants using the vertical Hessian method. Tobias Böhmer, Martin Kleinschmidt, and Christel M. Marian
   J. Chem. Phys. (2024)
   DOI: 10.1063/5.0220361
   Contribution: The implementation and validation of the VH method was carried out by me. I visualised all scientific results and I wrote and revised the manuscript.

2. Balancing TADF properties in π-bridged donor-acceptor systems by sterical constraints: The best of three worlds. Jeremy Kaminski, Tobias Böhmer and Christel M. Marian
   J. Phys. Chem. C (2024)
   DOI: 10.1021/acs.jpcc.4c03865
   Contribution: To this work I contributed the quantum chemical calculations of compound Comp 4-diMe and Comp 5-Me+diOMe. All computations of vibronic emission spectra were performed by me. I visualised most of the scientific results and assisted writing and reviewing the manuscript.

3. Unexpected quasi-axial conformer in thermally activated delayed fluorescence DMAC-TRZ. Pushing green OLEDs to blue. Kleitos Stavrou, Larissa G. Franca, Tobias Böhmer, Luka M. Duben, Christel M. Marian and Andrew P. Monkman
   Adv. Funct. Mater., 2300910 (2023)
   DOI: 10.1002/adfm.20230091
   Contribution: The quantum chemical investigation of excited state properties and emission properties of DMAC-TRZ was carried out by me. I wrote the original draft for the theoretical results section and provided the corresponding figures.

4. Intersystem crossing and intramolecular triplet excitation energy transfer in spiro[9,10-dihydro-9-oxoanthracene-10,2´- 5´,6´-benzindan] investigated by DFT/MRCI methods. Simon Metz, Tobias Böhmer, Ben Raunitschke and Christel M. Marian
   Can. J. Chem., 101, 633-640 (2023)
   DOI: 10.1139/cjc-2022-0259
   Contribution: I partially contributed quantum chemical investigation of the emission properties of AN.

List of Manuscripts in Preparation

1. The effect of conformational constraints and oxygen quenching on TADF in donor-acceptor systems. Dragana Sretenović, Laura N. Kloeters, Jeremy M. Kaminski, Tobias Böhmer, Philipp Schmeinck, Suren Felekyan, Oleg Opanasyuk, Gereon A. Sommer, Mina Chalani, Guido J. Reiß, Christoph Janiak, Christel M. Marian, Ralf Kühnemuth, Thomas J. J. Müller and Claus A. M. Seidel
   Manuscript in preparation for *Chemical Science*
   Latest version from 21.01.2025
   Contribution: I performed the quantum chemical investigation of Comp 4-diMe and Comp 5-Me+diOme and provided all the vibronic spectra and the nonradiative rate constants along the interpolated path. The theoretical results were partially visualized by me.

2. Boosting the Fluorescence Quantum Yield of N-Methyl-Acridone by Hydrogen Bonding in Solution and Solid State. Matthias Jantz, David Klaverkamp, Lennart Bunnemann, Benedikt Bendel, Takin Haj Hassani Sohi, Tobias Böhmer, Christel M. Marian, Vera Vasylyeva-Shor, Markus Suta, Constantin Czekelius and Peter Gilch
   Latest version from 22.01.2025
   Manuscript in preparation for the *Journal of American Chemical Society*
   Contribution: I performed all the quantum chemical computations on all of the NMA derivatives and visualized the theoretical results.

Contents

1 Introduction

Since the invention of the light bulb, lighting technologies have become an integral part of our daily lives. However, traditional incandescent bulbs convert more than 94% of the energy into heat, making them inefficient in terms of light production.[1] To address this drawback, more efficient technologies such as gas discharge lamps, halogen lamps, and **L**ight **E**mitting **D**iodes (LEDs) have been developed and commercialized since the 20th century. These innovations marked a significant step toward energy-saving lighting solutions.

Even today, advancements in lighting technology continue to play a central role, particularly in display technologies. Since their first demonstration[2] in 1987, **O**rganic **L**ight **E**mitting **D**iodes (OLEDs) have been a focus of research. These optoelectronic semiconductor-based devices offer numerous advantages that make them highly attractive for modern applications. OLEDs are known for their low energy consumption, excellent color quality, and flexible designs. They are already widely used in commercial applications, including smartphones, televisions, and other displays.[3,4]

Despite their success, OLEDs remain at the forefront of scientific research, particularly in improving their efficiency, brightness, color brilliance, and lifespan. To further enhance the performance of this innovative technology, it is crucial to thoroughly understand and optimize the underlying processes in luminescent materials. The continued development of OLEDs holds the potential to significantly shape the future of lighting and display technologies.

1.1 Architecture of OLEDs

The basic structure of an OLED is relatively simple.[5–7] Essentially, it consists of an emission layer sandwiched between an anode (usually indium tin oxide, a material that is both conductive and transparent) and a cathode (typically a less noble metal such as magnesium, calcium, barium, or aluminum). When a voltage is applied across the electrodes, both electrons and holes are driven toward the emission layer. In this layer, the injected electrons and holes meet, and during their recombination, energy is released, which excites the surrounding emitter molecules. These molecules then emit the excitation energy in the form of light.

Due to the energetically high barriers for electron injection into the emission layer, a single-layer design is highly inefficient. For this reason, modern OLEDs

are typically composed of multiple layers. In addition to the electrodes and emission layer, a hole injection layer and hole transport layer are applied on the anode, while an electron injection layer and electron transport layer are added on top of the cathode. This multi-layer structure facilitates the transport of both electrons and holes toward the emission layer and shifts the recombination zone to the center of the device. These additional layers help balance the charges, reduce charge density within individual layers, and prevent charge leakage at the opposite electrode.

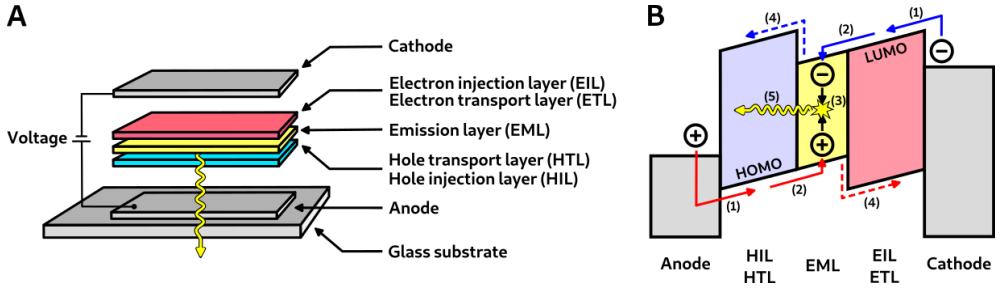

Figure 1.1: Schematic picture of the architecture of a multi-layer OLED (**A**) and a scheme including all the processes which lead to the emission of light in an OLED (**B** 1: Injection of the electron/hole, 2: Transport of the electron/hole, 3: Recombination of the electron and hole and formation of an exciton, 4: Charge leackage, 5: Emission of a photon). Both schemes were inspired by the works of Brütting *et al.*[8]

The multi-layer structure is crucial for achieving high efficiency in OLEDs, but it significantly increases the complexity of device fabrication. The organic materials used for the various layers must exhibit good processability in solution, high conductivity, transparency, and mechanical durability. These layers are typically applied through sublimation or spin-coating, resulting in devices that are generally thinner than 100 nm, allowing them to be flexible. However, the efficiency of OLEDs is influenced by several factors beyond the multi-layer structure. These include the orientation of the emitter molecules, the balance between radiative and nonradiative processes, the charge-carrier balance (which determines how effectively holes and electrons recombine), and the radiative exciton fraction (which determines how many excitons emit light radiatively according to quantum mechanical selection rules).[8] Optimizing these factors is key to enhancing the overall performance of OLED devices.

1.2 Luminescence in OLEDs

Since the introduction of OLEDs, various generations of these devices have been developed. While their basic structure remains largely similar, the mechanisms in the emission layer differ significantly. The underlying principle of these generations starts from the same point: based on spin statistics, electrical excitation generates 25% singlet excitons and 75% triplet excitons.[9,10] Typically, with a singlet ground state, fluorescence from the lowest excited singlet state is the predominating process for the dissipation of the excitation energy. The spin-forbidden transition from the triplet state leads to most of the triplet population

being lost as nonradiative heat dissipation.

In the first generation of OLEDs, only fluorescent emitter materials were used, which inherently limited the internal quantum efficiency to 25%. This is because, without substantial **S**pin–**O**rbit **C**oupling (SOC), the triplet excitons can only relax nonradiatively, making them effectively lost for light generation through electrical excitation. Consequently, only singlet excitons can relax radiatively to the electronic ground state. Despite their significant limitation in quantum efficiency, fluorescent emitters are still commonly used for display applications because they typically exhibit very narrow emission bands.

The second generation of OLEDs introduced phosphorescent emitters, which, unlike their fluorescent counterparts, could theoretically achieve an internal quantum efficiency of 100%. This is achieved by using organometallic complexes in the emission layer. Following electrical excitation, singlet excitons are converted to triplet excitons via **I**nter**s**ystem **C**rossing (ISC). Due to the strong SOC provided by heavy metals like iridium or platinum, theoretically 100% of the excitons can radiatively relax to the electronic ground state. However, while this generation offers high internal quantum efficiency, the emission from the triplet state occurs on microsecond timescales, leaving ample time for chemical reactions in the electronically excited triplet state, potentially leading to degradation reactions. From an industrial perspective, the use of heavy metals is also problematic, as electronic components containing these metals are expensive and difficult to recycle, posing challenges for large-scale industrial applications.

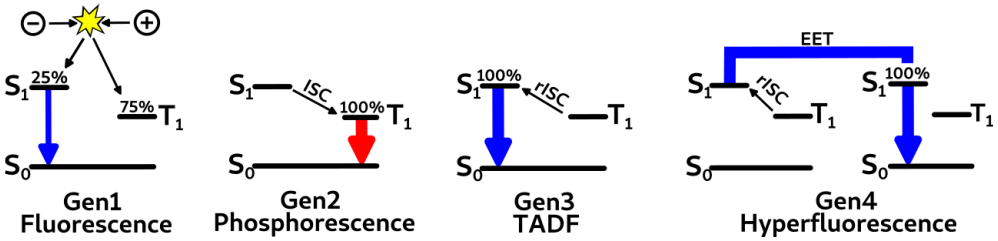

Figure 1.2: Schematic picture of the different OLED generations including the underlying spin statistics of an electric excitation. From left to right: Gen1 Fluorescence OLED, Gen2 Phosphorescence OLED, Gen3 TADF OLED, Gen4 Hyperfluorescence OLED.

The disadvantages of the use of heavy metals provided sufficient motivation to develop a third generation of OLEDs. The goal of this generation is to design organic molecules with electronic states and corresponding energies such that the energy gap between the lowest excited singlet and triplet states is small, enabling **r**everse **I**nter**s**ystem **C**rossing (rISC) and a delayed fluorescence. This process is known as **T**hermally **A**ctivated **D**elayed **F**luorescence (TADF) and occurs when the energy barrier between the lowest excited states is overcome *e.g.* with the help of thermal energy. Like the second generation, this approach theoretically allows for harvesting 100% of the excitons, while also ensuring fast fluorescence and avoiding the use of expensive and toxic heavy metals. However, in comparison to phosphorescent emitters, their operational stability is very limited.

For the sake of completeness, the fourth generation of OLEDs should also be mentioned. In this generation, two types of emitter molecules are combined in the emission layer: fluorescent emitters and TADF emitters. After the TADF emitter is electrically excited, triplet excitons are converted back into singlets via rISC. The excitation energy is then transferred to the singlet states of the fluorescent emitter through **E**xcitation **E**nergy **T**ransfer (EET), after which the fluorescent emitter returns to the electronic ground state, emitting a photon. A key advantage of this generation is that it combines the efficiency of TADF emitters in harvesting singlet excitons with the narrow-band emission of fluorescent emitters. However, this generation remains the subject of ongoing research and is not yet commercially available.

1.3 Motivation and Objectives

This doctoral thesis originates from a project within the **R**esearch **T**raining **G**roup (RTG) 2482 (**Mod**ulation of **I**nter**s**ystem **C**rossing (ModISC)). The central topic of ModISC is to understand and influence the radiative and nonradiative decay processes of emitter molecules, such as those used in an emission layer, as described in section 1.1. For this purpose, various classes of organic and organometallic emitter molecules were synthesized, examined spectroscopically, and their properties investigated through quantum chemical calculations. Chemical modifications and variations of the molecular environment were then used to investigate how these processes can be modulated and optimized. The most promising molecules were then also incorporated into devices, and their luminescent properties were tested in practical applications.

The role of theoretical chemistry within the RTG is to explain and validate experimental phenomena and to develop design principles to make structural proposals that show desired photophysical properties. Reliable methods for describing and simulating the underlying processes are essential for providing accurate explanations and predictions. As part of the project area C2 (Efficient Methods for ISC and IC in Solution and Complex Environments), my predecessor Mario Bracker developed a method for calculating non-adiabatic coupling elements, ultimately aimed at computing rate constants for **I**nternal **C**onversion (IC). At the start of my PhD, the plan was to extend the in-house program VIBES to simulate vibronic transitions in the presence of external solvent molecules. However, it quickly became evident that the conventional method provided only an imprecise description of vibronic transitions in systems undergoing significant geometric changes during these transitions, even without the presence of external solvent molecules. Traditional approaches result in unphysically broad vibrationally resolved absorption and emission spectra and, in some cases, yield unreliable rate constants for nonradiative processes. Such systems often represent promising emitter molecules and the accurate simulation of their photophysical properties is of great interest but it could not be achieved by the use of common approaches. This challenge became the primary motivation for implementing a new model to simulate vibronic transitions more reliably.

This work aims to provide a comprehensive overview of how the simulation of vibronic transitions is practically conducted. To achieve this, it is essential to briefly discuss possible transition processes between electronic states that can follow an electronic excitation. The associated quantitative rules used to estimate the speed and intensity of these processes will also be briefly covered. Regarding vibronic transitions, this thesis will offer an extensive overview of both the fundamental experimental methods and the simulation techniques for vibronic transitions. It will discuss the conventional (adiabatic) approaches used to simulate vibronic transitions and specifically explore the various alternative (vertical) methods available for their simulation. The functionality of both models will be explained, along with their respective strengths and weaknesses. Special attention will be given to the mathematical limitations that arise due to the well-known Duschinsky transformation.

A detailed discussion will be provided on the implementation of the **V**ertical **H**essian (VH) method and how users can effectively utilize it. This will involve explaining the fundamental routines of the program and highlighting where differences arise due to the new implementation. For the updated version of the program new keywords will be introduced that allow the user to modify the output of the computation.

Finally, several application examples from different project areas where the VH method has already been successfully applied will be presented. Additionally, ongoing projects that have not yet been published, but whose results were made possible only through the use of the VH method, will be outlined briefly.

2 Theory

This chapter aims to provide a brief overview of the fundamental experimental and quantum chemical methods used to investigate vibronic transitions. The objective is to demonstrate that within the quantum chemical toolbox vibronic spectroscopy is a vital component in obtaining a comprehensive understanding of molecular properties and excited state decay pathway mechanisms. The focus will primarily be on the theoretical foundations of vibrational spectroscopy, along with its computational simulations. This includes common theoretical considerations and alternative approaches implemented and tested in this work.

2.1 Excited State Processes

Ideally, a preceding quantum chemical investigation using **D**ensity **F**unctional **T**heory (DFT) or **T**ime-**D**ependent **D**ensity **F**unctional **T**heory (TDDFT) provides a clear understanding of the electronic ground state and the relevant electronically excited states (see section 7.1 in the appendix for computational details) for a given system. Consequently, the next logical step is to examine the mechanisms by which these states can be populated, how population transfer between these states can occur and how excitation energy can be dissipated.[11,12] Broadly, these processes are categorized into radiative (release of excitation energy via photon emission) and nonradiative (intra- or intermolecular transfer of excitation energy to another electronic state or into vibrational, rotational, or translational degrees of freedom) processes. The following section provides a brief discussion of the different processes that can occur upon excitation.

Excitation: Molecules can typically be excited to higher electronic states through a process known as absorption, which involves the interaction of light and matter. Given the speed of light ($c = 2.99 \times 10^8$ m/s) and a typical molecular radius of several angstrom, the interaction time between a single photon and the molecule is estimated to be on the order of 10^{-18} seconds, indicating that the absorption process occurs within this attosecond timescale. Generally, photoabsorption happens from the electronic ground state to an electronically excited state. It is important to note that depending on the temperature, different vibrational levels of the ground state are populated, and photoexcitation typically leads to higher vibrational levels of the electronically excited state. This process is often the starting point for subsequent decay and relaxation processes in the excited state. It is important to note that molecules can be excited not only by light but also by other factors, leading to different types of luminescence. These include mechanical stress (triboluminescence), temperature (thermolu-

minescence), applied voltage (electroluminescence), and chemical reactions (chemoluminescence). As discussed in section 1.2, the initial conditions can vary depending on the excitation method. For instance, photoexcitation from a singlet ground state typically results in the formation of 100% singlet excitons, while electrical excitation, based on spin-statistical considerations, produces a ratio of 25% singlet and 75% triplet excitons.[9,10]

Excited State Absorption: An excitation can also originate from an already excited state. When a photon interacts with an electronically excited molecule, it can promote the molecule to higher excited electronic states of the same multiplicity, depending on the energy of the photon. This phenomenon is called **E**xcited **S**tate **A**bsorption (ESA) and is deliberately used to investigate the energetic positions of electronic states and their involvement in the decay pathway mechanism following the excitation. Triplet states, in particular, can be effectively studied using this approach, as they are not accessible through photon absorption from the singlet ground state and are only populated during the decay process.

Vibrational Relaxation: The next process following the excitation is known as **V**ibrational **R**elaxation (VR). On the timescale of molecular collisions (10^{-14} – 10^{-12} s), excited molecules interact and collide with other molecules or the surrounding solvent, dissipating a portion of their vibrational energy. VR oftentimes is a cascading process until the molecule reaches the lowest vibrational level of the respective electronic state. In addition to solvent-mediated relaxation, **I**nternal **V**ibrational **R**elaxation (IVR) can occur. IVR involves the redistribution of vibrational energy within the molecule itself, typically through coupling between vibrational modes. Experimental studies[13,14], such as femtosecond infrared pump-probe spectroscopy, have confirmed that IVR occurs on sub-picosecond timescales, often faster than solvent-mediated processes. For example, experiments on different isotopes of water, show rapid redistribution of vibrational energy among modes with frequencies close in energy. This internal redistribution typically precedes or accompanies VR, facilitating efficient energy dissipation.

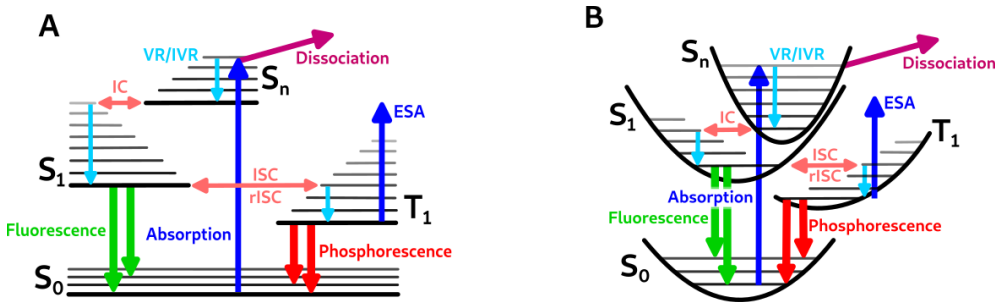

Figure 2.1: **A:** Schematic Jabłonski diagram with all single photon processes and decay mechanisms. **B:** Schematic diagram of the same processes using a picture of harmonic potentials.

Internal Conversion: IC is a process which involves the transition of a molecule from the vibrational ground state of an excited electronic state to another elec-

tronic state of the same multiplicity, but to a higher vibrational level. It is followed by rapid IVR into the vibrational ground state of the new electronic state. This process is typically very efficient due to the small energy gaps between excited states, especially compared to the energy gap between any excited state and the electronic ground state. IC can take place on the subpicosecond time scale when conical intersections between electronic states are involved. This cascade of relaxation processes is also described by Kasha's rule.[15] In some cases, where there are significant energy gaps between higher-lying excited states and fluorescence rate constants can compete with IC rate constants, emission can occur from these higher excited states.[16,17]

Fluorescence: The release of excitation energy in the form of a photon, while maintaining the same multiplicity, is known as fluorescence. This process is spin-allowed and occurs on timescales of $10^{-9} - 10^{-8}$ seconds for strong fluorophores. However, in molecules with weakly allowed transitions or dominant nonradiative decay pathways, fluorescence lifetimes can be much longer. Due to the dissipation of a portion of vibrational energy via VR, fluorescence occurs at lower frequencies compared to the incident radiation.

Intersystem Crossing: ISC is a competing process to fluorescence, where the population is transferred from a singlet to a triplet state. This transition is spin-forbidden, and only occurs on reasonable timescales due to SOC. The rate of ISC is highly dependent on the strength of the coupling between the singlet and triplet states. Once in the triplet regime, similar rules apply as for the singlet states, with excitation energy being dissipated through IC and VR until the system reaches the lowest excited triplet state.

Phosphorescence: Phosphorescence refers to the radiative transition from the lowest excited triplet state to the electronic ground state. Like ISC, this process involves a change in multiplicity and is therefore spin-forbidden. As a result, triplet states are long-lived, and phosphorescence rate constants are typically low, ranging from $10^{0}\,\mathrm{s}^{-1}$ to $10^{6}\,\mathrm{s}^{-1}$.

Delayed Fluorescence: A phenomenon that has gained significant attention in the past decade is delayed fluorescence. It occurs when there is a process called rISC from the triplet regime to the singlet regime, followed by fluorescence from the lowest excited singlet state. The rISC process is typically associated with an energy barrier that, if sufficiently small, can be overcome by thermal energy.

Photochemical Reactions: In the excited state, the excitation energy can also be used to initiate chemical reactions. These reactions occur very quickly, on the timescale of molecular collisions, typically in the range of $10^{-12}\,\mathrm{s}$ to $10^{-10}\,\mathrm{s}$. Examples of unimolecular reactions include photoisomerization and photodissociation. Photochemical reactions, however, are an undesirable process, particularly in the display industry, as the photoproducts exhibit different photophysical properties, thereby altering the behavior of the device.

2.2 Vibrational and Vibronic Spectroscopy

As already mentioned in section 2.1, molecular vibrations are involved in many radiative and nonradiative processes. The following sections will focus on how transitions between these states can be studied and highlight the importance of molecular vibrations. The aim is to demonstrate how vibronic transitions can be investigated experimentally and simulated using quantum chemical methods.

2.2.1 An Experimental Perspective

The experimental molecular vibration spectroscopy deals with all types of interactions between electromagnetic radiation and matter.[18] The resulting changes in molecular motions of these interactions can be observed through various types of experiments. Particularly in the gas phase, vibrational effects can be resolved, providing insights into the vibrational structure of complex systems. Figure 2.2 illustrates different spectroscopic methods in which molecular vibrations play a crucial role. They provide information about the energy of electronic and vibrational states and offer insights into important molecular vibrations during vibronic transitions. These methods will be briefly described in the following sections.

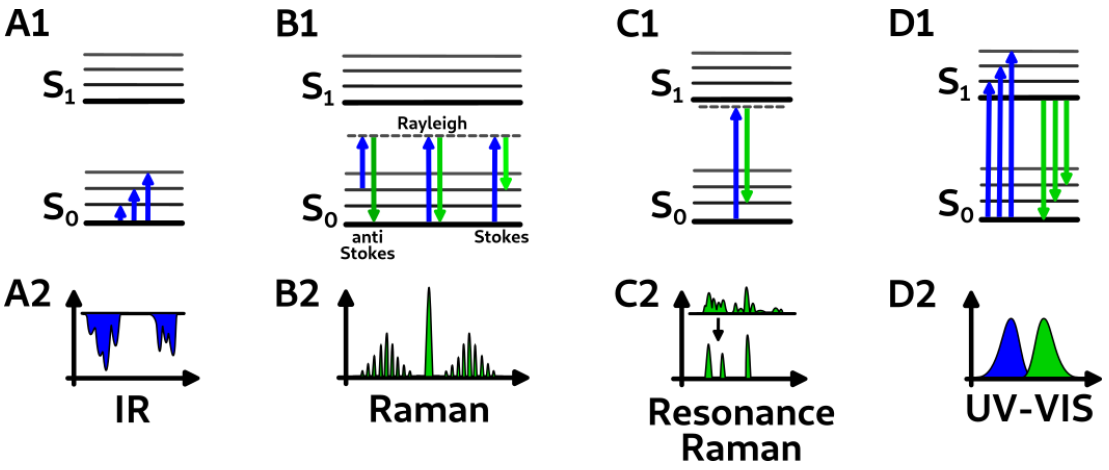

Figure 2.2: Schematic picture of a selection of experimental techniques to investigate molecular vibrations. The top panels (**A1**-**D1**) contain a schematic mechanism of IR spectroscopy (**A1**/**A2**), Raman spectroscopy (**B1**/**B2**), resonance Raman spectroscopy (**C1**/**C2**) and UV-VIS spectroscopy (**D1**/**D2**). The bottom panels (**A2**-**D2**) contain the corresponding schemes of exemplary spectra that result from these kind of experiments.

2.2.1.1 Infrared Spectroscopy

When molecules are exposed to **I**nfra**r**ed (IR) light, the incident radiation is compared with the light transmitted through the sample. This technique is known as transmission IR spectroscopy. The possible interactions between the incident photon and the molecule of interest involve the excitation of molecular rotations and molecular vibrations. IR spectra display bands with reduced intensity when

incoming radiation has been absorbed and molecules have been excited into different vibrational levels (see figure 2.2 A2).

Normal mode vibrations can absorb photons with energies corresponding to their vibrational frequencies (see figure 2.2 A1). As a result, the bands in an IR spectrum can be used to identify specific vibrations associated with functional groups or combinations of atoms, even in an unknown sample.

2.2.1.2 Raman Spectroscopy

In Raman spectroscopy[19], photons are scattered by molecules in a sample and exhibit a different energy after scattering than before. This energy can be higher (anti-Stokes Raman scattering) or lower (Stokes Raman scattering), depending on whether energy was absorbed or released during the elastic scattering process (see figure 2.2 B1). The energy difference between the scattered light that is unchanged in terms of energy (Rayleigh scattering) and the Raman scattering provides insight into the energy of vibrational levels of the given system. However, Raman scattering is much less intense compared to the Rayleigh scattering, making it typically very difficult to detect (see figure 2.2 B2).

2.2.1.3 Resonance Raman Spectroscopy

Resonance Raman spectroscopy[20,21] is a type of spectroscopy related to Raman spectroscopy. In this technique, the incident radiation is tuned to a frequency close to that of the electronic transition (see figure 2.2 C1). The advantage of resonance Raman spectroscopy is that the resulting spectra have significantly higher intensity and are usually much simpler. This simplicity arises because typically only a small number of normal modes contribute to the spectrum (see figure 2.2 C2).

Resonance Raman spectra are used when the signal of conventional Raman spectra is too complex or weak to allow for a meaningful interpretation, or when the molecules are present in very low concentrations in a solution, making detection via conventional Raman spectroscopy difficult. It has also been experimentally demonstrated that the intense resonance Raman bands can be attributed to those vibronic transitions where the geometry shifts from the ground state to the excited state along a normal mode. Consequently, only the normal modes that exhibit a dominant displacement during vibronic excitation appear in the resonance Raman spectrum. This rule is said to apply to both totally symmetric and non-totally symmetric vibrations[21] and allows for an additional geometric information compared to common IR or Raman spectroscopy.

2.2.1.4 UV-VIS Spectroscopy

Ultra**v**iolet (UV)-**Vis**ible (VIS) spectroscopy is not specifically a type of vibrational spectroscopy but rather a part of vibronic spectroscopy. Upon irradiation molecules change their electronic state and their vibrational state (vibronic

transition) at the same time. The energy of the photons used for excitation is significantly higher compared to IR and Raman spectroscopy (see figure 2.2 D1), enabling excitations into electronic states that are much higher in energy. In solution, both absorption and emission spectra typically show broad, featureless bands. However, in the gas phase, vibrational progressions can occur and be detected during absorption and emission processes. These progressions represent the superposition of electronic transitions and the individual vibronic transitions between different vibrational levels of the respective electronic states. Thus, as an addition to vibrational spectroscopy, UV-VIS spectroscopy can provide valuable insights into the vibrational structure of molecules.

2.2.2 A Theoretical Perspective

We observe that molecular vibrations play a significant role in experimental methods and photophysical phenomena in general. Consequently, it is essential to formulate a meaningful quantum chemical description of electronic transitions that incorporates molecular vibrations. The following sections aim to present theoretical considerations for quantifying vibronic transitions and to demonstrate how both vibronic spectra and nonradiative rate constants can be calculated. Additionally, general guidelines and principles will be outlined to estimate the rate constants of these processes.

2.2.2.1 Fermi's Golden Rule and Condon Approximation

Fermi's golden rule[22,23] is widely used in quantum mechanical perturbation theory to quantify the probability of transitions between vibrational levels, specifically from an initial state $|\Psi_a\rangle$ with vibrational level ν_{aj} to a final state $|\Psi_b\rangle$ with vibrational levels ν_{bk}. Fermi's golden rule is widely applicable in many different contexts, including deriving rate constants and lifetimes of electronic states, and it provides important insights into phenomena such as radioactive decay, the absorption and emission of light quanta, and the cross-section of chemical reactions. It is important to note, however, that Fermi's golden rule is not suitable for describing ultrafast non-adiabatic transitions, such as those involving conical intersections. The static approach which is employed using Fermi's golden rule, is insufficient for these cases. In such situations, non-adiabatic dynamic simulations are required. In this work we apply it to nonradiative processes like ISC and rISC[24,25], where SOC is the dominant interaction driving the transition. In this case Fermi's golden rule can be formulated as follows:

$$k_{nr} = \frac{2\pi}{\hbar} \left| \sum_k \langle \nu_{bk}, \Psi_b | \, \hat{H}_{SO} \, | \Psi_a, \nu_{aj} \rangle \right|^2 \delta(E_{aj} - E_{bk}) \tag{2.1}$$

where $\hbar$ represents reduced Planck's constant, and $\hat{H}_{SO}$ is the SOC operator. The Dirac delta function δ ensures energy conservation during the transition from the initial to the final state.

Equation 2.1 is typically expanded into a Taylor series and truncated after the first term.[25] Additionally, similar to the Born-Oppenheimer approximation, it is assumed that the electronic and vibrational parts can be separated. These simplifications lead to the expressions for ISC and rISC in the so-called Condon approximation:

$$k_{ISC}^{FC} = \frac{2\pi}{\hbar} \sum_{\alpha} \left| \langle \Psi_{T_b^\alpha} | \, \hat{H}_{SO} \, | \Psi_{S_a} \rangle \right|^2 \sum_{k} |\langle \nu_{bk} | \nu_{aj} \rangle|^2 \; \delta(E_{aj} - E_{bk}) \tag{2.2}$$

$$k_{rISC}^{FC} = \frac{2\pi}{3\hbar} \sum_{\alpha} \left| \langle \Psi_{S_a} | \, \hat{H}_{SO} \, | \Psi_{T_b^\alpha} \rangle \right|^2 \sum_{j} |\langle \nu_{aj} | \nu_{bk} \rangle|^2 \; \delta(E_{bk} - E_{aj}) \tag{2.3}$$

Both equations are identical except for the swapped indices and, compared to equation 2.1, the fine-structure components, α, of the triplet state, which must be taken into account for ISC and rISC processes, specifically.

It can be seen that calculating rate constants is fairly straightforward and can be divided into the calculation of the electronic coupling matrix element and the vibrational overlap, also known as **F**ranck–**C**ondon **F**actors (FCFs). Figure 2.3 illustrates an example of how the FCFs can be determined based on the vibrational wave functions of two different electronic states.

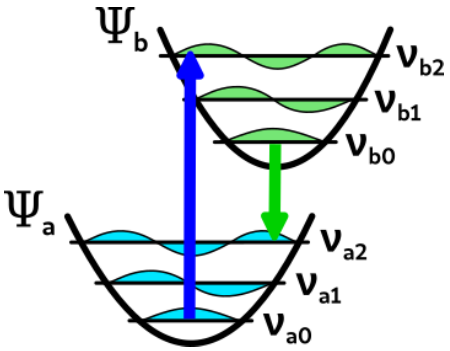

Figure 2.3: Schematic representation of two electronic states that are slightly spatially displaced including the most probable vibronic transitions from the inital state Ψ_a to the final state Ψ_b and *vice versa*. The blue and green arrows are pointing toward the FCP for absorption and emission, respectively.

It is assumed that the molecule starts in the vibrational ground state of the lowest electronic state before excitation. According to the **F**ranck–**C**ondon (FC) principle, the arrangement of the nuclei remains unchanged during the electronic excitation (represented by the vertical line in the diagram). The excitation is most likely to occur into the vibrational level that lies directly above the initial point. This specific point on the **P**otential **E**nergy **S**urface (PES) of the final state is referred to as the **F**ranck–**C**ondon **P**oint (FCP); however, it is more commonly described as the FC region, since molecules oscillate around the equilibrium geometry in the initial state, even at a temperature of $0\,\mathrm{K}$.

Two peculiarities are worth noting here. (I) Calculating the FCF for all possible combinations of a large number of vibrational levels is computationally

demanding and only practical if the number of vibrational levels is significantly limited. In practice, the expressions already discussed (and those to follow) are implicitly computed via the correlation function in the time domain, followed by Fourier transformation (see section 2.2.2.5). (II) Despite its limitations, the Condon approximation simplifies the calculation of transition probabilities and has made it possible to compute rate constants for nonradiative processes in large molecules, which are still at the forefront of current research, by allowing for a computational approach with a reasonable computational effort to systems with a meaningful number of atoms.

2.2.2.2 Temperature Effects

Radiative and nonradiative processes are often highly temperature-dependent.[26] Particularly, for processes that require overcoming a specific energy barrier, the modeling of temperature effects becomes essential. As depicted in section 2.1, rISC from low-lying triplet states to singlet states requires an activation energy, just as ISC from singlet states to higher triplet states does. Instead of considering a single vibrational level, the simulation of temperature effects assumes a transition between a Boltzmann distribution of vibrational states of the initial into the vibrational states of the final state. Generally, the rate constant k_{nr} for a nonradiative transition, starting from the thermal equilibrium of the initial state, can be expressed as an ensemble average for a distribution of transitions from various vibrational levels j of the initial state to a distribution of vibrational levels k of the final state[24,26,27]:

$$k_{nr} = \sum_j P(E_{aj})\, k_{nr}^{j\to k} \tag{2.4}$$

$$= \sum_j \frac{1}{Z} e^{\frac{-E_{aj}}{k_B T}}\, k_{nr}^{j\to k} \tag{2.5}$$

Here, the rate constant $k_{nr}^{j\to k}$ for the nonradiative transition from a vibrational level j of the initial state to a vibrational level k of the final state is scaled according to the Boltzmann distribution of the respective initial state, $P(E_{aj})$. T is the temperature, and k_B is the Boltzmann constant.

For the rate constants of ISC and rISC, under the assumption of the Condon approximation (see equations 2.2 and 2.3) and the contribution of temperature effects such as in equation 2.5, we can derive:

$$k_{\mathrm{ISC}}^{\mathrm{FC,T}} = \frac{2\pi}{\hbar Z} \sum_\alpha \left| \langle \Psi_{T_b^\alpha} | \hat{H}_{SO} | \Psi_{S_a} \rangle \right|^2 \sum_{kj} e^{\frac{-E_{aj}}{k_b T}} \left| \langle \upsilon_{bk} | \upsilon_{aj} \rangle \right|^2 \delta(E_{aj} - E_{bk}) \tag{2.6}$$

$$k_{\mathrm{rISC}}^{\mathrm{FC,T}} = \frac{2\pi}{3\hbar Z} \sum_\alpha \left| \langle \Psi_{S_a} | \hat{H}_{SO} | \Psi_{T_b^\alpha} \rangle \right|^2 \sum_{kj} e^{\frac{-E_{bk}}{k_b T}} \left| \langle \upsilon_{aj} | \upsilon_{bk} \rangle \right|^2 \delta(E_{bk} - E_{aj}) \tag{2.7}$$

Just like in section 2.2.2.1, these two equations differ in their prefactors, where the fine-structure components α of the triplet state are taken into account. Additionally, note that for rISC, the order of the initial and final states is reversed compared to ISC, which results in the indices being swapped accordingly.

2.2.2.3 El-Sayed Rules

The evaluation of the expressions in equations 2.6 and 2.7 involves significant computational effort. Consequently, it is often practical to apply a qualitative rule as an initial approximation. The most widely used qualitative rule for estimating rate constants is the El-Sayed rule. It can be found in the 'IUPAC Glossary of Terms for Photochemistry' and state: "The rate constant of intersystem crossing is relatively large if the radiationless transition involves a change of orbital type."[28]

For phosphorescent emitters, a typical scenario following photo- or electrical excitation involves the nonradiative transition from the lowest excited singlet state to the triplet manifold. Significant rate constants, however, would only be expected for ${}^1\pi\pi^* \rightsquigarrow {}^3n\pi^*$ transitions, but not for ${}^1\pi\pi^* \rightsquigarrow {}^3\pi\pi^*$ transitions and *vice versa*. A contextual embedding and a much more detailed explanation of this rule can be found in the review article by C.M. Marian.[24]

Note, that this rule is intended solely for the qualitative assessment of rate constants and was established under the assumption of fixed geometries. However, El-Sayed forbidden transitions can be significantly accelerated by molecular vibrations. The following section introduces expressions that include molecular vibrations that can break symmetry and lead to a substantial increase of SOC.

2.2.2.4 Beyond the Condon Approximation

The direct SOC, as shown in equations 2.2 and 2.3 (or equation 2.6 and 2.7 when including temperature contributions), is calculated at a fixed geometry. However, as mentioned earlier, it is known that SOC can vary significantly depending on the underlying geometry. Especially when the **S**pin–**O**rbit **C**oupling **M**atrix **E**lements (SOCMEs) are small, large changes may occur along the normal modes of the molecule.[24,29] In these cases, it becomes necessary to expand the current expressions for calculating nonradiative rate constants by incorporating the so-called vibronic SOC. In **H**erzberg–**T**eller (HT)-type schemes, this is done by expanding the Hamiltonian around the equilibrium geometry using a Taylor series expansion. When limited to linear terms, two additional terms appear alongside the pure FC terms: the FC/HT crossterm and the pure HT term, which are specifically expressed below for ISC:

$$k_{ISC}^{FC/HT} = \frac{4\pi}{\hbar} \sum_{\alpha} \sum_{k} \left(\langle \Psi_{T_b^\alpha} | \hat{H}_{SO} | \Psi_{S_a} \rangle \langle \nu_{bk} | \nu_{aj} \rangle \right. \\ \left. \sum_{a} \frac{\partial \langle \Psi_{T_b^\alpha} | \hat{H}_{SO} | \Psi_{S_a} \rangle}{\partial Q_a} \langle \nu_{bk} | Q_a | \nu_{aj} \rangle \, \delta(E_{aj} - E_{bk}) \right) \tag{2.8}$$

$$k_{ISC}^{HT} = \frac{2\pi}{\hbar} \sum_{\alpha} \sum_{k} \left(\frac{\partial \langle \Psi_{T_b^\alpha} | \hat{H}_{SO} | \Psi_{S_a} \rangle}{\partial Q_a} \langle \nu_{bk} | Q_a | \nu_{aj} \rangle \right. \\ \left. \sum_{b} \frac{\partial \langle \Psi_{T_b^\alpha} | \hat{H}_{SO} | \Psi_{S_a} \rangle}{\partial Q_b} \langle \nu_{bk} | Q_b | \nu_{aj} \rangle \, \delta(E_{aj} - E_{bk}) \right) \tag{2.9}$$

Of course temperature effects can also be included in this formalism. Analogous to Equation 2.4, a Boltzmann distribution can be assumed for the population of the vibrational levels of the initial state. This allows for a more realistic representation of the population of the initial state upon vibronic excitation or decay.

2.2.2.5 Time-Dependent Approaches

As mentioned earlier in section 2.2.2.1, one drawback of the static, time-independent approaches is that the computational effort for the explicit calculation of the FCFs is tremendous. For this reason, time-dependent or dynamic methods are more commonly used today, based on transferring Fermi's golden rule into the Heisenberg picture, which primarily avoids the need for explicit FCF calculations. This method is not new[30] but has already been successfully applied to compute electronic absorption spectra[31], circular dichroism spectra[32], resonance Raman spectra[33], as well as IC and EET rate constants.[31,34,35]

For a vibrationally cold initial state ($\nu = 0$), based on Fermi's golden rule and assuming the Condon approximation, the rate constant for ISC can be formulated as follows:

$$k_{ISC}^{corr} = \left|\langle \Psi_S | \, \hat{H}_{SO} \, | \Psi_T \rangle\right|^2 \int_{-\infty}^{\infty} \mathrm{d}t G(t) e^{it\left(\Delta E_{ST}^0 + \frac{1}{2}\,\mathrm{Tr}(\Omega_S)\right)} \tag{2.10}$$

where a time integration of the so-called generating function $G(t)$ is performed. The generating function is obtained using Mehler's formulas[36], which provide an analytic expression only in the harmonic oscillator approximation. In the simplest case (neglecting vibronic effects or temperature contributions), the generating function is given by:

$$\begin{aligned} G(t) =& 2^{\frac{N}{2}} \sqrt{\frac{\det \mathbf{S}^{-1}\Omega_S\Omega_T}{\det\left(\mathbf{J}^{\mathrm{T}}\Omega_{\mathrm{T}}\mathbf{B}\mathbf{J} + \Omega_{\mathrm{S}}\right)\det\left(\mathbf{J}^{\mathrm{T}}\Omega_{\mathrm{T}}\mathbf{B}^{-1}\mathbf{J} + \Omega_{\mathrm{S}}\right)}} \\ & \times e^{\mathbf{D}^T\left(\Omega_T\mathbf{B}\mathbf{J}\left(\mathbf{J}^T\Omega_T\mathbf{B}\mathbf{J}+\Omega_S\right)^{-1}\mathbf{J}^T\Omega_T\mathbf{B}-\Omega_T\mathbf{B}\right)\mathbf{D}} \end{aligned} \tag{2.11}$$

The specific expression for the generating function varies when accounting for temperature contributions[27], vibronic effects[37] or when IC rate constants[38] are computed. Nevertheless, the mathematical foundation mentioned above and the requirement of numerical time integration remain unchanged.

2.2.2.6 The Energy Gap Law

The energy gap law is based on the original considerations of Englman and Jortner[39] (similar considerations were made around the same time by Fisher[40]). It was derived to provide a qualitative rule for rate constants of nonradiative processes in large molecules. Thus, it represents a useful tool for the evaluation of decay pathway mechanisms in large molecules.

To make general statements about the rate constants of nonradiative transitions across various systems of different sizes, it is necessary to establish certain

approximations. In this context, Englman and Jortner proposed the following rigorous assumptions:

1. **Neglect of interference effects:** It is assumed that the rate constants of competing relaxation processes within an excited system can be calculated independently. In other words, each decay process occurs independently. The validity of the derived equations hinges on this assumption, which significantly simplifies the problem.

2. **Two-identical-states model:** A two-state model (also known as displaced oscillator model) is assumed, where transitions are only considered between two discrete electronic states. Potential decay processes to other electronic states are disregarded. Furthermore, the normal mode vibrations and corresponding frequencies of both electronic states are assumed to be identical.

3. **Factorization of vibronic coupling matrix elements:** Analogous to the Condon approximation, the vibronic coupling matrix elements are factorized into a product of electronic coupling elements and FC vibrational overlaps. This allows for the independent consideration of electronic and vibrational components.

4. **Harmonic oscillator approximation:** The PESs are described using harmonic oscillators.

With these approximations, two different scenarios can be distinguished: (I) The weak-coupling limit (see figure 2.4 A) is characterized by a small spatial displacement between the two harmonic oscillators. The PES are only shifted vertically relative to each other and do not intersect. This scenario is often referred to as nested states. (II) In the strong-coupling limit (see figure 2.4 B), however, the oscillators exhibit a significant geometric displacement relative to each other, meaning the involved electronic states have different geometries. The PES intersect at a certain point, requiring a different set of equations for this case.

The transition probability in the weak-coupling limit is highly dependent on the energy difference between the two involved electronic states, ΔE_{ST}. Significant vibrational overlaps can only occur between two harmonic oscillators when the energy gap is vanishingly small. This arises from the consideration that the overlap of the associated Hermite polynomials, $\langle H_n(Q)|H_m(Q)\rangle$, approaches zero unless $n = m$. Consequently, the smaller the energy gap, the larger the nonradiative rate constant. In fact, the transition probability decreases exponentially as the energy gap increases.

In the strong-coupling limit, however, the overlap of two Hermite polynomials with different quanta does not automatically approach to zero. In fact, the overlap is greatest near the intersection of the two PES. As a result, the transition probability exhibits a Gaussian-like behavior. Not only the energy gap but also the reorganization energy and the energy between the crossing point and the minimum of the final state (which are included in the parameter λ) become

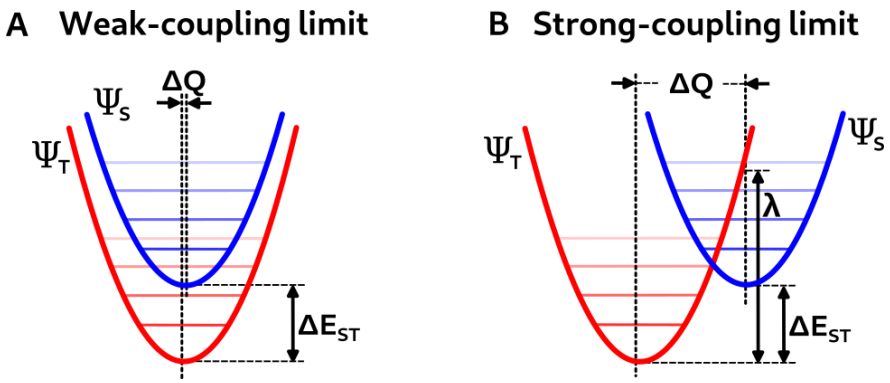

Figure 2.4: Schematic representation of two identical harmonic oscillators for a singlet (Ψ_S) and a triplet (Ψ_T) state. In the weak-coupling limit (**A**) both harmonic oscillators exhibit a small spatial displacement in all normal coordinates **Q** and in the strong-coupling limit (**B**) both harmonic oscillators exhibit a strong spatial displacement and the PES cross.

important factors in estimating the rate constant.

In reality the transition probabilty depends on various additional parameters which can be found in a review article by Marian.[24] It is important to note that the energy gap law is based on the harmonic oscillator model, making it unrealistic for very large energy gaps, such as those encountered during a transition from a triplet or singlet state to the electronic ground state. Additionally, the PES of the electronic states are usually different, and a model of two identical and merely displaced harmonic oscillators is inaccurate for this scenario. Differences in vibrational frequencies as well as rotations of the normal modes are not accounted for; however, it could be shown that the inclusion of Duschinsky mixing for the computation of rate constants of non radiative processes is crucial.[41] Moreover, spin-vibronic effects must also be considered, as they can significantly impact non radiative transitions.[29] Consequently, the energy gap law alone leads to an unreliable prediction of complicated decay pathway mechanisms. Nevertheless, despite these limitations, the energy gap law provides a useful tool for the qualitative assessment of rate constants for nonradiative processes.

2.3 Duschinsky Transformation

As previously mentioned, a vibronic transition always occurs between two different electronic states. Each state represents a minimum on a different PES and thus has a distinct nuclear arrangement. Consequently, the two sets of normal modes also differ. The normal modes of the final state may be rotated or mixed relative to those of the initial state. This phenomenon was first described by Duschinsky when extending the FC principle from diatomic to polyatomic systems.[42] Duschinsky proposed that the normal modes of both states could be related through a linear transformation – the Duschinsky transformation. Specifically, a rotation matrix and a displacement vector are used to map the normal modes of one state to those of the other. The more the rotation matrix deviates from a unit matrix, the greater the so-called Duschinsky mixings, indicating stronger mixing of normal modes. Various studies[41,43] emphasize the importance of considering Duschinsky mixings when calculating nonradiative rate constants and vibronic spectra.

The formalism for calculating the Duschinsky rotation matrix and displacement vector varies depending on the chosen method and the degree of introduced approximations. Generally, this is divided into adiabatic and vertical models, and numerous comprehensive review articles[44–46] compare both approaches.

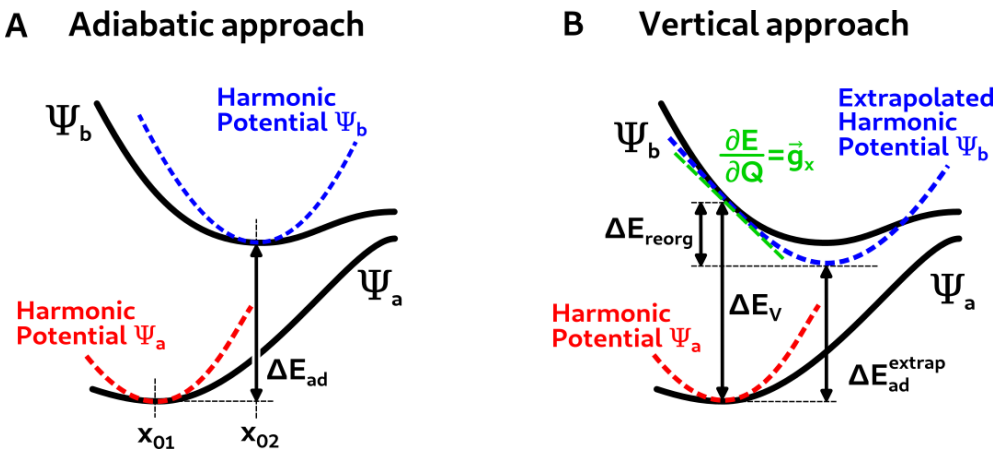

Figure 2.5: Schematic picture of the adiabatic (**A**) and vertical (**B**) approaches including the key parameters that are required for the computation of the Duschinsky rotation matrix and the displacement vector. This scheme was slightly adapted from **Publication No.1**.

The adiabatic and vertical models will be briefly introduced and compared in the following sections.

2.3.1 Adiabatic Approaches

The PES of a given system can be approximated by a harmonic potential. It is constructed around the minimum geometry of the respective electronic state of interest. For an N-atomic system, the harmonic potential for the initial state (V_1) can be expressed in matrix notation as follows:

$$V_1(\mathbf{Q}_1) = \frac{1}{2}\mathbf{Q}_1^T \mathbf{\Omega}_1^2 \mathbf{Q}_1 \tag{2.12}$$

where the normal modes are represented in the matrices $\mathbf{Q}$ (with a dimensionality of $3N-6$ for non-linear molecules and $3N-5$ for linear molecules), and the corresponding frequencies are included in the diagonal matrix $\mathbf{\Omega}$. The normal coordinates are defined as a mass-weighted deviation of the coordinates from the equilibrium geometry:

$$\mathbf{L}_1 \mathbf{Q}_1 = \mathbf{M}^{\frac{1}{2}}(x - x_{01}) \tag{2.13}$$

where $\mathbf{L}$ represents the eigenvectors of the force constant matrix, and $\mathbf{M}$ is the diagonal mass matrix for mass weighting. In the adiabatic case, the equilibrium geometries of both initial and final states are known, allowing for the construction of the harmonic potential of the final state in a similar manner. This approach is referred to as the **A**diabatic **H**essian (AH) method, as the data that is required to construct the harmonic potentials can be directly obtained from the analysis of the Hessian matrix.

As previously described, both sets of normal coordinates can be related to each other using the linear Duschinsky transformation:

$$\mathbf{Q}_1 = \mathbf{J}\mathbf{Q}_2 + \vec{K} \tag{2.14}$$

In the linear transformation, the set of normal modes of the final state is rotated and shifted onto the set of normal modes of the initial state using the Duschinsky rotation matrix $\mathbf{J}$ and the displacement vector $\vec{K}$. This means that the normal modes of the final state are represented in the basis of the initial state.

The harmonic potential of the final state can be expressed similarly to equation 2.12 in its own basis and, using equation 2.14, in the basis of the initial state as follows:

$$V_2(\mathbf{Q}_2) = E_{ad} + \frac{1}{2}\mathbf{Q}_2^T \mathbf{\Omega}_2^2 \mathbf{Q}_2 \tag{2.15}$$

$$V_2(\mathbf{Q}_1) = E_{ad} + \frac{1}{2}\mathbf{Q}_1^T \mathbf{J}\mathbf{\Omega}_2^2 \mathbf{J}^T \mathbf{Q}_1 - \vec{K}^T \mathbf{J}\mathbf{\Omega}_2^2 \mathbf{J}^T \mathbf{Q}_1 + \frac{1}{2}\vec{K}^T \mathbf{J}\mathbf{\Omega}_2^2 \mathbf{J}^T \vec{K} \tag{2.16}$$

In the preceding formula, E_{ad} represents the adiabatic energy difference between the minima of the harmonic potentials. For the optimized geometries, frequency calculations for both electronic states yield a set of normal modes along with their corresponding frequencies. For the rotation matrix and the displacement vector, straightforward terms can be derived in the adiabatic case according to

equations 2.17 and 2.18. A detailed derivation of the Duschinsky transformation in general and the corresponding expressions for the rotation matrix and the displacement vector transformation in the adiabatic case can be found in section 7.3 of the appendix.

$$\mathbf{J} = \mathbf{L}_1^{-1}\,\mathbf{L}_2 \tag{2.17}$$

$$\vec{K} = \mathbf{L}_1^{-1}\,\mathbf{M}^{\frac{1}{2}}\,(x_{02} - x_{01}) \tag{2.18}$$

Different models have been designed to reduce the computational effort of the AH method. Assuming that the structure of a vibronic spectrum is predominantly influenced by the displacement of the two harmonic potentials relative to each other, it can be simplified by defining that the potentials of the initial and final states are the same except for a spatial shift. This model is referred to as the **A**diabatic **S**hift (AS) model, where, by definition, the rotation matrix is an identity matrix ($\mathbf{J}^{(AS)} = \mathbf{1}$) and the frequencies of both states are identical ($\mathbf{\Omega}_2^{(AS)} = \mathbf{\Omega}_1$). However, since Duschinsky mixing effects cannot be neglected without compromising the quality of the results[41], a model was introduced that serves as an approximation between the AH and the AS models. The so-called **A**diabatic **S**hift and **F**requencies (ASF) model takes into account the changes in the harmonic frequencies during the vibronic transition. While the Duschinsky rotation effects are still neglected ($\mathbf{J}^{(ASF)} = \mathbf{1}$), the frequencies are adjusted ($\mathbf{\Omega}_2^{(ASF)} = \sqrt{diag\,(\mathbf{J}\mathbf{\Omega}_2^2\mathbf{J}^T)}$).

In the adiabatic approach, the harmonic potential in all the previously mentioned models is generated at the minimum of the PES of the initial and final states, where it is, by definition, the most accurate. For this reason, adiabatic models typically provide reliable information about the 0-0 transition, *i.e.* the onset of a vibronic spectrum. However, if the potentials are strongly displaced from one another, the actual potential at the FC point may deviate significantly from the constructed harmonic potential. This is one of the reasons why vertical models were introduced to address these issues.

2.3.2 Vertical Approaches

As an alternative to adiabatic models, the harmonic potential of the final state in vertical models is not created at the minimum of the PES. Instead, it is extrapolated toward the minimum using a second-order expansion based on data available at the FC point. The major technical advantage of vertical models is that the data calculated solely at the optimized geometry of the initial state is sufficient to perform a meaningful simulation of the vibronic transition. In the application examples that will be presented later in chapter 4, we demonstrate that vertical models outperform adiabatic models for systems experiencing significant geometrical changes during vibronic transitions. This advantage allows for the simulation of vibronic transitions for a broader range of compounds, where traditional adiabatic approaches fail and provide unreliable results.

In the so-called **V**ertical **H**essian (VH) method, the harmonic PES of the final state can be expressed in the basis of the normal modes of the inital state as

follows, using the vertical energy E_V between the minimum of the initial state and the FC point, the gradients $\vec{g}_x$, and the Hessian matrix $\mathbf{F}_x$ of the final state in Cartesian coordinates:

$$V_2(\mathbf{Q}_1) = E_V + \vec{g}^T\mathbf{Q}_1 + \frac{1}{2}\mathbf{Q}_1\mathbf{F}\mathbf{Q}_1 \tag{2.19}$$

with

$$\vec{g} = \mathbf{M}^{-\frac{1}{2}}\mathbf{L}_1\vec{g}_x \tag{2.20}$$

$$\mathbf{F} = \mathbf{L}_1^T\mathbf{M}^{-\frac{1}{2}}\mathbf{F}_x\mathbf{L}_1\mathbf{M}^{-\frac{1}{2}} \tag{2.21}$$

The linear Duschinsky transformation can also be applied in vertical models. The expressions for the rotation matrix and the displacement vector differ as follows:

$$\mathbf{Q}_1 = \mathbf{J}^{(VH)}\mathbf{Q}^{(VH)} + \vec{K}^{(VH)} \tag{2.22}$$

$$\vec{K}^{(VH)} = -\mathbf{J}^{(VH)}(\mathbf{\Omega}^{(VH)})^{-2}(\mathbf{J}^{(VH)})^T\vec{g} \tag{2.23}$$

Simplifications also exist for the VH method, analogous to the adiabatic alternatives, such as neglecting Duschinsky rotation effects. In the so-called **V**ertical **G**radient (VG) method, it is assumed that both states are only spatially shifted relative to each other and that the Hessian matrix of the final state at the FC point is identical to that of the initial state. This implies that the normal modes and their frequencies must be the same, and similar to the AS method, it holds that $\mathbf{J}^{(VG)} = \mathbf{1}$. As a result, diagonalizing the Hessian matrix and extrapolating the displacement vector for the transformation between the initial and final states is not necessary, and the expression for the displacement vector reduces to $\vec{K} = -\mathbf{\Omega}^{-2}\vec{g}$.

Analogous to the ASF model, the frequencies of the normal modes for the final state can also be adjusted in the vertical approach. In the so-called **V**ertical **G**radient and **F**requencies (VGF) model, Duschinsky rotation effects are ignored ($\mathbf{J}^{(VGF)} = \mathbf{1}$), and the normal mode frequencies are adjusted ($\mathbf{\Omega}^{(VGF)^2} = \sqrt{diag(\mathbf{F})}$).

In general, vertical models provide results of similar quality as adiabatic models for semi-rigid molecules (*i.e.* molecules that do not undergo significant geometrical changes upon excitation or vibronic transition), supporting the reliable application of the harmonic approximation. However, for systems that undergo significant geometric changes during the vibronic transition and whose geometries differ largely between the initial and final states, vertical models can yield significantly better results than adiabatic ones. However, if information about the final state is not accessible, for example, due to difficulties or high computational costs in optimization near crossing PESs, vertical models prove to be a useful alternative.

3 The Program VIBES

In section 2.2.2.1, we saw that rate constants for nonradiative processes can be quantified using Fermi's golden rule and that the expression for calculating the rate constant can be divided into a pure electronic SOCME and the FC integral. For the calculation of these integrals, the in-house program VIBES was developed in the group for theoretical and computational chemistry in Düsseldorf. The static computation of FC integrals (*i.e.* the computation in the energy domain) was implemented by Jörg Tatchen and are based on the *HOTFCHT* program by Roland Berger[47], to calculate FC integrals using the recursive Doktorov method.[48,49] The program has been continuously expanded and adapted since its original version. A dynamic calculation of FC integrals via the integration of the correlation function (see section 2.2.2.5) and the ability to account for temperature effects (see section 2.2.2.2) were introduced by Mihaljo Etinski. And through the work of Mario Bracker[38], the VIBES program can now also calculate IC rate constants, incorporating non-adiabatic coupling elements.

The following chapters do not aim to provide a detailed description of the mathematical background of the adaptations mentioned above and how they were implemented. In this case I strongly recommend to have a look into the original publications and theses that were cited accordingly. The next section rather provides an overview of the functionalities of the VIBES program, with a special focus on the latest modifications that are a part of this work and allow calculations in the internal coordinate system and using vertical approaches (see section 2.3.2) for the computation of Duschinsky mixing effects.

3.1 Implementation

The source code of the VIBES program is composed of various subroutines, originally written in Fortran70, Fortran90, and, in some parts, C++. At the beginning of this work, the main parts of the existing source code were translated into the Fortran90 programming language to increase comprehensibility. The subroutines for the computation and integration of the correlation function were kept in C++ due to their complexity and because there was no need for any adjustments.

The following sections contain generalized flowcharts that depict the sequence of processes within the program or specific sections of it. Oval shaped boxes represent input files, incoming data as well as output files and resulting data. Rectangular boxes denote the associated processes and subroutines. Additionally, diamond boxes indicate where the flow is non-linear, highlighting potential

branches in the program and the decisions that result in these programatic variations.

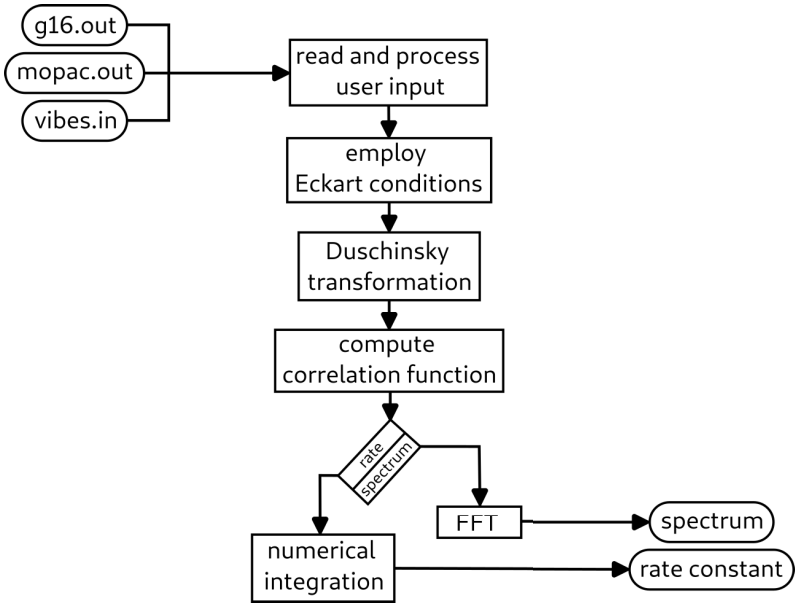

3.1.1 Reading the Input

As an initial step, the VIBES program reads the input data. It includes interfaces designed to import output files from quantum chemistry software packages such as Gaussian16[50] and Mopac.[51] Typically, the essential data are extracted from geometry optimizations or corresponding frequency calculations. These include the geometries of the initial and final states ($\mathbf{X}_1$, $\mathbf{X}_2$), which are stored in $(3N)\times(3)$ matrices, where each row contains the three Cartesian coordinates of an atom. The corresponding normal modes ($\mathbf{Q}_1$, $\mathbf{Q}_2$) are stored in $(3N-6)\times(3N)$ matrices, with each row representing the atomic displacements in atomic units for one of these normal modes. A separate vector ($\vec{\omega}_1$, $\vec{\omega}_2$) stores the eigenvalues of the normal modes, *i.e.*, the frequencies. The atomic masses (m_1, m_2) are identified internally based on the atom type, and from this information, a mass matrix, M, can be generated, if required.

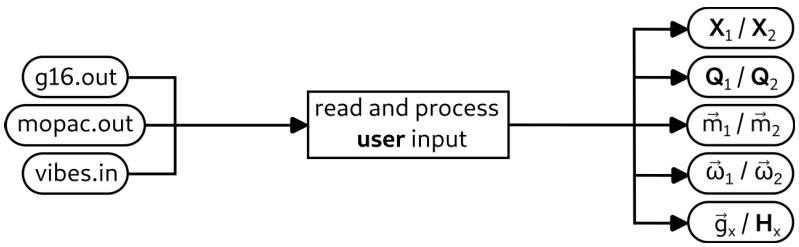

VIBES is controlled by the user through specific keywords. These keywords are stored in a separate input file and passed to the program via standard input. This way, the user can determine key parameters and the desired methods for calculating the Duschinsky rotation matrix, the displacement vector, and the corresponding method for the calculation of rate constants. The individual

keywords will be explained in detail in a dedicated section of the appendix (see section 7.2).

For VG or VH calculations, it is crucial to consider that during the frequency calculation, the binary checkpoint file is required in addition to the Gaussian16 output file. The standard output file contains only a fraction of the full Hessian matrix and gradients, whereas the checkpoint file always includes these matrices in full, regardless of the number of atoms. The gradient vector and Hessian matrix can be extracted from the binary Gaussian16 checkpoint file using the *formchk* routine provided by Gaussian, which converts the binary file into a readable format. From the resulting formatted checkpoint file, the corresponding $(3N{-}6){\times}(1)$ dimensional gradient vector ($\vec{g}_x$) and the $(3N{-}6){\times}(3N)$ dimensional Hessian matrix ($\mathbf{H}_x$) can be extracted. Specifically, in the checkpoint file only the lower triangular part of the Hessian matrix is stored, which must be converted into a symmetric matrix upon extraction.

3.1.2 Frequency Scaling

The harmonic potential serves as an approximation of the actual PES of an electronic state. While the harmonic potential is accurate near the minimum of the surface, it diverges significantly from the true potential at larger deviations from the equilibrium geometry. Although anharmonic potentials provide a much more realistic description, the computational cost associated with them for systems of interest is substantial. An approximate way to incorporate anharmonicity in vibronic transition simulations is by adjusting the harmonic oscillator frequencies using a scaling factor.[52,53]

For frequency scaling in the VIBES program, a scaling factor can be specified in the input file using the keyword *$freqscale* (see section 7.2). It is important to note that the scaling factor depends on the basis set but can be retrieved from a database for a large number of basis sets.[54] During input processing, the scaling factor is applied to the frequencies of each normal mode, and subsequent calculations are performed using the scaled frequency vector.

3.1.3 Eckart Conditions

Employing Eckart conditions[55,56] is essential for calculating vibrational contributions to a vibronic transition. These conditions are used to separate vibrational degrees of freedom from translational and rotational degrees of freedom. The goal is to minimize the contributions of the latter, so the focus can be solely on the vibrational contributions. In the VIBES program, a so-called pseudo-rotation matrix is used, which ensures that the vector product of two geometries of a given system approaches zero. The implemented method is based on a procedure described by Dymarsky *et al.*[57] and addresses challenges where the employment of Eckart conditions fails due to intermediate singular matrices.[58]

In the first step, the center of mass is computed for both geometries. Using these position vectors, both geometries can be shifted to the origin of the coordinate

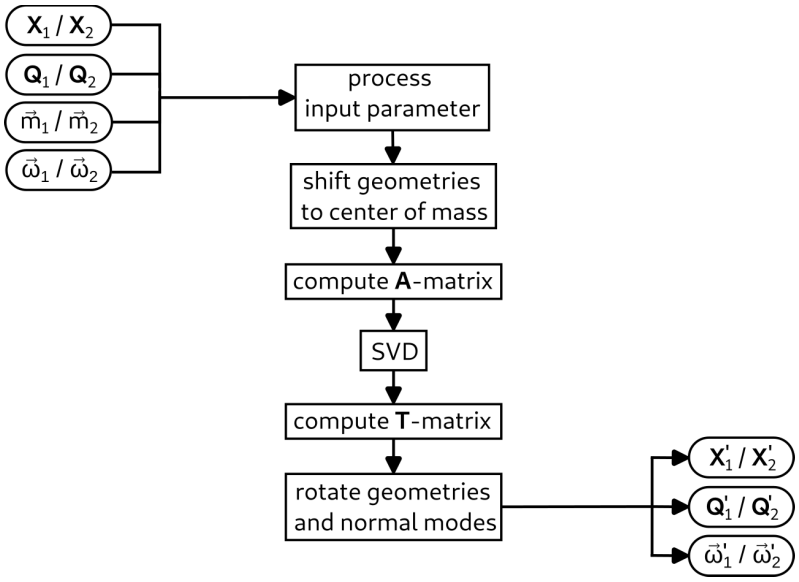

system, ensuring that the contributions from translational degrees of freedom are eliminated.

In the second step, the rotation matrix $\mathbf{T}$ that satisfies the Eckart conditions must be determined. The goal is to ensure the following equation holds true:

$$\sum_{k=1}^{N} m_k \, \mathbf{T}\mathbf{R}_k^I \times \mathbf{R}_k^{II} = 0 \tag{3.1}$$

where the mass-weighted vector product between the position of an atom k in one state $\mathbf{R}_k^{II}$ and the rotated position of this atom in the other state $\mathbf{R}_k^I$ should equal zero. This ensures that the rotational contributions are minimized, allowing the focus to be solely on the vibrational contributions. Equation 3.1 can be rewritten in an equivalent form defining a matrix $\mathbf{A}$:

$$\mathbf{A}_{ij} = \sum_{k=1}^{N} \mathbf{m}_k \, \mathbf{R}_k^I \, \left(\mathbf{R}_k^{II}\right)^T \tag{3.2}$$

Using **S**ingular **V**alue **D**ecomposition (SVD), the matrix $\mathbf{A}$ can be decomposed into its component matrices $\mathbf{U}$ and $\mathbf{V}$, which are required according to the procedure by Dymarsky *et al.*[57] to compute the rotation matrix $\mathbf{T}$. In the final step, this rotation matrix is used to align the two geometries and transform the corresponding normal modes accordingly.

$$\mathbf{A} = \mathbf{U}\mathbf{\Sigma}\mathbf{V}^T \tag{3.3}$$

where the matrix $\mathbf{\Sigma}$ contains all the pivot elements.

This routine is also used to detect normal modes with imaginary frequencies. If detected, the corresponding normal mode alongside its frequency is discarded and the dimensionality of the normal mode matrix and frequency vector of both initial and final state will be decreased accordingly. Finally, the rotated geometries and normal modes are passed to the main program for any further computations.

3.1.4 Duschinsky Transformation

In the VIBES program, various *deltabuild* routines handle relating two sets of normal modes of the initial and final states. This is done using the linear Duschinsky transformation (see section 2.3). Generally, the Duschinsky rotation matrix and displacement vector are generated from the normal modes, their respective frequencies, and atomic masses. Depending on the user input, the appropriate routine is selected based on the chosen coordinate system (Cartesian or internal) and the selected method (adiabatic or vertical). The following section will provide a brief outline of the implementation of the AH method in Cartesian coordinates, as well as the VH method in Cartesian coordinates. Key differences in their respective implementations will be briefly covered for other possibilities to perform the Duschinsky transformation.

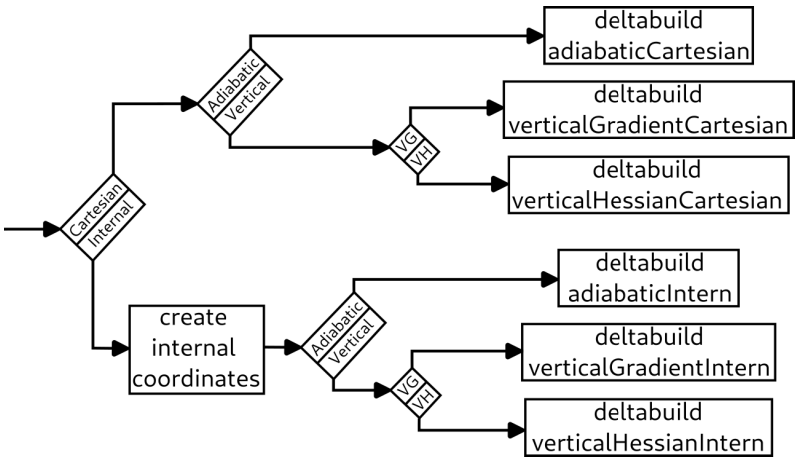

3.1.4.1 Adiabatic Model in Cartesian Coordinates

The conventional approach for calculating the Duschinsky rotation matrix and the displacement vector is the adiabatic case in Cartesian coordinates (see section 2.3.1). To compute the rotation matrix and the displacement vector, the subroutine requires data about the Cartesian coordinates and the normal mode vibrations with their respective frequencies for both electronic states.

First, the $(3N-6)\times(1)$ dimensional Cartesian displacements $\Delta\vec{x}$ are calculated. Similar to what was shown in equation 2.13, these are derived from the mass-weighted displacements:

$$\Delta\vec{x} = \mathbf{M}^{\frac{1}{2}}(\vec{x}_{01} - \vec{x}_{02}) \tag{3.4}$$

The $(3N-6)\times(1)$ dimensional displacement vector $\vec{K}$ is then calculated by multiplying the Cartesian displacements with the normal modes of the final state $\mathbf{Q}_2$ and scaling them with the corresponding frequencies $\vec{\omega}_2$ of the final state. Finally, the vector elements are scaled by a prefactor of 0.1722 $\sqrt{\mathrm{mol} * \mathrm{kg}^{-1} * \mathrm{m}^{-1}}$. This prefactor ensures that the displacement vector becomes dimensionless. A derivation of the prefactor can be found in section 7.3 of the appendix.

The $(3N-6)\times(3N-6)$ dimensional rotation matrix **J** is determined solely by the matrix-matrix multiplication of the normal modes of the initial and final states, as described in Equation 2.17.

Subsequently, the user is provided with an overview of the normal modes, their Duschinsky mixings, and other characteristic parameters of the Duschinsky transformation (these will be explained later in section 3.2).

3.1.4.2 Vertical Model in Cartesian Coordinates

As described in section 2.3.2, unlike in the adiabatic case, the vertical approach assumes that the normal modes of the final state at its minimum geometry, or the optimized geometry itself, are not known. Instead, the normal modes are calculated at the FC point and extrapolated toward the minimum using the Cartesian gradients and the Hessian matrix at that point.

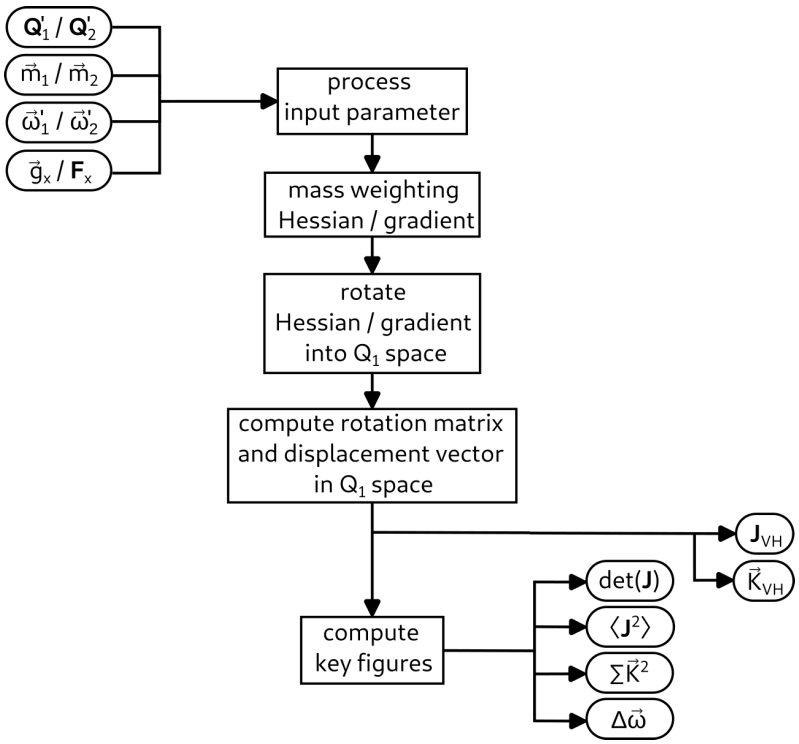

First, the gradients and the Hessian matrix of the final state are mass-weighted and transformed into the basis of the initial state according to equations 2.20 and 2.21.

In this basis, the Duschinsky rotation matrix is calculated through the diagonalization of the Hessian matrix ($\mathbf{J} = \mathrm{diag}(\mathbf{F})$), and the displacement vector is determined according to equations 2.22 and 2.23. These are then returned to the main program. Similar to the adiabatic models, the key parameters of the Duschinsky transformation (to be explained later in section 3.2) are output. Additionally, the user is provided with information on the extrapolated energy difference between the initial and final states.

3.1.4.3 Adiabatic Model in Internal Coordinates

The *deltabuild* routines in internal coordinates first require a transformation of the data into the internal coordinate system. Specifically, this means that alternative expressions for the normal mode vibrations and the Cartesian coordinate differences, for example from equation 3.4, must be found in the internal coordinate system.

To achieve this, internal coordinates for the given system must first be identified. These coordinates are generally classified into bond lengths, bond angles, and dihedral angles. The latter are further subdivided into out-of-plane bending motions (such as the inversion motion of ammonia) and torsions. Following the most common approach by Wilson *et al.* [59], so-called s-vectors can be generated along these motions. These vectors represent the direction of the largest possible geometric change for an internal coordinate and form the basis for the transformation matrix, known as the Wilson B-matrix, which enables the transformation between Cartesian and internal coordinates.

The detailed formalism for identifying all internal coordinates, constructing the transformation matrix, and addressing methodological specifics for transforming Cartesian to internal coordinates has been extensively described in many other articles. [60,61] As part of my master's thesis, I implemented the coordinate transformation into the VIBES program based on these articles. For a comprehensive overview of the implemented routine and the equations used for the coordinate transformation, please refer to my master's thesis. [62]

3.1.5 Generating Function

The primary task of the *ika* routines is to compute the generating function. The specific terms to be calculated for the correlation function differ depending on the chosen method. In section 2.2.2.5, the specific term for ISC without considering temperature effects has already been presented. However, the user can decide whether the generating function is evaluated by accounting for vibronic effects or by including non-adiabatic coupling elements for the calculation of IC rate constants. In all cases, it is possible to compute the correlation function with or without considering temperature effects. Similar to the *deltabuild* routines, a dedicated *ika* routine has been implemented for each formalism.

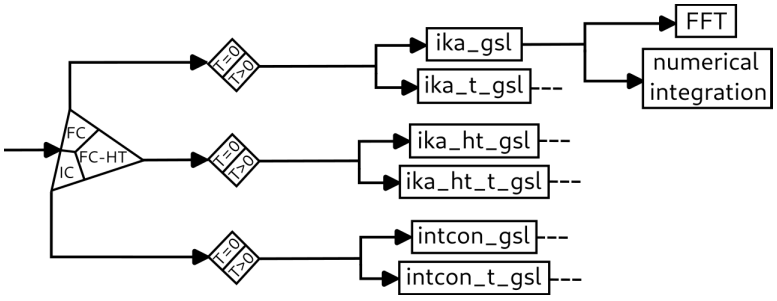

Since the implementation is very similar in all cases, and the correlation function only differs in minor details, the implementation will be explained using one of

these routines as an example. For this purpose, the routine most commonly used in practical applications has been selected: the FC case considering temperature effects with $T > 0K$.

Generating Function for FC with Temperature

The *ika* routine expects as input the previously calculated Duschinsky rotation matrix, the displacement vector, and the corresponding frequencies of the normal modes for the initial and final states. Together with the energy difference, all necessary information is available to evaluate the expression for the generating function.

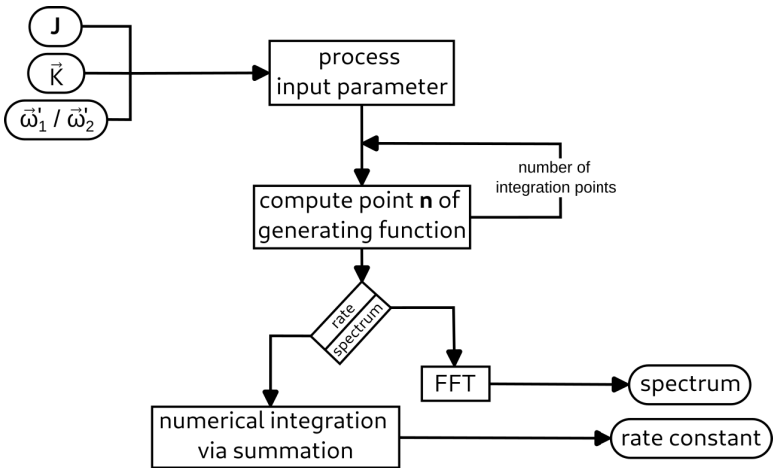

The calculation of a single point in the generating function involves a straightforward sequence of matrix-matrix multiplications. To compute a rate constant, numerical integration is performed, generating as many points of the function as specified by the user in the integration settings. These results are temporarily stored in a vector and the individual points are summed at the end of the integration process. The resulting rate constant is included in the standard output of the VIBES program.

If a spectrum is required, this vector containing the generating function is passed to a routine for a **F**ast **F**ourier **T**ransformation (FFT). For the FFT to work, the number of integration points must be a power of 2. If the specified number of points does not meet this requirement, it is adjusted to the nearest power of 2. Once the spectrum is calculated, it is saved in a separate output file.

3.2 Validation and Testing of the Implementation

The validation of the implementation was a key component of **Publication No.1**. In addition to comparing adiabatic and vertical models as discussed in section 2.3, various key figures were introduced to assess the performance of these models and determine whether comparable or improved results could be achieved relative to the common adiabatic approach for calculating rate constants or vibronic spectra in different test scenarios. These metrics were adapted from the review article by Ferrer and Santoro[44] and applied to custom test examples.

The following section explains the metrics used to evaluate the performance of adiabatic and vertical methods. It is important to note that these parameters do not necessarily need to be calculated and are not required for the subsequent computation of the correlation function. They are solely intended to rationalize the results of both methods and critically analyze the outcomes. However, since the computation of these metrics accounts for only a negligible fraction of the total computational time, they have been integrated into the standard workflow of a VIBES calculation.

3.2.1 Measures to Rate the Performance

Duschinsky rotation matrix determinant: As mentioned in section 2.3, two sets of normal modes can be related via the linear Duschinsky transformation. Using the rotation matrix **J** and the displacement vector $\vec{K}$ within the chosen formalism (see sections 2.3.1 and 2.3.2), the normal modes of one state can be mapped onto the normal modes of the other state. However, a study by Özkan[63] demonstrated that this transformation is neither strictly linear nor orthogonal. The non-orthogonality of this transformation results in a determinant of the rotation matrix that deviates from 1.[63,64] The validity of the Duschinsky transformation diminishes as the determinant diverges further from 1. It therefore serves as a valuable metric to assess whether the chosen formalism and parameter set for calculating the rotation matrix remain valid for a given application or if the results might contain systematic errors.

Average Duschinsky projection: Independent of the determinant of the rotation matrix, the so-called Duschinsky projection provides insights into the degree of Duschinsky mixing (providing a measure of how strongly the normal modes of the initial state couple with those of the final state). For instance, a column of the rotation matrix indicates how a single normal mode of the initial state couples with all the normal modes of the final state. Each vector (or matrix) element can range between 0 and 1, where values closer to 1 represent stronger couplings and a clearer correspondence between normal modes of the two electronic states. The average projection can be calculated using the following expression:

$$\langle \mathbf{J}^2_{max} \rangle = \frac{1}{M} \sum_{i=1}^{M} \max_{1 \leq f \leq M} \left(\mathbf{J}^2_{if} \right) \tag{3.5}$$

where M denotes the number of the normal mode, and the indices i and j

correspond to the row and column of the respective rotation matrix element $\mathbf{J}_{ij}$.

Energies: Since both adiabatic and vertical approaches are different approximations to the 'true' PES, it can be assumed that each model is better suited for specific scenarios. For instance, the energy of the 0-0 transition, which corresponds to the onset of a vibronic spectrum, is better described when the potential is constructed at the minimum. Conversely, the shape or the maximum of the spectrum are better captured by an accurate description of the FC region. To compare the performance of adiabatic and vertical models, the adiabatic energy difference and the extrapolated energy difference can be utilized. These allow for an assessment of the magnitude of the methodological error. Deviations in the calculated energy difference primarily result in a bathochromic or hypsochromic shift when simulating vibronic spectra, whereas their impact on nonradiative rate constants can be much more significant. This is because the energy gap between electronic states for ISC or rISC is typically much smaller than the energy gap between electronic states during photon absorption or emission.

Sum of squared displacement: Large geometric displacements during a vibronic transition manifest as significant elements in the displacement vector. Specifically, normal modes that represent changes in the molecular framework which can potentially transform the geometry of the initial state into the geometry of the final state exhibit high displacement values. Therefore, the sum of all squared displacements:

$$D^2 = \vec{K}^T \vec{K} \tag{3.6}$$

is used as a metric to evaluate the geometric displacements of the systems investigated in this work. Typically, these systems represent promising emitter molecules and share a common feature: low-lying electronic states involved in the decay mechanism that exhibit significant geometric differences. Often, the examined structures have markedly different dihedral angles. Consequently, low-frequency torsional modes show large displacements. Such vibrations are poorly described by the harmonic approximation. Toniolo and Persico[65] proposed replacing these specific modes with periodic sinusoidal potentials; however, vertical models also promise improved descriptions of torsional modes. As a direct consequence, the displacements in vertical models are generally expected to be smaller in magnitude.

0-0 vibrational overlap: The overlap of vibrational wave functions in their vibrational ground states (ν_{a0} and ν_{b0}) serves as another metric to assess how spatially displaced the harmonic oscillators are in the respective method. This overlap can take values between 0 and 1, with an overlap of exactly 1 occurring only in the case of nested states mentioned in section 2.2.2.6. Thus, the overlap can be used as a measure of the spatial displacement between the harmonic oscillators.

3.2.2 Benchmark

To validate the implementation of the VH method, four test systems of varying sizes and complexities (see figure 3.1) were selected and analyzed using the key measures (see section 3.2.1) for both adiabatic and vertical approaches. These systems had previously been used by Baiardi *et al.*[60] to validate the transformation from Cartesian to internal coordinates for vibronic spectrum calculations. Extending this study to the VH method, following the approach of Baiardi, represents a logical progression, especially since these systems were also used to test my implementation of internal coordinates for vibronic spectra in the VIBES program.[62]

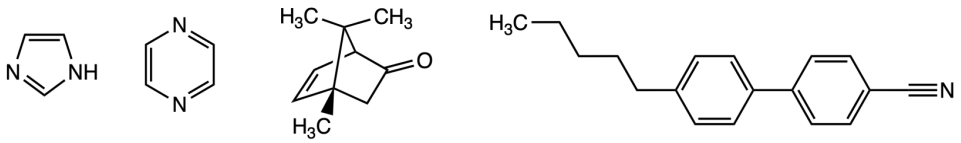

Figure 3.1: Lewis structures of the molecules that were investigated in the benchmark. From left to right: Imidazole (IM), pyrazine (PY), (1S)-dehydro-epicamphor (EPIC), 4-Pentyl-4'-cyanobiphenyl (CB).

Imidazole (IM) and **Py**razine (PY) were chosen as representative small molecules with photophysical properties of significant interest. IM plays a critical role in biological systems, participating in a variety of photoreactions.[66] PY, on the other hand, is characterized by pronounced vibronic interactions between low-lying electronically excited states.[67] Both systems undergo substantial geometric changes upon electronic excitation, posing challenges for generating meaningful spectra using the AH method alone. The epicamphor derivative, (1S)-Dehydro-**EPIC**amphor (EPIC), represents a different kind of challenge due to its complex topology. In this case, adiabatic simulations in Cartesian coordinates fail to capture the nuances of a vibrationally resolved spectrum. Baiardi *et al.*[60] demonstrated that switching to internal coordinates could significantly improve absorption and emission spectra. Moreover, meaningful results can also be achieved with a vertical approach in Cartesian coordinates. Although the geometric changes upon excitation are relatively small and the determinant of the Duschinsky rotation matrix is close to unity (indicating near-linearity in the transformation), the VH method notably enhances the calculation of spatial displacements. The cyanobiphenyl derivative, 4-Pentyl-4'-**C**yano**B**iphenyl (CB), presents unique challenges for vibronic spectrum calculations due to its low-frequency modes, particularly dihedral deformations, which result in substantial spatial displacements. Spectra simulated using the AH method are often structureless, overly broad, and computations yield unreliable rate constants. Internal coordinates offer a pathway to improved accuracy, especially for the treatment of linear components like cyano groups.[60] The VH method further enhances the description of low-frequency modes, which are not only prevalent in CB but also common in many donor–acceptor systems.

Benchmark Results

The following tables show a summary of the most important key measures (mentioned above in section 3.2.1) computed using adiabatic and vertical approaches.

Table 3.1: Summary of key metrics comparing the VH and AH methods for IM and PY: $\det(\mathbf{J})$ (Duschinsky matrix determinant), $\langle \mathbf{J}^2_{max} \rangle$ (average Duschinsky projection), D^2 (squared displacements), and S_{0-0} (0-0 vibrational overlap), along with vertical, reorganization, and adiabatic energy differences.

	IM ($S_0 \rightarrow S_1$)			**PY** ($S_0 \rightarrow S_1$)	
	AH	VG	VH	AH	VH
$\det(\mathbf{J})$	0.980	1.000	1.000	0.999	1.000
$\langle \mathbf{J}^2_{max} \rangle$	0.522	1.000	0.741	0.707	0.918
D^2	33.317	10.438	12.417	2.247	1.501
S_{0-0}	4.5×10^{-4}	7.4×10^{-2}	2.3×10^{-2}	4.5×10^{-1}	4.9×10^{-1}
$\#\omega_{imag}$	–	–	4	–	0
$\Delta E_V [\mathrm{cm}^{-1}]$	–	55617	55617	–	32950
$\Delta E_{reorg} [\mathrm{cm}^{-1}]$	–	5669	6139	–	566
$\Delta E_{ad} [\mathrm{cm}^{-1}]$	46173	49948	49478	32083	32384

Table 3.2: Summary of key metrics comparing the VH and AH methods for EPIC and CB: $\det(\mathbf{J})$ (Duschinsky matrix determinant), $\langle \mathbf{J}^2_{max} \rangle$ (average Duschinsky projection), D^2 (squared displacements), and S_{0-0} (0-0 vibrational overlap), along with vertical, reorganization, and adiabatic energy differences.

	EPIC ($S_0 \rightarrow S_1$)		**CB** ($S_0 \rightarrow S_1$)	
	AH	VH	AH	VH
$\det(\mathbf{J})$	0.992	1.000	0.980	1.000
$\langle \mathbf{J}^2_{max} \rangle$	0.700	0.699	0.709	0.720
D^2	30.995	15.135	26.304	5.777
S_{0-0}	1.8×10^{-3}	4.0×10^{-3}	4.7×10^{-3}	6.8×10^{-2}
$\#\omega_{imag}$	–	2	–	4
$\Delta E_V [\mathrm{cm}^{-1}]$	–	32645	–	35323
$\Delta E_{reorg} [\mathrm{cm}^{-1}]$	–	2821	–	1771
$\Delta E_{ad} [\mathrm{cm}^{-1}]$	29584	29824	32909	33552

Tables 3.1 and 3.2 demonstrate that the use of vertical approaches generally increases the determinant of the Duschinsky rotation matrix ($\det(\mathbf{J})$) to a value of 1. This outcome is a result of the extrapolation process, indicating that the linear Duschinsky transformation is only fully valid in vertical models. Examining the Duschinsky rotation matrices reveals two notable features:

1. **Reduced Dimensionality**: In the VH method, dimensionality is reduced because normal modes with imaginary eigenvalues in the frequency analysis at the FCP are excluded from the calculation.

2. **Decreased Duschinsky Mixing**: The mixing effects are significantly diminished, due to fewer and less scattered off-diagonal elements, with the matrix elements concentrating closer to the diagonal.

This reduction in mixing is directly reflected in the average Duschinsky projection $\langle \mathbf{J}^2_{max} \rangle$, which increases for all examples, indicating a general decrease in mixing effects.

In all test systems, the sum of all displacements (D^2) decreases, and the 0-0 overlap (S_{0-0}) slightly increases. This indicates that in the VH formalism, the extrapolated geometry of the final state in the basis of the initial state is less displaced compared to the adiabatic approach. It also suggests that the geometric displacements cannot be fully captured by a linear transformation in the adiabatic approach, and extrapolation of the PES positively influences the displacements.

The extrapolated adiabatic energy difference, derived from the vertical excitation energy ΔE_V from the minimum of the initial state to the FCP and the reorganization energy ΔE_{reorg} to the extrapolated minimum, provides a reasonable estimate compared to the actual adiabatic energy difference ΔE_{ad}. However, for the test molecule IM, the extrapolated energy difference of $49478\ \mathrm{cm}^{-1}$ is approximately 3000 wavenumbers higher than the true value. We attribute this discrepancy to the relatively high number of normal modes with imaginary eigenvalues compared to the total number of normal modes. Therefore, the number of imaginary normal modes is assumed to be a critical factor affecting the performance of the VH method.

Application Example: CZT1

The following section will demonstrate that key metrics can also be applied to larger systems, yielding valuable insights. For this purpose, results for a zinc complex (**C**arbene-**Z**inc-**T**hiolate **1**: [Zn($^{4\text{-H}}$bdt)($^{\text{Menth}}$cAAC)] (CZT1), see figure 3.2) are presented, which has already been investigated in **Publication No.1** for a comparative study of adiabatic and vertical models. CZT1 is part of a series of complexes from a previous study[68] and an intriguing test system due to its multiple conformers, whose excited states exhibit different geometric changes.

In a quantum chemical investigation of CZT1, which was mainly conducted by Markus Putscher[68], we successfully optimized the quasi-planar conformer ($\Omega_{S0} = 10°$), the ortho conformer ($\Omega_{S0} = 76°$), and a tilted conformer ($\Omega_{S0} = 40°$), with the latter being the most favorable in terms of energy. A rotational pathway revealed that the conformers can interconvert, with a maximum rotational barrier of only $4\ \mathrm{kJ/mol}$, which is expected to be easily surmountable. Consequently, it was hypothesized that under ambient conditions, an equilibrium between the conformers would occur, allowing them to be detected simultaneously in experimentally measured spectra.

The study addressed this question in part by simulating the photophysical properties of all conformers of CZT1. Here, we will focus on the emission process, as this is where the largest impact of using vertical models was observed. Figure 3.3 shows both the experimental emission spectrum of CZT1 and the theoretical emission spectra calculated using the AH and VH methods.

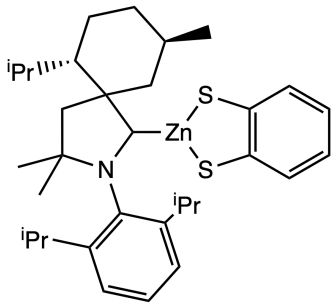

Figure 3.2: Lewis structure of CZT1. The dihedral angle measured at the electronic ground state Ω_{S0} is formed between the carbene-zinc plane and the zinc-sulfur plane.

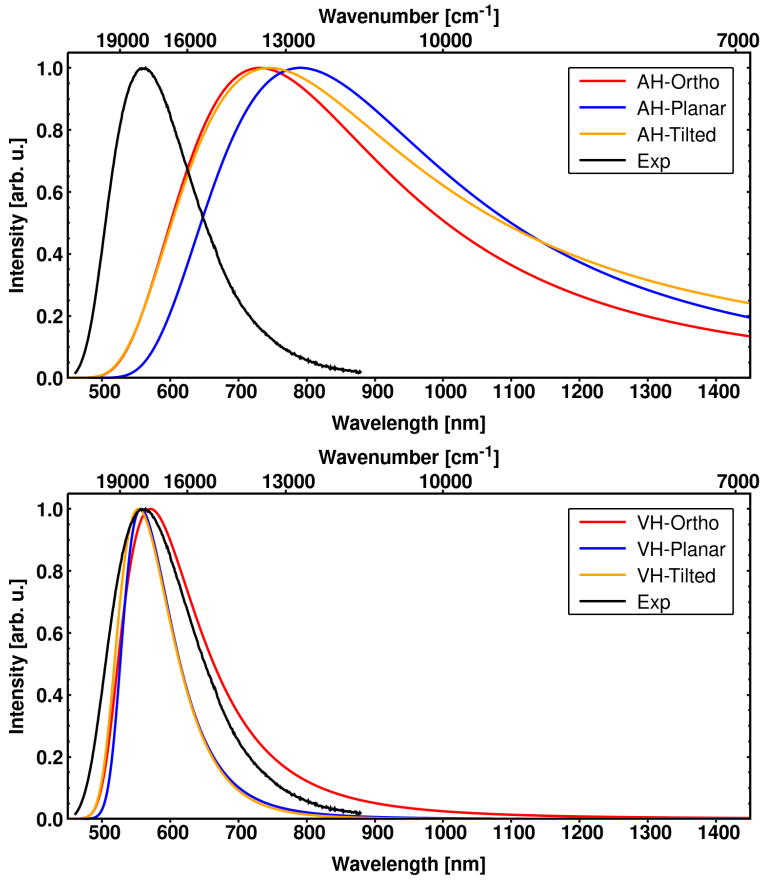

Figure 3.3: Experimental[68] and simulated emission spectra of CZT1 using the AH and VH methods. 16384 integration points, a time interval of $300\ \mathrm{fs}$, a damping factor of $100\ \mathrm{cm}^{-1}$ and a temperature of $300\ \mathrm{K}$ were used for the computations.

It is evident that the simulated spectra, regardless of the method used, exhibit only a featureless band. Generally, the emission spectra of the different conformers differ only marginally, with slight variations in emission maxima and onsets. Notably, however, the spectra calculated with the AH method are significantly broader compared to the experimental results (with a **F**ull **W**idth at **H**alf **M**aximum (FWHM) ranging from 6400 to $7400\ \mathrm{cm}^{-1}$). Their onsets do not match the experiment, and the spectra extend to higher wavelengths with the intensity not approaching to zero in the considered spectral regime.

In contrast, the spectra calculated using the VH method are much narrower (with a FWHM ranging from 2750 to $4350\,\mathrm{cm}^{-1}$) and align well with the experimental spectrum in both spectral shape and width. Additionally, the onsets of all VH spectra are in good agreement with the experimental data.

During the review process of **Publication No.1**, the question arose whether simplified models like the VG method (see section 2.3.2) could be used instead of the VH method to achieve comparable results with less computational effort (avoiding the explicit calculation of the Hessian matrix for the final state at the FCP). Figure 3.4 shows the emission spectra of all conformers calculated using the VG method.

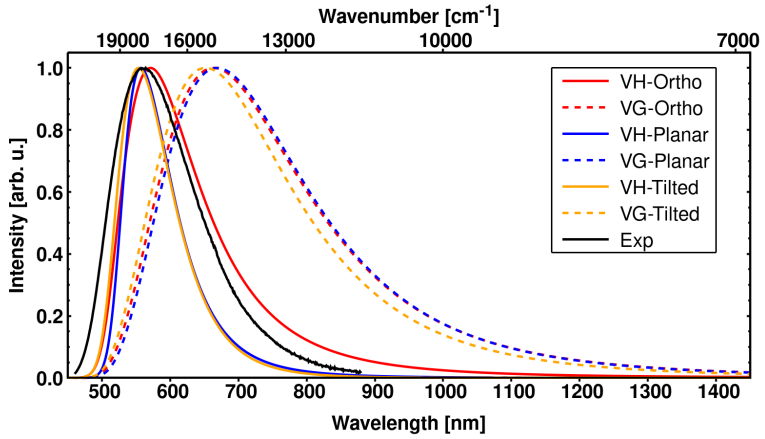

Figure 3.4: Experimental[68] and simulated emission spectra of CZT1 using the VG and VH methods. 16384 integration points, a time interval of $300\,\mathrm{fs}$, a damping factor of $100\,\mathrm{cm}^{-1}$ and a temperature of $300\,\mathrm{K}$ were used for the computations.

Although the resulting spectra are narrower than those obtained from the AH calculations, they remain significantly too broad compared to the experiment (FWHM $\approx 5500\,\mathrm{cm}^{-1}$). The emission maxima do not align with the experimental data and are shifted too far to longer wavelengths. These findings also corroborate the conclusions of a study by Etinski[41], which emphasized that incorporating Duschinsky mixings is essential for improving the simulation of vibronic transitions.

The benchmark metrics introduced earlier can also be applied to CZT1 to compare adiabatic and vertical models. The conclusions align with those drawn from the benchmark set, but a significant improvement in performance is observed when using the VH method for the tilted conformer. Here, the determinant of the Duschinsky rotation matrix increases ($\det(\mathbf{J}_{\mathrm{AH}}) = 0.9899$ and $\det(\mathbf{J}_{\mathrm{VH}}) = 1.000$), as does the average Duschinsky projection ($\mathrm{AH} = 0.6070$ and $\mathrm{VH} = 0.7080$), while the spatial displacements decrease dramatically ($D^2_{\mathrm{AH}} = 96.501$ and $D^2_{\mathrm{VH}} = 25.630$).

The computed normal modes at the FC region for the final state show only a single imaginary eigenvalue. The following tables 3.3 and 3.4 summarize the

results for all conformers.

Table 3.3: Summary of key metrics comparing the VH and AH methods for the ortho and planar conformers of CZT1: $\det(\mathbf{J})$ (Duschinsky matrix determinant), $\langle \mathbf{J}^2_{max} \rangle$ (average Duschinsky projection), D^2 (squared displacements), and S_{0-0} (0-0 vibrational overlap). Also the wavelength of the emission maximum, λ_{em}^{max}, and the FWHM are given.

	Ortho			**Planar**		
	AH	VG	VH	AH	VG	VH
$\det(\mathbf{J})$	0.998	1.000	1.000	0.996	1.000	1.000
$\langle \mathbf{J}^2_{max} \rangle$	0.612	1.000	0.661	0.661	1.000	0.725
D^2	29.710	29.478	27.667	45.230	41.587	32.309
S_{0-0}	2.5×10^{-4}	6.3×10^{-3}	1.1×10^{-3}	3.4×10^{-5}	3.1×10^{-5}	1.5×10^{-4}
$\#\omega_{imag}$	–	–	2	–	–	2
λ_{em}^{max} [nm]	731	669	571	746	664	557
FWHM [cm^{-1}]	6688	5445	4060	6403	5510	2751

Table 3.4: Summary of key metrics comparing the VH and AH methods for the tilted conformer of CZT1: $\det(\mathbf{J})$ (Duschinsky matrix determinant), $\langle \mathbf{J}^2_{max} \rangle$ (average Duschinsky projection), D^2 (squared displacements), and S_{0-0} (0-0 vibrational overlap). Also the wavelength of the emission maximum, λ_{em}^{max}, and the FWHM are given.

	Tilted			**Sum**	
	AH	VG	VH	VH	EXP
$\det(\mathbf{J})$	0.990	1.000	1.000	–	–
$\langle \mathbf{J}^2_{max} \rangle$	0.607	1.000	0.708	–	–
D^2	90.501	27.594	25.630	–	–
S_{0-0}	1.0×10^{-7}	1.0×10^{-3}	1.6×10^{-3}	–	–
$\#\omega_{imag}$	–	–	1	–	–
λ_{em}^{max} [nm]	792	652	553	559	564
FWHM [cm^{-1}]	7427	5423	3019	3259	4350

For completeness, figure 3.5 shows the calculated spectrum that most closely matches the experimental spectrum. It was generated as a Boltzmann-weighted sum of the VH spectra. The spectra were weighted based on the ground-state energies of the conformers (Ortho: $3.3\,\mathrm{kJ/mol}$ – 15%, Planar: $0.0\,\mathrm{kJ/mol}$ – 58%, Tilted: $1.9\,\mathrm{kJ/mol}$ – 27%) at room temperature ($298.15\,\mathrm{K}$) and subsequently summed. This simulation clearly confirms that the experimental spectrum represents the combined emission behavior of all conformers simultaneously.

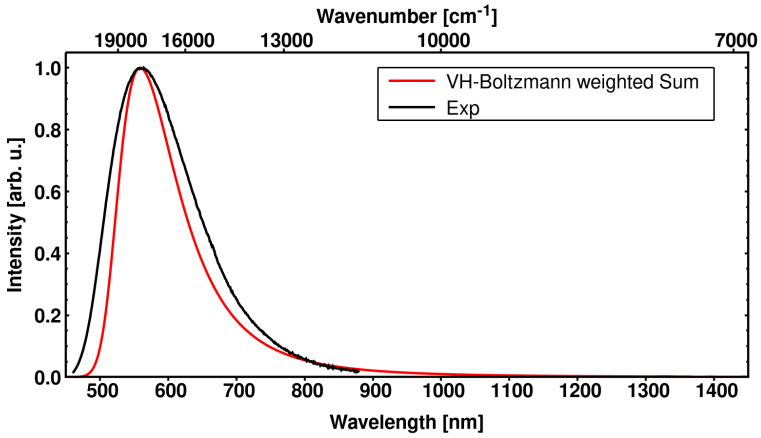

Figure 3.5: Experimental[68] and Boltzmann-weighted emission spectra of CZT1 using the VH methods. 16384 integration points, a time interval of $300\ \mathrm{fs}$, a damping factor of $100\ \mathrm{cm}^{-1}$ and a temperature of $300\ \mathrm{K}$ were used for the computations.

3.3 Parallelization

At the beginning of this work, the VIBES program only ran serially on a single **C**entral **P**rocessing **U**nit (CPU). For interesting systems with an increasing number of atoms, the CPU time required to calculate a meaningful spectrum or rate constant quickly exceeded 24 hours. For this reason, parallelizing the source code was of great interest.

In the first step, the goal was to identify which subroutines consumed the most CPU time, making them particularly suitable for parallelization. For this purpose, the profiler *gprof* [69] was used. To determine the most time-consuming routines in the program, various test calculations were performed. These include computations of vibronic spectra and nonradiative rate constants with or without temperature contributions, as well as different integration intervals and steps. In figure 3.6 (left), the percentage share of the five most computationally intensive routines in the total computation time is plotted for each test computation.

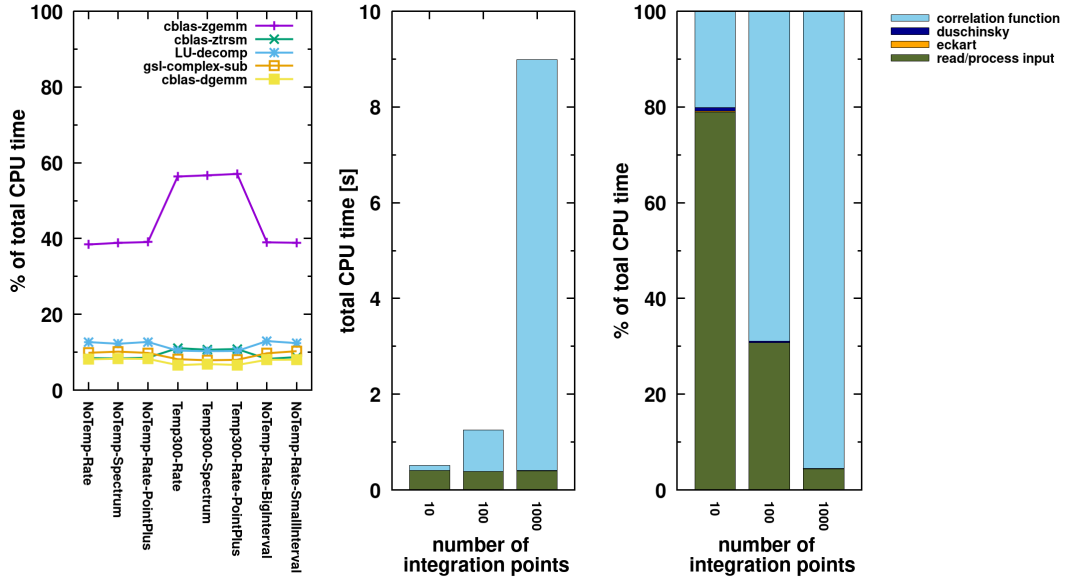

Figure 3.6: Different computations for profiling the serial VIBES source code and the identification of the computationally most expensive routines. Explanation of the different keywords: **NoTemp** = No temperature contributions, **Rate** / **Spectrum** = Computation of a rate constant or a spectrum, **PointPlus** = Computation with additional integration points, **BigInterval** / **SmallIntervall** = Computation with different integration intervals.

It is evident that, although there are significant differences between calculations with and without temperature effects, the conclusion remains the same. The routine with the largest percentage share (39-57%) of the total computation time is the *cblas-zgemm* routine, responsible for matrix-matrix multiplication of complex-valued matrices. Close behind, with a share between 7% and 13%, are the routines *cblas-ztrsm*, *LU-decomp*, *gsl-complex-sub*, and *cblas-ztrsv*, which handle scalar-matrix multiplication, vector-matrix multiplication, and **L**ower

Upper (LU) decomposition of matrices. These routines are primarily used for calculating the correlation function, and this step scales with the number of integration points for the numerical integration chosen by the user. To verify this scaling effect, test calculations with 10, 100, or 1,000 integration points were performed. With 1,000 integration points, 95% of the computation time falls on the routines that are responsible for calculating and integrating the correlation function. It is therefore logical to parallelize this routine. Figure 3.6 also shows that the portion of the serial program code responsible for reading and processing the input is independent of the number of integration points and takes up an insignificant percentage of the total computation time when calculating meaningful rate constants and spectra.

The parallelization was implemented using the **O**pen **M**ulti-**P**rocessing (OMP) framework to take advantage of shared-memory parallelism. The main parallelized section involves a *for* loop that scales with the number of integration points, as each point can be calculated independently. By employing a dynamic scheduling scheme for the *for* loop, the workload is distributed across threads based on system availability and thread readiness. This approach enhances efficiency by dynamically balancing the workload across multiple cores and minimizes thread idle times. With OMP, each thread can process a subset of these integration points in parallel, significantly reducing the total computational time.

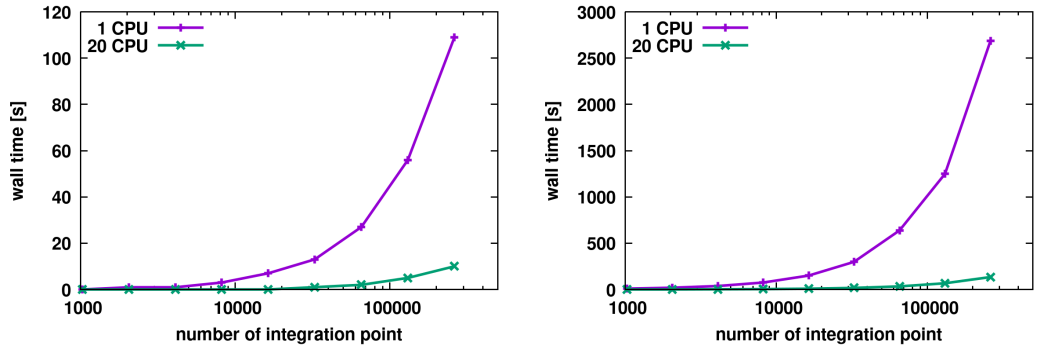

Figure 3.7: Computation of an ISC rate constant for IM (left) and the campher derivative EPIC (right) using the serial and parallel source code.

For testing, rate constants were calculated for IM (see figure 3.7 (left)) and the camphor derivative EPIC (see figure 3.7 (right)) using both the serial and parallelized (20-CPU) versions of the source code across varying numbers of integration points. The results show a substantial increase in elapsed real time (wall time) as the number of integration points rises. However, the parallel version enables calculations with significantly more integration points within an acceptable wall time. For example, by using approximately 260,000 integration points, the wall time for calculating a rate constant can be reduced from around 45 minutes to just 2 minutes with the parallelized code.

Additionally, the speed-up achieved remains largely unaffected by system size, indicating that the parallelized approach should offer similar substantial gains in computational efficiency even for much larger systems. This efficiency suggests

that our parallelized implementation scales well, making high-precision rate constant calculations feasible within practical time frames, even for complex systems with numerous atoms.

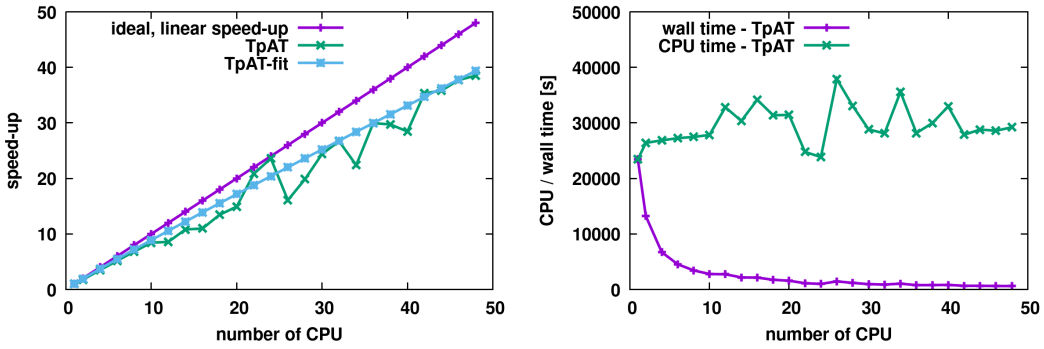

Figure 3.8: Visualization of the speed-up for parallel VIBES computations. The computations were performed for an exemplary TADF emitter TpAT[70]. Comparison to the ideal linear speed-up (left) and the wall- and CPU-time dependent on the number of CPUs used for the computation.

Figure 3.8 presents the results for a promising TADF emitter (TpAT[70]) across varying CPU counts. On the left, the theoretical linear speed-up, shown in purple, represents the maximum achievable improvement. As expected, VIBES does not experience superlinear speed-up effects (*e.g.*, from efficient cache use), but rather tends to encounter losses due to significantly increased overhead. In green, the actual speed-up achieved in spectral calculations is displayed, which falls short of the ideal linear trend. Since these calculations were not run on dedicated hardware, small variations in computational times are possible due to fluctuations in overhead capacity on individual nodes. To mitigate these discrepancies, each calculation was averaged over three runs, with a light blue linear trendline added to visualize this averaged data.

At this point, it is crucial to differentiate between wall time and CPU time. Figure 3.8 (right) illustrates both for TpAT as a function of the number of CPUs. While there is a dramatic reduction in wall time, the actual CPU time increases. Although parallelization may seem to deliver faster results for the user, in reality, the parallel computation involves significant additional overhead, making it more computationally expensive to run calculations across many CPUs simultaneously. For the current parallelized version of the VIBES program, this means that users should, whenever possible, opt for the lowest feasible CPU count to minimize computational costs, particularly if they can afford the additional time needed for a calculation. This approach ensures the most efficient use of resources without an unnecessary overhead cost.

4 Results

The primary objective of this work was the development and implementation of a new method for describing vibronic transitions. The results presented herein are derived from various collaborative projects and studies of different TADF emitters and organic fluorophores. Whenever conventional methods for calculating vibronic transitions failed to produce meaningful results, it provided an opportunity to investigate the underlying issues and apply the newly developed VH method to address these challenges. The application in actual projects allowed for a deeper understanding of the limitations of traditional methods and highlighted the advantages of vertical approaches. For the sake of clarity, the results will be divided into distinct project areas, each addressing specific aspects of the application of the VH method.

- Project Areas I and II (see sections 4.1 and 4.2) focus on the investigation of radiative and nonradiative processes in TADF emitters and the optimization of their photophysical properties. For the well-known emitter DMAC-TRZ, where traditional methods struggled to reliably describe its excited-state decay pathways, it was necessary to use the VH method and approaches that go beyond Condon approximation to explain the photophysical properties (see **Publication No.3**). Additionally, the VH method was used to provide critical corrections to a previously proposed decay mechanism of a TADF emitter called AN, improving the theoretical description of its behavior (see **Publication No.4**). In the framework of the RTG ModISC, we further investigated the influence of different conformers and chemical substitutions on ISC and rISC rates, offering new insights into the design and optimization of emitters comprising a donor–acceptor motif (see **Publication No.2** and **Manuscript No.1**).

- Project Area III (see section 4.3) extends the scope to highly efficient organic fluorescent emitters, specifically NMA derivatives. A quantum chemical investigation of these molecules focused on elucidating their fluorescence decay mechanisms, highlighting the effects of chemical substitutions, and inter- and intramolecular hydrogen bonding (see **Manuscript No.2**). As this project has not yet been published, initial results and insights, including those obtained using the newly implemented VH method, will be presented in this section.

Collectively, these results demonstrate the capability of the VH method to address significant challenges in studying vibronic transitions, advancing theoretical understanding and expanding the toolkit for exploring photophysical processes in complex molecular systems.

4.1 Project Area I - Radiative Processes

In Project Area I, we will explore radiative processes in TADF emitters featuring a donor–acceptor motif in greater detail. As discussed in section 2.1, these processes include both absorption and emission. For TADF emitters, the primary focus is on prompt and delayed fluorescence, as phosphorescence plays a less significant role. Furthermore, ESA measurements are utilized experimentally to identify electronic states involved in the decay mechanisms, offering valuable insights into the overall process.

4.1.1 Symmetry-forbidden Transitions and Dual Emission

First, we will examine a system where, in addition to the orientation of the donor and acceptor[71,72], conformational effects[73–75] (e.g. the coexistence of multiple different conformers) also play a role in influencing the photophysical properties of the system and can, for instance, promote dual fluorescence. For this purpose, we collaborated with the research group of Prof. Dr. Andrew Monkman from Durham, UK, to take a closer look at the well-known TADF emitter DMAC-TRZ[72,76], consisting of a 9,9-**Di**-**M**ethyl-9,10-Dihydro-**Ac**ridine (DMAC) and a 2,4,6-**Tri**phenyl-1,3,5-Tria**z**ine (TRZ) unit (see figure 4.1). These results formed a significant part of **Publication No.3** and the bachelor's thesis of Luka Duben[77], which I was mentoring as part of this project.

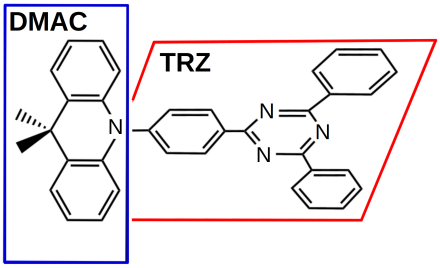

Figure 4.1: Lewis structure of DMAC-TRZ. The planes indicate the 9,9-**Di**-**M**ethyl-9,10-Dihydro-**Ac**ridine donor (blue) and 2,4,6-**Tri**phenyl-1,3,5-Tria**z**ine acceptor (red) moieties and show their perpendicular arrangement.

Initial experimental spectra (see figure 4.2) recorded in rigid matrix materials revealed spectral features that had not previously been addressed in the literature[72,78] and are absent in solution. For instance, the absorption spectrum exhibits a double band behaviour only in **M**ethyl-**C**yclo**h**exane (MCH) and the polymer matrix Zeonex® (see figure 4.2 A and C). Embedding DMAC-TRZ into Zeonex® also leads to an emission peak at a higher energy than previously reported in the literature (see figure 4.2 D). This led to the hypothesis that DMAC-TRZ, similar to well-documented phenothiazines[74,79], exhibits the effects of conformational heterogeneity mentioned earlier. A more detailed quantum chemical investigation (technical details can be found in section 7.1 of the appendix) of the system was conducted to elucidate the origin of these spectral features.

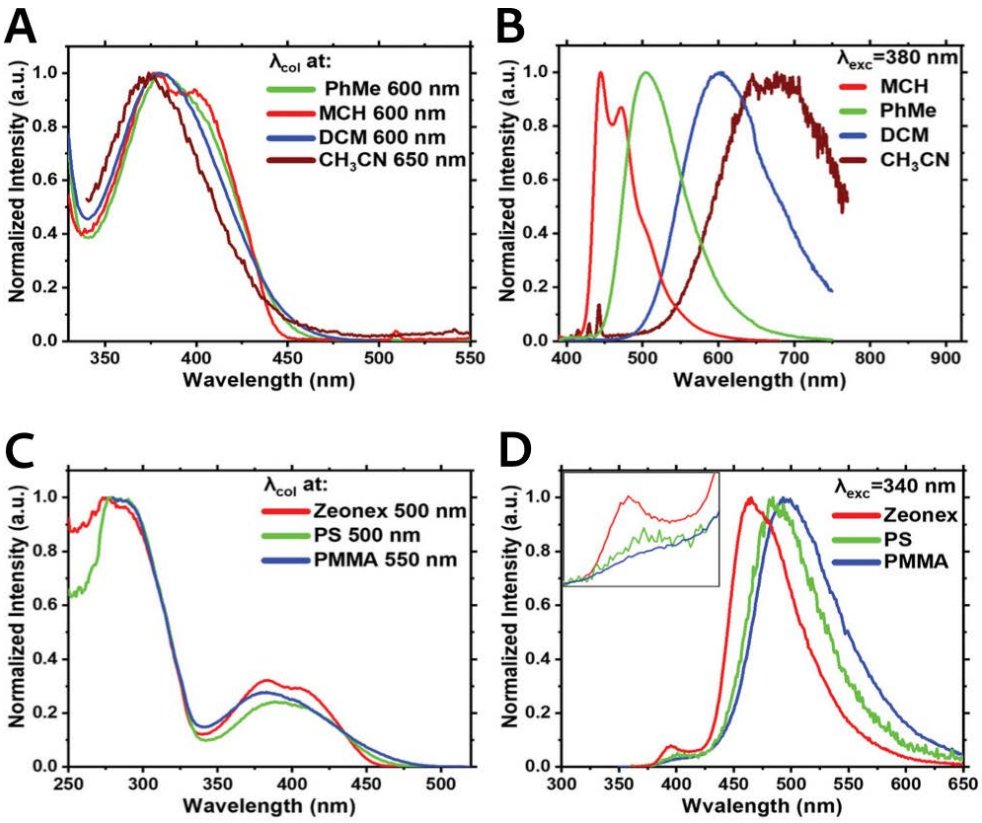

Figure 4.2: Excitation (**A**) and photoluminescence (**B**) spectra of DMAC-TRZ in different solvents at room temperature. Excitation (**C**) and photoluminescence (**D**) spectra of 1 wt.% DMAC-TRZ in diffferent polymer hosts at room temperature.

It was demonstrated that two different stable conformers exist for DMAC-TRZ. The **Q**uasi-**E**quatorial (QE) conformer, where the donor and acceptor are orthogonal to each other but remain individually planar, is well-documented in the literature and has been extensively studied experimentally.[72] The **Q**uasi-**A**xial (QA) conformer, where the DMAC adopts a bent structure and forms an angle of approximately 40 degrees with the TRZ plane, is new for this molecule, though similar QA conformers have been reported for structurally related phenothiazines.[74,79]

Further investigations were done in MCH environment. It was chosen to be a suitable solvent owing to the amount of experimental data available and its structural similarity to the matrix material Zeonex®. Ground state optimizations indicate that the QE conformer is energetically more favorable than the QA conformer (by 0.19 eV with zero-point vibrational energy correction). Consequently, the QE conformer is expected to be the predominant conformer in solution at room temperature.

We conducted an analysis of the state energies for the lowest excited states of both conformers, revealing significant differences between them. The vertical excitation energies of the QE conformer, calculated from the electronic ground state, indicate that the lowest excited singlet state ($E_V(^1\pi\pi^*(CT)) = 3.06\,\mathrm{eV}$)

exhibits a **C**harge **T**ransfer (CT) character, where electron density is transferred from the DMAC donor to the TRZ acceptor. At the ground state geometry, both a **L**ocal **E**xcitation (LE) triplet state ($E_V(^3\pi\pi^*(LE)) = 3.05\,\mathrm{eV}$) and a CT triplet state ($E_V(^3\pi\pi^*(CT)) = 2.97\,\mathrm{eV}$) are energetically lower. Owing to the energetically close CT states ($\Delta E_{ST}^{vert} = 0.09\,\mathrm{eV}$) and the rISC-mediating LE triplet state, the QE conformer meets the fundamental criteria of a classical TADF emitter.

A detailed analysis of the QA conformer reveals a different picture. Vertically, the lowest excited singlet state lies significantly higher in energy and can no longer be classified solely as a CT state. Instead, it represents a hybrid state combining CT and LE excitation, with substantial involvement of the bridging phenyl ring. Energetically beneath this singlet state are three triplet states: the lowest triplet state shares a similar hybrid character but is vertically more than 0.6 eV lower in energy, while the other two triplet states exhibit a mix of CT and LE characteristics, with strong contributions from the bridging phenyl ring and LE character localized on the acceptor unit. The significant energy gap between the lowest excited singlet and triplet states in this system clearly indicates that no classical TADF mechanism can be expected for this conformer.

Optimizing the relevant excited states mentioned above yields the adiabatic state diagram (see figure 4.3). We can see that CT states are stabilized more than the LE states. Nevertheless the lowest excited LE triplet state remains in energetic proximity to the lowest excited singlet state ($\Delta E_{ST}^{adia}(^1\pi\pi^*(CT) \leftrightarrow {}^3n\pi^*(LE)) = 0.08\,\mathrm{eV}$) for the QE conformer. For the QA conformer, the adiabatic energy difference between the lowest excited singlet and triplet states is slightly lower compared to the vertical energy gap ($\Delta E_{ST}^{adia}(^1\pi\pi^*(CT/LE) \leftrightarrow {}^3n\pi^*(CT/LE)) = 0.43\,\mathrm{eV}$), while the order of the electronic state is identical.

Consequently, the conclusions drawn from the vertical excitation energies discussed above remain unchanged. Our computations predict that a significant concentration of the QA conformer would negatively impact the TADF properties of DMAC-TRZ, making its presence undesirable.

From the vertical excitation energies and their associated oscillator strengths, the absorption properties of both conformers can be calculated. The calculations show that the experimental wavelength range covers the excitation from the electronic ground state to the first excited singlet state only. Figure 4.4 presents both the experimentally measured and the calculated absorption spectra for this range and for both conformers.

As stated above, the $S_1 \leftarrow S_0$ transition of the QA conformer exhibits a mix of CT and LE excitation, with a vertical excitation energy of 3.35 eV (371 nm), which aligns well with the experimental results. Similarly, the lowest energy $S_1 \leftarrow S_0$ CT transition of the C_{2v} symmetric QE conformer has a vertical excitation energy of 3.06 eV (405 nm), corresponding to a second band observed in the experiment. However, this A_2-symmetric transition is electric dipole forbidden in the FC approximation, resulting in an absorption spectrum with negligible intensity.

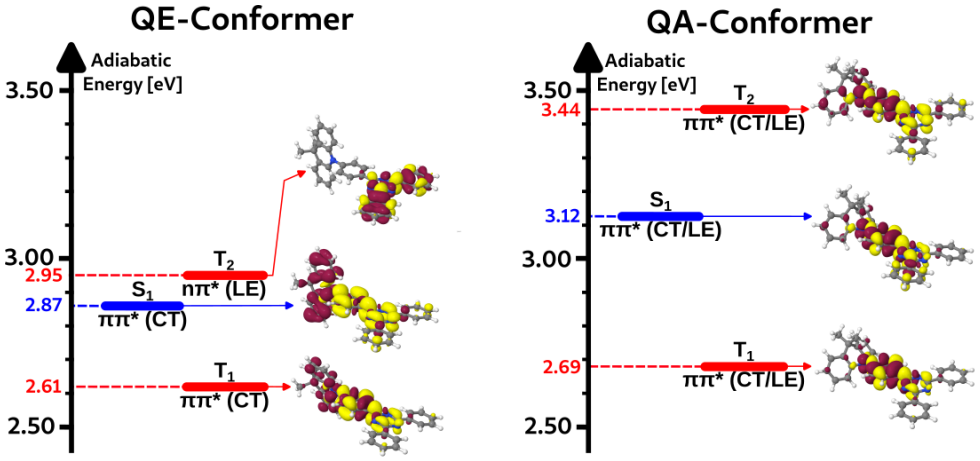

Figure 4.3: Adiabatic state diagram for the QE (left) and QA (right) conformer of DMAC-TRZ including the corresponding difference densities (red - decrease of electronic density; yellow - increase of electronic density) of the relevant singlet (blue) and triplet (red) states.

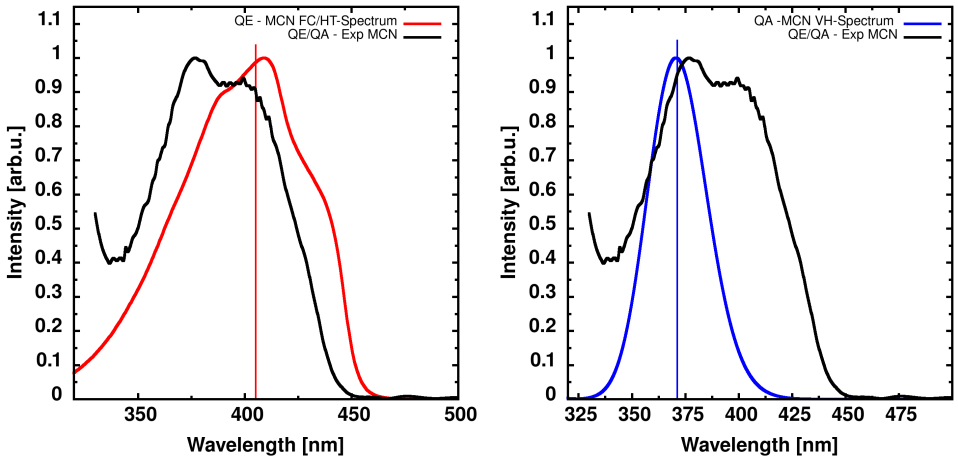

Figure 4.4: Experimental and computational absorption spectra for the QE (left) and QA conformer (right) of DMAC-TRZ. The electric dipole forbidden transition of the QE conformer was simulated using the FC/HT formalisms. All spectra are normalized with respect to the experimental emission maximum and were supplemented with the vertical excitation energies computed at **D**ensity **F**unctional **T**heory and **M**ulti**r**eference **C**onfiguration **I**nteraction (DFT/MRCI) level of theory.

In this case, it was necessary to go beyond the Condon approximation. The geometry of the electronic ground state was displaced along all normal modes, and the transition dipole moment was recalculated. These displacements generally had a significant effect on the transition dipole moment only for specific normal modes (see figure 4.5). Large gradients were calculated, for instance, for mode 1 (rotational vibration with $\omega_1 = 8.17\,\mathrm{cm}^{-1}$) and mode 7 (rotational vibration of the bridging phenyl ring of TRZ with $\omega_7 = 52.33\,\mathrm{cm}^{-1}$). These are modes that strongly break the C_{2v} symmetry.

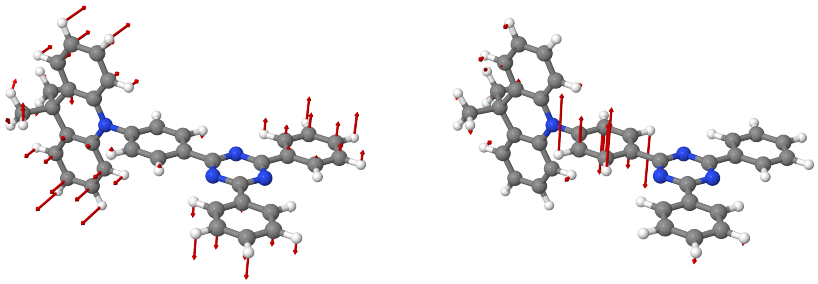

Figure 4.5: Graphical representation of the normal modes that strongly break the C_{2v} symmetry of DMAC-TRZ. Mode 1 (rotational vibration with $\omega_1 = 8.17\,\mathrm{cm}^{-1}$, left) and mode 7 (rotational vibration of the bridging phenyl ring of TRZ with $\omega_7 = 52.33\,\mathrm{cm}^{-1}$, right) with scaled red arrows to highlight the atomic movements.

As stated earlier, the energetic difference between the optimized electronic ground states of both conformers will result in a vastly different ratio of their concentrations in solution. Despite this disparity, we expect that in the experiment, both conformers will absorb nearly equally. Due to the low concentration of the optically very bright QA conformer and the predominant QE conformer with an electric dipole forbidden transition, we expect the absorption bands to overlap. Effects of a rigid matrix material however could influence the ratio between the conformers and make these peaks being distinguishable.

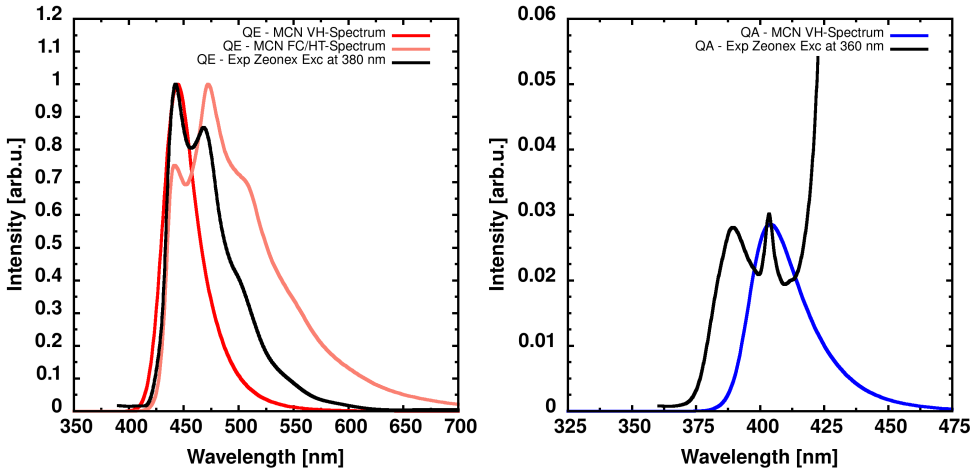

Figure 4.6: Experimental and computational emission spectra for the QE (left) and QA conformer (right) of DMAC-TRZ. The electric dipole forbidden transition of the QE conformer required going beyond Condon approximation. The computational results using the vertical approach are supplemented with FC/HT computations. All spectra are normalized with respect to the experimental emission maximum.

Figure 4.6 shows both the experimental and calculated emission spectra for fluorescence from the lowest excited singlet state of both conformers. The

calculations were performed using the VH method. It can be observed that the position and onset of the spectra align well with the experiment, although information about the vibrational progression is generally lacking.

Similarly to the absorption process, for the QE conformer, gradients along all normal modes were additionally calculated to generate a spectrum beyond the Condon approximation. The spectrum calculated using this method displays a vibrational structure comparable to the experiment, although the intensity distribution of the vibronic transitions differs slightly. In all cases, however, the emission peaks in the experimental spectra can be unambiguously assigned to the calculated spectra of the different conformers. Thus, the dual fluorescence is identified as an effect arising from conformational heterogeneity.

Ultimately, the question arose as to why DMAC-TRZ still exhibits such efficient TADF properties and whether the coexistence of two conformers can be exploited. To address this, investigations were carried out to determine whether the conformers can interconvert. This is most easily assessed using a linearly interpolated path (see figure 4.7). This method involves interpolating geometries between the two conformers at specific intervals. The dihedral angle between the donor and acceptor was chosen as the pathway coordinate for this purpose.

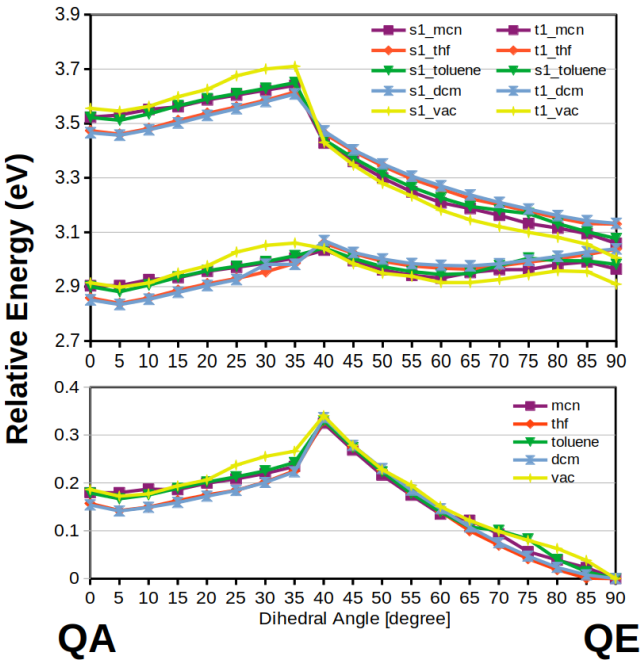

Figure 4.7: Linearly interpolation pathway between the QE and QA conformer of DMAC-TRZ. The coordinate for the interpolation is the dihedral angle between the DMAC donor and TRZ acceptor with an increment of 5 degrees.

The interpolated path for DMAC-TRZ was calculated in various **P**olarizable **C**ontinuum **M**odel (PCM) solvent environments using an increment of 5 degrees. As previously described, it can be observed that the QE conformer is energetically more favorable in the electronic ground state. Through rotation along the

donor–acceptor axis, the QE conformer can be converted into the QA conformer, requiring an energy barrier of slightly more than 0.3 eV to be overcome. A similar profile is observed for the calculated potentials of the singlet manifold, although the barrier between the conformers in the excited singlet state is nearly twice as high, reaching up to 0.6 eV. However, the energetic barrier is significantly smaller in the excited triplet manifold, where the triplet state of the QA conformer is even energetically lowest. Nevertheless, from these results we conclude that at ambient conditions interconversion is unlikely.

Our quantum chemical investigation demonstrated that the photophysical properties of DMAC-TRZ are significantly influenced by two distinct conformers. However, due to non-negligible energy barriers, these conformers cannot easily interconvert. This fact proves advantageous, as a notable concentration of the QA conformer, which exhibits poor TADF properties, should be avoided. From the theoretical results we conclude that significant spectral contributions of the QA conformer can only be seen because the unfavorable conformation is fixed in a rigid matrix environment. Furthermore, we concluded that since interconversion is unlikely some form of EET mechanism must exist between the QA and QE conformer in order to effectively make use of the excitons on the QA conformer. This energy transfer can only be suppressed at low concentrations, which makes specific spectral features observable.

For more detailed measurements of DMAC-TRZ in different solvent and matrix environments, additional measurements with respect to the EET process as well as the incorporation of the emitter into an OLED device, readers are referred to the original publication (see **Publication No.3**).

4.1.2 Excited-State Absorption

For another potential TADF emitter, featuring a spiro-bridged anthracenone (**A**) donor and naphthalene (**N**) acceptor (spiro[9,10-dihydro-9-oxoanthracene-10,2'-5'6'-benzindan] (AN)), Dobkowski *et al.*[80] proposed the following decay mechanism in butyronitrile. Upon excitation of the system, the lowest-lying $^1n\pi^*(\mathbf{A})$ singlet state localized on the anthracenone is rapidly populated. It was suggested that the excitation energy is subsequently transferred from this state via the $^3n\pi^*(\mathbf{A})$ state to the lowest excited triplet state, the $^3\pi\pi^*(\mathbf{N})$. The full proposed mechanism can be summarized as follows:

$$[^1\pi\pi^*(\mathbf{N}) + {}^1\pi\pi^*(\mathbf{A})] \rightsquigarrow {}^1n\pi^*(\mathbf{A}) \rightsquigarrow {}^3n\pi^*(\mathbf{A}) \rightsquigarrow {}^3\pi\pi^*(\mathbf{N})$$

The ISC from the $^1n\pi^*$ to the $^3n\pi^*$ state was reported with a rate constant of $3\times10^{10}\,\mathrm{s}^{-1}$. However, this appears rather unrealistic, as this transition is El-Sayed forbidden (see section 2.2.2.3), and significantly lower rate constants would be expected. These discrepancies were addressed in our separate study (see **Publication No.4**).

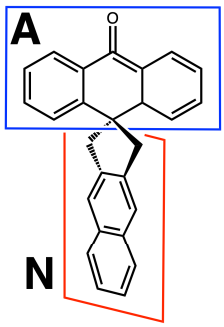

Figure 4.8: Lewis structure of AN. The planes indicate the donor (blue) and acceptor (red) moieties and show their perpendicular arrangement.

Our detailed quantum chemical investigation[81] of this decay mechanism reveals that it must proceed differently (technical details can be found in section 7.1 in the appendix). We identified a $\pi\pi^*$ triplet state on the anthracenone ($^3\pi\pi^*(\mathbf{A})$), of which the exact position could not be experimentally determined but was suspected to be near the lowest excited singlet state on the anthracenone ($^1n\pi^*(\mathbf{A})$). According to our calculations, this state represents the energetically lowest triplet state in butyronitrile and is expected to be populated via efficient ISC from the $^1n\pi^*(\mathbf{A})$ state on the anthracenone.

We confirmed the involvement of this state through the VH method and by calculating the ESA originating from the $^3\pi\pi^*(\mathbf{A})$ state. The procedure is explained in detail below: Figure 4.9 displays the vertical transition (red vertical line) from the energetically lowest triplet state, T_1, to the T_{20} state. This is the only state with a significant oscillator strength in the energy regime of the experimentally measured ESA. Consequently, this vibronic transition was selected for a vibrationally resolved calculation using the VIBES program. The result is represented by the blue curve. The calculated ESA spectrum matches the experimentally

observed spectrum exceptionally well. The vibrational progression can be unambiguously assigned to this vibronic transition. Compared to the experiment, the onset of the spectrum is only slightly red-shifted. Additionally, the fact that the calculated spectrum shows significant intensities at high wavenumbers can be attributed to the usage of the harmonic approximation. The 'true' PES must diverge strongly from the used harmonic potential leading to unreliably high intensities for higher wavenumbers.

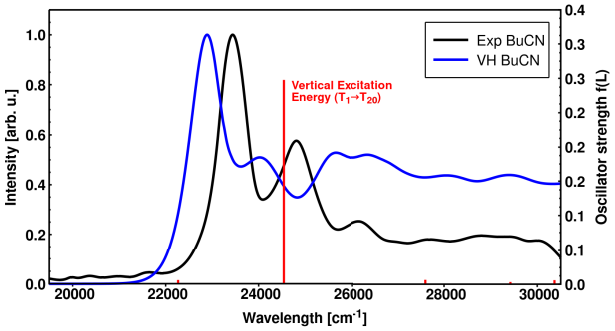

Figure 4.9: Experimental[80] and computed short-time excited state absorption spectrum using the VH method as well as the vertical excitation wavelength and oscillator strength computed at DFT/MRCI level of theory.

A major technical advantage of the VH method is that the final state (T_{20}) used to calculate the ESA from the lowest excited triplet state did not require optimization which is often not a feasible procedure due to the presence of numerous conical intersections and the high density of higher-lying electronic states. The oscillator strength computed at DFT/MRCI level of theory was sufficient to identify a bright transition in this wavelength regime. The gradients and Hessian matrix could be calculated without the need for an expensive optimization of the T_{20} state. Consequently, the vertical transition from the DFT/MRCI calculation could be straightforwardly supplemented with the information about vibrational resolution.

This simulation provided an unambiguous assignment of this transition to the experimentally measured spectrum, thereby confirming that the $^3\pi\pi^*(\mathbf{A})$ state must be populated after electronic excitation and has to be included in the decay pathway scheme shown above. But of course, the ESA spectrum represents only a small component for the elucidation of the overall decay pathway mechanism. For a comprehensive investigation of the properties of the excited states and the rate constants of the processes between them, the reader is referred to our original study.[81] (see **Publication No.4**)

4.2 Project Area II - Nonradiative Processes

A central topic of several studies[82,83] is the emitter series consisting of a **T**ri**a**ryl**a**mine (TAA) donor and a **T**ere**p**hthalo**n**itrile (TPN) acceptor. Various sterically demanding substituents are attached to the bridging phenyl group. The goal of these studies was to understand and quantify the influence of these substituents on the photophysical properties and to check if systematic chemical substitution can be used to tune and promote TADF properties. Our theoretical investigation (see **Publication No.2**) focuses particularly on the oscillator strengths, the emission wavelengths, the SOC, and the rate constants of nonradiative processes of the emitter molecules in this series.

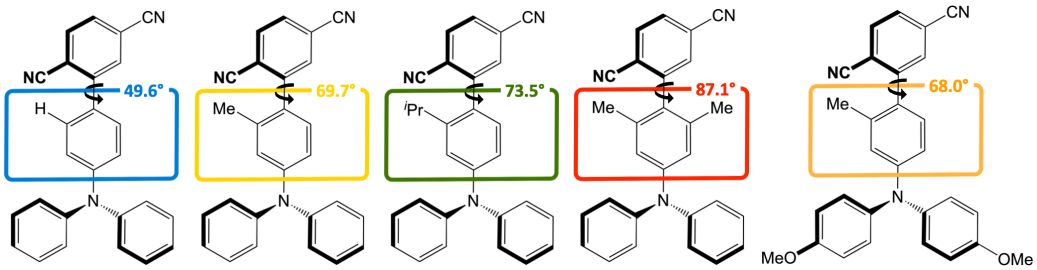

Figure 4.10: Lewis structures of the investigated emitter series consisting of a TAA donor and a TPN acceptor exhibiting different sterically demanding substituents and consequently different dihedral angles between the two moieties. From left to right: **Comp 1-H**, **Comp 2-Me**, **Comp 3-iPr**, **Comp 4-diMe**, **Comp 5-Me+diOMe**.

Figure 4.10 shows the structural formulas of the investigated emitters. They were synthesized by Laura Kloeters from the group of Prof. Dr. Thomas J. J. Müller (Organic Chemistry, Heinrich Heine University) and were thouroughly investigated by Dragana Sretenović and her co-workers from the group of Prof. Dr. Claus A. M. Seidel (Molecular Physical Chemistry, Heinrich Heine University). In this series, the molecules exhibit varying dihedral angles between the donor and acceptor, depending on the substituent on the bridging phenyl ring. The molecules are named according to their position in the emitter series and their substituents as follows: **Comp 1-H**, **Comp 2-Me**, **Comp 3-iPr**, **Comp 4-diMe**, **Comp 5-Me+diOMe**. As the steric demand of the substituents increases from **Comp 1-H** to **Comp 4-diMe**, it leads to a more orthogonal alignment of the donor and acceptor regions. **Comp 5-Me+diOMe** is structurally similar to **Comp 2-Me** and thus exhibits a comparable dihedral angle. However, the introduction of methoxy groups on the TAA donor increases its donor strength and thus changes it photophysical properties.

In the following discussion, we will primarily focus on **Comp 2-Me**, as TADF was unequivocally demonstrated for this molecule. **Comp 5-Me+diOMe** is included for comparison due to its structural similarity, and trends will be identified for the remaining molecules in the series.

The absorption behavior of the emitters in this series is comparable (see figure 4.11 top panel). The first bright transition ($S_1 \leftarrow S_0$) can be attributed to a CT

transition. However, this transition becomes symmetry-forbidden as the donor and acceptor adopt a more orthogonal orientation due to the decreasing overlap of the involved orbitals, resulting in a significant decrease in oscillator strength across the series.

The changes in intensity of the higher-energy absorption bands are more complex and can be explained by a shift in their character, representing a mix of CT and LE transitions (see **Publication No.2**). To rule out the possibility that these changes are purely electronic effects rather than conformational ones, we examined the absorption spectrum of **Comp 2-Me** at various dihedral angles between the donor and acceptor. Figure 4.11 (bottom panel) clearly illustrates how the oscillator strengths of individual low-energy excitations change depending on the dihedral angle. Regardless of the substituent, the absorption spectra of the corresponding compounds can be derived from this figure.

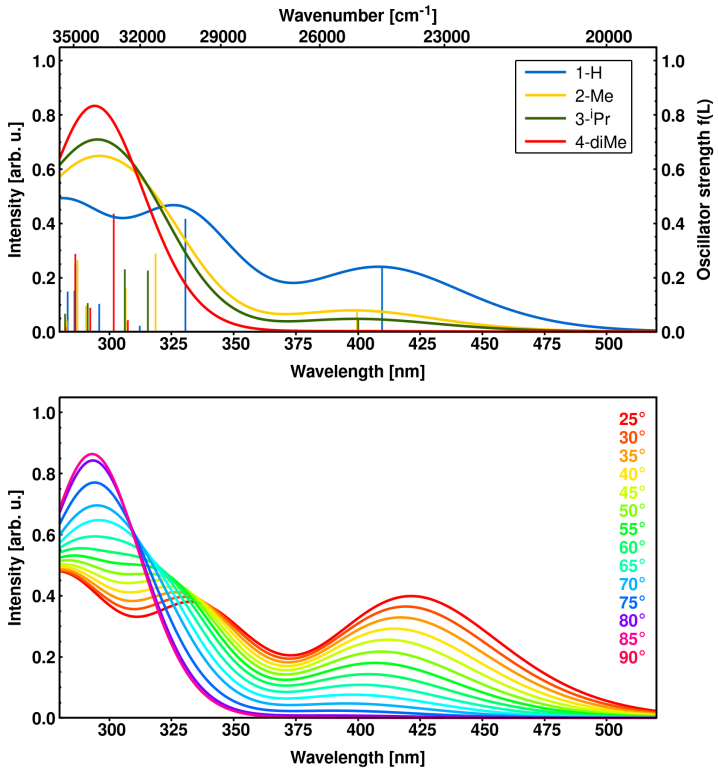

Figure 4.11: Absorption spectra of all compounds investigated in the emitter series at the optimized ground state geometry (top) and corresponding absorption spectra of **Comp 2-Me** for different dihedral angles between donor and acceptor with an increment of 5 degrees (bottom).

In the course of this investigation, we also examined numerous other properties that can help to understand the decay process. In figure 4.12, alongside the oscillator strength, we also observe the evolution of the characters of the electronic excitation for the lowest excited singlet and triplet states, as well as the adiabatic energy difference between these states. It is clearly evident that the electronic states always exhibit a mixed character, with the CT contribution increasing for an orthogonal alignment of donor and acceptor. The dip in the

CT contribution near orthogonality for the lowest triplet state can be explained by a crossing state with LE character, which must energetically lie below the CT states at 90 degrees. Different studies have already shown that such a crossing of a nearby LE state with the lowest CT states can promote efficient rISC.[70,84,85] We observe that the calculated adiabatic energy difference around 90 degrees reaches values low enough to fulfill the fundamental requirement for efficient rISC, and thus for delayed fluorescence.

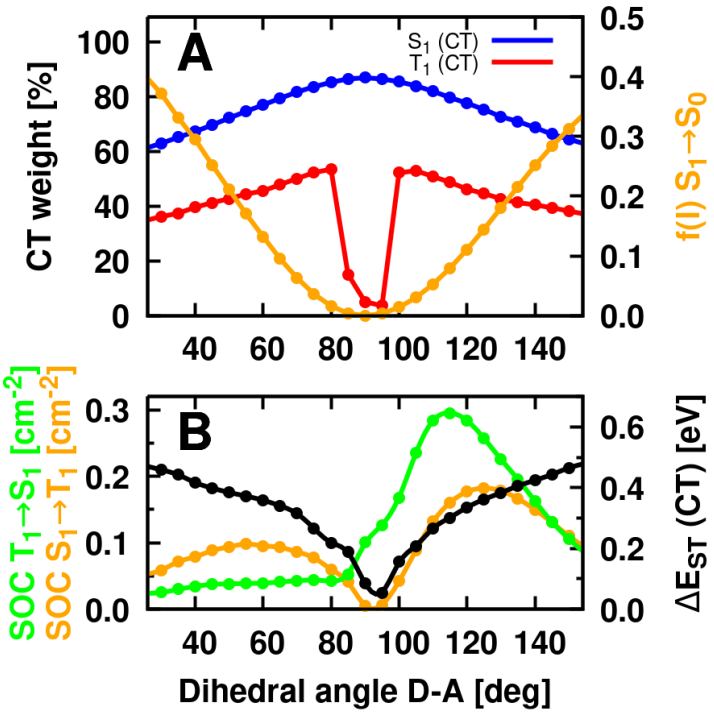

Figure 4.12: Properties of DFT/MRCI wave functions of **Comp 2-Me** resulting from single-point calculations along relaxed TDDFT paths of the S_1 and T_1 states. **A**: CT character of the first excited singlet (blue) and triplet (red) state. Oscillator strength for the $S_1 \rightarrow S_0$ transition (orange) of **Comp 2-Me**. **B**: ΔE_{ST} (black) and sum of squared SOCMEs between S_1 and T_1 states (ISC = orange, rISC = green) of **Comp 2-Me**.

In addition to the adiabatic energy difference, an examination of the evolution of the SOCME($S_1 \rightarrow T_1$) for ISC and SOCME($T_1 \rightarrow S_1$) for rISC reveals that the rate constants of nonradiative processes must also strongly depend on the dihedral angle. It is plausible that low-frequency normal modes, such as dihedral vibrations, could induce such twists between the donor and acceptor moieties. Consequently, they may have a similar impact on other photophysical properties as they do on absorption behavior.

In both **Publication No.1** and **Publication No.2**, we investigated the deactivation processes of this emitter series and calculated nonradiative rate constants for this purpose. The rate constants are particularly intriguing for this emitter series because, although TADF has been experimentally confirmed, the theoretically calculated adiabatic state energies of the involved singlet and triplet

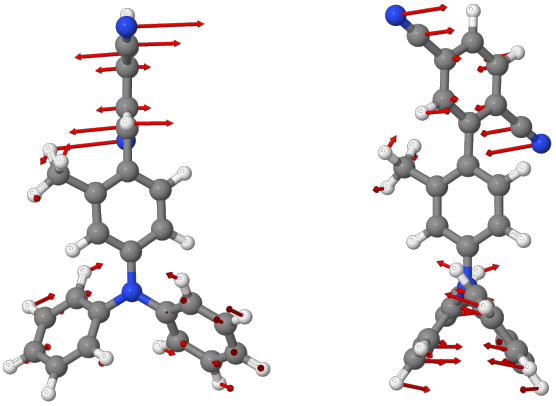

Figure 4.13: Low-frequency normal mode vibration (rotational vibration with $\omega_1 = 21.03\,\mathrm{cm}^{-1}$) of **Comp 2-Me** from two different perspectives with scaled arrows to highlight the atomic movements.

states using TDDFT show differences that are too large. Specifically, an energy difference exceeding 0.4 eV typically implies negligible rate constants for rISC and, consequently, no delayed fluorescence. Just as absorption is highly sensitive to the orientation between donor and acceptor, as shown in figure 4.12, the energy difference is equally affected. A detailed discussion of the causes behind the excessively large theoretical energy difference is provided in **Publication No.2**. However, we wanted to make meaningful estimates of the rate constants across the emitter series with the available results. For this reason, we employed the VH method to calculate rate constants along an interpolated path, which is a procedure that is impossible using adiabatic models.

To estimate the rate constants for **Comp 2-Me**, we used geometries derived from the interpolated pathways of the excited states presented above. From these geometries, the gradients and Hessian matrices for the final state of the vibronic transition were calculated, allowing the corresponding PES of the final state to be extrapolated. Without additional geometry optimizations, we determined the ISC and rISC rate constants for donor–acceptor dihedral angles between 25 and 90 degrees. For the sake of completeness, the fluorescence rate constant was also included in the analysis. Figure 4.14 provides an overview of all rate constants as a function of the dihedral angle between the donor and acceptor units.

Notably, the fluorescence rate constant remains high, reaching up to $1.13 \times 10^8\,\mathrm{s}^{-1}$ and staying nearly constant over a wide range of dihedral angles, with a sharp drop to $3.02 \times 10^4\,\mathrm{s}^{-1}$ at exactly 90 degrees. A similar trend can be observed for ISC, which is efficient with rate constants in the range of $10^6 - 10^7\,\mathrm{s}^{-1}$. However, the greatest impact of varying the dihedral angle is observed for rISC, which increases from $1.00 \times 10^0\,\mathrm{s}^{-1}$ at 45 degrees to a maximum of $2.17 \times 10^6\,\mathrm{s}^{-1}$ at 85 degrees. Near orthogonality, these results indicate that both processes can effectively compete. Conversely, this also implies that efficient rISC can only be expected for dihedral angles close to 90 degrees.

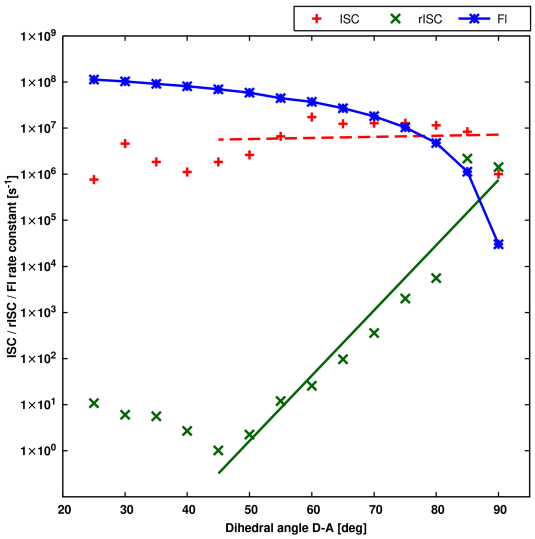

Figure 4.14: Graphical representation of the computed ISC (red), rISC (green) and fluorescence (blue) rate constants as a function of the dihedral angle between donor and acceptor of **Comp 2-Me** including trend lines from 45 (T_1 dihedral angle is 42 degrees) to 90 degrees.

We did a similar analysis for **Comp 5-Me+diOMe** of which the results are shown in figure 4.15. There we present the rate constants, divided into their electronic and vibrational components. It is evident that the transitions are slower (due to very small SOC) when donor and acceptor exhibit a dihedral angle of exactly 90 degrees to each other. However, significantly higher SOC can be achieved for twisted geometries. In contrast, the vibrational overlap behaves oppositely, with the highest values for geometries where the donor and acceptor are nearly orthogonal.

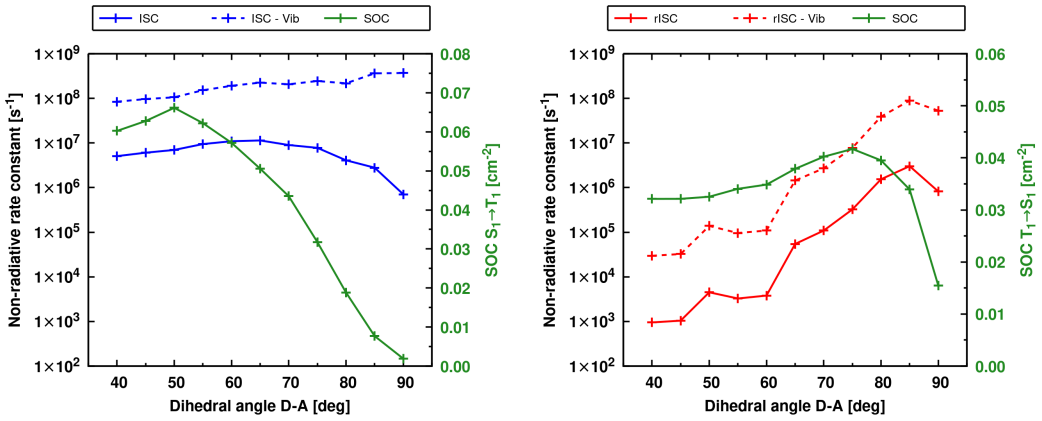

Figure 4.15: Graphical representation of the vibrational overlap (assuming a SOCME of $1\ \mathrm{cm}^{-1}$), the computed sum over the squared SOC matrix elements and the ISC and rISC rate constant as a function of the dihedral angle between donor and acceptor of **Comp 5-Me+diOMe**.

Similarly to the interpretation of the data for **Comp 2-Me**, the resulting overall rate constant for ISC remains nearly constant across all dihedral angles inves-

tigated. The impact on the rISC rate constant, however, is dramatic. Between dihedral angles of 40 degrees and 85 degrees, the rISC rate constant increases by more than three orders of magnitude and only at a dihedral angle of approximately 85 degrees does rISC become competitive with ISC. This leads us to the conclusion that from a theoretical perspective, the likelihood of observing TADF increases as the dihedral angle between donor and acceptor approaches 90 degrees. However, at precisely 90 degrees, the symmetry-forbidden nature of the transition is expected to prevent efficient rISC.

4.3 Project Area III - Hydrogen Bonding in Acridones

Hydrogen bonds are a crucial component in chemical and biological systems. In proteins, for instance, hydrogen bonds act as the driving force that determines how molecules bind to binding pockets, thereby defining chemical reactions at the reactive centers of proteins and enzymes.

However, hydrogen bonds also play a significant role in much smaller systems. Fluorescent acridone derivatives, for example, are widely used in pharmaceuticals as fluorescent markers[86,87] or as triplet sensitizers.[88] The order of electronic states in acridones is highly dependent on the choice of solvent, or more precisely, on the interactions between the acridone and its environment.[89,90] By tuning the polarity and proticity of the solvent, acridone can be turned into either a dark triplet sensitizer or a bright fluorescent sensitizer. Besides that, an experimental study[91] has already demonstrated that hydrogen bonds can significantly influence the energy of electronically excited states, thereby affecting chemical reactions. The aim of a study, which has not yet been published (see **Manuscript No.2**), was to investigate whether the targeted formation of hydrogen bonds could further enhance the fluorescent properties of acridone and its derivatives.

The investigation of hydrogen bonds poses a unique challenge in theoretical chemistry, which will be adressed in greater detail in the following sections.

4.3.1 Theoretical Assessment of Hydrogen Bond Strengths Including the Basis Set Superposition Error

Theoretical studies can provide insights into how strong the interaction energy between two interacting molecules can be. The term 'interaction energy' refers to the energy gain released upon coordination or the formation of a hydrogen bond, which must be overcome to spatially separate these molecules again.

The interaction energies of various partners have already been tabulated in other studies.[92–94] These studies show that interaction energies strongly depend on the choice of hydrogen bond donor and acceptor. However, some general trends can be identified. For example, the interaction energy is maximized at a donor–acceptor distance of about 3 Å.[95] Besides the distance, the donor–acceptor orientation significantly impacts the bond strength. In a study by Hao *et al.*[95], three different orientational changes were tested while maintaining a constant distance. All tests showed: The interaction energy is highest when the donor and acceptor are linearly aligned, with minimal dihedral angles.

The decisive factor, however, appears to be the specific combination of hydrogen bond donor and acceptor. For the molecules investigated in this project area, no specific hydrogen bond strengths have been reported. However, a study by Wenrui *et al.*[93] suggests that interactions between ureas and carbonyl compounds, with binding energies of up to 57 kJ/mol in structurally similar systems, constitute strong hydrogen bonds.

For quantum chemical calculations of binding strengths between the components of a specific system and their comparison with experimental data, a rough estimation is insufficient. Interaction energies can generally be determined using DFT single-point calculations. However, the computation becomes non-trivial due to the overlap of the basis sets used to approximate the electronic wave functions of the interacting systems as they come closer together.

Basis Set Superposition Error and Counterpoise Procedure

When two atoms or molecules, **A** and **B**, approach each other, they can interact through various forces such as dispersion interactions, electrostatic interactions or the formation of chemical bonds such as covalent bonds or like in the present case hydrogen bonds. These interactions can be either attractive or repulsive. The interaction energy E_{int} is typically determined by calculating the difference between the energy of the complex, **AB**, and the energies of the individual components, **A** and **B**:

$$E_{int} = E(\mathbf{AB})^{\mathbf{AB}} - E(\mathbf{A})^{\mathbf{A}} - E(\mathbf{B})^{\mathbf{B}} \tag{4.1}$$

where $E(\mathbf{AB})^{\mathbf{AB}}$ is the energy of the complex within the basis of the complex itself and $E(\mathbf{A})^{\mathbf{A}}$ as well as $E(\mathbf{B})^{\mathbf{B}}$ are the energies of the corresponding components within their own basis. However, upon using equation 4.1 the interaction energies are often significantly overestimated. Benchmark results for a $(He)_2$ dimer[96] as well as for $(HF)_2$ and $(H_2O)_2$ dimers[97] show that the geometric parameters, dipole moments and interaction energies are strongly dependent on (I) the size of the utilized basis set, (II) the type of orbitals within the system and (III) the level of theory that is employed.

The origin for the poor results is the so-called **B**asis **S**et **S**uperposition **E**rror (BSSE). This error occurs because the wave function of each component in the basis of the complex has more basis functions available than in the basis of the individual component alone, leading to more accurate calculations of important properties, such as the total energy of a system. As a result, the energies in a mixed basis are compared with the energies of the components in their unmixed basis. This mismatch can be quantified as BSSE.

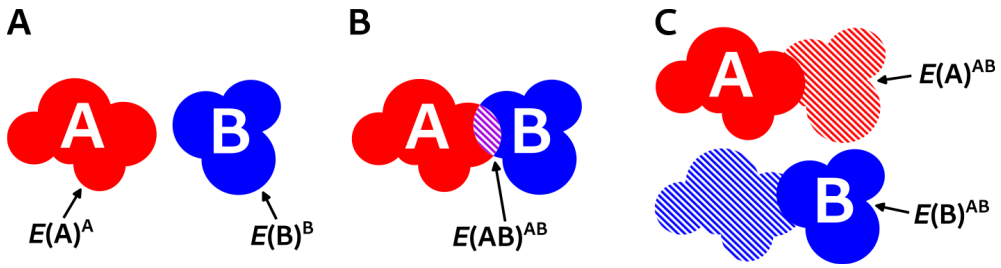

Figure 4.16: Schematic representation of (**A**) two monomers with their own basis and well separated to each other or (**B**) two monomers with their own basis appraoching and interacting with each other. (**C**) Two monomers with a basis including the ghost basis of the other monomer for the CP correction procedure.

One approach to minimize the error is to use an extremely large basis set. However, this is not feasible for large molecules and is therefore not considered a practical method for correcting the BSSE. A reasonable approach prevents the BSSE *a priori* by replacing the classical Hamiltonian operator with one where all terms that allow mixing of different basis functions are removed, as originally described by Mayer and Vibók.[98,99] This method excludes the occurrence of the BSSE from the outset. The second approach is the so-called **C**ounter**p**oise (CP) method, which is applied *a posteriori*. It aims to estimate the BSSE for a defined basis set and correct the interaction energy of the two components. In the simplest case, the energies of both the components and the complex are calculated using the same basis set, specifically that of the complex.

$$E_{BSSE}(\mathbf{A}) = E(\mathbf{A})^{\mathbf{AB}} - E(\mathbf{A})^{\mathbf{A}} \tag{4.2}$$

$$E_{BSSE}(\mathbf{B}) = E(\mathbf{B})^{\mathbf{AB}} - E(\mathbf{B})^{\mathbf{B}} \tag{4.3}$$

Determining the BSSE within the CP correction procedure by Boys and Bernardi[100] by combining the correction terms in equation 4.2 and 4.3 with the uncorrected expression of the interaction energy in equation 4.1 yields:

$$E_{int}^{CP}(\mathbf{AB}) = E(\mathbf{AB})^{\mathbf{AB}} - E(\mathbf{A})^{\mathbf{AB}} - E(\mathbf{B})^{\mathbf{AB}} \tag{4.4}$$

Special caution is necessary when the geometry of the dimer changes significantly after complexation or reorientation of the individual components, **A** and **B**. The resulting deformation energy can be a crucial part of the interaction energy between the components and must not be neglected in such cases:

$$E_{int}^{CP} = E(\mathbf{AB})^{\mathbf{AB}} - E(\mathbf{A})^{\mathbf{AB}} - E(\mathbf{B})^{\mathbf{AB}} + E_{def} \tag{4.5}$$

where $E(\mathbf{A})^{\mathbf{AB}}$ now is the energy of the individual component **A** in the basis of the complex **AB** and E_{def} is the deformation energy.

So far, the BSSE has primarily been discussed in the context of discrete molecules or complexes. However, it is also possible to expand the CP correction procedure to trimers or small clusters of molecules. It is also conceivable that different parts of a single molecule interact with each other, *i.e.*, intramolecularly. The CP correction procedure can be applied to such systems by dividing the discrete molecule into fragments. The interaction energy can then be calculated using the previously mentioned equations without issue. Valdés *et al.*[101] demonstrated that the BSSE significantly affects the determined geometries and interaction energies of [n]helicenes and Phe-Gly-Phe tripeptides. However, the results depend on the amount of fragments the molecule is divided into and how the fragmentation is performed. The challenge lies in the absence of a standardized strategy for fragmenting individual molecules to calculate the BSSE using the CP correction procedure.

4.3.2 Investigated NMA derivatives

The acridone derivatives investigated are shown in figure 4.17. The structural designs were proposed and synthesized by Lennart Bunnemann from the group of Prof. Dr. Constantin Czekelius (Asymmetric Synthesis, Heinrich Heine University Düsseldorf). Additionally, the photophysical properties were studied by Matthias Jantz from the group of Prof. Dr. Peter Gilch (Femtosecond Spectroscopy, Heinrich Heine University Düsseldorf). Additional conformations or aggregates will be shown and mentioned when relevant.

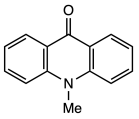

(a) NMA

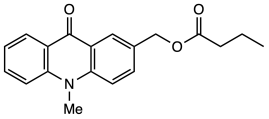

(b) NMAM-B

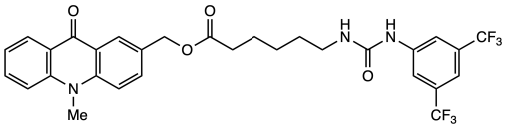

(c) NMAM-bFPUH / open

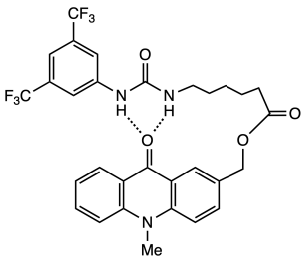

(d) NMAM-bFPUH / closed

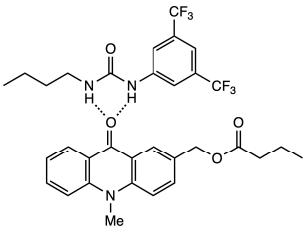

(e) NMAM-B + tFMPBU

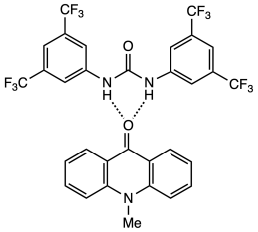

(f) NMA + Schreiner's catalyst

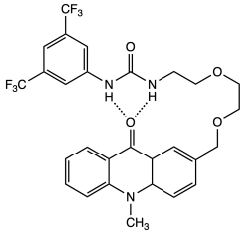

(g) NMAM-bFPUH with PEG

Figure 4.17: Lewis structures of the compounds that were investigated in this report.

The following results were obtained as part of two bachelor's theses by B.Sc. Dana Koch and B.Sc. Hendrik Knaup. I assisted both to perform the computations for their theses during this project and continued the quantum chemical investigation of these systems. The key findings have been integrated and supplemented at the relevant sections here.

Introducing the Relevant Excited States

For a quantification of the effect of intra- and intermolecular hydrogen bond formation the electronic ground state as well as the lowest excited singlet and triplet $\pi\pi^*$ and $n\pi^*$ states (see figure 4.18) were investigated for the compounds presented above (see figure 4.17).

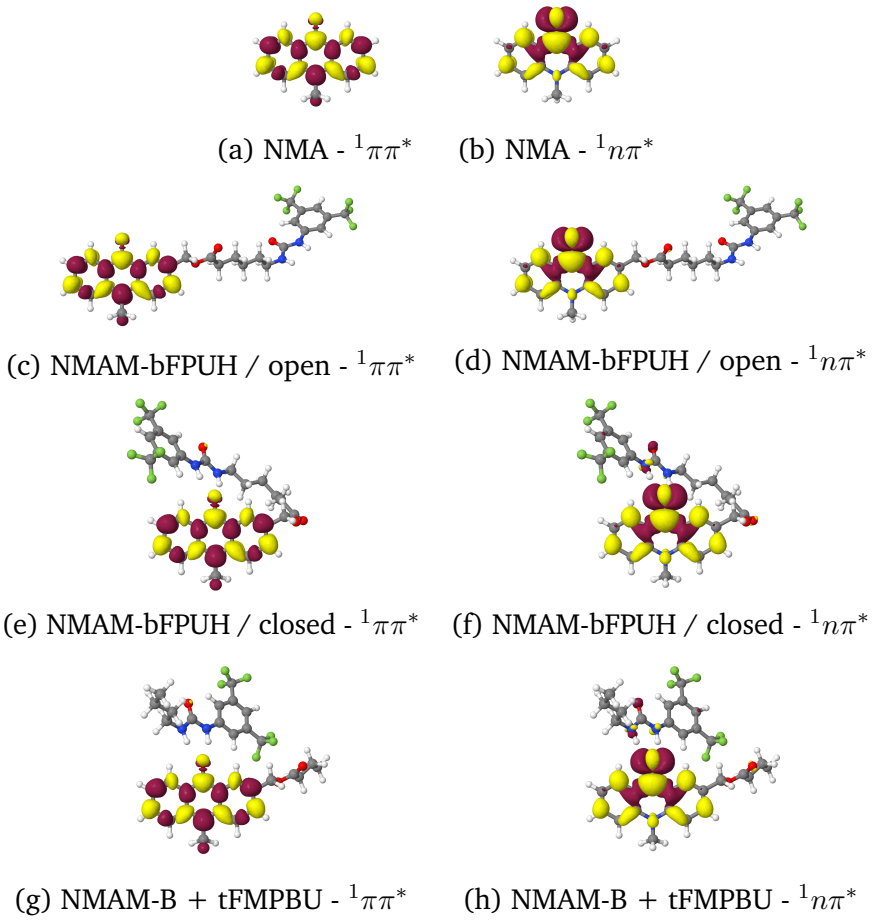

(a) NMA - $^1\pi\pi^*$ (b) NMA - $^1n\pi^*$

(c) NMAM-bFPUH / open - $^1\pi\pi^*$ (d) NMAM-bFPUH / open - $^1n\pi^*$

(e) NMAM-bFPUH / closed - $^1\pi\pi^*$ (f) NMAM-bFPUH / closed - $^1n\pi^*$

(g) NMAM-B + tFMPBU - $^1\pi\pi^*$ (h) NMAM-B + tFMPBU - $^1n\pi^*$

Figure 4.18: Exemplary difference densities (red - decrease of electron density; yellow - increase of electron density) for the lowest excited singlet $\pi\pi^*$ and $n\pi^*$ states for a range of molecules. Geometries and difference densities for the corresponding triplet states differ slightly.

N-**M**ethyl **A**cridone (**NMA**) as well as the derivative **NMAM-bFPUH** in its open conformation serve as exemplary compounds without hydrogen bond formation. **NMAM-bFPUH** in its closed conformation forms intramolecular hydrogen bonds whereas the combination of another **NMA** derivative **NMAM-B** forms intermolecular hydrogen bonds to the urea derivative **tFMPBU**.

From figure 4.19 its clearly visible that for the unsubstituted **NMA** without hydrogen bonds the lowest excited $^3\pi\pi^*$ state is well separated from the $T_2^{n\pi^*}$, $S_1^{\pi\pi^*}$ and $S_2^{n\pi^*}$ states. A chemical substitution with the ester substituent depicted in figure 4.17 has a minor effect on the energetic levels of the lowest excited singlet and triplet states. However, upon coordination and hydrogen bond formation

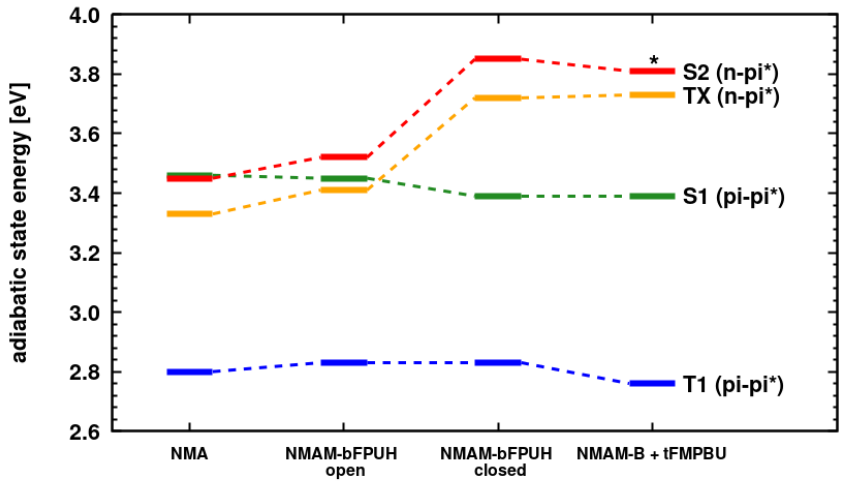

Figure 4.19: Summary of adiabatic energies of the lowest excited $\pi\pi^*$ and $n\pi^*$ states within the singlet and triplet regime for **NMA**, **NMAM-bFPUH** in its open and closed form and **NMAM-B + tFMPBU** computed with the DFT/MRCI method (BH-LYP / def2-SVP / PCM-THF). The energy of the $S_{n\pi^*}$ state (highlighted with a '*') was taken from the $T_{n\pi^*}$ geometry, since the actual electronic state could not be optimized.

the lowest excited $n\pi^*$ states are strongly destabilized by about 0.35 eV.

While for **NMA** the lowest excited singlet state is of $n\pi^*$ character it is a $\pi\pi^*$ excitation for **NMAM-bFPUH** in its closed form and for **NMAM-B + tFMPBU**. The formation of hydrogen bonds (regardless of the fact that the formation can happen intra- and intermolecular) strongly affects the energetic order of the lowest excited singlet and triplet states.

In figure 4.20 we take a closer look at the vertical excitation energies at the optimized geometry of every excited state investigated of **NMAM-bFPUH** in its open form specifically. While figure 4.19 already showed that $S_1^{\pi\pi^*}$ and $T_2^{n\pi^*}$ are in close energetic proximity, figure 4.20 hints toward a low energetic barrier ($\Delta E \approx 0.1\,eV$) for proceeding from the $\pi\pi^*$ state to the $n\pi^*$ state regime. This indicates that the ISC in **NMAM-bFPUH** might require thermal activation. At room temperature, **NMAM-bFPUH** in its open form (as well as **N-Methyl Acridone (NMA)** and **NMAM-B**, as their state diagrams look essentially the same) is expected to decay radiationlessly (according to El-Sayed's rules; see section 2.2.2.3) via intermediate population of the lowest excited $n\pi^*$ state ($S_1^{\pi\pi^*} \rightarrow T_2^{n\pi^*} \rightarrow T_1^{\pi\pi^*}$).

The energetic shift of the lowest excited $n\pi^*$ states upon hydrogen bond formation (shown in figure 4.19) will prevent the intermediate population of the $T_2^{n\pi^*}$ state and promote fluorescence.

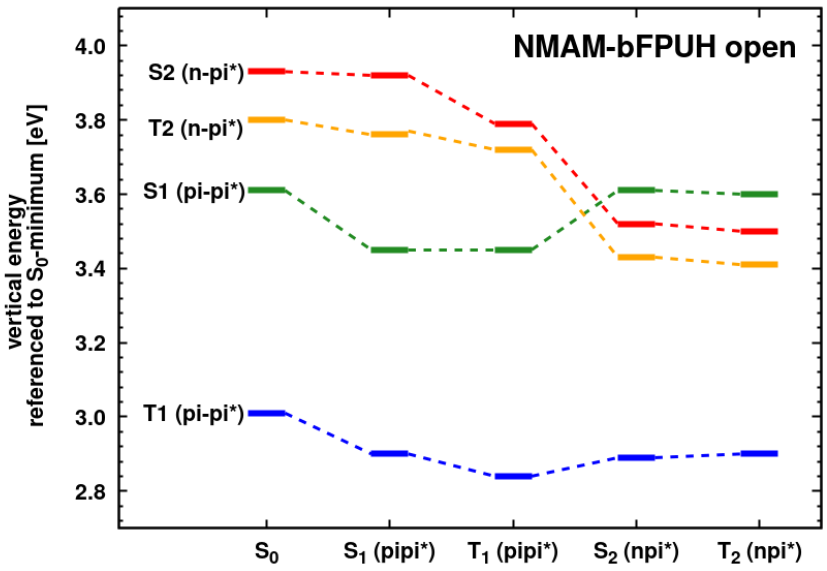

Figure 4.20: Summary of vertical excitation energies of the lowest excited $\pi\pi^*$ and $n\pi^*$ states within the singlet and triplet regime for **NMAM-bFPUH** in its open form at the electronig optimized electronic ground state and excited state geometries computed with the DFT/MRCI method (BH-LYP / def2-SVP / PCM-THF). All energies are relative to the energy of the electronic ground state at its optimized geometry.

4.3.3 Intermolecular Hydrogen Bonds

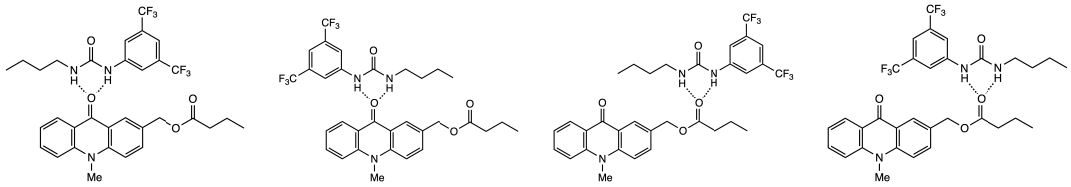

(a) Conf. 1 (b) Conf. 2 (c) Conf. 3 (d) Conf. 4

Figure 4.21: Different arrangements of **NMAM-B** and **tFMPBU** with a formation of a hydrogen bond between either the ketone and the urea or between the ester and the urea and different orientations to each other.

The hydrogen bond formation of four different orientations of **NMAM-B** and **tFMPBU** (see figure 4.21) will be addressed in the following. Conformer 1 and 2 form hydrogen bonds between the urea and the ketone and conformer 3 and 4 between the urea and the ester. A comparison of the ground state energies of all conformers shows that conformer 1 and 2 are slightly more stable (by about 0.1 eV).

As depicted in figure 4.21, in **NMAM-B** and **tFMPBU** the carbonyl oxygen forms a bifurcated hydrogen bond with the urea derivative. Despite being slightly asymmetric (see table 4.1) for the sake of simplicity both hydrogen bonds formed are treated equally. The hydrogen bond formation energy is comparable for all compounds with a strength of more than 5 kcal/mol (see figure 4.22). The hydrogen bond energy of conformer 1 and 2 is slightly higher which matches the trend of their overall stability.

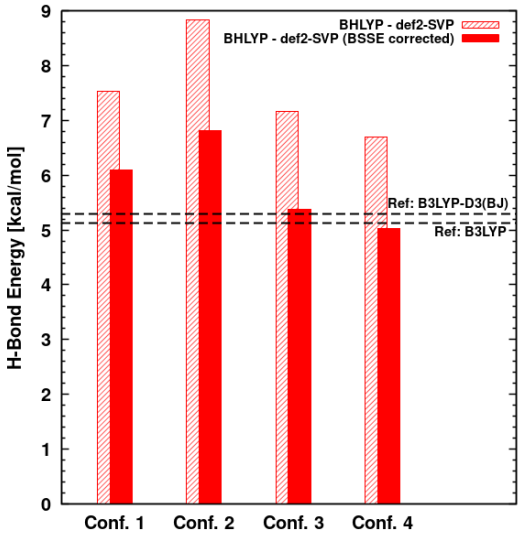

Figure 4.22: Uncorrected (hatched) and BSSE-corrected (solid) formation energy per hydrogen bond for all conformers of **NMAM-B + tFMPBU**. Computed using DFT (BH-LYP / def2-SVP / Vacuum) single point computations.

Note that the given reference energies in figure 4.22 are hydrogen bond energies and stem from a benchmark over a variety of RNA base pairs with a hydrogen bond between a secondary amine and a ketone (5.29 $\pm$ 1.29 kcal/mol[94,95]) and a theoretical investigation of hydrogen bond interactions between ureas and carbonyl compounds (3-7 kcal/mol for a range of different urea derivatives and carbonyls[93]). While both studies contain molecules that are substantially different from the conformers investigated here, the hydrogen bond formation energies are in the same order of magnitude and lie within the given confidence interval. Also the theoretical protocol to compute the hydrogen bond energies besides the used basis sets and functionals is the same.

Table 4.1: Summary of key characteristics for hydrogen bonds. Bond lengths are given in Å , the angles in degrees and the vibrational frequencies in cm^{-1} for Conf. 1-4 of **NMAM-B + tFMPBU**.

	$N_1 - O$	$N_2 - O$	$N_1 - H_1 - O$	$N_2 - H_2 - O$	$C = O_{Ketone}$	$C = O_{Ester}$
Conf. 1	2.93	2.87	151.6	158.2	1679 / 1722	1847
Conf. 2	2.85	2.95	159.5	150.9	1680 / 1721	1844
Conf. 3	2.99	2.96	154.0	157.6	1754	1799 / 1815
Conf. 4	2.94	3.02	159.8	152.2	1756	1795 / 1810

Figure 4.22 also illustrates that the BSSE is significant with approximately 3 kcal/mol for the entire molecule (and about 1.5 kcal/mol per formed hydrogen bond) and should not be neglected. The following table lists the interaction energies and the BSSE for various functionals, also taking solvent effects into account. The results show that across all the methods the interaction energy is slightly higher in solution ($6.66 \pm 0.39\mathrm{kcal/mol}$) than in vacuum ($5.85 \pm 0.40\mathrm{kcal/mol}$).

Table 4.2: Summary of the interaction energies and the BSSE computed on different levels of theory for Conformer 1 of **NMAM-B + tFMPBU**.

Method	Interaction energy [kcal/mol]	BSSE [kcal/mol]
DFT / BHLYP / def2-SVP / vacuum	6.13	2.91
DFT / BHLYP / def2-SVP / toluene	6.93	3.03
DFT / BHLYP / 6-31G* / vacuum	6.16	2.84
DFT / BHLYP / 6-31G* / toluene	6.98	2.94
DFT / B3LYP / def2-SVP / vacuum	5.29	3.60
DFT / B3LYP / def2-SVP / toluene	6.11	3.74
DFT / B3LYP / 6-31G* / vacuum	5.37	3.48
DFT / B3LYP / 6-31G* / toluene	6.21	3.60
DFT / PEB0 / def2-SVP / vacuum	6.07	3.02
DFT / PBE0 / def2-SVP / toluene	6.87	3.14
DFT / PBE0 / 6-31G* / vacuum	6.06	2.99
DFT / PBE0 / 6-31G* / toluene	6.88	3.09

4.3.4 Intramolecular Hydrogen Bonds

Our theoretical investigations of **NMAM-bFPUH** showed that two distinct conformers can be optimized. They will be called **open** (no self-coordination between the urea and the ketone) and **closed** (upon self-coordination of the urea group to the ketone) in the following. According to our first theoretical results, the **closed** conformer is higher in energy compared to the corresponding **open** conformer in **T**etra**h**ydro**f**uran (THF) despite intramolecular hydrogen bond formation. This indicates that the closure is an endothermic process in **NMAM-bFPUH**. The energy gain via hydrogen bond formation is annihilated by forcing the molecule to be in a bent and strained conformation. It was therefore proposed to investigate pairs of conformers with different chain lengths in order to find the optimal chain length to form intramolecular hydrogen bonds. To this end, the number of methylene groups was decreased and increased starting from the initially investigated compound having a total of 5 methylene groups. Also, it was proposed to use **P**oly-**E**thylene **G**lycol (PEG) as a building block for the chain in order to reduce the strain upon hydrogen bond formation.

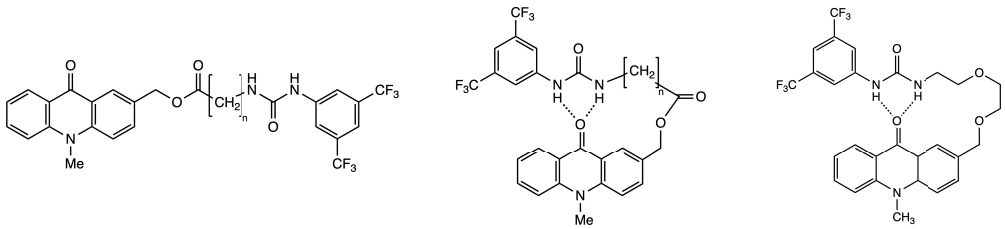

Figure 4.23: Lewis structure of the investigated the **open** (left) and **closed** (middle) form of **NMAM-bFPUH** ($n = 5$) with different chain lengths ($n = 3, 4, 6, 7$) and with a PEG chain instead (right).

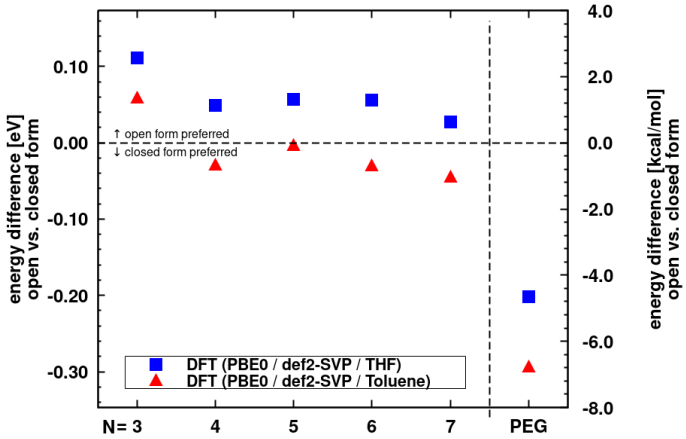

Figure 4.24: Energetic difference in eV and kcal/mol between the optimized electronic ground state energies of conformers with different chain lengths in their **open** and **closed** form using DFT (PBE0 / def2-SVP / PCM-THF) and DFT (PBE0 / def2-SVP / PCM-toluene). A positive energy denotes that the **closed** conformer is higher in energy by that amount and the preferred form is **open** and *vice versa*.

Figure 4.24 shows that independent from the chain length in **NMAM-bFPUH** in THF the **open** conformer is slightly lower in energy while in toluene the **open** conformer is slightly higher in energy than the **closed** form. In general, the results hint toward longer chains being more favourable for a closure mechanism. It should be noted, that the theoretical energy predictions at that specific level of theory are afflicted by an error of about 0.1 eV. This leads to the interpretation that the energetic difference between the conformers is close to thermal energy and both the **open** and **closed** form are present at the same time in solution. We expect the transition between those conformations to be a dynamical process.

However, for **NMAM-bFPUH** with a PEG chain the **closed** form is 0.20 eV (in THF) and 0.29 eV (in toluene) lower in energy and thus more stable than the **open** form. In solution clearly the **closed** form is favored.

The Effects of Water Aggregation

In order to investigate the effect of water aggregation to the **open** and **closed** form of **NMAM-bFPUH**, an explicit water molecule was placed close to the ketone in the **open** form and between the urea and the ketone in the **closed** form. Figure 4.25 illustrates the water coordinaten for the **open** and **closed** conformation.

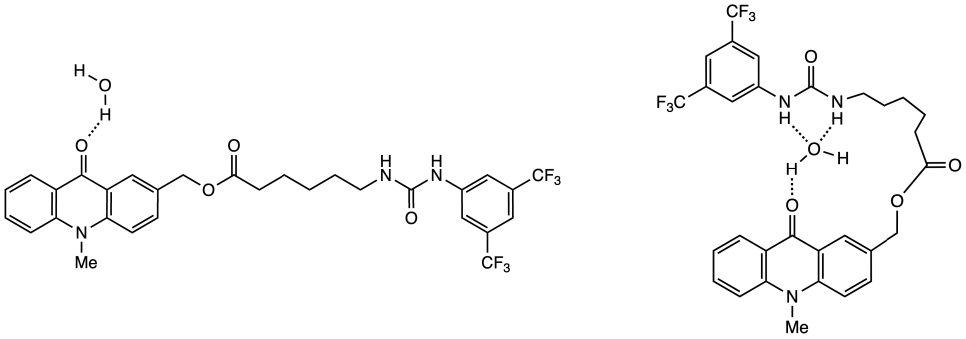

Figure 4.25: Lewis structures of the **open** and **closed** conformation of **NMAM-bFPUH** with a water molecule coordinating to the ketone and between the urea and the ketone, respectively.

Figure 4.26 contains the vertical excitation energies at the optimized geometry of the electronic ground states to the lowest excited singlet and triplet states. This way, the effect of a different conformation and the aggregation of a single water molecule can be estimated. Note, that the vertical excitation energies are not suitable to elaborate on the decay pathway mechanism for which adiabatic energies of the corresponding states at their respective optimized geometries are required. However, as previously shown for acridone[89] or flavin derivatives[102], the solvent shifts of vertical excitation energies are useful to get an idea of the influence of the solvent coordination while at the same time saving a lot of computational resources.

With that being said, figure 4.26 shows that the coordination of a single water molecule alone strongly affects the energy of the lowest excited $n\pi^*$ states while

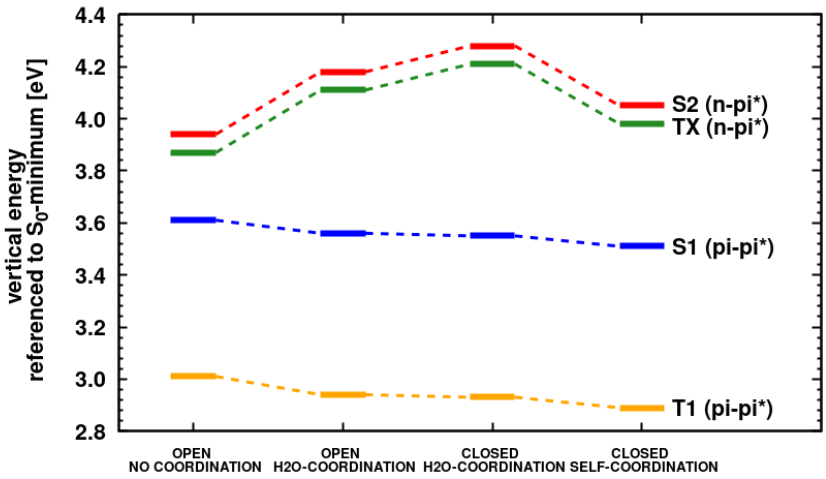

Figure 4.26: Vertical excitation energies of the lowest excited singlet (blue / red) and triplet (orange / green) states from the respective ground state energy for **NMAM-bFPUH** with and without water coordination computed with the DFT/MRCI method (BH-LYP / def2-SVP / PCM-THF).

the energy of the $\pi\pi^*$ states remains nearly unaltered. The effect becomes even stronger when a water molecule is located between the urea and the ketone. The **open** conformer with water coordination as well as the **closed** form with water coordination both show a stronger shift of the $n\pi^*$ states than the intramolecular hydrogen bond formation via self-coordination alone. To get an estimate of the adiabatic state energies upon water coordination the solvent shift was added to or subtracted from the correspondent adiabatic state energy without water coordination (the estimated adiabatic state energies are summarized in table 4.3).

Table 4.3: Estimated effect of the explicit water solvation shift from figure 4.26 on the adiabatic energies taken from figure 4.19. Energies and the corresponding solvent shift in brackets are given in eV.

	$T_1^{\pi\pi^*}$	$S_1^{\pi\pi^*}$	$T_2^{n\pi^*}$	$S_2^{n\pi^*}$
NMAM-bFPUH / open	2.76 (-0.07)	3.40 (-0.05)	3.65 (+0.24)	3.76 (+0.24)
NMAM-bFPUH / closed	2.87 (+0.04)	3.35 (+0.04)	3.96 (+0.23)	4.08 (+0.23)

Also, upon water coordination in the electronic ground state the **closed** conformer is lower in energy (by about 0.18 eV using DFT (PBE0 / def2-SVP / PCM-THF)) and thus more stable than the **open** conformer.

4.3.5 Combining NMA with Schreiner's Catalyst

The full vertical and adiabatic state diagrams of **NMA** in toluene are given in figure 4.27. The vertical state diagram presents a rough idea about the PES of the lowest excited $\pi\pi^*$- and $n\pi^*$-states and the energetic barriers to get from one electronic state to the other. The most probable decay pathway mechanism is depicted in the corresponding adiabatic state diagram.

Upon electronic excitation from the ground state into the lowest excited singlet state ($S_{\pi\pi^*}$) geometrical relaxation happens along the PES of this singlet state. Despite a high fluorescence rate constant of $k_f = 7.7 \times 10^7\,\mathrm{s}^{-1}$ ($\tau = 13\,ns$) this is followed by a fast IC into the adiabatically lower lying $S_{n\pi^*}$ state. From there, the $S_{n\pi^*}$ state is depopulated via El-Sayed allowed ISC (see 2.2.2.3) into the lowest excited $T_{\pi\pi^*}$ state. Due to efficient nonradiative decay, **NMA** is expected to show little to no fluorescence in toluene.

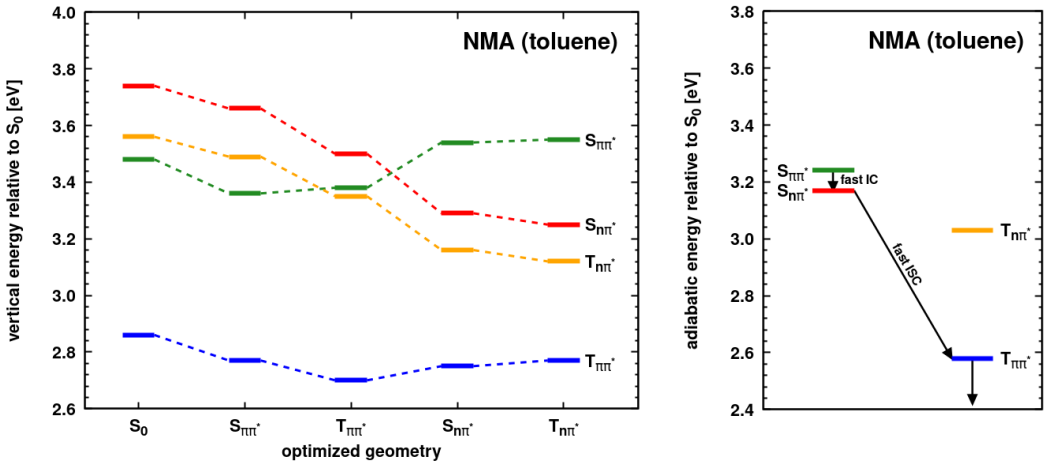

Figure 4.27: Vertical (left) and adiabatic (ZPVE corrected, right) excitation energies of NMA in toluene at the respective optimized geometries computed with the DFT/MRCI method (R2016 / BH-LYP / def2-SVP / PCM-Toluene).

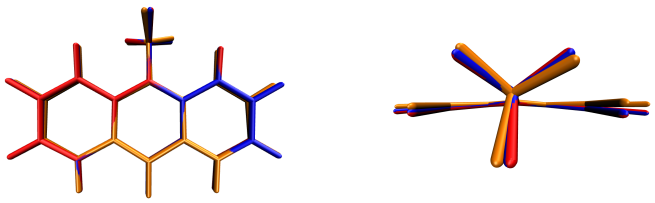

Figure 4.28: Overlay of the optimized geometries of **NMA** in toluene (blue) and THF (red) as well as the experimental crystal structure with optimized positions of the hydrogen atoms (orange).

Figure 4.28 shows that independent from the solvent the computationally optimized geometries show negligible geometrical changes compared to the experimental crystal structure. The aromatic plane of **NMA** is slightly more tilted (3.6° in toluene, 3.5° in THF and 1.6° in crystal) and the methyl group a little more displaced from the aromatic plane (6.8° in toluene, 6.5° in THF and 4.2° in

crystal) in solvent compared to the crystal structure. Due to minor changes in the optimized geometries (**R**oot-**M**ean-**S**quare **D**eviation (RMSD) $= 0.004 - 0.067$ Å) the computational results for the solvent models and crystal structure are expected to be readily comparable.

Figure 4.29 shows the vibrationally resolved absorption and emission spectra for the optimized geometries in toluene and THF environment. Both spectra show a strong vibrational progression (C-C stretch vibration $\approx$ 1450 cm^{-1} and out-of-plane motion of the CH_3-group $\approx$ 130 cm^{-1}) and a very small Stokes shift of 225 cm^{-1} in toluene and 167 cm^{-1} in THF. Compared to the experimental absorption and emission maxima, the computational results are shifted only by about 900 cm^{-1}. The shape and vibronic progression of both computed spectra shows excellent agreement with the experiment.

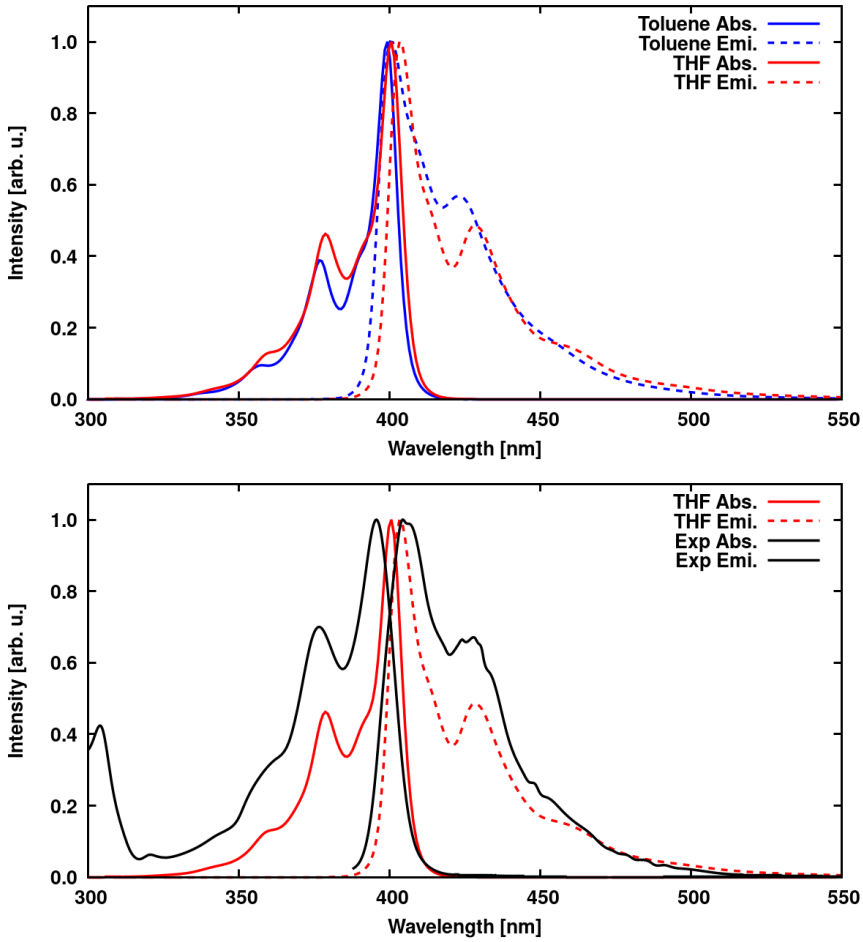

Figure 4.29: Vibrationally resolved absorption (solid lines) and emission (dashed lines) spectra for **NMA** in toluene (blue) and THF (red) at 298 K. The computations were performed using the VH method.

Table 4.4 additionally shows the energy gaps between the lowest excited singlet and triplet states for both adiabatic and vertical approaches. The extrapolated energy gaps for the absorption and emission processes are comparable hinting toward a reliable extrapolation process. However, the absolute value of the

extrapolated energy gap is slightly higher in energy compared to the computed values using the AH method. Also the energy gap is regardless of the method slightly bigger in toluene compared to THF.

Table 4.4: Energy gap between the lowest excited singlet and triplet states using the AH and VH (extrapolated) method for **NMA** in toluene and THF.

	NMA in toluene	**NMA** in THF
ΔE_{ST} (VH abs, extrapolated) [cm^{-1}]	27248	26910
ΔE_{ST} (VH emi, extrapolated) [cm^{-1}]	27102	26727
ΔE_{ST} (AH 0-0 corrected) [cm^{-1}]	26100	25852

As depicted in figure 4.30, upon coordination of Schreiner's catalyst to **NMA** two hydrogen bonds are formed. Since both molecules are symmetric, both hydrogen bonds are equivalent (also see table 4.5). The hydrogen bond between **NMA** and Schreiner's catalyst is comparably strong (BSSE corrected interaction energy of 10.21 kcal/mol in THF and 9.51 kcal/mol in toluene for each hydrogen bond computed with the DFT method (BHLYP / def2-SVP / PCM)). The study by Zheng *et al.*[93] already showed that hydrogen bonds formed between carbonyls and 1,3-bis(trifluoromethyl)phenyl substituted ureas and thioureas tend to be the strongest within the combinations and examples that were investigated.

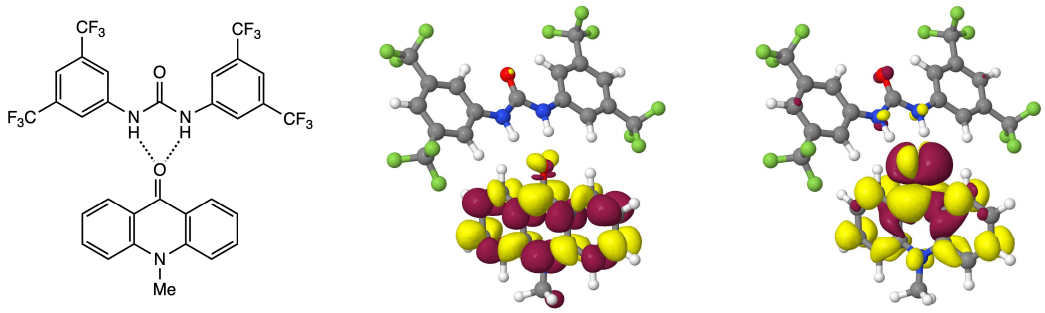

Figure 4.30: Lewis structure of **NMA** with Schreiner's catalyst and the respective difference densities of the lowest excited $\pi\pi^*$ and $n\pi^*$ states (red - decrease of electron density; yellow - increase of electron density).

Table 4.5: Summary of key characteristics for hydrogen bonds for **NMA** + Schreiner's catalyst. Bond lengths are given in Å , angles in degrees and vibrational frequencies in cm^{-1}.

	$N_1 - O$	$N_2 - O$	$N_1 - H_1 - O$	$N_2 - H_2 - O$	$C = O_{Ketone}$
NMA + Schreiner's catalyst	2.84	2.84	157.2	157.0	1669 / 1710

Figure 4.31 shows the vertical excitation energies from the lowest excited $\pi\pi^*$ and $n\pi^*$ states. The formation of hydrogen bonds slightly decreases the energy of the lowest excited $\pi\pi^*$ states (by about 0.1 eV) whereas the lowest excited $n\pi^*$ states are strongly destabilized (by about 0.5 eV). Thus, the $n\pi^*$ states and $\pi\pi^*$ states are not in close energetic proximity anymore and the most probable

deactivation pathway changes. Upon vertical electronic excitation from the ground state into the lowest excited singlet state ($S_{\pi\pi^*}$) geometrical relaxation happens. The transition from the $S_{\pi\pi^*}$ to the lowest excited $T_{\pi\pi^*}$ state is El-Sayed forbidden which is why fluorescence will outcompete the radiationless deactivation via ISC ($k_f = 9.4 \times 10^7\ \mathrm{s}^{-1}$ and $\tau = 10.7\ ns$). Upon coordination with Schreiner's catalyst **NMA** is expected to show a significant fluorescence intensity.

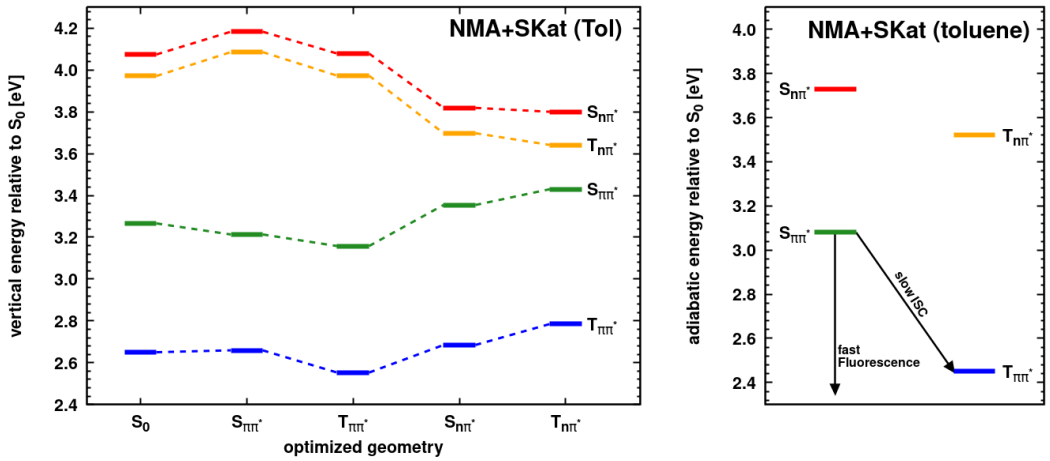

Figure 4.31: Vertical (left) and adiabatic (ZPVE corrected, right) excitation energies of **NMA**+Schreiner's catalyst in toluene at the respective optimized geometries computed with the DFT/MRCI method (R2016 / BH-LYP / def2-SVP / PCM-Toluene).

For a meaningful comparison with the experimental crystal structure, Markus Putscher performed **Q**uantum **M**echanics (QM)/**M**olecular **M**echanics (MM) calculations for **NMA**+Schreiner's catalyst. In order to do so, the parameters of the unit cell were extracted from the available data. A supercell consisting of 350 aggregates of **NMA** and Schreiner's catalyst was constructed based on the experimental crystal structure. One aggregate (QM region) was optimized within the vicinity of all other molecules (MM region). Subsequently, the surrounding molecules were exported as point charges and used as an implicit crystal environment for all further calculations. The vertical excitation energies at the optimized ground state were computed using the DFT/MRCI method.

Figure 4.32 shows that the optimized structures of **NMA**+Schreiner's catalyst in the investigated solvents align with the experimental crystal structure. There are negligible changes in the geometry of the two monomers of the aggregate. Only the orientation of the **NMA** and the catalyst toward each other deviates in solvation compared to the experimental crystal structure. More importantly, the optimized geometry within the simulated solid state environment shows negligible changes compared to the optimized structures in vacuum, toluene and THF (RMSD $= 0.009 - 0.012$ Å). The vertical excitation energy from the electronic ground state to the lowest excited singlet state ($E = 3.51$ eV or $E = 353$ nm) only slightly deviates from the excitation energies in toluene ($E = 3.49$ eV or $E = 356$ nm) and THF ($E = 3.47$ eV or $E = 358$ eV).

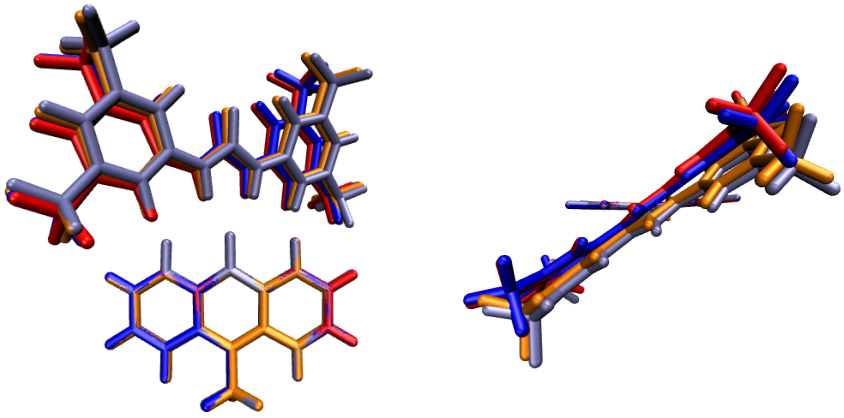

Figure 4.32: Overlay of the optimized geometries of **NMA**+Schreiner's catalyst in toluene (blue), THF (red) and the experimental crystal structure with relaxed hydrogen atoms (orange) aligned to **NMA**. The optimized geometry within simulated solid state environment is depicted in cyan also aligned to **NMA**.

Simulated absorption and emission spectra for **NMA**+Schreiner's catalyst in toluene and THF are shown in figure 4.33. At $298\ \mathrm{K}$ both absorption and emission are significantly broader compared to the corresponding spectra of **NMA** alone in figure 4.29. Vibrational progression at $298\ \mathrm{K}$ was not clearly visible which is why also absorption and emission spectra without temperature contributions were computed. Vibrational progression originates mainly from a C-C stretch vibration ($\approx$ 1480 cm^{-1}) and a low-frequency butterfly vibration on the **NMA** ($\approx$ 23 cm^{-1}). Due to temperature contributions also the Stokes shift increases in toluene (3650 cm^{-1}) and THF (3900 cm^{-1}).

Similar to the results shown earlier for **NMA** alone, table 4.6 shows the energy gaps between the lowest excited singlet and triplet states for both vertical and adiabatic approaches computed for **NMA**+Schreiner's catalyst. The difference between the extrapolated energy gap and the 'true' adiabatic energy difference is smaller. The absolute values remain higher in toluene compared to those in THF.

Table 4.6: Energy gap between the lowest excited singlet and triplet states using the AH and VH (extrapolated) method for **NMA**+Schreiner's catalyst in toluene and THF.

	NMA+ Schreiner's catalyst in toluene	**NMA**+ Schreiner's catalyst in THF
ΔE_{ST} (VH abs, extrapolated) [cm^{-1}]	25168	25019
ΔE_{ST} (VH emi, extrapolated) [cm^{-1}]	25295	25022
ΔE_{ST} (AH 0-0 corrected) [cm^{-1}]	24881	24552

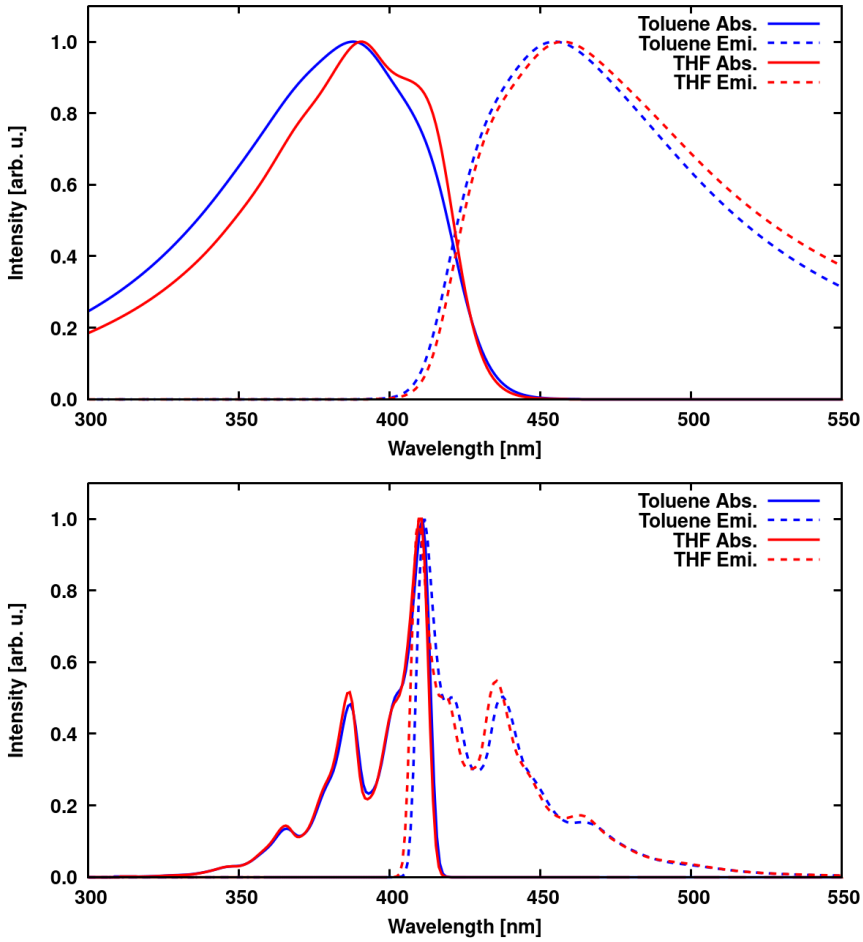

Figure 4.33: Vibrationally resolved absorption (solid lines) and emission (dashed lines) spectra for **NMA**+Schreiner's catalyst in toluene (blue) and THF (red) at $298\,\mathrm{K}$ (top panel) and without temperature contributions (bottom panel). The computations were performed using the VH method.

5 Conclusion

This work highlights the importance of vibronic spectroscopy, both as an experimental method and as part of the quantum chemical toolbox. Molecular vibrations play a crucial role in the characterization and identification of structures in physical and theoretical chemistry. In the context of this work, established and promising TADF emitters as well as efficient fluorophores were investigated. However, simulations using conventional adiabatic approaches did not always yield meaningful results. Compared to experimental results, the simulated spectra are featureless and excessively broad. Therefore, it became necessary to expand our repertoire of quantum chemistry approaches for the description of vibronic transitions.

Within the scope of this thesis the implementation of the VH method into the VIBES program was demonstrated. It is fundamentally based on a review article by Ferrer *et al.* and it was shown that the program structure can be entirely preserved, while the VH branch requires the Hessian matrix and gradients as additional input parameters. Based solely on this data, it is possible to extrapolate the PES and the corresponding normal mode vibrations of the final state. The equations for calculating the Duschinsky rotation matrix and the displacement vector were presented for both adiabatic and vertical approaches.

The implementation was tested using a small benchmark set. The performance of adiabatic and vertical approaches was critically evaluated based on various metrics. For the benchmark systems, it can be shown that the linear Duschinsky transformation is not fully valid when employing adiabatic approaches, as indicated by a determinant of the rotation matrix deviating from 1. Methodologically driven the VH method increases the determinant to 1 and reduces Duschinsky mixing effects. However, it should be noted that the extrapolated adiabatic energy difference deviates from the 'true' adiabatic energy gap. Consequently, the onset of vibronic spectra might be shifted, and rate constants may differ in magnitude. Additionally, the quality of the results seems to correlate with the number of normal modes with imaginary eigenvalues, demanding a suitable strategy for the treatment of such normal modes. The more of them need to be discarded for a calculation, the larger is the energetic difference between the extrapolated and the 'true' adiabatic energy.

Numerous application projects have demonstrated the versatility of the VH method, showing that it is particularly well-suited for intriguing TADF systems exhibiting a donor–acceptor motif, as these often exhibit normal modes that are challenging to describe using the conventional AH approach.

For the well-known emitter DMAC-TRZ, the goal was to explain experimental features that had not been mentioned in the literature until now and only appeared in MCH as well as in rigid matrix materials like Zeonex®. A quantum chemical investigation confirmed the existence of two distinct conformers whose significant geometric differences not only result in fundamentally different photophysical properties but also necessitate distinct methods for accurately describing these properties. Specifically, the symmetry-forbidden nature of the relevant vibronic transitions required going beyond Condon approximation to get meaningful results.

For the spiro-bridged donor–acceptor system AN, the vertical approach was used to unambiguously assign the experimentally measured ESA spectrum to an excited state whose involvement in the decay mechanism had been hypothesized by Dobkowski *et al.* but could not be definitively proven.

Ultimately, a series of organic donor–acceptor compounds with various sterically demanding substituents was used to investigate the influence of the donor–acceptor orientation on radiative and nonradiative processes. We used the vertical approach to recompute ISC and rISC rate constants along a linearly interpolated pathway. Through this series, we demonstrated that an almost orthogonal orientation is beneficial for TADF behavior owing to non-negligible oscillator strengths, SOC and a low energy gap between the lowest excited singlet and triplet states. However, an exact 90-degree alignment results in symmetry-forbidden transitions, leading to a significant decrease of emission. This project was the first-ever application of the VH method for computing nonradiative rate constants.

Within the application examples presented in this thesis, I could show that vertical models come with certain challenges. Extrapolation is an approximation, meaning that, for instance, the adiabatic energy difference can only be defined approximately. As a result, vibronic spectra are usually slightly shifted compared to experimental data. Also, a quantification of the impact of the extrapolation process on rate constants requires further analysis. In these cases, calculations using vertical models are recommended as supplementary to calculations with adiabatic models. When choosing the method, a careful evaluation of the systems is still required.

Finally, the technical and practical advantages offered by the application of the VH method should be summarized. We observed cases where the optimization of the final electronic state can be omitted and be replaced by an extrapolation based on the data available at the FC region. This resulted in a significant reduction in computational effort. Furthermore, the VH method enabled us to calculate meaningful spectra, comparable to experimental results, even for systems that exhibit significant geometric changes after electronic excitation. The vertical approaches prove to be a solid foundation for investigating nonradiative rate constants along an interpolated path and provide a theoretical analysis that would not have been possible with adiabatic models. All in all, we could show

that the simulation of vibronic transitions could be improved for a variety of different systems upon using vertical approaches.

6 References

6.1 Bibliography

[1] D. C. Agrawal, H. S. Leff, and V. J. Menon. Efficiency and Efficacy of Incandescent Lamps. *Am. J. Phys.*, 64(5):649–654, 05 1996.

[2] C. W. Tang and S. A. VanSlyke. Organic Electroluminescent Diodes. *Appl. Phys. Lett.*, 51(12):913–915, 09 1987.

[3] S. Reineke, M. Thomschke, B. Lüssem, and K. Leo. White Organic Light-Emitting Diodes: Status and Perspective. *Rev. Mod. Phys.*, 85:1245–1293, Jul 2013.

[4] X. Yang, G. Zhou, and W. Y. Wong. Recent Design Tactics for High Performance White Polymer Light-Emitting Diodes. *J. Mater. Chem. C*, 2:1760–1778, 2014.

[5] A. Salehi, X. Fu, D. H. Shin, and F. So. Recent Advances in OLED Optical Design. *Adv. Func. Mat.*, 29(15):1808803, 2019.

[6] O. Nuyken, S. Jungermann, V. Wiederhirn, E. Bacher, and K. Meerholz. Modern Trends in Organic Light-Emitting Devices (OLEDs). *Monatsh. für Chem.*, 137(7):811–824, 2006.

[7] O. Ostroverkhova. Organic Optoelectronic Materials: Mechanisms and Applications. *Chem. Rev.*, 116(22):13279–13412, 2016.

[8] W. Brütting, J. Frischeisen, T. D. Schmidt, B. J. Scholz, and C. Mayr. Device Efficiency of Organic Light-Emitting Diodes: Progress by Improved Light Outcoupling. *Phys. Status Solidi A*, 210(1):44–65, 2013.

[9] C. Adachi and A. S. D. Sandanayaka. The Leap from Organic Light-Emitting Diodes to Organic Semiconductor Laser Diodes. *CCS Chemistry*, 2(4):1203–1216, 2020.

[10] J. Wang, A. Chepelianskii, F. Gao, and N. C. Greenham. Control of Exciton Spin Statistics Through Spin Polarization in Organic Optoelectronic Devices. *Nat. Comm.*, 3(1):1191, 2012.

[11] H. H. Jaffe and A. L. Miller. The Fates of Electronic Excitation Energy. *J. Chem. Ed.*, 43(9):469, 1966.

[12] P. W. Atkins, J. De Paula, and J. Keeler. *Atkins' Physical Chemistry*. Oxford University Press, sixth edition, 1999.

[13] M. Pastorczak, M. Nejbauer, and C. Radzewicz. Femtosecond Infrared Pump–Stimulated Raman Probe Spectroscopy: The First Application of the Method to Studies of Vibrational Relaxation Pathways in the Liquid HDO/D2O System. *Phys. Chem. Chem. Phys.*, 21:16895–16904, 2019.

[14] M. Banno, K. Ohta, S. Yamaguchi, S. Hirai, and K. Tominaga. Vibrational Dynamics of Hydrogen-Bonded Complexes in Solutions Studied with Ultrafast Infrared Pump-Probe Spectroscop. *Acc. Chem. Res.*, 42(9):1259–1269, 2009.

[15] M. Kasha. Characterization of Electronic Transitions in Complex Molecules. *Discuss. Faraday Soc.*, 9:14–19, 1950.

[16] G. Viswanath and M. Kasha. Confirmation of the Anomalous Fluorescence of Azulene. *J. Chem. Phys.*, 24(3):574–577, 03 1956.

[17] T. Itoh. Fluorescence and Phosphorescence from Higher Excited States of Organic Molecules. *Chem. Rev.*, 112(8):4541–4568, 2012.

[18] S. Califano. *Vibrational States*. A Wiley-Interscience publication. Wiley, 1976.

[19] A. Orlando, F. Franceschini, C. Muscas, S. Pidkova, M. Bartoli, M. Rovere, and A. Tagliaferro. A Comprehensive Review on Raman Spectroscopy applications. *Chemosensors*, 9(9):262, 2021.

[20] P. W. Atkins, J. De Paula, and J. Keeler. *Atkins' Physical Chemistry*. Oxford University Press, sixth edition, 1999.

[21] A. Y. Hirakawa and M. Tsuboi. Molecular Geometry in an Excited Electronic State and a Preresonance Raman Effect. *Science*, 188(4186):359–361, 1975.

[22] J. Orear and E. Fermi. *Nuclear Physics: A Course Given by Enrico Fermi at the University of Chicago*. Midway reprints. University of Chicago Press, 1950.

[23] H. Haken and H. C. Wolf. *Molekülphysik und Quantenchemie*. Springer-Lehrbuch. Springer, Berlin ; Heidelberg, fünfte, völlig neubearbeitete und erweiterte auflage edition, 2006.

[24] C. M. Marian. Understanding and Controlling Intersystem Crossing in Molecules. *Annu. Rev. Phys. Chem.*, 72(72):617–640, 2021.

[25] C. M. Marian. Spin–Orbit Coupling and Intersystem Crossing in Molecules. *WIREs Comput. Mol. Sci.*, 2(2):187–203, 2012.

[26] S. Banerjee, A. Baiardi, J. Bloino, and V. Barone. Temperature Dependence of Radiative and Nonradiative Rates from Time-Dependent Correlation Function Methods. *J. Chem. Theory Comput.*, 12(2):774–786, 2016.

[27] M. Etinski, J. Tatchen, and C. M. Marian. Thermal and Solvent Effects on the Triplet Formation in Cinnoline. *Phys. Chem. Chem. Phys.*, 16(10):4740, 2014.

[28] S. E. Braslavsky. Glossary of Terms Used in Photochemistry, 3rd Edition (IUPAC Recommendations 2006). *Pure Appl. Chem.*, 79(3):293–465, 2007.

[29] T. J. Penfold, E. Gindensperger, C. Daniel, and C. M. Marian. Spin-Vibronic Mechanism for Intersystem Crossing. *Chem. Rev.*, 118(15):6975–7025, 2018.

[30] D. A. McQuarrie. Statistical Mechanics, University Science Books. *Sausalito, CA*, pages 194–221, 2000.

[31] Y. Niu, Q. Peng, C. Deng, X. Gao, and Z. Shuai. Theory of Excited State Decays and Optical Spectra: Application to Polyatomic Molecules. *J. Phys. Chem. A*, 114(30):7817–7831, 2010.

[32] J. Seibt, A. Lohr, F. Würthner, and V. Engel. Circular Dichroism and Absorption Spectroscopy of Merocyanine Dimer Aggregates: Molecular Properties and Exciton Transfer Dynamics from Time-Dependent Quantum Calculations. *Phys. Chem. Chem. Phys.*, 9:6214–6218, 2007.

[33] S. Y. Lee and E. J. Heller. Time-Dependent Theory of Raman Scattering. *J. Chem. Phys.*, 71(12):4777–4788, 12 1979.

[34] M. Hayashi, A. M. Mebel, K. K. Liang, and S. H. Lin. Ab Initio Calculations of Radiationless Transitions Between Excited and Ground Singlet Electronic States of Ethylene. *J. Chem. Phys.*, 108(5):2044–2055, 02 1998.

[35] R. Islampour and S. H. Lin. On the Theory of Photoinduced Intramolecular Electron Transfer. *J. Phys. Chem.*, 95(25):10261–10266, 1991.

[36] F. G. Mehler. Ueber die Entwicklung einer Function von beliebig vielen Variablen nach Laplaceschen Functionen hoeherer Ordnung. *J. für Reine Angew. Math.*, 1866(66):161–176, 1866.

[37] M. Etinski, V. Rai-Constapel, and C. M. Marian. Time-Dependent Approach to Spin-Vibronic Coupling: Implementation and Assessment. *J. Chem. Phys.*, 140(11):114104, 03 2014.

[38] M. Bracker, C. M. Marian, and M. Kleinschmidt. Internal Conversion of Singlet and Triplet States Employing Numerical DFT/MRCI Derivative Couplings: Implementation, Tests, and Application to Xanthone. *J. Chem. Phys.*, 155(1):014102, 07 2021.

[39] R. Englman and J. Jortner. The Energy Gap Law for Radiationless Transitions in Large Molecules. *Mol. Phys.*, 18(2):145–164, 1970.

[40] S. Fischer. Correlation Function Approach to Radiationless Transitions. *J. Chem. Phys.*, 53(8):3195–3207, 10 1970.

[41] M. Etinski. The Role of Duschinsky Rotation in Intersystem Crossing: a Case Study of Uracil. *J. Serb. Chem. Soc.*, 76(12):1649–1660, 2011.

[42] F. Duschinsky. *Acta. Physicochim.*, 7:551–566, 1937.

[43] G. J. Small. Herzberg–Teller Vibronic Coupling and the Duschinsky Effect. *J. Chem. Phys.*, 54(8):3300–3306, 04 1971.

[44] F. J. Avila Ferrer and F. Santoro. Comparison of Vertical and Adiabatic Harmonic Approaches for the Calculation of the Vibrational Structure of Electronic Spectra. *Phys. Chem. Chem. Phys.*, 14:13549–13563, 2012.

[45] M. Biczysko, J. Bloino, F. Santoro, and V. Barone. *Time-Independent Approaches to Simulate Electronic Spectra Lineshapes: From Small Molecules to Macrosystems*, chapter 8, pages 361–443. John Wiley & Sons, Ltd, 2011.

[46] J. Bloino, M. Biczysko, F. Santoro, and V. Barone. General Approach to Compute Vibrationally Resolved One-Photon Electronic Spectra. *J. Chem. Theory Comput.*, 6(4):1256–1274, 2010.

[47] R. Berger, C. Fischer, and M. Klessinger. Calculation of the Vibronic Fine Structure in Electronic Spectra at Higher Temperatures. 1. Benzene and Pyrazine. *J. Phys. Chem. A*, 102(36):7157–7167, 1998.

[48] E. V. Doktorov, I. A. Malkin, and V. I. Man'Ko. Dynamical Symmetry of Vibronic Transitions in Polyatomic Molecules and the Franck-Condon Principle. *J. Mol. Spec.*, 56(1):1–20, 1975.

[49] E. V Doktorov, I. A. Malkin, and V. I. Man'Ko. Dynamical Symmetry of Vibronic Transitions in Polyatomic Molecules and the Franck-Condon Principle. *J. Mol. Spec.*, 64(2):302–326, 1977.

[50] *Gaussian 16, Revision A.03, M. J. Frisch, G. W. Trucks, H. B. Schlegel, G. E. Scuseria, M. A. Robb, J. R. Cheeseman, G. Scalmani, V. Barone, G. A. Petersson, H. Nakatsuji et al., Gaussian, Inc., Wallingford CT, 2016.*

[51] J. J. P. Steward. Steward Computational Chemistry. `http://OpenMOPAC.net`, 2016. Accessed: (22.10.2024).

[52] A. P. Scott and L. Radom. Harmonic Vibrational Frequencies: An Evaluation of Hartree-Fock, Moeller-Plesset, Quadratic Configuration Interaction, Density Functional Theory, and Semiempirical Scale Factors. *J. Phys. Chem.*, 100(41):16502–16513, 1996.

[53] K. K. Irikura, R. D. Johnson, and R. N. Kacker. Uncertainties in Scaling Factors for ab Initio Vibrational Frequencies. *J. Phys. Chem. A*, 109(37):8430–8437, 2005.

[54] Vibrational Frequency Scaling Factors. `https://cccbdb.nist.gov/vsfx.asp`. Accessed: 2024-09-25.

[55] C. Eckart. Some Studies Concerning Rotating Axes and Polyatomic Molecules. *Phys. Rev.*, 47:552–558, Apr 1935.

[56] A. Sayvetz. The Kinetic Energy of Polyatomic Molecules. *J. Chem. Phys.*, 7(6):383–389, 06 1939.

[57] A. Y. Dymarsky and K. N. Kudin. Computation of the Pseudorotation Matrix to Satisfy the Eckart Axis Conditions. *J. Chem. Phys.*, 122(12):124103, 03 2005.

[58] H. L. Strauss and H. M. Pickett. Conformational Structure, Energy, and Inversion Rates of Cyclohexane and some Related Oxanes. *J. Am. Chem. Soc.*, 92(25):7281–7290, 1970.

[59] E. B. Wilson, J. C. Decius, and P. C. Cross. *Molecular Vibrations: The Theory of Infrared and Raman Vibrational Spectra*. Dover Books on Chemistry Series. Dover Publications, 1980.

[60] A. Baiardi, J. Bloino, and V. Barone. General Formulation of Vibronic Spectroscopy in Internal Coordinates. *J. Chem. Phys.*, 144(8):084114, 02 2016.

[61] J. R. Reimers. A Practical Method for the Use of Curvilinear Coordinates in Calculations of Normal-Mode-Projected Displacements and Duschinsky Rotation Matrices for Large Molecules. *The Journal of Chemical Physics*, 115(20):9103–9109, 11 2001.

[62] T. Böhmer. Calculation of Adiabatic Franck-Condon-Spectra using Internal Coordinates. Master's thesis, Heinrich Heine University Düsseldorf, Düsseldorf, Germany, 2021. Available at `https://www.theochem.hhu.de/fileadmin/redaktion/Fakultaeten/Mathematisch-Naturwissenschaftliche_Fakultaet/Chemie/Theo_Chem/Abschlussarbeiten/Boehmer.Tobias_MSc.pdf`.

[63] I. Özkan. Franck-Condon Principle for Polyatomic Molecules: Axis-switching Effects and Transformation of Normal Coordinates. *J. Mol. Spectros.*, 139(1):147–162, 1990.

[64] J. T. Hougen and J. K. G. Watson. Anomalous Rotational Line Intensities in Electronic Transitions of Polyatomic Moleculs: Axis-Switching. *Can. J. Phys.*, 43(2):298–320, 1965.

[65] A. Toniolo and M. Persico. Efficient Calculation of Franck–Condon Factors and Vibronic Couplings in Polyatomics. *J. Comput. Chem.*, 22(9):968–975, 2001.

[66] G. Balakrishnan, A. A. Jarzecki, Q. Wu, P. M. Kozlowski, D. Wang, and T. G. Spiro. Mode Recognition in UV Resonance Raman Spectra of Imidazole: Histidine Monitoring in Proteins. *J. Phys. Chem. B*, 116(31):9387–9395, 2012.

[67] F. Dinkelbach and C. M. Marian. Vibronic and Spin-Orbit Coupling Effects in the Absorption Spectra of Pyrazine: A Quantum Chemical Approach. *J. Serb. Chem. Soc.*, 84(8):819–836, 2019.

[68] M. Mitra, O. Mrózek, M. Putscher, J. Guhl, B. Hupp, A. Belyaev, C. M. Marian, and A. Steffen. Structural Control of Highly Efficient Thermally Activated Delayed Fluorescence in Carbene Zinc(II) Dithiolates. *Angew. Chem. Int. Ed.*, 63(7):e202316300, 2024.

[69] S. L. Graham, P. B. Kessler, and M. K. Mckusick. Gprof: A Call Graph Execution Profiler. In *Proceedings of the 1982 SIGPLAN Symposium on Compiler Construction*, SIGPLAN '82, page 120–126, New York, NY, USA, 1982. Association for Computing Machinery.

[70] J. M. Kaminski, A. Rodríguez-Serrano, F. Dinkelbach, H. Miranda-Salinas, A. P. Monkman, and C. M. Marian. Vibronic Effects Accelerate the Intersystem Crossing Processes of the Through-Space Charge Transfer States in the Triptycene Bridged Acridine–Triazine Donor–Acceptor Molecule TpAT-tFFO. *Chem. Sci.*, 13:7057–7066, 2022.

[71] D. K. A. Phan Huu, S. Saseendran, R. Dhali, L. G. Franca, K. Stavrou, A. P. Monkman, and A. Painelli. Thermally Activated Delayed Fluorescence: Polarity, Rigidity, and Disorder in Condensed Phases. *J. Am. Chem. Soc.*, 144(33):15211–15222, 2022.

[72] R. Dhali, D. K. A. Phan Huu, F. Bertocchi, Cr. Sissa, F. Terenziani, and A. Painelli. Understanding TADF: a Joint Experimental and Theoretical Study of DMAC-TRZ. *Phys. Chem. Chem. Phys.*, 23:378–387, 2021.

[73] H. Tanaka, K. Shizu, H. Nakanotani, and C. Adachi. Dual Intramolecular Charge-Transfer Fluorescence Derived from a Phenothiazine-Triphenyltriazine Derivative. *J. Phys. Chem. C*, 118(29):15985–15994, 2014.

[74] M. K. Etherington, F. Franchello, J. Gibson, T. Northey, J. Santos, J. S. Ward, H. F. Higginbotham, P. Data, A. Kurowska, P. L. Dos Santos, D. R. Graves, A. S. Batsanov, F. B. Dias, M. R. Bryce, T. J. Penfold, and A. P. Monkman. Regio- and Conformational Isomerization Critical to Design of Efficient Thermally-Activated Delayed Fluorescence Emitters. *Nat. Comm.*, 8(1):14987, 2017.

[75] Y. Z. Shi, K. Wang, S. L. Zhang, X. C. Fan, Y. Tsuchiya, Y. T. Lee, G. L. Dai, J. X. Chen, C. J. Zheng, S. Y. Xiong, X. M. Ou, J. Yu, D. S. Jie, C. S. Lee, C. Adachi, and X. H. Zhang. Characterizing the Conformational Distribution in an Amorphous Film of an Organic Emitter and Its Application in a "Self-Doping" Organic Light-Emitting Diode. *Angew. Chem. Int. Ed.*, 133(49):26082–26087, 2021.

[76] W. L. Tsai, M. H. Huang, W. K. Lee, Y. J. Hsu, K. C. Pan, Y. H. Huang, H. C. Ting, M. Sarma, Y. Y. Ho, H. C. Hu, C. C. Chen, M. T. Lee, K. T. Wong, and C. C. Wu. A Versatile Thermally Activated Delayed Fluorescence Emitter for Both Highly Efficient Doped and Non-Doped Organic Light Emitting Devices. *Chem. Commun.*, 51:13662–13665, 2015.

[77] L. M. Duben. Quantum Chemical Characterization of Conformers of the Donor-Acceptor Compound DMAC-TRZ. Master's thesis, Heinrich Heine University Düsseldorf, Düsseldorf, Germany, 2022. Available at https://www.theochem.hhu.de/fileadmin/redaktion/Fakultaeten/Mathematisch-Naturwissenschaftliche_Fakultaet/Chemie/Theo_Chem/Abschlussarbeiten/Duben._Luka_BSc.pdf.

[78] M. Y. Wong and E. Zysman-Colman. Purely Organic Thermally Activated Delayed Fluorescence Materials for Organic Light-Emitting Diodes. *Adv. Mat.*, 29(22):1605444, 2017.

[79] H. Tanaka, K. Shizu, H. Nakanotani, and C. Adachi. Dual Intramolecular Charge-Transfer Fluorescence Derived from a Phenothiazine-Triphenyltriazine Derivative. *J. Phys. Chem. C*, 118(29):15985–15994, 2014.

[80] J. Dobkowski, A. Gorski, M. Kijak, M. Pietrzak, K. Redeckas, and M. Vengris. Combined Picosecond Time-Resolved UV–Vis and NMR Techniques Used for Investigation of the Excited State Intramolecular Triplet–Triplet Energy Transfer. *J Phys. Chem. A*, 123(32):6978–6985, 2019.

[81] S. Metz, T. Böhmer, B. Raunitschke, and C. M. Marian. Intersystem Crossing and Intramolecular Triplet Excitation Energy Transfer in spiro[9,10-dihydro-9-oxoanthracene-10,2'-5',6'-benzindan] Investigated by DFT/MRCI Methods. *Can. J. Chem.*, 101(9):633–640, 2023.

[82] G. A. Sommer, L. N. Mataranga-Popa, R. Czerwieniec, T. Hofbeck, H. H. H. Homeier, T. J. J. Müller, and H. Yersin. Design of Conformationally Distorted Donor–Acceptor Dyads Showing Efficient Thermally Activated Delayed Fluorescence. *J. Phys. Chem. Lett.*, 9(13):3692–3697, 2018.

[83] J. M. Kaminski, T. Böhmer, and C. M. Marian. Balancing TADF Properties in π-Bridged Donor–Acceptor Systems by Sterical Constraints: The Best of Three Worlds. *J. Phys. Chem. C*, 128(33):13711–13721, 2024.

[84] T. J. Penfold, F. B. Dias, and A. P. Monkman. The Theory of Thermally Activated Delayed Fluorescence for Organic Light Emitting Diodes. *Chem. Commun.*, 54:3926–3935, 2018.

[85] P. K. Samanta, D. Kim, V. Coropceanu, and J. L. Brédas. Up-Conversion Intersystem Crossing Rates in Organic Emitters for Thermally Activated Delayed Fluorescence: Impact of the Nature of Singlet vs Triplet Excited States. *J. Am. Chem. Soc.*, 139(11):4042–4051, 2017.

[86] Yasuhisa H., Tomoya H., Atushi S., Masayasu K., Hiroaki O., and Hiroaki S. Acridone-tagged DNA as a New Probe for DNA Detection by Fluorescence Resonance Energy Transfer and for Mismatch DNA Recognition. *Bioorg. Med. Chem. Lett.*, 16(14):7013–7020, 2008.

[87] K. A. Thom, F. Wieser, K. Diestelhorst, A. Reiffers, C. Czekelius, M. Kleinschmidt, M. Bracker, C. M. Marian, and P. Gilch. Acridones: Strongly

Emissive HIGHrISC Fluorophores. *J. Phys. Chem. Lett.*, 12(24):5703–5709, 2021.

[88] A. Dadabhoy, S. Faulkner, and P. G. Sammes. Small Singlet–Triplet Energy Gap of Acridone Enables Longer Wavelength Sensitisation of Europium(III) Luminescence. *J. Chem. Soc., Perkin Trans. 2*, pages 2359–2360, 2000.

[89] V. Rai-Constapel and C. M. Marian. Solvent Tunable Photophysics of Acridone: a Quantum Chemical Perspective. *RSC Adv.*, 6:18530–18537, 2016.

[90] J. Meissner, B. Kosper, C. M. Marian, and R. Weinkauf. Lowest Triplet and Singlet States in N-Methylacridone and N,N'-Dimethylquinacridone: Theory and Experiment. *J. Phys. Chem. A*, 125(40):8777–8790, 2021.

[91] R. E. Galian, G. Litwinienko, J. Pérez-Prieto, and K. U. Ingold. Kinetic Solvent Effects on the Reaction of an Aromatic Ketone π,π^* Triplet with Phenol. Rate-Retarding and Rate-Accelerating Effects of Hydrogen-Bond Acceptor Solvents. *J. Am. Chem. Soc.*, 129(30):9280–9281, 2007.

[92] S. Raub, A. Steffen, A. Kämper, and C. M. Marian. AIScore — Chemically Diverse Empirical Scoring Function Employing Quantum Chemical Binding Energies of Hydrogen-Bonded Complexes. *J. Chem. Inf. Model.*, 48(7):1492–1510, 2008.

[93] W. Zheng, Y. Fu, L. Liu, and Q. Guo. Hydrogen Bonding Interaction between Ureas or Thioureas and Carbonyl Compounds. *Acta. Phys-Chim. Sin.*, 23(7):1018–1024, 2007.

[94] H. Dong, W. Hua, and S. Li. Estimation on the Individual Hydrogen-Bond Strength in Molecules with Multiple Hydrogen Bonds. *J. Phys. Chem. A*, 111(15):2941–2945, 2007.

[95] M. H. Hao. Theoretical Calculation of Hydrogen-Bonding Strength for Drug Molecules. *J. Chem. Theory Comput.*, 2(3):863–872, 2006.

[96] The Basis Set Superposition Error (BSSE), 2005. `https://www.cup.uni-muenchen.de/ch/compchem/basis/bsse1.html` [Accessed: 07/2024].

[97] N. R. Kestner and J. E. Combariza. Basis Set Superposition Errors: Theory and Practice. *Rev. Comp. Chem.*, pages 99–132, 1999.

[98] I. Mayer. Towards a "Chemical" Hamiltonian. *Int. J. Quantum Chem.*, 23(2):341–363, 1983.

[99] I. Mayer and Á. Vibók. SCF Equations in the Chemical Hamiltonian Approach. *Chem. Phys. Let.*, 148(1):68–72, 1988.

[100] S.F Boys and F. Bernardi. The Calculation of Small Molecular Interactions by the Differences of Separate Total Energies. Some Procedures with Reduced Errors. *Mol. Phys.*, 19(4):553–566, 1970.

[101] H. Valdés, V. Klusḱ, Michal Pitoňḱ, Otto Exner, I. Starý, P. Hobza, and L. Rulíšek. Evaluation of the Intramolecular Basis Set Superposition Error in the Calculations of Larger Molecules: [n]helicenes and Phe-Gly-Phe Tripeptide. *J. Comput. Chem.*, 29(6):861–870, 2008.

[102] M. Bracker, M. K. Kubitz, C. Czekelius, C. M. Marian, and M. Kleinschmidt. Computer-Aided Design of Fluorinated Flavin Derivatives by Modulation of Intersystem Crossing and Fluorescence. *ChemPhotoChem*, 6(7):e202200040, 2022.

[103] D. Jacquemin, B. II Moore, A. Planchat, C. Adamo, and J. Autschbach. Performance of an Optimally Tuned Range-Separated Hybrid Functional for 0–0 Electronic Excitation Energies. *J. Chem. Theory Comput.*, 10(4):1677–1685, 2014.

[104] T. M. Henderson, A. F. Izmaylov, G. Scalmani, and G. E. Scuseria. Can Short-Range Hybrids Describe Long-Range-Dependent Properties? *J. Chem. Phys.*, 131(4):044108, 07 2009.

[105] F. Weigend and R. Ahlrichs. Balanced Basis Sets of Split Valence, Triple Zeta Valence and Quadruple Zeta Valence Quality for H to Rn: Design and Assessment of Accuracy. *Phys. Chem. Chem. Phys.*, 7:3297–3305, 2005.

[106] E. Runge and E. K. U. Gross. Density-Functional Theory for Time-Dependent Systems. *Phys. Rev. Lett.*, 52:997–1000, Mar 1984.

[107] E. K. U. Gross and W. Kohn. Time-Dependent Density-Functional Theory. In P. O. Löwdin, editor, *Density Functional Theory of Many-Fermion Systems*, volume 21 of *Advances in Quantum Chemistry*, pages 255–291. Academic Press, 1990.

[108] A. Dreuw and M. Head-Gordon. Single-Reference ab Initio Methods for the Calculation of Excited States of Large Molecules. *Chem. Rev.*, 105(11):4009–4037, 2005.

[109] S. Hirata and M. Head-Gordon. Time-dependent Density Functional Theory Within the Tamm–Dancoff Approximation. *Chemical Physics Letters*, 314(3):291–299, 1999.

[110] E. Cancés, B. Mennucci, and J. Tomasi. A New Integral Equation Formalism for the Polarizable Continuum Model: Theoretical Background and Applications to Isotropic and Anisotropic Dielectrics. *J. Chem. Phys.*, 107(8):3032–3041, 08 1997.

[111] S. Grimme and M. Waletzke. A Combination of Kohn–Sham Density Functional Theory and Multi-Reference Configuration Interaction Methods. *J. Chem. Phys.*, 111(13):5645–5655, 10 1999.

[112] C. M. Marian, A. Heil, and M. Kleinschmidt. The DFT/MRCI Method. *WIREs Comput. Mol. Sci*, 9(2):e1394, 2019.

[113] I. Lyskov, M. Kleinschmidt, and C. M. Marian. Redesign of the DFT/MRCI Hamiltonian. *J. Chem. Phys.*, 144(3):034104, 01 2016.

[114] M. Kleinschmidt, C. M. Marian, M. Waletzke, and S. Grimme. Parallel Multireference Configuration Interaction Calculations on Mini-β-Carotenes and β-Carotene. *J. Chem. Phys.*, 130(4):044708, 01 2009.

[115] A. D. Becke. A New Mixing of Hartree–Fock and Local Density-Functional Theories. *J. Chem. Phys.*, 98(2):1372–1377, 01 1993.

[116] J. Tatchen, N. Gilka, and C. M. Marian. Intersystem Crossing Driven by Vibronic Spin–Orbit Coupling: A Case Study on Psoralen. *Phys. Chem. Chem. Phys.*, 9:5209–5221, 2007.

[117] M. Etinski, J. Tatchen, and C. M. Marian. Time-Dependent Approaches for the Calculation of Intersystem Crossing Rates. *J. Chem. Phys.*, 134(15):154105, apr 2011.

[118] T. Böhmer, M. Kleinschmidt, and C. M. Marian. Toward the Improvement of Vibronic Spectra and Non-Radiative Rate Constants Using the Vertical Hessian Method. *J. Chem. Phys.*, 161(9):094114, 09 2024.

[119] C. Adamo and V. Barone. Toward Reliable Density Functional Methods Without Adjustable Parameters: The PBE0 Model. *J. Chem. Phys.*, 110(13):6158–6170, 04 1999.

[120] J. D. Chai and M. Head-Gordon. Long-Range Corrected Hybrid Density Functionals With Damped Atom–Atom Dispersion Corrections. *Phys. Chem. Chem. Phys.*, 10:6615–6620, 2008.

[121] Martin Kleinschmidt, Jörg Tatchen, and Christel M. Marian. Spin–Orbit Coupling of DFT/MRCI Wavefunctions: Method, Test Calculations, and Application to Thiophene. *J. Comput. Chem.*, 23(8):824–833, 2002.

[122] O. Weingart, A. Nenov, P. Altoè, I. Rivalta, J. Segarra-Martí, I. Dokukina, and M. Garavelli. COBRAMM 2.0 —A Software Interface for Tailoring Molecular Electronic Structure Calculations and Running Nanoscale (QM/MM) Simulations. *J. Mol. Model.*, 24(9):271, 2018.

[123] D. R. Dombrowski, T. Schulz, M. Kleinschmidt, and C. M. Marian. R2022: A DFT/MRCI Ansatz with Improved Performance for Double Excitations. *J. Phys. Chem. A*, 127(8):2011–2025, 2023.

6.2 List of Abbreviations

AH	**A**diabatic **H**essian
AN	spiro[9,10-dihydro-9-oxoanthracene-10,2'-5'6'-benzindan]
AS	**A**diabatic **S**hift
ASF	**A**diabatic **S**hift and **F**requencies
BO	**B**orn-**O**ppenheimer
BSSE	**B**asis **S**et **S**uperposition **E**rror
CB	4-Pentyl-4'-**C**yano**B**iphenyl
CI	**C**onfiguration **I**nteraction
CIS	**C**onfiguration **I**nteraction **S**ingles
CISD	**C**onfiguration **I**nteraction **S**ingles **D**oubles
CP	**C**ounter**p**oise
CPU	**C**entral **P**rocessing **U**nit
CSF	**C**onfiguration **S**tate **F**unction
CT	**C**harge **T**ransfer
CZT1	**C**arbene-**Z**inc-**T**hiolate **1**: [Zn($^{4\text{-H}}$bdt)($^{\text{Menth}}$cAAC)]
DFT	**D**ensity **F**unctional **T**heory
DFT/MRCI	**D**ensity **F**unctional **T**heory and **M**ulti**r**eference **C**onfiguration **I**nteraction
DMAC	9,9-**D**i-**M**ethyl-9,10-Dihydro-**Ac**ridine
EET	**E**xcitation **E**nergy **T**ransfer
EPIC	(1S)-Dehydro-**EPIC**amphor
ESA	**E**xcited **S**tate **A**bsorption
FC	**F**ranck–**C**ondon
FCF	**F**ranck–**C**ondon **F**actor
FCP	**F**ranck–**C**ondon **P**oint
FFT	**F**ast **F**ourier **T**ransformation
FWHM	**F**ull **W**idth at **H**alf **M**aximum
HF	**H**artree-**F**ock

HOMO	**H**ighest **O**ccupied **M**olecular **O**rbital
HT	**H**erzberg–**T**eller
IR	**I**nfra**r**ed
IC	**I**nternal **C**onversion
IM	**Im**idazole
ISC	**I**nter**s**ystem **C**rossing
IVR	**I**nternal **V**ibrational **R**elaxation
LE	**L**ocal **E**xcitation
LED	**L**ight **E**mitting **D**iode
LU	**L**ower **U**pper
LUMO	**L**owest **O**ccupied **M**olecular **O**rbital
MCH	**M**ethyl-**C**yclo**h**exane
ModISC	**Mod**ulation of **I**nter**s**ystem **C**rossing
MRCI	**M**ulti**r**eference **C**onfiguration **I**nteraction
NMA	**N**-**M**ethyl **A**cridone
NMAM-B	**N**-**M**ethyl **A**cridone-**M**ethyl-**B**utyrat
NMAM-bFPUH	**N**-**M**ethyl **A**cridone-**M**ethyl-6-(3-(3,5-**b**is(**T**rifluoromethyl)**P**henyl)**U**reido)**H**exanoat)
MM	**M**olecular **M**echanics
OLED	**O**rganic **L**ight **E**mitting **D**iode
OMP	**O**pen **M**ulti-**P**rocessing
PCM	**P**olarizable **C**ontinuum **M**odel
PES	**P**otential **E**nergy **S**urface
PEG	**P**oly-**E**thylene **G**lycol
PY	**Py**razine
QA	**Q**uasi-**A**xial
QE	**Q**uasi-**E**quatorial
QM	**Q**uantum **M**echanics
rISC	**r**everse **I**nter**s**ystem **C**rossing

RMSD	**R**oot-**M**ean-**S**quare **D**eviation
RTG	**R**esearch **T**raining **G**roup
SES	**S**olvent **E**xcluding **S**urface
SOC	**S**pin–**O**rbit **C**oupling
SOCME	**S**pin–**O**rbit **C**oupling **M**atrix **E**lement
SVD	**S**ingular **V**alue **D**ecomposition
TAA	**T**ri**a**ryl**a**mine
TADF	**T**hermally **A**ctivated **D**elayed **F**luorescence
TDA	**T**amm-**D**ancoff **A**pproximation
TDDFT	**T**ime-**D**ependent **D**ensity **F**unctional **T**heory
tFMPBU	1-(3,5-bis (**t**ri-**F**luoro**m**ethyl)**P**henyl)-3-**Bu**tylurea)
THF	**T**etra**h**ydro**f**uran
TPN	**T**ere**p**hthalo**n**itrile
TRZ	2,4,6-**Tr**iphenyl-1,3,5-Tria**z**ine
UV	**U**ltra**v**iolet
VG	**V**ertical **G**radient
VGF	**V**ertical **G**radient and **F**requencies
VH	**V**ertical **H**essian
VIS	**Vis**ible
VR	**V**ibrational **R**elaxation

6.3 List of Figures

6.4 List of Tables

7 Appendix

7.1 Project Specific Computational Details

The technical details varied for each project due to the fundamentally different nature of the systems that were studied. For instance, calculations required different basis sets and functionals depending on the specific system. Additionally, standard calculations were not sufficient for all systems and had to be complemented, for example, by computations accounting for vibronic effects and going beyond Condon approximation. Furthermore, the methods evolved over time, leading to variations in the choice of methodology across different projects. As a result, no uniform approach could be established for calculating vertical excitation energies, for example. The computational details are therefore tailored to each project and will be explained in the subsequent sections.

Technical Details: DMAC-TRZ Project

The ground and excited state geometries of both conformers of DMAC-TRZ were optimized using the Gaussian16[50] program package and DFT at LC-wHPBE[104]/def2-SVP(P)[105] level of theory. The utilization of the range-separated hybrid functional required a tuning procedure[103] for the range-separation parameter ω (see figure 7.1). TDDFT[106–108] was used for the optimization of the excited singlet states. Additionaly, the Tamm-Dancoff approximation[109] was used for the optimization of the excited triplet states. Solvent–solute interactions (MCH) were included through the PCM.[110] The analytic calculation of harmonic vibrational frequencies was performed using the Gaussian16 program.

Vertical and adiabatic excitation energies and optical electronic properties were calculated using the DFT/MRCI[111–114] method. 20 roots were calculated for each singlet and triplet manifold (BH-LYP[115], Grid = m4, scfconv = 8, denconv = 1d-7, esel = 1.0). The R2016[113] Hamiltonian was used.

Vibronic spectra and nonradiative rate constants were computed using the VIBES[27,37,38,116–118] program. For symmetry forbidden transitions the expressions had to be expanded to a Herzberg-Teller scheme. Numerical derivatives of the electric dipole transition moments and the SOCMEs with respect to the normal coordinates were computed using the GRADIENATOR[67] by distorting the geometry from its equilibrium geometry along each normal mode vibration in positive and negative direction. We utilized the VH Method[118] to obtain vibrationally resolved absorption and emission spectra for both conformers.

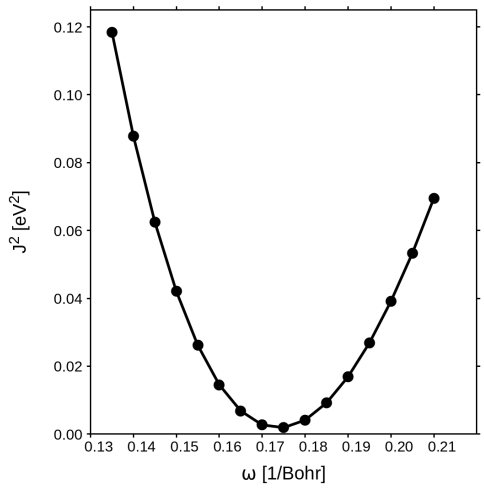

Figure 7.1: Optimal tuning procedure[103] for the range-separated hybrid functional LC-wHPBE.[104] A range-separation parameter of $\omega = 0.175\ \mathrm{bohr}^{-1}$ was chosen.

Technical Details: AN Project

The ground and excited state geometries of AN were optimized using the Gaussian16[50] program package and DFT at PBE0[119]/def2-TZVP[105] level of theory. TDDFT[106–108] was used for the optimization of the excited singlet states. Additionaly, the Tamm-Dancoff approximation[109] was used for the optimization of the excited triplet states. Solvent–solute interactions were included through the PCM[110] (Butyronitrile). The analytic calculation of harmonic vibrational frequencies was performed using the Gaussian16 program.

The normal mode frequencies and coordinates were further utilized to generate FCFs and FC weighted densities of states for determining spectral profiles and rate constants. The phosphorescence spectra were computed using the AH method and the VH method[44,118] was used to compute the triplet absorption spectrum for a transition that was identified using the DFT/MRCI method (BH-LYP[115], Grid = m4, scfconv = 8, denconv = 1d-7, esel = 1.0).

Technical Details: TAA-TPN Project

The ground and excited state geometries of all emitters in the series consiting of a TAA donor and TPN acceptor were optimized using the Gaussian16[50] program package and DFT at ωB97X-D[120]/def2-SVP(P)[105] level of theory. The utilization of the range-separated hybrid functional required a tuning procedure[103] for the range-separation parameter ω (see figure 7.2). TDDFT[106–108] was used for the optimization of the excited singlet states. Additionaly, the Tamm-Dancoff approximation[109] was used for the optimization of the excited triplet states. Solvent–solute interactions were included through the PCM[110] (Toluene). The analytic calculation of harmonic vibrational frequencies was performed using the Gaussian16 program.

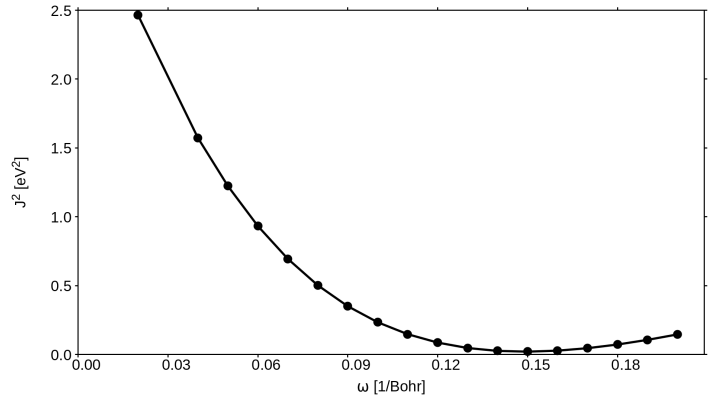

Figure 7.2: Optimal tuning procedure[103] for the range-separated hybrid functional ωB97X-D.[104] A range-separation parameter of $\omega = 0.15\mathrm{bohr}^{-1}$ was chosen.

Vertical and adiabatic excitation energies and optical electronic properties were calculated using the DFT/MRCI[111–114] method. 20 roots were calculated for each singlet and triplet manifold (BH-LYP[115], Grid = m4, scfconv = 8, denconv = 1d-7, esel = 1.0). The R2016[113] Hamiltonian was used. SOCMEs were computed in atomic mean-field approximation using SPOCK.[121] Vibronic spectra and nonradiative rate constants were computed using the VIBES[27,37,38,116–118] program and the utilization of the VH method.[118] For symmetry forbidden transitions the expressions had to be expanded to a Herzberg-Teller scheme. Numerical derivatives of the electric dipole transition moments and the SOCMEs with respect to the normal coordinates were computed using the GRADIENATOR[67] by distorting the geometry from its equilibrium geometry along each normal mode vibration in positive and negative direction.

Technical Details: NMA Derivatives Project

The ground and excited state geometries of all NMA derivatives were optimized using the Gaussian16[50] program package and DFT at PBE0[119]/def2-SVP(P)[105] level of theory. TDDFT[106–108] was used for the optimization of the excited singlet states. Additionaly, the Tamm-Dancoff approximation[109] was used for the optimization of the excited triplet states. Solvent–solute interactions were included through the PCM[110] (Toluene and THF) and QM/MM models[122] (Crystal environment; these computations specifically were performed by Markus Putscher). The analytic calculation of harmonic vibrational frequencies was performed using the Gaussian16 program.

Vertical and adiabatic excitation energies and optical electronic properties were calculated using the DFT/MRCI[111–114] method. 10 roots were calculated for each singlet and triplet manifold (BH-LYP[115], Grid = m4, scfconv = 8, denconv = 1d-7, esel = 1.0). The R2016[113] and R2022[123] Hamiltonian were used.

Vibronic spectra and nonradiative rate constants were computed using the VIBES[27,37,38,116–118] program and utilizing the VH method.[118]

7.2 VIBES Input keywords

The following section explains the keywords that allow the user to operate the VIBES program, control the calculations, and manage the generated output. All essential keywords are collected in a single file and passed to the program when executing a calculation.

General keywords

```
$end
```

The input of keywords is concluded with $end. Only entries provided by the user before this keyword will be considered for the calculation. It is the only keyword that is mandatory and is required to run a computation. For all other keywords there are default values that are applied if they are not present in the input file.

```
$# any_keyword
```

Quick editing and modification of the input can be achieved by commenting out individual keywords by placing a # at the beginning of the line. Entries in such lines are ignored by the program.

Method specific keywords

```
$method = [static / dynamic]
```

This keyword defines the method used to calculate the vibrational overlap. In the static approach, the FCF are explicitly calculated. For large molecules, it becomes necessary to significantly limit the number of quanta from and into which transitions can occur, as the number of overlap integrals to be computed increases substantially. In the dynamic approach, all components required for the calculation of the correlation function are computed. The desired rate constant or spectrum is then obtained through numerical integration or an FFT of the correlation function.

```
$vertical [gradient / hessian] [abs / emi]
```

This keyword selects whether, and if so, which vertical model is used for the simulation of the vibronic transition. The options are VH and VG. In both cases, it must also be specified whether the process formally corresponds to absorption (energy increase, positive vertical energy difference) or emission (energy decrease, negative vertical energy difference). This specification is necessary to correctly calculate and display the extrapolated adiabatic energy difference and is necessary even for the computation of nonradiative rate constants.

$spectrum

By default, the VIBES program calculates a rate constant. However, if the user wishes to calculate the vibronic spectrum, this keyword must be specified.

$interval = REAL

This keyword defines the time interval over which the correlation function is integrated. The input is provided as a REAL value in femtoseconds.

$npoints = INT

This keyword determines the number of integration points for the numerical integration of the correlation function. It should be noted that, as a prerequisite for the FFT in the calculation of a vibronic spectrum, the number of integration points must be a power of 2. If this condition is not met by the user, the number of integration points will be rounded to the nearest power of 2, which may be either higher or lower. Also, in case the computed rate constant is negative, it is recommended to increase the number of integration points.

$temperature = REAL

The temperature can be controlled using this keyword. It should be noted that the consideration of temperature effects is not enabled by default. Temperature effects will only be taken into account if the keyword is specified and the selected temperature is non-zero. The temperature can be specified with arbitrary precision as a REAL value.

$damping = REAL

This keyword defines the width of the Gaussian function used to dampen the correlation function, specified in wavenumbers as a REAL.

Keywords for specific data supply

$deltae = REAL

The adiabatic energy difference between the initial and final states of the vibronic transition can be defined using this keyword. It is important to specify whether the process is an absorption or emission process. The energy difference can be given with arbitrary precision as a REAL in wave numbers but the sign may change according to the kind of process.

```
$eta = REAL
```

This keyword defines the energy interval in wave numbers to seek for vibrational state of the final electronic state in the static approach. For the dynamic approach, however, it can be omitted. If it is defined the value will be used as a synonym for the $damping keyword that defines the damping factor of the correlation function.

```
$elec = REAL
```

As described in section 2.2.2.1, the calculation of rate constants and vibronic spectra is divided into the calculation of the electronic and vibrational parts. The electronic coupling matrix element must be calculated beforehand and provided to the VIBES program through this keyword. The specification of the SOCME is essential for the calculation of rate constants, but not necessary for the calculation of vibronic spectra within the Condon approximation. The matrix element is provided as a REAL in wave numbers.

```
$deriv INT0
INT1  REAL1
INT2  REAL2
...     ...
```

The derivatives of the transition dipole moment or the SOC with respect to the normal mode vibrations can be specified with this keyword. INT0 expects the number of normal modes for which numerical gradients will be provided and the subsequent lines will be filled with the number of the normal mode and the correspondent derivative. This keyword is used if the derivative is summed over all three Cartesian directions.

```
$alpha_x/y/z = REAL
```

The direct coupling of the x-, y- and z-component of the operator (*e.g.* SOC) can be supplied using this keyword. It is only used when $deriv is given.

```
$derx/y/z INT0
INT1  REAL1
INT2  REAL2
...     ...
```

The derivatives of the transition dipole moment or the SOC with respect to the normal mode vibrations can be specified with this keyword. INT0 expects the number of normal modes for which numerical gradients will be provided and the subsequent lines will be filled with the number of the normal mode and the correspondent derivative.

```
$nac INT0
INT1  REAL1
INT2  REAL2
...     ...
```

Non-adiabatic coupling elements with respect to all normal modes can be specified here for the calculation of IC rate constants.

```
$vibs [gaufreq / mopac]
FILENAME1
FILENAME2
```

The normal modes and corresponding frequencies necessary for simulating the vibronic transition can be extracted from previously performed frequency analyses using this keyword. The user has the option to choose between two different interfaces: one to Gaussian16 and one to Mopac. The next two lines should then contain the file names where the corresponding normal modes are located. When performing frequency analyses with the Gaussian16 program, it is important to ensure that the normal modes and frequencies are specified with sufficient accuracy (*freq=HPModes*).

```
$coord-files
FILENAME1
FILENAME2
```

Similar to the normal modes and corresponding frequencies, the geometries of the initial and final states can also be defined. The geometry can also be taken from the frequency calculation.

General stearing keywords

```
$zeromoment = REAL
```

This keyword defines the threshold to decide whether one of the moments of inertia is vanishingly small. The default value is defined to be 1×10^{-4}.

```
$modediscard = REAL
```

This keyword allows defining the threshold for the minimum frequency of a normal mode that should still be used for further calculations. All frequencies that have an eigenvalue below that threshold will be discarded.

Keywords to control the output

```
$transout REAL
```

This keyword can be used in the static approach only. It defines whether information is printed about FC integrals that are larger than the defined threshold. The threshold is given as a REAL. Be careful selecting a threshold that is too small. It can greatly effect the number of integrals that a printed.

```
$print = INT

$print 1: normal output
$print 10: add quants, delta and duschinskymatrix
$print 20: add more from deltabuild
$print 30: add eckart things
$print 40: add gaussread/mopacread things
$print 50: add internal things
```

Various additional information can be provided to the user. This can assist in understanding or further analyzing important normal modes or Duschinsky mixings. For the relevant supplementary information, this keyword can be used with a suitable integer.

```
$debug
```

To activate all settings at once, the debug view can be started. However, this is only recommended for program development and not for general use of the VIBES program.

7.3 Supplemenatry Derivations

Derivation of the Duschinsky Transformation

For two different sets of normal coordinates $\mathbf{Q}_1$ and $\mathbf{Q}_2$ the relationship between normal mode eigenvectors ($\mathbf{L}_1$ and $\mathbf{L}_2$) and spatial displacements in Cartesian coordinates, x, can be expressed as follows:

$$\mathbf{L}_1\mathbf{Q}_1 = \mathbf{M}^{\frac{1}{2}}(x - x_{01}) \tag{7.1}$$

$$\mathbf{L}_2\mathbf{Q}_2 = \mathbf{M}^{\frac{1}{2}}(x - x_{02}) \tag{7.2}$$

Equation 7.2 can be reformulated with respect to the variable x.

$$\mathbf{M}^{-\frac{1}{2}}\mathbf{L}_2\mathbf{Q}_2 = \mathbf{M}^{-\frac{1}{2}}\mathbf{M}^{\frac{1}{2}}(x - x_{02}) \tag{7.3}$$

$$\mathbf{M}^{-\frac{1}{2}}\mathbf{L}_2\mathbf{Q}_2 + x_2 = x \tag{7.4}$$

Combining equation 7.1 and 7.4 yields:

$$\mathbf{L}_1\mathbf{Q}_1 = \mathbf{M}^{\frac{1}{2}}(x - x_{01}) \tag{7.5}$$

$$\mathbf{L}_1\mathbf{Q}_1 = \mathbf{M}^{\frac{1}{2}}(\mathbf{M}^{-\frac{1}{2}}\mathbf{L}_2\mathbf{Q}_2 + x_{02} - x_{01}) \tag{7.6}$$

$$\mathbf{L}_1^{-1}\mathbf{L}_1\mathbf{Q}_1 = \mathbf{L}_1^{-1}\mathbf{L}_2\mathbf{Q}_2 + \mathbf{L}_1^{-1}\mathbf{M}^{\frac{1}{2}}(x_{02} - x_{01}) \tag{7.7}$$

Leading to the Duschinsky transformation equation:

$$\mathbf{Q}_1 = \mathbf{J}\mathbf{Q}_2 + \mathbf{K} \tag{7.8}$$

where $\mathbf{J} = \mathbf{L}_1^{-1}\mathbf{L}_2$ is the Duschinsky rotation matrix and $\mathbf{K} = \mathbf{L}_1^{-1}\mathbf{M}^{\frac{1}{2}}(x_{02} - x_{01})$ is the displacement vector in Cartesian coordinates.

Derivation of the Prefactor for the Displacement Vector

Since both the mass-weighted coordinate difference and the frequencies of the normal modes are not dimensionless, the displacement vector is made dimensionless by applying a prefactor, $conv$. This prefactor, adopted from the program *HOTFCHT* by Roland Berger[47], is calculated as follows:

$$\begin{aligned} conv &= \sqrt{\frac{4 * \pi^1 * c}{10 * N_A * h}} * 10^{-10} \\ &= \sqrt{\frac{4 * 3.1415^2 * 2.9979 \times 10^8}{10 * 6.0260 \times 10^{23} * 6.6260 \times 10^{-34}}} * 10^{-10} \sqrt{\frac{m * s^{-1}}{mol^{-1} * kg * m^2 * s^{-1}}} \\ &= 0.1722 \sqrt{\frac{mol}{kg * m}} \end{aligned} \tag{7.9}$$

7.4 Included Papers

Paper No.1

Toward the improvement of vibronic spectra and nonradiative rate constants using the vertical Hessian method

Tobias Böhmer, Martin Kleinschmidt, and Christel M. Marian
J. Chem. Phys. (2024)
DOI: 10.1063/5.0220361

Contribution: The implementation and validation of the VH method was carried out by me. I visualised all scientific results and I wrote and revised the manuscript.

The Journal of Chemical Physics ARTICLE pubs.aip.org/aip/jcp

Toward the improvement of vibronic spectra and non-radiative rate constants using the vertical Hessian method

Cite as: J. Chem. Phys. 161, 094114 (2024); doi: 10.1063/5.0220361
Submitted: 24 May 2024 • Accepted: 15 August 2024 •
Published Online: 5 September 2024

Tobias Böhmer, Martin Kleinschmidt, and Christel M. Marian[a)]

AFFILIATIONS

Institute for Theoretical and Computational Chemistry, Faculty of Mathematics and Natural Sciences, Heinrich Heine University Düsseldorf, Universitätsstraße 1, 40225 Düsseldorf, Germany

[a)]Author to whom correspondence should be addressed: christel.marian@hhu.de

ABSTRACT

For the computation of vibrationally resolved electronic spectra, various approaches can be employed. Adiabatic approaches simulate vibronic transitions using harmonic potentials of the initial and final states, while vertical approaches extrapolate the final state potential from the gradients and Hessian at the Franck–Condon point, avoiding a full exploration of the potential energy surface of the final state. Our implementation of the vertical Hessian (VH) method has been validated with a benchmark set of four small molecules, each presenting unique challenges, such as complex topologies, problematic low-frequency vibrations, or significant geometrical changes upon electronic excitation. We assess the quality of both adiabatic and vertical approaches for simulating vibronic transitions. For two types of donor–acceptor compounds with promising thermally activated delayed fluorescence properties, our computations confirm that the vertical approaches outperform the adiabatic ones. The VH method significantly reduces computational costs and yields meaningful emission spectra, where adiabatic models fail. More importantly, we pioneer the use of the VH method for the computation of rate constants for non-radiative processes, such as intersystem crossing and reverse intersystem crossing along a relaxed interpolated pathway of a donor–acceptor compound. This study highlights the potential of the VH method to advance computational vibronic spectroscopy by providing meaningful simulations of intricate decay pathway mechanisms in complex molecular systems.

I. INTRODUCTION

Vibronic spectroscopy exploits the interaction of light and matter to determine fundamental properties of molecules. It is a crucial component in photochemistry to characterize chemical systems regarding their photophysical attributes. Various experimental methods such as one-photon, two-photon absorption, and one-photon emission experiments;[1,2] resonance Raman spectroscopy;[3,4] and circular polarized luminescence spectroscopy are available for investigating these properties. Quantum chemical simulations aid in elucidating experiments and making precise predictions,[5] necessitating a robust framework for describing molecular vibrations under light interactions.

Vibronic spectroscopy involves electronic and vibrational transitions at the same time, distinguishing it from mere electronic excitations. In general, there are two approaches for the description of vibronic transitions. The time-independent (TI)[6–8] approach builds vibronic spectra by computing individual vibrational transitions independent of each other. Despite recent advancements in the algorithms of Berger *et al.*[9] and efficient strategies for reducing the number of Franck–Condon (FC) integrals that need to be computed,[10] this approach remains prohibitively expensive for large systems. The time-dependent (TD)[11–13] approach, on the other hand, involves the Fourier transformation of the autocorrelation function of the transition dipole moment to obtain the envelope of all vibronic transitions at the same time, pioneered by Heller.[14,15]

The complex description of the kinetic energy operator in curvilinear coordinates, as well as the associated problems with its description in Cartesian coordinates, has been addressed by

Podolski.[16] Currently, robust algorithms exist for transforming the energy operator[17,18] and molecular motions[19–25] into the internal coordinate system. Recent advancements enable the consideration of Herzberg–Teller effects[26,27] for the computation of vibronic transitions and propose to use adiabatic and vertical approaches[28–31] to relate vibrational motions of two distinct electronic states.

Adiabatic models, such as adiabatic Hessian (AH), rely on utilizing the harmonic potentials at the minimum geometries of both the initial and final states. In particular, AH exploits harmonic approximation to describe the potential energy surface (PES) around the equilibrium geometries of the electronic states as a quadratic function. This yields meaningful results for rigid systems for which spatial displacements are small and the harmonic approximation is valid. In contrast, the vertical Hessian (VH) approach only requires the optimized geometry of the initial state of a vibronic transition. The Hessian matrix and gradients at the FC point are sufficient to extrapolate the PES of the final state. This efficient strategy minimizes computational overhead by circumventing the necessity for a full exploration of the PES. Cerezo and co-workers[31,32] could show that vertical approaches outperform adiabatic approaches for the simulation of vibronic spectra, particularly for application cases where AH fails due to the inability of Cartesian coordinates in describing curvilinear displacements.

This study shortly highlights the differences between adiabatic and vertical approaches. We apply both approaches to compounds comprising donor–acceptor motifs with promising photophysical properties. Donor–acceptor compounds typically exhibit low-lying charge-transfer states. While the separation of electron and hole densities ensures a small energy splitting, conducive to favorable thermally activated delayed fluorescence (TADF) conditions, the orthogonal alignment of the donor and acceptor moiety is responsible for vanishingly small spin–orbit coupling matrix elements between the lowest excited singlet and triplet states. These emitters emerge as promising TADF candidates when low-frequency vibrations twist both donor and acceptor moieties toward each other. However, these twisting modes result in large spatial displacements and, therefore, pose challenges for the simulation of vibronic transitions. We show that use of the VH method can greatly improve simulated emission spectra and non-radiative rate constants for such problematic application cases.

II. THEORETICAL BACKGROUND

A vertical model was initially introduced by Hazra *et al.*[33] in 2004 to simulate the photophysical properties of ethylene in the gas phase. Avila Ferrer *et al.*[34] established a standardized nomenclature for various methods of simulating vibronic transitions. While all approaches have the same description of the initial state PES, they differ in constructing and approximating the PES of the final state. Our implementation of the VH method is rooted in the theoretical framework outlined by Avila Ferrer *et al.*[34] The equations were adapted and supplemented with derivations as needed.

A. Adiabatic approaches

For an N-atomic system, we consider an electronic transition from an initial state $|\Psi_1\rangle$ to a final state $|\Psi_2\rangle$. The harmonic potential of the initial state V_1 can be expressed in matrix form as follows:

$$V_1(\mathbf{Q}_1) = \frac{1}{2}\,\mathbf{Q}_1^{\mathrm{T}}\,\Omega_1^2\,\mathbf{Q}_1. \tag{1}$$

The diagonal matrix Ω_1 contains all normal mode frequencies of the initial state, whereas $\mathbf{Q}_1$ comprises the corresponding normal modes in vector form. For a set of normal coordinates, the relationship between the normal modes in vector form and the spatial displacements [difference of Cartesian coordinates (see Fig. 1) at a displaced geometry x and the equilibrium geometry of the initial state x_{01}] is given by the following expression:

$$\mathbf{L}_1\mathbf{Q}_1 = \mathbf{M}^{\frac{1}{2}}(x - x_{01}), \tag{2}$$

where $\mathbf{L}_1$ comprises the eigenvectors of the force constant matrix of the initial state, which are massweighted using $\mathbf{M}$. Two sets of normal modes can be related to each other through the so-called Duschinsky transformation,[35]

$$\mathbf{Q}_1 = \mathbf{J}\mathbf{Q}_2 + \mathbf{K}, \tag{3}$$

where $\mathbf{J}$ denotes the Duschinsky rotation matrix and $\mathbf{K}$ is the displacement vector.

Analogous to Eq. (1), the potential energy surface for the final state in its own basis and in the basis of the initial state can be written as follows:

$$V_2(\mathbf{Q}_2) = E_{ad} + \frac{1}{2}\,\mathbf{Q}_2^{\mathrm{T}}\,\Omega_2^2\,\mathbf{Q}_2, \tag{4}$$

$$V_2(\mathbf{Q}_1) = E_{ad} + \frac{1}{2}\mathbf{Q}_1^{\mathrm{T}}\mathbf{J}\Omega_2^2\mathbf{J}^{\mathrm{T}}\mathbf{Q}_1 - \mathbf{K}^{\mathrm{T}}\mathbf{J}\Omega_2^2\mathbf{J}^{\mathrm{T}}\mathbf{Q}_1 + \frac{1}{2}\mathbf{K}^{\mathrm{T}}\mathbf{J}\Omega_2^2\mathbf{J}^{\mathrm{T}}\mathbf{K}, \tag{5}$$

where E_{ad} is the energy difference between the two minima of the electronic states investigated and $1/2\mathbf{K}^{\mathrm{T}}\mathbf{J}\Omega^2\mathbf{J}^{\mathrm{T}}\mathbf{K}$ is the so-called reorganization energy from the FC point to the extrapolated minimum of the final state. Thus, $E_V = E_{ad} + E_{reorg}$ only yields an approximated value for the vertical excitation energy in adiabatic models and an estimate for the adiabatic energy in vertical models.

In addition to the AH method, Avila Ferrer *et al.*[34] also presented two approaches that use further limitations in order to simplify the simulation of vibronic transitions. For the so-called adiabatic shift (AS) model, only spatial displacements are taken into account since they are expected to dominate the structure of the spectra and the Duschinsky rotation effect is neglected. For the adiabatic shift and frequency (ASF) approach, the normal mode frequencies of the final state are extrapolated alongside the use of the gradients while still neglecting the Duschinsky mixing.

Since the construction of the final state PES within the adiabatic approach is performed at the minimum geometry of the corresponding initial and final states, where the harmonic approximation is most suitable, AH is expected to provide meaningful information about the 0–0 transitions and the onset of a spectrum. However, when the minimum geometries of the initial and final states are significantly displaced, the constructed harmonic potential of the final state can deviate strongly from the actual PES in the FC region. Therefore, we introduce vertical approaches in Sec. II B.

B. Vertical approaches

In contrast to adiabatic approaches, the potential energy surface of the final state in vertical approaches is extrapolated based

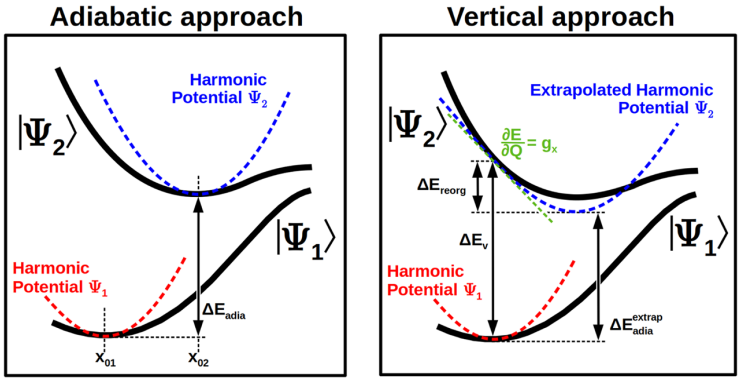

FIG. 1. Schematic picture for the adiabatic (left) and vertical (right) approaches. The strongly displaced (x_{01} and x_{02}) anharmonic potentials of two distinct electronic states $|\Psi_1\rangle$ and $|\Psi_2\rangle$ are indicated by the solid black lines. The corresponding dashed lines (red—initial state, blue—final state) represent the (extrapolated) harmonic potentials.

on vertical data (see Fig. 1). Using the vertical energy E_V from the equilibrium geometry of the initial state to the FC point of the final state, the gradients g_x, and the Hessian matrix $\mathbf{F}_x$ in Cartesian coordinates, the potential energy surface of the final state can be written as follows:

$$V_2(\mathbf{Q}_1) = E_V + g_x^{\mathrm{T}} x + \frac{1}{2} x^{\mathrm{T}} \mathbf{F}_x x \tag{6}$$

with

$$g = \mathbf{M}^{-\frac{1}{2}} \mathbf{L}_1 g_x, \tag{7}$$

$$\mathbf{F} = \mathbf{L}_1^{\mathrm{T}} \mathbf{M}^{-\frac{1}{2}} \mathbf{F}_x \mathbf{L}_1 \mathbf{M}^{-\frac{1}{2}}. \tag{8}$$

The Duschinsky rotation matrix within the vertical approach $\mathbf{J}_{VH}$ can be obtained through the diagonalization of the Hessian matrix $\mathbf{F}$,

$$\mathbf{J}_{VH} \mathbf{F} (\mathbf{J}_{VH})^{\mathrm{T}} = (\Omega_{VH})^2, \tag{9}$$

$$\mathbf{K}_{VH} = -\mathbf{J}_{VH} (\Omega_{VH})^{-2} (\mathbf{J}_{VH})^{\mathrm{T}} g. \tag{10}$$

In addition, for the vertical approaches, simplifications exist that either ignore the Duschinsky rotation effect, as in the vertical gradient (VG) model or adapt the normal mode frequencies while assuming vanishing Duschinsky mixings (vertical gradient and frequency model, VGF).

In the vertical approach, oftentimes normal modes with an imaginary frequency arise for the final state, as the frequency calculation is performed at a non-stationary point. A harmonic potential for these normal modes would result in a downward parabola, and the extrapolated potential would tend toward negative infinity. Therefore, it is necessary to implement a strategy for the treatment of normal modes with imaginary frequencies. For the calculation of vibronic spectra and non-radiative rate constants within this study, these modes are discarded. The focus is on the modes that influence the vibronic transitions most, while the technically problematic normal modes are ignored. Götze *et al.*[24] could already show that this approach is valid for large molecules since the number of normal modes with imaginary frequencies that occur is small.

Models such as AS, VG, or VGF—mentioned earlier—neglect the effect of Duschinsky mixing and also use the normal modes of the initial state with real frequencies for the final state (known as IMDHO model[36,37]), avoiding the occurrence of imaginary frequencies. However, the PES of two electronic states may differ significantly and thus these methods are no adequate models for the simulation of photophysical properties of the molecules investigated in this study. Toniolo and Persico[38] proposed to use a periodic potential for strongly anharmonic normal modes with imaginary frequencies to compute FC factors in the TI model. On the other hand, Hazra *et al.*[33] presented a meaningful alternative within the TD framework. They assume separability of the excited-state potential along its normal mode coordinates and compute a complete one-dimensional potential for imaginary frequency modes while freezing all the other normal modes. However, these strategies are associated with a high computational effort and are not feasible for large molecules.

C. Computation of vibronic spectra and non-radiative rate constants

The calculation of vibronic spectra and non-radiative rate constants is carried out using the program VIBES,[39,40] originally programmed by Jörg Tatchen in 2006 for the computation of intersystem crossing (ISC) rate constants employing a direct, TI approach. Several extensions have been added since then. Non-radiative rate constants and vibronic spectra can be computed using a dynamic TD approach,[39,40] and recently, corresponding equations for the computation of internal conversion (IC) rate constants were implemented.[41] In all cases, temperature effects can be considered using a Boltzmann distribution.

In the TI approach, FC factors are explicitly calculated. However, for large systems, the numerous possible vibronic transitions result in a high computational effort. For this reason, the number of

normal modes and vibrational levels that are taken into account have to be strongly limited. In the TD approach, on the other hand, FC factors are implicitly calculated via an analytical expression and no restrictions are needed. Within the framework of TD perturbation theory, the non-radiative rate constant for a vibronic transition from an initial singlet state $|\Psi_S\rangle$ to a final triplet state $|\Psi_T\rangle$, with given normal coordinates $\mathbf{Q}$ and the corresponding normal mode frequencies Ω, can be expressed using Fermi's golden rule. Both the electronic states can be related via Duschinsky transformation as in Eq. (3). In a case study on uracil, Etinski[42] could show that the inclusion of Duschinsky mixings for non-radiative processes between distinct electronic states with an energy gap of less than 6000 cm^{-1} is crucial. For this reason, we decided to compute all rate constants either with the AH or the VH method, both of which include Duschinsky mixing effects. With ΔE_{ST} being the energetic difference between the optimized geometries of both electronic states, respectively, the ISC rate constant in Condon approximation, for example, can be written as follows:

$$k_{ISC} = \frac{1}{Z}|\langle\Psi_S|\hat{H}_{SO}|\Psi_T\rangle|^2 \int_{-\infty}^{\infty} G(t) e^{\frac{it}{\hbar}\Delta E^0_{ST}} dt, \tag{11}$$

with the canonical partition function Z and the correlation function $G(t)$ between the harmonic oscillator eigenfuntions for the singlet and triplet states. For $G(t)$, an analytical expression can be derived within the harmonic oscillator model using Mehler's formula for Hermite polynomials,[43,44]

$$G(t) = \sqrt{\frac{\det(\mathbf{S}_S^{-1}\mathbf{S}_T^{-1}\Omega_S\Omega_T)}{\det(\mathbf{J}^T\Omega_T\mathbf{B}_T\mathbf{J}+\Omega_S\mathbf{B}_S)}}\sqrt{\frac{1}{\det(\mathbf{J}^T\Omega_T\mathbf{B}_T^{-1}\mathbf{J}+\Omega_S\mathbf{B}_S^{-1})}} \times e^{\mathbf{K}^T(\Omega_T\mathbf{B}_T\mathbf{J}(\mathbf{J}^T\Omega_T\mathbf{B}_T\mathbf{J}+\Omega_S\mathbf{B}_S)^{-1}\mathbf{J}\Omega_T\mathbf{B}_T-\Omega_T\mathbf{B}_T)\mathbf{K}}, \tag{12}$$

where $\mathbf{S}$ and $\mathbf{B}$ are diagonal matrices with $\mathbf{S}_{Sii} = \sinh((1/k_BT - it)\omega_{Si})$ and $\mathbf{S}_{Tii} = \sinh(i\omega_{T\ i}t)$ as well as $\mathbf{B}_{Sii} = \tanh(\omega_{S\ i}/2(1/k_BT))$ and $\mathbf{B}_{Tii} = \tanh(i\omega_{Ti}t/2)$. For the computation of non-radiative rate constants, a time-integration of Eq. (11) has to be performed, which is done numerically.

Domcke and co-workers[45] could show that the vibrational intensity distribution for an electronic transition depends, in the first place, on the PES of the final state in the Franck–Condon region. They derived a short-time expression for the computation of FC integrals that involves only the gradient of the final state at the initial state geometry. A different approach employs an approximation to Fermi's golden rule by using a cumulant expansion.[46,47] Etinski derived an extension to the computation of rate constants for ISC using a short-time approximation starting from the second-order cumulant expansion by keeping only the terms up to second order in time,[40]

$$k_{ISC}^{short} = |\langle\Psi_S|\hat{H}_{SO}|\Psi_T\rangle|^2 \sqrt{\frac{\pi}{\frac{1}{16}\sum_{i,j=1}^{N}\frac{\mathbf{R}_{ij}^2}{\omega_{S_i}\omega_{S_j}} + \frac{1}{4}\sum_{i=1}^{N}\frac{\mathbf{A}_i^2}{\omega_{S_i}}}} \times \exp\left(-\frac{\left(\frac{1}{4}\sum_{i,j=1}^{N}\frac{\mathbf{R}_{ij}}{\omega_{S_i}} + C - \Delta E^0_{ST}\right)^2}{\frac{1}{4}\sum_{i,j=1}^{N}\frac{\mathbf{R}_{ij}^2}{\omega_{S_i}\omega_{S_j}} + \sum_{i=1}^{N}\frac{\mathbf{A}_i^2}{\omega_{S_i}}}\right), \tag{13}$$

where $\mathbf{R} = \mathbf{J}^T\Omega_T^2\mathbf{J} - \Omega_S^2$, $C = 1/2\mathbf{K}^T\Omega_T^2\mathbf{K}$, and $\mathbf{A} = \mathbf{J}^T\Omega_T^2\mathbf{K}$. This approach is implemented in the program VIBES and was used here to compare the resulting rate constants for non-radiative processes using a short-time approximation [see Eq. (13)] to the outcome obtained by using the complete correlation function [see Eq. (11)]. The short-time approximation expression is attractive because there is no need for a numerical integration but the rate constant for a non-radiative transition can be computed analytically.

III. COMPUTATIONAL DETAILS

The molecular geometries and vibrational frequencies were computed with the Gaussian16 program package[48] employing B3-LYP[49] functional and 6-31G(d)[50,51] basis set for the benchmark molecules at (TD)DFT[52–54] level of theory with Tamm–Dancoff approximation[55] (TDA) for the triplet states to avoid triplet instabilities. The solvent environment was simulated using the polarizable continuum model[56–58] (PCM) with a solvent excluding surface (SES) implemented in Gaussian16. Vertical excitation energies were determined with a combined density functional theory and multireference configuration interaction (DFT/MRCI) method[59–61] using the R2016[62] Hamiltonian (or R2022[63] Hamiltonian when mentioned), employing a selection threshold of 0.8 Hartree with the associated parameter set. Spin–orbit coupling matrix elements were calculated utilizing the atomic mean-field approximation with the SPOCK.[64–66] All the vibronic spectra and non-radiative rate constants were computed with the recently adapted VIBES[39,40] program using the adiabatic and vertical approaches explained in this work (the vibronically resolved one-photon spectra are proportional to the Fourier transform of the underlying correlation function). The implementation of the VH method is rooted in the theoretical framework of Avila Ferrer *et al.*[34]

IV. BENCHMARK

To verify the implementation of the VH method, four test systems of varying size and complexity (Fig. 2) were selected and investigated using both adiabatic and vertical approaches. These examples were previously used to validate the transformation from Cartesian coordinates to internal coordinates for the computation of vibronic spectra in a study by Baiardi *et al.*[67] Since we utilized these systems for the testing of the implementation of internal coordinates in our own program code for the calculation of vibronic spectra, an extension of the study to the VH method, following the approach of Baiardi *et al.*, is a logical progression.

Imidazole (**IM**) and pyrazine (**PY**) serve as case studies of comparable size, for which there is significant interest in precisely simulating their photophysical properties and processes. **IM** is a substantial component of complex biological systems and, therefore, an important part in a range of biological photoreactions.[68] **PY,** on the other hand, is known for its prominent vibronic interactions between low-lying electronically excited states.[69] Both test cases undergo significant geometric changes upon electronic excitation, making the simulation of meaningful spectra challenging based on the AH method. The epicamphor derivative [(1S)-dehydroepicamphor, **EPIC**] presents a challenge in internal coordinates due to its complex topology, making simulations using an adiabatic approach in Cartesian coordinates inaccurate. Switching from the description in Cartesian to internal coordinates could already improve the simulated absorption and emission spectra.[67] However,

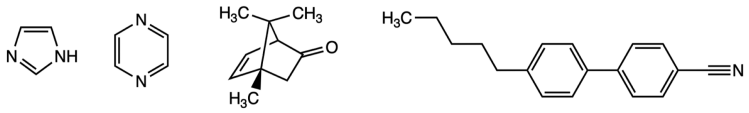

FIG. 2. Lewis structures of the molecules that were investigated in the benchmark. From left to right: imidazole (**IM**), pyrazine (**PY**), (1S)-dehydro-epicamphor (**EPIC**), and 4-Pentyl-4′-cyanobiphenyl (**CB**).

meaningful results can also be obtained using a vertical approach in Cartesian coordinates. While the geometric changes upon excitation are relatively small and a Duschinsky rotation determinant close to unity indicates a linear transformation, the effect of the VH method on the calculated spatial displacements is significant. The cyanobiphenyl derivative (4-Pentyl-4′-cyanobiphenyl, **CB**) poses a particular challenge for the calculation of vibronic spectra because low-frequency modes, typically manifesting as dihedral deformation vibrations, result in significant spatial displacements. Simulated spectra using the AH method are structure-less, too broad, and the calculated rate constants are unreliable. The use of internal coordinates promises to improve the treatment of linear components, such as cyano groups.[67] Meanwhile the focus of the VH method is on improving the description of low-frequency modes that besides in **CB** often occur in typical donor–acceptor systems as well.

A. Measures to rate the performance

To measure the performance of both adiabatic and vertical approaches, we define a range of parameters suitable for comparison. These parameters are not typically calculated within the standard framework of adiabatic or vertical approaches and are intended to help rationalize the results and critically compare both approaches in this study. They provide meaningful clues regarding the reliability for the simulation of vibronic transitions and can demonstrate that vertical approaches yield better and more valid results for strongly displaced systems. For the specific applications in this study, these criteria strongly advocate for the use of vertical approaches.

1. Duschinsky rotation determinant

Two sets of normal modes from different electronic states of a polyatomic molecule can be related via Duschinsky transformation as written in Eq. (3). Özkan's study[70] from 1990 revealed that this transformation is neither linear nor orthogonal. Upon employing Eckart conditions, two molecule-fixed axis systems can be related via a 3×3 rotation matrix $\mathbf{T}$ (which is referred to as axis-switching matrix). It is a unit matrix for a diatomic molecule, but for a polyatomic system, it is a function of the vibrational modes. The non-orthogonality of the transformation matrix results in a determinant that deviates from 1, indicating the transformation's limited applicability.[70,71] The validity of the Duschinsky transformation decreases with a smaller determinant. Therefore, the determinant serves as a useful measure for assessing its applicability in simulating vibronic transitions. On the one hand, that means we expect the AH and VH approaches to yield the same results for a Duschinsky determinant equal to 1. On the other hand, a Duschinsky determinant strongly deviating from 1 is calling for the use of the VH method.

For the vertical approach, the force constant matrix for the final state's PES is constructed at the optimized ground state geometry. The resulting eigenvectors that describe the rotation and spatial displacement between the initial state and the extrapolated final state are identical. Axis-switching effects[70,71] do not arise for this approach, and the determinant of the Duschinsky rotation matrix is expected to reach a value of exactly 1.[72]

2. Average Duschinsky projection

Independent of the determinant of the Duschinsky rotation matrix, the so-called average Duschinsky projection $\langle \mathbf{J}^2_{\max} \rangle$ indicates the strength of the couplings between the normal modes of the initial and final states. A column of the Duschinsky rotation matrix $\mathbf{J}$, for example, shows the coupling between one mode of the initial state and all the other modes of the final state. The corresponding vector (or matrix) elements can have absolute values ranging from 0 to 1.

The average Duschinsky projection over all normal modes of a given system is calculated as follows:

$$\langle \mathbf{J}^2_{\max} \rangle = \frac{1}{M} \sum_{i=1}^{M} \max_{1 \le f \le M} \left(\mathbf{J}^2_{if} \right), \tag{14}$$

where M represents the number of normal modes and the indices i and f denote the rotation matrix elements corresponding to vectors of the initial and final states, respectively. In consequence, an averaged Duschinsky projection value close to 1 indicates that the normal modes of the initial state can be clearly projected onto the normal modes of the final state. Conversely, a value significantly different from 1 suggests that the normal modes are strongly mixed. Using the VH method should increase the average Duschinsky projection compared to the AH method, especially for the rotation matrix elements of low-frequency vibrational modes.

3. Sum of squared displacements

Large geometrical changes upon vibronic transition, for example, are reflected in the displacement vector $\mathbf{K}$. Typically, normal modes exhibit significant displacements when they describe nuclear motions that are capable of transforming the geometry of the initial state into the geometry of the final state,

$$D^2 = \mathbf{K}^T \mathbf{K}. \tag{15}$$

The excited states of typical through-bond donor–acceptor systems oftentimes differ markedly in their dihedral angle. Such differences in the nuclear framework are described by low-frequency

vibrational torsional modes, for which the harmonic approximation, in general, provides only a poor description. Since these modes are either better described using an approach or completely omitted due to an imaginary frequency, the sum of all squared displacements is expected to decrease dramatically for critical application cases when switching from the AH method to either the VG or VH method. The sum of squared displacements D^2 is, therefore, a good measure for the displacement of the equilibrium geometries.

4. Energies

Both adiabatic and vertical approaches are approximations. As outlined in Sec. II, in the case of the AH method, the harmonic potentials are constructed around the minimum structure and are thus accurate for small geometric deviations from the equilibrium structures. In contrast, the vertical approach constructs the harmonic potential from the FC point but deviates due to extrapolation at the minimum of the final state. The errors of both methods will inevitably increase as the potential surfaces, or their minima, are more displaced from each other. However, these assumptions also imply that the approaches are well-suited for different application areas. An accurate description of the harmonic potential at the FC point results in a favorable description of the emission maxima and band structures, while the 0-0 energy and thus the onset of vibronic spectra are better described by harmonic potentials constructed at the minimum. Therefore, comparing the extrapolated adiabatic energy difference with the actual adiabatic energy difference facilitates the assessment of how well the extrapolation reflects the actual PES. This comparison is crucial for evaluating systematic errors associated with the VH method made by extrapolation.

In vibronic spectra, discrepancies between the extrapolated and true adiabatic energy differences result in shifted onsets while maintaining the spectral shape. In contrast, for non-radiative rate constants, the impact of the error can be significant, depending on the magnitude of the energy difference between the corresponding electronic states of a vibronic transition. While this value proves valuable for gauging the quality of VH calculations and evaluating the systematic error that is caused by the extrapolation, it will not be used to decide which approach should be applied for a meaningful simulation of a vibronic transition.

B. Benchmark results

For all the four test systems (see Fig. 2), the key characteristics mentioned in Sec. IV A are presented in Table I. Upon using the VH method, the Duschinsky determinant generally increases to a value of exactly 1. The increase in linearity is methodologically driven by extrapolation. The graphical representation of the Duschinsky rotation matrix (shown in Fig. 3), computed using both adiabatic and vertical approaches, immediately shows two peculiarities: (i) a reduced dimensionality of the rotation matrix in the VH method due to the omission of normal modes of the final state with imaginary frequencies and the corresponding counterparts of the initial state, and (ii) strongly reduced Duschinsky mixing effects (overall less off-diagonal matrix elements with higher values each) that directly manifest in an increased average Duschinsky projection ($AH = 0.522$ and $VH = 0.657$ for **IM**). The number of imaginary frequencies that occur for the frequency analysis at the optimized initial state geometry is different for each molecule in the benchmark set. It should be noted that for **IM**, 4 of 21 normal modes have an imaginary eigenvalue, while **PY** does not show any problematic normal modes and, consequently, has the same dimensionality in both approaches.

Independent of the investigated test system, the sum of all the squared spatial displacements decreases ($AH = 33.317$ and $VH = 6.286$ for **IM**). At the same time, the 0-0 overlap increases by a maximum of three orders of magnitude. This means that in the basis of the initial state, the extrapolated geometry of the final state is always less spatially displaced from the optimized geometry of the initial state.

A glance at the vertical excitation and reorganization energies shows that they are always reasonable estimates for the approximation of the "true" adiabatic energy difference between the corresponding electronic states. It should be noted that for the absorption case, the reorganization energy has to be subtracted from the vertical excitation energy, whereas it has to be added in case of emission. The extrapolated energy gap deviates most in the case of **IM**, which is a direct consequence of the large number of normal modes with

TABLE I. Summary of the above-mentioned key characteristics to measure the performance of the VH method compared to the AH approach.

	IM ($S_0 \rightarrow S_1$)			**PY** ($S_0 \rightarrow S_1$)		**EPIC** ($S_0 \rightarrow S_1$)		**CB** ($S_0 \rightarrow S_1$)	
Method and molecule	AH	VG	VH	AH	VH	AH	VH	AH	VH
Duschinsky determinant	0.980	1.000	1.000	0.999	1.000	0.992	1.000	0.980	1.000
Average Duschinsky projection	0.522	1.000	0.741	0.707	0.918	0.700	0.699	0.709	0.720
Sum of squared displacements	33.317	10.438	12.417	2.247	1.501	30.995	15.135	26.304	5.777
0-0 overlap	4.5×10^{-4}	7.4×10^{-2}	2.3×10^{-2}	4.5×10^{-1}	4.9×10^{-1}	1.8×10^{-3}	4.0×10^{-3}	4.7×10^{-3}	6.8×10^{-2}
Imaginary frequencies	⋯	⋯	4	⋯	0	⋯	2	⋯	4
$E^{ST}_{vert}(\mathrm{cm}^{-1})$	⋯	55 617	55 617	⋯	32 950	⋯	32 645	⋯	35 323
$E^{ST}_{reorg}(\mathrm{cm}^{-1})$	⋯	5669	6139	⋯	566	⋯	2821	⋯	1771
$E^{ST}_{adia}(\mathrm{cm}^{-1})$	46 173	49 948	49 478	32 083	32 384	29 584	29 824	32 909	33 552

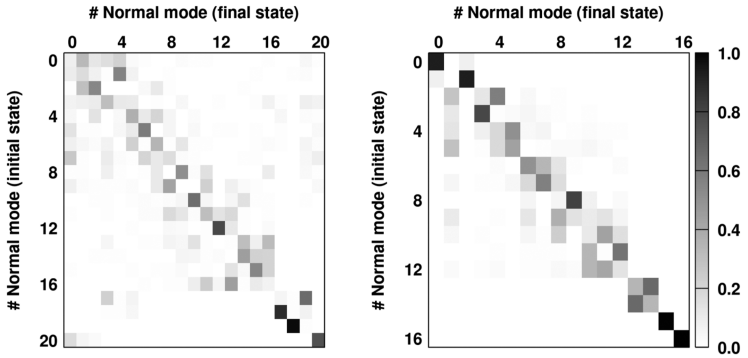

FIG. 3. Graphical representation of the Duschinsky rotation matrices of **IM** ($S_0 \rightarrow S_1$) using the adiabatic (left) and vertical (right) approaches. A shade of gray is associated to the matrix elements J_{ij}^2.

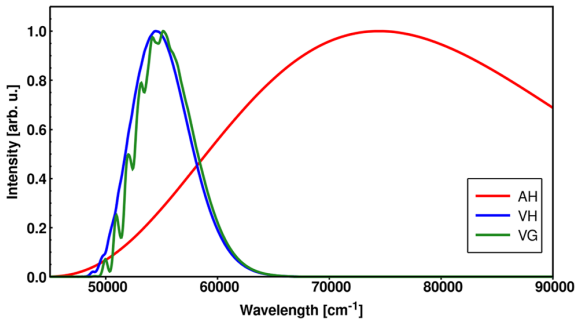

FIG. 4. Computational absorption spectra for **IM** ($S_0 \rightarrow S_1$) using the AH (red), VG (green), and VH (blue) approaches.

imaginary eigenvalues that have been omitted for the VH computation. This is why the number of problematic normal modes is considered to be a decisive factor for the performance of the VH method.

Figure 4 shows the absorption spectrum for **IM** ($S_0 \rightarrow S_1$) using adiabatic and vertical approaches. Both VG and VH spectra show a narrow absorption band compared to the adiabatic approach, while there is a slight vibrational progression for the VG computation, which is not observed in the experiment.[73]

V. COMPUTATION OF EXCITED STATE ABSORPTION SPECTRA IN AN EXCITATION ENERGY TRANSFER STUDY

Excitation energy transfer (EET) is a ubiquitous phenomenon in nature and has emerged as a promising mechanism to improve the efficiency of optical devices.[74–76] For the triplet EET (TEET), which is a short-range Dexter process, excitation energy can be transferred upon close contact between an electronically excited donor molecule and an acceptor molecule. To mitigate reliance on accidental encounters between donor and acceptor molecules and in order to control the orientation of both moieties, they can be covalently linked. After electronic excitation, these photosensitizers can undergo intramolecular TEET on a nanosecond timescale, thereby enhancing efficiency and precision in energy transfer dynamics. A promising type of molecule for an efficient TEET mechanism comprises a spiro-linked anthracenone (**A**) and naphthalene (**N**) moiety (**AN**) (see Fig. 5). In an earlier study,[77] we investigated the photophysical properties of (**AN**) in butyronitrile (BuCN) to clarify inconsistencies in the excited state energy dissipation pathway proposed by Dobkowski *et al.*[78] The experimentalists investigated the absorption behavior after certain delay times to prove the occurrence of TEET and the population of the triplet state on the acceptor moiety (**N**) after the electronic excitation of the donor (**A**). The experimental investigations indicated that after a delay time of 5000 ps after the first excitation, the lowest excited triplet state would be populated. A transient triplet absorption experiment reveals a spectrum in the spectral range of 23 000–26 000 cm^{-1} with multiple peaks (see Fig. 5, black). DFT/MRCI calculation at the optimized geometry of

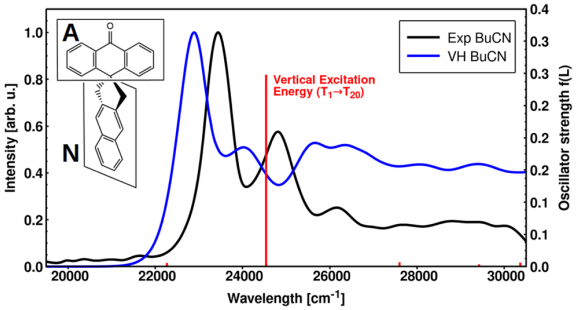

FIG. 5. Experimental long-time (5000 ps) triplet excited state absorption spectrum of **AN** in BuCN (black) in comparison with the computed vibrationally resolved spectrum using the VH method (blue). The line spectrum of the respective vibronic transition ($T_1 \rightarrow T_{20}$) is shown in red and was computed using the DFT/MRCI level of theory.

the lowest triplet state confirms a bright single electronic transition in this wavelength regime ($T_1 \rightarrow T_{20}$) with oscillator strength of 0.29. In order to prove that the experimental spectral features originate from a vibronic transition of this band, we used the VH approach to simulate the vibrationally resolved triplet excited state absorption spectrum from the lowest excited triplet state to the T_{20} (see Fig. 5, blue).

The advantage of the VH method at this point is that the final state T_{20} did not have to be optimized to obtain a meaningful vibronic spectrum. Optimizing higher excited states is not a feasible procedure due to the vast amount of excited states close in energy and numerous conical intersections between them. Instead, the PES of T_{20} was extrapolated from the FC point using a frequency analysis at the optimized geometry of the initial state T_1. The vertical excitation energy (ΔE_V = 24 540 cm^{-1}), which is readily available using a DFT/MRCI calculation at the optimized geometry of the T_1, was used to extrapolate the adiabatic energy difference (ΔE_{adia} = 23 773 cm^{-1}). The VH method gives rise to the vibrational features of this transition (C–C stretch vibration with a frequency of 1463 cm^{-1} on the **N** part). Except for a small shift (≈540 cm^{-1}), the computed spectral shape and vibrational progression show a very good agreement with the experiment. Deviations at higher wavenumbers are attributed to the effect of anharmonicity. The VH simulation could prove that in the experiment the vibrational structure of a single individual electronic transition can be observed and TEET occurred after electronic excitation.

VI. COMPUTATION OF EMISSION SPECTRA FOR DONOR–ACCEPTOR COMPOUNDS

Metal–organic as well as purely organic compounds featuring a donor–acceptor motif serve as a promising class of compounds for a wide range of luminescent applications. The intrinsic separation of electron and hole densities gives rise to low-lying charge-transfer states with minimal energy separation. Upon electronic excitation, these compounds can directly emit fluorescence (prompt fluorescence), whereas the triplet population has to undergo nonradiative reverse intersystem crossing (rISC) first, followed by delayed fluorescence. The energetic barrier for this process is usually small enough to be overcome under ambient conditions. Hence, this decay pathway mechanism is called thermally activated delayed fluorescence (TADF). The efficiency of TADF not only hinges on the energy gap between the lowest excited singlet and triplet states but is also strongly affected by the spin–orbit coupling (SOC) between the corresponding states and the transition dipole strength of the emissive state.[79,80] Herein, we present two case studies of compounds with promising photophysical properties.

A. Metal–organic donor–acceptor compound

Metal–organic complexes containing earth-abundant 3d metals have been explored in recent literature for luminescent applications.[81–83] Initially, precious 4d and 5d metals gained prominence owing to their SOC strength promoting spin-forbidden transitions, which is particularly advantageous in light-emitting diodes. Employing zinc, a 3d metal that is not taking part in the electronic excitations, on the one hand prevents non-radiative decay due to low-lying metal-centered states but on the other hand does not

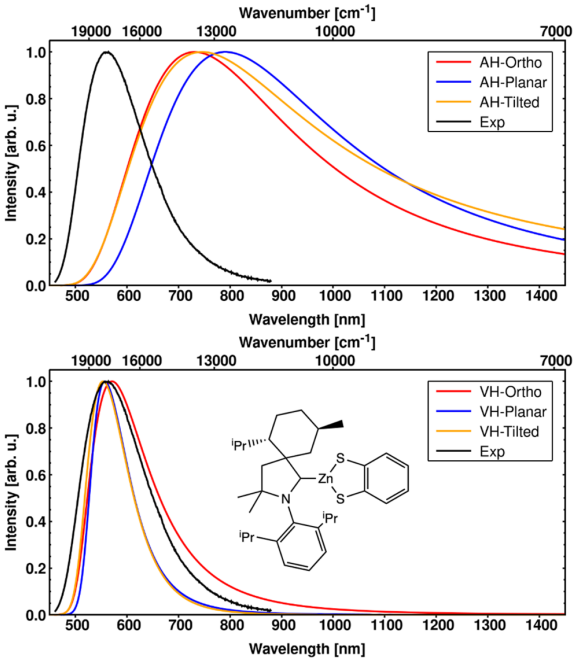

FIG. 6. Experimental emission spectrum from the S-LLCT ($\pi\pi^*$)-state of **CZT1** at 298 K[84] in comparison with the computational results for all conformers using the adiabatic (upper panel) and vertical (lower panel) approaches at 298 K, respectively. The Lewis structure of **CZT1** is included in the lower panel.

provide SOC strength. The necessary SOC originates from heavier elements incorporated into the ligands of the complex, such as sulfur atoms in the case of [Zn(^{H}bdt)(^{Menth}cAAC)] (**CZT1**, see Fig. 6). **CZT1** comprises a donor–acceptor motif and is among the three compounds that were previously investigated by Mitra *et al.*[84] showcasing the promising TADF properties of carbene zinc(II) dithiolate complexes. Particularly for **CZT1**, a series of different stable conformers were optimized, which are energetically very similar. The conformers differ only in the arrangement of the ligands to each other. Namely, the ortho, tilted, and planar conformers could be identified. For each of these conformers, a distinct set of low-lying electronically excited states was investigated. The aim of this study was to determine whether the various conformers exhibit fundamentally different photophysical properties and which of these conformers is observed in the experimental spectra. For this purpose, absorption and emission spectra were calculated. However, calculating the emission spectra was challenging due to significant geometric changes between electronically excited singlet states and the electronic ground state. Emission spectra were generated (see Fig. 6) for every conformer using both the adiabatic and the vertical approach and were compared to the experimental emission spectrum.

The computation of vibronic spectra using the AH method yields very broad (FWHM$_{AH}$ > 7000 cm^{-1}) and featureless emission

bands. The resulting spectral band shapes and, more importantly, their emission maxima could not be compared to the experimental data. The same is true for the corresponding simulations using the VG approach [see Fig. S2 (left) in the supplementary material]. When omitting the Duschinsky mixings for the extrapolation of the final state PES, a low-frequency normal mode remains that exhibits a large displacement [see Fig. S2 (right) in the supplementary material]. The VH method, on the other hand, yields three much narrower spectra ($FWHM_{VH}$ = 2750–4060 cm^{-1}) that also match the experimental emission maximum.

The most pronounced effect of the VH method could be observed for the tilted conformer. Here, the determinant of the Duschinsky rotation matrix [$\det(\mathbf{J})_{AH}$ = 0.9899 and $\det(\mathbf{J})_{VH}$ = 1.000] and the average Duschinsky projection (AH = 0.6070 and VH = 0.7080) increase, whereas the spatial displacements decrease dramatically (D^2_{AH} = 96.501 and D^2_{VH} = 25.630). The computed normal modes at the Franck–Condon region for the final state exhibit only a single imaginary eigenvalue.

It should be noted that for the planar conformer the use of the VH method resulted in unphysical and excessively large displacements for a single low frequency mode. For this reason, we decided to neglect this mode specifically for all further calculations of the vibronic transition.

Due to the fact that the conformers are in close energetic proximity and the simulated emission spectra are almost superimposable, the experimental features were assigned to all three conformers at the same time. The conformers cannot be distinguished based on the computational results of the VH method. In fact, a weighted sum of the emission spectra accordant with the Boltzmann population of these conformers yields the best agreement with the experiment (Sec. S1).

B. Organic donor–acceptor compound

Within the context of an upcoming study,[80] we investigated a series of different twisted biphenyl donor–acceptor compounds with different sterical substituents. The aim was to understand how chemical substitution with increasingly sterically demanding substituents affects the alignment of the donor and acceptor moieties and, consequently, alters a wide range of characteristics crucial for efficient TADF behavior. The computational results and methodological details for a similar compound, **TAA-DCN5**, will be presented in this study. It consists of a triarylamine (TAA) donor with two methoxy groups as electron resonance-donating substituents and a di-cyanobenzene (DCN) acceptor (see Fig. 7).

Simulating the vibrationally resolved emission behavior for **TAA-DCN5** using the AH method yields a very broad ($FWHM_{AH}$ = 7400 cm^{-1}) spectrum. There is a slight vibrational progression visible that cannot be seen in the experiment at all. Despite the good agreement of the experimental and AH emission maxima, we do not consider the results of the AH computation to be a meaningful representation of the experiment.

A computation of the emission spectrum using the VH method greatly improves the spectral width ($FWHM_{VH}$ = 4700 cm^{-1}), and no vibrational progression occurs as expected for an emission from a charge-transfer state. For this vibronic transition, the spatial displacements are smaller using the VH approach than for the AH method (D^2_{AH} = 23.094 and D^2_{VH} = 8.470). However, compared to the experimental spectrum, the computed emission spectrum is slightly shifted to shorter wavelengths.

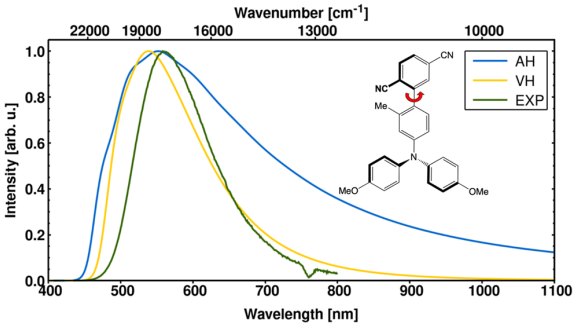

FIG. 7. Experimental emission spectrum of **TAA-DCN5** in toluene at room temperature[85] and the corresponding computational results using the AH and VH method at 300 K. All the spectra were normalized with respect to their emission maximum.

VII. COMPUTATION OF NON-RADIATIVE RATE CONSTANTS

For **TAA-DCN5** in particular, the electronic ground state exhibits a dihedral angle between the donor and acceptor moiety of 68°, whereas it is smaller for the excited states [$D-A(S_1)$ = 67° and $D-A(T_1)$ = 43°].

Within the scope of the study of the purely organic twisted donor–acceptor compound introduced in Sec. VI B, also the computation of rate constants for non-radiative processes, such as ISC ($S_1 \rightsquigarrow T_1$) and rISC ($S_1 \leftsquigarrow T_1$), was of interest. It is known that these quantities are strongly dependent on the energy gap between the initial and final state of a vibronic transition, and from our previous study,[80] we know that the energy gap strongly correlates with the dihedral angle between the donor and acceptor moiety. Thus, investigating the non-radiative rate constants as a function of the dihedral rotation between the donor and acceptor is a theoretical consideration which aims to show the effect of geometrical distortion on the excited-state behavior. This consideration required examination of the vibronic progression from non-stationary points on the PES of either the singlet or the triplet state, which excludes adiabatic approaches for the simulation of non-radiative rate constants. Instead, we used the VH method for this purpose.

We computed a relaxed interpolated pathway for **TAA-DCN5** starting from a geometry with a dihedral angle of 70° (the optimized geometry of the electronic ground state exhibits a dihedral angle of 68°) and an increment of 5° in both directions (see Fig. 8). The PES scans were used to determine the vertical excitation energy E_V at each point of the PES scan of both excited states (see Tables S4 and S5 in the supplementary material). The ΔE_V value decreases with an increasing dihedral angle for both interpolated pathways, however, the absolute value is larger for the relaxed triplet scan.

The VH method was then utilized to re-extrapolate the PES of the respective final state and the corresponding adiabatic energy

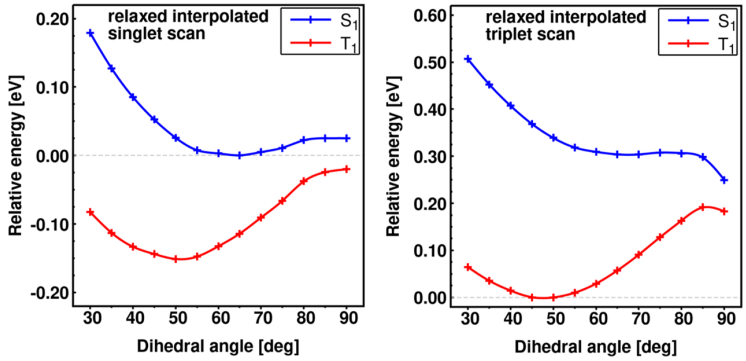

FIG. 8. Relaxed interpolated pathways for the lowest excited singlet state (left, normalized with respect to the S_1 minimum) and triplet state (right, normalized with respect to the T_1 minimum) with vertical excitation energies computed at the DFT/MRCI level of theory for geometries with dihedral angles of 30°–90° and an increment of 5°.

difference. For the computation of meaningful non-radiative rate constants (ISC and rISC), it is crucial that the extrapolated adiabatic energy gap can be determined reliably. The reorganization energies and the extrapolated adiabatic energy gaps are presented in Tables S4 and S5. In general, the absolute amount of reorganization is larger for the extrapolation of the triplet PES due to higher gradients and a steeper potential.

Figure 9 shows that the ISC rate constant is almost unaffected by the dihedral angle, reaching values ranging from 7.1×10^5 (90°) to 1.1×10^7 (65°). While the vibronic overlap is slightly increasing, the SOC matrix elements are dramatically decreasing, reaching a minimal amount for a dihedral angle of 90° (see Fig. S4 and Table S4 in the supplementary material). The rISC, on the other hand, is strongly affected by the relative orientation of the donor and acceptor, with rate constants ranging from 9.5×10^2 (40°) to 3.0×10^6 (85°). The sudden drop of rISC at 90° is attributed to strongly decreased SOC matrix elements at that geometry (see Fig. S5 and Table S5 in the supplementary material). Along this path, the fluorescence rate constant decreases from 8.5×10^7 (40°) to 4.1×10^4 (90°).

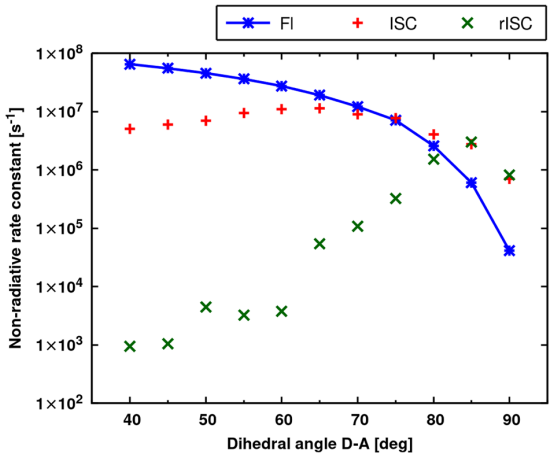

FIG. 9. DFT/MRCI fluorescence rate constants (blue) of **TAA-DCN5** for various points on the relaxed interpolated pathway between 40° and 90°, $S_1 \rightsquigarrow T_1$ ISC (red) and $S_1 \leftsquigarrow T_1$ rISC (green) rate constants in toluene (PCM) at 298 K.

We performed similar calculations using the short-time approximation as in Eq. (13). The computed ISC rate constants for both approaches are almost superimposable, leading to the conclusion that ISC, in general, is only slightly affected by the dihedral angle of the donor–acceptor system. However, while the computed rate constants for rISC are about an order of magnitude higher using the short-time approximation (see Fig. S6 in the supplementary material), the trend shown in Fig. 9 remains the same.

The investigation of radiative and non-radiative rate constants as a function of the dihedral angle between the donor and acceptor leads to the conclusion that the TADF behavior of **TAA-DCN5** is strongly influenced by the dihedral angle between donor and acceptor moiety. Low vibrational frequency normal modes can directly influence that characteristic. A meaningful simulation of these rate constants required the application of the VH method. It could be used to quantify that behavior and compute meaningful non-radiative rate constants between two distinct electronic states.

VIII. CONCLUSIONS

There is a wide range of diverse approaches and methodologies for simulating vibronic transitions and calculating vibrationally resolved spectra and non-radiative rate constants. Notably, our investigation confirms that the VH method offers a significant advantage in terms of computational efficiency when computing excited-state absorption spectra. Circumventing the necessity for a full exploration of a PES for highly excited electronic states facilitates and expedites the identification of experimental spectral features. Meaningful spectra could be obtained on the base of initial state information at its optimized minimum geometry, without the necessity of a full exploration of the final state PES, especially when there

is a large displacement between the geometries of the initial and final states.

For both metal–organic and purely organic compounds featuring a donor–acceptor motif, the VH method proved indispensable in simulating meaningful emission spectra. This was especially evident in the case of **CZT1**, where the AH approach yielded excessively broad emission spectra, while the VH method provided a better agreement with the experimental data. Similarly, for systems undergoing significant geometrical changes upon electronic excitation, such as **TAA-DCN5**, only the VH method could provide meaningful results, shedding light on the intricate interplay of donor–acceptor rotations and TADF properties.

Our investigation pioneers the use of a vertical approach for the computation of rate constants for non-radiative processes. Despite the lack of prior literature data on this specific application, our results underscore the efficacy of the VH method in quantifying the influence of donor–acceptor rotations on key characteristics for TADF, such as the rate constants for non-radiative processes (ISC and rISC). The investigation of these photophysical properties along a relaxed interpolated pathway required to go beyond adiabatic approaches that are commonly used in the literature. Our approach demonstrates a promising use of the VH method for reliable rate constant calculations, reinforcing its potential as a versatile instrument for computational vibronic spectroscopy.

Overall, our findings advocate for the adoption of the VH method as a powerful tool for the simulation of vibronic transitions and elucidating the intricate spectroscopic properties and decay pathway mechanisms of complex donor–acceptor systems. This method not only enhances the accuracy of spectral simulations but also extends its applicability to the reliable calculation of rate constants, marking a significant step forward in computational vibronic spectroscopy.

SUPPLEMENTARY MATERIAL

See the supplementary material for complete datasets for the application examples presented in Secs. VI A, VI B, and VII.

ACKNOWLEDGMENTS

We acknowledge the financial support from the Deutsche Forschungsgemeinschaft (DFG; German Research Foundation) through GRK 2482, Project No. 396890929. We thank the reviewers for their time and effort in reviewing this manuscript. We sincerely appreciate their valuable comments and suggestions, which have significantly enhanced our work.

AUTHOR DECLARATIONS

Conflict of Interest

The authors have no conflicts to disclose.

Author Contributions

Tobias Böhmer: Conceptualization (lead); Methodology (lead); Software (lead); Validation (lead); Visualization (lead); Writing – original draft (lead). **Martin Kleinschmidt**: Funding acquisition (lead); Supervision (supporting); Writing – original draft (supporting). **Christel M. Marian**: Funding acquisition (supporting); Supervision (lead); Writing – original draft (supporting).

DATA AVAILABILITY

The data that support the finding of this study are available within the article and its supplementary material.

REFERENCES

[1] S. Pascal, S. David, C. Andraud, and O. Maury, Chem. Soc. Rev. **50**, 6613 (2021).
[2] P. Macak, Y. Luo, and H. Ågren, Chem. Phys. Lett. **330**, 447 (2000).
[3] B. Robert, Photosynth. Res. **101**, 147 (2009).
[4] L. A. K. Staveley, *The Characterization of Chemical Purity: Organic Compounds* (Elsevier, Bradford, Yorkshire, 2016).
[5] M. Bracker, M. K. Kubitz, C. Czekelius, C. M. Marian, and M. Kleinschmidt, ChemPhotoChem **6**, e202200040 (2022).
[6] P. T. Ruhoff, Chem. Phys. **186**, 355 (1994).
[7] M. Dierksen and S. Grimme, J. Chem. Phys. **120**, 3544 (2004).
[8] J.-L. Chang, J. Chem. Phys. **128**, 174111 (2008).
[9] R. Berger, C. Fischer, and M. Klessinger, J. Phys. Chem. A **102**, 7157 (1998).
[10] H.-C. Jankowiak, J. L. Stuber, and R. Berger, J. Chem. Phys. **127**, 234101 (2007).
[11] S. Mukamel, S. Abe, and R. Islampour, J. Phys. Chem. **89**, 201 (1985).
[12] J. Tang, M. T. Lee, and S. H. Lin, J. Chem. Phys. **119**, 7188 (2003).
[13] W. Liang, H. Ma, H. Zang, and C. Ye, Int. J. Quantum Chem. **115**, 550 (2015).
[14] E. J. Heller, Acc. Chem. Res. **14**, 368 (1981).
[15] D. J. Tannor and E. J. Heller, J. Chem. Phys. **77**, 202 (1982).
[16] B. Podolsky, Phys. Rev. **32**, 812 (1928).
[17] B. T. Sutcliffe and J. Tennyson, Mol. Phys. **58**, 1053 (1986).
[18] N. Handy, Mol. Phys. **61**, 207 (1987).
[19] E. B. Wilson, J. C. Decius, and P. C. Cross, *Molecular Vibrations the Theory of Infrared and Raman Vibrational Spectra* (McGraw-Hill, New York, 1955).
[20] D. F. McIntosh, K. H. Michaelian, and M. R. Peterson, Can. J. Chem. **56**, 1289 (1978).
[21] A. Toniolo and M. Persico, J. Comput. Chem. **22**, 968 (2001).
[22] R. L. Hilderbrandt, J. Mol. Struct. **13**, 33 (1972).
[23] J. R. Reimers, J. Chem. Phys. **115**, 9103 (2001).
[24] J. P. Götze, B. Karasulu, and W. Thiel, J. Chem. Phys. **139**, 234108 (2013).
[25] A. Baiardi, J. Bloino, and V. Barone, J. Chem. Theory Comput. **11**, 3267 (2015).
[26] A. Baiardi, J. Bloino, and V. Barone, J. Chem. Theory Comput. **9**, 4097 (2013).
[27] A. Manian, R. A. Shaw, I. Lyskov, W. Wong, and S. P. Russo, J. Chem. Phys. **155**, 054108 (2021).
[28] F. Santoro and D. Jacquemin, Wiley Interdiscip. Rev.: Comput. Mol. Sci. **6**, 460 (2016).
[29] J. Cerezo and F. Santoro, J. Chem. Theory Comput. **12**, 4970 (2016).
[30] F. J. Avila Ferrer, J. Cerezo, E. Stendardo, R. Improta, and F. Santoro, J. Chem. Theory Comput. **9**, 2072 (2013).
[31] J. Cerezo and F. Santoro, J. Comput. Chem. **44**, 626 (2023).
[32] J. Cerezo, J. Zúñiga, A. Requena, F. J. Ávila Ferrer, and F. Santoro, J. Chem. Theory Comput. **9**, 4947 (2013).
[33] A. Hazra, H. H. Chang, and M. Nooijen, J. Chem. Phys. **121**, 2125 (2004).
[34] F. J. Avila Ferrer and F. Santoro, Phys. Chem. Chem. Phys. **14**, 13549 (2012).
[35] F. Duschinsky, Acta Physicochim. U. R. S. S. **7**, 551 (1937).
[36] L. Seidner, G. Stock, A. L. Sobolewski, and W. Domcke, J. Chem. Phys. **96**, 5298 (1992).
[37] T. Petrenko and F. Neese, J. Chem. Phys. **137**, 234107 (2012).
[38] A. Toniolo and M. Persico, J. Chem. Phys. **115**, 1817 (2001).
[39] M. Etinski, J. Tatchen, and C. M. Marian, Phys. Chem. Chem. Phys. **16**, 4740 (2014).

[40]M. Etinski, J. Tatchen, and C. M. Marian, J. Chem. Phys. **134**, 154105 (2011).
[41] M. Bracker, C. M. Marian, and M. Kleinschmidt, J. Chem. Phys. **155**, 014102 (2021).
[42]M. Etinski, J. Serb. Chem. Soc. **76**, 1649 (2011).
[43]J. J. Markham, Rev. Mod. Phys. **31**, 956 (1959).
[44]F. Mehler, J. Reine Angew. Math. **1866**, 161.
[45]W. Domcke, L. Cederbaum, H. Köppel, and W. von Niessen, Mol. Phys. **34**, 1759 (1977).
[46]R. Kubo, J. Phys. Soc. Jpn. **17**, 1100 (1962).
[47]J. Huh and R. Berger, Sci. Rep. **7**, 17561 (2017).
[48]M. J. Frisch, G. W. Trucks, H. B. Schlegel, G. E. Scuseria, M. A. Robb, J. R. Cheeseman, G. Scalmani, V. Barone, G. A. Petersson, H. Nakatsuji, X. Li, M. Caricato, A. V. Marenich, J. Bloino, B. G. Janesko, R. Gomperts, B. Mennucci, H. P. Hratchian, J. V. Ortiz, A. F. Izmaylov, J. L. Sonnenberg, D. Williams-Young, F. Ding, F. Lipparini, F. Egidi, J. Goings, B. Peng, A. Petrone, T. Henderson, D. Ranasinghe, V. G. Zakrzewski, J. Gao, N. Rega, G. Zheng, W. Liang, M. Hada, M. Ehara, K. Toyota, R. Fukuda, J. Hasegawa, M. Ishida, T. Nakajima, Y. Honda, O. Kitao, H. Nakai, T. Vreven, K. Throssell, J. A. Montgomery, Jr., J. E. Peralta, F. Ogliaro, M. J. Bearpark, J. J. Heyd, E. N. Brothers, K. N. Kudin, V. N. Staroverov, T. A. Keith, R. Kobayashi, J. Normand, K. Raghavachari, A. P. Rendell, J. C. Burant, S. S. Iyengar, J. Tomasi, M. Cossi, J. M. Millam, M. Klene, C. Adamo, R. Cammi, J. W. Ochterski, R. L. Martin, K. Morokuma, O. Farkas, J. B. Foresman, and D. J. Fox, *GAUSSIAN 16, Revision A.03*, Gaussian, Inc., Wallingford, CT, 2016.
[49]A. D. Becke, J. Chem. Phys. **96**, 2155 (1992).
[50]G. A. Petersson, A. Bennett, T. G. Tensfeldt, M. A. Al-Laham, W. A. Shirley, and J. Mantzaris, J. Chem. Phys. **89**, 2193 (1988).
[51] G. A. Petersson and M. A. Al-Laham, J. Chem. Phys. **94**, 6081 (1991).
[52]E. Runge and E. K. U. Gross, Phys. Rev. Lett. **52**, 997 (1984).
[53]M. A. L. Marques and E. K. U. Gross, *A Primer in Density Functional Theory* (Springer Berlin Heidelberg, 2003), pp. 144–184.
[54]F. Furche and R. Ahlrichs, J. Chem. Phys. **117**, 7433 (2002).
[55]S. Hirata and M. Head-Gordon, Chem. Phys. Lett. **314**, 291 (1999).
[56]R. Cammi, S. Corni, B. Mennucci, and J. Tomasi, J. Chem. Phys. **122**, 104513 (2005).
[57]J. Tomasi, B. Mennucci, and R. Cammi, Chem. Rev. **105**, 2999 (2005).
[58]G. Scalmani, M. J. Frisch, B. Mennucci, J. Tomasi, R. Cammi, and V. Barone, J. Chem. Phys. **124**, 094107 (2006).
[59]S. Grimme and M. Waletzke, J. Chem. Phys. **111**, 5645 (1999).
[60]C. M. Marian, A. Heil, and M. Kleinschmidt, Wiley Interdiscip. Rev.: Comput. Mol. Sci. **9**, e1394 (2019).
[61] M. Kleinschmidt, C. M. Marian, M. Waletzke, and S. Grimme, J. Chem. Phys. **130**, 044708 (2009).
[62]I. Lyskov, M. Kleinschmidt, and C. M. Marian, J. Chem. Phys. **144**, 034104 (2016).
[63]D. R. Dombrowski, T. Schulz, M. Kleinschmidt, and C. M. Marian, J. Phys. Chem. A **127**, 2011 (2023).
[64]M. Kleinschmidt, J. Tatchen, and C. M. Marian, J. Comput. Chem. **23**, 824 (2002).
[65]M. Kleinschmidt and C. M. Marian, Chem. Phys. **311**, 71 (2005).
[66]M. Kleinschmidt, J. Tatchen, and C. M. Marian, J. Chem. Phys. **124**, 124101 (2006).
[67]A. Baiardi, J. Bloino, and V. Barone, J. Chem. Phys. **144**, 084114 (2016).
[68]G. Balakrishnan, A. A. Jarzecki, Q. Wu, P. M. Kozlowski, D. Wang, and T. G. Spiro, J. Phys. Chem. B **116**, 9387 (2012).
[69]F. Dinkelbach and C. M. Marian, J. Serb. Chem. Soc. **84**, 819 (2019).
[70]J. T. Hougen and J. K. G. Watson, Can. J. Phys. **43**, 298 (1965).
[71] I. Özkan, J. Mol. Spectros. **139**, 147 (1990).
[72]G. M. Sando and K. G. Spears, J. Phys. Chem. A **105**, 5326 (2001).
[73]N.-u. H. Khan, S. Agrawal, R. I. Kureshy, S. H. R. Abdi, K. J. Prathap, and R. V. Jasra, Eur. J. Org Chem. **2008**, 4511.
[74]R. A. Keller, J. Am. Chem. Soc. **90**, 1940 (1968).
[75]P. J. Wagner and P. Klán, J. Am. Chem. Soc. **121**, 9626 (1999).
[76]L. D. Elliott, S. Kayal, M. W. George, and K. Booker-Milburn, J. Am. Chem. Soc. **142**, 14947 (2020).
[77]S. Metz, T. Böhmer, B. Raunitschke, and C. M. Marian, Can. J. Chem. **101**, 633 (2023).
[78]J. Dobkowski, A. Gorski, M. Kijak, M. Pietrzak, K. Redeckas, and M. Vengris, J. Phys. Chem. A **123**, 6978 (2019).
[79]C. M. Marian, Annu. Rev. Phys. Chem. **72**, 617 (2021).
[80]J. Kaminski, T. Böhmer, and C. M. Marian, J. Phys. Chem. C **128**, 13711 (2024).
[81] A. Steffen and B. Hupp, in *Comprehensive Coordination Chemistry III*, edited by E. C. Constable, G. Parkin, and L. Que, Jr. (Elsevier, Oxford, 2021), pp. 466–502.
[82]O. S. Wenger, J. Am. Chem. Soc. **140**, 13522 (2018).
[83]C. Förster and K. Heinze, Chem. Soc. Rev. **49**, 1057 (2020).
[84]M. Mitra, O. Mrózek, M. Putscher, J. Guhl, B. Hupp, A. Belyaev, C. M. Marian, and A. Steffen, Angew. Chem., Int. Ed. **63**, e202316300 (2024).
[85]D. Sretenović, "Photophysical properties of chromophores studied by multimodal fluorescence spectroscopy," Ph.D. thesis (Heinrich Heine University Düsseldorf, 2024).

S1 Computational results for CZT1

The emission spectra of each conformer was weighted based on the Boltzmann distribution (Ortho: 3.3 kJ/mol – 15%, Planar: 0.0 kJ/mol – 58%, Tilted: 1.9 kJ/mol – 27%) at room temperature (298.15K). The weighted sum of all emission spectra is shown in the following:

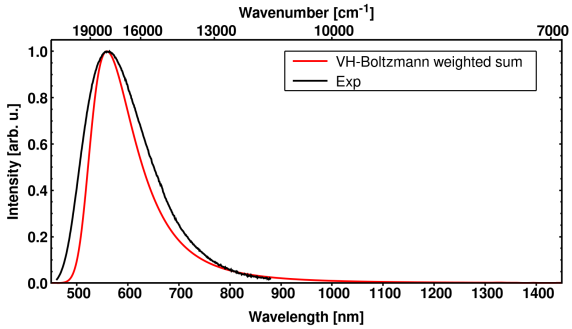

Figure S1: Experimental emission spectrum from the S-LLCT ($\pi\pi^*$) state of **CZT1** at 298 K[1] (black) in comparison with the Boltzmann weighted sum of the VH spectra of all conformers at 298 K (red).

In addition to the computational results using the VH method, presented in the main study, we included the computed emission spectra for **CZT1** using the VG method in Figure S2. Compared to the results using the VH approach (presented in the main text) and the experimental values, these spectra are too broad (FWHM $\approx$ 5500 cm^{-1}) and the emission maximum is too far into the red region.

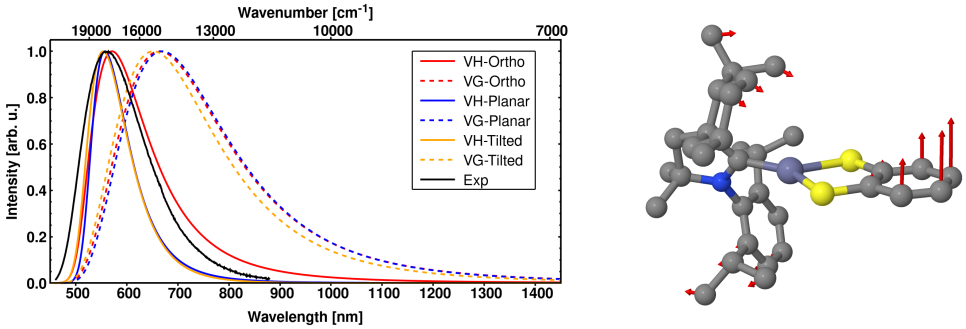

Figure S2: **Left**: Experimental emission spectrum from the S-LLCT ($\pi\pi^*$) state of **CZT1** at 298 K[1] (black) in comparison with the computational spectra using the VH and VG approach. **Right**: Low-frequency vibrational mode that exhibits a large spatial displacement.

Table S1 contains the detailed results for all three investigated conformers of **CZT1** in section VI A using the AH, VG and VH method. We added the key characteristics of the experimental emission spectrum and the weighted sum of all computational results displayed above in Figure S1.

Table S1: Summary of the key characteristics for the comparison of the vertical and adiabatic approaches for the ortho and planar conformers of **CZT1**.

method and molecule	**Ortho**			**Planar**		
	AH	VG	VH	AH	VG	VH
Duschinsky determinant	0.998	1.000	1.000	0.996	1.000	1.000
Average Duschinsky projection	0.612	1.000	0.661	0.661	1.000	0.725
Sum of squared displacements	29.710	29.478	27.667	45.230	41.587	32.309
0-0 overlap	2.5×10^{-4}	6.3×10^{-3}	1.1×10^{-3}	3.4×10^{-5}	3.1×10^{-5}	1.5×10^{-4}
Imaginary Frequencies	–	–	2	–	–	2
λ_{em}^{max} [nm]	731	669	571	746	664	557
FWHM [cm^{-1}]		5445	4060		5510	2751

Table S2: Summary of the key characteristics for the comparison of the vertical and adiabatic approaches for the tilted conformer and the Boltzmann-weighted sum of all conformers of **CZT1**.

method and molecule	**Tilted**			**Sum**	
	AH	VG	VH		EXP
Duschinsky determinant	0.990	1.000	1.000	–	–
Average Duschinsky projection	0.607	1.000	0.708	–	–
Sum of squared displacements	90.501	27.594	25.630	–	–
0-0 overlap	1.0×10^{-7}	1.0×10^{-3}	1.6×10^{-3}	–	–
Imaginary Frequencies	–	–	1	–	–
λ_{em}^{max} [nm]	792	652	553	559	564
FWHM [cm^{-1}]		5423	3019	3259	4350

From Figure S2 (left) as well as from Table S1 and S2 we can conclude that the displacement is significantly larger for the AH appraoch than for the vertical appraoches. For all compounds, the normal mode depicted in Figure S2 (right) exhibits a high spatial displacement and is not well described without Duschinsky mixing.

To assess whether omitting low-frequency normal modes systematically improves the simulated spectra, we conducted VG computations excluding the normal modes typically discarded in VH computations (see Table S1 and S2). Figure S3 compares the different VG computations, showing that the results are nearly identical. The emission maxima are only slightly shifted to higher wavenumbers, and the FWHM decreases marginally. From this, we conclude that (i) considering Duschinsky rotation effects is essential and (ii) that low-frequency normal modes must not be arbitrarily neglected.

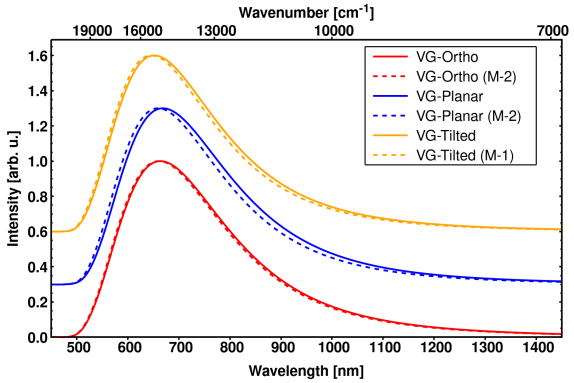

Figure S3: Computed vibronic emission spectra of **CZT1** at 298 K using the VG approach with (dashed lines) and without (solid lines) omission of low-frequency normal modes that exhibit an imaginary frequency at the FC region. To enhace clarity, the results for the planar (blue) and tilted (orange) conformers were shifted by 0.3 and 0.6 arbitrary units, respectively.

S2 Computational results for TAA-DCN5

Table S3 contains the detailed computational results for the emission properties of **TAA-DCN5** investigated in section VI B as well as the experimental results taken from the PhD thesis[2] of Dragana Sretenović .

Table S3: Summary of the key characteristics for the comparison of the vertical and adiabatic approach for **TAA-DCN5**.

method and molecule	**TAA-DCN5**		
	AH	VH	EXP
Duschinsky determinant	0.997	1.000	–
Average Duschinsky projection	0.709	0.729	–
Sum of squared displacements	24.656	10.000	–
0-0 overlap	2.8×10^{-3}	7.2×10^{-2}	–
Imaginary Frequencies	–	1	–
λ_{em}^{max} [nm]	552	538	558
FWHM [cm^{-1}]	7400	4700	3607

S3 Detailed results for the computation of non-radiative rate constants

Table S4: Summary of all key ingredients required for the computation of the intersystem crossing (ISC) rate constants for **TAA-DCN5** using the VH method. The index "vib" indicates a non-radiative rate constant assuming a SOCME of $1\,cm^{-2}$ to show the vibrational contribution.

dihedral angle	E_V [cm^{-1}]	E_{extrap} [cm^{-1}]	$E_{adia-extrap}$ [cm^{-1}]	$k_{ISC-vib}$ [s^{-1}]	SOC^2 [cm^{-2}]	k_{ISC} [s^{-1}]
40	1764.35	1602.12	3366.47	8.43×10^7	0.06024	5.08×10^6
45	1582.18	940.89	2523.07	9.66×10^7	0.06277	6.06×10^6
50	1429.87	1648.96	3078.83	1.06×10^8	0.06615	6.99×10^6
55	1252.97	1419.76	2672.73	1.52×10^8	0.06223	9.46×10^6
60	1094.3	2852.95	3947.25	1.92×10^8	0.05720	1.10×10^7
65	922.01	2918.95	3840.96	2.26×10^8	0.05057	1.14×10^7
70	772.11	8437.15	9209.26	2.07×10^8	0.04351	9.00×10^6
75	623.74	2026.07	2649.81	2.45×10^8	0.03176	7.78×10^6
80	482.84	1138.70	1621.54	2.17×10^8	0.01886	4.10×10^6
85	401.20	248.89	650.09	3.64×10^8	0.00768	2.79×10^6
90	366.08	29.93	396.01	3.71×10^8	0.00191	7.09×10^5

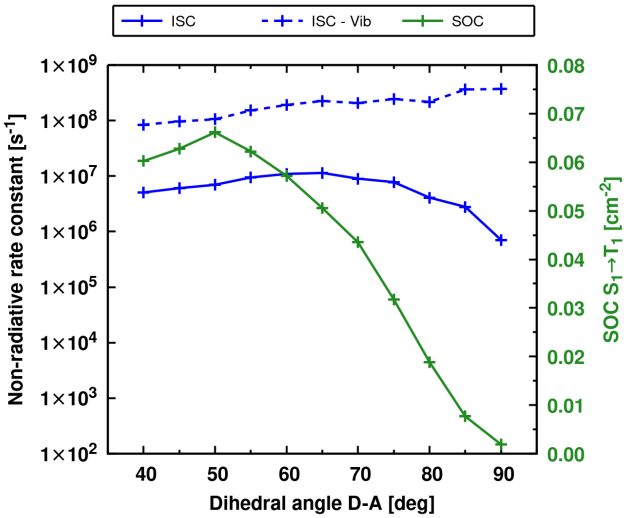

Figure S4: Graphical representation of the vibrational overlap (assuming a SOC matrix element of $1\,cm^{-2}$), the computed sum over the squared SOC matrix elements and the ISC rate constant as a function of the dihedral angle between donor and acceptor of **TAA-DCN5**.

Table S5: Summary of all key ingredients required for the computation of the reverse intersystem crossing (rISC) rate constants for **TAA-DCN5** using the VH method. The index "vib" indicates a non-radiative rate constant assuming a SOC matrix element of 1 cm^{-2} to show the vibrational contribution.

dihedral angle	$\mathbf{E_V}$ [cm^{-1}]	$\mathbf{E_{extrap}}$ [cm^{-1}]	$\mathbf{E_{adia-extrap}}$ [cm^{-1}]	$\mathbf{k_{ISC-vib}}$ [s^{-1}]	$\mathbf{SOC^2}$ [cm^{-2}]	$\mathbf{k_{ISC}}$ [s^{-1}]
40	3166.78	1256.72	1910.06	2.96×10^4	0.03211	9.52×10^2
45	2970.14	1050.66	1919.48	3.25×10^4	0.03213	1.04×10^3
50	2734.20	905.35	1828.85	1.38×10^5	0.03253	4.50×10^3
55	2487.29	871.48	1615.81	9.61×10^4	0.03405	3.27×10^3
60	2259.92	792.58	1467.34	1.09×10^5	0.03486	3.80×10^3
65	1988.21	900.06	1088.15	1.44×10^6	0.03789	5.46×10^4
70	1716.72	867.58	849.14	2.71×10^6	0.04022	1.09×10^5
75	1450.06	899.98	550.08	7.78×10^6	0.04171	3.25×10^5
80	1155.31	891.32	263.99	3.89×10^7	0.03953	1.54×10^6
85	855.51	751.34	104.17	8.93×10^7	0.03393	3.03×10^6
90	539.47	395.16	144.31	5.30×10^7	0.01549	8.21×10^5

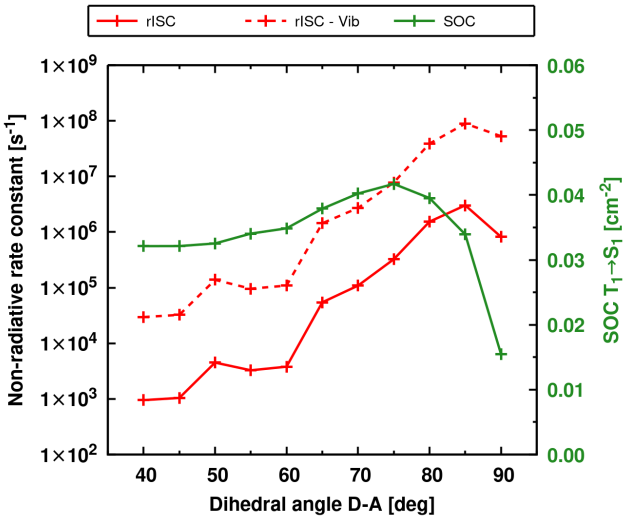

Figure S5: Graphical representation of the vibrational overlap (assuming a SOC matrix element of 1 cm^{-2}), the computed sum over the squared SOC matrix elements and the rISC rate constant as a function of the dihedral angle between donor and acceptor of **TAA-DCN5**.

We computed the rate constants of the non-radiative processes using the full correlation function as well as the short time approximation presented in section II C. Figure S6 contains the computed rate constants for ISC (left) and rISC (right). For ISC, the results obtained by using the complete correlation function are comparable to those from the short-time approximation. However, for rISC, the short-time approximation produces rate constants that are higher by an order of magnitude compared to those calculated with the full correlation function.

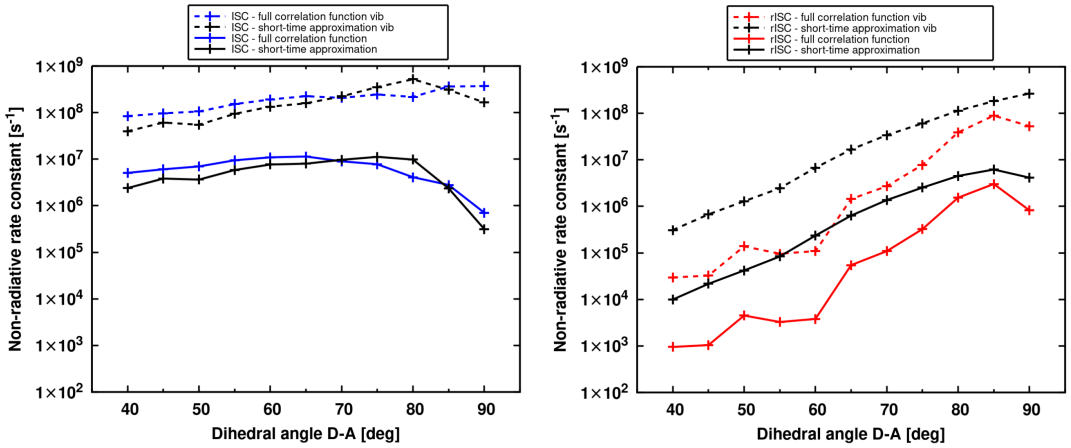

Figure S6: Graphical representation of the vibrational overlap (assuming a SOC matrix element of 1cm^{-2}), the ISC rate constant (left) and the rISC rate constant (right) as a function of the dihedral angle between donor and acceptor of **TAA-DCN5**.

References

(1) Mitra, M.; Mrózek, O.; Putscher, M.; Guhl, J.; Hupp, B.; Belyaev, A.; Marian, C. M.; Steffen, A. Structural Control of Highly Efficient Thermally Activated Delayed Fluorescence in Carbene Zinc(II) Dithiolates. *Angew. Chem. Int. Ed.* **2024**, *63*, e202316300.

(2) Sretenović, D. Photophysical Properties of Chromophores studied by Multimodal Fluorescence Spectroscopy. Ph.D. thesis, Heinrich Heine University Düsseldorf, 2024.

Paper No.2

Balancing TADF properties in π-bridged donor-acceptor systems by sterical constraints: The best of three worlds. Jeremy Kaminski

Tobias Böhmer and Christel M. Marian
J. Phys. Chem. C (2024)
DOI: 10.1021/acs.jpcc.4c03865

Contribution: To this work I contributed the quantum chemical calculations of compound **5d** and **5e**. All computations of vibronic emission spectra were performed by me. I visualised most of the scientific results and assisted writing and reviewing the manuscript.

THE JOURNAL OF PHYSICAL CHEMISTRY C
A JOURNAL OF THE AMERICAN CHEMICAL SOCIETY

pubs.acs.org/JPCC

Article

Balancing TADF Properties in π-Bridged Donor–Acceptor Systems by Sterical Constraints: The Best of Three Worlds

Published as part of The Journal of Physical Chemistry C virtual special issue "TADF-Active Systems: Mechanism, Applications, and Future Directions".

Jeremy M. Kaminski, Tobias Böhmer, and Christel M. Marian*

Cite This: J. Phys. Chem. C 2024, 128, 13711–13721

Read Online

ACCESS | Metrics & More | Article Recommendations | Supporting Information

ABSTRACT: Key parameters that steer the efficiency of thermally activated delayed fluorescence (TADF) are the energetic splitting ΔE_{ST} between S_1 and T_1, their mutual spin–orbit coupling (SOC) and the transition dipole strength μ of the S_1 emission. Small ΔE_{ST} values, resonable SOC and high values of μ are difficult to achieve simultaneously. Using high-level quantum chemical methods, we have investigated the course of these parameters as functions of the donor–acceptor torsion angle in a series of conformationally constrained triarylamine–terephthalonitrile systems. Potential energy surface crossings between triplet states of charge-transfer and local-excitation character close to 90° indicate that a three-state model of the TADF kinetics might not be appropriate. The smallest adiabatic ΔE_{ST} values are obtained for a hybrid solvent model comprising two explicit toluene molecules in addition to a polarizable continuum model of solvation. Due to the substantial geometrical displacements of the S_1 and T_1 potentials in the torsion angle, the adiabatic Hessian method does not provide meaningful rate constants for reverse intersystem crossing. The recently developed vertical Hessian approach remedies this problem.

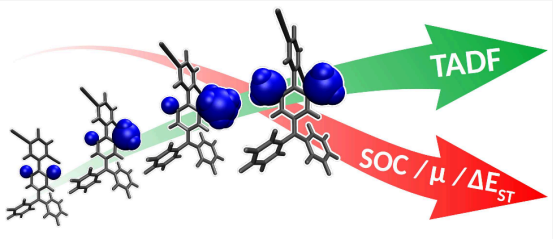

INTRODUCTION

Organic light-emitting diodes (OLEDs) have emerged as a promising technology for display and lighting applications, particularly in compact devices such as smartphones and smartwatches.[1] The external quantum efficiency of an OLED is primarily determined by the total internal charge-to-photon conversion ratio, i.e., the internal quantum efficiency and the light out-coupling efficiency of the device.[2] From a technical perspective, achieving uniform performance across all primary colors remains an ongoing challenge. While highly luminescent red[3−5] and green[6−8] emitters are already known, there is still great interest to find deep-blue emitters with similar effectiveness.

The principle of thermally activated delayed fluorescence (TADF) has proven to be a promising approach to overcome the efficiency limitations of OLEDs.[1,9] Initial studies on TADF date back to 1929.[10] Since 2012, when Adachi and co-workers reported the first highly efficient TADF-based OLEDs,[11] a rapid development of TADF materials with excellent electroluminescence performance could be observed.[12] A key target in the design of novel TADF emitters is the energy difference between the lowest excited singlet and triplet states, ΔE_{ST}: A small ΔE_{ST} value is crucial for the efficiency of reverse intersystem crossing (rISC),[13,14] a thermally activated nonradiative process necessary for converting optically dark triplet excitons into singlet excitons which eventually emit delayed fluorescence. In this way, an internal quantum efficiency of 100% can be achieved by TADF emitters in principle, thereby maximizing the overall device performance. Challenges persist in the development and implementation of TADF-based OLEDs. These include the need for deep-blue TADF emitters, improvement of triplet state lifetimes, inhibition of exciton annihilation through aggregation in thin films, and ensuring operational stability.[15] Addressing these challenges requires comprehensive research efforts to refine TADF systems for practical applications and industrial production.

A promising type of molecules in this regard are purely organic donor–acceptor (D–A) systems. In contrast to commercially available transition metal complexes, which often exhibit symmetrical, nearly spherical shapes, organic D–A systems have the advantage that their molecular structures resemble those of the host or matrix materials. Through the ordered structure of the molecules within the

Received: June 10, 2024
Revised: July 15, 2024
Accepted: July 23, 2024
Published: August 7, 2024

layers of an OLED device, the external quantum efficiency is significantly improved.[16] In D−A compounds, electron and hole densities are spatially separated, yielding states of charge-transfer (CT) character as the lowest excited states with intrinsically very small singlet−tripet energy gaps. Unfortunately, spin−orbit coupling (SOC) between ^{1}CT and ^{3}CT states, a prerequisite for efficient ISC and rISC, is very small as well. It was shown, however, that a locally excited (LE) triplet state in energetic proximity of the CT states can mediate the interconversion of singlet and triplet populations.[17−19] From a theoretical perspective, accurately predicting the adiabatic energy difference between the excited singlet and triplet states remains a challenging task because it requires a balanced treatment of CT and LE states in the presence of a solvent environment.[14]

This study aims to shine light on how to modulate the characteristics of a known TADF emitter,[20] consisting of a triarylamine (TAA) donor and a 1,4-dicyanobenzene (terephthalonitrile, TPN) acceptor (Figure 1b). Dicyanobenzenes

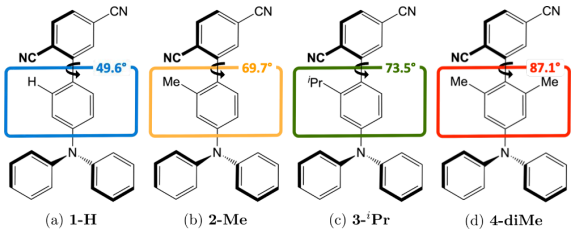

Figure 1. Investigated emitter series consisting of a triarylamine (TAA) donor and a terephthalonitrile (TPN) acceptor unit. Labeling: Consecutive numbers in the order of increasing substitutional effect plus name of the substituent. Differences are highlighted by colored boxes. The torsion angle between the phenylene bridge and the TPN acceptor of the most stable conformer is indicated in the upper right of each colored box.

have been commonly used as acceptor units since the development of the first TADF-based OLED emitters.[11] Due to their high photoluminescence efficiencies, dicyano-based N-heterocyclics have played an important role in the design of high-performance TADF materials.[11,21] Triphenylamines show excellent hole-transporting capabilities. Moreover, their steric demand is able to diminish aggregation-caused quenching.[22] Despite these advantageous properties and their high thermal and electrochemical stabilities, triphenylamine-based TADF emitters are rather uncommon.[23,24] A problem appears to be the increased ΔE_{ST} value in comparison to D−π−A TADF emitters containing N-heterocyclic donors such as carbazole or dimethylacridine.[24] However, if the ΔE_{ST} values could be improved, triphenylamines might represent promising donors.

By means of quantum chemistry, we investigate the influence of the chemical substitution (Figure 1a−d) on key characteristics of this emissive system (oscillator strength, spin−orbit coupling, and rate constants for radiative and nonradiative processes) while the emission remains in the blue wavelength regime that is of strong interest. Furthermore, we discuss the challenges met in the simulation of their excited-state properties. Conclusions drawn from the observed trends are not considered system-specific but can be generalized and applied to improve the design principles for other TADF emitters.

METHODS

Molecular geometries and vibrational frequencies of the investigated TADF emitter series were determined with Gaussian 16[25] employing the optimally tuned, range-separated ωB97X-D density functional[26,27] and the split-valence double-ζ def2-SV(P) basis set.[28−30] The optimal tuning procedure followed the scheme recommended by many authors.[31−35] It yields a value of ω = 0.15 for the range separation parameter where Koopmans' theorem is fulfilled best (Figure S8). Geometries of singlet excited states were optimized with time-dependent density functional theory (TDDFT),[36−38] for excited triplet states including the Tamm-Dancoff approximation (TDA).[39] Unless noted otherwise, the polarizable continuum model (PCM)[40−42] was utilized to mimic the toluene environment using the solvent excluding surface (SES) implemented in Gaussian 16.

Excitation energies and excited-state properties were determined with the combined density functional theory and multireference configuration interaction (DFT/MRCI) method[43,44] using the tight R2016[45] parameter set. Spin−orbit coupling matrix elements were computed in atomic mean-field approximation using SPOCK.[46,47] Temperature-dependent vibronic spectra and (r)ISC rate constants were calculated with a recent extension[48] of the VIBES program,[49,50] enabling the use of internal coordinates and the application of the vertical Hessian (VH) method which are better suited for a pair of potential energy surfaces with large displacements in a dihedral angle than Cartesian coordinates and the adiabatic Hessian (AH) approach. Numerical derivatives of the electric dipole transition moments and of the spin−orbit coupling matrix elements with respect to the normal coordinates, required for computing radiative or (r)ISC rate constants in Herzberg−Teller approximation,[19,51,52] were generated with the GRADIENATOR toolbox.[53,54] A detailed analysis of the CT and LE contributions to the DFT/MRCI transition densities was carried out with a local version of the TheoDORE program.[55]

RESULTS AND DISCUSSION

For each compound in the investigated D−A series (except for **4-diMe**), two conformers can be found in the electronic ground state, even for seemingly symmetric bridges. In particular, the nonequivalency of the **1-H** conformers is caused by the propellar structure of the TAA donor unit. The steric demand of the substituents at the bridge increases from **1-H** to **4-diMe**, entailing increasingly perpendicular D−A arrangements (Figure 1 and Table 1). The shallow potential energy surface of the electronic ground state may be the reason for finding only one **4-diMe** conformer. A detailed analysis of the different conformers is omitted here, as this is the subject of a forthcoming paper.[56] The following results focus on the energetically most stable conformer of each compound.

Table 1. Torsion Angle/° between Donor and Acceptor for All Compounds in the Electronic Ground-State and in the Lowest Excited Singlet and Triplet States

	Compound			
	1-H	**2-Me**	**3-^{i}Pr**	**4-diMe**
S_0	49.6	69.7	73.5	87.1
S_1 (CT)	34.3	65.9	65.2	81.8
T_1 (CT)	20.9	41.7	39.5	49.3

https://doi.org/10.1021/acs.jpcc.4c03865
J. Phys. Chem. C 2024, 128, 13711−13721

Absorption Spectra. Figure 2 shows the computed absorption spectra in toluene solution. Due to the multi-

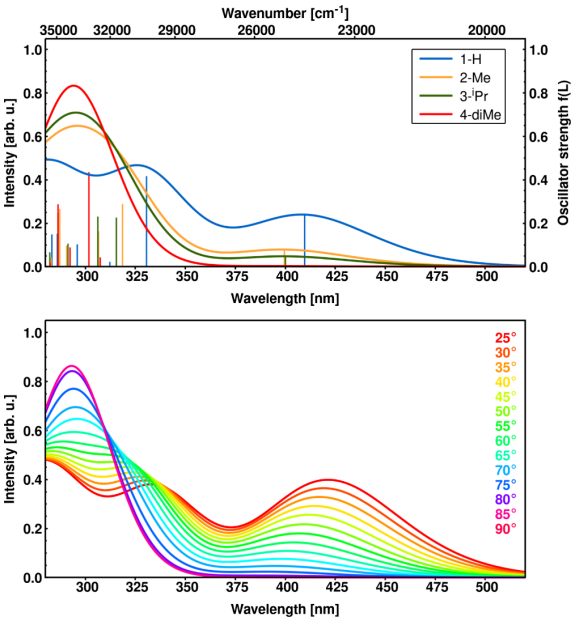

Figure 2. (Top) Computed absorption spectra of **1-H** (blue), **2-Me** (orange), **3-^{i}Pr** (green), and **4-diMe** (red) in toluene solution. (Bottom) Simulated absorption spectra of **2-Me** at fixed D−A torsion angles along a relaxed scan of the electronic ground-state relaxed PES. All DFT/MRCI line spectra were broadened with Gaussians of 4400 cm^{-1} full width at half maximum.

configurational character of the excited singlet wave functions (Tables S2−S5), the analysis of the transitions is not straightforward. A close look at the molecular orbitals (MOs) involved in the transitions (Figures S1−S4) further reveals that some of the frontier MOs are delocalized, thus further complicating the designation as CT or LE transition or an admixture thereof. To aid the assignment, we partitioned each molecule into a donor and an acceptor fragment and analyzed the corresponding DFT/MRCI one-particle transition density matrices by means of the TheoDORE[55] toolkit.

The first peak at ca. 400 nm is assigned to the $S_1 \leftarrow S_0$ transition. It is mainly characterized by an electron transfer from the highest occupied molecular orbital (HOMO) of the donor to the lowest unoccupied molecular orbital (LUMO) of the acceptor. We observe a clear correlation between the intensity of the $S_1 \leftarrow S_0$ absorption peak and the torsion angle between the donor and acceptor moieties: The larger this dihedral angle, the more pronounced is the CT character and the weaker is the oscillator strength of the $S_1 \leftarrow S_0$ transition. The intensity decrease is accompanied by a small blue shift of the absorption wavelength, ranging from **1-H** (410 nm) to **4-diMe** (396 nm). Note that the CT contributions to the corresponding T_1 states are markedly smaller, save for **4-diMe** with nearly orthogonal D−A orientation.

The $S_2 \leftarrow S_0$ transitions of **1-H**, **2-Me**, and **3-^{i}Pr** are dominated by a HOMO → LUMO + 1 CT excitation mixed with varying amounts of LE_{TAA} configurations. The admixture of CT and LE character is most pronounced for **1-H** where the molecular planes of the phenylene bridge and the TPN acceptor are twisted by about 50°, thus enabling substantial π-conjugation in LUMO + 1 (Figure S1). With increasing steric strain, the π-conjugation is diminished in this series and disappears completely in **4-diMe** where the HOMO → LUMO + 1 CT excitation forms the leading term of the $S_4 \leftarrow S_0$ transition. The decrease of the π-conjugation in LUMO + 1 explains the strong blue shift of the excitation wavelength from 331 nm in **1-H** over 319 nm in **2-Me** and 315 nm in **3-^{i}Pr** to 286 nm in **4-diMe** and the concomitant reduction of the oscillator strength in this series (Table S1).

The $S_3 \leftarrow S_0$ and $S_5 \leftarrow S_0$ transitions are mainly characterized by LE_{TAA} contributions. To understand their intensity patterns, it is useful to study the donor fragment first. The absorption spectrum of the unsubstituted D_3-symmetric triphenylamine molecule shows one strong *E*-symmetric $\pi\pi^*$ band with maximum at about 300 nm.[57] When the molecular point group is reduced to C_2, the band splits into an *A*- and a *B*-symmetric component with perpendicular directions of the transition dipole vectors. In the D−A compounds investigated in this work, the *A*-polarized transition forms the lowest LE_{TAA}-type excitation. Its transition dipole and the dipole vectors of the CT excitations are arranged in a close to collinear fashion, i.e., they can strongly couple. Depending on the directions of the interacting dipoles, their combination can either enhance or reduce the oscillator strengths of the mixed LE/CT transitions. In the $S_2 \leftarrow S_0$ transition of **1-H**, these vectors point in the same direction and thus lead to an enhancement of absorption strength whereas their negative superposition causes the $S_3 \leftarrow S_0$ absorption to be weak. With decreasing CT contribution to the S_3 wave function of the emitter molecule, the $S_3 \leftarrow S_0$ absorption peak becomes more and more intense. This modulating effect is even more pronounced when an additional phenylene bridge is inserted between donor and acceptor, thus increasing their mutual distance.[58] The *B*-symmetric component of the LE_{TAA} transition can be associated with the $S_5 \leftarrow S_0$ transition. Because its transition dipole vector points in a direction perpendicular to the D−A axis, it cannot couple to a CT excitation. Hence, wavelengths and intensities of the $S_5 \leftarrow S_0$ transition are only marginally affected by the substitution.

The lowest-lying LE_{TPN} configuration, which gives rise to a shallow band with an onset at about 320 nm in the native TPN molecule in water solution,[59] contributes mainly to the $S_4 \leftarrow S_0$ transition in **1-H**, **2-Me**, and **3-^{i}Pr**. Its excitation wavelength does not vary strongly among these compounds, as may be expected for a predominantly local transition. Due to the increased steric hindrance between the cyano group in the ortho-position of the linkage and the substituents of the bridge, this transition is blue-shifted in compound **4-diMe**, where it forms the $S_6 \leftarrow S_0$ band with an excitation wavelength of 283 nm.

Interestingly, the impact of the substituents on the absorption spectra is not primarily driven by electronic effects. Rather, it seems to correlate with the torsion angle between the donor and acceptor units which varies between ∼50° (**1-H**) and ∼87° (**4-diMe**) in the respective minimum nuclear arrangements, see Figure 1 and Table 1. To prove this correlation, we computed the absorption spectrum of compound **2-Me** as a function of the torsion angle while optimizing all other geometry parameters of the ground-state potential energy surface (PES). The agreement between the computed absorption spectra of **1-H** to **4-diMe** (Figure 2, top) and the simulated spectra of compound **2-Me** for fixed torsion

https://doi.org/10.1021/acs.jpcc.4c03865
J. Phys. Chem. C 2024, 128, 13711−13721

angles between 25° and 90° (Figure 2, bottom) is striking and substantiates our assumption that the observed changes in the absorption profiles mainly have a steric rather than an electronic origin.

Torsional Effects on Excited-State Properties. The torsion angle between donor and acceptor does not only have strong impact on the absorption properties of the compounds. As shown in Figure 3, it affects several other excited-state

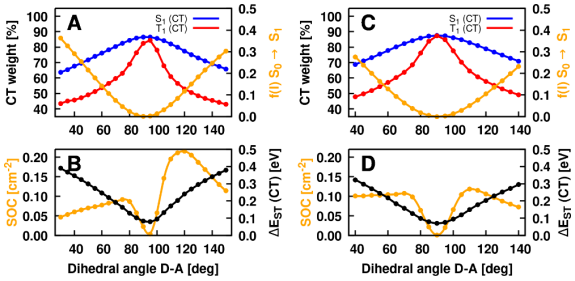

Figure 3. (A) CT character of the first excited singlet (blue) and triplet (red) state. Oscillator strength for the $S_1 \leftarrow S_0$ transition (orange) of **2-Me**. (B) ΔE_{ST} (black) and sum of squared SOCMEs (orange) between S_1 and T_1 states of **2-Me**. (C and D) Corresponding data for **4-diMe**. All data were computed at the DFT/MRCI level of theory along a relaxed scan of the torsion angle in the electronic ground state.

properties of the emitters as well. In particular, we investigated the oscillator strength f(I) of the $S_1 \leftarrow S_0$ transition of compound **2-Me** and the CT contributions to the S_1 and T_1 states (Figure 3A), their mutual spin−orbit coupling matrix elements (SOCMEs), as well as the energy gap ΔE_{ST} (Figure 3B). Corresponding data for **4-diMe** can be found in Figure 3C,D. Knowledge of their functional dependencies on the torsional coordinate is considered a key toward understanding the photophysics of these chromophores.

A perpendicular D−A orientation favors the CT character of the first excited singlet and triplet states and lowers their energetic splitting ΔE_{ST} to a minimum value. Concomitantly, the oscillator strength of the $S_1 \leftarrow S_0$ transition vanishes due to the missing overlap of hole and particle densities which are located on donor and acceptor, respectively. Direct SOC between states of CT character involving the same orbitals is expected to be close to zero as well.[52] Accordingly, a strictly perpendicular arrangement does not seem to be as advantageous as expected when judging solely on the basis of ΔE_{ST}. Lowering the torsion angle to values describing nearly coplanar D−A arrangements strongly increases $f(I)$, but widens the energy gap. An increased ΔE_{ST} value, next to lowered SOC, minimizes the possibility of observing TADF. As a realistic compromise between these extremes, a twist of the donor and acceptor moeties by about ±10° away from orthogonality could markedly improve the situation: The mutual SOCME between S_1 and T_1 increases steeply while the CT weight of the S_1 and T_1 wave functions and the ΔE_{ST} values are still close to their optima.

Similar conclusions can be drawn for compound **4-diMe**. The fact that the graphs for torsion angles <90° and >90°, displayed in Figure 3C,D, are not perfect mirror images of one another, although the bridge is symmetrically substituted, is a consequence of the propellar structure of the TAA unit.

However, the qualitative picture changes when the nuclear frame is allowed to adapt to the electronic structure of the excited states. In particular, the S_1−T_1 energy gap does no longer approach zero for a perpendicular orientation of donor and acceptor. Moreover, the data suggest that a three-state model of the excited-state decay, comprising only the S_0, ^{1}CT, and ^{3}CT states and their mutual couplings, might not be sufficient. The reasons underlying this behavior are discussed below.

Geometry Relaxation Effects on the S_1 and T_1 States. For all compounds, the minimum of the T_1 PES is located at much smaller torsion angles than the one of the S_1 PES (Table 1). Geometry relaxation of **2-Me** in the S_1 state, for example, yields a minimum at 65.9°, whereas the minimum of the T_1 state is found at 41.7°. The eligability of the applied quantum chemical methods to determine the equilibrium structures of the excited states may be judged from a convincing match of our results with recent time-resolved near-infrared spectroscopy measurements.[60] The disparity of the S_1 and T_1 equilibrium torsion angles is rooted in the fact that exchange interactions which stabilize triplet-coupled open-shell determinants with respect to singlet-coupled ones are much stronger in LE $\pi\pi^*$ states than in CT states where the overlap of the involved open-shell electron densities is small. Consequentially, the contributions of LE configurations to the T_1 wave function are much higher than to the corresponding S_1 wave function. Moreover, the percentage of LE contributions is seen to vary with the torsion angle in the investigated D−A compounds.

Relaxed scans of the first excited singlet and triplet PESs for fixed values of the torsional coordinate while optimizing all other nuclear degrees of freedom were computed at the TDDFT/ωB97X-D level of theory. For **2-Me**, properties derived from single-point DFT/MRCI calculations along these paths are shown in Figure 4. The analysis of the one-particle

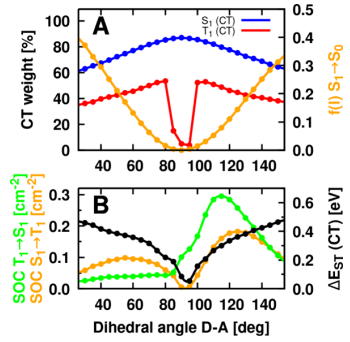

Figure 4. Properties of DFT/MRCI wave functions resulting from single-point calculations along relaxed TDDFT paths of the S_1 and T_1 states. (A) CT character of the first excited singlet (blue) and triplet (red) state. Oscillator strength for the $S_1 \rightarrow S_0$ transition (orange) of **2-Me**. (B) ΔE_{ST} (black) and sum of squared SOCMEs between S_1 and T_1 states (ISC: orange, rISC: green) of **2-Me**.

transition density matrix reveals that the S_1 state has predominantly CT character across the considered range of torsion angles, reaching its maximum at 90°. The large exchange interactions in LE $\pi\pi^*$ states stabilize ^{3}LE states which are therefore energetically much closer to the CT states than their singlet counterparts. For this reason, the wave function of the T_1 state exhibits substantial contributions from LE configurations both on the TAA donor and TPN acceptor

https://doi.org/10.1021/acs.jpcc.4c03865
J. Phys. Chem. C 2024, 128, 13711−13721

moieties (Figures S5 and S6). The LE character is particularly pronounced at torsion angles close to planarity. With increasing interplanar D−A angle, the CT contributions to the T_1 wave function rise to about 50% until they suddenly drop as the torsion angle approaches 85° (Figure 4A), indicating a major change in the electronic structure of the T_1 state and a breakdown of the Born−Oppenheimer approximation. In the LE regime, the T_1 state originates mainly from a local excitation on the TPN acceptor moiety, $^3LE_{TPN}$, while the T_2 state is predominantly of CT type.

The change in the electronic structure of the T_1 state when switching from the CT to the LE regime is reflected in a sudden increase of the mutual S_1−T_1 SOC close to an orthogonal D−A arrangement (Figure 4B). The leading configurations of the ^1CT and $^3LE_{TPN}$ states share the electron accepting orbital on the TPN moiety, but the hole orbitals are different. This means that the S_1 and $^3LE_{TPN}$ states are singly excited with respect to one another, an important property in view of the effective one-electron nature and symmetry properties of the SOC operator. The energetically accessible PES crossing of the T_1 and T_2 states therefore has interesting consequences for the ISC and rISC probabilities: A three-state equilibrium model, underlying the Arrhenius analysis of the prompt and delayed fluorescence decay times, is not considered appropriate for describing the kinetic scheme of ISC and rISC processes in **2-Me**. The analysis of the excited-state energy profiles of **1-H**, **3-iPr**, and **4-diMe** suggests similar excited-state decay characteristics for these compounds as well.

Emission Properties. For the theoretical simulation of emission properties, the commonly used adiabatic Hessian (AH) method[61,62] results in featureless and very broad emission spectra (Figure 5a). Due to large-amplitude motions in low-frequency vibrational modes, the harmonic oscillator model, which uses the respective equilibrium geometry as offset for the Taylor expansion of the PES, is not appropriate. In the compounds studied in this work, mainly the torsional coordinate between donor and acceptor is involved. The vertical Hessian (VH) method for the computation of vibronic spectra[48] yields emission bands with spectral origins and peak maxima (Figure 5b) in excellent agreement with the experiment.[63]

Because the harmonic approximation tends to overestimate the Franck−Condon (FC) factors between the initial vibrational level in the electronically excited state and higher vibrational quanta of torsional modes in the electronic ground state, the computed spectra are somewhat broader than their experimental counterparts (Figure 5b, shown for **2-Me**). The emission spectra of **1-H**, **2-Me**, and **3-iPr** are almost superimposable with maxima at 499, 495, and 496 nm, respectively, while the **4-diMe** emission (λ_{max} = 513 nm) is somewhat red-shifted. The oscillator strength of the $S_1 \rightarrow S_0$ emission follows the trend observed already for absorption, i.e., we see a large step between **1-H** and **2-Me**, very similar values for **2-Me** and **3-iPr** and a reduction by a factor of 10 when moving to **4-diMe** (Table 2). Pure radiative lifetimes (without consideration of competitive nonradiative channels) vary between 10 and 590 ns in this series. Radiative lifetimes in the 500 ns regime may appear long, but they are not untypical for organic D−A TADF emitters.

Singlet−Triplet Energy Gap ΔE_{ST}. The ability of a molecule to emit TADF critically depends on the size of the singlet−triplet energy gap ΔE_{ST}. In earlier work by Sommer et al.,[20] a value of 980 cm^{-1} (122 meV) had been derived for the energy difference between the S_1 and T_1 states of **2-Me** on the basis of an Arrhenius plot. In the same work, a quantum chemically determined energy separation of 840 cm^{-1} (104 meV) was reported. Note, however, that this value resulted from single-point TDDFT calculations at the optimized S_0 geometry, i.e., in the absorption region. This vertical energy gap is therefore neither directly comparable to the 0−0 energy difference underlying the Arrhenius equations nor to the energy shifts derived from the maxima of the fluorescence and phosphorescence spectra. Since TADF is not an ultrafast process that proceeds on the subpicosecond time scale, the nuclear arrangement has the time to adapt to the electronic potentials of the S_1 and T_1 states, respectively.

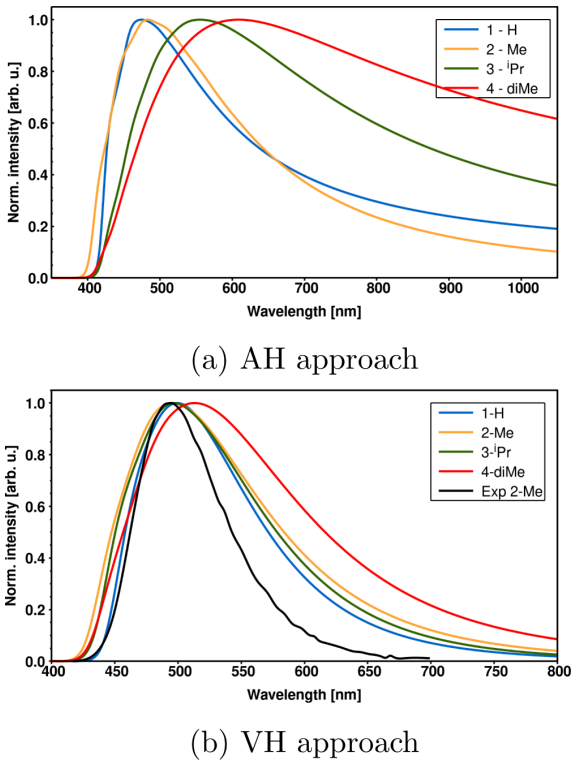

Figure 5. Computed emission spectra of **1-H** (blue), **2-Me** (orange), **3-^{i}Pr** (green), and **4-diMe** (red) in toluene solution at 300 K in comparison with an experimental emission spectrum of **2-Me** in toluene at 300 K.[63] (a) adiabatic Hessian approach and (b) vertical Hessian approach.

Table 2. Computed $S_1 \rightarrow S_0$ Emission Wavelengths/nm of DFT/MRCI Line Spectra (vert.), Adiabatic Hessian (AH), and Vertical Hessian (VH) Spectra[a]

	Compound			
	1-H	**2-Me**	**3-^{i}Pr**	**4-diMe**
vert.	482	484	490	492
f(l)	0.348	0.090	0.071	0.006
$\tau_{rad.}$	10	39	51	590
AH	474	483	555	609
VH	499	495	496	513

[a]Oscillator strengths $f(l)$ and radiative lifetimes τ_{rad}/ns are obtained from the Einstein relation at the S_1 minimum.

https://doi.org/10.1021/acs.jpcc.4c03865
J. Phys. Chem. C 2024, 128, 13711−13721

The data presented in Table 1 reveal that the torsion angles of the S_1 and S_0 equilibrium structures are similar whereas T_1 has its minimum at markedly reduced values of the torsional coordinate. As a consequence, geometry relaxation in the excited state increases the ΔE_{ST} values substantially (Table 3). The consideration of zero-point vibrational energy corrections changes the overall picture only slightly.

Table 3. DFT/MRCI computed S_1 - T_1 energy differences ΔE_{ST}/meV in toluene solution

	Compound			
	1-H	2-Me	3-^{i}Pr	4-diMe
$\Delta E_{ST,vert}$ [a,b]	341	192	162	73
$\Delta E_{ST,adiab}$ [a]	501	438	428	333
$\Delta E_{ST,adiab}$ [c]	—	263	—	—
$\Delta E_{ST,0-0}$ [a]	510	481	463	322

[a]PCM. [b]Evaluated at the S_0 minimum geometry. [c]Hybrid solvent model, see text.

We thus have to face the situation that the computed S_1−T_1 0−0 energy gaps are significantly larger than expected for a TADF emitter. This may have a variety of reasons which are analyzed and discussed in the following.

In liquid solutions, the primarily excited solute does not only relax internal nuclear degrees of freedom. For all but ultrafast processes, the reorganization of the solvent environment has to be taken into consideration as well. Initially, the electronic ground state of the emitter molecule and the solvent are in equilibrium. Upon electronic excitation, the charge distribution changes almost instantaneously, effectuating that the solvent degrees of freedom must adapt to the new situation. Since solute and solvent have different response times, a slow evolution from the nonequilibrium to the equilibrium solvation occurs.

Solvent reorganization effects on spectroscopic properties are notoriously difficult to model, however. To simulate the coupling between the solute and solvent, typically a two step process is used in a polarizable continuum model (PCM): (i) Directly after the vertical transition process, the final state of the solute experiences an electrostatic field corresponding to a solvent polarization frozen to the initial state. (ii) A dynamic component of the solvent polarization rearranges to equilibrate with the final state charge density of the solute. While in linear response models the latter process is computed from the transition density, state-specific models like the corrected linear response (cLR) approach[64] incorporate solvent reorganization effects on the basis of electron density differences between initial and final states, including a density-dependent relaxation of the solvent polarization.[65]

The cLR model works extremely well for CT excitations of polar transition metal complexes such as carbene coinage metal amides.[66,67] In these compounds, the CT excitation reduces the static dipole moment of the molecule. Applied to **2-Me** that exhibits a much larger static dipole moment in the S_1 state than in the S_0 state, the cLR model apparently overshoots: The cLR corrections lower the emission energy in toluene solution by about 5000 cm^{-1} (Table S6) in comparison to a PCM environment. Considering the good agreement of the PCM-computed emission spectrum with its experimental counterpart (Figure 5b), this energy shift seems too strong and speaks against the applicability of the cLR model in the present case.

Recently, Mewes and co-workers advertised a state-specific ROKS/PCM approach,[14,68] which appears to work well for many organic D−A systems but fails to reproduce the published experimental ΔE_{ST} value for a few emitter compounds including **2-Me**.[20] The adiabatic energy separations between the S_1 and T_1 states of **2-Me** in toluene, reported in that study, are significantly larger than the experimentally derived value and rather resemble the computational results of the present work.

Instead of employing a continuum model for describing solvation effects, explicit toluene molecules could be used to form a solvent shell. To obtain a representative, statistically balanced distribution, extensive molecular dynamics simulations would have to be carried out[69] which is beyond the scope of the present work. Here, we persued a middle way and placed two toluene molecules close to the π-bridge using the Quantum Cluster Growth extension of the CREST program[70,71] (Figure 6). These two toluene molecules were then

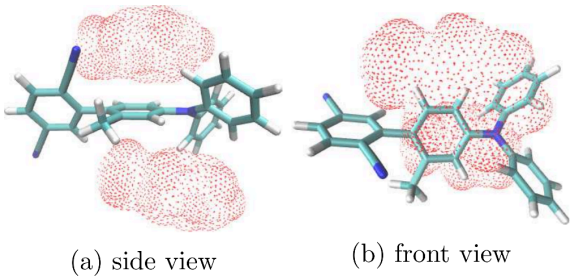

Figure 6. Optimized structure of **2-Me** in the electronic ground state with two explicit toluene solvent molecules. The red crosses indicate the van der Waals surfaces of the toluene molecules.

explicitly included in our quantum chemical calculations of the excited-state properties, and the whole complex was enclosed by a PCM cavity. While effects of this hybrid solvation model on the relaxed geometries are minimal, the electronic effect lowers the CT excitations in comparison to the implicit solvent model (Table S7). We do not see any indications for an exciplex formation. Rather, we attribute the preferential stabilization of the solute in the S_1 state to attractive interactions between its strong electric dipole moment and the highly polarizable π-electron clouds of the toluene molecules. As the electric dipole moment of **2-Me** in the T_1 state is much smaller than in S_1, the explicit consideration of the solvent−solute interactions results in a decreased ΔE_{ST} gap as desired.

Rate Constants. The attempt to model explicit solvent interactions by two quantum chemically treated toluene molecules greatly improves the adiabatic singlet−triplet energy gap of **2-Me** from 0.44 eV (PCM) to 0.26 eV (hybrid solvent model). Within the harmonic oscillator model, the adiabatic Hessian (AH) approach[49] (Figure 7, left), commonly used so far in our group, yields room-temperature ISC rate constants of 3×10^6 s^{-1} (PCM) and 2×10^6 s^{-1} (hybrid solvent model) in FC approximation. As expected, the ΔE_{ST} value has larger impact on the rISC process, for which rate constants of 2×10^{-2} s^{-1} (PCM) and 6×10^1 s^{-1} (hybrid solvent model) are obtained. The computed ΔE_{ST} value is thus still too large to yield rISC rate constants which are compatible with the experimentally determined TADF lifetime of ≈30 μs.[20]

https://doi.org/10.1021/acs.jpcc.4c03865
J. Phys. Chem. C 2024, 128, 13711−13721

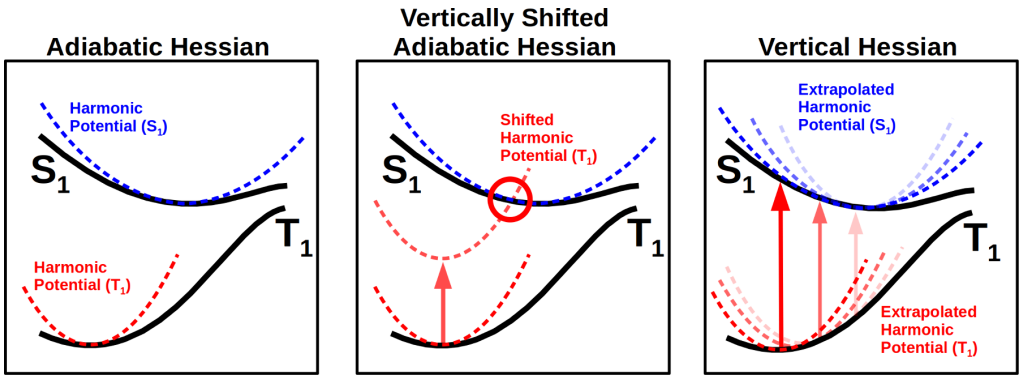

Figure 7. Schematic comparing the adiabatic Hessian (AH, left), vertically shifted adiabatic Hessian (center), and vertical Hessian (VH, right) approaches.

Could the crossing of the ^{1}CT and ^{3}CT PESs with the $^3LE_{TPN}$ PES in the neighborhood of a perpendicular conformation (see the Geometry Relaxation Effects on the S1 and T1 States section) play a decisive role? The spin-vibronic mechanism is known to substantially accelarate TADF in organic donor—acceptor compounds exhibiting a low-lying ^{3}LE state energetically close to the ^{3}CT and ^{1}CT states.[19] For example, by including spin-vibronic interactions by means of a Herzberg—Teller-like expansion of the coupling, we could successfully explain the complicated excited-state decay behavior of the through-space CT TADF emitter TpAT-tFFO[72,73] and of the well-known through-bond CT TADF emitter DMAC-TRZ.[74,75] Going beyond the FC approximation in the case of **2-Me** in an implicit solvent environment increases the rISC rate constant at room temperature merely to 9×10^{-2} s^{-1}, a value still much too small to explain the experimentally observed TADF.

In a second attempt to remedy the problem, we simply adjusted the singlet—triplet energy gaps by vertically shifting the harmonic potentials of S_1 and T_1 (Figure 7, center). The rate constants computed for ΔE_{ST} values between 50 and 400 meV in AH approximation are presented in Tables S8 and S9. With a decreasing singlet—triplet energy gap, the rISC rate constant increases by several orders of magnitude. Although the results meet our expectations at first sight, they are not fully credible. Since the S_1 and T_1 states are not nested, a strong energetic shift could lead to crossing potential energy surfaces. We observe this situation for **4-diMe** (Tables S8 and S9, ΔE_{ST} < 100 meV) where rISC is faster than ISC.

Earlier theoretical studies suggest that the static picture underlying the AH approach is not sufficient to model the TADF process in conformationally flexible emitters.[19] For example, Penfold and co-workers presented an extensive study using quantum nuclear dynamics to enlighten the excited-state processes in a copper phenanthroline complex undergoing large-amplitude flattening distortions.[76−78] A similar dynamic mechanism was postulated for linear carbene metal amides, where the torsional motion about the metal—ligand bond plays a key role for the understanding of its photophysics.[66,79] A simplified 3-state model that accounts for the spin-vibronic coupling of a ^{1}CT, ^{3}CT, and ^{3}LE state to a conformational degree of freedom associated with the torsion angle was presented lately by Dhali et al.[75] Their analysis is based on a scan of the torsional coordinate in the optimized electronic ground-state, however. For **2-Me**, the energy profiles of the relaxed excited-state scans are quite different from the unrelaxed energy profiles along the ground-state scan. The simplified 3-state model of Dhali et al. therefore does not appear applicable in the present case.

The above-mentioned studies point toward a dynamic kinetic scheme in which the population transfer between the S_1 and T_1 surfaces and the radiative decay of the S_1 population to the S_0 potential occur at different points in coordinate space. For **2-Me**, the ΔE_{ST} gap is smallest for an orthogonal D—A orientation and, therefore, rISC is expected to occur primarily here. In contrast, the electric dipole transition probability is very low at 90° but increases appreciably as the torsion angle gets smaller (Figure 4 and Table S11). Fluorescence is therefore preferentially emitted in less twisted conformations.

To mimic the dynamic behavior of the ISC and rISC processes in **2-Me** without resorting to costly quantum dynamics simulations, we applied a vertical Hessian (VH) approach to determine rate constants at fixed torsion angles of the relaxed S_1 path (Figure 7, right). The VH method is well established for computing absorption and emission spectra,[61,62,80,81] but it has, to our knowledge, so far not been applied by other groups to determine vibrational densities of states for nonradiative transitions such as ISC and rISC. Briefly, this method uses the gradients and Hessians of the initial and final electronic states at the fixed geometry of the initial state to extrapolate the course of the PESs and to compute FC factors. In the limit of strictly parabolic PESs, the VH and AH methods are supposed to yield identical results. The AH method is known to yield promising results for the onset of a vibronic spectrum and the 0—0 transitions. In contrast, in the strong coupling case, which is characterized by large geometric displacements of the minima in at least one vibrational coordinate,[82] we expect the VH model to be more realistic, especially in cases in which these displacements are related to low-frequency modes. Details of the method and its implementation are presented in a separate paper by Böhmer et al.[48]

Application of the VH method to the $S_1 \rightsquigarrow T_1$ ISC in **2-Me** yields rate constants ranging between 10^6 and 10^7 s^{-1} upon variation of the torsion angle (Figure 8). Interestingly, the highest value is obtained for 60°, close to the equilibrium geometry of the S_1 state. In contrast, the reverse $S_1 \leftsquigarrow T_1$ ISC process speeds up dramatically as the torsion angle increases. Starting from values of the order of 1 s^{-1} at the T_1 minimum, the rISC rate constant grows roughly exponentially to about 5

https://doi.org/10.1021/acs.jpcc.4c03865
J. Phys. Chem. C 2024, 128, 13711−13721

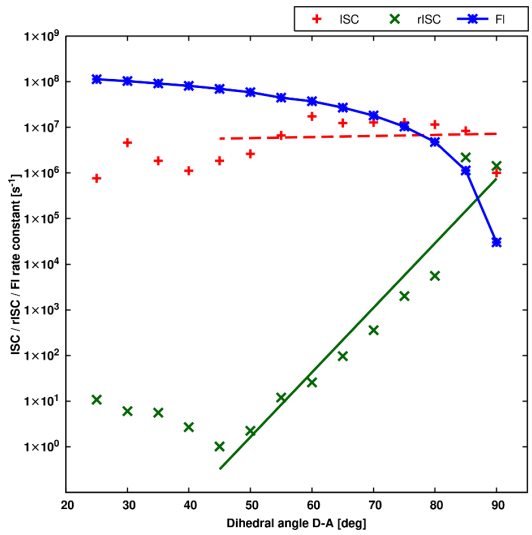

Figure 8. DFT/MRCI fluorescence rate constants of **2-Me** based on the Einstein relation, $S_1 \rightsquigarrow T_1$ ISC and $S_1 \leftsquigarrow T_1$ rISC rate constants in toluene (PCM) at 298 K. Note the logarithmic scale on the *y*-axis. The computed rate constants were supplemented by an exponential fitting from 45 (T_1 minimum) to 90 deg.

$\times 10^3$ s^{-1} for an angle of 80°. This value appears to be in the right ballpark in view of the experimentally observed delayed fluorescence lifetime of 357.5 μs[63] of **2-Me**. The sudden jump of the rISC rate constant to values between 10^6 and 10^7 s^{-1} for torsion angles between 85° and 90° is only partially caused by the diminishing S_1-T_1 energy gap. A large portion of this increase is due to the leading $^3LE_{TPN}$ character of the T_1 state in this regime and the concomitant enhancement of the SOC.

In the case of **4-diMe**, we computed ISC and rISC rate constants for a torsion angle of 81.8°, corresponding to the dihedral angle of the S_1 minimum structure. The VH method yields an extrapolated energy gap of 635 cm^{-1} and a rate constant of k_{ISC} = 3.9 × 10^6 s^{-1} for the forward $S_1 \rightsquigarrow T_1$ process, similar to the computed ISC rate constants of **2-Me**. The backward transition proceeds at a much shorter time scale in **4-diMe** than the corresponding process in **2-Me**. For $S_1 \leftsquigarrow T_1$, the VH method yields an extrapolated energy gap of −716 cm^{-1} and a rate constant of k_{rISC} = 4.6 × 10^4 s^{-1}, in good agreement with the experimentally observed delayed fluorescence lifetime of 18.4 μs[63] of **4-diMe**.

CONCLUSIONS

In this work, we have investigated the impact of chemical substitution on the TADF properties of triarylamine−terephthalonitrile emitters that exhibit blue emission wavelengths by means of advanced quantum chemical methods. The substituents, one (**2-Me**) or two methyl groups (**4-diMe**) or an isopropyl residue (**3-^{i}Pr**), are attached to the donor in the ortho position of the donor−acceptor linkage. The inductive effects brought about by the subsitution are found to be minimal. Rather, we attribute the variation of the photophysical properties among the compounds predominantly to the sterical strain exerted by the substituents. We could prove a clear correlation between the D−A twist angle and the absorption profile of a compound. For the respective most stable conformer, this dihedral angle varies between ∼50° (**1-H**) and ∼87° (**4-diMe**) in the electronic ground state. Similar dihedral angles are observed for the equilibrium structures of the S_1 states which exhibit ^{1}CT character. The corresponding T_1 states are markedly less twisted due to the admixture of $^3LE_{TAA}$ configurations. This disparity results in adiabatic ΔE_{ST} values which are much larger than the energy gaps determined from experimental data on the basis of Arrhenius plots.

Part of the problem seems to be caused by the continuum model of the solvent−solute interactions which does not fully account for the solvent reorganization effects following the primary excitation of the S_1 state. The shortcomings of the solvent model are not a specific problem of the methods employed in the present work but are a common phenomenon discussed in the literature. For **2-diMe**, a hybrid model was set up comprising two explicitly treated toluene molecules in addition to the surrounding self-consistent reaction field. The interaction between the highly polarizable π-electron clouds of the toluene molecules and the electric dipole moment of the solute in the excited state preferentially stabilizes the S_1 potential energy and improves the ΔE_{ST} value. However, the magnitude of the resulting adiabatic singlet−triplet energy gap still appears to be incompatible with the experimentally observed delayed fluorescence lifetimes.

Potential energy scans of the torsional coordinate in the excited state reveal the presence of a further low-lying electronic state, so far not discussed in the relevant literature. While the S_1 state retains ^{1}CT character at all considered nuclear arrangements, an energetically accessible crossing between states of ^{3}CT and $^3LE_{TPN}$ character is observed close to the perpendicular arrangement of the donor and acceptor moieties. Due to the presence of this conical intersection, a three-state kinetic model of the TADF processes resting only on the S_0 ground state and the ^{1}CT and ^{3}CT excited states and their mutual couplings appears inappropriate. Spin-vibronic interactions, accounted for by means of a Herzberg−Teller-type expansion of the S_1-T_1 SOC, change the picture only marginally.

Like other conformationally flexible through-bond D−A systems, the TAA-TPN emitters face the situation that the vertical singlet−triplet energy gap is small and hence rISC is large only for a perpendicular alignment of the donor and acceptor units where the transition dipole moment and hence the emission probability vanish. While a static description of the TADF process, based on rate constants for an equilibrated population of the excited singlet and triplet state, is unable to deal with the problem, a quantum dynamical treatment is prohibitively expensive considering the microsecond time scale of the TADF kinetics. Relaxed scans of the excited state potentials and scans along the torsional coordinate in the electronic ground state yield qualitatively different results in the series of compounds, questioning the credibility of simplified dynamic models.

To mimic the dynamical behavior of a system undergoing large-amplitude motions without resorting to costly dynamics simulations, we here advocate the application of the vertical Hessian (VH) method. The VH method is well established for computing FC spectra, but has, to our knowledge, not been employed by other groups for determining rate constants of nonradiative transitions. This method uses the gradients and Hessians of the initial and final electronic states at the fixed geometry of the initial state to extrapolate the course of the PESs and to compute the FC factors and the vibrational

https://doi.org/10.1021/acs.jpcc.4c03865
J. Phys. Chem. C 2024, 128, 13711−13721

density of states. Due to the large displacement of the S_1 and T_1 minima in the torsional coordinate, we expect the VH model to yield more realistic rate constants than the commonly used adiabatic approaches.

Evidently, the steric demand of the substituents controls the D−A torsion angle and hence the ΔE_{ST} value. The ratio between $S_1 \rightsquigarrow T_1$ ISC and $S_1 \leftsquigarrow T_1$ rISC probabilities is negligibly small for the unsubstituted compound and maximizes in this series for the dimethylated compound. We therefore consider **4-diMe** the most promising candidate for showing TADF behavior. The increased percentage of the delayed component does not remedy the problem that its overall radiative rate constant of $\sim 2 \times 10^6\ s^{-1}$ is rather low but not untypical for an organic D−A compound.

■ ASSOCIATED CONTENT

Supporting Information

The Supporting Information is available free of charge at https://pubs.acs.org/doi/10.1021/acs.jpcc.4c03865.

> Characterization of the excited singlet states in the absorption region showing the wave function composition and molecular orbitals of all compounds, emission spectra using the adiabatic Hessian approach, solvent shifts and rate constants according to various models, and procedure for the optimization of the range-separation parameter (PDF)

■ AUTHOR INFORMATION

Corresponding Author

Christel M. Marian − *Institute of Theoretical and Computational Chemistry, Faculty of Mathematics and Natural Sciences, Heinrich Heine University Düsseldorf, 40225 Düsseldorf, Germany;* orcid.org/0000-0001-7148-0900; Email: christel.marian@hhu.de

Authors

Jeremy M. Kaminski − *Institute of Theoretical and Computational Chemistry, Faculty of Mathematics and Natural Sciences, Heinrich Heine University Düsseldorf, 40225 Düsseldorf, Germany*

Tobias Böhmer − *Institute of Theoretical and Computational Chemistry, Faculty of Mathematics and Natural Sciences, Heinrich Heine University Düsseldorf, 40225 Düsseldorf, Germany;* orcid.org/0009-0004-2823-5300

Complete contact information is available at: https://pubs.acs.org/10.1021/acs.jpcc.4c03865

Author Contributions

J.M.K. and T.B. contributed equally to this work.

Notes

The authors declare no competing financial interest.

■ ACKNOWLEDGMENTS

The authors thank the Deutsche Forschungsgemeinschaft (DFG, German Research Foundation) for financial support through GRK 2482, project no. 396890929, and the members of the research training network ModISC, in particular Dragana Sretenović and Ralf Kühnemuth, for valuable discussions.

■ REFERENCES

(1) Teng, J.-M.; Wang, Y.-F.; Chen, C.-F. Recent progress of narrowband TADF emitters and their applications in OLEDs. *J. Mater. Chem. C* **2020**, *8*, 11340−11353.

(2) Tenopala-Carmona, F.; Lee, O. S.; Crovini, E.; Neferu, A. M.; Murawski, C.; Olivier, Y.; Zysman-Colman, E.; Gather, M. C. Identification of the key parameters for horizontal transition dipole orientation in fluorescent and TADF organic light-emitting diodes. *Adv. Mater.* **2021**, *33*, 2100677.

(3) Kim, J. H.; Yun, J. H.; Lee, J. Y. Recent progress of highly efficient red and near-infrared thermally activated delayed fluorescent emitters. *Adv. Opt. Mater.* **2018**, *6*, 1800255.

(4) Zhang, Y.; Zhang, D.; Cai, M.; Li, Y.; Zhang, D.; Qiu, Y.; Duan, L. Towards highly efficient red thermally activated delayed fluorescence materials by the control of intra-molecular $\pi-\pi$ stacking interactions. *J. Nanotechnol.* **2016**, *27*, 094001.

(5) Zhang, Y.-L.; Ran, Q.; Wang, Q.; Liu, Y.; Hänisch, C.; Reineke, S.; Fan, J.; Liao, L.-S. High-efficiency red organic light-emitting diodes with external quantum efficiency close to 30% based on a novel thermally activated delayed fluorescence emitter. *Adv. Mater.* **2019**, *31*, 1902368.

(6) Braveenth, R.; Lee, H.; Kim, S.; Raagulan, K.; Kim, S.; Kwon, J. H.; Chai, K. Y. High efficiency green TADF emitters of acridine donor and triazine acceptor D−A−D structures. *J. Mater. Chem. C* **2019**, *7*, 7672−7680.

(7) Zhou, D.; Tong, G. S. M.; Cheng, G.; Tang, Y.-K.; Liu, W.; Ma, D.; Du, L.; Chen, J.-R.; Che, C.-M. Stable tetradentate gold(III)-TADF emitters with close to unity quantum yield and radiative decay rate constant of up to $2 \times 10^6\ s^{-1}$: High-efficiency green OLEDs with operational lifetime (LT90) longer than 1800 h at 1000 cd m^{-2}. *Adv. Mater.* **2022**, *34*, 2206598.

(8) Huang, Z.; Xiang, S.; Zhang, Q.; Lv, X.; Ye, S.; Guo, R.; Wang, L. Highly efficient green organic light emitting diodes with phenanthroimidazole-based thermally activated delayed fluorescence emitters. *J. Mater. Chem. C* **2018**, *6*, 2379−2386.

(9) Endo, A.; Ogasawara, M.; Takahashi, A.; Yokoyama, D.; Kato, Y.; Adachi, C. Thermally activated delayed fluorescence from Sn^{4+}-porphyrin complexes and their application to organic light-emitting diodes-A novel mechanism for electroluminescence. *Adv. Mater.* **2009**, *21*, 4802−4806.

(10) Perrin, F. La fluorescence des solutions−Induction moléculaire.−Polarisation et durée d'émission.−Photochimie. *Ann. Phys.* **1929**, *10*, 169−275.

(11) Uoyama, H.; Goushi, K.; Shizu, K.; Nomura, H.; Adachi, C. Highly efficient organic light-emitting diodes from delayed fluorescence. *Nature* **2012**, *492*, 234−238.

(12) Wong, M. Y.; Zysman-Colman, E. Purely organic thermally activated delayed fluorescence materials for organic light-emitting diodes. *Adv. Mater.* **2017**, *29*, 1605444.

(13) Arjona-Esteban, A.; Szafranowska, B.; Ochsmann, J. In *Luminescence*; Pyshkin, S., Ed.; IntechOpen: Rijeka, 2019; Chapter 6.

(14) Kunze, L.; Hansen, A.; Grimme, S.; Mewes, J.-M. PCM-ROKS for the description of charge-transfer states in solution: Singlet−triplet gaps with chemical accuracy from open-shell Kohn−Sham reaction-field calculations. *J. Phys. Chem. Lett.* **2021**, *12*, 8470−8480.

(15) Liang, X.; Tu, Z.-L.; Zheng, Y.-X. Thermally activated delayed fluorescence materials: towards realization of high efficiency through strategic small molecular design. *Chem.—Eur. J.* **2019**, *25*, 5623−5642.

(16) Naqvi, B. A.; Schmid, M.; Crovini, E.; Sahay, P.; Naujoks, T.; Rodella, F.; Zhang, Z.; Strohriegl, P.; Bräse, S.; Zysman-Colman, E.; Brütting, W. What controls the orientation of TADF emitters? *Front. Chem.* **2020**, *8*, 750.

(17) Nobuyasu, R. S.; Ren, Z.; Griffiths, G. C.; Batsanov, A. S.; Data, S. P.; Yan; Monkman, A. P.; Bryce, M. R.; Dias, F. B. Rational design of TADF polymers using a donor−acceptor monomer with enhanced TADF efficiency induced by the energy alignment of charge transfer and local triplet excited states. *Adv. Opt. Mater.* **2016**, *4*, 597−607.

(18) Etherington, M. K.; Gibson, J.; Higginbotham, H. F.; Penfold, T. J.; Monkman, A. P. Revealing the spin−vibronic coupling mechanism of thermally activated delayed fluorescence. *Nat. Commun.* **2016**, *7*, 13680.
(19) Penfold, T. J.; Gindensperger, E.; Daniel, C.; Marian, C. M. Spin-vibronic mechanism for intersystem crossing. *Chem. Rev.* **2018**, *118*, 6975−7025.
(20) Sommer, G. A.; Mataranga-Popa, L. N.; Czerwieniec, R.; Hofbeck, T.; Homeier, H. H.; Müller, T. J.; Yersin, H. Design of conformationally distorted donor−acceptor dyads showing efficient thermally activated delayed fluorescence. *J. Phys. Chem. Lett.* **2018**, *9*, 3692−3697.
(21) Cao, X.; Zhang, D.; Zhang, S.; Tao, Y.; Huang, W. CN-containing donor−acceptor-type small-molecule materials for thermally activated delayed fluorescence OLEDs. *J. Mater. Chem. C* **2017**, *5*, 7699−7714.
(22) Chen, S.; Xu, X.; Liu, Y.; Yu, G.; Sun, X.; Qiu, W.; Ma, Y.; Zhu, D. Synthesis and characterization of n-type materials for non-doped organic red-light-emitting diodes. *Adv. Funct. Mater.* **2005**, *15*, 1541−1546.
(23) Wang, S.; Yan, X.; Cheng, Z.; Zhang, H.; Liu, Y.; Wang, Y. Highly efficient near-infrared delayed fluorescence organic light emitting diodes using a phenanthrene-based charge-transfer compound. *Angew. Chem., Int. Ed.* **2015**, *54*, 13068−13072.
(24) Lin, C.-Y.; Lu, C.-H.; Kuo, K.-H.; Wang, M.; Tang, Y.; Dou, Y.; Hu, B.; Wu, C.-C.; Wong, K.-T. Highly efficient blue thermally activated delayed fluorescence emitters with a triphenylamine-based macrocyclic donor. *Adv. Opt. Mater.* **2023**, *11*, 2202292.
(25) Frisch, M. J., Trucks, G. W., Schlegel, H. B., Scuseria, G. E., Robb, M. A., Cheeseman, J. R., Scalmani, G., Barone, V., Petersson, G. A., Nakatsuji, H. et al. *Gaussian 16*, revision A.03; Gaussian, Inc.: Wallingford, CT, 2016.
(26) Chai, J.-D.; Head-Gordon, M. Long-range corrected hybrid density functionals with damped atom−atom dispersion corrections. *Phys. Chem. Chem. Phys.* **2008**, *10*, 6615−6620.
(27) Chai, J.-D.; Head-Gordon, M. Systematic optimization of long-range corrected hybrid density functionals. *J. Chem. Phys.* **2008**, *128*, 084106.
(28) Schäfer, A.; Horn, H.; Ahlrichs, R. Fully optimized contracted Gaussian basis sets for atoms Li to Kr. *J. Chem. Phys.* **1992**, *97*, 2571−2577.
(29) Weigend, F.; Ahlrichs, R. Balanced basis sets of split valence, triple zeta valence and quadruple zeta valence quality for H to Rn: Design and assessment of accuracy. *Phys. Chem. Chem. Phys.* **2005**, *7*, 3297.
(30) Weigend, F. Accurate Coulomb-fitting basis sets for H to Rn. *Phys. Chem. Chem. Phys.* **2006**, *8*, 1057−1065.
(31) Baer, R.; Livshits, E.; Salzner, U. Tuned range-separated hybrids in density functional theory. *Annu. Rev. Phys. Chem.* **2010**, *61*, 85−109.
(32) Kronik, L.; Stein, T.; Refaely-Abramson, S.; Baer, R. Excitation gaps of finite-sized systems from optimally tuned range-separated hybrid functionals. *J. Chem. Theory Comput.* **2012**, *8*, 1515−1531.
(33) Kronik, L.; Kümmel, S. Dielectric screening meets optimally tuned density functionals. *Adv. Mater.* **2018**, *30*, 1706560.
(34) Jacquemin, D.; Moore, B.; Planchat, A.; Adamo, C.; Autschbach, J. Performance of an optimally tuned range-separated hybrid functional for 0−0 electronic excitation energies. *J. Chem. Theory Comput.* **2014**, *10*, 1677−1685.
(35) Bokareva, O. S.; Grell, G.; Bokarev, S. I.; Kühn, O. Tuning range-separated density functional theory for photocatalytic water splitting systems. *J. Chem. Theory Comput.* **2015**, *11*, 1700−1709.
(36) Runge, E.; Gross, E. K. U. Density-functional theory for time-dependent systems. *Phys. Rev. Lett.* **1984**, *52*, 997−1000.
(37) Marques, M. A. L.; Gross, E. K. U. In *A Primer in Density Functional Theory*; Fiolhais, C., Nogueira, F., Marques, M. A. L., Eds.; Springer: Berlin, 2003; pp 144−184.
(38) Furche, F.; Ahlrichs, R. Adiabatic time-dependent density functional methods for excited state properties. *J. Chem. Phys.* **2002**, *117*, 7433−7447.
(39) Hirata, S.; Head-Gordon, M. Time-dependent density functional theory within the Tamm−Dancoff approximation. *Chem. Phys. Lett.* **1999**, *314*, 291−299.
(40) Cammi, R.; Corni, S.; Mennucci, B.; Tomasi, J. Electronic excitation energies of molecules in solution: State specific and linear response methods for nonequilibrium continuum solvation models. *J. Chem. Phys.* **2005**, *122*, 104513.
(41) Tomasi, J.; Mennucci, B.; Cammi, R. Quantum mechanical continuum solvation models. *Chem. Rev.* **2005**, *105*, 2999−3094.
(42) Scalmani, G.; Frisch, M. J.; Mennucci, B.; Tomasi, J.; Cammi, R.; Barone, V. Geometries and properties of excited states in the gas phase and in solution: Theory and application of a time-dependent density functional theory polarizable continuum model. *J. Chem. Phys.* **2006**, *124*, 094107.
(43) Grimme, S.; Waletzke, M. A combination of Kohn−Sham density functional theory and multi-reference configuration interaction methods. *J. Chem. Phys.* **1999**, *111*, 5645−5655.
(44) Marian, C. M.; Heil, A.; Kleinschmidt, M. The DFT/MRCI method. *WIREs Comput. Mol. Sci.* **2019**, *9*, e1394.
(45) Lyskov, I.; Kleinschmidt, M.; Marian, C. M. Redesign of the DFT/MRCI Hamiltonian. *J. Chem. Phys.* **2016**, *144*, 034104.
(46) Kleinschmidt, M.; Tatchen, J.; Marian, C. M. Spin-orbit coupling of DFT/MRCI wavefunctions: Method, test calculations, and application to thiophene. *J. Comput. Chem.* **2002**, *23*, 824−833.
(47) Kleinschmidt, M.; Marian, C. M. Efficient generation of matrix elements for one-electron spin−orbit operators. *Chem. Phys.* **2005**, *311*, 71−79.
(48) Böhmer, T., Kleinschmidt, M., Marian, C. M. Toward the improvement of vibronic spectra and non-radiative rate constants using the vertical Hessian method. *J. Chem. Phys.* **2024**, under revision.
(49) Etinski, M.; Tatchen, J.; Marian, C. M. Thermal and solvent effects on the triplet formation in cinnoline. *Phys. Chem. Chem. Phys.* **2014**, *16*, 4740.
(50) Etinski, M.; Tatchen, J.; Marian, C. M. Time-dependent approaches for the calculation of intersystem crossing rates. *J. Chem. Phys.* **2011**, *134*, 154105.
(51) Etinski, M.; Rai-Constapel, V.; Marian, C. M. Time-dependent approach to spin-vibronic coupling: Implementation and assessment. *J. Chem. Phys.* **2014**, *140*, 114104.
(52) Marian, C. M. Understanding and controlling intersystem crossing in molecules. *Annu. Rev. Phys. Chem.* **2021**, *72*, 617−640.
(53) Dinkelbach, F.; Marian, C. M. Vibronic and spin−orbit coupling effects in the absorption spectra of pyrazine: A quantum chemical approach. *J. Serb. Chem. Soc.* **2019**, *84*, 819−836.
(54) Rodriguez-Serrano, A.; Dinkelbach, F.; Marian, C. M. Intersystem crossing processes in the 2CzPN emitter: A DFT/MRCI study including vibrational spin−orbit interactions. *Phys. Chem. Chem. Phys.* **2021**, *23*, 3668−3678.
(55) Plasser, F. TheoDORE: A toolbox for a detailed and automated analysis of electronic excited state computations. *J. Chem. Phys.* **2020**, *152*, 084108.
(56) Sretenović, D.; Kloeters, L. N.; Kaminski, J. M.; Böhmer, T.; Schmeinck, P.; Sommer, G. A.; Chalani, M.; Felekyan, S.; Kühnemuth, R.; Reiß, G. J. et al. The effect of conformational constraints and oxygen quenching on TADF in donor-acceptor systems. **2024**, in preparation.
(57) Amthor, S.; Noller, B.; Lambert, C. UV/Vis/NIR spectral properties of triarylamines and their corresponding radical cations. *Chem. Phys.* **2005**, *316*, 141−152.
(58) Wiefermann, J.; Kaminski, J. M.; Pankert, E.; Hertel, D.; Meerholz, K.; Marian, C. M.; Müller, T. J. Highly luminescent blue emitter with balanced hybridized locally and charge-transfer excited-states emission. *ChemPhotoChem.* **2023**, *7*, e202200265.

(59) Balan, B.; Gopidas, K. R. Photoinduced electron transfer in α-cyclodextrin-based supramolecular dyads: A free-energy-dependence study. *Chem.Eur. J.* **2006**, *12*, 6701−6710.
(60) Haselbach, W.; Kaminski, J. M.; Kloeters, L. N.; Müller, T. J. J.; Weingart, O.; Marian, C. M.; Gilch, P.; Nogueira de Faria, B. E. A thermally activated delayed fluorescence emitter investigated by time-resolved near-infrared spectroscopy. *Chem.Eur. J.* **2023**, *29*, e202202809.
(61) Götze, J. P.; Karasulu, B.; Thiel, W. Computing UV/vis spectra from the adiabatic and vertical Franck−Condon schemes with the use of Cartesian and internal coordinates. *J. Chem. Phys.* **2013**, *139*, 234108.
(62) Ferrer, F. J. A.; Santoro, F. Comparison of vertical and adiabatic harmonic approaches for the calculation of the vibrational structure of electronic spectra. *Phys. Chem. Chem. Phys.* **2012**, *14*, 13549−13563.
(63) Sretenović, D. Photophysical properties of chromophores studied by multimodal fluorescence spectroscopy. PhD thesis, Heinrich Heine University Düsseldorf, 2024.
(64) Caricato, M.; Mennucci, B.; Tomasi, J.; Ingrosso, F.; Cammi, R.; Corni, S.; Scalmani, G. Formation and relaxation of excited states in solution: A new time dependent polarizable continuum model based on time dependent density functional theory. *J. Chem. Phys.* **2006**, *124*, 124520.
(65) Guido, C. A.; Jacquemin, D.; Adamo, C.; Mennucci, B. Electronic excitations in solution: the interplay between state specific approaches and a time-dependent density functional theory description. *J. Chem. Theory Comput.* **2015**, *11*, 5782−5790.
(66) Föller, J.; Marian, C. M. Rotationally assisted spin-state inversion in carbene−metal−amides is an artifact. *J. Phys. Chem. Lett.* **2017**, *8*, 5643−5647.
(67) Lüdtke, N.; Föller, J.; Marian, C. M. Understanding the luminescence properties of Cu(I) complexes: A quantum chemical perusal. *Phys. Chem. Chem. Phys.* **2020**, *22*, 23530−23544.
(68) Froitzheim, T.; Grimme, S.; Mewes, J.-M. Either accurate singlet−triplet gaps or excited-state structures: Testing and understanding the performance of TD-DFT for TADF emitters. *J. Chem. Theory Comput.* **2022**, *18*, 7702−7713.
(69) Parac, M.; Doerr, M.; Marian, C. M.; Thiel, W. QM/MM calculation of solvent effects on absorption spectra of guanine. *J. Comput. Chem.* **2010**, *31*, 90−106.
(70) Pracht, P.; Bohle, F.; Grimme, S. Automated exploration of the low-energy chemical space with fast quantum chemical methods. *Phys. Chem. Chem. Phys.* **2020**, *22*, 7169−7192.
(71) Spicher, S.; Plett, C.; Pracht, P.; Hansen, A.; Grimme, S. Automated molecular cluster growing for explicit solvation by efficient force field and tight binding methods. *J. Chem. Theory Comput.* **2022**, *18*, 3174−3189.
(72) Kaminski, J. M.; Rodríguez-Serrano, A.; Dinkelbach, F.; Miranda-Salinas, H.; Monkman, A. P.; Marian, C. M. Vibronic effects accelerate the intersystem crossing processes of the through-space charge transfer states in the triptycene bridged acridine−triazine donor−acceptor molecule TpAT-tFFO. *Chem. Sci.* **2022**, *13*, 7057−7066.
(73) Miranda-Salinas, H.; Rodriguez-Serrano, A.; Kaminski, J. M.; Dinkelbach, F.; Hiromichi, N.; Kusakabe, Y.; Kaji, H.; Marian, C. M.; Monkman, A. P. Conformational, host, and vibrational effects giving rise to dynamic TADF behavior in the through-space charge transfer, triptycene bridged acridine−triazine donor acceptor TADF molecule TpAT-tFFO. *J. Phys. Chem. C* **2023**, *127*, 8607−8617.
(74) Stavrou, K.; Franca, L. G.; Böhmer, T.; Duben, L. M.; Marian, C. M.; Monkman, A. P. Unexpected quasi-axial conformer in thermally activated delayed fluorescence DMAC-TRZ, pushing green OLEDs to blue. *Adv. Funct. Mater.* **2023**, *33*, 2300910.
(75) Dhali, R.; Phan Huu, D. K. A.; Bertocchi, F.; Sissa, C.; Terenziani, F.; Painelli, A. Understanding TADF: a joint experimental and theoretical study of DMAC-TRZ. *Phys. Chem. Chem. Phys.* **2021**, *23*, 378−387.
(76) Eng, J.; Penfold, T. J. Understanding and designing thermally activated delayed fluorescence emitters: beyond the energy gap approximation. *Chem. Rec.* **2020**, *20*, 831−856.
(77) Capano, G.; Penfold, T.; Chergui, M.; Tavernelli, I. Photophysics of a copper phenanthroline elucidated by trajectory and wavepacket-based quantum dynamics: a synergetic approach. *Phys. Chem. Chem. Phys.* **2017**, *19*, 19590−19600.
(78) Capano, G.; Chergui, M.; Rothlisberger, U.; Tavernelli, I.; Penfold, T. J. A quantum dynamics study of the ultrafast relaxation in a prototypical Cu(I)−phenanthroline. *J. Phys. Chem. A* **2014**, *118*, 9861−9869.
(79) Thompson, S.; Eng, J.; Penfold, T. J. The intersystem crossing of a cyclic (alkyl)(amino) carbene gold (i) complex. *J. Chem. Phys.* **2018**, *149*, 014304 DOI: 10.1063/1.5032185.
(80) Hazra, A.; Chang, H. H.; Nooijen, M. First principles simulation of the UV absorption spectrum of ethylene using the vertical Franck−Condon approach. *J. Chem. Phys.* **2004**, *121*, 2125−2136.
(81) Cerezo, J.; Santoro, F. FCclasses3: Vibrationally-resolved spectra simulated at the edge of the harmonic approximation. *J. Comput. Chem.* **2023**, *44*, 626−643.
(82) Englman, R.; Jortner, J. The energy gap law for radiationless transitions in large molecules. *Mol. Phys.* **1970**, *18*, 145−164.

Supporting Information: Balancing TADF Properties in π-Bridged Donor–Acceptor Systems by Sterical Constraints: The Best of Three Worlds

Jeremy M. Kaminski,[†,‡] Tobias Böhmer,[†,‡] and Christel M. Marian[*,†]

†*Institute of Theoretical and Computational Chemistry, Faculty of Mathematics and Natural Sciences, Heinrich Heine University Düsseldorf, Universitätsstraße 1, 40225 Düsseldorf*

‡*These authors contributed equally to this work.*

E-mail: christel.marian@hhu.de

Absorption Spectra

Table S1: DFT/MRCI-R2016 computed oscillator strengths f(l), vertical absorption wavelengths λ_{abs}/nm and wave function composition of low-lying electronic states at the respective ground-state geometry of the most stable conformer.

		Compound			
		1-H	**2-Me**	**3-^{i}Pr**	**4-diMe**
$\mathbf{S_1 \leftarrow S_0}$	λ_{abs} **(f(l))**	410 (0.237)	400 (0.077)	400 (0.047)	396 (0.002)
	[% **CT/LE$_{TAA}$/LE$_{TPN}$**]	70/10/9	80/6/4	82/5/4	87/2/2
$\mathbf{S_2 \leftarrow S_0}$	λ_{abs} **(f(l))**	331 (0.417)	319 (0.289)	315 (0.226)	307 (0.044)
	[% **CT/LE$_{TAA}$/LE$_{TPN}$**]	40/41/9	31/59/2	26/64/2	7/85/0
$\mathbf{S_3 \leftarrow S_0}$	λ_{abs} **(f(l))**	312 (0.022)	307 (0.163)	306 (0.231)	302 (0.436)
	[% **CT/LE$_{TAA}$/LE$_{TPN}$**]	4/86/0	9/82/1	12/80/1	15/77/1
$\mathbf{S_4 \leftarrow S_0}$	λ_{abs} **(f(l))**	296 (0.103)	291 (0.096)	291 (0.106)	286 (0.247)
	[% **CT/LE$_{TAA}$/LE$_{TPN}$**]	25/4/58	15/6/68	18/7/64	63/24/4
$\mathbf{S_5 \leftarrow S_0}$	λ_{abs} **(f(l))**	286 (0.151)	287 (0.266)	292 (0.089)	286 (0.288)
	[% **CT/LE$_{TAA}$/LE$_{TPN}$**]	2/91/0	1/93/0	0/93/1	1/94/0

Table S2: Composition of the DFT/MRCI wave functions of the five lowest excited singlet states of 1-H at the ground-state geometry. The orbitals involved in the excitation are displayed in Figure S1.

State	%	Transition		
S_1	81.2	H	→	L
	2.3	H-3	→	L
	2.1	H-1	→	L
	1.8	H	→	L+1
S_2	76.3	H	→	L+1
	4.6	H	→	L+4
	1.6	H-3	→	L+1
	1.5	H-1	→	L+1
	1.1	H	→	L
S_3	71.3	H	→	L+2
	2.5	H-2	→	L+1
	2.0	H-5	→	L+1
	1.8	H-2	→	L+4
	1.7	H-1	→	L+3
	1.4	H-2	→	L
	1.4	H-5	→	L
	1.2	H-3	→	L+5
	1.1	H-1	→	L+5
S_4	23.4	H-7	→	L
	19.6	H-3	→	L
	15.2	H-1	→	L
	10.5	H-6	→	L+1
	4.3	H	→	L
	3.3	H-6	→	L
	2.5	H	→	L+4
	2.3	H-6	→	L+4
	1.8	H-2	→	L
	1.7	H	→	L+1
	1.2	H-3	→	L+1
S_5	58.5	H	→	L+3
	16.9	H	→	L+5
	3.4	H-1	→	L+2
	2.8	H-3	→	L+3
	1.5	H-4	→	L+6
	1.2	H-2	→	L+7
	1.1	H-5	→	L+1
	1.1	H-5	→	L

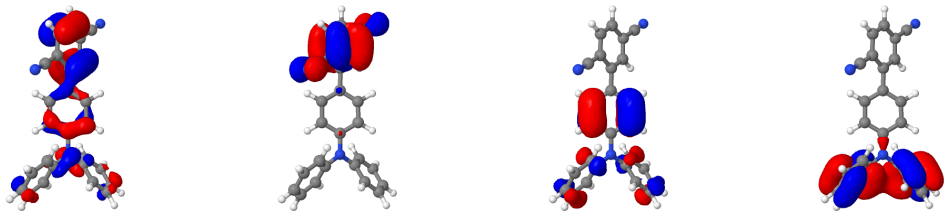

(a) H-7 (b) H-6 (c) H-5 (d) H-4

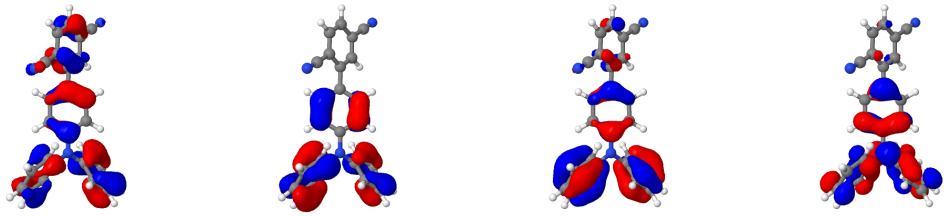

(e) H-3 (f) H-2 (g) H-1 (h) H

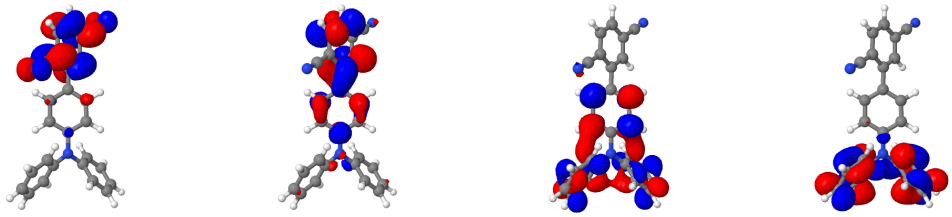

(i) L (j) L+1 (k) L+2 (l) L+3

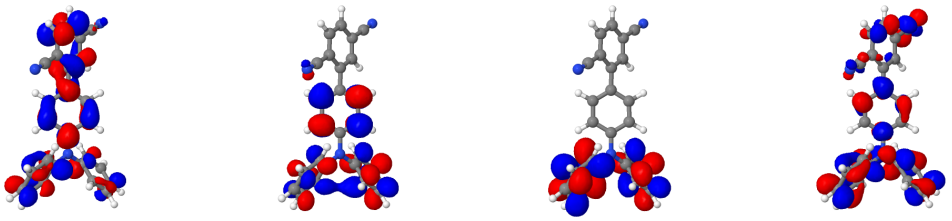

(m) L+4 (n) L+5 (o) L+6 (p) L+7

Figure S1: BH-LYP molecular orbitals (cutoff 0.03) mainly involved in the first five singlet excitations of **1-H** at the ground-state geometry.

Table S3: Composition of the DFT/MRCI wave functions of the five lowest excited singlet states of 2-Me at the ground-state geometry. The orbitals involved in the excitation are displayed in Figure S2.

State	%	Transition		
S1	84.4	H	→	L
	1.5	H-4	→	L
	1.3	H-3	→	L
S2	62.0	H	→	L+1
	10.9	H	→	L+3
	4.8	H	→	L+2
	3.6	H	→	L+4
	1.7	H-4	→	L+1
S3	69.0	H	→	L+2
	7.3	H	→	L+1
	2.4	H-1	→	L+3
	2.0	H-2	→	L+4
	1.7	H-1	→	L+1
	1.0	H-5	→	L+6
S4	39.6	H-7	→	L
	13.9	H-6	→	L+1
	8.4	H-3	→	L
	7.3	H-1	→	L
	5.2	H-4	→	L
	3.7	H	→	L+3
	2.0	H-4	→	L+1
	1.9	H	→	L
	1.5	H-6	→	L+3
	1.0	H	→	L+4
S5	62.4	H	→	L+4
	19.1	H	→	L+3
	3.9	H	→	L+5
	1.2	H-2	→	L+2

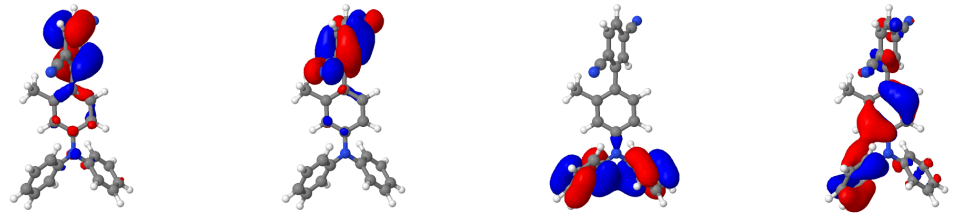

(a) H-7 (b) H-6 (c) H-5 (d) H-4

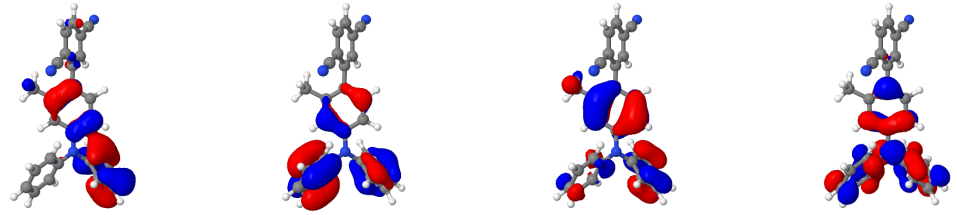

(e) H-3 (f) H-2 (g) H-1 (h) H

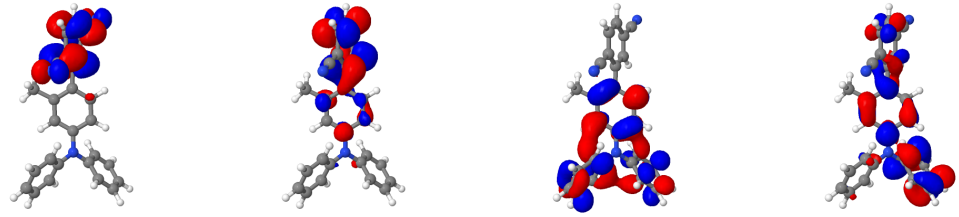

(i) L (j) L+1 (k) L+2 (l) L+3

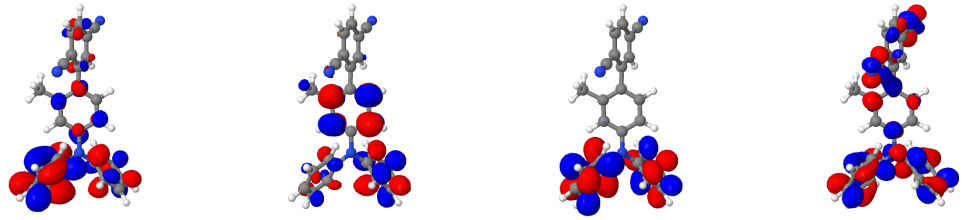

(m) L+4 (n) L+5 (o) L+6 (p) L+7

Figure S2: BH-LYP molecular orbitals (cutoff 0.03) mainly involved in the first five singlet excitations of **2-Me** at the ground-state geometry.

Table S4: Composition of the DFT/MRCI wave functions of the five lowest excited singlet states of 3-^{i}Pr at the ground-state geometry. The orbitals involved in the excitation are displayed in Figure S3.

State	%	Transition		
S1	85.0	H	→	L
	1.7	H-4	→	L
	1.0	H-3	→	L
S2	51.7	H	→	L+1
	17.6	H	→	L+3
	9.9	H	→	L+2
	1.6	H-4	→	L+1
	1.3	H-1	→	L+3
	1.2	H-1	→	L+2
	1.1	H	→	L+4
S3	65.4	H	→	L+2
	12.6	H	→	L+1
	2.0	H-1	→	L+3
	1.7	H-2	→	L+4
	1.4	H	→	L+3
	1.3	H-1	→	L+1
S4	38.2	H-7	→	L
	13.1	H-6	→	L+1
	10.2	H-1	→	L
	8.0	H-3	→	L
	5.7	H	→	L+3
	3.7	H-4	→	L
	1.8	H-4	→	L+1
	1.5	H	→	L
	1.3	H-6	→	L+3
	1.1	H-2	→	L
S5	76.1	H	→	L+4
	5.8	H	→	L+5
	2.3	H	→	L+3
	1.5	H-2	→	L+2
	1.0	H-8	→	L+4

L

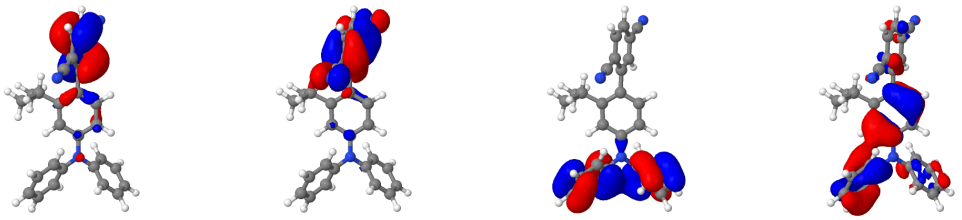

(a) H-7 (b) H-6 (c) H-5 (d) H-4

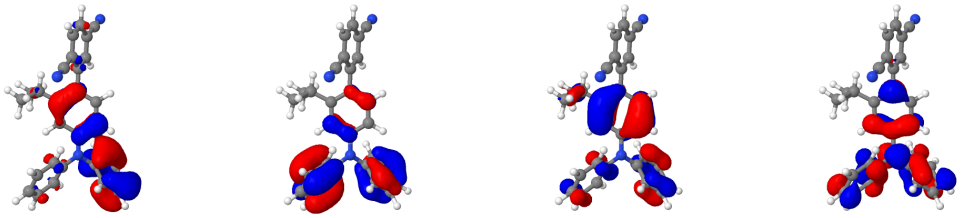

(e) H-3 (f) H-2 (g) H-1 (h) H

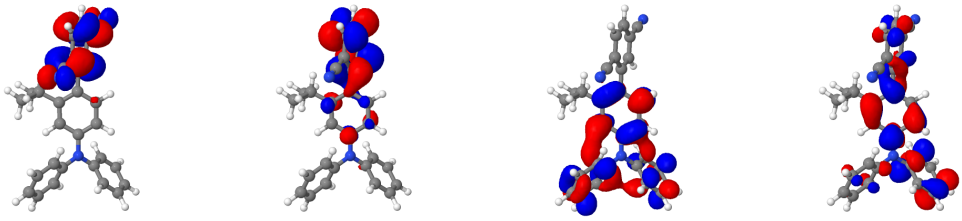

(i) L (j) L+1 (k) L+2 (l) L+3

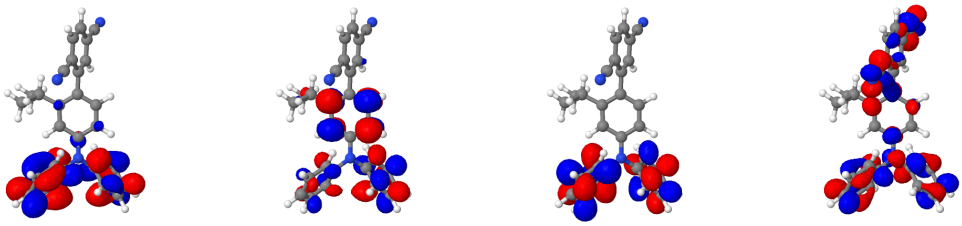

(m) L+4 (n) L+5 (o) L+6 (p) L+7

Figure S3: BH-LYP molecular orbitals (cutoff 0.03) mainly involved in the first five singlet excitations of **3-iPr** at the ground-state geometry.

Table S5: Composition of the DFT/MRCI wave functions of the five lowest excited singlet states of 4-diMe at the ground-state geometry. The orbitals involved in the excitation are displayed in Figure S4.

State	%	Transition		
S1	86.2	H	→	L
	2.9	H-4	→	L
	1.2	H-2	→	L
S2	63.8	H	→	L+3
	10.3	H	→	L+1
	4.8	H-1	→	L+2
	2.7	H-2	→	L+4
	1.3	H-4	→	L+6
	1.1	H	→	L+2
	1.0	H-5	→	L+5
S3	61.9	H	→	L+2
	17.5	H	→	L+1
	5.4	H	→	L+3
	1.0	H-7	→	L
	0.9	H-8	→	L+2
S4	53.0	H	→	L+1
	21.5	H	→	L+2
	4.8	H	→	L+3
	2.8	H-4	→	L+1
	1.8	H-7	→	L
	1.2	H-2	→	L+1
S5	83.0	H	→	L+4
	2.4	H	→	L+6
	1.5	H-2	→	L+3
	1.2	H-8	→	L+4
	1.0	H	→	L+3

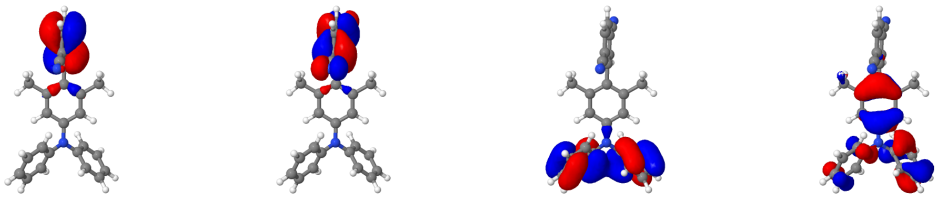

(a) H-7 (b) H-6 (c) H-5 (d) H-4

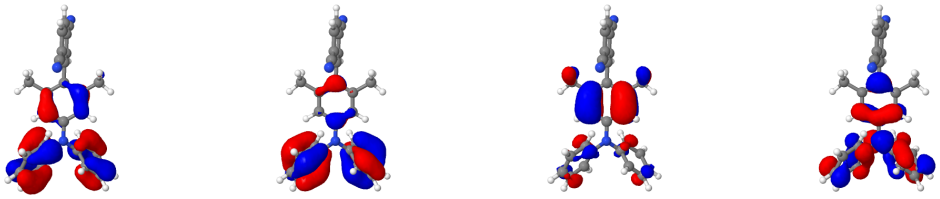

(e) H-3 (f) H-2 (g) H-1 (h) H

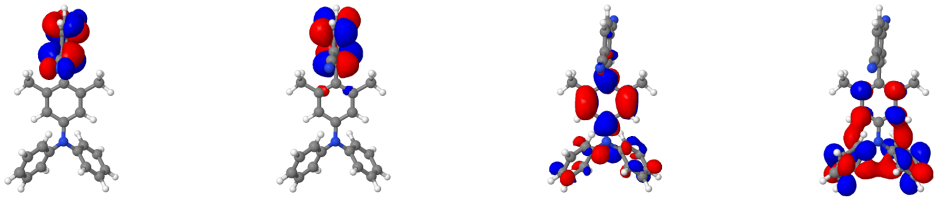

(i) L (j) L+1 (k) L+2 (l) L+3

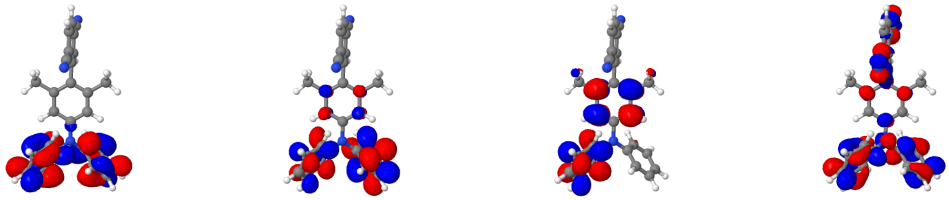

(m) L+4 (n) L+5 (o) L+6 (p) L+7

Figure S4: BH-LYP molecular orbitals (cutoff 0.03) mainly involved in the first five singlet excitations of **4-diMe** at the ground-state geometry.

Relaxed Interpolated Pathways

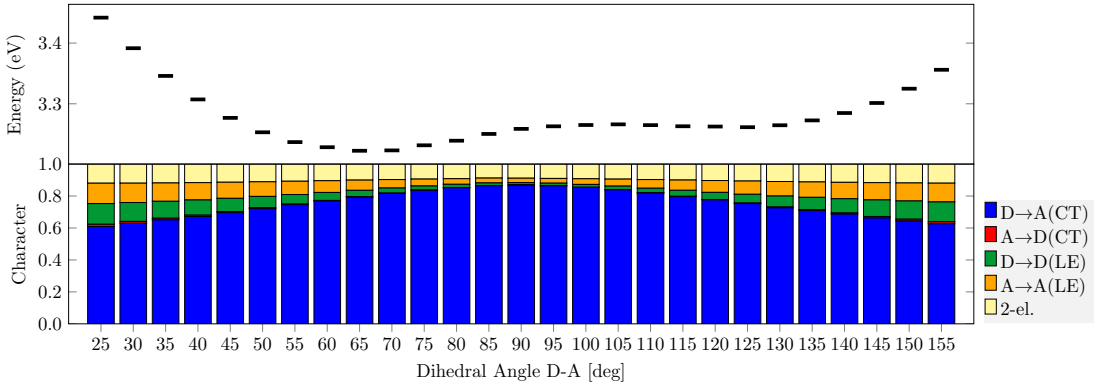

Figure S5: **2-Me**: Relaxed interpolated pathway for the lowest excited singlet state (S_1) at (TD)DFT/ωB97X-D level of theory (**Top**). Detailed analysis of the excited state character based on the transition densities at every optimized geometry of the relaxed interpolated pathway (**Bottom**).

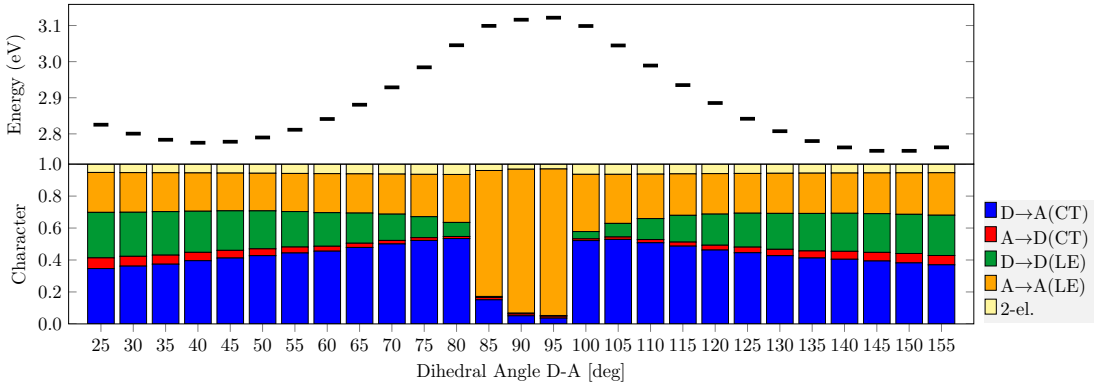

Figure S6: **2-Me**: Relaxed interpolated pathway for the lowest excited triplet state (T_1) at (TD)DFT/ωB97X-D level of theory (**Top**). Detailed analysis of the excited state character based on the transition densities at every optimized geometry of the relaxed interpolated pathway (**Bottom**).

Emission Spectra

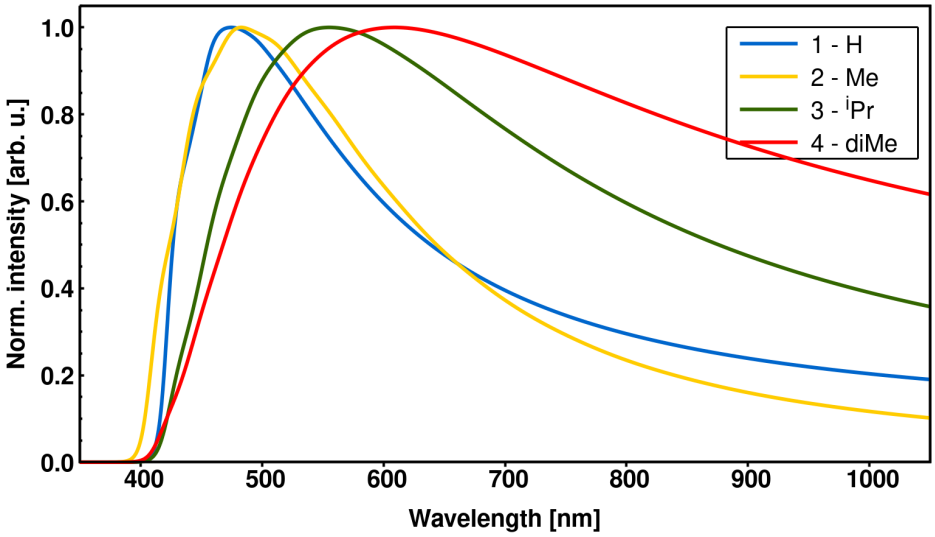

Figure S7: Computed emission spectra of **1-H** (blue), **2-Me** (yellow), **3-^{i}Pr** (green) and **4-diMe** (red) in toluene solution at 300 K using the AH method.

Solvation Effects

Table S6: The influence of PCM and cLR models on the vertical emission wavelength λ_{em} (DFT/MRCI-R2016) and adiabatic energy of the S_1 excited state of 2-Me.

	n-Hexane	**Toluene**	**Ethylethanoate**	**DMSO**
dielectric constant ϵ	1.8819	2.3741	5.9867	46.8260
Dihedral angle D-A S_0 [deg]	70.2	69.7	72.7	72.3
Dihedral angle D-A S_1 [deg]	66.3	65.4	58.5	56.0
$\lambda_{em,PCM}$ [cm^{-1} (nm)]	20536 (487)	20613 (485)	20533 (487)	20440 (489)
$\lambda_{em,cLR}$ [cm^{-1} (nm)]	16171 (618)	15530 (644)	12778 (783)	11962 (836)
E_{adia} (PCM/cLR) [eV]	2.96 / 2.36	2.94 / 2.23	2.94 / 1.87	2.92 / 1.73

Table S7: The influence of two explicit toluene solvent molecules (plus PCM) in comparison to implicit toluene solvation on different photophysical characteristics for 2-Me. Dihedral angle between donor and acceptor, absorption and emission oscillator strengths and wavelengths, vertical and adiabatic energies for S_1 and T_1, electric dipole moments and CT weight of respective excited states.

	S_0		S_1		T_1	
	Implicit	Explicit	Implicit	Explicit	Implicit	Explicit
D-A [deg]	69.7	63.4	65.9	64.3	41.7	41.0
E(S_1, vert.) [eV (nm)]	3.10	2.90	2.56 (484)	2.35 (528)	2.53	2.37
E(S_1, adia.) [eV]	–	–	2.94	2.73	3.00	2.88
μ(S_1) [D]	26.97	24.32	24.66	23.16	19.66	18.53
S_1 [% CT/LE_{TAA}/LE_{TPN}]	80/6/4	78/6/6	80/4/6	78/4/6	59/15/13	60/12/13
E(T_1, vert.) [eV (nm)]	2.91	2.72	2.36	2.19	2.03 (610)	1.95 (635)
E(T_1, adia.) [eV]	–	–	2.74	2.57	2.50	2.47
μ(T_1) [D]	20.28	20.07	20.32	20.67	13.71	14.16
T_1 [% CT/LE_{TAA}/LE_{TPN}]	59/22/11	64/14/12	65/10/17	70/8/13	40/26/24	45/21/23
k_F [s^{-1}]	–	–	2.6×10^7	2.2×10^7	–	–
ΔE, vert. [eV]	0.19 / 0.18			–		
ΔE, adia. [eV]	–			0.44 / 0.26		

Non-radiative Rate Constants for Vertically Shifted PES

Table S8: ISC rate constants k_{ISC} for all compounds with respect to different energy gaps and the true adiabatic energy gap between the singlet and triplet state within the Franck-Condon approximation in s^{-1}.

E_{adia} [meV]	Compound			
	1-H	**2-Me**	**3-^{i}Pr**	**4-diMe**
50	4.08×10^6	6.52×10^5	3.30×10^5	3.01×10^3
100	4.47×10^6	1.03×10^6	5.58×10^5	6.60×10^3
150	5.12×10^6	1.39×10^6	8.08×10^5	1.16×10^4
200	5.46×10^6	1.76×10^6	1.08×10^6	1.78×10^4
250	5.45×10^6	2.11×10^6	1.36×10^6	2.49×10^4
300	5.40×10^6	2.42×10^6	1.63×10^6	3.30×10^4
350	5.26×10^6	2.70×10^6	1.90×10^6	4.17×10^4
400	5.09×10^6	2.95×10^6	2.16×10^6	5.12×10^4
Actual ΔE	4.61×10^6	3.29×10^6	2.46×10^6	3.68×10^4

Table S9: rISC rate constants k_{rISC} for all compounds with respect to different energy gaps and the true adiabatic energy gap between the singlet and triplet state within the Franck-Condon approximation in s^{-1}.

E_{adia} [meV]	Compound			
	1-H	**2-Me**	**3-^{i}Pr**	**4-diMe**
50	5.39×10^5	6.33×10^4	7.59×10^4	1.31×10^4
100	8.53×10^4	1.46×10^4	1.86×10^4	4.17×10^3
150	1.41×10^4	2.86×10^3	3.92×10^3	1.07×10^3
200	2.18×10^3	5.20×10^2	7.59×10^2	2.37×10^2
250	3.14×10^2	9.02×10^1	1.38×10^2	4.79×10^1
300	4.51×10^1	1.50×10^1	2.41×10^1	8.92×10^0
350	6.32×10^0	2.42×10^0	4.05×10^0	1.38×10^0
400	8.44×10^{-1}	3.82×10^{-1}	6.65×10^{-1}	–
Actual ΔE	4.80×10^{-2}	1.85×10^{-2}	6.65×10^{-2}	4.01×10^0

Comparison FC vs. FC/HT Rate Constants

Table S10: Calculated radiative and non-radiative rate constants within Franck-Condon approximation and HT-type scheme in s^{-1} for 1-H to 4-diMe.

	Compound			
	1-H	**2-Me**	**3-^{i}Pr**	**4-diMe**
$\mathbf{k}_{F,FC}$	1.0×10^{8}	2.6×10^{7}	2.0×10^{7}	1.7×10^{6}
$\mathbf{k}_{F,FC/HT}$	–	1.9×10^{7}	–	2.6×10^{6}
$\mathbf{k}_{ISC,FC}$	4.6×10^{6}	3.3×10^{6}	2.5×10^{6}	3.7×10^{4}
$\mathbf{k}_{ISC,FC/HT}$	–	4.4×10^{6}	–	7.3×10^{5}
$\mathbf{k}_{rISC,FC}$	4.8×10^{-2}	1.9×10^{-2}	6.7×10^{-2}	4.0×10^{0}
$\mathbf{k}_{rISC,FC/HT}$	–	8.7×10^{-2}	–	1.3×10^{1}

Non-radiative Rate Constants within VH Approach

Table S11: Calculated fluorescence rate constants using DFT/MRCI-R2016 and non-radiative rate constants within the newly implemented VH approach in s^{-1} for 2-Me.

Dihedral angle D-A	$\mathbf{k}_{ISC}$	$\mathbf{k}_{rISC}$	$\mathbf{k}_{F}$
25	1.0×10^{6}	1.0×10^{0}	1.1×10^{8}
30	1.1×10^{6}	1.4×10^{6}	1.0×10^{8}
35	1.2×10^{7}	2.2×10^{6}	9.1×10^{7}
40	1.2×10^{7}	2.2×10^{0}	8.1×10^{7}
45	1.3×10^{7}	2.7×10^{0}	7.0×10^{7}
50	1.3×10^{7}	5.6×10^{0}	5.9×10^{7}
55	1.7×10^{7}	6.1×10^{0}	4.5×10^{7}
60	1.8×10^{6}	1.1×10^{1}	3.7×10^{7}
65	1.8×10^{6}	1.2×10^{1}	2.7×10^{7}
70	2.6×10^{6}	2.6×10^{1}	1.8×10^{7}
75	4.6×10^{6}	9.6×10^{1}	1.0×10^{7}
80	6.7×10^{6}	3.6×10^{2}	4.8×10^{6}
85	8.4×10^{6}	2.0×10^{4}	1.1×10^{6}
90	7.6×10^{5}	5.6×10^{4}	3.0×10^{4}

Optimization of the range-separation parameter ω

In order to get reliable values for excited state energies on TDDFT level of theory for TADF emitters range-separated exchange functionals were proposed to bring remedy. However, these functionals need to be tuned and adapted to the system. This is done by varying the range-separation parameter ω that stands for the inverse distance which assigns the change from DFT to HF exchange terms.

Since TADF emitters usually consist of a donor and an acceptor moiety the range-separation parameter ω is tuned towards the ionization potential and the electron affinity applying Koopmans´ theorem. As a matter of fact the value of J^2 is minimized in this procedure by determining the minimum of the target function:

$$J^2 = \sum_{i=0}^{1} [\epsilon_{HOMO}^{\omega}(N+i) + IP(N+i)]^2 \tag{1}$$

with $IP(N) = E(N-1) - E(N)$, and $IP(N+1) = E(N) - E(N+1)$.

Here, N is the number of electrons of the target molecule, ϵ_{HOMO}^{ω} is the HOMO energy and $IP(N)$ the vertical ionization potential. In Figure S8 the parameter optimization for **2-Me** in toluene is shown in the range between 0.00 and 0.20 bohr^{-1}. The optimal ω was set to 0.15 a_0^{-1} for all computations.

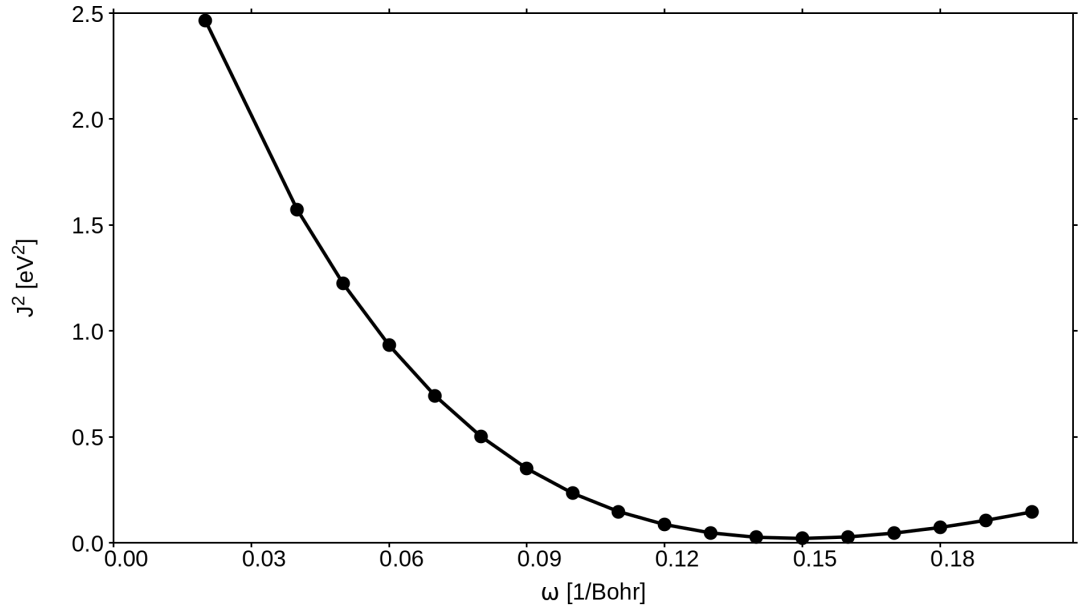

Figure S8: For the optimization of the range-seperated hybrid density functional ωB97X-D a tuning procedure was performed. ω was set to 0.15 a_0^{-1} for all computations.

Paper No.3

Unexpected quasi-axial conformer in thermally activated delayed fluorescence DMAC-TRZ. Pushing green OLEDs to blue.

Kleitos Stavrou, Larissa G. Franca, Tobias Böhmer, Luka M. Duben, Christel M. Marian and Andrew P. Monkman
Adv. Funct. Mater., 2300910 (2023)
DOI: 10.1002/adfm.20230091

Contribution: The quantum chemical investigation of excited state properties and emission properties of DMAC-TRZ was carried out by me. I wrote the original draft for the theoretical results section and provided the corresponding figures.

RESEARCH ARTICLE

ADVANCED FUNCTIONAL MATERIALS
www.afm-journal.de

Unexpected Quasi-Axial Conformer in Thermally Activated Delayed Fluorescence DMAC-TRZ, Pushing Green OLEDs to Blue

Kleitos Stavrou, Larissa G. Franca, Tobias Böhmer, Luka M. Duben, Christel M. Marian,* and Andrew P. Monkman**

Hidden photophysics is elucidated in the very well-known thermally activated delayed fluorescence (TADF) emitter, DMAC-TRZ. A molecule that, based on its structure, is considered not to have more than one structural conformation. However, based on experimental and computational studies, two conformers, a quasi-axial (QA) and a quasi-equatorial (QE) are found, and the effect of their co-existence on both optical and electrical excitation isexplored. The relative small population of the QA conformer has a disproportionate effect because of its strong local excited state character. The energy transfer efficiency from the QA to the QE conformer is high, even at low concentrations, dependent on the host environment. The current accepted triplet energy of DMAC-TRZ is shown to originate from the QA conformer, completely changing the understanding of DMAC-TRZ. The contribution of the QA conformer in devices helps to explain the good performance of the material in non-doped organic light-emitting diodes (OLEDs). Moreover, hyperfluorescence (HF) devices, using ν-DABNA emitter show direct energy transfer from the QA conformer to ν-DABNA, explaining the relatively improved Förster resonance energy transfer efficiency compared to similar HF systems. Highly efficient OLEDs where green light (TADF-only devices) is converted to blue light (HF devices) with the maximum external quantum efficiency remaining close to 30% are demonstrated.

1. Introduction

Organic Light Emitting Diodes (OLEDs) are a valuable alternative to conventional light-emitting devices. A key characteristic of efficient OLEDs is the exciton harvesting in the active layer of a device, which due to spin statistics forms 25% singlet and 75% triplet states.[1–3] The triplet state utilisation is forbidden by Pauli's principle and internal quantum efficiency (IQE) is limited to 25% for fluorescence materials.[4,5] Two classes of organic materials, the phosphorescent and the thermally activated delayed fluorescence (TADF) materials can overcome this problem by harvesting the triplet states.[6,7] Phosphorescent materials containing heavy atoms enhance the strong spin–orbit coupling (SOC) and activate triplet state radiative decay.[8] TADF molecules can convert triplet states into an emissive singlet state by reverse intersystem crossing (rISC) between the two states. This process is identified to be thermally activated by the vibronically coupled spin–orbit coupling mechanism, which is facilitated by a small energy gap between the triplet and singlet state (ΔE_{ST}) and the use of a third state to mediate the exchange.[9–12]

Conventional TADF molecules contain a donor (D) and an acceptor (A), a structure that promotes the formation of an intramolecular charge transfer (ICT) state between the two moieties.[13] This type of D-A molecule is characterized by an effective separation of the highest occupied molecular orbital (HOMO) and lowest unoccupied molecular orbital (LUMO) in the excited state through a near-orthogonal D-A relative orientation. The latter, minimizes the electron exchange energy to achieve very small ΔE_{ST} (typically below 200 meV) and enables efficient rISC at room temperature.[14–16] The presence of a ^{3}LE state (locally excited) within the ΔE_{ST} energy range, to vibrationally mix with the ^{3}CT (charge transfer), enhances rISC by allowing SOC with the ^{1}CT.[7,17–20]

In these already complex systems, extra parameters such as: intermolecular interactions between the same type of molecules (dimer/excimer) and different types of molecules (complex/exciplex), guest-host interactions (environmental dipole moment effect)[21] and conformational effects complicate the systems even more. On the latter, two types of conformation effects have been mainly explored so far: the distribution of

K. Stavrou, L. G. Franca, A. P. Monkman
Department of Physics
Durham University
Durham DH1 3LE, UK
E-mail: kleitos.stavrou@durham.ac.uk; a.p.monkman@durham.ac.uk
T. Böhmer, L. M. Duben, C. M. Marian
Institute of Theoretical and Computational Chemistry
Heinrich-Heine-University Düsseldorf
40204 Düsseldorf, Germany
E-mail: Christel.Marian@hhu.de
The ORCID identification number(s) for the author(s) of this article can be found under https://doi.org/10.1002/adfm.202300910.

DOI: 10.1002/adfm.202300910

dihedral angles between the D-A moieties[22–24] and the possible ground and/or excited state conformers (i.e., planar, axial, equatorial etc).[25–27] In the context of the second type of conformational effect, several D-A and D-A-D molecules have been reported whose donor unit is non-planar, leading to two configurations where the D-A are near orthogonal, i.e., axial and equatorial orientations.[26]

In 2014, Tanaka et al. reported PTZ-TRZ, a structural analogue of PXZ-TRZ that has a sulfur atom instead of oxygen in the donor unit.[25] This distorted the donor allowing axial and equatorial conformations to co-exist, and dual emission was observed originating from two ICT transitions derived from conformational heterogeneity (quasi-axial (QA) and quasi-equatorial (QE)). A similar effect was shown by Su et al., but instead of using a hetero atom, adamantane was attached to the acridine donor, showing the same dual conformational emission.[28] Other cases of D-A systems also presented dual conformer emission.[29] Such conformers in D-A-D systems have also been reported, and their photophysical behavior has been described in detail.[26,30]

In this work, we investigate the TADF emitter DMAC-TRZ,[31] a molecule that does not fulfill the requirements presented before to have dual conformer emission. Surprisingly, under specific conditions a QA conformer can be observed, although the QE conformer appears to be dominant. In solution state, the molecular interconversion from the QA to the QE is labile and the emission from the first only contributes to a very small extent. In solid-state however, because of the environmental restrictions (hindering molecular relaxation) the QA emission appears stronger. At low temperatures this effect is even stronger, while a structured QE CT emission can also be observed. The energy transfer process between the two conformer species appears to be very efficient, even at concentrations below 0.1 wt.%, and the TADF efficiency appears to increase with increasing concentration. Above 1 wt.% concentration, aggregation occurs and it appears to dominate above 5 wt.% loading, however, this enhances the TADF efficiency. Under specific conditions, at low temperature, the origin of the phosphorescence spectrum appears to come from the QA conformer, mainly because the lowest lying triplet state of the QE conformer has a pure CT character and if it can decay radiatively any phosphorescence would be vanishingly weak. In OLEDs the QA conformer appears to efficiently transfer its energy to the QE conformer and only in specific hosts a QA contribution can be seen. Using DMAC-TRZ as a sensitizer in hyperfluorescence (HF) OLEDs[32–34] the QA conformer can directly pump the terminal emitter (because of the terminal emitter higher oscillator strength and better spectral overlap compared to DMAC-TRZ QE conformer). Thus, Förster resonance energy transfer (FRET) from the QA conformer to the terminal emitter outcompetes the FRET from the QA to the QE conformer. This significantly improves the FRET efficiency of the system, compared to similar sensitizer-terminal emitter systems. HF OLEDs with maximum external quantum efficiency (EQE_{max}) close to 30% were fabricated but most importantly, a green TADF sensitizer was converted to blue HF OLED for the first time.

2. Results and Discussion

2.1. Basic Photophysics

The solvatochromic behavior of DMAC-TRZ in both excitation and emission measurements is shown in **Figure 1**. In MCH the excitation spectrum has two distinct bands with peaks at 376 nm (Ab1) and 413 nm (Ab2). Upon increased solvent polarity, the Ab2 band decreases in intensity and a tail appears at 450 nm, an expected behavior for a CT excited state, but loses in oscillator strength with increasing polarity. The Ab1 band appears unaffected and slightly blue-shifted in acetonitrile (CH_3CN).

Deconvolution of the excitation spectra in the four different solvents, using two Gaussians, shows an Ab1 band maximum of ≈376 nm in all cases (with a minor 5 nm hypsochromic shift in CH_3CN), and a full width half maximum (FWHM) of 55 ± 4 nm (Figure S1, Supporting Information). This behavior is expected from a strongly localized excited state. The Ab2 band maximum is observed at 413 nm in all solvents but reduces in intensity and increases in FWHM (from 35 nm in MCH to 63 nm in CH_3CN) with increasing solvent polarity. The latter follows the FWHM behavior of the emission spectrum (Figure 1b) and is undoubtedly from the CT state between the donor and acceptor moiety. The Ab2 band appears to have a mixed, local (LE) and CT character in MCH, giving a structured excitation and photoluminescence (PL) spectrum.

In MCH and upon excitation at wavelengths between 320 and 380 nm, a shorter wavelength emission band appears (Em1) with an emission maximum at 390 nm (Figure S2b, Supporting Information). The relative intensity of the Em1 band maximum is the highest when exciting at 360 nm, where the intensity of the Ab1 band is close to its maximum, and the Ab2 band is close to its minimum value (Figure S1a, Supporting Information). Interestingly, when exciting at shorter wavelengths (λ_{exc} < 310 nm) the Em1 band is not observed. The excitation profile of the Em1 band is well resolved, solvent independent (Figure S3a, Supporting Information) and appears very similar to the deconvoluted Ab1 spectra (Figures S1a and S2a, Supporting Information). With increasing solvent polarity, the relative PL intensity of Em1 band decreases and its peak position has a minor redshift, compared to the main PL (Em2) band (Figure 1b; Figure S3b, Supporting Information). The absorption and emission spectra of the individual D and A units were studied previously and are energetically in higher positions compared to the Ab1 and Em1, respectively.[35] Hence, these two distinct emission bands (Em1 and Em2) can only be assigned to two different conformers of the DMAC-TRZ molecule.[26]

Similar behavior is observed using a zeonex polymer matrix as a host (Figure S4, Supporting Information). Due to the steric hindrance from the solid-state matrix, conformational relaxation (or interconversion) is prevented to a much higher degree, in contrast to the solvent environments. Consequently, the Em1 band is more intense and provides better resolved excitation spectra upon collections between 390–420 nm (Figure S4a, Supporting Information). From the excitation spectra, two isosbestic points are observed, one at 325 nm and another at 390 nm, which suggest the presence of two distinct species.

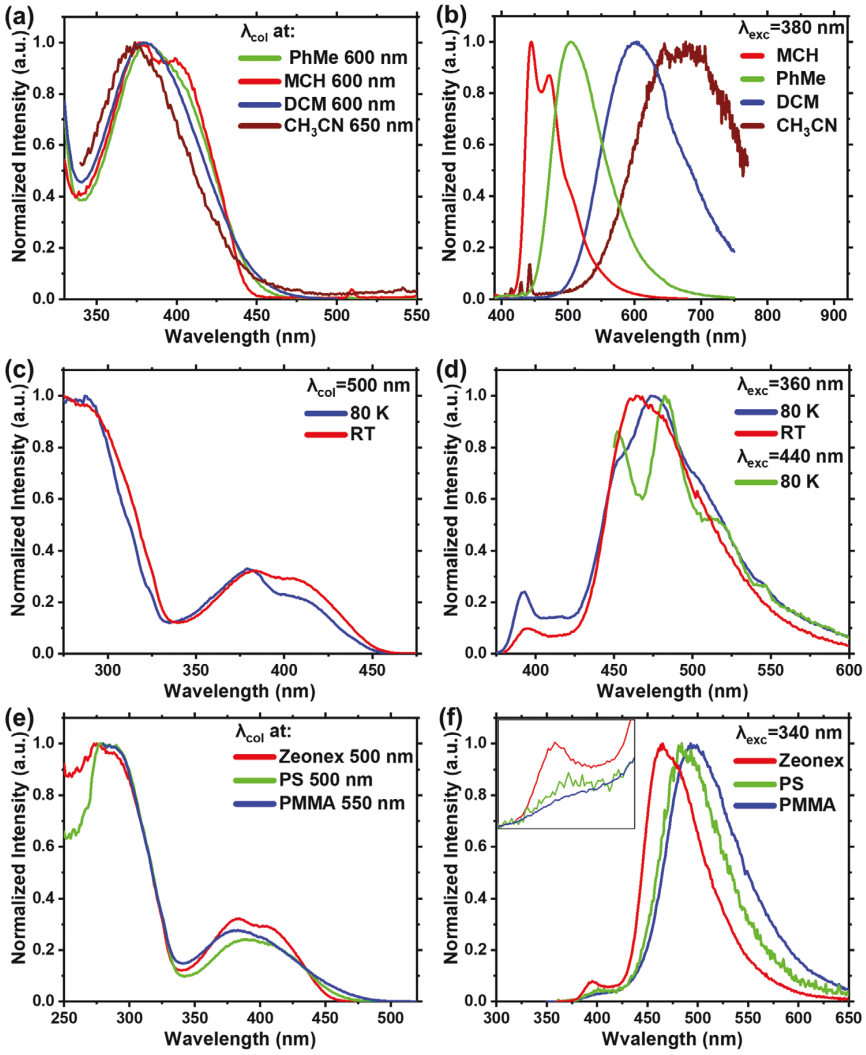

Figure 1. Steady state photophysics of DMAC-TRZ. a) Excitation and b) PL spectra of 20 μM concentration of DMAC-TRZ in different solvents, at room temperature. c) Excitation and d) PL spectra of 1 wt.% DMAC-TRZ in zeonex host, at room temperature (red) and 80 K (blue). e) Excitation and f) PL spectra of 1 wt.% DMAC-TRZ in different polymer hosts, at room temperature. Inset: Zoom in on the high energy band.

It is important to reiterate that the contribution of the local D and A units (below 325 nm) to the excitation spectra is minimal when collecting at wavelength where only Em1 emits. Low temperature steady state measurements of the same film show that the increased hindrance introduced by freezing the environment enhances the relative contribution of the Em1 band (Figure 1d; Figure S5, Supporting Information). From excitation spectra, a decrease in relative intensity of the Ab2 band and a better resolved Ab1 band can be observed (Figure 1c), while the Stokes shift between Ab1 and Em1 is very small (Figure S5d, Supporting Information). The Em2 band is more structured when compared to room temperature and appears better resolved upon direct excitation of the Ab2 band only (Figure 1d, green curve). This indicates that excess excitation energy broadens the spectrum. Here it is important to mention that the phosphorescence contribution to the total DMAC-TRZ emission, even at low temperature, is minimal as shown in our previous studies.[23]

Using two polymer hosts with stronger ground state dipole moment (*i.e.*, enhanced relative polarity) a bathochromic shift is observed in the Em2 band, both in excitation and emission spectra (Figure 1e,f). In polystyrene (PS), the Em1 band appears reduced in intensity by a factor of two (Figure S6, Supporting Information), while in PMMA by a factor of three (Figure S7, Supporting Information) compared to zeonex. The onset of the Em1 band appears to be the same in all cases while the peak has a small bathochromic shift and appears less resolved. This indicates that the excited state of Em1 conformer has a mixed (LE & CT) but stronger LE character compared to the Em2 CT conformer state (Figure 1f). Again, upon excitation at wavelengths

below 310 nm the Em1 is not observed. By collecting at the Em1 emission band, the excitation spectra are identical in all hosts (Figure S8, Supporting Information). The latter is in good agreement with the solution results, see above.

Small molecule hosts were also used, and the two bands were again observed in various hosts (Figure S9, Supporting Information). Unfortunately, the most common carbazole based hosts often used in OLED devices could not be used as most of them emit in the same region as the higher energy conformer (Em1), such as the case of BCPO. The UGH spectrum looks similar to the one in zeonex, with a small increase in the relative intensity due to possible extra steric hindrance from the host. DPEPO has a much smaller contribution from the Em1 band due to the shift of the CT absorption resulting to a better energy transfer from the high energy conformer (Em1) to the low one (Em2). Finally, neat film does not have any contribution from the Em1 band mainly because the intermolecular distance is minimal increasing the FRET efficiency between the two conformers.

2.2. Calculations

Quantum chemical calculations are used to understand the nature of these conformers. Two stable conformers of DMAC-TRZ, a QE conformer with planar DMAC donor and TRZ acceptor moieties arranged perpendicular to one another (**Figure 2**c) and a QA conformer in which DMAC adopts a kinked structure tilted by ≈40° with respect to the TRZ plane (Figure 2d). In MCH solution, the QE conformer is favored over the QA conformer by 0.19 eV including zero-point vibrational energy (ZPVE) corrections and hence represents the majority component. Combined density functional theory and multi-reference configuration interaction (DFT/MRCI) calculations yield vertical excitation energies of 3.06 eV (405 nm, Ab2) and 3.35 eV (371 nm, Ab1) for the S_1 states of the QE and QA conformers, respectively which compare favorably with the experimentally observed band maxima in this solvent (Figure 1b). However, while the $S_1 \leftarrow S_0$ transition of the QA minority conformer is characterized by a mixed CT/LE excitation with high oscillator strength, the $S_1 \leftarrow S_0$ CT transition of the C_{2v}-symmetric QE conformer is electric dipole forbidden in Franck–Condon (FC) approximation. Coupling between the electronic degrees of freedom and torsional vibrations about the molecular axis lends intensity to this CT transition which therefore becomes weakly allowed in Herzberg–Teller (HT) approximation (Figure S10) and for ensemble averages. That both peaks are observed with nearly equal intensity in the excitation spectrum is thus a consequence of the small concentration of the optically very bright QA conformer in MCH solution on the one hand and the necessity to vibronically enhance the electric dipole-forbidden transition of the QE majority conformer on the other hand. Examination of the experimentally measured QE absorption band (Ab2) in MCH reveals a weak vibrational structure arising from the vibronic coupling to the electronic transition (Figure 2a). The estimated vibronic energy spacing of this HT transition is 1170 cm^{-1} indicative of a coupled C—N band stretch,[36] most likely the C—N bridging bond between D and A. Even small changes in this bond length and torsion will radically change the radiative coupling, highlighting the sensitivity and important role of the C—N donor acceptor bridging bond plays in these TADF materials.

With regard to the photophysics of the QE conformer, the presence of a $T_{LE(TRZ)}$ state in energetic proximity of the

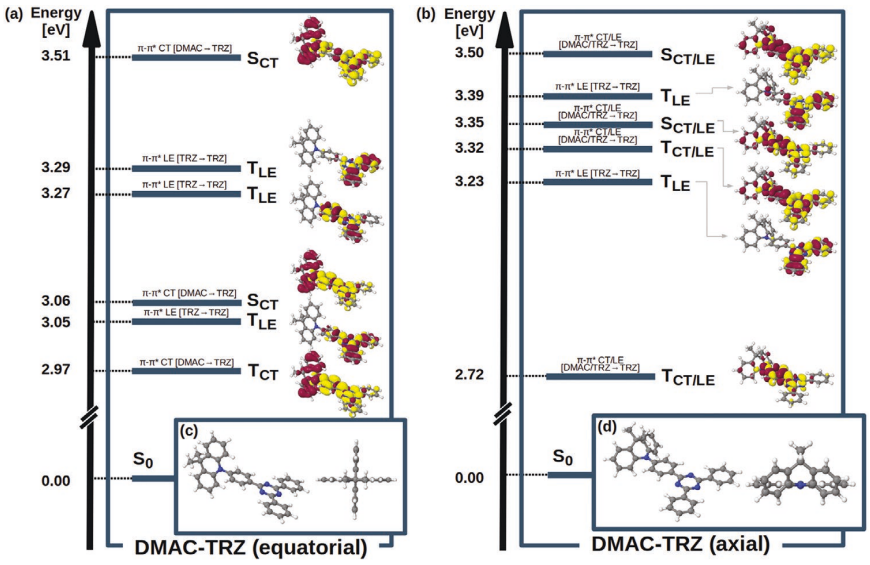

Figure 2. Calculated vertical DFT/MRCI excitation energies and state characteristics of the a) QE and b) QA conformers of DMAC-TRZ at the respective ground-state geometry in methylcyclohexane solution. The QE conformer is favored over the QA conformer by 0.19 eV including ZPVE corrections. A loss of electron density w.r.t. the electronic ground state is indicated in red, a gain in yellow. Geometric structures of the c) quasi-equatorial and d) quasi-axial conformers of DMAC-TRZ in the electronic ground state.

lowest-lying S_{CT} and T_{CT} states is noteworthy as it can mediate their ISC and rISC processes and lead to efficient TADF (Figure 2a).[11,37] For the QA conformer, two triplet states are found to lie below the S_1 state and a third one lies slightly above the S_1 state in the FC region (Figure 2b). The substantial energy gap between the S_1 and T_1 states, caused by the local $\pi\pi^*$ contributions to their wavefunctions, rule out TADF for this conformer. A detailed computational study investigating the role of the higher-lying triplet states in the photophysical deactivation pathways of both conformers is currently under way and will be presented in the near future.

The oscillator strength (f) of the two conformers in MCH was calculated to be 0.00006 for the QE conformer and 1.09379 for the QA conformer. The big difference can be explained by the strong local character of the QA conformer, compared to the CT character of the QE conformer. The population of both conformers in MCH can be approximately estimated from the ratio of the absorbance to the oscillator strength for the two individual conformers. This results to an approximate ratio of 99.9:0.1 population of QE to QA conformers, in MCH solution. This estimated population is completely dependent on the theoretically estimated transition oscillator strengths. Rama et al., previously reported the phosphorescence and excitation spectrum of DMAC-TRZ in frozen solution.[35] From the excitation spectrum results, which we now understand to include both QA and QE contributions, the QA population appears to be much larger in frozen solution at long delay times, compared to our estimate from room temperature MCH solution. This makes sense as the energy barrier crossing in solid state, which requires cooperative motion of the molecule, must be hindered, slowing down the interconversion and potentially giving a higher QA population. In solid state, and more specifically in evaporated films, where the solvent is not present, and the conformation entropy of the system will be different, the population of the QA conformer is expected to be much higher. Further, the QA conformer contribution in the PL spectrum is expected to be much higher due to matrix hindering possible interconversion between the two conformers, something that is possible in solution environments, especially with the presence of excess energy in the system. The latter is verified by the absence of the QA emission, in MCH solution, when exciting at wavelengths below 300 nm (Figure S2, Supporting Information).

2.3. Conformer Photophysics

At very low emitter concentrations (0.01 wt.%) in zeonex the maximum PL intensity of the QA conformer band (Em1) is comparable with that of the QE band (Em2) (Figure S11, Supporting Information). This observation can clearly be reconciled with low FRET due to the higher spatial separation between the individual molecules. With increasing concentration, the QA PL band decreases considerably in relative intensity monotonically (Figure S12, Supporting Information). Also, the high ground state dipole moment of DMAC-TRZ molecules, compared to the host, changes the ground state of the environment at higher concentrations (intermolecular interactions) and the QE absorption/emission stabilizes to a lower energy. Further, at higher concentrations there will be a higher probability for excitons to reach lower energy states on average because exciton hoping is more efficient, leading to higher QE PL peak shift.

From Figure S11a (Supporting Information) spectra, the mixed CT/LE character of both bands is clear, especially in zeonex host, because of their structured PL emission. With increasing host dipole moment, both bands lose their structured shape, and shift towards longer wavelengths. The QA band has a small bathochromic shift of 115 meV, going from 395 nm in zeonex to 410 nm in PMMA, which could occur due to increasing overlap with the QE absorption band. The QE band shifts by 247 meV, going from 448 nm in zeonex to 490 nm in PMMA (Figure S11b, Supporting Information). This indicates that the QA and QE conformers have stronger LE and CT character, respectively.

Temperature dependent steady state spectra of 0.01 wt.% DMAC-TRZ in zeonex are shown in Figure S13 (Supporting Information). Upon exciting both conformers (at 360 nm), structured emission is observed from both at room temperature. By lowering the temperature, the QA emission (395 nm) increases in relative intensity indicating that a possible conformational interconversion of the QA to the QE conformation is hindered because of the frozen matrix and low temperature (it is not due to singlet exciton migration enhancing the FRET radius, as this is highly unlikely at 0.01 wt.% in zeonex). The QE emission is also affected by the temperature, becoming more structured and the spectral band maxima changing from the 0–0 transition to the 0–1 transition. This effect is also observed with direct excitation ($\lambda_{exc} > 400$ nm) of the QE CT (Figure S13, Supporting Information) and is attributed to hindering of the torsion motions because of the frozen environment, and the spectra are better resolved. Further, in all PL spectra there is a weak emission band ≈500 nm which increases in relative intensity with decreasing temperature. This excited state can be directly populated upon excitation above 460 nm. To understand the origin of this band, excitation spectra at different collection wavelengths are shown in Figure S13b (Supporting Information). When collecting below 500 nm the behavior is the same as 1 wt.% in zeonex (Figure S5a, Supporting Information). Collecting above 500 nm, a further weak excitation band is observed between 450–500 nm (Figure S13b, Supporting Information). This new band does not appear in solution or at higher concentration solid state measurements and has the same structure at all temperatures. Thus, we can only assume that it is a dimer emission that can be formed in solid state, even at very low concentrations, and is only observed in low ground state dipole moment environments. It cannot be observed at higher concentrations or higher dielectric media because it overlaps with the redshifted CT emission. Nevertheless, the contribution of this species at room temperature can be considered minimal.

Using the Jacobian spectral (wavelength to eV) conversion, the PL spectra of 0.01 wt.% DMAC-TRZ in zeonex at 80 K and different excitations, we again identify three distinct emission bands (Figure S14a, Supporting Information). At 360 nm excitation, three regions with constant vibronic intervals are found; at high energy the QA conformer appears to have at least three observable vibronic contributions of 152 meV between 3.15 and 2.84 eV. After a short gap of 75 meV, the QE conformer

emits between 2.77 and 2.29 eV, again with 152 meV vibronic spacing. The third region below 2.29 eV has narrower spacing of 130 meV. Upon direct excitation of the low energy species (480 nm), the aggregated band appears well resolved with 130 meV vibronic spacing, similar to the 360 nm excitation (Figure S14b, Supporting Information).

The steady state behavior of 0.01 wt.% DMAC-TRZ in different polymer hosts is shown in Figure S15 (Supporting Information). An energy relaxation effect is observed upon excitation at 380 nm, which becomes less pronounced at lower temperatures for both the QA and QE conformers (Figure S15a, Supporting Information). The vibronic structure of the QE emission appears to be less defined in polystyrene and even less in PMMA. Exciting at 430 nm (mainly the QE conformer), the energy relaxation effect is clearer at room temperature, compared to 380 nm excitation, and reduces at lower temperatures (Figure S15b, Supporting Information). The latter could indicate that at low temperature the possible side group motions of the polymer chain are reduced, reducing the slow reorganizational effects that can lead to the relaxation of the CT energy.[22] At 0.01 wt.% loading, this cannot be an effect of energy migration to low energy sites in the density-of-states (DOS). Upon excitation at 460 nm, in polystyrene and PMMA we still observe the temperature dependent energy relaxation effect on the QE CT state, with polystyrene giving a structured emission compared to higher excitation energies (Figure S15c, Supporting Information). The very weak red aggregated/dimer emission band (PL_{max} = 525 nm) observed in zeonex cannot be observed in the other two hosts due to overlap with the QE CT PL. This can also be observed in the excitation spectra (Figure S16, Supporting Information).

Time-resolved spectra from 0.01 wt.% DMAC-TRZ in zeonex, at various temperatures are shown in Figures S3 and S17 (Supporting Information). At early time (0.5 ns time delay) and all temperatures, the emission (395 nm) comes mainly from the QA conformer (Figure S17a, Supporting Information), because of the faster radiative rate of the more strongly local character state. The contribution of the QE CT band is observed at 450 nm and appears to decrease in intensity with decreasing temperature, relative to the QA band. This verifies that the frozen matrix hinders the molecular relaxation of the QA to the QE conformation, resulting in a higher QA population, and thus stronger emission from the QA conformer at early times (<10 ns) (**Figure 3**a). At later prompt fluorescence (PF) times, the emission comes from the QE conformer and becomes more structured with decreasing temperature, indicating that under specific conditions a CT state can have vibronic character (note that the band does not blue shift at all).[38] At µs times, the room temperature measurement shows strong emission which comes from the QE CT band (Figure S17a, Supporting Information). In ms, the emission mainly comes from the phosphorescence with an energy onset of 2.75 eV (450 nm) and a small contribution of DF being observed at room temperature which decreases in contribution with decreasing temperature (small band below 450 nm). The PF emission area normalized spectra (Figure S17b, Supporting Information) clearly show the presence of two species (QA and QE conformer), with an iso-emissive point at 430 nm. A second iso-emissive point at 530 nm is only obvious at lower temperatures. This we assign to the aggregated species, as stated above.

The effect of temperature on the time-resolved spectra of 0.01 wt.% DMAC-TRZ in polystyrene and PMMA hosts are shown in Figure S18 (Supporting Information). In both cases a strong contribution from the QA conformer is observed in early times. Here it is worth mentioning that polystyrene and PMMA themselves emit at 380 nm, when excited at 355 nm (Figure S19, Supporting Information), but the PL contribution from the polystyrene is minor compared to the PMMA. As a result, the PMMA spectra have a strong contribution from the host itself (along with the QA emission) compared to the other

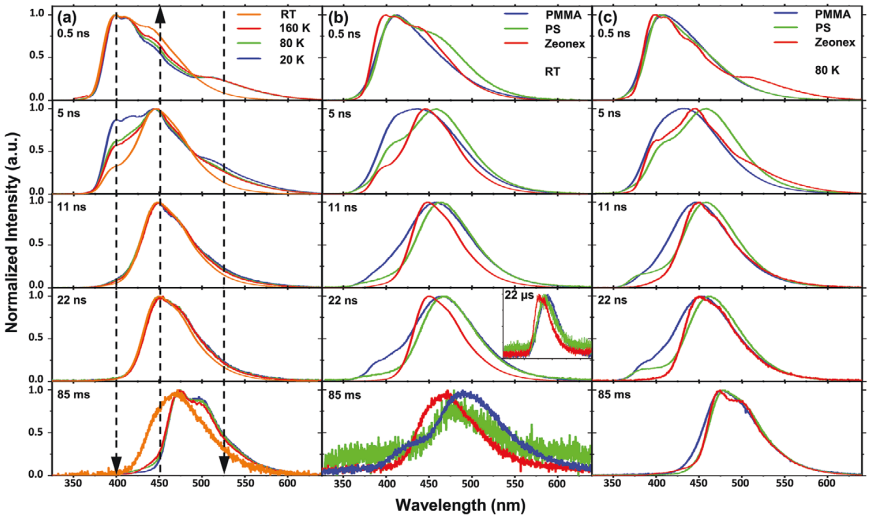

Figure 3. Time-resolved spectra of 0.01 wt.% DMAC-TRZ in a) zeonex at different temperatures and time delays. Time-resolved spectra of 0.01 wt.% DMAC-TRZ in three polymer hosts at different time delays at b) room temperature (Inset: DF spectra following the solvatochromism effect) and c) 80 K. Excitation wavelength 355 nm.

two hosts. At the later PF regime (t > 10 ns) both films have dual emission, the main band coming from the QE conformer and the high energy band (≈400 nm) from the host. In all three hosts, a high energy iso-emissive point is observed in the area normalized spectra, between QA and QE emission.

Comparing all three hosts one can see the large contribution from the QA conformer at early times, pumping the QE conformer which dominates after 10 ns and continues into the DF regime (Figure 3b). The QE TADF emission is clear at 22 µs as shown in the inset of Figure 3b. At 85 ms delay time, DF can still be observed in all hosts with PMMA having a high energy band which appears similar to the PMMA phosphorescence emission. The phosphorescence spectra are similar in all cases, with an energy onset of 2.75 eV, being in good agreement with our previous results.[23] PMMA film has slightly higher phosphorescence energy onset but is actually contribution for TADF emission, even at 80 K, because of the smaller ΔE_{ST} (Figure 3c).

Further analysis of the effect of the two conformers on the overall photophysics was made using time-resolved (TR) emission decays, shown in **Figure 4**. Zeonex host was chosen as a neutral environment. Upon excitation of the QA conformer at 375 nm, and collecting at 395 nm, where the QA conformer emits (Figure 4a), a dominant very fast component with lifetime less than 1.15 ns is found, contribution 86% (at 0.01 wt.%) and 99% (at 1 wt.%) (Figure 4b; Figure S20a, Supporting Information). This lifetime is assigned to the singlet lifetime of the QA conformer quenched by energy transfer to molecules in the QE conformation. This lifetime decreases with increasing concentration, as expected from a FRET related process. The unquenched PF lifetime of (isolated) QA conformers is 7.1 ± 0.2 ns with a population that decreases with increasing concentration. A third component appears from 0.1 wt.% loading, having the same lifetime as the QE PF component (Figure S20a, Supporting Information). The latter indicates that even though the emission of the QE state at 395 nm should be minimal, as the FRET efficiency increases less unquenched QA emission occurs and QE emission can be observed.

Collecting at 550 nm, (375 nm excitation wavelength) mainly the QE conformer emission is monitored (Figure 4c). The lifetime behavior appears to be similar with increasing concentration, with only a minor increase from 13 ns (0.01 wt.%) to 16.9 ns (1 wt.%) as the concentration increases due to possible stronger contribution from intermolecular (dimer/excimer) states (Figure S20b, Supporting Information). Upon excitation at 405 nm, where the QE conformer mainly absorbs, the results appear to be similar with 375 nm excitation (Figure 4d).

A larger concentration series in zeonex, from 0.01 wt.% up to 25 wt.% DMAC-TRZ loading, was studied using time-resolved PL spectra, to highlight the effect of the QA conformer contribution (Figure S21, Supporting Information). At 0.01 and 1 wt.% concentration the QA contribution is dominant at early times. With increasing concentration, the intermolecular separation decreases and the FRET efficiency increases resulting in a better energy transfer from the QA to the QE conformer. Because of the latter, at 25 wt.% loading no QA contribution is observed. Increasing the emitter concentration also has an impact on the QE emission spectrum which appears to red-shift (Figure S21, Supporting Information). The emission

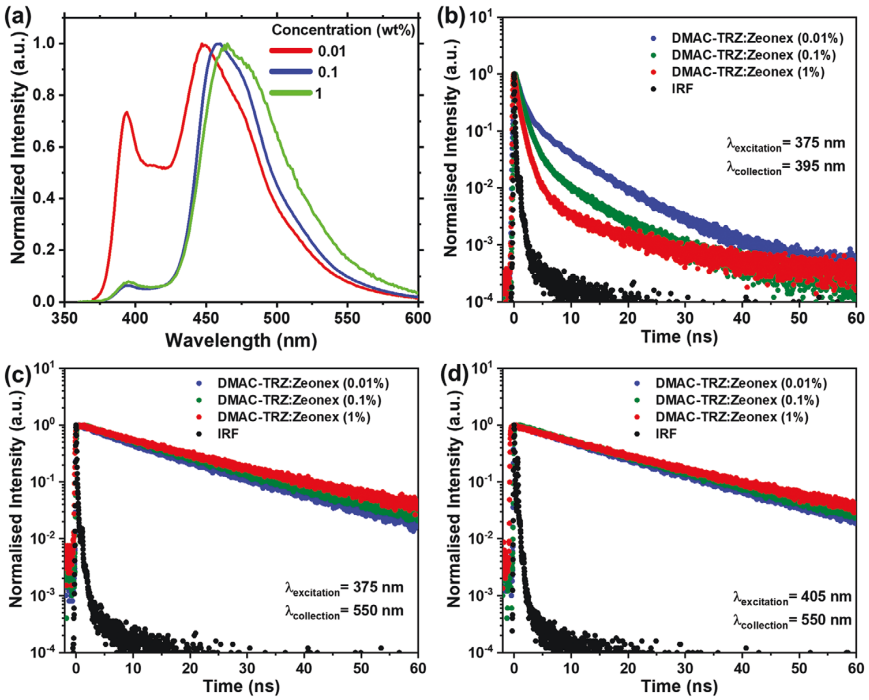

Figure 4. Photophysics of DMAC-TRZ in zeonex host, at different concentrations and room temperature. a) Steady state photoluminescence. b–d) time-resolved photoluminescence at different excitation and collection wavelengths.

spectrum of this band though appears to be the same in 5, 10, and 25 wt.%. The latter indicates that the ΔE_{ST} decreases with increasing concentration, up to a specific value (5 wt.%), due to the change of the environment's dielectric, and then remains stable.[23] The small decrease in ΔE_{ST} appears to have a disproportionate effect on the increase in DF contribution, especially for concentrations above 1 wt.% (Figure S22, Supporting Information). This implies that other phenomena might have an impact on the DF contribution.

Any potential DF contribution from the QA conformer is not observed because the DF TR-PL spectra, at all concentrations, have the QE conformer profile. This is because FRET is orders of magnitude faster than ISC causing most excited states to be transferred to the QE ^{1}CT state even at very low concentrations. Instead, aggregate emission has already been observed in DMAC-TRZ guest-host systems, especially for concentrations above 10 wt.%.[23] From the neat film PLQY, is clear that the aggregated state (dimer/excimer) efficiency is high with a value of 75%, compared to nearly 100% at 10 wt.% doped film in mCBPCN host.[23] Also, the through space analogue of DMAC-TRZ, TpAT-tFFO,[39] that has among the best TADF performance, is basically an exciplex of controlled D-A distance. Thus, we believe that the enhanced DF contribution comes from a faster intermolecular k_{rISC} and not a change of the environment's dielectric (because of the increasing concentration of the dopant), at least not at concentrations above 5 wt.%. Nevertheless, despite the improved k_{rISC}, the aggregated emission state has lower PLQY than DMAC-TRZ monomer due to enhanced non-radiative pathways.

We have previously reported the DMAC-TRZ triplet value to be at 2.75 eV (450 nm).[23] The triplet value of the individual donor and acceptor units have also been reported to have much higher values ($T_{D,A}$ > 3 eV).[35] In addition, TpAT-tFFO which is incapable of having a QA conformer, has been reported to have a ^{3}CT character lowest triplet state,[40] and its value depends on the distance between the D-A units. This experimentally has been difficult to prove and the lowest lying triplet energy was calculated to be above 3 eV.[39] All the above imply that the 'low' triplet value observed in DMAC-TRZ could either be due to the state being of ^{3}CT or of mixed ^{3}(CT/LE) character. As a mixed ^{3}(CT/LE) state is easier to observe, because the oscillator strength increases dramatically, we believe this is what we are observing in DMAC-TRZ and this then explains the structured phosphorescence emission observed in DMAC-TRZ, in specific environments (Figure S23, Supporting Information).

In our previous work[23] we showed that the triplet energy of DMAC-TRZ is temperature dependent. At 20 K, the phosphorescence spectrum is blue shifted compared to that at 80 K, observed in all hosts and neat film, except zeonex where the phosphorescence spectrum is identical at both temperatures (Figure S23, Supporting Information). At 80 K in mCPCN and mCBPCN, where the triplet value of the host is only slightly higher than the triplet value of the DMAC-TRZ, a Gaussian shape emission spectrum appears with a wavelength onset of 460 ± 1 nm in both cases, which is redshifted compared to the DMAC-TRZ:zeonex film at the same temperature. Energetically it is at the same position as the low temperature DF (coming from the QE CT state), which appears to contribute in the delayed regime, even at low temperatures (as low as 80 K), because of the efficient k_{rISC}.[23] At 20 K, in both hosts, where the DMAC-TRZ TADF contribution is minimal based on the time-resolved spectra,[23] the phosphorescence spectrum is blue shifted and appears identical to the phosphorescence spectrum measured in films of neat hosts (Figure S23b,c, Supporting Information). The host phosphorescence is dominant at 20 K, because we excite both the host and the guest, so at very low temperatures some host triplet states do not migrate to the guest sites at 1 wt.% concentration, and can be observed because of their stronger oscillator strength compared to the DMAC-TRZ lowest lying triplet. This must then have a strong ^{3}CT character. Although the host triplet appears to be the lowest observable triplet state of the system, this cannot be the case in the guest-host systems because DF emission from the QE ^{1}CT is observed at room temperature,[23] which means that the upconverted QE ^{3}CT are not quenched by the triplet of the host. . Therefore, the lowest energy triplet of DMAC-TRZ QE conformer must be below that of these two hosts.

When the hosts lowest lying triplet energy is much higher compared to the guest, this effect does not occur. In DPEPO host (T_1 ~ 3 eV),[41] the 80K phosphorescence spectrum of 1 wt.% DMAC-TRZ appears similar to that observed in mCBPCN and mCPCN hosts, another indication that DF is still observable at this temperature. At 20 K, a blue shift of the onset is observed towards 445 nm (from 460 nm), similar to the DMAC-TRZ:zeonex film, and far from the triplet value of DPEPO. In the absence of a host (i.e., neat film) a structured emission appears at 80 K with an onset of 475 nm, and is assigned to aggregated emission. Lowering to 20 K a second band appears, with the onset of the high energy band at 2.82 eV (440 nm), similar to what was observed in the high triplet energy hosts and in frozen solution[35] (Figure S23e, Supporting Information). This indicates that the two conformers have distinct lowest triplet states. The QE conformer has a strong CT character triplet state, which must be energetically slightly below the ^{1}CT but is difficult to observe in all environments because of its low oscillator strength. This explains why in mCPCN and mCBPCN we see host phosphorescence but no guest phosphorescence. Thus, the triplet value observed at 20 K, in DPEPO and zeonex films is attributed to the QA triplet value (not the QE triplet), which has a mixed CT/LE character and so is emissive enough to be observed. This is in good agreement with the calculations (Figure 2).

Conformational heterogeneity[23] is a parameter that could affect this determination, regarding the origin, of the triplet state discussed above. One could speculate that a molecule with lower dihedral twist angle between the donor and acceptor units could be the source of this triplet energy. Our previous studies,[22–24] show that conformational heterogeneity is environment dependent. Thus, the population of the low twisted angle D-A molecules should decrease with increasing dielectric, and in high dielectric DPEPO host this population will be negligible, thus its phosphorescence would be difficult, if not impossible, to observe. Further, a QE ^{3}CT with some local character should be easier to change with the environment dielectric, compared to a ^{3}LE with some CT character (which is the case of the QA conformer). Thus, we verify that the lowest triplet observed in different environments, which is dielectric independent, could only be the triplet of the QA conformer.

2.4. Devices

Devices were fabricated with a structure of ITO (anode) | NPB (HTL, 40 nm) | TSBPA (EBL, 10 nm) | DMAC-TRZ x wt.% in different hosts (EML, 30 nm) | TPBi (HBL, 10 nm) | POT2T (ETL, 40 nm) | LiF (EIL, 1 nm) and Al (cathode, 100 nm). For the emissive layer (EML) a concentration series of 5, 15, and 25 wt.% DMAC TRZ was used in a number of hosts with different ground state dipole moments (mCP, mCPCN, mCBPCN, BCPO, DPEPO, and neat film). The resultant EL spectra in each individual host are shown in Figure S24 (Supporting Information), and the contribution of the QA conformer appears in specific environments, similar to previous dual conformer emitter studies.[25] The QA electroluminescence (EL) contribution is strongest in mCP and decreases in intensity with increasing host dielectric, because of better spectral overlap between the EL of the QA and the absorption of the QE conformer (which redshifts with increasing dielectric constant). In mCPCN, the QA contribution appears to be minor and seems to set the environment threshold for complete FRET between the two conformers. In BCPO and DPEPO no contribution from the QA conformer can be observed. Possible host emission is excluded because of their different emission spectra, as shown in Figure S24f (Supporting Information). Also, if the emission was coming from the hosts, it should have been observed in mCPCN and BCPO devices too. In all cases, where the QA emission is observed, its relative intensity appears to decrease with increasing DMAC-TRZ concentration, mainly because of increasing quenching by the QE conformers.

To investigate further the QA effect on OLEDs, a new set of devices using DMAC-TRZ as a triplet harvesting/singlet sensitizer for v-DABNA as a terminal emitter was fabricated in mCBPCN host (device structure in **Figure 5**). Using this approach one can investigate the effect of energy transfer to the v-DABNA from the two conformers. Figure S25a (Supporting Information) shows the absorption and emission overlap between v-DABNA and DMAC-TRZ respectively, a critical parameter for efficient FRET.[32,42] To our understanding this system has the smallest spectral overlap so far reported yet achieves very high FRET efficiency, even at 1 wt.% v-DABNA loading.

The electrical response of the DMAC-TRZ only and HF-OLEDs appears to be similar, while the brightness of the HF-device is slightly lower (Figure 5b). The performance is comparable in the two cases and the EQE is divided into two regimes; below 1 mA cm^{-2} where the EQE is higher in the HF-OLED (≈30%); and above 1 mA cm^{-2} where the EQE is higher in the TADF only OLED (Figure 5c). Further, v-DABNA OLEDs in mCBPCN host were fabricated using the same device structure and although they cannot compete with the previously reported devices using DOBNA-OAr as a host,[43] they also show the common MR-TADF EQE response, with two different regimes (Figure S26, Supporting Information); a high performance one below 1 mA cm^{-2} and one above with low performance. The latter implies that at higher current densities the longer-lived DF lifetime of the v-DABNA terminal emitter results in excess triplet quenching mechanisms.

Focusing on the EL spectra one can observe that although there is a clear contribution of the sensitizer ≈500 nm

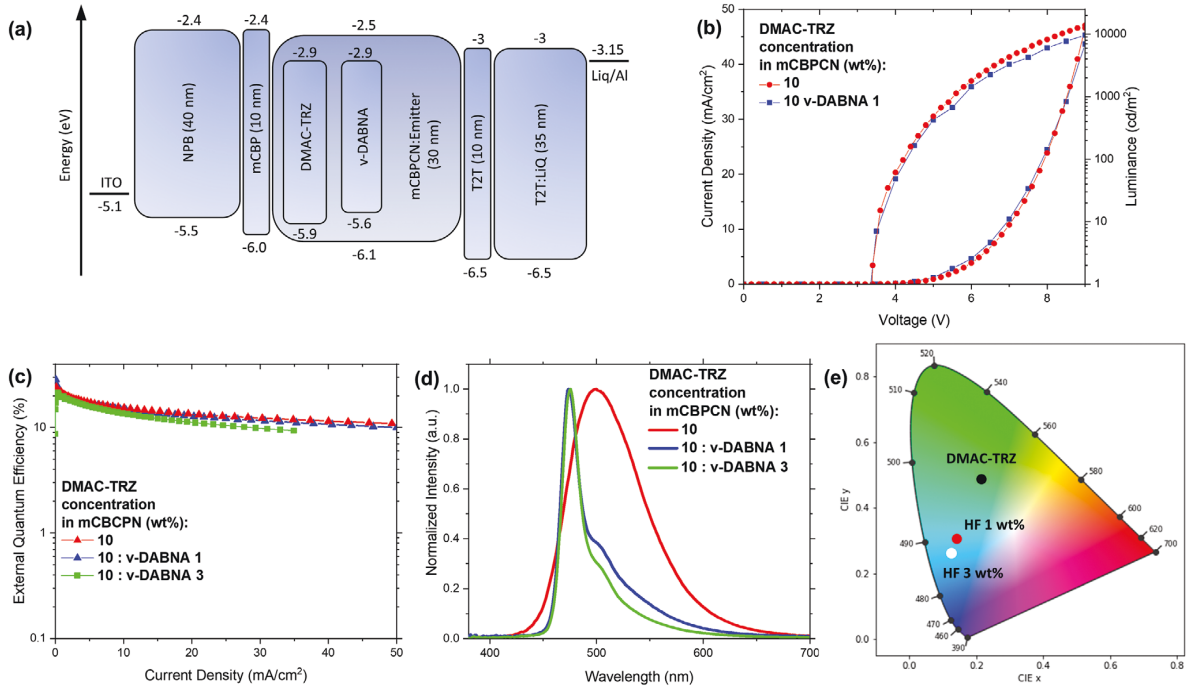

Figure 5. OLEDs performance. a) Device architecture, b) JVL curves, and c) EQE versus current density of TADF only and HF OLEDs. d) EL spectra and e) CIE coordinates collected at 8 V.

(Figure 5d), the results are comparable or even better compared to previously published studies using deeper blue sensitizers with similar quantum yield.[44,45] This does not seem possible considering the relatively lower FRET efficiency of the specific set of DMAC-TRZ/v-DABNA system. Thus, we suggest that the presence of the QA conformer acts as an extra (sensitizer emission) component that directly pumps the terminal emitter through efficient FRET, instead of just the QE conformer as seen in TADF only devices. The QA conformer PL spectrum has much better overlap with the v-DABNA absorption spectrum, compared to the QE absorption spectrum (Figure S25b,c, Supporting Information). Further, another important parameter for a high FRET radius is the extinction coefficient of the acceptor, which is orders of magnitude higher in v-DABNA. The FRET radius[32] from the QA conformer to the QE conformer or the terminal emitter (v-DABNA) was calculated to be 2.3 and 4.05 nm respectively. As a result, the energy of the initial QA population is expected to be mainly transferred to the v-DABNA molecules and not the QE configuration. FRET from the QE conformer to the terminal emitter is still occurring (Figure S25a, Supporting Information), but the efficiency is lower compared to the QA to terminal emitter energy transfer. To investigate further the energy transfer efficiency of the QE conformer to the terminal emitter, especially in the DF regime where triplet harvesting is critical for the OLED performance, time-resolved measurements in three different systems are shown in Figure S27a (Supporting Information). The HF-system (DMAC-TRZ:v-DABNA in mCBPCN) shows a small quenching of the late PF and early DF lifetime, compared to the DMAC-TRZ film but a much stronger quenching of longer DF contribution, following the v-DABNA film lifetime. The latter indicates that we have two different regimes, one with high and one with low FRET efficiency from the QE conformer to the terminal emitter. From the contour plot of the HF-system (Figure S27b, Supporting Information), one can observe a second spectral band increasing in the less efficient energy transfer regime ($15 < t < 1000$ ns). In the PF regime, the early time spectrum has an identical shape with the v-DABNA film, confirming the high FRET efficiency of the QA conformer to the terminal emitter (Figure S27c, Supporting Information). At later times, the second band appears and contributes equally to the PL spectrum as the terminal emitter. This is the effect of the more orthogonal D-A QE conformers, that have longer wavelength emission and longer PF lifetime as shown before.[23] In the DF regime, the opposite occurs. The longer wavelength QE conformer have shorter lifetime and can be seen at early DF times, thus can be observed in the HF system (Figure S27d, Supporting Information). Over time, only the shorter wavelength QE conformers decay radiatively and have better spectral overlap with the terminal emitter, thus the PL emission mainly originates from v-DABNA. This implies that the FRET efficiency between the QE conformer and the terminal emitter is highly inhomogeneous and is entirely dependent on the dihedral angle distribution of the QE conformers. At late PF and early DF regimes the FRET efficiency will be relatively poor, while at early PF and late DF the efficiency will be higher, with a FRET radius of 3.45 nm. This less efficient energy transfer process results in a very small contribution of the QE emission in the overall EL spectrum, at 1 wt.% concentration of v-DABNA (Figure 5d).

With increasing terminal emitter concentration, an increase of FRET efficiency occurs resulting in a smaller contribution of the TADF sensitizer as observed in the EL spectrum (Figure 5d) and is much closer to the v-DABNA only OLED (Figure S26a, Supporting Information). The EL spectra of both HF OLEDs (1 and 3 wt.% concentration) are stable with increasing voltage/current density (Figure S28, Supporting Information), excluding the presence of a current density dependent band and/or the contribution from and interfacial exciplex EL emission. The maximum EQE decreases with increased concentration, which we assume is, among other effects, due to stronger intermolecular interactions and excimer quenching,[32] but is still above 20%. The color coordinates shifted from (0.21, 0.47) to (0.16, 0.31) and (0.14, 0.27) in DMAC-TRZ only, HF OLED 1 and 3 wt.% respectively (Figure 5e). To our understanding this is the first set of HF OLEDs that convert green EL emission to blue.

3. Conclusion

DMAC-TRZ has been studied extensively before, but there are many aspects of its photophysics and device performance that have not been revealed until now.[18,22,23,31,35,46,47] The presence of a second conformer, the QA, has proven to be stronger than expected and its contribution to the photophysical performance in solid-state, especially at low concentrations, has proven to be dominant. At higher concentrations (above 1 wt.%), the FRET efficiency to the QE conformer increases greatly and its contribution cannot be easily observed, this could be why it was not observed until now. A key parameter for its strong contribution is the presence of a rigid host, that hinders possible conformational relaxation to the QE conformation, with the presence of excess (excitation) energy. The sensitivity of the two conformers to the environment appears to be different, indicating a stronger local character for the QA and a stronger CT character for the QE conformer, verified by quantum chemical calculations. The DF appears to originate purely from the QE conformer mainly because of the high ΔE_{ST} of the QA preventing the formation of rISC channels from the T_1 to S_1. Intermolecular interactions (dimer/excimer formation) improve the rISC rate and show that can be more efficient compared to the monomer performance. The triplet value mystery of DMAC-TRZ (the triplet is lower in energy than either the D or A units) has been resolved, with experimental proofs showing that the actual triplet value observed in DMAC-TRZ systems originates from the QA conformer and not the QE. OLEDs of DMAC-TRZ show the contribution of the QA conformer to the EL spectrum of the device, only in specific environments and low concentrations. To explore the energy transfer process of the two conformers, HF-devices using v-DABNA as the terminal emitter show high relative FRET efficiency compared to similar systems,[44,45] indicating that the QA conformer transfers its energy directly to the terminal emitter instead of the QE conformer. The efficient energy transfer resulted to the fabrication of the first OLEDs that convert green EL emission into blue using the HF approach.

Supporting Information

Supporting Information is available from the Wiley Online Library or from the author.

Acknowledgements

The authors thank Prof. Takuji Hatakeyama for providing the v-DABNA emitter. This project had received funding from the European Union's Horizon 2020 research and innovation programme under the Marie Skłodowska Curie grant agreement No 812872 (TADFlife). T.B., L.M.D., and C.M.M. acknowledge the Deutsche Forschungsgemeinschaft (DFG, German Research Foundation) – 396890929/GRK 2482 and MA1051/17-1. A.P.M. thanks the EPSRC for funding, EP/T02240X/1.

Conflict of Interest

The authors declare no conflict of interest.

Data Availability Statement

The data that support the findings of this study are available in the supplementary material of this article.

Keywords

acridine, dual conformations, FRET, hyperfluorescence, OLEDs, quasi-axial, TADFs

Received: January 25, 2023
Revised: February 16, 2023
Published online: March 14, 2023

[1] Z. Yang, Z. Mao, Z. Xie, Y. Zhang, S. Liu, J. Zhao, J. Xu, Z. Chi, M. P. Aldred, *Chem. Soc. Rev.* **2017**, *46*, 915.
[2] C. Adachi, M. A. Baldo, M. E. Thompson, S. R. Forrest, *J. Appl. Phys.* **2001**, *90*, 5048.
[3] J. R. Lakowicz, *Principles of Fluorescence Spectroscopy*, 3rd ed., Springer, New York **2006**.
[4] G. Méhes, H. Nomura, Q. Zhang, T. Nakagawa, C. Adachi, *Angew. Chem., Int. Ed.* **2012**, *51*, 11311.
[5] H. Wang, L. Xie, Q. Peng, L. Meng, Y. Wang, Y. Yi, P. Wang, *Adv. Mater.* **2014**, *26*, 5198.
[6] Y. Liu, G. Zhan, Z. W. Liu, Z. Q. Bian, C. H. Huang, *Chin. Chem. Lett.* **2016**, *27*, 1231.
[7] F. B. Dias, K. N. Bourdakos, V. Jankus, K. C. Moss, K. T. Kamtekar, V. Bhalla, J. Santos, M. R. Bryce, A. P. Monkman, *Adv. Mater.* **2013**, *25*, 3707.
[8] M. A. Baldo, D. F. O'Brien, Y. You, A. Shoustikov, S. Sibley, M. E. Thompson, S. R. Forrest, *Nature* **1998**, *395*, 151.
[9] P. L. Santos, J. S. Ward, P. Data, A. S. Batsanov, M. R. Bryce, F. B. Dias, A. P. Monkman, *J. Mater. Chem. C* **2016**, *4*, 3815.
[10] F. B. Dias, T. J. Penfold, A. P. Monkman, *Methods Appl. Fluoresc.* **2017**, *5*, 012001.
[11] M. K. Etherington, J. Gibson, H. F. Higginbotham, T. J. Penfold, A. P. Monkman, *Nat. Commun.* **2016**, *7*, 13680.
[12] T. J. Penfold, E. Gindensperger, C. Daniel, C. M. Marian, *Chem. Rev.* **2018**, *118*, 6975.
[13] Z. R. Grabowski, K. Rotkiewicz, W. Rettig, *Chem. Rev.* **2003**, *103*, 3899.
[14] L.-S. Cui, H. Nomura, Y. Geng, J. U. Kim, H. Nakanotani, C. Adachi, *Angew. Chem., Int. Ed.* **2017**, *56*, 1571.
[15] Y. Tao, K. Yuan, T. Chen, P. Xu, H. Li, R. Chen, C. Zheng, L. Zhang, W. Huang, *Adv. Mater.* **2014**, *26*, 7931.
[16] F. B. Dias, J. Santos, D. R. Graves, P. Data, R. S. Nobuyasu, M. A. Fox, A. S. Batsanov, T. Palmeira, M. N. Berberan-Santos, M. R. Bryce, A. P. Monkman, *Adv. Sci.* **2016**, *3*, 1600080.
[17] X. Cai, B. Gao, X. L. Li, Y. Cao, S. J. Su, *Adv. Funct. Mater.* **2016**, *26*, 8042.
[18] T.-A. Lin, T. Chatterjee, W.-L. Tsai, W.-K. Lee, M.-J. Wu, M. Jiao, K.-C. Pan, C.-L. Yi, C.-L. Chung, K.-T. Wong, C.-C. Wu, *Adv. Mater.* **2016**, *28*, 6976.
[19] P. L. dos Santos, J. S. Ward, D. G. Congrave, A. S. Batsanov, J. Eng, J. E. Stacey, T. J. Penfold, A. P. Monkman, M. R. Bryce, *Adv. Sci.* **2018**, *5*, 1700989.
[20] L. Yu, Z. Wu, G. Xie, C. Zhong, Z. Zhu, H. Cong, D. Ma, C. Yang, *Chem. Commun.* **2016**, *52*, 11012.
[21] V. Jankus, P. Data, D. Graves, C. McGuinness, J. Santos, M. R. Bryce, F. B. Dias, A. P. Monkman, *Adv. Funct. Mater.* **2014**, *24*, 6178.
[22] D. K. A. Phan Huu, S. Saseendran, R. Dhali, L. G. Franca, K. Stavrou, A. Monkman, A. Painelli, *J. Am. Chem. Soc.* **2022**, *144*, 15211.
[23] K. Stavrou, L. G. Franca, A. P. Monkman, *ACS Appl. Electron. Mater.* **2020**, *2*, 2868.
[24] D. Kelly, L. G. Franca, K. Stavrou, A. Danos, A. P. Monkman, *J. Phys. Chem. Lett.* **2022**, *13*, 6981.
[25] H. Tanaka, K. Shizu, H. Nakanotani, C. Adachi, *J. Phys. Chem. C* **2014**, *118*, 15985.
[26] M. K. Etherington, F. Franchello, J. Gibson, T. Northey, J. Santos, J. S. Ward, H. F. Higginbotham, P. Data, A. Kurowska, P. L. Dos Santos, D. R. Graves, A. S. Batsanov, F. B. DIas, M. R. Bryce, T. J. Penfold, A. P. Monkman, *Nat. Commun.* **2017**, *8*, 14987.
[27] Y. Z. Shi, K. Wang, S. L. Zhang, X. C. Fan, Y. Tsuchiya, Y. T. Lee, G. L.e Dai, J. X. Chen, C. J. Zheng, S. Y. Xiong, X. M. Ou, J. Yu, J. S. Jie, C. S. Lee, C. Adachi, X. H. Zhang, *Angew. Chem., Int. Ed.* **2021**, *60*, 25878.
[28] W. Li, X. Cai, B. Li, L. Gan, Y. He, K. Liu, D. Chen, Y. C. Wu, S. J. Su, *Angew. Chem., Int. Ed.* **2019**, *58*, 582.
[29] K. Wang, C.-J. Zheng, W. Liu, K. Liang, Y.-Z. Shi, S.-L. Tao, C.-S. Lee, X.-M. Ou, X.-H. Zhang, *Adv. Mater.* **2017**, *29*, 1701476.
[30] I. Marghad, F. Bencheikh, C. Wang, S. Manolikakes, A. Rérat, C. Gosmini, D. H. Kim, J. C. Ribierre, C. Adachi, *RSC Adv.* **2019**, *9*, 4336.
[31] W. L. Tsai, M. H. Huang, W. K. Lee, Y. J. Hsu, K. C. Pan, Y. H. Huang, H. C. Ting, M. Sarma, Y. Y. Ho, H. C. Hu, C. C. Chen, M. T. Lee, K. T. Wong, C. C. Wu, *Chem. Commun.* **2015**, *51*, 13662.
[32] K. Stavrou, A. Danos, T. Hama, T. Hatakeyama, A. Monkman, *ACS Appl. Mater. Interfaces* **2021**, *13*, 8643.
[33] K. Stavrou, S. Madayanad Suresh, D. Hall, A. Danos, N. A. Kukhta, A. M. Z. Slawin, S. Warriner, D. Beljonne, Y. Olivier, A. Monkman, E. Zysman-Colman, *Adv. Opt. Mater.* **2022**, *10*, 2200688.
[34] D. Hall, K. Stavrou, E. Duda, A. Danos, S. Bagnich, S. Warriner, A. M. Z. Slawin, D. Beljonne, A. Köhler, A. Monkman, Y. Olivier, E. Zysman-Colman, *Mater. Horiz.* **2022**, *9*, 1068.
[35] R. Dhali, D. K. A. Phan Huu, F. Bertocchi, C. Sissa, F. Terenziani, A. Painelli, *Phys. Chem. Chem. Phys.* **2021**, *23*, 378.
[36] Y. Qian, X. Li, A. R. Harutyunyan, G. Chen, Y. Rao, H. Chen, *J. Phys. Chem. A* **2020**, *124*, 9156.
[37] J. Gibson, A. P. Monkman, T. J. Penfold, *ChemPhysChem* **2016**, *17*, 2956.
[38] D. De Sa Pereira, C. Menelaou, A. Danos, C. Marian, A. P. Monkman, *J. Phys. Chem. Lett.* **2019**, *10*, 3205.

[39] Y. Wada, H. Nakagawa, S. Matsumoto, Y. Wakisaka, H. Kaji, *Nat. Photonics* **2020**, *14*, 643.
[40] J. M. Kaminski, A. Rodríguez-Serrano, F. Dinkelbach, H. Miranda-Salinas, A. P. Monkman, C. M. Marian, *Chem. Sci.* **2022**, *13*, 7057.
[41] J. Zhang, D. Ding, Y. Wei, H. Xu, *Chem. Sci.* **2016**, *7*, 2870.
[42] T. Förster, *Ann. Phys.* **1948**, *437*, 55.
[43] Y. Kondo, K. Yoshiura, S. Kitera, H. Nishi, S. Oda, H. Gotoh, Y. Sasada, M. Yanai, T. Hatakeyama, *Nat. Photonics* **2019**, *13*, 678.
[44] S. O. Jeon, K. H. Lee, J. S. Kim, S. G. Ihn, Y. S. Chung, J. W. Kim, H. Lee, S. Kim, H. Choi, J. Y. Lee, *Nat. Photonics* **2021**, *15*, 208.
[45] C. Y. Chan, M. Tanaka, Y. T. Lee, Y. W. Wong, H. Nakanotani, T. Hatakeyama, C. Adachi, *Nat. Photonics* **2021**, *15*, 203.
[46] Y. Wada, K. Shizu, S. Kubo, T. Fukushima, T. Miwa, H. Tanaka, C. Adachi, H. Kaji, **2016**, *9*, 032102.
[47] Y. Wada, H. Nakagawa, H. Kaji, *Chem. – Asian J.* **2021**, *16*, 1073.

ADVANCED FUNCTIONAL MATERIALS

Supporting Information

for *Adv. Funct. Mater.,* DOI: 10.1002/adfm.202300910

Unexpected Quasi-Axial Conformer in Thermally Activated Delayed Fluorescence DMAC-TRZ, Pushing Green OLEDs to Blue

Kleitos Stavrou, Larissa G. Franca, Tobias Böhmer, Luka M. Duben, Christel M. Marian,* and Andrew P. Monkman**

Supporting Information

Unexpected quasi-axial conformer in thermally activated delayed fluorescence DMAC-TRZ, pushing green OLEDs to blue.

Kleitos Stavrou,[a]* Larissa G. Franca,[a] Tobias Böhmer,[b] Luka M. Duben,[b] Christel M. Marian,[b]* Andrew P. Monkman[a]*

[a]Department of Physics, Durham University, Durham DH1 3LE, U.K. E-mail: a.p.monkman@durham.ac.uk, kleitos.stavrou@durham.ac.uk

[b]Institute of Theoretical and Computational Chemistry, Heinrich-Heine-University Düsseldorf, 40204 Düsseldorf, Germany, E-mail: christel.marian@hhu.de

Table of Contents

General information:

Computational Details.

The molecular equilibrium geometries were optimised with Gaussian16[1] employing the LC-ω*-HPBE[2] density functional. The range separation parameter was set to ω=0.195 a_0^{-1} for the QE conformer, as determined by Dhali et al.[3] in an optimal tuning procedure. For the QA conformer a slightly smaller value of ω=0.175 a_0^{-1} was found to be optimal. For all atoms, the split-valence def2-SV(P) basis set was utilised.[4] A methyl cyclohexane environment was mimicked with a polarisable continuum model [PCM] as implemented in Gaussian16. Electronic spectra were computed with the combined density functional theory and multireference configuration interaction DFT/MRCI method[5] in the short parameterisation form suggested by Lyskov et al.[6] To this end, the PCM point charges were exported and transferred to the Turbomole program package[7] which was used to generate molecular orbitals and three-index two-electron integrals required by the DFT/MRCI program. Energies and wavefunctions of 20 excited singlet and 20 triplet states were solved for in the DFT/MRCI step. Franck–Condon and Herzberg–Teller spectra were computed with a modified version of the VIBES program.[8]

Photophysical measurements.

Steady-state absorption and emission spectra were measured using a double beam Shimadzu UV-3600 UV/VIS/NIR spectrophotometer and a Horiba Jobin Yvon Fluorolog-3 spectrofluorometer, respectively. Solution-state samples were dissolved at 20 μM concentration. Solid-state samples were prepared from toluene solutions of host and guest molecules at specific mass ratios, and dried in vacuum following drop-casting upon sapphire or quartz substrates. Fresh samples were used for all steady state measurements to minimize the possibility of emitter degradation. Time-resolved measurements were performed using a spectrograph (Horiba Triax) and a Stanford Computer Optics 4Picos ICCD camera, where samples were excited with a Nd:YAG laser (EKSPLA, 10 Hz, 355 nm) under vacuum.

Device Fabrication.

OLEDs were fabricated on patterned indium tin oxide (ITO)-coated glass (VisionTek Systems) with a sheet resistance of 15 Ω/sq. After sonicating in acetone and isopropanol, oxygen-plasma cleaned substrates were loaded into a Kurt J. Lesker Super Spectros deposition chamber, and both the small molecule and cathode layers were thermally evaporated at pressure below 10–7 mbar. The materials used for the production of the TADF-only devices were N,N-bis(naphthalene-1-yl)-N,-bis(phenyl)benzidine (NPB) as the transport layer (HTL), 4,4'-(Diphenylsilanediyl)bis(N,N-diphenylaniline) (TSBPA) as the electron blocking layer (EBL), the emissive layer (EML) had DMAC-TRZ as terminal emitter at 5, 10 and 25 wt% concentration in different hosts (mCP, mCPCN, mCBPCN, BCPO, DPEPO and neat film), 2,2',2''-(1,3,5-Benzinetriyl)-tris(1-phenyl-1-H-benzimidazole) (TPBi) as the hole blocking layer (HBL), 2,4,6-tris[3-(diphenylphosphinyl)phenyl]-1,3,5-triazine (PO-T2T) as the electron transport layer, lithium fluoride (LiF) as electron injection layer and aluminum (Al) as cathode. The materials used for the hyperfluorescence OLEDs were N,N-bis(naphthalene-1-yl)-N,-

bis(phenyl)benzidine (NPB) as HTL, 3,3′-Di(9H-carbazol-9-yl)-1,1′-biphenyl (mCBP) as EBL, the EML had 3,3′-di(carbazol-9-yl)-5-cyano-1,1′-biphenyl (mCBPCN) as host, DMAC-TRZ as the sensitizer and v-DABNA as the terminal emitter, 2,4,6-tris(biphenyl-3-yl)-1,3,5-triazine (T2T) as the hole blocking layer (HBL), T2T and 8-hydroxyquinolinolato-lithium (Liq) as the electron transport/injection layer (ETL/EIL), and aluminium (Al) cathode. NPB, mCP, mCBP, TSBPA, PO-T2T and T2T were purchased from SigmaAldrich, TSBPA and mCBPCN from Ossila and sublimed before use. Sublimed DMAC-TRZ was purchased from Lumtec. v-DABNA was synthesized and purified by Prof. Hatakeyama group.

Device Characterization

Freshly evaporated devices were transferred into a calibrated 6-inch integrating sphere (Labsphere) in a glovebox, and their electrical properties were measured using a source meter (Keithley 2400). Emission spectra were simultaneously measured using both a calibrated fiber coupled spectrometer (Ocean optics USB4000) and a photodiode, for low luminance. All devices were evaluated at 293 K and under N2 atmosphere.

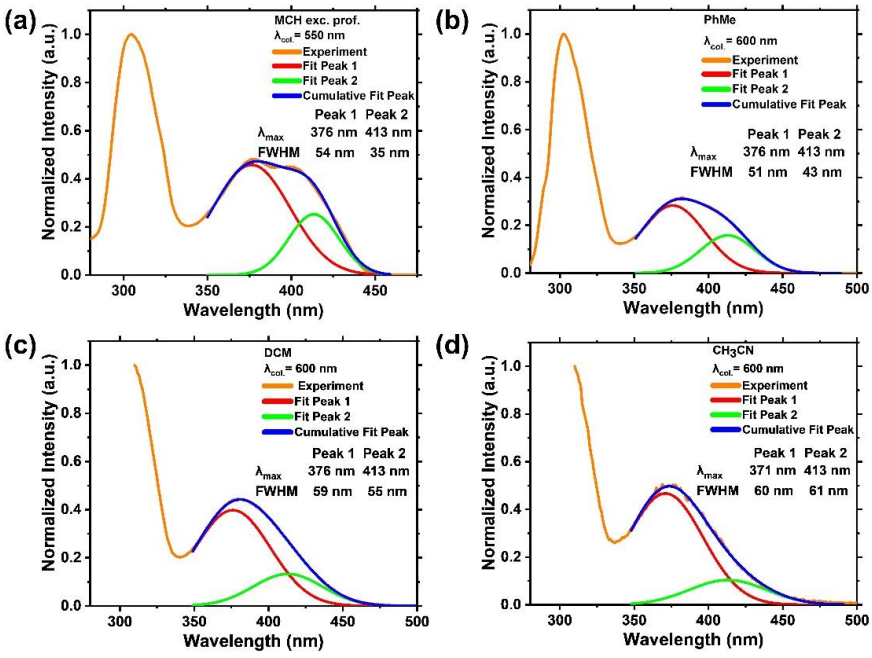

Figure S1. Deconvoluted excitation spectra of 20 μM concentration of DMAC-TRZ in (a) MCH, (b) PhMe, (c) DCM and (d) CH_3CN solvent, at room temperature. Red Ab1 band and green Ab2 band,

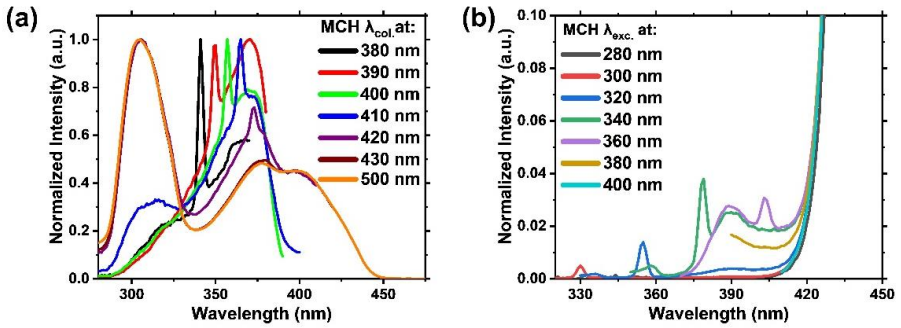

Figure S2. (a) Excitation and (b) PL spectra (of Em1) of 20 µM DMAC-TRZ in MCH, using different collection and excitation wavelengths respectively, at room temperature. Sharp peaks in the spectra are Raman peaks of the solvent.

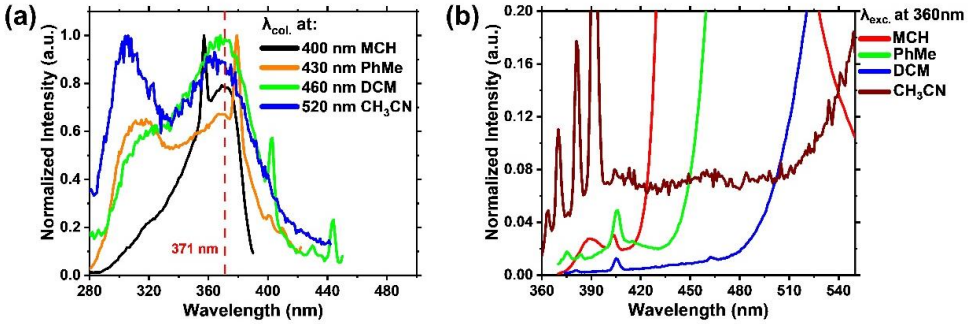

Figure S3. (a)Ab1 excitation and (b) Em1 PL spectra of 20 µM DMAC-TRZ in different solvents, using different collection and excitation wavelengths respectively, at room temperature. Sharp peaks in the spectra are Raman peaks of the solvent.

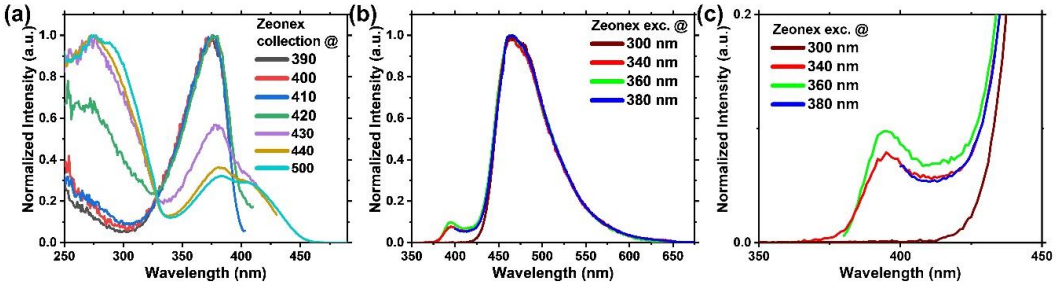

Figure S4. (a) Excitation and (b) PL spectra of 1 wt% DMAC-TRZ in zeonex host, at room temperature, using different collection and excitation wavelengths, respectively. (c) zoom in high energy band.

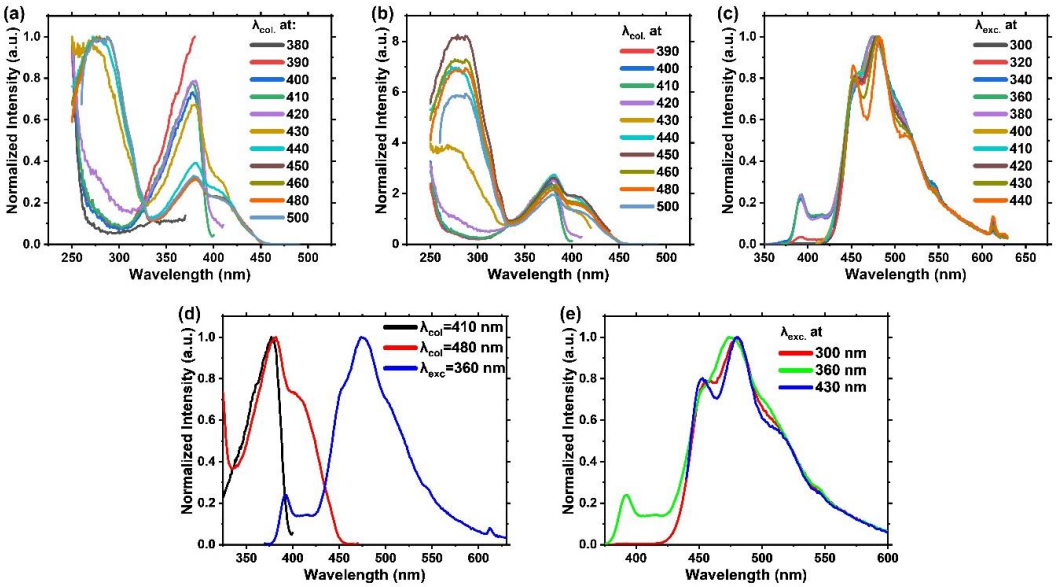

Figure S5. Excitation (a) Normalized, (b)Emission intensity normalized and (c)PL spectrum using different collection and excitation wavelengths respectively, of 1 wt% DMAC-TRZ in Zeonex, at 80 K. (d)excitation and (e) PL spectra of the two conformers of 1 wt% DMAC-TRZ in Zeonex, at 80K

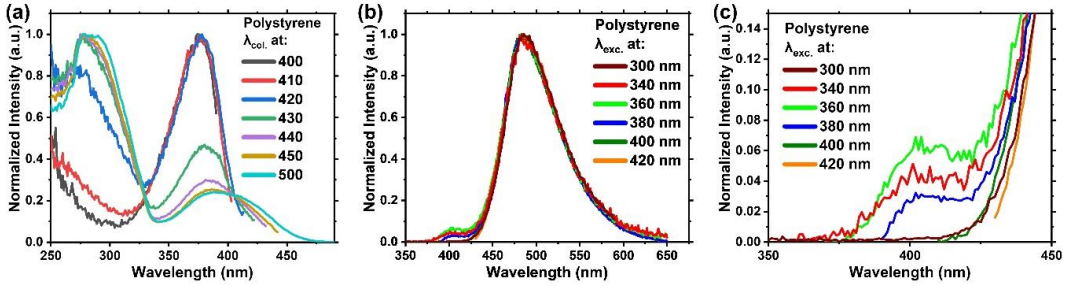

Figure S6. (a) Excitation and (b) PL spectra of 1 wt% DMAC-TRZ in polystyrene host, at room temperature, using different collection and excitation wavelengths, respectively. (c) zoom in high energy band.

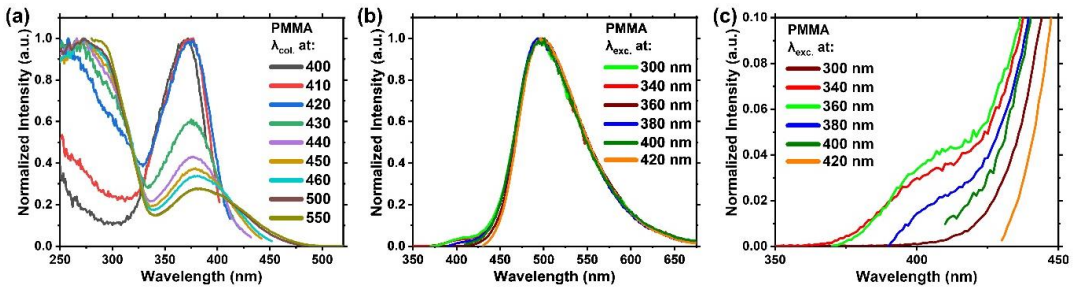

Figure S7. (a) Excitation and (b) PL spectra of 1 wt% DMAC-TRZ in PMMA host, at room temperature, using different collection and excitation wavelengths, respectively. (c) zoom in high energy band.

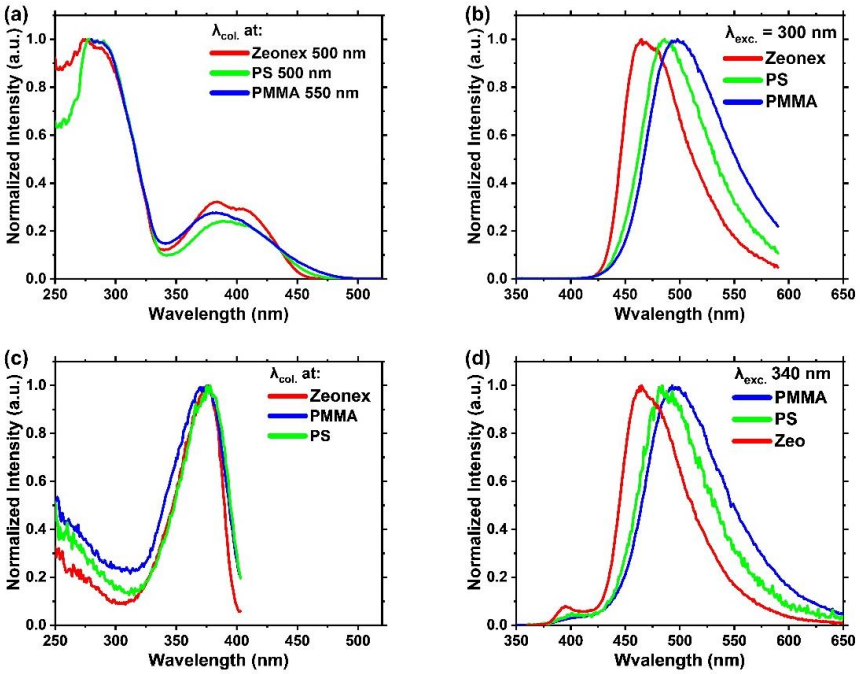

Figure S8. (a), (c) Excitation and (b), (d) PL spectra of 1 wt% DMAC-TRZ in different hosts, at room temperature. Collecting at (a) 500-550 nm, (c) 410 nm and exciting at (b) 300 nm and (d) 340 nm.

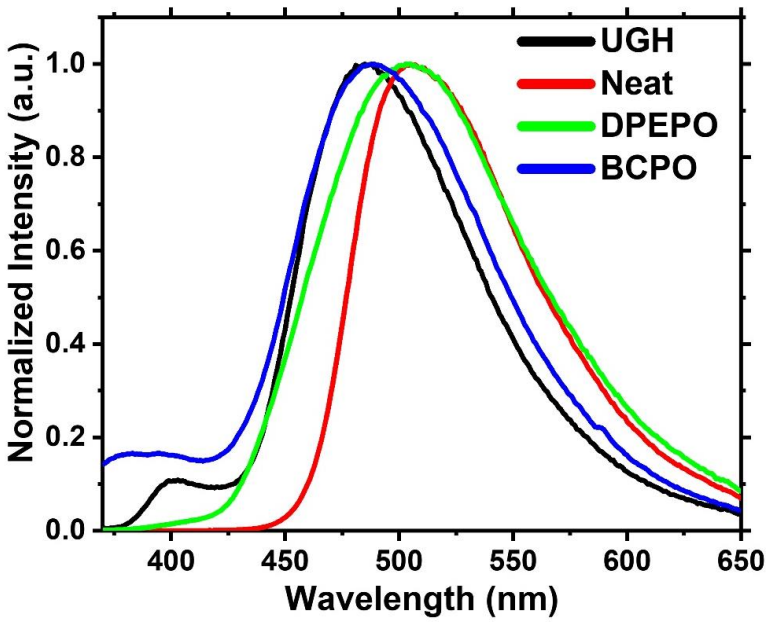

Figure S9. PL spectra of 1 wt% DMAC-TRZ in different small molecule hosts, at room temperature. Excitation wavelength 360 nm.

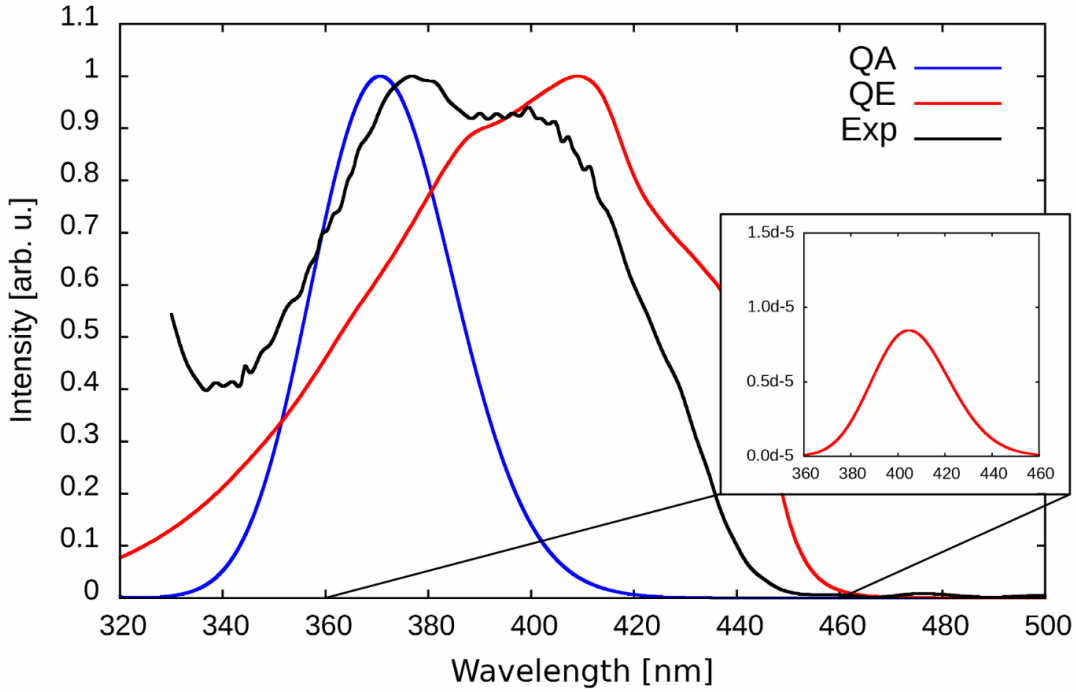

Figure S10. The peak hights of the calculated Herzberg–Teller (QE) and Franck–Condon (QA) absorption spectra are normalized to unity and compared to the experimental excitation spectrum at room temperature in methylcyclohexane solution. The inset shows the computed Franck–Condon absorption spectrum of a QE conformer with nearly orthogonal orientation of the DMAC and TRZ molecular planes.

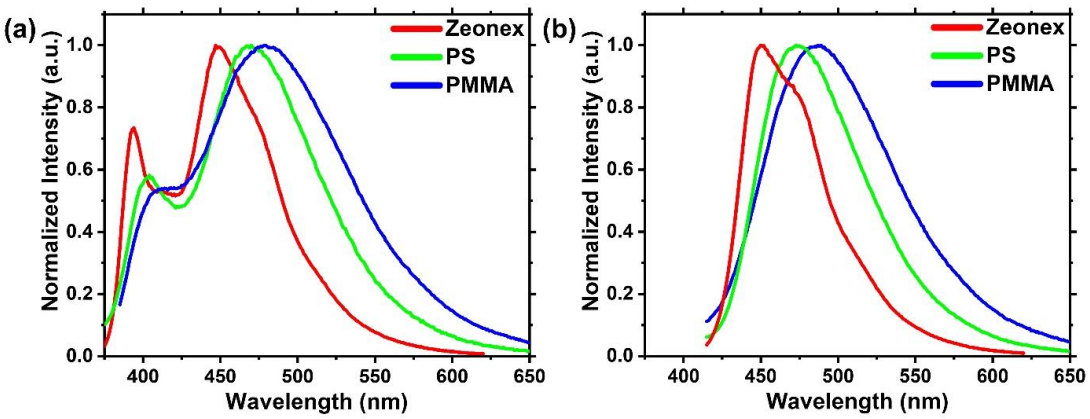

Figure S11. Solid-state photophysics of 0.01 wt% DMAC-TRZ films. Photoluminescence spectra in different polymer hosts exciting at (a) 360 nm (380nm for PMMA film) and (b) 400 nm, at room temperature.

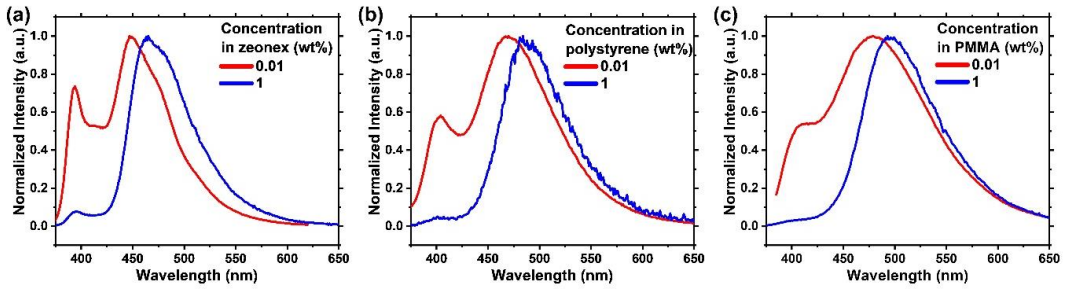

Figure S12. PL spectra of 0.01 and 1 wt% DMAC-TRZ in (a) Zeonex, (b) Polystyrene and (c) PMMA host, at room temperature. Excitation wavelength 360 nm (380 nm for PMMA film).

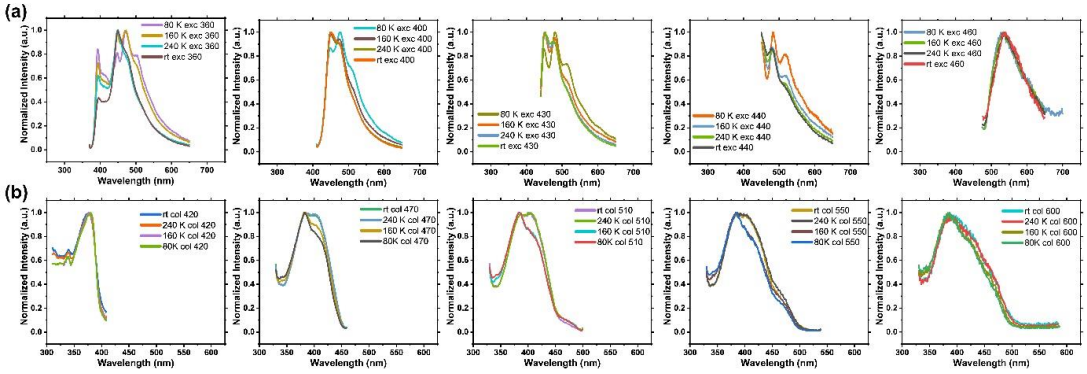

Figure S13. Steady state measurement of 0.01 wt% DMAC-TRZ in zeonex. (a) PL and (b) excitation spectra at different temperatures and excitation/collection wavelength respectively.

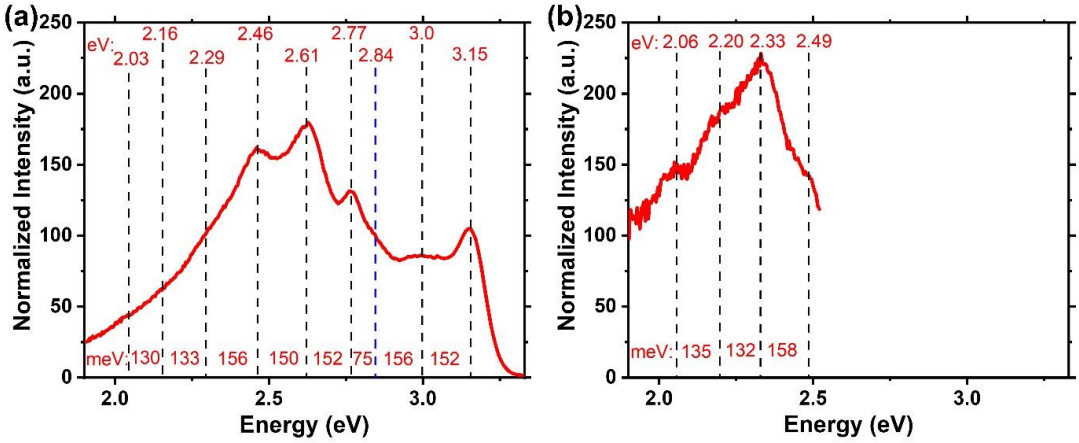

Figure S14. Jacobian conversion of 0.01 wt% DMAC-TRZ in zeonex, at 80 K. Excitation wavelength (a) 360 nm and (b) 480 nm.

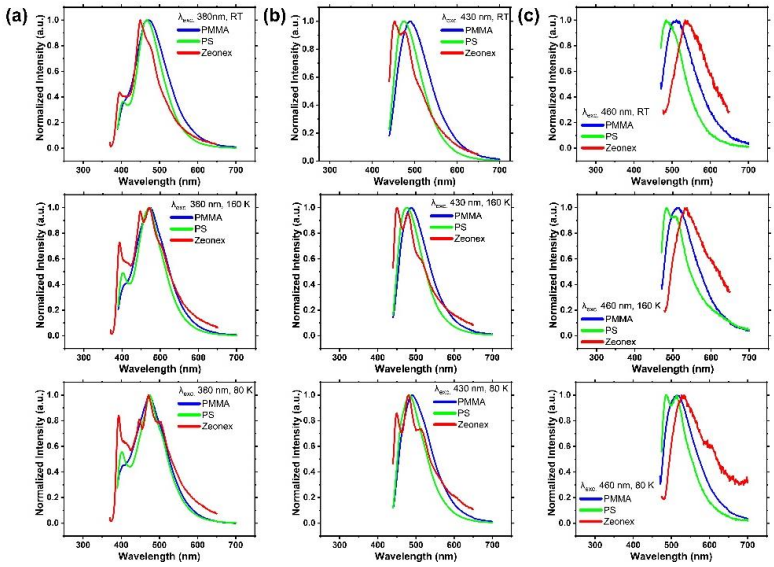

Figure S15. PL spectra of 0.01 wt% DMAC-TRZ in different hosts and different excitation wavelengths. At (a) RT, (b) 160 K and (c) 80 K.

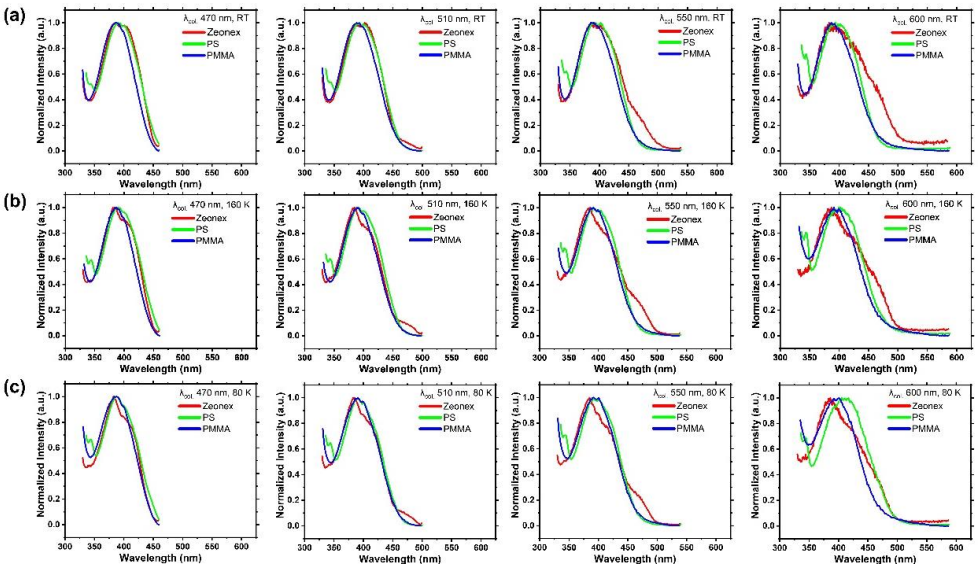

Figure S16. Excitation spectra of 0.01 wt% DMAC-TRZ in different hosts and different excitation wavelengths. At (a) RT, (b) 160 K and (c) 80 K.

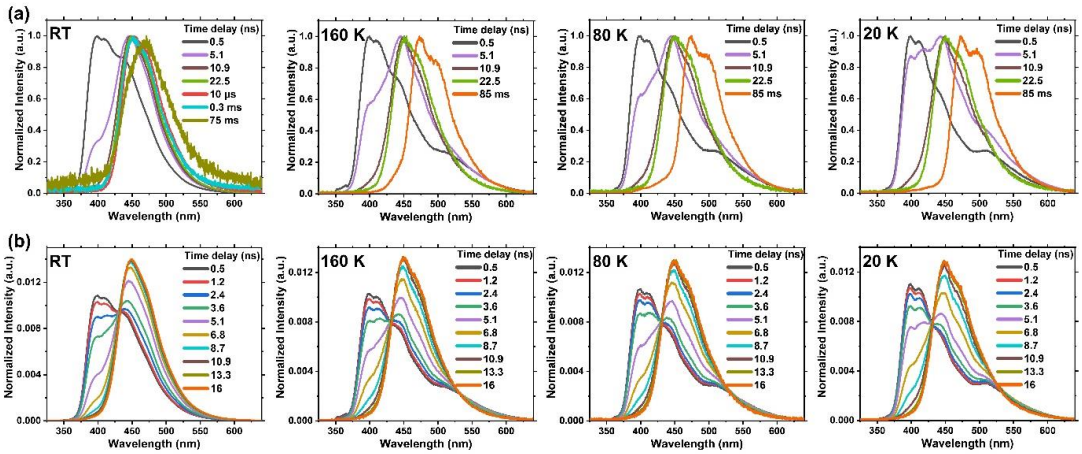

Figure S17. Time-resolved spectra of 0.01 wt% DMAC-TRZ in zeonex, in different temperatures. (a) Normalized (0,1) spectra and (b) area normalized spectra. Excitation wavelength 355 nm.

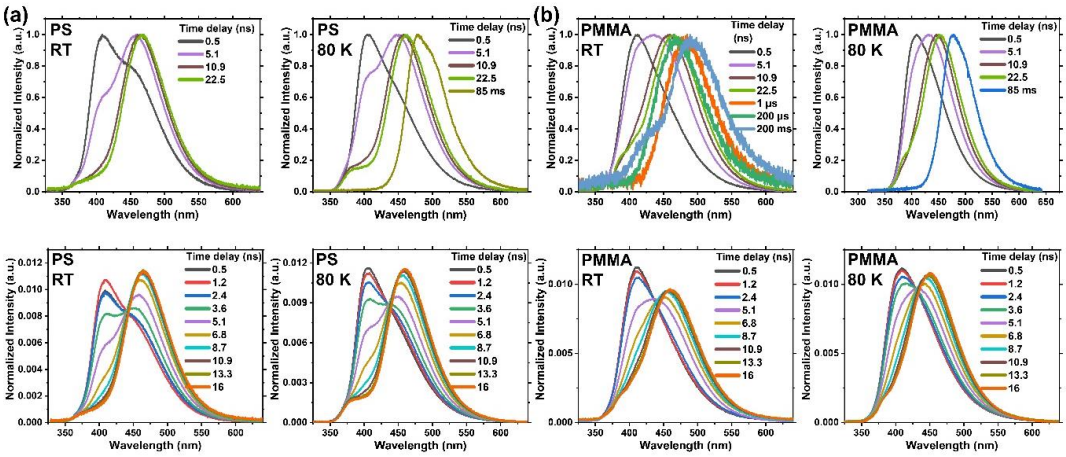

Figure S18. Time-resolved spectra of 0.01 wt% DMAC-TRZ in (a) polystyrene and (b) PMMA, at room temperature and 80 K. Top figures Normalized (0,1) spectra and bottom figures area normalized spectra. Excitation wavelength 355 nm.

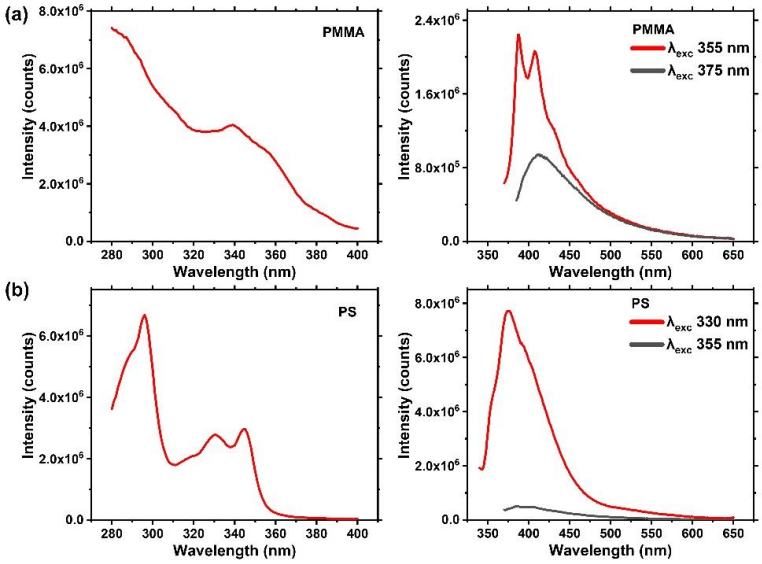

Figure S19. Steady state excitation (left) and PL (right) spectra of (a) PMMA and (b) Polystyrene, at room temperature.

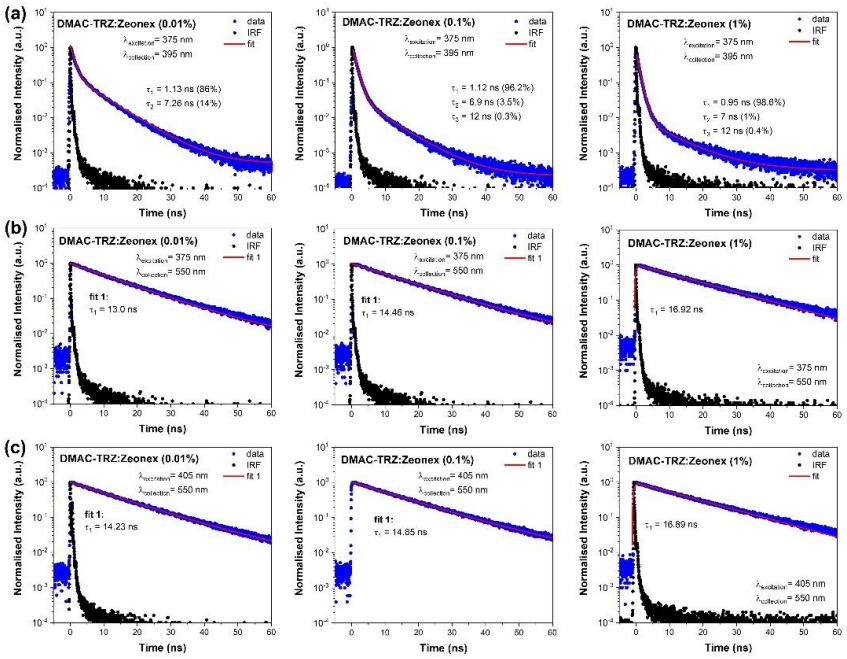

Figure S20. Time-resolved PL decays of different concentrations of DMAC-TRZ in zeonex host, at room temperature. Excitation wavelength 375 and 405 nm. Collection wavelength 395 and 550 nm.

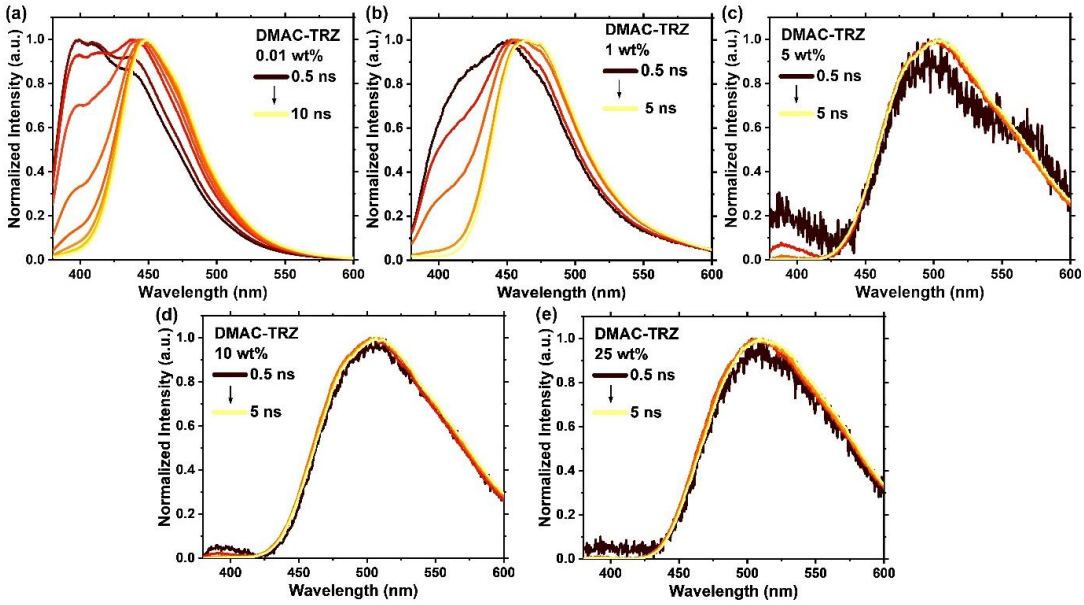

Figure S21. Time-resolved PL spectra of DMAC-TRZ in zeonex host at (a) 0.01 wt%, (b) 1 wt%, (c) 5 wt%, (d) 10 wt% and (e) 25 wt% concentration, at room temperature. Excitation wavelength 355 nm.

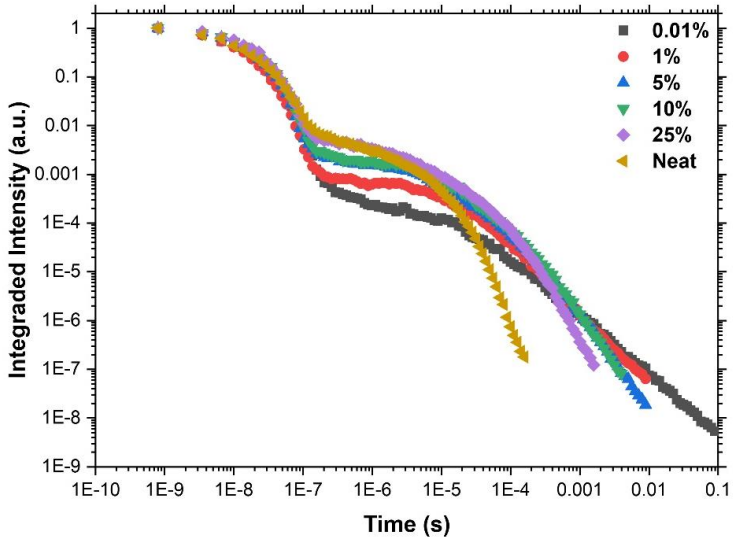

Figure S22. Time-resolved PL decays of different concentrations of DMAC-TRZ in zeonex host, at room temperature. Excitation wavelength 355 nm.

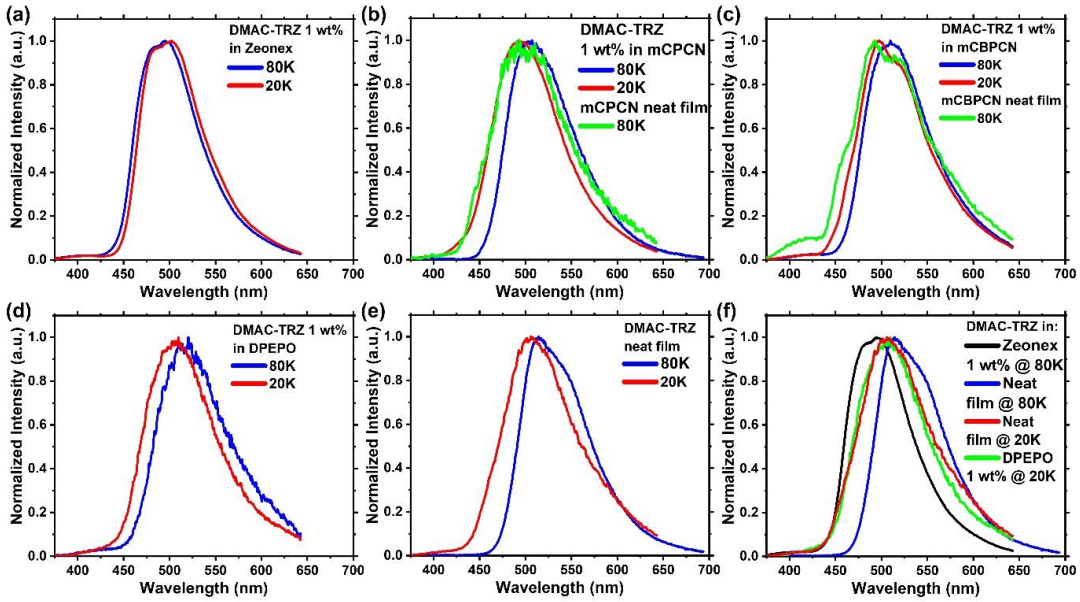

Figure S23. Solid-state photophysics of 1 wt% DMAC-TRZ films. Phosphorescence spectra in different hosts, at 80 and 20 K. Excitation wavelength 355 nm. Delay time 85 ms.

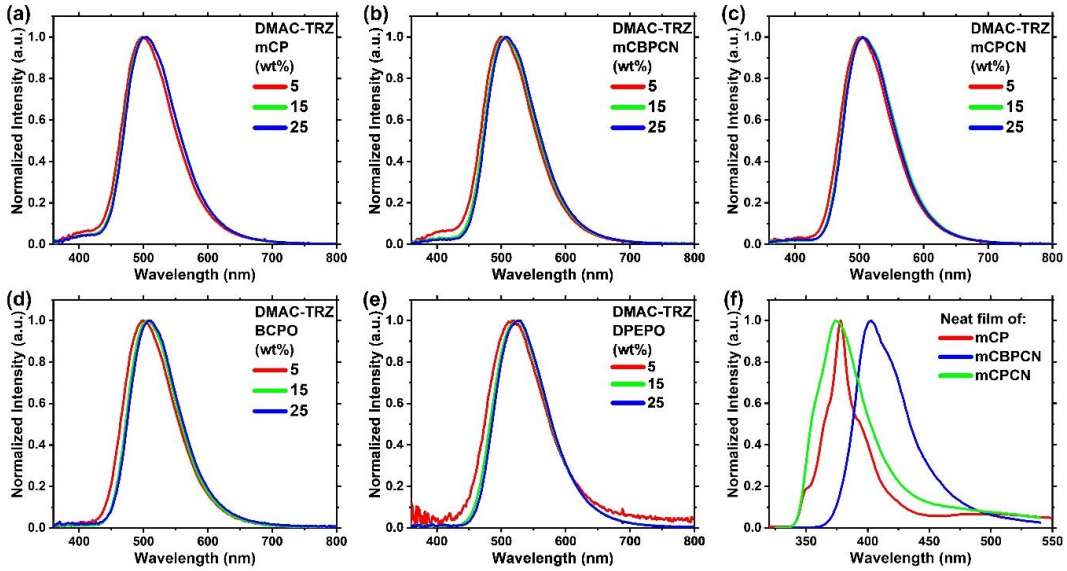

Figure S24. Electroluminescence spectra of DMAC-TRZ OLEDs in different concentrations and different hosts. (f) PL spectra of the three hosts.

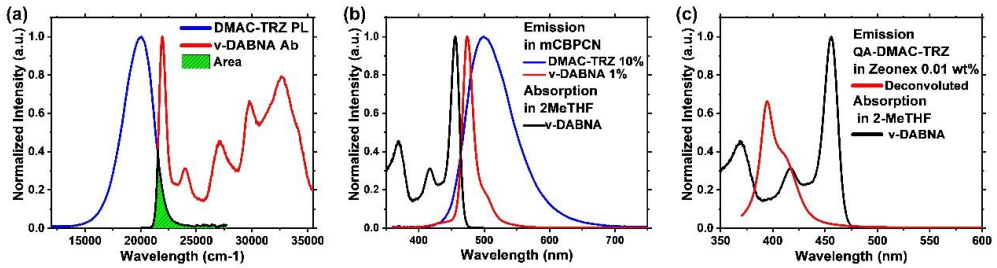

Figure S25. (a) Absorption-PL overlap between v-DABNA and DMAC-TRZ respectively in wavenumbers. (b), (c) Absorption-PL overlap between v-DABNA and DMAC-TRZ two conformers.

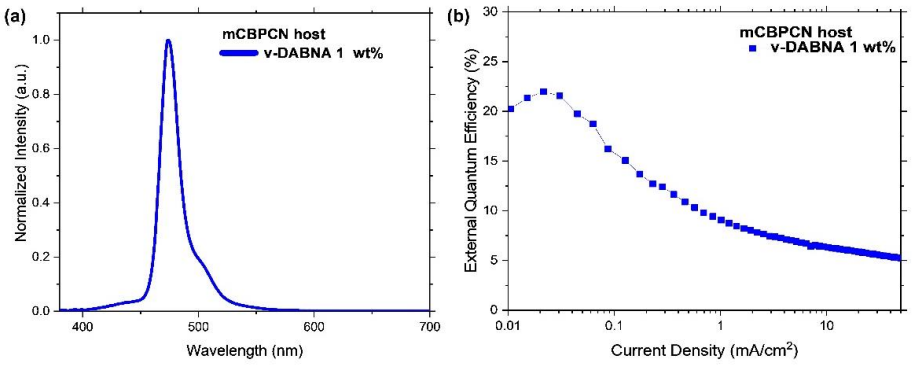

Figure S26. MR-TADF OLED. (a) Electroluminescence spectrum at 8 V, and (b) EQE vs current density of v-DABNA in mCBPCN OLEDs

XC

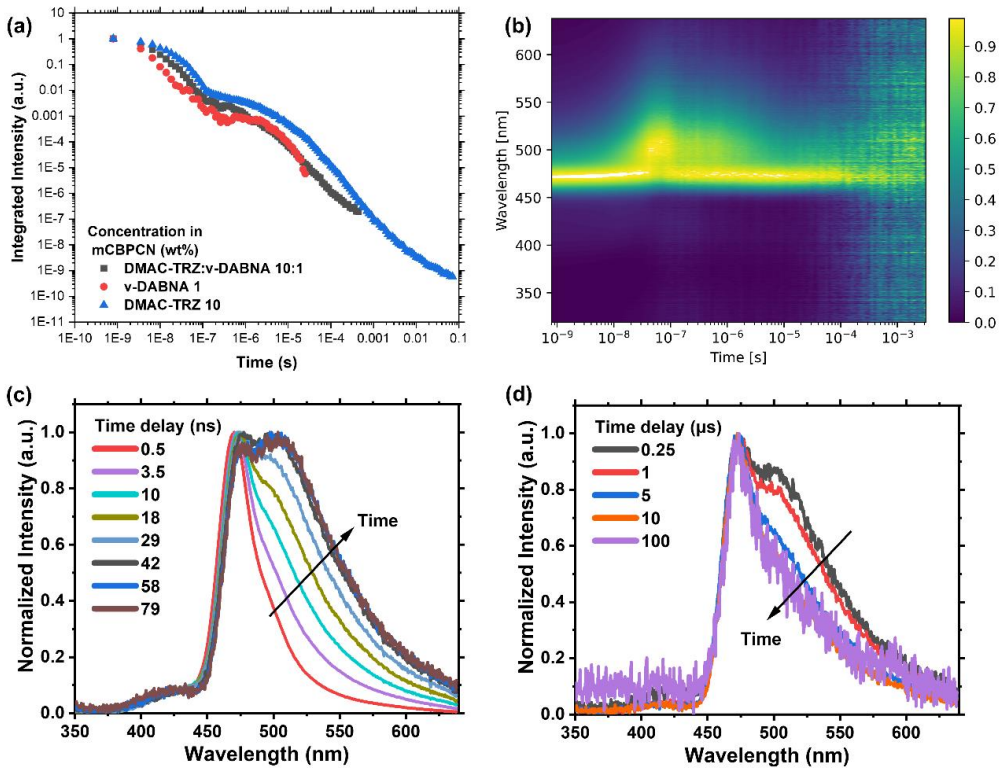

Figure S27. Time-resolved PL (a) decays of DMAC-TRZ, v-DABNA and DMAC-TRZ:v-DABNA in mCBPCN host, at room temperature. (b) Contour plot and time resolved spectra of (c) prompt and (d) delayed fluorescence emission of DMAC:TRZ:v-DABNA in mCBPCN host, at room temperature.. Excitation wavelength 355 nm.

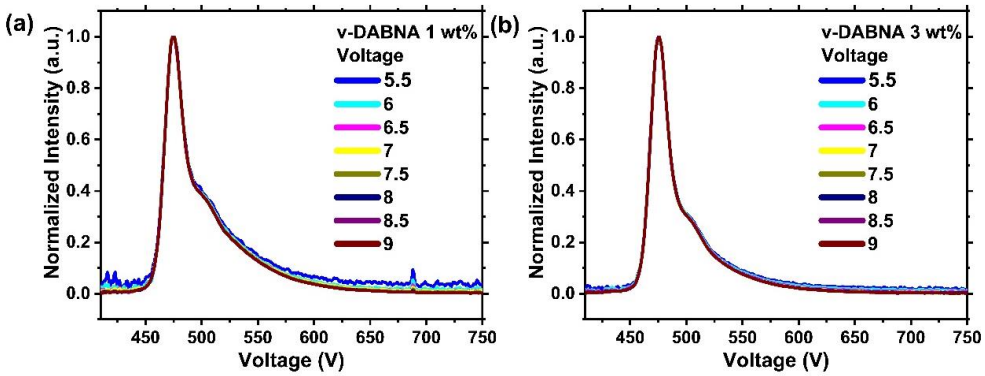

Figure S28. Voltage stability of electroluminescence spectrum of the HF-OLEDs at (a) 1 wt% and (b) 3 wt% concentration of v-DABNA.

References

[1] M. J. Frisch, G. W. Trucks, H. B. Schlegel, G. E. Scuseria, M. A. Robb, J. R. Cheeseman, G. Scalmani, V. Barone, G. A. Petersson, H. Nakatsuji, X. Li, M. Caricato, A. Marenich, J. Bloino, B. G. Janesko, R. Gomperts, B. Mennucci, H. P. Hratchian, J. V. Ortiz, A. F. Izmaylov, J. L. Sonnenberg, D. Williams-Young, F. Ding, F. Lipparini, F. Egidi, J. Goings, B. Peng, A. Petrone, T. Henderson, D. Ranasinghe, V. G. Zakrzewski, J. Gao, N. Rega, G. Zheng, W. Liang, M. Hada, M. Ehara, K. Toyota, R. Fukuda, J. Hasegawa, M. Ishida, T. Nakajima, Y. Honda, O. Kitao, H. Nakai, T. Vreven, K. Throssell, J. A. Montgomery Jr., J. E. Peralta, F. Ogliaro, M. Bearpark, J. J. Heyd, E. Brothers, K. N. Kudin, V. N. Staroverov, T. Keith, R. Kobayashi, J. Normand, K. Raghavachari, A. Rendell, J. C. Burant, S. S. Iyengar, J. Tomasi, M. Cossi, J. M. Millam, M. Klene, C. Adamo, R. Cammi, J. W. Ochterski, R. L. Martin, K. Morokuma, O. Farkas, J. B. Foresman, D. J. Fox, Gaussian 16, Revision A.03. 2016; *Gaussian Inc., Wallingford CT*.

[2] O. A. Vydrov, G. E. Scuseria, *J. Chem. Phys.* **2006**, *125*, 234109.

[3] R. Dhali, D. K. A. Phan Huu, F. Bertocchi, C. Sissa, F. Terenziani, A. Painelli, *Phys. Chem. Chem. Phys.* **2021**, *23*, 378.

[4] A. Schäfer, A. Klamt, D. Sattel, J. C. W. Lohrenz, F. Eckert, *Phys. Chem. Chem. Phys.* **2000**, *2*, 2187.

[5] S. Grimme, M. Waletzke, *J. Chem. Phys.* **1999**, *111*, 5645.

[6] I. Lyskov, M. Kleinschmidt, C. M. Marian, *J. Chem. Phys.* **2016**, *144*, 034104.

[7] TURBOMOLE V7.5 2020. A development of University of Karlsruhe and Forschungszentrum Karlsruhe GmbH, 1989−2007, TURBOMOLE GmbH, since 2007; available from http://www.turbomole.com.

[8] M. Etinski, V. Rai-Constapel, C. M. Marian, *J. Chem. Phys.* **2014**, *140*, 114104.

Paper No.4

Intersystem crossing and intramolecular triplet excitation energy transfer in spiro[9,10-dihydro-9-oxoanthracene-10,2´- 5´,6´-benzindan] investigated by DFT/MRCI methods.

Simon Metz, Tobias Böhmer, Ben Raunitschke and Christel M. Marian
Can. J. Chem., 101, 633-640 (2023)
DOI: 10.1139/cjc-2022-0259

Contribution: I partially contributed quantum chemical investigation of the emission properties of **AN**.

Canadian Journal of Chemistry

Article

Intersystem crossing and intramolecular triplet excitation energy transfer in spiro[9,10-dihydro-9-oxoanthracene-10,2′-5′,6′-benzindan] investigated by DFT/MRCI methods

Simon Metz, Tobias Böhmer, Ben Raunitschke, and Christel M. Marian

Institute of Theoretical and Computational Chemistry, Heinrich Heine University Düsseldorf, Universitätsstr. 1, Düsseldorf, 40225, Germany

Corresponding author: **Christel M. Marian** (email: christel.marian@hhu.de)

Abstract

Recent experimental studies of a spiro-linked anthracenone (**A**)–naphthalene (**N**) compound (**AN**) in butyronitrile (BuCN) solution (Dobkowski et al., J. Phys. Chem. A **2019**, *123*, 6978) proposed an excited-state energy dissipation pathway [$^1\pi\pi^*$(**N**) + $^1\pi\pi^*$(**A**)]$\sim^1n\pi^*$(**A**)$\sim^3n\pi^*$(**A**)$\sim^3\pi\pi^*$(**N**). However, a detailed theoretical study employing combined density functional theory and multireference configuration interaction methods, performed in the present work, suggests that the photoexcitation decay follows a different pathway. In BuCN solution, the intersystem crossing (ISC) follows the well-established El-Sayed rule and involves the $^3\pi\pi^*$(**A**) state which is found to be the lowest excited triplet state localized on the anthracenone moiety. Because the Dexter triplet excitation energy transfer (TEET) to the first excited triplet state of the naphthalene subunit is forbidden in C_{2v} symmetry, it is mandatory to go beyond the Condon approximation in modeling this process. Nonadiabatic coupling matrix elements were computed to obtain a TEET rate different from zero. Our calculations yield time constants of 5 ps for the $^1n\pi^*$(**A**)$\sim^3\pi\pi^*$(**A**) ISC and of 3 ps for the subsequent $^3\pi\pi^*$(**A**)$\sim^3\pi\pi^*$(**N**) TEET in BuCN whereas the energy dissipation involving the $^3n\pi^*$(**A**) state as an intermediate occurs on a much longer time scale.

Key words: multireference methods, intersystem crossing, nonadiabatic coupling, intramolecular triplet energy transfer, solvent effects

1. Introduction

Excitation energy transfer (EET) between a triplet sensitizer and a triplet acceptor is a common chemical process used to photoinitiate radical reactions[1] or triplet–triplet annihilation upconversion.[2] To be less dependent on accidental encounters between the donor and acceptor molecules, covalently linked photosensitizers undergoing intramolecular triplet EET (TEET) on the nanosecond or even picosecond time scale have been devised.[3–9] The donor fragments of these compounds typically comprise aromatic ketones with triplet quantum yields close to unity. Their first-order spin–orbit coupling (SOC) originates from interactions between electrons occupying the lone-pair n and the p_π orbitals of the carbonyl oxygen, in agreement with El-Sayed's rules.[10,11] Owing to the weaker exchange interaction of the open shells in $n\pi^*$ states as compared to $\pi\pi^*$ states, the first excited singlet (S_1) states of aromatic ketones typically exhibit $n\pi^*$ electronic structure whereas the first excited triplet (T_1) state may have $\pi\pi^*$ or $n\pi^*$ characteristics, depending on the chemical composition of the aromatic ketone and the solvent polarity.[11] In any case, aromatic ketones possess small to medium-sized singlet–triplet energy gaps with close-lying $^1n\pi^*$, $^3n\pi^*$, and $^3\pi\pi^*$ states. With regard to the conditions promoting efficient intramolecular TEET,[5] the combination of an aromatic ketone, playing the role of the singlet acceptor and triplet donor, and a conjugated hydrocarbon fragment, acting as a singlet donor and triplet acceptor, appears ideal. In contrast to aromatic ketones, oligoacenes exhibit large S_1–T_1 energy gaps.[12,13] The chances are, therefore, high that the $S_1 \leftarrow S_0$ transition of the acene is located energetically above the $S_1 \rightarrow S_0$ transition of the ketone. In this way, quenching of the excited-state population on the ketone moiety by singlet EET is prevented. The energetically low-lying triplet acceptor T_1 state on the other hand increases the likelihood that the TEET from the ketone to the oligoacene is irreversible.

In this paper, we report extensive quantum chemical calculations on spiro[9,10-dihydro-9-oxoanthracene-10,2′-5′,6′-benzindan] (**AN**) (Chart 1) which is composed of an anthracenone (**A**) and a naphthalene (**N**) subunit, held relatively rigidly at right angles to each other by a spiran linkage. When the molecule is excited with 312 nm radiation in toluene[14] or 308 nm radiation in butyronitrile (BuCN)

Fig. 1. Scan along the dimensionless normal coordinate of the imaginary vibrational mode at the C_{2v}-symmetric ground-state geometry in vacuum. The energy profile of the DFT (PBE0/def2-TZVP) calculations show a shallow double minimum structure whereas the DFT/MRCI energy profile has a minimum at the symmetry point.

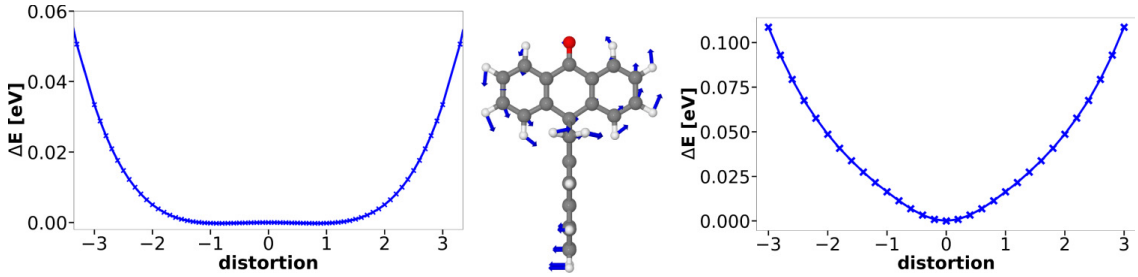

(a) DFT (PBE0/def2-TZVP) (b) imag. mode (c) DFT/MRCI (def2-TZVP)

solution,[15] the fluorescence of the **N** moiety is quenched, while phosphorescence characteristic of **N** is observed with a relatively large quantum yield. Direct excitation of the S_1(**A**)←S_0 transition at 362 nm leads to phosphorescence from the T_1(**N**) state as well,[14] clearly suggesting that **AN** undergoes intramolecular triplet(**A**)–triplet(**N**) energy transfer. Less clear is the nature of the involved triplet(**A**) state. Based on the results of combined experimental and computational studies of **AN** in BuCN solution, Dobkowski et al.[15] proposed an excited-state energy dissipation path $[^1\pi\pi^*(\mathbf{N}) + {}^1\pi\pi^*(\mathbf{A})] \sim {}^1n\pi^*(\mathbf{A}) \sim {}^3n\pi^*(\mathbf{A}) \sim {}^3\pi\pi^*(\mathbf{N})$. The first step was associated with a time constant of 1.6 ± 0.2 ps. The second and third steps occur within 35 ± 3 ps, but τ_{ISC} and τ_{TEET} could not be temporally resolved. The kinetic scheme suggests that the ${}^1n\pi^*(\mathbf{A}) \sim {}^3n\pi^*(\mathbf{A})$ intersystem crossing (ISC) proceeds at a rate constant of 3×10^{10} s^{-1} or more which is surprising in view of El-Sayed's rules,[10,11] which require a change of orbital character for fast and efficient ISC. A recent quantum chemical study of the ISC processes in the isolated **A** molecule[16] has shown that the El-Sayed-forbidden direct $S_1(^1n\pi^*) \sim T_1(^3n\pi^*)$ passage is comparatively slow ($k_{ISC}^{HT} = 4 \times 10^9$ s^{-1} including spin-vibronic interactions in Herzberg–Teller (HT) approximation) and cannot compete against the much faster El-Sayed-allowed $S_1(^1n\pi^*) \sim T_2(^3\pi\pi^*)$ transition which proceeds with a rate constant of $k_{ISC}^{HT} = 5 \times 10^{11}$ s^{-1}. The exact energetic location of the $T_2(\pi\pi^*)$ state of the **A** molecule is not known experimentally, but it is reasonable to assume that it is almost isoenergetic to the S_1 state in nonpolar solvents and below S_1 in polar environments.[17] Earlier experiments on **AN** in *n*-hexane found a longer rise time of the triplet excited-state absorption (ESA) of 80 ± 20 ps.[14] Polar solvents such as BuCN cause the $\pi\pi^*$ states of aromatic ketones to shift bathochromically with respect to apolar environments whereas the $n\pi^*$ states are shifted hypsochromically. Therefore the question arises whether the larger time constant in the older work by Maki et al.[14] is just a consequence of the lower temporal resolution of their apparatus, as supposed by Dobkowski et al.,[15] or whether **AN** follows different photoexcitation decay paths in apolar (*n*-hexane) and polar (BuCN) environments.

Although no evidence of an El-Sayed-allowed two-step mechanism ${}^1n\pi^*(\mathbf{A}) \sim {}^3\pi\pi^*(\mathbf{A}) \sim {}^3n\pi^*(\mathbf{A})$ was reported for **AN**, one may wonder where the ${}^3\pi\pi^*(\mathbf{A})$ state of **AN** is located energetically in relation to the ${}^3n\pi^*(\mathbf{A})$ state and whether it plays a mediating role in the fast ${}^1n\pi^*(\mathbf{A}) \sim {}^3n\pi^*(\mathbf{A})$ ISC process. Alternatively, if the ${}^3\pi\pi^*(\mathbf{A})$ state turns out to be the lower one of the two triplet (**A**) states in polar solvents, the question arises whether the ${}^3n\pi^*(\mathbf{A})$ state is involved at all in the energy dissipation pathway of **AN**. Further, it is interesting to know which of the two processes, ISC or TEET, is the slower one and thus the rate-determining step for the build-up of the ESA signal of the **N** moiety. Finally, since Dexter EET from the ${}^3n\pi^*(\mathbf{A})$ and ${}^3\pi\pi^*(\mathbf{A})$ states to the first excited ${}^3\pi\pi^*(\mathbf{N})$ state is symmetry forbidden in first order (vide infra), the question arises why TEET is so efficient in **AN** and which vibrational modes promote the TEET between the **A** and **N** moieties. Our present theoretical study strives to answer these questions based on extensive quantum chemical computations of energy schemes, spectral properties and rate constants of intramolecular transitions employing combined density functional theory (DFT) and multireference configuration interaction (MRCI) methods.

2. Computational methods

The Gaussian 16 program package[18] was used for all geometry optimizations and vibrational frequency analyses. The ground-state equilibrium structure was determined using Kohn–Sham density functional theory (KS-DFT) in conjunction with the PBE0 hybrid functional[19,20] and the def2-TZVP basis set.[21] Solvent–solute interactions were included through the polarizable continuum model.[22] For the optimization of the excited singlet states, time-dependent DFT (TDDFT) was used while the Tamm–Dancoff approximation (TDA) to TDDFT was applied for locating the triplet minima. The normal mode frequencies and coordinates were further utilized to generate Franck–Condon (FC) factors and FC-weighted densities of states (FCWDOS) for determining spectral profiles and rate constants.

Two general routes have been implemented into the VIBES source code[23,24] and were used to compute vibronic spectra.

The phosphorescence spectra were computed using the Adiabatic Hessian approach whereas for the vibrationally resolved triplet absorption spectra the Vertical Hessian (VH) method was used. The latter is suitable to describe the vibronic transitions around the FC region without the requirement of effectively computing the final state's equilibrium geometry.[25,26] For the VH method, the gradients and Hessian matrix of the respective final state are calculated at the optimized geometry of the initial state. This information is utilized to extrapolate the potential energy surface (PES) from the nonstationary point. The derivatives are used to generate the frequencies and normal modes at the extrapolated equilibrium geometry of the final state. Modes with an imaginary frequency are eliminated for both electronic states. The omission is valid as long as the modes that are expected to affect the spectral shape the most are still included.[26] The reorganization energy was estimated based on the vertical excitation energies to determine the offset of the spectrum according to the following equation.[27]

$$E_v = E_{ad} + \frac{1}{2}\mathbf{K}^T\mathbf{J}\overline{\overline{\Omega}}^2\mathbf{J}^T\mathbf{K} \quad (1)$$

Here, **K** is the displacement vector, **J** the Duschinsky rotation matrix, and $\overline{\overline{\Omega}}$ the diagonal frequency matrix of the final state. Vertical (E_v) and adiabatic (E_{ad}) excitation energies were calculated employing the R2016 Hamiltonian[28] of the DFT/MRCI method[29,30] and a configuration selection threshold of 1.0 E_h. Herein, Kohn–Sham BH-LYP[31,32] molecular orbitals (MOs) of the closed-shell ground-state determinant served as one-particle basis set. To take account of solute–solvent interactions in the KS-DFT MO optimization, the point charges from the preceding Gaussian 16 calculations were imported into Turbomole.[33] The cbas auxiliary basis sets from the Turbomole library[34] were utilized to construct the two-electron integrals in the resolution-of-the-identity approximation. Fragment-based analyses of the DFT/MRCI wavefunctions were performed with Theodore.[35] Electronic spin–orbit coupling matrix elements and component-averaged phosphorescence lifetimes were obtained with the SPOCK program.[36,37] ISC and internal conversion (IC) rate constants were determined for a temperature of 300 K via a fast Fourier transformation ansatz employing the VIBES program.[24,38] The derivatives with respect to the normal coordinates, required for the HT expansion of the SOC, and the nonadiabatic coupling matrix elements (NACMEs) of the triplet states, promoting the IC, were computed at the DFT/MRCI level using finite difference techniques.[38,39] Further computational details may be found in the Supplementary Material (SM).

3. Results and discussion

3.1. Molecular symmetry

Before we present our theoretical results on **AN** in detail, a short discussion of the molecular symmetry properties appears appropriate. Using DFT (B3LYP/6-311+G(d,p)), Dobkowski et al.[15] determined a double minimum structure for **AN** in the electronic ground state in which the **N** unit is tilted by ca. ±15° with respect to the mirror plane perpendicular to the **A** molecular plane and including the C=O bond. We found a similar nuclear arrangement in our DFT (PBE0/def2-TZVP) calculations (Fig. S1a of the SM). While the TDDFT-TDA optimization of the lowest locally excited (LE) triplet state on the **N** part yielded a C_{2v} symmetrical minimum, symmetry-broken solutions were obtained for the lowest excited singlet state and two triplet LE states on the **A** part of the molecule (see Fig. S2a of the SM for the $^3\pi\pi^*$ (**A**) state). Subsequent DFT/MRCI calculations suggest, however, that the true minima of these states have C_{2v}-symmetric structures (Fig. 1, and Fig. S2c).

Chart 1: Chemical structures of anthracenone (**A**), naphthalene (**N**) and spiro[9,10-dihydro-9-oxoanthracene-10,2′-5′,6′-benzindan] (**AN**).

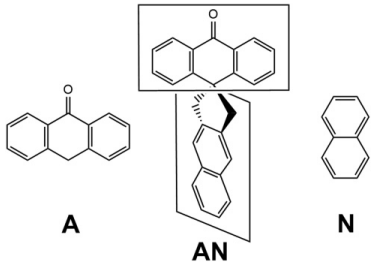

The tilt of **N** unit in the electronic ground state has only a minor effect on the computed $S_n \leftarrow S_0$ line spectrum (Fig. S3 of the SM). Its comparison with the measured static absorption spectrum can therefore not be used to probe the true equilibrium structure of the compound. In contrast to the electronic line spectra, the vibrational fine-structure of the phosphorescence emission depends heavily on the choice of the ground-state potential. While the FC factors of the C_{2v}-symmetric T_1 and S_0 potentials represent the intensity distribution in the experimental phosphorescence spectrum almost perfectly, the symmetry-broken solutions produce too intense vibrational transitions in the low-energy part of the spectrum (Fig. S4 of the SM), thus nourishing our suspicion that the symmetry-broken solutions are artifacts of the (TD)DFT treatment. Such artifacts have been encountered earlier in other heteroaromatic compounds whose geometrical structures are well known.[40,41] In the following sections, therefore mainly the properties determined at the C_{2v} symmetric geometries will be discussed. For being able to compute meaningful FC spectra and nonradiative rate constants, the negative eigenvalue of the Hessian has to be corrected. To this end, the curvature of the PBE0/def2-TZVP energy profile at larger displacements was used to fit a harmonic frequency. For more details see the SM (Fig. S1b).

3.2. The Franck–Condon region

Most of the low-lying excited states possess wavefunction expansions with more than one leading term (Tables S1 and S2 of the SM). For their further categorization, a fragmentation-based analysis was performed (Fig. S6 of the

Fig. 2. Renormalized absorption spectrum of **AN** in BuCN. The computed line spectrum was broadened by Gaussians with 1500 cm^{-1} FWHM. In orange, a digitized experimental stationary absorption spectrum[15] in BuCN at room temperature is shown.

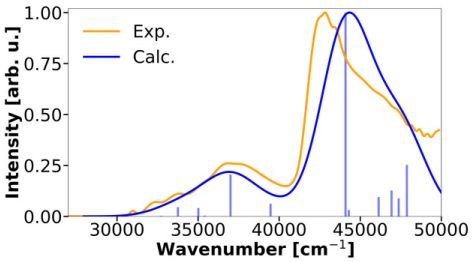

SM). The calculated normalized absorption spectrum in BuCN solution fits well with the experimental room temperature stationary absorption spectrum (Fig. 2). Both show their first intense band with a maximum at about 37 000 cm^{-1} which originates from a LE $\pi\pi^*$ on the **A** moiety and a very intense peak at about 43 000–44 000 cm^{-1} which stems from a multiconfigurational LE state on the **N** subunit, correlating with the bright ^1B_b state of **N** in Platt's nomenclature.[42] For the interpretation of the experimental transient absorption (TA) spectra, which was recorded with an excitation wavelength of 308 nm (32500 cm^{-1}) by Dobkowski et al.,[15] the high-energy part of the static absorption spectrum is of no relevance, however.

The S_1 state has a vertical excitation energy of about 29 900 cm^{-1} in BuCN solution and corresponds to an optically dark $n\pi^*$ LE on the **A** part of the molecule. Even the next two singlet transitions at ca. 32 700 and 32 800 cm^{-1}, respectively, are barely visible in the computed spectrum (Fig. 2). S_2 is a state of mixed charge-transfer **N**→**A** and LE(**A**) character, S_3 a multiconfigurational LE state correlating with the very weak ^1L_b transition of **N**. The shoulder around 34 000 cm^{-1} is assigned to the lowest $^1\pi\pi^*$ excitation on **A** and the shoulder around 35 000 cm^{-1} to the ^1L_a transition of **N**.

The T_1 state, located about 6000 cm^{-1} below S_1, is a LE $^3\pi\pi^*$ (**N**) state. Like in the isolated **N** molecule,[43] it is not the counterpart of the lowest lying $^1\pi\pi^*$ state but shares the electronic structure with the ^1L_a state. The next two triplet states are both local excitations on the **A** moiety. In the isolated molecule, which may serve as a proxy for the photophysical properties of **AN** in an apolar solvent such as *n*-hexane, the T_2 state is the triplet counterpart of the S_1 state with $n\pi^*$ excitation character, while a triplet state stemming from a local $\pi\pi^*$ excitation on the **A** part forms the T_3 state. A BuCN environment reverses the order of these two triplet states in comparison to vacuum conditions. As we will see below, the close energetic proximity of the $^3\pi\pi^*$ (**A**) and $^3n\pi^*$ (**A**) states has a large impact on the ISC and TEET kinetics of **AN** in different media.

Fig. 3. Difference densities of the excited states at their respective minimum geometries in BuCN. Red areas lose electron density in comparison to the ground state, whereas yellow areas gain electron density.

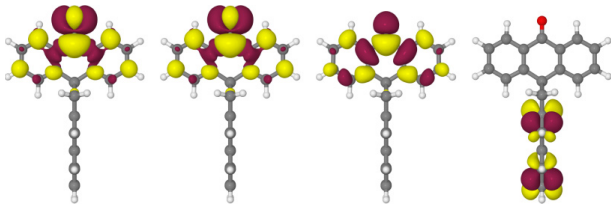

(a) $^1n\pi^*$ **A** - S_0 (b) $^3n\pi^*$ **A** - S_0 (c) $^3\pi\pi^*$ **A** - S_0 (d) $^3\pi\pi^*$ **N** - S_0

Table 1. ZPVE-corrected DFT/MRCI adiabatic energies of the low-lying excited states of **AN** in vacuum and BuCN.

State	Vacuum (cm^{-1})	BuCN (cm^{-1})
$^1n\pi^*$ (**A**)	25 295	26 496
$^3n\pi^*$ (**A**)	23 320	25 267
$^3\pi\pi^*$ (**A**)	24 587	24 137
$^3\pi\pi^*$ (**N**)	19 972	19 903

3.3. Excited-state properties

Difference densities of the excited states at their respective C_{2v}-symmetric minimum geometries (Fig. 3) reveal that the S_1, T_1, T_2, and T_3 states have LE character. Their adiabatic excitation energies in vacuum and BuCN, corrected for zero-point vibrational energies (ZPVEs), are listed in Table 1. While PES crossings between the $^1n\pi^*$ (**A**) state and the $^3\pi\pi^*$ (**A**) and $^3\pi\pi^*$ (**N**) states can be made out in vacuum (Fig. 4*a*), the $^1n\pi^*$ (**A**) state is located energetically above the three triplet states at all considered geometries in BuCN (Fig. 4*b*). In contrast, several intersections between the triplet potentials are observed in the latter medium. Here, the $^3\pi\pi^*$ (**N**) state clearly is the lowest among the triplet states in the FC region and at the optimized $^3\pi\pi^*$ (**N**) geometry, but it is located very close to the $^3n\pi^*$ (**A**) state at the $^1n\pi^*$ (**A**) and $^3n\pi^*$ (**A**) minimum geometries and even crosses the $^3\pi\pi^*$ (**A**) potential on the path connecting the $^3n\pi^*$ (**A**) and $^3\pi\pi^*$ (**A**) minima (Fig. 4*b*). As will be seen below, the close energetic proximity of the T_1, T_2, and T_3 states at the $^3n\pi^*$ (**A**) and $^3\pi\pi^*$ (**A**) minimum structures facilitates the TEET.

3.4. Photoexcitation decay pathways

While the spectral position of the $^3\pi\pi^*$ (**N**) state is nearly unaffected by a solvent environment, solvent–solute interactions stabilize the $^3\pi\pi^*$ (**A**) state whereas they destabilize the $^3n\pi^*$ (**A**) state with the effect that the adiabatic order of the two triplet LE(**A**) states is reversed. Therefore, it may well be that the relaxation of **AN** after photoexcitation in *n*-hexane and BuCN follows different pathways.

According to Dobkowski et al.,[15] the ISC in **AN** proceeds along the $^1n\pi^*$ (**A**)~$^3n\pi^*$ (**A**) pathway with a time constant τ_{ISC} smaller than 35 ps in BuCN. Maki et al.[14] found a longer rise time of about 80 ± 20 ps for the T_n ←T_1 absorption in *n*-hexane. Our calculations yield a high rate constant of 7.8 ×

Fig. 4. DFT/MRCI energies of the low-lying excited states of **AN** at the optimized triplet geometries relative to the C_{2v}-symmetric electronic ground state minimum in (a) vacuum and (b) BuCN.

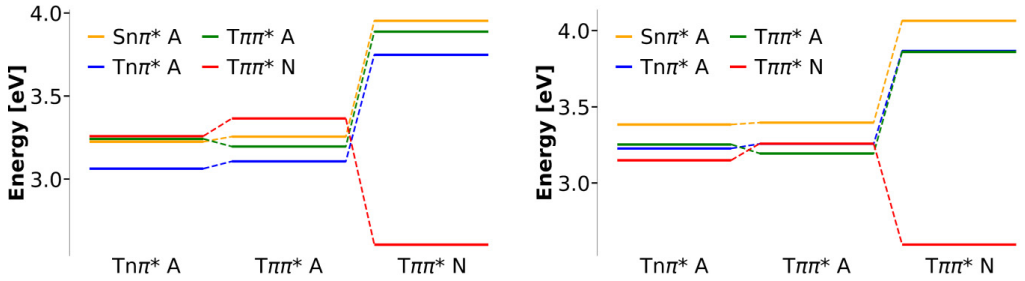

10^{11} s^{-1} ($\tau \approx 1$ ps) for the El-Sayed-allowed $^1n\pi^*$ (**A**)~$^3\pi\pi^*$ (**A**) process in the isolated **AN**. In BuCN solution, this rate constant decreases to 2.2×10^{11} s^{-1}, but with a time constant of about $\tau_{ISC} \approx 5$ ps the $^1n\pi^*$ (**A**)~$^3\pi\pi^*$ (**A**) ISC may still be considered ultrafast. Because the $^1n\pi^*$ (**A**)~$^3n\pi^*$ (**A**) transition is El-Sayed forbidden, its ISC rate constant is very small in Condon approximation. Spin-vibrational interactions increase the ISC rate constant to 1.6×10^{10} s^{-1} ($\tau \approx 62$ ps). Applying BuCN solvent shifts to the potentials, the $^1n\pi^*$ (**A**)~$^3n\pi^*$ (**A**) ISC rate constant changes to 2.5×10^{10} s^{-1} ($\tau \approx 41$ ps). Hence, both deexcitation pathways allow an efficient local singlet–triplet ISC on the **A** moiety on a time scale which fits the kinetic scheme proposed by the experimentalists.

An unambiguous assignment of the intermediate triplet state is possible, however, when the calculated ESA spectra are compared with the TA spectrum recorded for a short delay time of 0.5 ps in BuCN (Fig. 5*a*). The band with the highest intensity in this TA spectrum has a maximum around 29 500 cm^{-1}. In addition, a weaker band with several maxima in the 22 000–25 000 cm^{-1} regime can be made out. Both features are nearly perfectly matched by the calculated ESA spectrum of the $^3\pi\pi^*$ (**A**) state. An additional low-energy peak around 19 500 cm^{-1} is also visible in the unrestricted DFT ESA spectrum presented by Dobkowski et al.,[15] but has not been observed in the TA experiment for unknown reasons. For comparison, we computed the ESA spectra of the $^3n\pi^*$ (**A**) and $^1n\pi^*$ (**A**) states at the DFT/MRCI level of theory as well. Both possess spectral profiles which differ markedly from the measured TA spectrum (Fig. 5*a*). At variance with Dobkowski et al.,[15] we therefore conclude that the intermediate state populated predominantly after 0.5 ps in the experiment in BuCN solution is the $^3\pi\pi^*$ (**A**) state and not the $^3n\pi^*$ (**A**) state.

This conclusion is corroborated by our calculated TEET rate constants. In weakly coupled systems, the rate constant of an EET between a donor and an acceptor molecule is conveniently evaluated according to a Fermi golden rule expression.[44]

$$(2) \qquad k_{EET} = \frac{2\pi}{\hbar} |V_{DA}^{(el-el)}|^2 \, \mathrm{FCWDOS}$$

The FCWDOS contains all information about the population of the donor vibrational states at a given temperature and their overlaps with the acceptor vibrational states at the energy of the initial donor state. The electronic coupling matrix element $V_{DA}^{(el-el)}$ is composed of a Coulomb part $J_{DA}^{(el-el)}$ which gives rise to Förster resonance energy transfer (FRET)[45] in case of a dipole-allowed transition and an exchange part $K_{DA}^{(el-el)}$ which is the origin of Dexter energy transfer.[46] Due to spin selection rules, only the latter contributes to TEET.

The monomer transition density approach determines an estimate for $V_{DA}^{(el-el)}$ from the ground- and excited-state properties of separate donor and acceptor molecules, i.e., the monomers. It was originally devised for computing the Coulomb coupling between the FRET partners beyond the ideal dipole approximation.[47,48] An extension of this method, which includes Dexter terms in addition to Förster terms, was successfully applied to model intramolecular EET as well.[49] In the framework of this approach, the exchange part of the electronic coupling between the donor and acceptor subunits of the EET systems can be approximated by

$$(3) \qquad K_{DA}^{(el-el)} = -\frac{1}{2} \sum_{ijkl} \rho_{ij}^{(A)} \, (il|kj) \, \rho_{kl}^{(D)}$$

where $\rho_{ij}^{(A)}$ denotes an element of the transition density matrix between the ground and the excited states of the acceptor subunit in the MO basis, $\rho_{kl}^{(D)}$ a transition density matrix element of the donor subunit, and $(il|kj)$ an electronic repulsion integral in Mulliken convention

$$(4) \qquad (il|kj) \equiv \left\langle i(r_1)\, k(r_2) \left| r_{12}^{-1} \right| l(r_1)\, j(r_2) \right\rangle \; .$$

In the particular case of the intramolecular TEET in the **AN** molecule, all electronic coupling matrix elements employing either $^3n\pi^*$ (**A**) or $^3\pi\pi^*$ (**A**) as the initial state and $^3\pi\pi^*$ (**N**) as the final state vanish in C_{2v} symmetry. To see this, we focus on the leading configurations of the respective wavefunction expansion (Tables S3–S10 and Figs. S7–S10 of the SM). The $^3\pi\pi^*$ (**N**) acceptor state results mainly from an excitation involving the highest occupied MO (HOMO) and the second lowest unoccupied MO (LUMO+1). (For MO plots, see Fig. S5 of the SM.) These MOs transform according to the a_2

Fig. 5. (a) Short-time and (b) long-time DFT/MRCI triplet and singlet ESA spectra in BuCN in comparison to digitized experimental TA spectra with time delays of (a) 0.5 ps and (b) 5000 ps read from reference.[15] The computed short-time line spectra were normalized with respect to the intensity of the highest peak of the $^3\pi\pi^*$(**A**) ESA spectrum and were broadened by Gaussians with 1500 cm^{-1} FWHM. In addition to the Gaussian-broadened line spectrum of the long-time ESA spectrum, a vibrationally resolved ESA spectrum computed within the Vertical Hessian Franck–Condon scheme is shown.

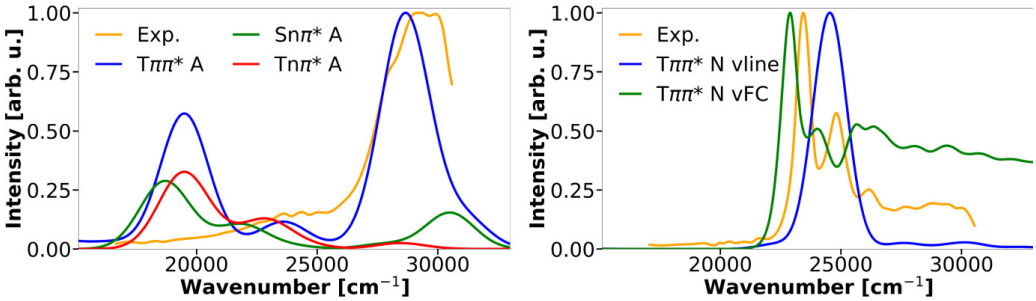

and b_1 irreducible representations (irreps), respectively, and can be equated with the MOs i and j in eqs. 3 and 4. The $^3n\pi^*$ (**A**) excitation involves HOMO-6 and LUMO. In this case, the donor MOs k and l transform according to the b_2 and b_1 irreps, respectively. The electron repulsion integral $(il|kj)$ can adopt values different from zero only, if the direct products of the four MO irreps contain the totally symmetric representation a_1, but $a_2 \otimes b_1 \otimes b_2 \otimes b_1 = b_1 \neq a_1$. Therefore, the $^3n\pi^*$ (**A**)$\rightsquigarrow^3\pi\pi^*$(**N**) Dexter TEET is forbidden in Condon approximation. If we start the Dexter TEET from the $^3\pi\pi^*$ (**A**) state instead, HOMO-5 and LUMO are involved, both transforming according to the b_1 irrep. Even in this case, the direct product representation, $a_2 \otimes b_1 \otimes b_1 \otimes b_1 = b_2$, is not totally symmetric and the integral vanishes. For obtaining a TEET rate different from zero it is therefore mandatory to go beyond the Condon approximation.

Lowering the molecular symmetry to the kinked structure, shown in Fig. S1 of the SM, transfers the acceptor orbitals to the a'' (HOMO) and a' (LUMO+1) irreps of the C_s point group, respectively. The donor orbitals exhibit a' (HOMO-6), a'' (HOMO-5), and a'' (LUMO), respectively. Therefore, while the $^3n\pi^*$ (**A**)$\rightsquigarrow^3\pi\pi^*$ (**N**) TEET becomes symmetry-allowed upon deflection of the anthracenone moiety, the $^3\pi\pi^*$ (**A**)$\rightsquigarrow^3\pi\pi^*$ (**N**) TEET remains symmetry forbidden.

Instead of expanding the Dexter coupling term in an HT-like series, we computed NACMEs between the triplet donor and acceptor states using a finite difference approach recently developed in our group.[38] Many, but small NACMEs associated with b_1-symmetric coupling modes are found which enable the $^3n\pi^*$ (**A**)$\rightsquigarrow^3\pi\pi^*$ (**N**) transition. In the $^3\pi\pi^*$ (**A**)$\rightsquigarrow^3\pi\pi^*$ (**N**), five prominent derivative couplings involving b_2-symmetric vibrational modes, shown in Fig. S11 of the SM, promote the TEET.

With room temperature rate constants of approximately $k_{IC} = 1.5 \times 10^9$ s^{-1} in vacuum and of $k_{IC} = 1.6 \times 10^9$ s^{-1} in BuCN, the $^3n\pi^*$ (**A**)$\rightsquigarrow^3\pi\pi^*$ (**N**) transition is much too slow to explain the experimentally observed rise times of the $^3\pi\pi^*$ (**N**) ESA. In contrast to the $^3n\pi^*$ (**A**)$\rightsquigarrow^3\pi\pi^*$ (**N**) TEET, the $^3\pi\pi^*$ (**A**)$\rightsquigarrow^3\pi\pi^*$ (**N**) TEET experiences a substantial impact of the solvent environment. The energetic proximity of the three triplet states at the relaxed $^3\pi\pi^*$ (**A**) geometry in BuCN and the nearby crossing between the $^3\pi\pi^*$ (**A**) and $^3\pi\pi^*$ (**N**) PESs promotes their nonadiabatic coupling and accelerates the TEET between the $^3\pi\pi^*$ (**A**) and $^3\pi\pi^*$ (**N**) states of **AN** for which we obtain a rate constant of $k_{IC} = 3.2 \times 10^{11}$ s^{-1} in BuCN compared to $k_{IC} = 4.9 \times 10^9$ s^{-1} in vacuum. Note that the NACMEs and hence the IC rate constants are very sensitive with respect to the energetic splittings of the triplet states at the $^3\pi\pi^*$ (**A**) minimum geometry and thus prone to uncertainties. The values of computed rate constants might vary depending on the computational setup, but they are expected to be in the right ballpark. The consecutive $^1n\pi^*$ (**A**)$\rightsquigarrow^3\pi\pi^*$ (**A**) ISC (time constant of about 5 ps in BuCN) and $^3\pi\pi^*$ (**A**)$\rightsquigarrow^3\pi\pi^*$ (**N**) TEET (time constant of about 3 ps in BuCN) processes represent the only $^1n\pi^*$ (**A**)$\rightsquigarrow^3\pi\pi^*$ (**N**) pathway whose time constant falls within the experimentally determined risetime of the $^3\pi\pi^*$ (**N**) ESA of 35 ps.[15]

For a delay time of 5000 ps after the primary excitation the lowest triplet state, $^3\pi\pi^*$ (**N**), is supposed to be populated. The experimental TA spectrum exhibits a band with several maxima and minima between ca. 23 000 and 26 000 cm^{-1}. The DFT/MRCI calculations find only one strong electronic transition ($1^3B_2 \rightarrow 4^3B_2$) in this wavenumber regime. To prove that the experimentally observed fine structure of this band has a vibrational origin, we computed an FC spectrum of this transition using the VH approach. The good agreement between this spectrum and the experimental TA spectrum (Fig. 5*b*) is obvious and corroborates our assumption that the peaks do not stem from multiple electronic transitions but can be explained by vibrational progressions of the intense T_{20}(**N**)$\leftarrow T_1$(**N**) ESA.

A vibrationally resolved phosphorescence emission spectrum of the $^3\pi\pi^*$ (**N**) state is displayed in Fig. 6*a* together with the experimental spectrum measured at 77 K. Save for an overall shift by about 1000 cm^{-1}, the spectra match very well. The vibrational spacing of about 1550 cm^{-1} is attributed

Fig. 6. (*a*) Phosphorescence spectra of **AN** in BuCN at 77 K. Blue: computed FC spectra with origin at the DFT/MRCI adiabatic energy (solid line) and shifted by 1000 cm^{-1} (dashed line). Green: digitized spectrum read from reference.[15] (*b*) Totally symmetric vibrational mode in the electronic ground state causing the visible vibrational progression in the phosphorescence spectrum.

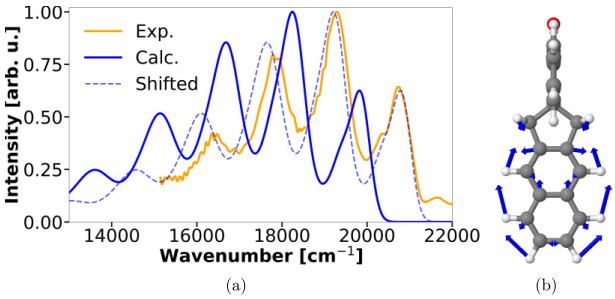

Fig. 7. Proposed kinetic scheme of the ISC and TEET processes following the photoexcitation of **AN** in BuCN solution and in vacuum at room temperature.

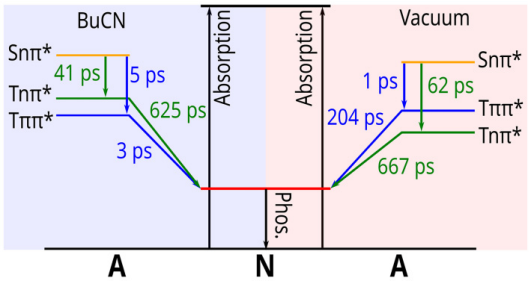

to the totally symmetric deformation mode of the **N** subunit with wavenumber 1556 cm^{-1} in the electronic ground state (Fig. 6*b*).

4. Summary and conclusions

In this paper, we investigated the electronic structures of the low-lying electronic states of **AN** and their intramolecular transition probabilities with the objective to clarify inconsistencies in the excited-state energy dissipation mechanism proposed in recent work by Dobkowski et al.[15] The main results of our computational study are summarized in Fig. 7. We have been able to locate the $^3\pi\pi^*$ (**A**) state of **AN**. In BuCN solution, it represents the lowest excited triplet state of the anthracenone moiety, energetically very close to the $^3n\pi^*$ (**A**) and $^1n\pi^*$ (**A**) states. The $^3\pi\pi^*$ (**A**) state is readily populated via ISC from the $^1n\pi^*$ (**A**) state on the picosecond time scale. A conical intersection close to the $^3\pi\pi^*$ (**A**) minimum enables efficient TEET to the $^3\pi\pi^*$ (**N**). This excited-state energy dissipation pathway is much faster than the one proposed by Dobkowski et al.[15] in BuCN solution, namely $^1n\pi^*$(**A**)$\sim$$^3n\pi^*$(**A**)$\sim$$^3\pi\pi^*$(**N**), which entails an El-Sayed-forbidden ISC process. The rate-determining step in the latter pathway is the TEET which proceeds at the timescale of several hundred picoseconds according to our calculations and therefore does not represent the favored energy dissipation route. The MRCI methods used in this work allow to compute ESA spectra of all possible intermediate states. Comparison with the experimentally determined TA spectra of Dobkowski et al.[15] clearly identify the $^3\pi\pi^*$ (**A**) state as the origin of the TA spectrum at short time delay.

Supporting information

Further technical details of the computations, handling of symmetry-broken solutions, conformational effects on the absorption and phosphorescence spectra; MO plots; DFT/MRCI excitation energies of low-lying singlet and triplet states of all complexes at selected minimum geometries, Theodore analyses of the wavefunction characteristics of low-lying states in BuCN.

Acknowledgements

This research was funded by the Deutsche Forschungsgemeinschaft (DFG, German Research Foundation) - 396890929/GRK 2482.

Article information

History dates

Received: 30 September 2022
Accepted: 9 November 2022
Accepted manuscript online: 22 December 2022

Notes

This paper is one of a selection of papers from the 12th Triennial Congress of the World Association of Theoretical and Computational Chemists (WATOC 2020).

Data availability

The corresponding author can provide further data upon request.

Author information

Author ORCIDs

Christel M. Marian https://orcid.org/0000-0001-7148-0900

Author contributions

Investigation: SM
Visualization: SM, TB
Writing – original draft: SM, TB, CM
Methodology: TB
Software: TB
Investigation: BR

Conceptualization: CM
Funding acquisition: CM
Project administration: CM
Supervision: CM

Competing interests

The authors declare there are no competing interests.

Supplementary material

Supplementary data are available with the article at https://doi.org/10.1139/cjc-2022-0259.

References

(1) Dormán, G.; Nakamura, H.; Pulsipher, A.; Prestwich, G. D., Chem. Rev. **2016**, *116*, 15284–15398. doi:10.1021/acs.chemrev.6b00342.
(2) Bharmoria, P.; Bildirir, H., Chem. Soc. Rev. **2020**, *49*, 6529–6554. doi:10.1039/D0CS00257G.
(3) Keller, R. A., J. Am. Chem. Soc. **1968**, *90*, 1940–1944. doi:10.1021/ja01010a002.
(4) Cowan, D. O.; Baum, A. A., J. Am. Chem. Soc. **1971**, *93*, 1153–1162. doi:10.1021/ja00734a021.
(5) Amrein, W.; Schaffner, K., Helvet. Chim. Acta **1975**, *58*, 397–415. doi:10.1002/hlca.19750580209.
(6) Sigman, M. E.; Closs, G. L., J. Phys. Chem. **1991**, *95*, 5012–5017. doi:10.1021/j100166a022.
(7) Wagner, P. J.; Klán, P., J. Am. Chem. Soc. **1999**, *121*, 9626–9635. doi:10.1021/ja990224l.
(8) Wöll, D.; Laimgruber, S.; Galetskaya, M.; Smirnova, J.; Pfleiderer, W.; Heinz, B.; Gilch, P.; Steiner, U. E., J. Am. Chem. Soc. **2007**, *129*, 12148–12158. doi:10.1021/ja072355p.
(9) Elliott, L. D.; Kayal, S.; George, M. W.; Booker-Milburn, K., J. Am. Chem. Soc. **2020**, *142*, 14947–14956. doi:10.1021/jacs.0c05069.
(10) El-Sayed, M. A.; Tinti, D. S.; Owens, D. V., Chem. Phys. Lett. **1969**, *3*, 339–342. doi:10.1016/0009-2614(69)80248-4.
(11) Marian, C. M., Annu. Rev. Phys. Chem. **2021**, *72*, 616–640. doi:10.1146/annurev-physchem-061020-053433.
(12) Marian, C. M.; Gilka, N., J. Chem. Theory Comput. **2008**, *4*, 1501–1515. doi:10.1021/ct8001738.
(13) Hajgató, B.; Szieberth, D.; Geerlings, P.; De Proft, F.; Deleuze, M. S., J. Chem. Phys. **2009**, *131*, 224321. doi:10.1063/1.3270190.
(14) Maki, A. H.; Weers, J. G.; Hilinski, E. F.; Milton, S. V.; Rentzepis, P. M., J. Chem. Phys. **1984**, *80*, 2288–2297. doi:10.1063/1.447016.
(15) Dobkowski, J.; Gorski, A.; Kijak, M.; Pietrzak, M.; Redeckas, K.; Vengris, M., J. Phys. Chem. A **2019**, *123*, 6978–6985. doi:10.1021/acs.jpca.9b03414.
(16) Metz, S.; Marian, C. M., ChemPhotoChem *2022*, e202200098.
(17) Kobayashi, T.; Nagakura, S., Chem. Phys. Lett. **1976**, *43*, 429–434. doi:10.1016/0009-2614(76)80593-3.
(18) Frisch, M. J.; et al., Gaussian 16 Revision C.01 **2016**, Gaussian Inc., Wallingford, CT.
(19) Perdew, J. P.; Burke, K.; Ernzerhof, M., Phys. Rev. Lett. **1996**, *77*, 3865–3868. doi:10.1103/PhysRevLett.77.3865.
(20) Adamo, C.; Barone, V., J. Chem. Phys. **1999**, *110*, 6158–6170. doi:10.1063/1.478522.
(21) Schäfer, A.; Horn, H.; Ahlrichs, R., J. Chem. Phys. **1992**, *97*, 2571–2577. doi:10.1063/1.463096.
(22) Cancès, E.; Mennucci, B.; Tomasi, J., J. Chem. Phys. **1997**, *107*, 3032. doi:10.1063/1.474659.
(23) Etinski, M.; Tatchen, J.; Marian, C. M., J. Chem. Phys. **2011**, *134*, 154105. doi:10.1063/1.3575582.
(24) Etinski, M.; Rai-Constapel, V.; Marian, C. M., J. Chem. Phys. **2014**, *140*, 114104. doi:10.1063/1.4868484.
(25) Computational Strategies for Spectroscopy: from Small Molecules to Nano Systems; John Wiley & Sons, **2012**, pp. 361–389.
(26) Götze, J. P.; Karasulu, B.; Thiel, W., J. Chem. Phys. **2013**, *139*, 234108. doi:10.1063/1.4844055.
(27) Ferrer, A.; José, F.; Santoro, F., Phys. Chem. Chem. Phys. **2012**, *14*, 13549–13563. doi:10.1039/c2cp41169e.
(28) Lyskov, I.; Kleinschmidt, M.; Marian, C. M., J. Chem. Phys. **2016**, *144*, 034104. doi:10.1063/1.4940036.
(29) Grimme, S.; Waletzke, M., J. Chem. Phys. **1999**, *111*, 5645–5655. doi:10.1063/1.479866.
(30) Marian, C. M.; Heil, A.; Kleinschmidt, M., WIREs Comput. Mol. Sci. **2019**, *9*, e1394. doi:10.1002/wcms.1394.
(31) Lee, C.; Yang, W.; Parr, R. G., Phys. Rev. B **1988**, *37*, 785–789. doi:10.1103/PhysRevB.37.785.
(32) Becke, A. D., J. Chem. Phys. **1993**, *98*, 1372–1377. doi:10.1063/1.464304.
(33) TURBOMOLE GmbH. **2019**
(34) Weigend, F.; Häser, M.; Patzelt, H.; Ahlrichs, R., Chem. Phys. Lett. **1998**, *294*, 143–152. doi:10.1016/S0009-2614(98)00862-8.
(35) Plasser, F., J. Chem. Phys. **2020**, *152*, 084108. doi:10.1063/1.5143076.
(36) Kleinschmidt, M.; Tatchen, J.; Marian, C. M., J. Comput. Chem. **2002**, *23*, 824–833. doi:10.1002/jcc.10064.
(37) Kleinschmidt, M.; Tatchen, J.; Marian, C. M., J. Chem. Phys. **2006**, *124*, 124101. doi:10.1063/1.2173246.
(38) Bracker, M.; Marian, C. M.; Kleinschmidt, M., J. Chem. Phys. **2021**, *155*, 014102. doi:10.1063/5.0056182.
(39) Dinkelbach, F.; Marian, C. M., J. Serb. Chem. Soc. **2019**, *84*, 819–836. doi:10.2298/JSC190510048D.
(40) Bracker, M.; Dinkelbach, F.; Weingart, O.; Kleinschmidt, M., Phys. Chem. Chem. Phys. **2019**, *21*, 9912–9923. doi:10.1039/C9CP00805E.
(41) Dinkelbach, F.; Bracker, M.; Kleinschmidt, M.; Marian, C. M., J. Phys. Chem. A **2021**, *125*, 10044–10051. doi:10.1021/acs.jpca.1c09150.
(42) Platt, J. R., J. Chem. Phys. **1949**, *17*, 484–495. doi:10.1063/1.1747293.
(43) Vosskötter, S.; Konieczny, P.; Marian, C. M.; Weinkauf, R., Phys. Chem. Chem. Phys. **2015**, *17*, 23573–23581. doi:10.1039/C5CP01826A.
(44) Hennebicq, E.; Pourtois, G.; Scholes, G. D.; Herz, L. M.; Russell, D. M.; Silva, C.; Setayesh, S.; Grimsdale, A. C.; Müllen, K.; Brédas, J.-L.; Beljonne, D., J. Am. Chem. Soc. **2005**, *127*, 4744–4762. doi:10.1021/ja0488784.
(45) Förster, T., Ann. Phys. (Berlin) **1948**, *437*, 55–75. doi:10.1002/andp.19484370105.
(46) Dexter, D. L., J. Chem. Phys **1953**, *21*, 836–850. doi:10.1063/1.1699044.
(47) Fink, R.; Pfister, J.; Schneider, A.; Zhao, H.; Engels, B., Chem. Phys. **2008**, *343*, 353–361. doi:10.1016/j.chemphys.2007.08.021.
(48) Fink, R. F.; Pfister, J.; Zhao, H. M.; Engels, B., Chem. Phys. **2008**, *346*, 275–285. doi:10.1016/j.chemphys.2008.03.014.
(49) Spiegel, J. D.; Kleinschmidt, M.; Larbig, A.; Tatchen, J.; Marian, C. M., J. Chem. Theory Comput. **2015**, *11*, 4316–4327. doi:10.1021/acs.jctc.5b00501.

Supplementary Material for Intersystem Crossing and Intramolecular Triplet Excitation Energy Transfer in Spiro[9,10-dihydro-9-oxoanthracene-10,2´-5´,6´-benzindan] Investigated by DFT/MRCI Methods

Simon Metz, Tobias Böhmer, Ben Raunitschke, and Christel M. Marian*

Institute of Theoretical and Computational Chemistry, Heinrich-Heine-University Düsseldorf, Universitätsstr. 1, 40225 Düsseldorf, Germany

E-mail: Christel.Marian@hhu.de

September 30, 2022

Technical Details of the Computations

MRCI: 21 singlet, 20 triplet roots; standard parameter set; esel = 1.0 E_h

TTA: 64 triplet roots; short parameter set; esel = 0.8 E_h

HT expansion of ISC: 21 singlet, 20 triplet roots; short parameter set; esel = 0.8 E_h

NACMEs: 10 triplet roots; short parameter set; esel = 0.8 E_h; renorm parameter = 10^{-8}

FC spectra: 16000 grid points, integration interval 3000 fs, damping parameter η = 200 cm^{-1}

ISC and IC rate constants: 65536 grid points, integration interval 3000 fs, damping parameter η = 10 cm^{-1}

Handling of Symmetry-Broken Solutions

In order to calculate Franck–Condon spectra, the eigenvalue of the imaginary frequency of the symmetry-constrained saddle-point has to be corrected. To this end, a (TD)DFT scan is carried out along the normal mode. The curvature of the outer part (red encircled points in Figure S1) is used to fit a harmonic frequency to this energy profile, as done in previous works.[1,2] The fit, shown in Figure S1, yields a harmonic frequency of 13 cm^{-1}, which is close to the absolute value of the imaginary frequencies of –14.58 cm^{-1}. This is also true for the ground-state geometry in BuCN and the $^1n\pi^*$ **A** vacuum geometry. As a result, all other imaginary frequencies for this kind of normal mode were used as absolute values. To test how strongly the Franck–Condon overlaps depend on the eigenvalue of this low-frequency mode, a few calculations with different values were performed which yielded almost identical rate constants and spectra.

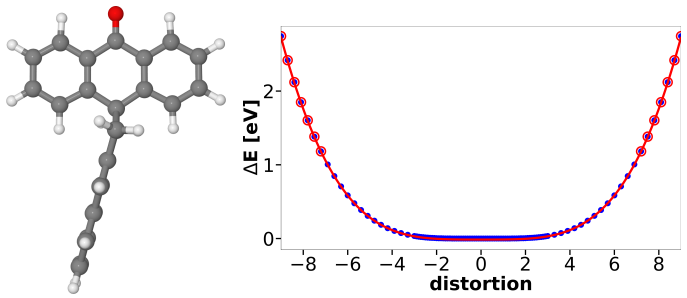

(a) (b)

Figure S1: DFT (PBE0/def2-TZVP) minimum structure of the electronic ground state in BuCN an scan along the dimensionless normal coordinate of the imaginary vibrational mode at the C_{2v}-symmetric ground state geometry. Red encircled points are used for the fit of the harmonic potential (red line).

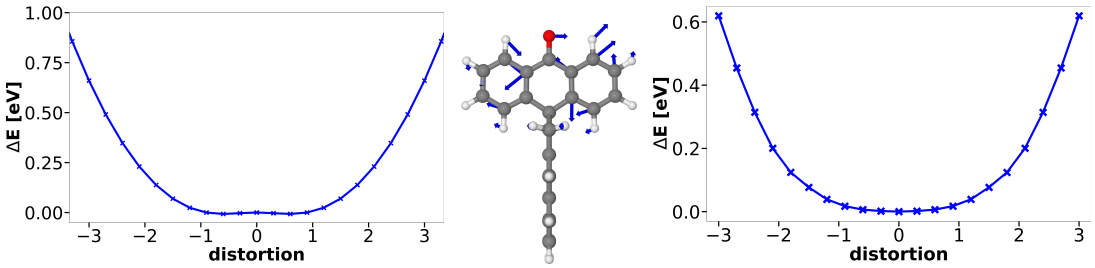

(a) TDDFT-TDA (PBE0/def2-TZVP) (b) imag. mode (c) DFT/MRCI (def2-TZVP)

Figure S2: Scan along the dimensionless normal coordinate of the imaginary vibrational mode at the C_{2v}-symmetric $^3\pi\pi^*$ (**A**) state geometry. The energy profile of the TDDFT-TDA (PBE0/def2-TZVP) calculations show a shallow double minimum structure whereas the DFT/MRCI energy profile has a minimum at the symmetry point.

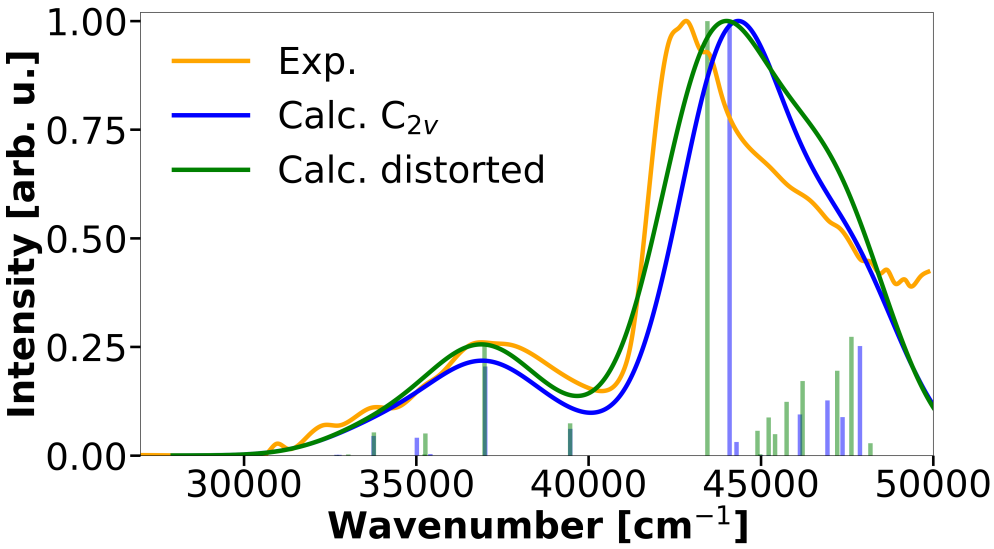

Figure S3: Calculated stationary absorption spectra in BuCN. The bars represent the transitions with their normalized oscillator strength. Blue: C_{2v} symmetric ground state; green: distorted ground-state geometry; orange: digitized spectrum read from Figure 6 of Ref.[3]

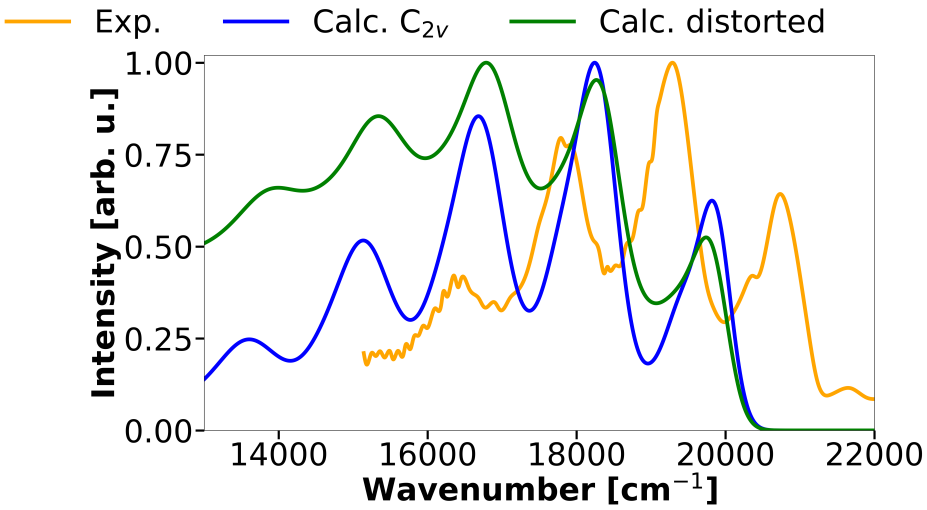

Figure S4: Calculated phosphorescence spectra in BuCN at 77K in comparison to experimental spectra. Blue: C_{2v} symmetric ground state; green: distorted ground-state geometry; orange: digitized spectrum read from Figure 3 of Ref.[3]

Molecular Orbitals

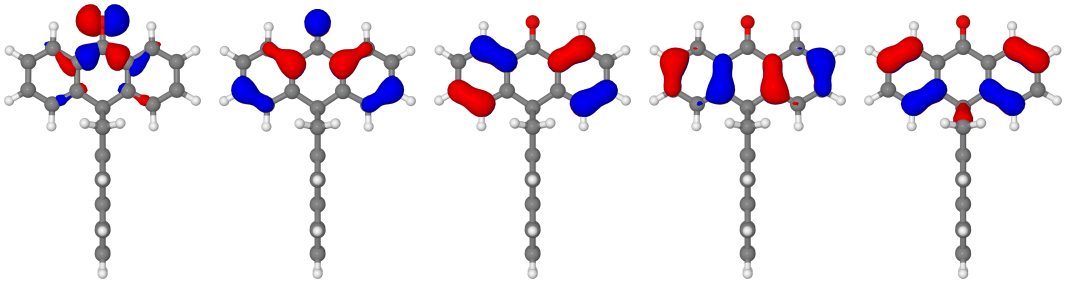

(a) HOMO-6 (b) HOMO-5 (c) HOMO-4 (d) HOMO-3 (e) HOMO-2

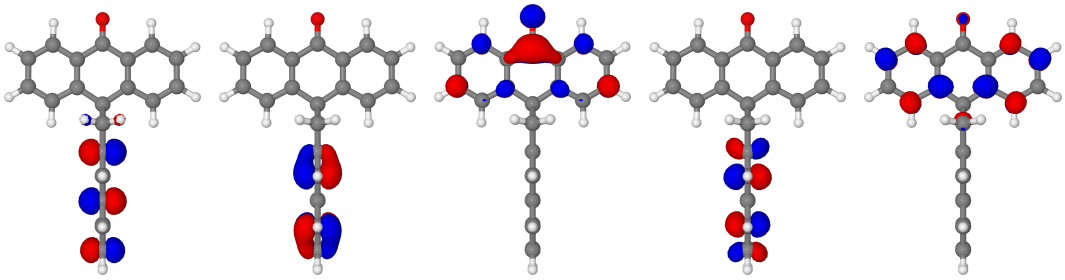

(f) HOMO-1 (g) HOMO (h) LUMO (i) LUMO+1 (j) LUMO+2

Figure S5: BH-LYP frontier molecular orbitals at the C_{2v} symmetrical ground state geometry in BuCN.

Excited-State Characteristics

Table S1: DFT/MRCI vertical excitation energies of low lying singlet and triplet states of the C_{2v} symmetrical ground state in vacuum.

State	ΔE	Transition	% weight
S_1 ($^1n\pi^*$ **A**)	3.58	HOMO-6→LUMO	77.5
S_2	4.07	HOMO-1→LUMO+1	46.2
		HOMO →LUMO+2	24.2
S_3	4.20	HOMO →LUMO	41.6
		HOMO-3→LUMO	29.9
T_1 ($^3\pi\pi^*$ **N**)	2.95	HOMO →LUMO+1	83.9
T_2 ($^3n\pi^*$ **A**)	3.37	HOMO-6→LUMO	77.7
T_3 ($^3\pi\pi^*$ **A**)	3.52	HOMO-5→LUMO	66.2
T_4	3.66	HOMO-4→LUMO	41.7
		HOMO-3→LUMO	19.8

Table S2: DFT/MRCI vertical excitation energies of low lying singlet and triplet states of the C_{2v} symmetrical ground state in BuCN.

State	ΔE	Transition	% weight
S_1 ($^1n\pi^*$ **A**)	3.71	HOMO-6→LUMO	78.1
S_2	4.05	HOMO →LUMO	57.1
		HOMO-3→LUMO	21.7
S_3	4.06	HOMO-1→LUMO+1	45.1
		HOMO →LUMO+2	21.0
T_1 ($^3\pi\pi^*$ **N**)	2.96	HOMO →LUMO+1	84.2
T_2 ($^3n\pi^*$ **A**)	3.51	HOMO-6→LUMO	78.5
T_3 ($^3\pi\pi^*$ **A**)	3.51	HOMO-5→LUMO	67.3
T_4	3.60	HOMO-4→LUMO	41.5
		HOMO-3→LUMO	24.5

Table S3: DFT/MRCI vertical excitation energies of low lying singlet and triplet states of the C_{2v} symmetrical $^1n\pi^*$ **A** in BuCN.

State	ΔE	Transition	% weight
S_1 ($^1n\pi^*$ **A**)	3.19	HOMO-6→LUMO	79.2
S_2	3.78	HOMO →LUMO	66.6
		HOMO-3→LUMO	9.7
S_3	3.97	HOMO-2→LUMO	72.2
T_1 ($^3\pi\pi^*$ **N**)	2.97	HOMO →LUMO+1	83.9
T_2 ($^3n\pi^*$ **A**)	3.03	HOMO-6→LUMO	80.1
T_3 ($^3\pi\pi^*$ **A**)	3.04	HOMO-5→LUMO	76.9
T_4	3.36	HOMO-3→LUMO	52.2
		HOMO-4→LUMO	20.6

Table S4: DFT/MRCI vertical excitation energies of low lying singlet and triplet states of the C_{2v} symmetrical $^1n\pi^*$ **A** in vacuum.

State	ΔE	Transition	% weight
S_1 ($^1n\pi^*$ **A**)	2.93	HOMO-6→LUMO	78.2
S_2	3.96	HOMO →LUMO	51.0
		HOMO-5→LUMO	16.7
		HOMO-4→LUMO	11.6
S_3	4.06	HOMO-2→LUMO	59.9
T_1 ($^3n\pi^*$ **A**)	2.77	HOMO-6→LUMO	79.2
T_2 ($^3\pi\pi^*$ **A**)	2.94	HOMO-3→LUMO	77.0
T_3 ($^3\pi\pi^*$ **N**)	2.96	HOMO →LUMO+1	83.6
T_4	3.42	HOMO-4→LUMO	56.2
		HOMO-5→LUMO	13.0

Table S5: DFT/MRCI vertical excitation energies of low lying singlet and triplet states of the C_{2v} symmetrical $^3n\pi^*$ **A** in BuCN.

State	ΔE	Transition	% weight
S_1 ($^1n\pi^*$ **A**)	3.20	HOMO-6→LUMO	79.2
S_2	3.79	HOMO →LUMO	66.1
		HOMO-3→LUMO	12.2
S_3	3.98	HOMO-2→LUMO	72.2
T_1 ($^3\pi\pi^*$ **N**)	2.97	HOMO →LUMO+1	83.9
T_2 ($^3n\pi^*$ **A**)	3.04	HOMO-6→LUMO	80.0
T_3 ($^3\pi\pi^*$ **A**)	3.07	HOMO-5→LUMO	76.7
T_4	3.38	HOMO-3→LUMO	42.4
		HOMO-4→LUMO	29.9

Table S6: DFT/MRCI vertical excitation energies of low lying singlet and triplet states of the C_{2v} symmetrical $^3n\pi^*$ **A** in vacuum.

State	ΔE	Transition	% weight
S_1 ($^1n\pi^*$ **A**)	2.92	HOMO-6→LUMO	78.1
S_2	3.96	HOMO →LUMO	50.6
		HOMO-4→LUMO	15.4
		HOMO-5→LUMO	15.3
S_3	4.06	HOMO-2→LUMO	56.8
T_1 ($^3n\pi^*$ **A**)	2.76	HOMO-6→LUMO	79.1
T_2 ($^3\pi\pi^*$ **A**)	2.94	HOMO-3→LUMO	76.7
T_3 ($^3\pi\pi^*$ **N**)	2.95	HOMO →LUMO+1	83.5
T_4	3.43	HOMO-4→LUMO	47.8
		HOMO-5→LUMO	21.0

Table S7: DFT/MRCI vertical excitation energies of low lying singlet and triplet states of the C_{2v} symmetrical $^3\pi\pi^*$ **A** in BuCN.

State	ΔE	Transition	% weight
S_1 ($^1n\pi^*$ **A**)	3.11	HOMO-6→LUMO	79.3
S_2	3.68	HOMO →LUMO	69.1
		HOMO-5→LUMO	9.3
S_3	3.91	HOMO-3→LUMO	71.5
T_1 ($^3\pi\pi^*$ **A**)	2.91	HOMO-4→LUMO	78.2
T_2 ($^3n\pi^*$ **A**)	2.97	HOMO-6→LUMO	80.3
T_3 ($^3\pi\pi^*$ **N**)	2.97	HOMO →LUMO+1	83.9
T_4	3.22	HOMO-2→LUMO	71.0

Table S8: DFT/MRCI vertical excitation energies of low lying singlet and triplet states of the C_{2v} symmetrical $^3\pi\pi^*$ **A** in Vacuum.

State	ΔE	Transition	% weight
S_1 ($^1n\pi^*$ **A**)	2.84	HOMO-6→LUMO	78.2
S_2	3.88	HOMO →LUMO	54.3
		HOMO-5→LUMO	18.2
S_3	4.01	HOMO-4→LUMO	68.2
T_1 ($^3n\pi^*$ **A**)	2.69	HOMO-6→LUMO	79.2
T_2 ($^3\pi\pi^*$ **A**)	2.78	HOMO-2→LUMO	77.6
T_3 ($^3\pi\pi^*$ **N**)	2.95	HOMO →LUMO+1	83.4
T_4	3.28	HOMO-3→LUMO	68.7

Table S9: DFT/MRCI vertical excitation energies of low lying singlet and triplet states of the C_{2v} symmetrical $^3\pi\pi^*$ **N** in BuCN.

State	ΔE	Transition	% weight
S_1 ($^1n\pi^*$ **A**)	3.73	HOMO-6→LUMO	77.5
S_2	3.76	HOMO →LUMO+1	87.1
S_3	3.83	HOMO →LUMO	80.7
T_1 ($^3\pi\pi^*$ **N**)	2.26	HOMO →LUMO+1	87.7
T_2 ($^3\pi\pi^*$ **A**)	3.53	HOMO-5→LUMO	67.0
T_3 ($^3n\pi^*$ **A**)	3.53	HOMO-6→LUMO	77.9
T_4	3.61	HOMO-4→LUMO	40.2
		HOMO-3→LUMO	24.7

Table S10: DFT/MRCI vertical excitation energies of low lying singlet and triplet states of the C_{2v} symmetrical $^3\pi\pi^*$ **N** in vacuum.

State	ΔE	Transition	% weight
S_1 ($^1n\pi^*$ **A**)	3.60	HOMO-6→LUMO	76.9
S_2	3.74	HOMO →LUMO+1	86.9
S_3	3.82	HOMO-1→LUMO+1	44.2
		HOMO →LUMO+3	17.7
		HOMO →LUMO+4	13.9
T_1 ($^3\pi\pi^*$ **N**)	2.25	HOMO →LUMO+1	87.5
T_2 ($^3n\pi^*$ **A**)	3.39	HOMO-6→LUMO	77.3
T_3 ($^3\pi\pi^*$ **A**)	3.53	HOMO-5→LUMO	65.7
T_4	3.64	HOMO-1→LUMO+1	50.7
		HOMO →LUMO+3	15.6
		HOMO →LUMO+4	12.7

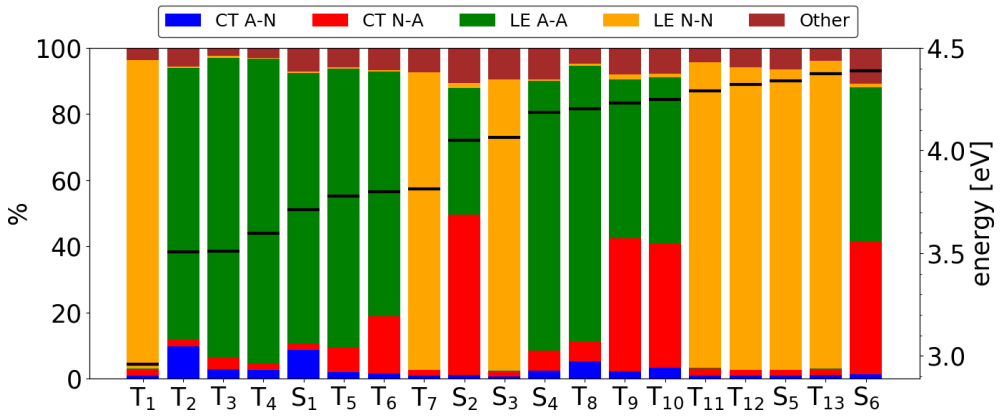

Figure S6: Theodore analysis at the ground state geometry in BuCN for excited states with a vertical excitation energy below 4.5 eV. Orange: local excitation on the naphthalene, green: local excitation on the anthracenone, blue: charge-transfer from the anthracenone to the naphthalene, red: charge-transfer from the naphthalene to the anthracenone, brown: other contribution such as 2-electron excitations.

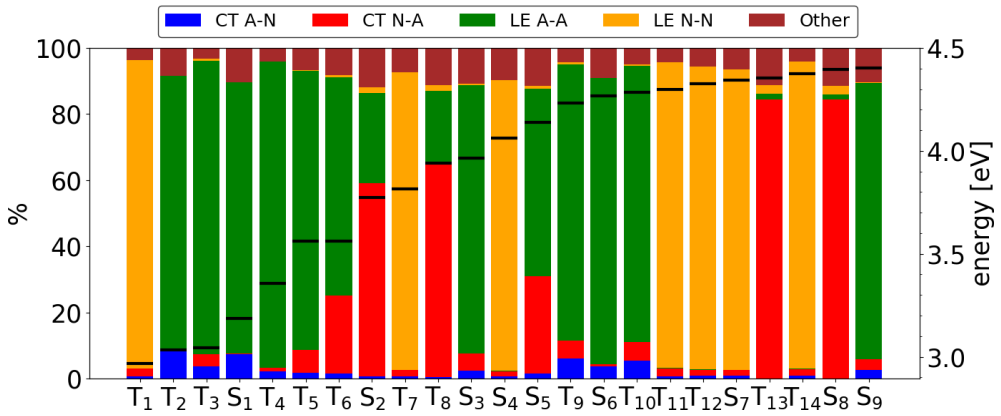

Figure S7: Theodore analysis at the $^1n\pi^*$ geometry in BuCN for excited states with a vertical excitation energy below 4.5 eV. Orange: local excitation on the naphthalene, green: local excitation on the anthracenone, blue: charge-transfer from the anthracenone to the naphthalene, red: charge-transfer from the naphthalene to the anthracenone, brown: other contribution such as 2-electron excitations.

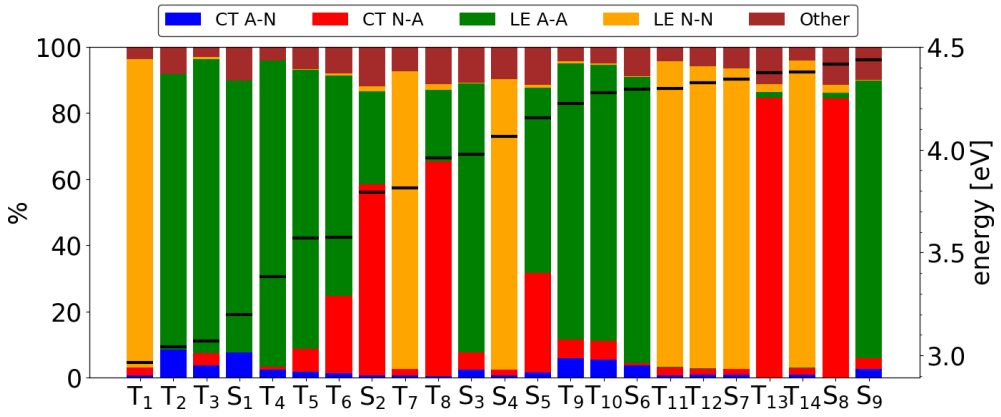

Figure S8: Theodore analysis at the $^3n\pi^*$ geometry in BuCN for excited states with a vertical excitation energy below 4.5 eV. Orange: local excitation on the naphthalene, green: local excitation on the anthracenone, blue: charge-transfer from the anthracenone to the naphthalene, red: charge-transfer from the naphthalene to the anthracenone, brown: other contribution such as 2-electron excitations.

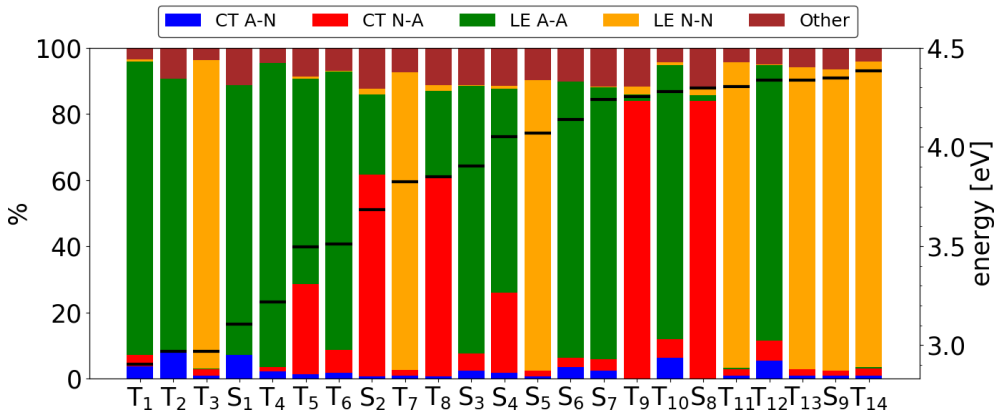

Figure S9: Theodore analysis at the $^3\pi\pi^*$ (**A**) geometry in BuCN for excited states with a vertical excitation energy below 4.5 eV. Orange: local excitation on the naphthalene, green: local excitation on the anthracenone, blue: charge-transfer from the anthracenone to the naphthalene, red: charge-transfer from the naphthalene to the anthracenone, brown: other contribution such as 2-electron excitations.

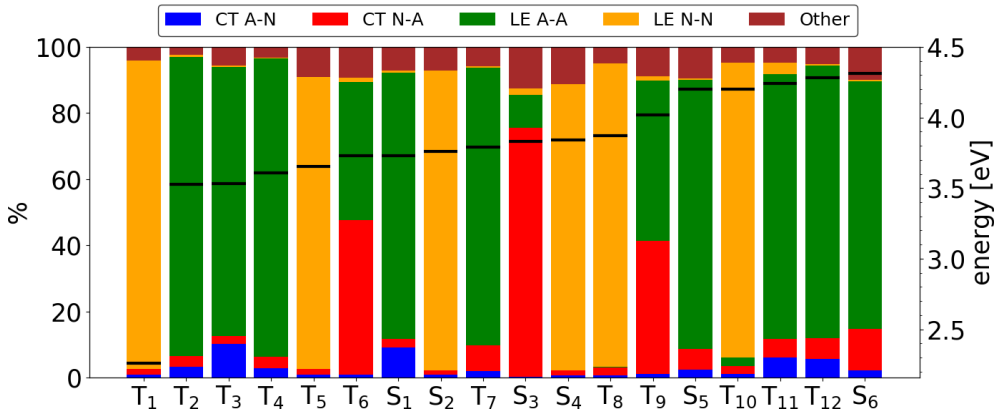

Figure S10: Theodore analysis at the $^3\pi\pi^*$ (**N**) geometry in BuCN for excited states with a vertical excitation energy below 4.5 eV. Orange: local excitation on the naphthalene, green: local excitation on the anthracenone, blue: charge-transfer from the anthracenone to the naphthalene, red: charge-transfer from the naphthalene to the anthracenone, brown: other contribution such as 2-electron excitations.

Vibrational Coupling Modes

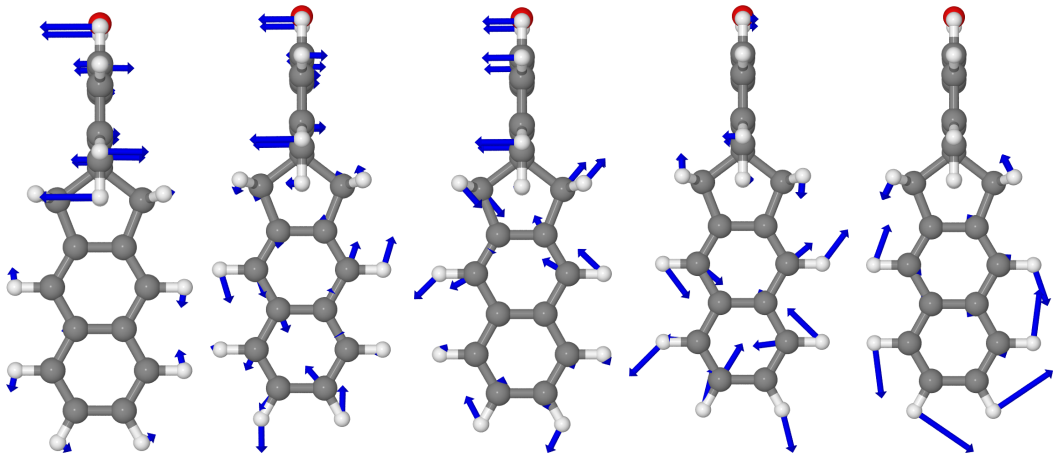

(a) mode 19 (b) mode 29 (c) mode 39 (d) mode 55 (e) mode 91

Figure S11: B_2 symmetric coupling vibrational modes promoting the TEET between the $^3\pi\pi^*$ (**A**) and $^3\pi\pi^*$ (**N**) of **AN** in BuCN.

References

(1) Bracker, M.; Dinkelbach, F.; Weingart, O.; Kleinschmidt, M. Impact of fluorination on the photophysics of the flavin chromophore: a quantum chemical perspective. *Phys. Chem. Chem. Phys.* **2019**, *21*, 9912–9923.

(2) Dinkelbach, F.; Bracker, M.; Kleinschmidt, M.; Marian, C. M. Large inverted singlet–triplet energy gaps are not always favorable for triplet harvesting: Vibronic coupling drives the (reverse) intersystem crossing in heptazine derivatives. *J. Phys. Chem. A* **2021**, *125*, 10044–10051.

(3) Dobkowski, J.; Gorski, A.; Kijak, M.; Pietrzak, M.; Redeckas, K.; Vengris, M. Combined picosecond time-resolved UV-Vis and NMR techniques used for investigation of the excited state intramolecular triplet-triplet energy transfer. *J. Phys. Chem. A* **2019**, *123*, 6978–6985.

Manuscript No.1

The effect of conformational constraints and oxygen quenching on TADF in donor-acceptor systems

Dragana Sretenović, Laura N. Kloeters, Jeremy M. Kaminski, Tobias Böhmer, Philipp Schmeinck, Suren Felekyan, Oleg Opanasyuk, Gereon A. Sommer, Mina Chalani, Guido J. Reiß, Christoph Janiak, Christel M. Marian, Ralf Kühnemuth, Thomas J. J. Müller and Claus A. M. Seidel
Manuscript in preparation for *Chemical Science*
Latest version from 21.01.2025

Contribution: I performed the quantum chemical investigation of Comp 4-diMe and Comp 5-Me+diOme and provided all the vibronic spectra and the nonradiative rate constants along the interpolated path. The theoretical results were partially visualized by me.

The effect of conformational constraints and oxygen quenching on TADF in donor-acceptor systems

Dragana Sretenović,[a] Laura N. Kloeters,[b] Jeremy M. Kaminski,[c] Tobias Böhmer,[c] Philipp Schmeinck,[d] Suren Felekyan,[a] Oleg Opanasyuk,[a] Gereon A. Sommer,[b] Mina Chalani,[a] Guido J. Reiß,[d] Christoph Janiak,[d] Christel M. Marian,*[c] Ralf Kühnemuth,*[a] Thomas J. J. Müller*[b] and Claus A. M. Seidel*[a]

[a] Dr. D. Sretenović, Dr. S. Felekyan, Dr. O. Opanasyuk, M. Chalani, Dr. R. Kühnemuth, Prof. Dr. C. A. M. Seidel
Institut für Physikalische Chemie
Mathematisch-Naturwissenschaftliche Fakultät
Heinrich-Heine-Universität Düsseldorf
Universitätsstr. 1, 40225 Düsseldorf, Germany
E-Mail: ralf.kuehnemuth@hhu.de, cseidel@hhu.de

[b] Dr. L. N. Kloeters, Dr. G. A. Sommer, Prof. Dr. T. J. J. Müller
Institut für Organische Chemie und Makromolekulare Chemie
Mathematisch-Naturwissenschaftliche Fakultät
Heinrich-Heine-Universität Düsseldorf
Universitätsstr. 1, 40225 Düsseldorf, Germany
E-Mail: ThomasJJ.Mueller@uni-duesseldorf.de

[c] J. M. Kaminski, T. Böhmer, Prof. Dr. C. M. Marian
Institut für Theoretische Chemie und Computerchemie
Mathematisch-Naturwissenschaftliche Fakultät
Heinrich-Heine-Universität Düsseldorf
Universitätsstr. 1, 40225 Düsseldorf, Germany
E-Mail: christel.marian@hhu.de

[d] Dr. P. Schmeinck, Dr. G. J. Reiß, Prof. Dr. C. Janiak
Institut für Anorganische Chemie und Strukturchemie
Mathematisch-Naturwissenschaftliche Fakultät
Heinrich-Heine-Universität Düsseldorf
Universitätsstr. 1, 40225 Düsseldorf, Germany

Manuscript stage: In preparation for *Chemical Science.* The current version can be subjected to further changes such as adding or removing text or figures as well as author contributions.

Keywords: TADF, Fluorescence, Spectroscopy, steric effects, MRCI calculations

Abstract

To be filled in

Introduction

Thermally activated delayed fluorescence (TADF) has become an important design principle of metal free dyes and their applications range from non-doped organic light-emitting diodes (OLEDs),[1-3] over biomedicine[4] to photocatalysis.[5] In particular, increasing the energy efficiency of emitters in OLEDs takes enormous effort and has become the major interdisciplinary challenge for devising novel emissive molecules by synthesis, photophysics and theory.[6, 7] One decisive key factor for enabling high internal quantum efficiency of TADF emitters is the singlet-triplet energy difference (ΔE_{ST}).[8] Small ΔE_{ST} values allow for efficient reverse intersystem crossing (rISC) that leads to the depopulation of non-emissive triplet states T_1 into emissive singlet states S_1. Realization of small singlet-triplet energy gaps by molecular motifs could be for example achieved in conjugated donor-acceptor systems with steric distortion.[9] This steric distortion leads to the hole (donor) and electron (acceptor) of a conjugated donor-acceptor system and is achieved by conformational fixation, for instance in spiro systems or by bis-ortho disubstitution.

However, at complete orthogonalization of the donor and acceptor units, the emission transition dipole moment might reduce to zero, which causes a dramatic loss of emission quantum yield. Therefore, fine-tuning of ΔE_{ST} by conformational constraint of the angle between donor and acceptor parts warranting a small energy gap with a concomitant sufficiently large fluorescence rate constant appears to be an option for modulating singlet-triplet transitions.[10] Besides this approach based upon conformational design, the presence of oxygen as a quencher of both singlet and triplet state might also affect the TADF characteristics of donor-acceptor dyes. Herein, we report the investigation of conformational effects on the photophysics as well as on TADF properties of a TADF system that we chose as a meaningful model.[11, 12] Introducing substituents with different steric demand on the phenylene bridge of the reference system causes a conformational constraint in the ground state and this effect on the TADF properties is scrutinized by experimental and computational approaches. Photophysical measurements also consider the effects of oxygen quenching on the prompt and delayed fluorescence lifetimes.

Results and Discussion

Synthesis

Five donor-acceptor systems including the primordial system that already has been shown to possess TADF properties[11, 12] are accessible by a concise two-step sequence. Starting from *para*-bromo anilines **1** and aryl iodides **2**, the brominated triphenylamine donor substrates **3** are synthesized by Ullmann coupling in the presence of catalytic amounts of copper iodide and 1,10-phenanthroline and potassium *tert*-butoxide as a base in 31–86% yield (Scheme 1).[13] The donor substrates **3** subsequently react in a bromine-lithium exchange-borylation-Suzuki (BLEBS) sequence[14] with 2-iodoterephthalonitrile (**4**) as an acceptor component to give after workup and purification by flash chromatography on silica gel the target compounds **5** in 14-99% yield.[12] While this one-pot sequence proceeds smoothly with $Pd(PPh_3)_4$ for monosubstituted phenyl bridges, the sterically demanding donor substrate **3d** with *ortho,ortho'*-disubstitution requires the catalyst system $Pd_2(dba)_3$/2-biphenyl)dicyclohexylphosphane (CyJohnPhos) and K_3PO_4 as a base in the Suzuki step to give the desired product **5d** in low yield. The molecular structures of the title compounds **5** were unambiguously assigned by comprehensive ^1H and ^{13}C NMR spectroscopy and the molecular composition was determined by combustion analysis and/or mass spectrometry (see SI Chapter 1, Figures S1-S26).

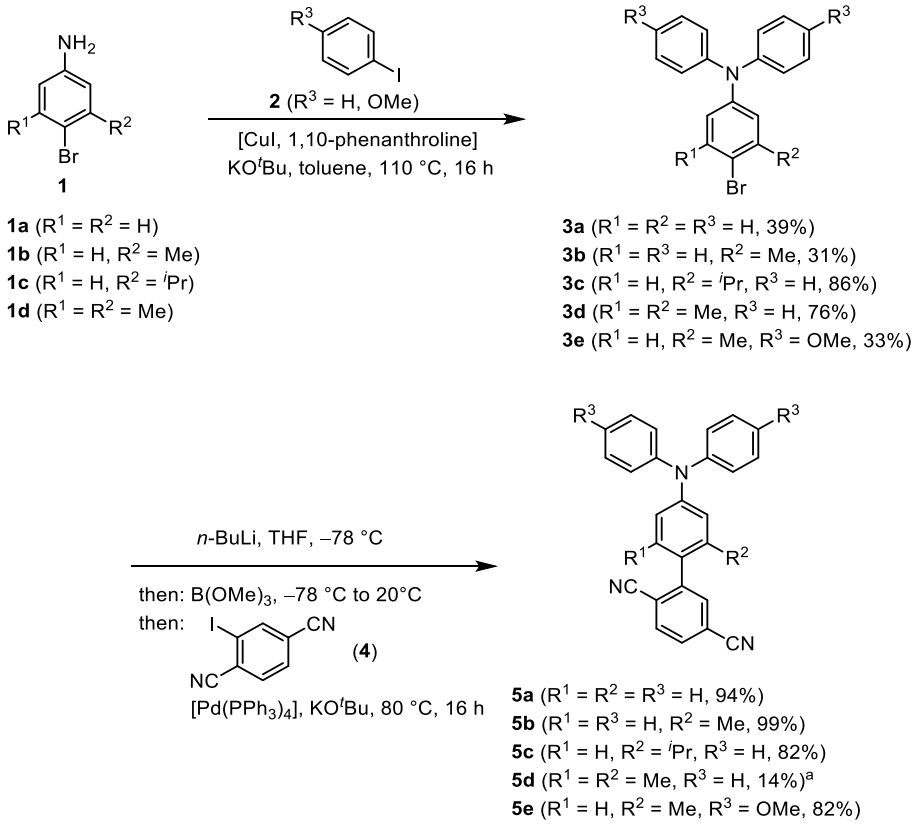

Scheme 1. Synthesis of donor-acceptor systems **5** with torsionally constrained phenylene-bridge via Ullmann arylation and one-pot bromine-lithium-exchange-borylation-Suzuki coupling (BLEBS) sequence [[a]$Pd_2(dba)_3$/2-biphenyl)dicyclohexylphosphane (CyJohnPhos) and K_3PO_4 are employed in the Suzuki step].

Geometric properties: Theory and experiment

Placing *ortho*-substituents on the phenylene bridge adjacent to the terephthalonitrile acceptor causes significant torsion of the donor-acceptor axes as seen in the crystal structure as well as from theoretical investigations ([a] Molecule A. [b] Molecule B. See Figures S29-S33. [c] The second minimum of **5c** can only be seen in a two-dimensional scan in which θ $D-A$ and the isopropyl rotation angle ω are varied (**see** B).

Figure 1A, B and D). One-dimensional relaxed KS-DFT scans of the ground-state potential energy surface along the donor-acceptor dihedral angle θ_{D-A} reveals two separate conformers for **5a**, **5b** and **5e**. A second conformer cannot be found for the corresponding relaxed scan of **5c**. Unlike for the other compounds the rotational degree of freedom for the sterically demanding isopropyl group (see ω in [a] Molecule A. [b] Molecule B. See Figures S29-S33. [c] The

second minimum of **5c** can only be seen in a two-dimensional scan in which θ $D-A$ and the isopropyl rotation angle ω are varied (**see** B).

Figure 1C) has to be considered. Its steric demand possibly hinders rotation around the donor-acceptor ligating sigma bond (Figure S27). The rotational barrier was estimated from variable temperature (VT) NMR spectra (Figure S28). From the coalescence temperature (T_c = 343 K) the rate constant k_{T_c} and thereby the Gibbs free enthalpy of activation for rotation of the isopropyl group can be calculated to $\Delta G_c^{\ddagger}$ = 74 kJ/mol (for details, see SI Chapter 1.1).[15] This value lies within the same order of magnitude for hindered *iso*-propyl rotations[16] as well as for hindered *ortho,ortho'*-biaryl rotations.[17] It can also be seen in a computed two-dimensional scan including the donor-acceptor dihedral angle and the isopropyl rotation ([a] Molecule A. [b] Molecule B. See Figures S29-S33. [c] The second minimum of **5c** can only be seen in a two-dimensional scan in which θ $D-A$ and the isopropyl rotation angle ω are varied (**see** B).

Figure 1B). The rotational barrier starting from the energetically most stable conformer (θ_{D-A}: 75°, ω: -5°) is computed to be marginally smaller (ca. 50 kJ/mol) than in experiment. For **5d** the donor-acceptor arrangement is nearly perpendicular, and due to the flat potential energy surface only one conformer could be confirmed.

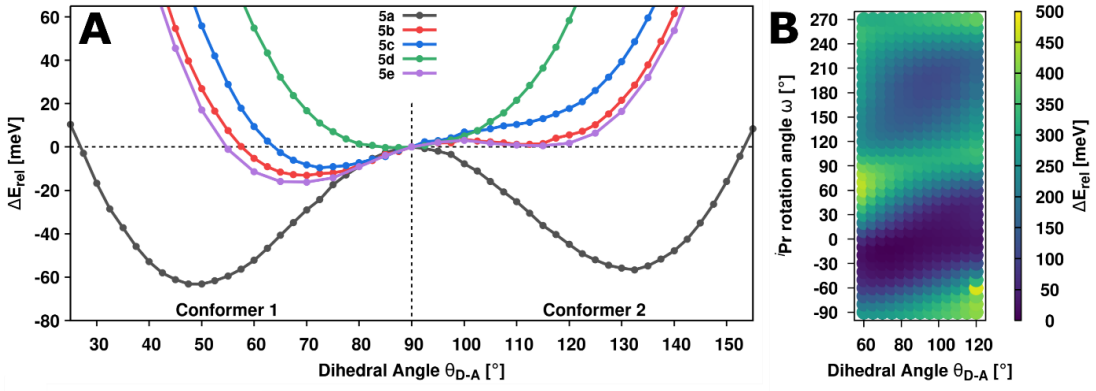

C

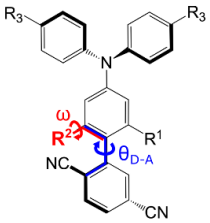

D

Structure	R¹	R²	R³	Theory (single molecule in toluene) Dihedral Angle θ_{D-A} [°] Conformer 1	Theory (single molecule in toluene) Dihedral Angle θ_{D-A} [°] Conformer 2	Experiment (crystal) Dihedral Angle θ_{D-A} [°] Conformer 1
5a	H	H	H	49.6	131.2	n.d.
5b	H	Me	H	69.7	110.7	55.1(2)[a] / 54.7(2)[b]
5c	H	^{i}Pr	H	73.5	95.8[c]	69.51(7)[a] / 68.3(2)[b]
5d	Me	Me	H	87.1	---	73.10(7)
5e	H	Me	OMe	68.0	112.3	58.2(1)

[a] Molecule A. [b] Molecule B. See Figures S29-S33. [c] The second minimum of **5c** can only be seen in a two-dimensional scan in which θ_{D-A} and the isopropyl rotation angle ω are varied (see **B**).

Figure 1. A. One-dimensional relaxed KS-DFT scans of the ground-state potential energy surface of **5a**-**5e** along the donor-acceptor dihedral angle θ_{D-A}. **B.** Two-dimensional relaxed KS-DFT scan of the ground state potential energy surface of **5c** along the donor-acceptor

dihedral angle θ_{D-A} including the ^{i}Pr rotation along rotation angle ω. **C.** General chemical structure of the investigated compounds **5a**-**5e**. **D.** Interplanar dihedral angles θ_{D-A} of the structures **5a-5e** from the relaxed ground-state KS-DFT scans and the crystal structure analyses (for more details, see SI Chapter 2).

The preceding experimental and theoretical investigations show that in solution and at room temperature the rotational degrees of freedom around the biaryl σ-bond are restricted and, therefore, these systems can be considered conformationally constrained in the electronic ground state.

Spectroscopy

We examined two factors influencing the photophysical properties in our study: the influence of steric torsion variations within the linker between the donor and acceptor (compound series **5a-5d**), and the increased donor strength (compound **5e**).

Compound **5a** has the smallest torsion angle, which results in the closest spatial proximity of its hole and electron densities. Thus, this compound has the highest absorption coefficient for its lowest-energy absorption maximum among all five compounds (Figure 2A). The theoretical S_0-S_1 oscillator strengths (***f***) corroborates this trend (Figure 2B) of an increasing charge transfer character for compounds **5a-5d**. The theoretically predicted absorption and emission spectra are in excellent agreement with the experimental spectra (Figure 2C). From **5a** to **5d**, the increasing torsion angle leads to a more significant decoupling of the donor and acceptor, and consequently lower absorption coefficients (Figure 2D). The fluorescence emission maxima for compounds **5a-5d** in toluene are in the range of 490 nm to 500 nm. The donor variation in **5e** already significantly influences the fluorescence emission spectrum, shifting it bathochromically in comparison with its counterpart **5b** (dashed purple and red lines, respectively, Figure 2A and C).

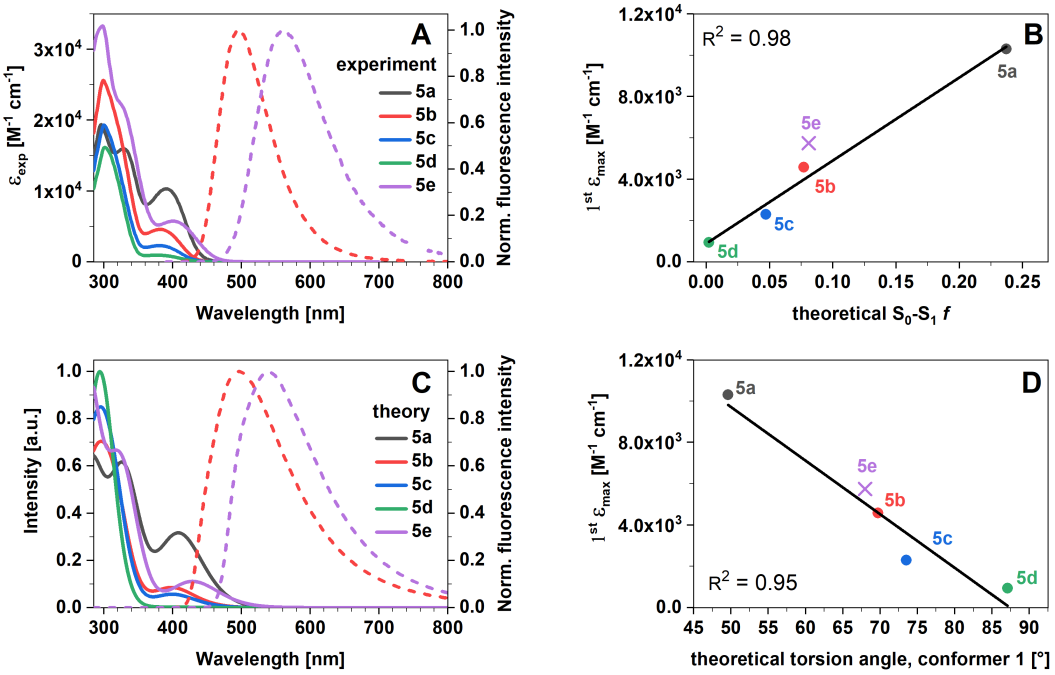

Figure 2. A. and **C.** *Left y-axis*: Experimental and theoretical absorption spectra of compounds **5a**-**5e** in toluene. The line spectra of all compounds were broadened with Gaussians of 4400 cm^{-1}. *Right y-axis*: Experimental and theoretical fluorescence emission spectra of compounds **5b** and **5e** in toluene (dashed red and purple lines, respectively). The corresponding spectra of compounds **5a**, **5c** and **5d** are similar to **5b** (see Figures S38 & S39). The range between 750 and 770 nm in the experimental spectra is excluded due to the presence of second-order diffracted excitation light. **B.** The correlation between the experimental absorption coefficient (ε_{exp}) and the theoretical oscillator S_0-S_1 strength ***f***. The first absorption maximum (1^{st} ε_{max}) was used for the correlation as it corresponds to the S_0-S_1 transition. **D.** The correlation between the first experimental absorption maximum (1^{st} ε_{max}) and the theoretical torsion angle of conformer 1.

Both the absorption and fluorescence experimental spectra were transformed into the transition dipole moment representations[18] (SI Chapter 3.1, Figure S38) to determine the 0-0 energies ($\tilde{\nu}_{00}$), the full widths at half maxima of the emission bands (emission FWHM) and the Stokes shift ($\Delta\tilde{\nu}_s$) (

Table ***1***).

Table 1. Spectroscopic and photophysical parameters of compounds **5a-5e** in toluene. The wavelength maxima of the 1st and 2nd bands with the lowest absorption energies (λ_{max}), absorption coefficients (ε), and fluorescence emission maxima (λ_{em}) refer to the spectra in the wavelength domain. 0-0 energies ($\tilde{\nu}_{00}$), full widths at half maxima of the emission bands (emission FWHM), and Stokes shift ($\Delta\tilde{\nu}_s$) were derived from the corrected absorption and fluorescence emission spectra (Figure S38).

Parameters (at 296 K)	**5a**	**5b**	**5c**	**5d**	**5e**
1^{st} λ_{max} [nm]	391	382	381	377	401
1^{st} ε_{max} [M^{-1} cm^{-1}]	10309	4586	2289	941	5750
S_0-S_1 ***f***, theory [a]	0.237	0.077	0.047	0.002	0.081
λ_{em} [nm]	493	497	492	497	558
2^{nd} λ_{max} [nm]	330	299	300	301	298
2^{nd} ε_{max} [M^{-1} cm^{-1}]	15979	25648	19324	16166	33333
$\tilde{\nu}_{00}$ [cm^{-1}]	22472	22624	22676	22624	20790
Emission FWHM [cm^{-1}]	3606	3990	3916	4106	4417
$\Delta\tilde{\nu}_s$ [cm^{-1}]	5421	6022	6077	6385	7090
Lippert-Mataga slope [cm^{-1}] [b]	22650	22191	24094	23810	19132 [c]
μ_E-μ_G [D], theory [d]	19.1	22.9	22.7	24.0	25.3
Φ_{PF}^{Air} [e]	0.59	0.36	0.29	0.20	0.16
$\Phi_{PF}^{N_2}$ [f]	0.76	0.60	0.56	0.53	0.36
Φ_{DF} [g]	0.00	0.07	0.10	0.28	0.04
Φ_{TF} [h]	0.76	0.67	0.67	0.81	0.40
k_F^{SB} [10^7 s^{-1}] [i]	7.4	3.4	1.7	0.7	3.2
$\tau_F^{SB\ Air}$ [ns] [j]	8.0	10.6	17.0	29.1	5.1
$\tau_F^{SB\ N_2}$ [ns] [j]	10.3	17.6	33.0	77.1	11.6
$\langle\tau\rangle_F^{Air}$ [ns] [k]	7.3	12.3	14.7	17.5	10.8
$\langle\tau\rangle_F^{N_2}$ [ns] [k]	9.4	20.4	28.5	46.5	24.6
τ_{DF} at 296 K [μs]	-	1130	373.6	19.6	37,4

[a] Calculated S_0-S_1 oscillator strengths ***f***. **[b]** See SI Chapter 3.2, Figure S40. **[c]** The fluorescence of **5e** was quenched in dimethylformamide and acetonitrile. These two data points were excluded from the Lippert-Mataga analysis (Figure S40E). **[d]** Theoretical values for the difference between the static dipole moments of the excited and ground states (μ_E-μ_G) in implicit toluene solution at DFT/MRCI level of theory. **[e]** The quantum yield of prompt fluorescence measured in air-saturated toluene (Φ_{PF}^{Air}) was determined using the relative method with Rhodamine 6G in ethanol (air) as a reference (Φ_F^r = 0.94).[19, 20] **[f]** The quantum yield of prompt fluorescence for a nitrogen-purged solution ($\Phi_{PF}^{N_2}$) was calculated according to eq. 1. **[g]** The quantum yield of delayed fluorescence determined by TCSPC offset analysis (see SI Chapter 3.3, eqs. S11-S14). **[h]** The total fluorescence quantum yield calculated as $\Phi_{TF} = \Phi_{PF}^{N_2} + \Phi_{DF}$. **[i]** The radiative rate constants (k_F^{SB}) predicted by Strickler-Berg analysis[22] (see SI Chapter 3.4). **[j]** The fluorescence lifetimes were estimated according to eqs. S15 and S16. **[k]** The fluorescence-weighted lifetimes of prompt fluorescence measured by TCSPC. Individual decay times and species fractions are compiled in SI Chapter 3.5, Tables S11-S15.

Compound **5a** had the highest fluorescence quantum yield in air-saturated toluene (Φ_{PF}^{Air}) of 60%, measured relative to Rhodamine 6G in ethanol (air) as a reference (Φ_F^r = 0.94).[19, 20] To determine the prompt fluorescence quantum yield in nitrogen ($\Phi_{PF}^{N_2}$), we multiplied the quantum yield in air-saturated solution (Φ_{PF}^{Air}) by the ratio of the fluorescence-weighted prompt fluorescence lifetimes in nitrogen and air, $\langle\tau\rangle_F^{N_2}$ and $\langle\tau\rangle_F^{Air}$ (eq. 1). The individual decay times and species fractions are compiled in Tables S11–S15 (SI Chapter 3.5). A significant increase in prompt fluorescence lifetime was observed in nitrogen-purged toluene solution (Figure 3A-E), indicating that singlet states are quenched to some extent by oxygen (SI Chapter 3.6.1).

$$\Phi_{PF}^{N_2} = \Phi_{PF}^{air} \cdot \frac{\langle\tau\rangle_F^{N_2}}{\langle\tau\rangle_F^{Air}} \quad 1$$

Triplet states are more sensitive to oxygen quenching than singlet states, as they have a longer lifetime and therefore the probability of collisions leading to quenching is higher.[21] For compounds **5a**-**5e**, TADF was not detected in the air-saturated toluene solutions. However, in nitrogen, substantial variations in the TADF lifetimes were observed depending on the deoxygenation procedure used during sample preparation. This finding could be explained by the Stern-Volmer equation,[20] which predicts that for longer lifetimes small changes in quencher concentration may cause larger deviations in measured lifetimes (SI Chapter 3.6.2, Figure S46). Thus, sample preparation was one of the most challenging aspects of this study. To prevent the ingress of oxygen, all samples were stored in sealed glass ampoules after being thoroughly bubbled with nitrogen and subjected to the freeze-pump-thaw cycle (SI Chapter 3.7, Figure S47). The longest lifetimes obtained in this study are presented in Figure 3 and

Table *1*. To confirm the temperature dependence of the delayed fluorescence of compounds **5b-5e**, we conducted a series of time-resolved measurements in liquid solutions in a temperature range from 180 K to 300 K (Figure 3G-J), considering the melting point of toluene at 178.1 K (see SI Chapter 3.8). Time-resolved emission spectra of compounds **5b-5e** as additional evidence for TADF can be found in SI Chapter 3.9 (Figure S50).

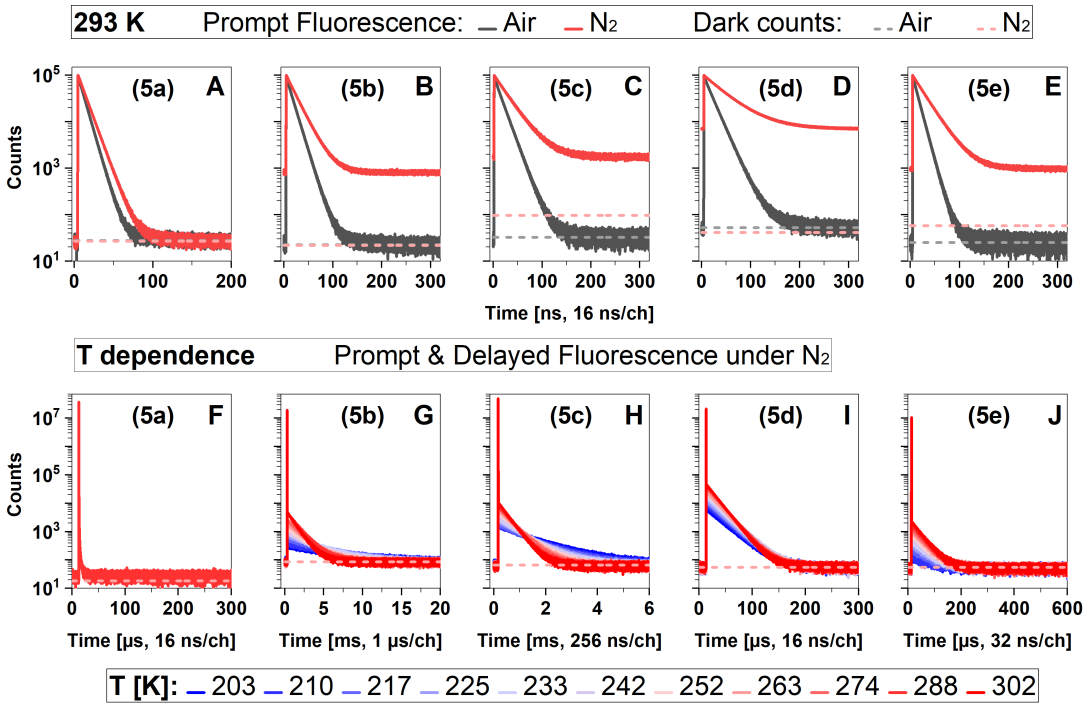

Figure 3. A-E: Prompt fluorescence of compounds **5a-5e** in air-saturated and nitrogen-purged solutions in toluene measured by TCSPC. **F-J:** Prompt and delayed fluorescence of compounds **5a-5e** in nitrogen-purged toluene solutions. The counts corresponding to the dark count rate of the detector (93 Hz) are indicated by a light grey or light red dashed line for air-saturated or nitrogen-purged solutions, respectively. The measurement conditions are described in detail in the Experimental Section.

Compound **5a** did not exhibit TADF under these conditions (Figure 3F). As the torsion angle increases from **5b** to **5d**, the quantum yield and the amplitude of TADF increase, and the TADF lifetime becomes shorter. This study presents an effective design strategy for improving TADF properties in compounds by fine-tuning the steric torsion at the donor-acceptor linker and ensuring a substantial spatial separation between hole and electron densities.

Compound **5e**, despite possessing nearly identical torsion angle as **5b** ([a] Molecule A. [b] Molecule B. See Figures S29-S33. [c] The second minimum of **5c** can only be seen in a two-dimensional scan in which θ_{D-A} and the isopropyl rotation angle ω are varied (**see** B).

Figure 1D), demonstrates enhanced TADF features due to its increased donor strength. However, due to the very low prompt fluorescence quantum yield of **5e**, compound **5b** remains brighter under nitrogen where both prompt and delayed fluorescence are operative (see Φ_{TF} in

Table ***1***).

Kinetic model

The simplest model, consistent with theoretical predictions for this class of fluorophores,[11] is a three-state system with small energy gap between the excited S_1 and T_1 states. The corresponding rate matrix (eq. S22) has been solved analytically and yields relaxation times for prompt and delayed fluorescence, $1/k_p$ and $1/k_d$, respectively (eqs. S23 and S24). These two observables are not sufficient to independently determine all rate constants involved in this kinetic scheme. Tsuchiya *et al.*[23] presented an approach to incorporate quantum yields, in particular the relative fraction of the delayed fluorescence, $P_d = F_d/(F_p+F_d)$, as additional independent observable for each temperature. Assuming negligible direct relaxation of T_1 to the ground state, i.e., $k_{r\_T} + k_{nr\_T} \equiv k_T \ll k_{rISC}$, three primary rate constants (k_{ISC}, k_{rISC} and $k_S \equiv k_{rad\_S} + k_{IC\_S}$) now are readily available:

$$k_{rISC} = k_d(1 - P_d)^{-1} \quad (2)$$

$$k_{ISC} = k_p P_d - k_d((P_d)^{-1} - 1)^{-1} \quad (3)$$

$$k_{rad\_S} + k_{IC\_S} = k_S = k_p(1 - P_d) \quad (4)$$

The disregard of k_T is justified by the observed temperature dependence of k_{rISC} (see Figure 4). The Marcus plots show no indication for the appearance of a second process depopulating T_1 at low temperatures. This would have to be expected since k_T is assumed to have a much smaller temperature dependence than k_{rISC} and should dominate the T_1 depopulation in that temperature range.

The derived intersystem crossing rates, $k_{ISC}(T)$, of compound **5b-5e** showed a clear increase with rising temperatures (Figure 4), indicating an activated process. Thus, we postulate an expanded kinetic model by adding a transition to a higher triplet state T_2 (Scheme 2).

Assuming $k_{IC\_T} \gg k_{ISC}(2)$ this system behaves like a pseudo three-state system with $k_{ISC} = k_{ISC}(1) + k_{ISC}(2)$.

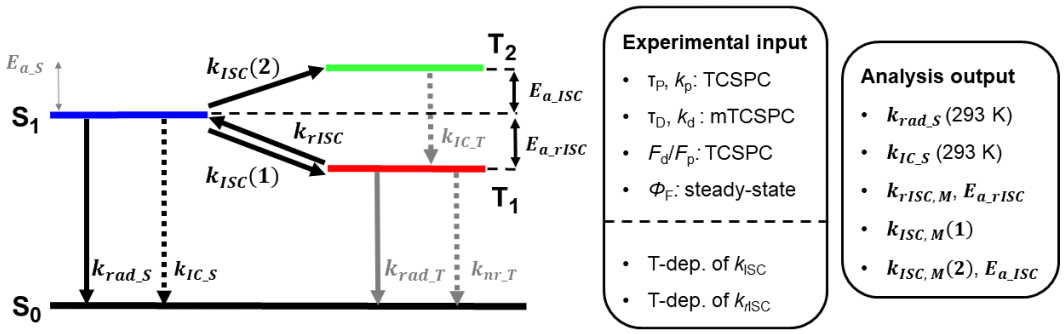

Scheme 2. 4-state system. *Experimental input*: The temperature-dependence of k_{ISC} and k_{rISC} were not directly obtained from the measurements. *Assumptions*: (i) Negligible direct relaxation of T_1 to the ground state, i.e., $k_{rad\_T} + k_{nr\_T} \equiv k_T \ll k_{rISC}$; and (ii) Internal conversion from T_2 to T_1 is a very fast process, i.e., $k_{IC\_T} \gg k_{ISC}(2)$. Thus, this system behaves like a pseudo three-state system. *Analysis output*: k_{rad_S} and k_{IC_S} follow the Arrhenius approach, while k_{rISC} and k_{ISC} are described using Marcus theory (denoted with a subscript 'M'). The activation energy E_{a_ISC} always refers to the energy required for intersystem crossing from the S_1 to T_2 state, as no activation energy is required for intersystem crossing from S_1 to T_1. For further details, see equations 5-9.

Marcus & Arrhenius plots

Rate constants related to spin conversion processes are often described using Marcus theory.[24] For the rate constants of reverse intersystem crossing and intersystem crossing, we obtain:

$$k_{rISC} = \frac{k_{0\_rISC}}{\sqrt{T}} e^{-(E_{a\_rISC})/kT} \quad (5)$$

$$\Rightarrow k_{rISC}\sqrt{T} = k_{0\_rISC}\, e^{-(E_{a\_rISC})/kT} \quad (6)$$

and

$$k_{ISC} = \frac{k_{ISC,M}(1)}{\sqrt{T}} + \frac{k_{0\_ISC,M}(2)}{\sqrt{T}} e^{-(E_{a\_ISC}(2))/kT} \quad (7)$$

$$\Rightarrow k_{ISC}\sqrt{T} = k_{ISC,M}(1) + k_{0\_ISC,M}(2)\, e^{-(E_{a\_ISC}(2))/kT}, \quad (8)$$

respectively. The sums of the radiative and nonradiative rates from S_1 to the ground state are described by an Arrhenius type approach:

$$k_{rad\_S} + k_{IC\_S} = k_S = k_{0\_S}\, e^{-(E_{a\_S})/kT} \quad (9)$$

The temperature dependence of the rate constants described by the Marcus and Arrhenius approach (see equations 5-9) are shown Figure 4. The final primary kinetic parameters resulting from fits to the corresponding Marcus and Arrhenius plots are given in Table 2.

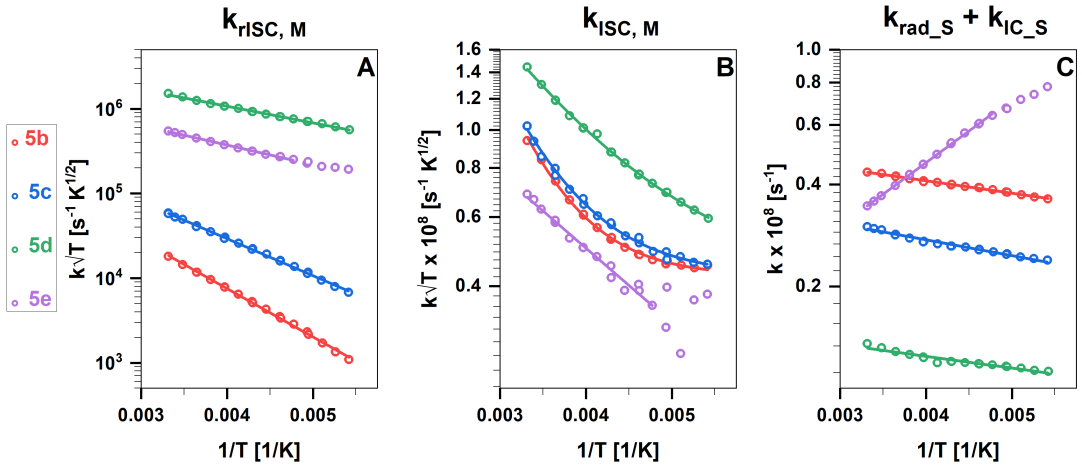

Figure 4. Temperature dependence of k_{rISC} (Panel **A**) and k_{ISC} (Panel **B**) is analysed using the Marcus approach (subscript 'M', see equations 5-8). Panel **C** shows the sum of radiative and nonradiative rate constants from S_1 to the ground state ($k_{rad\_S} + k_{IC\_S}$) based on the Arrhenius approach (eq. 9). The raw data can be found in SI Chapter 3.8, Figure S48 and Tables S17-S20. Data for compound **5e** below 220 K was excluded from the fits due to increased noise levels caused by aggregation (see Figure S52).

Table 2. The final primary kinetic parameters obtained from the fits shown in Figure 4. See equations 5-9 for further details.

Compound		**5b**	**5c**	**5d**	**5e**
$k_{ISC}(1)$	[10^6 s^{-1} $K^{½}$]	42.4 ± 0.4	42.6 ± 0.8	40 ± 2	0 (fixed)
$k_{0\_ISC}(2)$	[10^9 s^{-1} $K^{½}$]	13 ± 3	6 ± 2	1.4 ± 0.2	0.29 ± 0.02
$E_{a\_ISC,M}(2)$	[meV]	142 ± 5	122 ± 6	67 ± 3	38 ± 2
k_{0_rISC}	[10^6 s^{-1} $K^{½}$]	1.45 ± 0.09	1.64 ± 0.07	6.5 ± 0.2	3.19 ± 0.09
$E_{a\_rISC,M}$	[meV]	113 ± 2	86.7 ± 0.8	39.0 ± 0.5	46.2 ± 0.6
k_{0_S}	[10^6 s^{-1}]	57.5 ± 0.4	42.2 ± 0.7	17.2 ± 0.4	8.3 ± 0.1

E_{a_S}	[meV]	7.3 ± 0.2	9.3 ± 0.3	7.0 ± 0.5	-37.0 ± 0.3
k_{ISC} (296 K)	[10^6 s^{-1}]	5.27	5.55	8.02	3.81
k_{rISC} (296 K)	[10^3 s^{-1}]	0.99	3.18	82.6	29.6
k_{rad_S} (296 K)	[10^6 s^{-1}]	29.0	19.6	11.2	14.3
k_{IC_S} (296 K)	[10^6 s^{-1}]	14.3	9.7	1.9	21.2

With increasing steric hindrance from **5b** to **5d** we observe a reduction of the activation energies for intersystem crossing and reverse intersystem crossing, E_{a_ISC} and E_{a_rISC} respectively, while the activation energy E_{a_S} is very similar for all three compounds (Figure 4).

To prove the necessity of a 4-state model, we conducted relaxed TDDFT scans of the energy profiles of the first excited singlet and triplet states along the torsional coordinate. Figure 5 presents relaxed S_1 (first row) and T_1 (second row) scans, along with the corresponding static dipole moments (third row). The results obtained using DFT/MRCI are summarized in so-called state diagrams (fourth row). For compounds **5b** (left column), **5d** (middle column) and **5e** (right column), it is evident that the minima of the triplet states occur at significantly lower dihedral angles compared to the singlet states. As expected, the energy gap between the lowest excited CT states decreases when the donor and acceptor moieties are arranged orthogonally.

However, the results from the relaxed T_1 scans require a more detailed analysis. Notably, the static dipole moments of the triplet states exhibit significant changes near an orthogonal orientation of the donor and acceptor moieties. Between 85 and 95°, a state switch occurs, leading to the LE(TPN) triplet state becoming the lowest in energy. The DFT/MRCI state diagrams further corroborate this finding, clearly showing that for compounds **5b** and **5d**, the states switch, with the locally excited triplet state having its minimum geometry at 90°. In contrast, for compound **5e**, due to the increased donor strength, the CT and LE regimes are too energetically separated for such a state switch to occur.

From both a theoretical and experimental perspective, the application of a 4-state model is essential for accurately describing these systems.

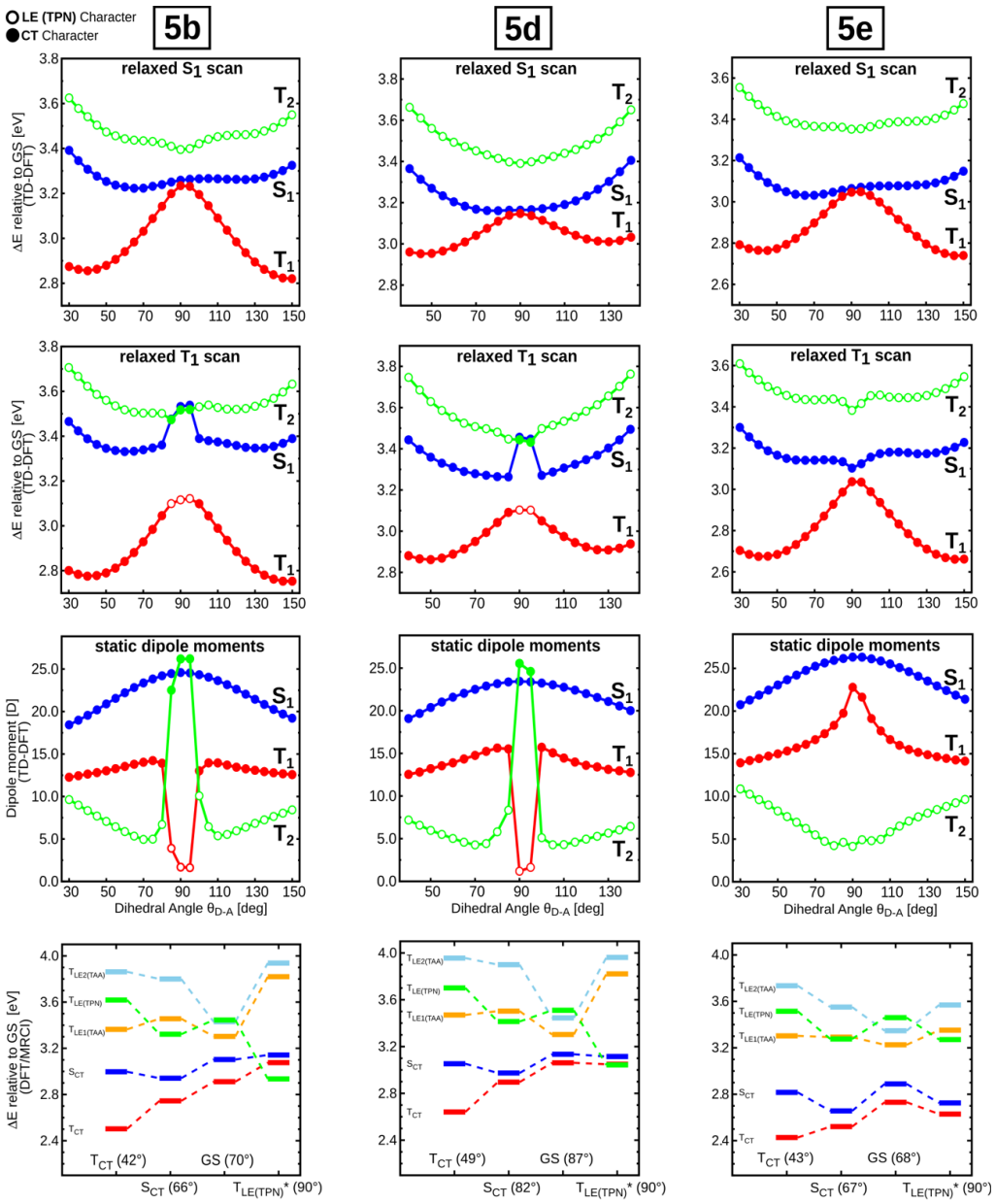

Figure 5. Relaxed scans of the lowest excited singlet and triplet state potential energy surface (S_1: first row, T_1: second row) as well as the static dipole moments of S_1, T_1 and T_2 states (third row) along the donor-acceptor dihedral angles for compound **5b**, **5d** and **5e** computed at TD-DFT level of theory. A change between CT (solid circles) and LE(TPN) character (hollow circles) can be observed close to orthogonality for compound **5b** and **5d**. Energy level diagrams comprising the vertical excitation energies for various excited states at different optimized geometries (x-axis) of compound **5b**, **5d** and **5e** computed at DFT/MRCI level of theory (fourth row). The * denotes that this geometry is not a minimum geometry but was optimized with a restricted dihedral angle between the donor and acceptor.

Discussion of kinetic parameters

From Figure 5 bottom panels we can extract the vertical energy differences between the lowest excited S_{CT} and T_{LE} states that are used to compute the rate constants using Marcus theory. We illustrated the influence of the steric constraints on these vertical energies from compound **5b** to compound **5d** (Figure 6A). From the resulting scheme we can estimate the transition barrier for the ISC process (S_{CT} ⇝T_{LE}) which decreases within the series. This agrees nicely with the experimental values (E_{a_ISC}) given in Table 2.

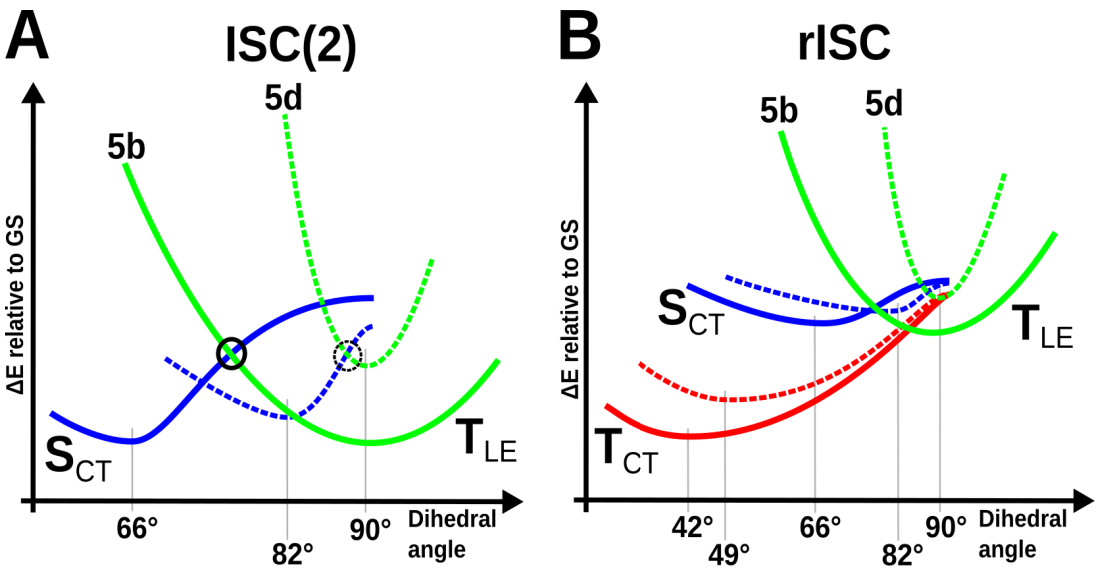

Figure 6. A: Schematic picture of the potential energy surfaces (PES) of S_{CT} and T_{LE} according to Marcus theory for **5b** (solid line) and **5d** (dashed line). The crossing point of the PES is an estimate for the transition barrier for (r)ISC process and is encircled in black. **B**: Schematic picture of the potential energy surfaces of $S_{CT,}$ T_{CT} and T_{LE} involved in the excited-state decay pathway of **5b**.

Due to large geometrical changes one cannot simply draw a Marcus-like picture to understand the corresponding rISC process. Within a separate theoretical study of these systems[25] we conclude that the rISC process is strongly dependent on the dihedral angle and that it can only occur if donor and acceptor are aligned nearly perpendicularly to each other. In that region we see a strong correlation between the lowest excited CT states and the lowest excited LE state.

Discussion of previously published data on 5b

The photophysical behaviour of compound **5b** has been investigated previously in Ref. 11. The general observation of TADF could only be confirmed qualitatively, the exact numbers for rate constants of ISC and rISC, k_{ISC} and k_{rISC}, and their dependence on temperature differ substantially in the current study. We have clear evidence that this deviation is caused by triplet quenching by residual oxygen in the previous measurements. A simple model assuming diffusion-controlled quenching was applied to simulate the effect (see Figure S51). Adding triplet quenching to the kinetic system will add an extra channel to depopulate the triplet and thus increase the apparent k_{rISC}, as reported. At the same time the temperature dependence of that rate will change, since the apparent activation energy for rISC (E_{a_rISC}) will now be affected by the temperature dependent diffusion coefficient of **5b** and O_2. We were able to quantitatively reproduce the published data and explain all experimental discrepancies using this approach (see SI Chapter 3.11).

Conclusion

To be filled in

Experimental Section

Spectroscopic conditions

Absorption spectra were measured on a Cary 4000 UV-Vis spectrophotometer (Agilent Technologies, USA), while fluorescence spectra were recorded on a Horiba Fluorolog FL3-22 spectrophotometer. Time-resolved measurements were conducted with a fluorescence lifetime and steady-state spectrometer FT300 (PicoQuant, Germany) equipped with a ColdEdge cryostat powered by a Sumitomo CH-204 cold head and HC-4E Helium compressor (Cryoandmore, Germany). Temperatures were regulated by a temperature controller, Model 335 (Lake Shore Cryotronics, USA), using a silicon diode sensor at the cold head. Sample temperatures were measured independently with a second diode (Model 540 group B, Scientific Instruments, USA; accuracy: ± 0.5 K) and used for all analyses. All samples were measured in UV Quartz Type Hellma QS 221.001 Fluorescence Cuvette Cells with an extension made of Quartz/Duran glass mixture. The light path was 10 mm. For the steady-state and time-resolved measurements in the nanosecond time regime, samples were excited with a supercontinuum laser excitation source (EXW-12 with EXTEND-UV spectral extension unit, NKT Photonics, Denmark). An excitation wavelength of 375 nm was set by tuning the frequency doubler. Time-correlated single photon counting (TCSPC) was achieved with HydraHarp 400 electronics (PicoQuant, Germany). The repetition rate was 4.88 MHz for **5a**, and 3.12 MHz for **5b-5e**. The time bin was 16 ps. For the time-resolved measurements in the microsecond and millisecond time ranges, samples were excited with a modulated continuous wave diode laser (Cobolt 375 nm MLD laser, Series 06-01, Hübner Photonics, Germany). In both cases, the excitation wavelength was 375 nm. A TCSPC and MCS board, Time Harp 260 (PicoQuant, Germany), provided photon counting and timing. The repetition rates were: 3.33 kHz for **5a** and **5d**, 0.05 kHz for **5b**, 0.15 kHz for **5c**, and 1.67 kHz for **5e**. The bin sizes were 16 ns for **5a** and **5d**, 1 μs for **5b**, 256 ns for **5c**, and 32 ns for **5e**. Signal detection was achieved with a hybrid PMT detector (PMA Hybrid 40, PicoQuant, Germany). Emission was detected under magic angle conditions. The detection wavelength was 490 nm for compounds **5a-5d**, and 560 nm for **5e**. All time-resolved measurements were conducted with a scripted measurement routine.

Analysis of time- and temperature-resolved data

Prompt (ns) fluorescence decays

A multi-exponential model function was fitted to the data using Python based custom software (Pyfia) applying an iterative reconvolution procedure. The instrumental function (IRF) was acquired measuring scattered light off a diluted Ludox® solution. Almost always three decay components were needed to fit the data (see SI), the fastest decay reflecting the highly quenched fluorescence of the aggregates (see below). The second fastest fraction (average photon fraction 1-2 %) is most likely due to a small portion of less quenched species. This was found in **5b-5d**. The remaining prompt fluorescence of the monomers was found to be monoexponential.

Delayed (µs & ms) fluorescence decays

To extract decay parameters from the time-resolved delayed fluorescence experiments a custom written LabView based batch routine was applied to fit a biexponential model function to the data. The short lifetime component represents the prompt fluorescence, broadened by the resolution of the experimental set-up ($\tau \approx 2$ µs) and was not further processed. The delayed fluorescence of the monomers was found to be monoexponential.

Offset analysis

The well-separated decay times for prompt and delayed fluorescence allowed for determination of the relative delayed fraction in the ns-decays by calculating the virtually constant offset generated by the delayed signal. Here only the dark count rate of the detector of 93 Hz needed to be considered. For more details, see SI chapter 3.3.2.

Computational Details

Molecular geometries and vibrational frequencies were determined with Gaussian 16[26] employing the optimally tuned, range-separated ωB97X-D density functional[27, 28] and the split-valence double zeta def2-SV(P) basis set.[29-31] The optimal tuning procedure followed the scheme recommended in Ref. 32, yielding a value of ω=0.15 for the range separation parameter. Geometries of singlet excited states were optimized with time-dependent density functional theory (TDDFT).[33-35] For triplet states, the Tamm-Dancoff approximation (TDA)[36] was employed. The polarizable continuum model (PCM)[37-39] was utilized to mimic the toluene solvent environment using the solvent excluding surface (SES) implemented in Gaussian 16. Excitation energies and excited-state properties were determined with the combined density functional theory and multireference configuration interaction (DFT/MRCI) method[40-42] using the tight R2016[43] parameter set. More detailed quantum chemical investigations of the emitter series were conducted in Ref. 25.

References

1. Y.-Z. Shi, H. Wu, K. Wang, J. Yu, X.-M. Ou and X.-H. Zhang, *Chemical Science*, 2022, **13**, 3625-3651.
2. X.-K. Chen, D. Kim and J.-L. Brédas, *Accounts of Chemical Research*, 2018, **51**, 2215-2224.
3. C. Adachi, *Japanese Journal of Applied Physics*, 2014, **53**, 060101.
4. F. Fang, L. Zhu, M. Li, Y. Song, M. Sun, D. Zhao and J. Zhang, *Advanced Science*, 2021, **8**, 2102970.
5. M. A. Bryden and E. Zysman-Colman, *Chemical Society Reviews*, 2021, **50**, 7587-7680.
6. S.-J. Zou, Y. Shen, F.-M. Xie, J.-D. Chen, Y.-Q. Li and J.-X. Tang, *Materials Chemistry Frontiers*, 2020, **4**, 788-820.
7. J. Bauri, R. B. Choudhary and G. Mandal, *Journal of Materials Science*, 2021, **56**, 18837-18866.
8. M. Zheng, Y. Li, Y. Wei, L. Chen, X. Zhou and S. Liu, *The Journal of Physical Chemistry Letters*, 2022, **13**, 2507-2515.
9. Paras, A. Dhiman and C. N. Ramachandran, *Chemical Physics Letters*, 2022, **801**, 139711.
10. P. Stachelek, J. S. Ward, P. L. Dos Santos, A. Danos, M. Colella, N. Haase, S. J. Raynes, A. S. Batsanov, M. R. Bryce and A. P. Monkman, *ACS Appl Mater Interfaces*, 2019, **11**, 27125-27133.
11. G. A. Sommer, L. N. Mataranga-Popa, R. Czerwieniec, T. Hofbeck, H. H. H. Homeier, T. J. J. Müller and H. Yersin, *The Journal of Physical Chemistry Letters*, 2018, **9**, 3692-3697.
12. W. Haselbach, J. M. Kaminski, L. N. Kloeters, T. J. J. Müller, O. Weingart, C. M. Marian, P. Gilch and B. E. Nogueira de Faria, *Chemistry*, 2023, **29**, e202202809.
13. C. Sambiagio, S. P. Marsden, A. J. Blacker and P. C. McGowan, *Chemical Society Reviews*, 2014, **43**, 3525-3550.
14. A. W. Franz and T. J. J. Müller, *Synthesis*, 2008, **2008**, 1121-1125.
15. J. Sandström, *Dynamic NMR Spectroscopy*, Academic Press, 1982.
16. E. Rochlin and Z. Rappoport, *The Journal of Organic Chemistry*, 1994, **59**, 3857-3870.
17. M. S. Sundar, G. Singh, R. S. Ampapathi and A. V. Bedekar, *Journal of Molecular Structure*, 2017, **1147**, 495-501.
18. W. W. Parson, *Modern optical spectroscopy*, Springer, 2007.
19. M. Fischer and J. Georges, *Chemical Physics Letters*, 1996, **260**, 115-118.
20. J. Lakowicz, *University of Maryland School of Medicine Baltimore*, 2006, **132**.
21. H. Kautsky, *Transactions of the Faraday Society*, 1939, **35**, 216-219.
22. S. J. Strickler and R. A. Berg, *The Journal of Chemical Physics*, 1962, **37**, 814-822.
23. Y. Tsuchiya, S. Diesing, F. Bencheikh, Y. Wada, P. L. dos Santos, H. Kaji, E. Zysman-Colman, I. D. W. Samuel and C. Adachi, *The Journal of Physical Chemistry A*, 2021, **125**, 8074-8089.

24. Y. Tsuchiya, K. Mizukoshi, M. Saigo, T. Ryu, K. Miyata, K. Onda and C. Adachi, *Faraday Discussions*, 2024, **250**, 233-250.
25. J. M. Kaminski, T. Böhmer and C. M. Marian, *The Journal of Physical Chemistry C*, 2024, **128**, 13711-13721.
26. M. J. Frisch, G. W. Trucks, H. B. Schlegel, G. E. Scuseria, M. A. Robb, J. R. Cheeseman, G. Scalmani, V. Barone, G. A. Petersson, H. Nakatsuji, X. Li, M. Caricato, A. V. Marenich, J. Bloino, B. G. Janesko, R. Gomperts, B. Mennucci, H. P. Hratchian, J. V. Ortiz, A. F. Izmaylov, J. L. Sonnenberg, Williams, F. Ding, F. Lipparini, F. Egidi, J. Goings, B. Peng, A. Petrone, T. Henderson, D. Ranasinghe, V. G. Zakrzewski, J. Gao, N. Rega, G. Zheng, W. Liang, M. Hada, M. Ehara, K. Toyota, R. Fukuda, J. Hasegawa, M. Ishida, T. Nakajima, Y. Honda, O. Kitao, H. Nakai, T. Vreven, K. Throssell, J. A. Montgomery Jr., J. E. Peralta, F. Ogliaro, M. J. Bearpark, J. J. Heyd, E. N. Brothers, K. N. Kudin, V. N. Staroverov, T. A. Keith, R. Kobayashi, J. Normand, K. Raghavachari, A. P. Rendell, J. C. Burant, S. S. Iyengar, J. Tomasi, M. Cossi, J. M. Millam, M. Klene, C. Adamo, R. Cammi, J. W. Ochterski, R. L. Martin, K. Morokuma, O. Farkas, J. B. Foresman and D. J. Fox, *Journal*, 2016.
27. J.-D. Chai and M. Head-Gordon, *The Journal of Chemical Physics*, 2008, **128**.
28. J.-D. Chai and M. Head-Gordon, *Physical Chemistry Chemical Physics*, 2008, **10**, 6615-6620.
29. A. Schäfer, H. Horn and R. Ahlrichs, *The Journal of Chemical Physics*, 1992, **97**, 2571-2577.
30. F. Weigend and R. Ahlrichs, *Physical Chemistry Chemical Physics*, 2005, **7**, 3297-3305.
31. F. Weigend, *Physical Chemistry Chemical Physics*, 2006, **8**, 1057-1065.
32. O. S. Bokareva, G. Grell, S. I. Bokarev and O. Kühn, *Journal of Chemical Theory and Computation*, 2015, **11**, 1700-1709.
33. E. Runge and E. K. U. Gross, *Physical Review Letters*, 1984, **52**, 997-1000.
34. M. Marques and E. Gross, *Lecture Notes in Physics*, 2003, **620**, 144-184.
35. F. Furche and R. Ahlrichs, *The Journal of Chemical Physics*, 2002, **117**, 7433-7447.
36. S. Hirata and M. Head-Gordon, *Chemical Physics Letters*, 1999, **314**, 291-299.
37. R. Cammi, S. Corni, B. Mennucci and J. Tomasi, *The Journal of Chemical Physics*, 2005, **122**.
38. J. Tomasi, B. Mennucci and R. Cammi, *Chemical Reviews*, 2005, **105**, 2999-3094.
39. G. Scalmani, M. J. Frisch, B. Mennucci, J. Tomasi, R. Cammi and V. Barone, *The Journal of Chemical Physics*, 2006, **124**.
40. S. Grimme and M. Waletzke, *The Journal of Chemical Physics*, 1999, **111**, 5645-5655.
41. C. M. Marian, A. Heil and M. Kleinschmidt, *WIREs Computational Molecular Science*, 2019, **9**, e1394.
42. M. Kleinschmidt, C. M. Marian, M. Waletzke and S. Grimme, *The Journal of Chemical Physics*, 2009, **130**.
43. I. Lyskov, M. Kleinschmidt and C. M. Marian, *The Journal of Chemical Physics*, 2016, **144**.

SUPPLEMENTARY INFORMATION

The effect of conformational constraints and oxygen quenching on TADF in donor-acceptor systems

Dragana Sretenović,[a] Laura N. Kloeters,[b] Jeremy M. Kaminski,[c] Tobias Böhmer,[c] Philipp Schmeinck,[d] Suren Felekyan,[a] Oleg Opanasyuk,[a] Gereon A. Sommer,[b] Mina Chalani,[a] Guido J. Reiß,[d] Christoph Janiak,[d] (Christel M. Marian,*[c] Ralf Kühnemuth,*[a] Thomas J. J. Müller*[b] and Claus A. M. Seidel*[a])

[a] Dr. D. Sretenović, Dr. S. Felekyan, Dr. O. Opanasyuk, M. Chalani, Dr. R. Kühnemuth, Prof. Dr. C. A. M. Seidel
Institut für Physikalische Chemie
Mathematisch-Naturwissenschaftliche Fakultät
Heinrich-Heine-Universität Düsseldorf
Universitätsstr. 1, 40225 Düsseldorf, Germany
E-Mail: ralf.kuehnemuth@hhu.de, cseidel@hhu.de

[b] Dr. L. N. Kloeters, Dr. G. A. Sommer, Prof. Dr. T. J. J. Müller
Institut für Organische Chemie und Makromolekulare Chemie
Mathematisch-Naturwissenschaftliche Fakultät
Heinrich-Heine-Universität Düsseldorf
Universitätsstr. 1, 40225 Düsseldorf, Germany
E-Mail: ThomasJJ.Mueller@uni-duesseldorf.de

[c] J. M. Kaminski, T. Böhmer, Prof. Dr. C. M. Marian
Institut für Theoretische Chemie und Computerchemie
Mathematisch-Naturwissenschaftliche Fakultät
Heinrich-Heine-Universität Düsseldorf
Universitätsstr. 1, 40225 Düsseldorf, Germany
E-Mail: christel.marian@hhu.de

[d] Dr. P. Schmeinck, Dr. G. J. Reiß, Prof. Dr. C. Janiak
Institut für Anorganische Chemie und Strukturchemie
Mathematisch-Naturwissenschaftliche Fakultät
Heinrich-Heine-Universität Düsseldorf
Universitätsstr. 1, 40225 Düsseldorf, Germany

Manuscript stage: In preparation for *Chemical Science.* The current version can be subjected to further changes such as adding or removing text or figures as well as author contributions.

The results included in this Supplementary Information are limited to the spectroscopic and theoretical data necessary for a proper understanding of the manuscript. Information on the synthesis and crystallographic data of **5b** is already available in the original publication by Sommer *et al*.[29]

Table of Contents

Chapter 1. Spectroscopy

1.1 Absorption and Steady-State Fluorescence Emission Spectra

Absorption and fluorescence spectra were redrawn in wavenumber scale ($\tilde{\nu}$). The absorption spectra were corrected by dividing the extinction coefficient by the wavenumber: $\varepsilon(\tilde{\nu})/\tilde{\nu}$, and the fluorescence spectra by dividing the fluorescence intensity by $\tilde{\nu}^3$.[12] Subsequently, both the corrected absorption and fluorescence spectra were normalized to their respective maximum (Figure S1).

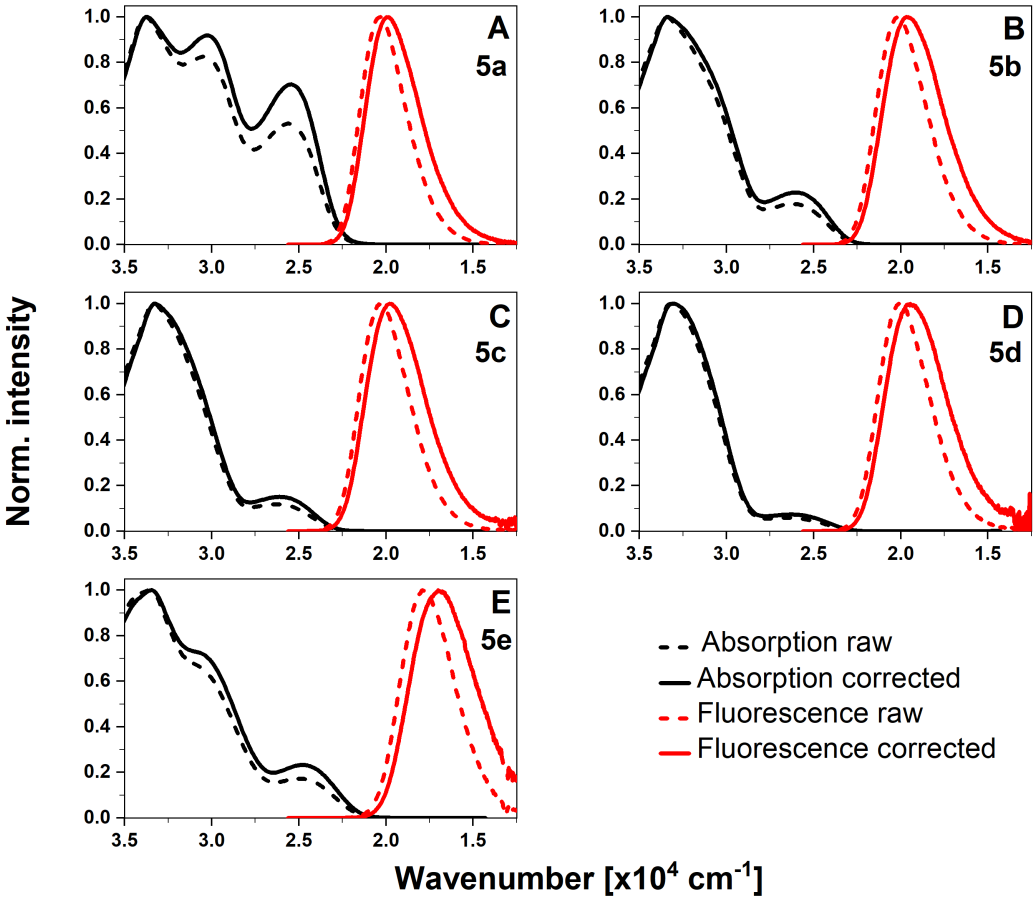

Figure S1. Absorption and fluorescence emission spectra of compounds **5a-5e** presented with and without corrections for comparison.

We derived several values from the corrected steady-state spectra, including the 0-0 energy ($\tilde{\nu}_{00}$), the full width at half maximum (FWHM) of the emission band, Stokes shift ($\Delta\tilde{\nu}_s$),

and radiative rate constants calculated according to the Strickler-Berg method (k_F^{SB}). All estimated values are compiled in Table 1 of the main text. The 0-0 energies ($\tilde{\nu}_{00}$) were determined as the intersection point between the corrected absorption and fluorescence emission spectra and ranged from 22472 cm^{-1} (**5a**) to 22676 cm^{-1} (**5c**). To calculate the FWHM of the emission band, we measured the distance in wavenumber units between two points with a normalized intensity of 0.5. The Stokes shift was determined as the distance between the first absorption maxima and the fluorescence maxima. To find the first absorption maximum, we deconvoluted the absorption spectra using a Gaussian fit. The calculated Stokes shift increased from 5421 cm^{-1} for **5a** to 6385 cm^{-1} for **5d**. These Stokes shift values were used in the Lippert-Mataga analysis[13, 14] (Figure S3).

1.2 Lippert-Mataga analysis

Lippert-Mataga analysis is based on the Lippert-Mataga equation (eq. S1).[13, 14]

$$\bar{\upsilon}_A - \bar{\upsilon}_F = \frac{2}{hc}\frac{(\mu_E - \mu_G)^2}{r^3} \cdot \Delta f + constant \qquad \text{eq. S1}$$

In this equation, $\tilde{\nu}_A$ and $\tilde{\nu}_F$ represent the wavenumbers (cm^{-1}) of the absorption and emission, h is Planck's constant, c the speed of light, μ_G and μ_E indicate the dipole moments of the ground and excited states, and r corresponds to the radius of the cavity in which the fluorophore is situated.[15] The orientation polarizability is defined as:

$$\Delta f = \frac{\varepsilon - 1}{2\varepsilon + 1} - \frac{n^2 - 1}{2n^2 + 1} \qquad \text{eq. S2}$$

where ε is the dielectric constant, and n is the refractive index of the solvent.

Table S1. The solvents employed in this study with their corresponding refractive indexes (*n*), dielectric constants (ε) and calculated orientation polarizabilities (*Δf*) according to eq. S2.

Solvent	***n***	**ε**	**Δ*f***
Toluene	1.496	2.38	0.014
Methyl tert-butyl ether (MTBE)	1.369	2.60	0.074
Anisole	1.517	4.33	0.112
Chlorobenzene	1.525	5.62	0.143
Ethyl Acetate	1.372	6.08	0.201
THF	1.407	7.58	0.210
DCM	1.424	8.93	0.217
DMF	1.431	36.7	0.274
Acetonitrile	1.344	37.5	0.305

To generate Lippert-Mataga plots (Figure S3), we determined the difference of the absorption and emission maxima in wavenumbers by measuring the respective spectra of compounds **5a-5e** in toluene, methyl *tert*-butyl ether (tBuMeEther), anisole, chlorobenzene, ethyl acetate, tetrahydrofuran (THF), dichloromethane (DCM), dimethylformamide (DMF), and acetonitrile (MeCN). The measurements revealed a positive solvatochromic effect (Figure S2), typically associated with charge-transfer states and TADF.

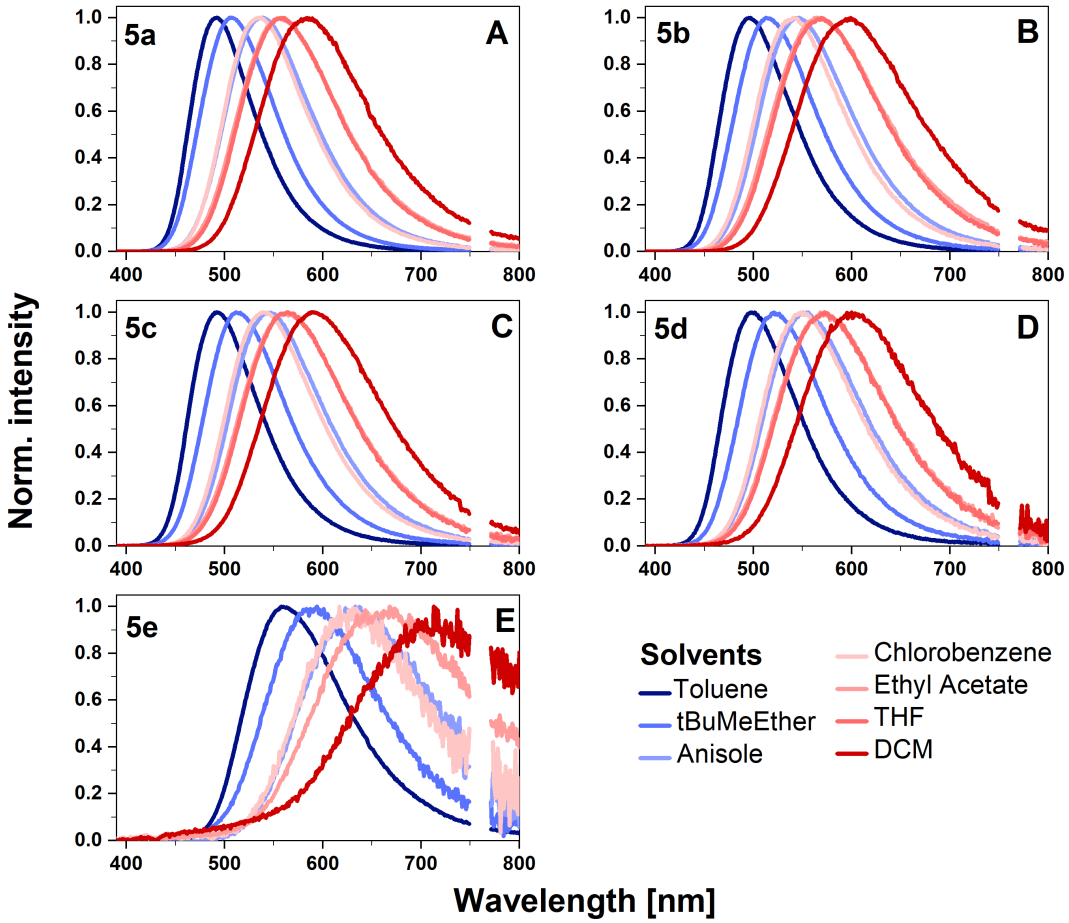

Figure S2. Fluorescence emission spectra of **5a-5e** (**A-E**) in the solvents indicated in the legend. Samples were excited at 375 nm. The range between 750 and 770 nm is excluded due to the presence of second-order diffracted excitation light.

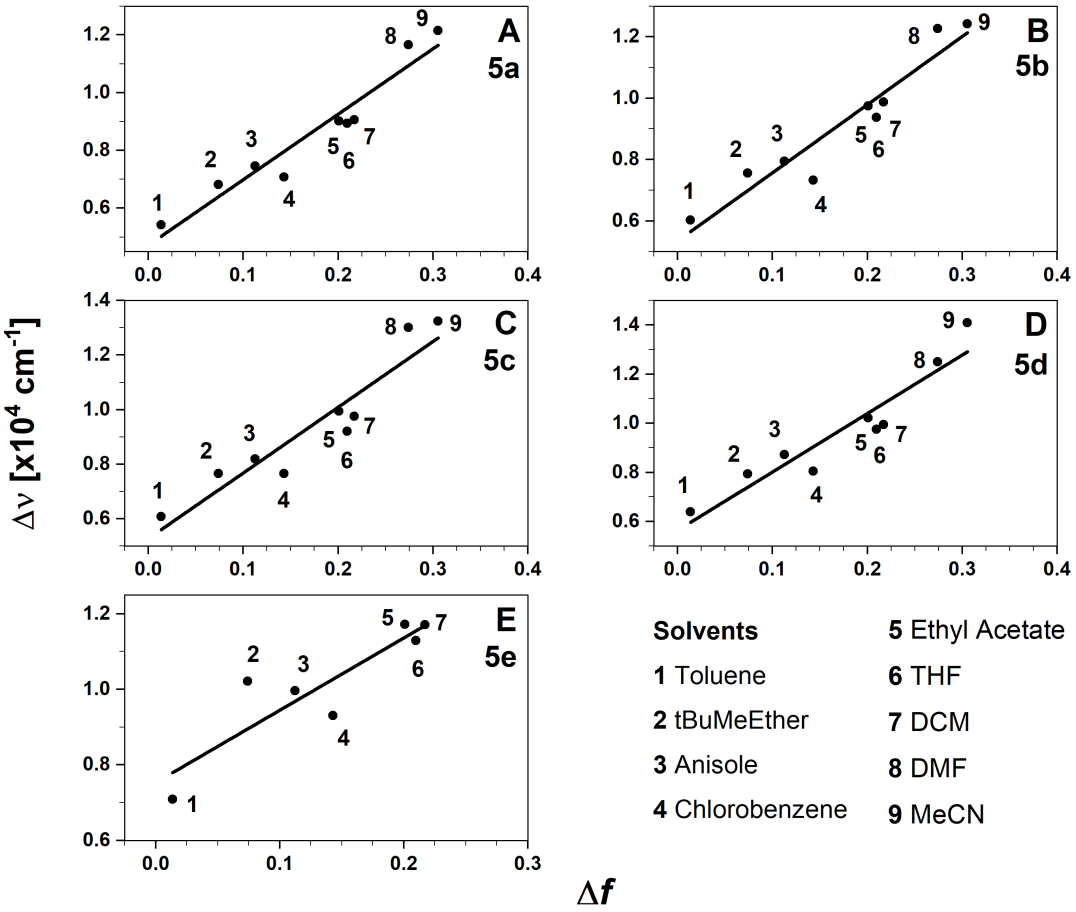

Figure S3. Lippert-Mataga diagrams for compounds **5a-5e** (**A-E**). The solvents used are marked with the numbers 1-9 and indicated in the legend. A linear regression is applied and the slopes are listed in Table S2. The Lippert-Mataga diagram of compound **5e** does not include DMF and MeCN, as the fluorescence is quenched in these solvents.

From the slope of the linear regression $\Delta\tilde{\nu}$ against Δf (Figure S3), the difference between the dipole moments of the ground and excited states can be estimated (eq. S*3*).

$$\mu_E - \mu_G = \Delta\mu = \sqrt{\frac{slope \cdot hc \cdot r^3}{2}} \qquad \text{eq. S3}$$

However, it is evident that the assumption of a spherical molecular shape is not valid for compounds **5a-5e**, and as a result, the calculated Δμ values do not accurately reflect reality. To

estimate the molecular radius, we used the theoretically predicted Δμ values, along with the slopes obtained from the Lippert-Mataga analysis (see Table S2).

Table S2. Estimation of molecular radius based on the slopes obtained from the Lippert-Mataga analysis (Figure S3) and the theoretically predicted Δμ values.

	5a	**5b**	**5c**	**5d**	**5e**
Slope [cm^{-1}], exp.	22650	22191	24094	23810	19132
μ_E-μ_G [D], theory	19.1	22.9	22.7	24.0	25.3
r (needed to get theory values) [Å]	5.5	6.2	6.0	6.2	7.0

1.3 Delayed fluorescence quantum yields

1.3.1 Approach with the steady-state data

One approach to determine the delayed fluorescence quantum yield (Φ_{DF}) uses steady-state data. In an air-saturated solution, only prompt fluorescence is observed due to the quenching of triplet states by oxygen. In a nitrogen-purged solution, both prompt and delayed fluorescence are operative. Thus, the integral of the steady-state fluorescence spectrum in air is proportional to Φ_{PF}, while in nitrogen is $\Phi_{PF} + \Phi_{DF}$.[16] However, the quantum yield of delayed fluorescence cannot be simply calculated as the difference between the steady-state fluorescence integrals in air and nitrogen as indicated in Ref. 16, since singlet states are also quenched by oxygen to a certain extent (see Table 1). The increase in the steady-state emission signal in nitrogen is therefore not only due to the delayed fluorescence, but also to the enhanced prompt fluorescence. To obtain an estimate of the delayed fluorescence quantum yield, it is important to consider the prompt fluorescence quantum yield in nitrogen ($\Phi_{PF}^{N_2}$, see eq. 1 of the main text) and not in air (Φ_{PF}^{air}) in the context of the total fluorescence emission in absence of oxygen (Φ_{TF}), eq. S4.

$$\Phi_{TF} = \Phi_{PF}^{N_2} + \Phi_{DF} \qquad \text{eq. S4}$$

The delayed fluorescence quantum yield is calculated from the eq. S5.

$$\Phi_{DF} = \Phi_{TF} - \Phi_{\mathrm{PF}}^{\mathrm{air}} \cdot \frac{\langle\tau\rangle_{\mathrm{F}}^{N_2}}{\langle\tau\rangle_{\mathrm{F}}^{\mathrm{Air}}} \qquad \text{eq. S5}$$

1.3.2 Approach with the time-resolved data (offset analysis)

Another method to assess the quantum yields of delayed fluorescence involves integrating the time-resolved decays recorded within the nanosecond time range (Table 1). The region within the decay offset in nitrogen is important because it contains long lifetime components such as delayed fluorescence (eq. S6 and eq. S7). The quantum yield of delayed fluorescence is estimated by comparing the TCSPC decay offsets obtained under air and nitrogen in the nanosecond time range (see eq. S8 and eq. S9).

$$offset\ (Air) = dark\ counts + afterpulses \qquad \text{eq. S6}$$

$$offset\ (N_2) = dark\ counts + afterpulses + F_{DF} \qquad \text{eq. S7}$$

$$F_{DF} = \int offset\ (N_2) - \int offset\ (Air) \qquad \text{eq. S8}$$

$$\Phi_{DF} = \frac{F_{DF}}{F_{PF}} \cdot \Phi_{\mathrm{PF}}^{N_2} \qquad \text{eq. S9}$$

where F_{DF} and F_{PF} are the integral fractions of delayed and prompt fluorescence.

1.4 Strickler-Berg analysis

The radiative rate constants ($k_{\mathrm{F}}^{\mathrm{SB}}$) were determined using the Strickler-Berg method,[17] by integrating the absorption and fluorescence spectra. To compute the absorption integral, we focused on the absorption band with the lowest energy, identifying it through comparison with the corresponding corrected fluorescence spectrum. This fluorescence spectrum was mirrored at the 0-0 energy point and scaled to match the height of the corrected absorption spectrum.[18] The calculated rate constants decreased from $7.4 \cdot 10^7$ s^{-1} for **5a** to $0.7 \cdot 10^7$ s^{-1} for **5d**. Furthermore, fluorescence lifetimes ($\tau_{\mathrm{F}}^{\mathrm{SB}}$) were estimated based on the radiative rate constant, accounting for the fluorescence quantum yields (eq. S10 and eq. S11, Table 1).

$$\tau_{\mathrm{F}}^{\mathrm{SB\ air}} = \frac{\phi_{\mathrm{PF}}^{\mathrm{air}}}{k_{\mathrm{F}}^{\mathrm{SB}}}$$ eq. S10

$$\tau_{\mathrm{F}}^{\mathrm{SB}\ N_2} = \frac{\phi_{\mathrm{PF}}^{N_2}}{k_{\mathrm{F}}^{\mathrm{SB}}}$$ eq. S11

However, the calculated lifetime values do not agree well with those measured by TCSPC, presumably due to the non-Condon effect.[19, 20] As the torsion angle increases in the series **5a-5d**, the discrepancies in lifetimes also grow, ranging from 9% for **5a** to 66% for **5d**.

1.5 Analysis of prompt fluorescence decays

A bi-exponential fit function is applied to characterize the experimental TCSPC data. Each emissive species is presented with its fraction (x_i) and lifetime (τ_i). Species-averaged lifetime $\langle\tau\rangle_x$ (eq. S12) and intensity-weighted lifetime $\langle\tau\rangle_F$ (eq. S13) are given, as well as the reduced χ_r^2 value as a measure of the goodness of the fit. The value $\chi_r^2 = 1$ is obtained with an optimal fit.

$$\langle\tau\rangle_x = \sum_{i=1}^{2} x_i\tau_i$$ eq. S12

$$\langle\tau\rangle_F = \frac{\sum_{i=1}^{2} x_i\tau_i^2}{\sum_{i=1}^{2} x_i\tau_i}$$ eq. S13

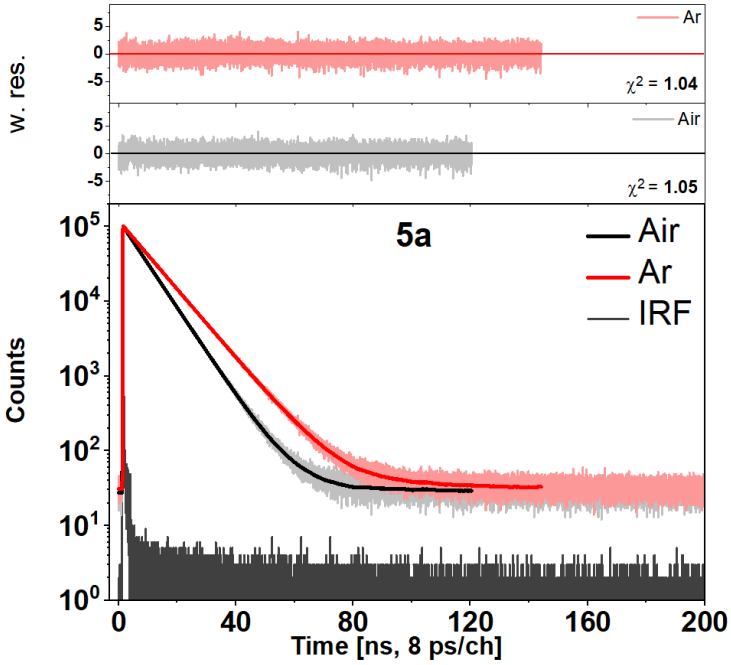

Figure S4. Prompt fluorescence of compound **5a** in air-saturated and nitrogen-purged solutions in toluene measured by TCSPC. Lifetime fit results with fixed lifetime fractions are shown in Table S3.

Table S3. Prompt fluorescence lifetime fit for compound **5a** with fixed lifetime fractions.

5a	x_1	τ_1 [ns]	x_2	τ_2 [ns]	$\langle\tau\rangle_x$ [ns]	$\langle\tau\rangle_F$ [ns]	χ_r^2
Air	0.96	7.37	0.04	0.76	7.09	7.34	1.05
Ar	0.96	9.44	0.04	0.17	9.06	9.44	1.04

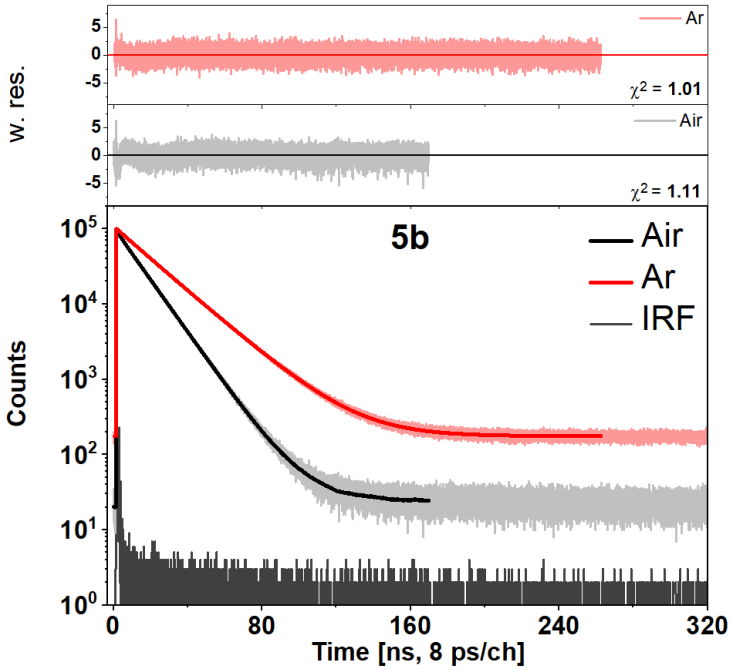

Figure S5. Prompt fluorescence of compound **5b** in air-saturated and nitrogen-purged solutions in toluene measured by TCSPC. Lifetime fit results with fixed lifetime fractions are shown in Table S4.

Table S4. Prompt fluorescence lifetime fit of compound **5b** with fixed lifetime fractions.

5b	x_1	τ_1 [ns]	x_2	τ_2 [ns]	$\langle\tau\rangle_x$ [ns]	$\langle\tau\rangle_F$ [ns]	χ_r^2
Air	0.89	12.46	0.11	1.50	11.22	12.29	1.11
Ar	0.89	20.91	0.11	14.83	20.23	20.41	1.01

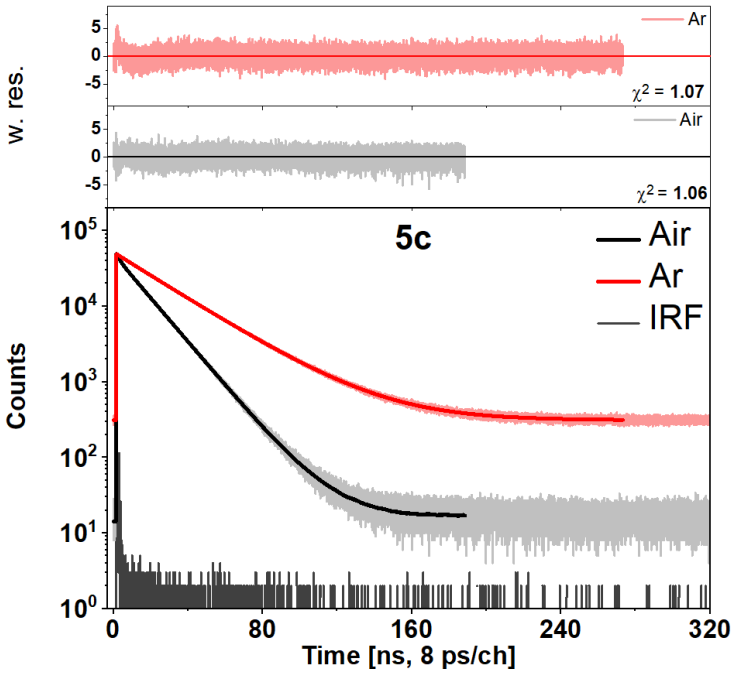

Figure S6. Prompt fluorescence of compound **5c** in air-saturated and nitrogen-purged solutions in toluene measured by TCSPC. Lifetime fit results with fixed lifetime fractions are shown in Table S5.

Table S5. Prompt fluorescence lifetime fit of compound **5c** with fixed lifetime fractions.

5c	x_1	τ_1 [ns]	x_2	τ_2 [ns]	$\langle\tau\rangle_x$ [ns]	$\langle\tau\rangle_F$ [ns]	χ_r^2
Air	0.85	14.96	0.15	1.66	13.01	14.71	1.06
Ar	0.85	29.40	0.15	21.09	28.18	28.49	1.07

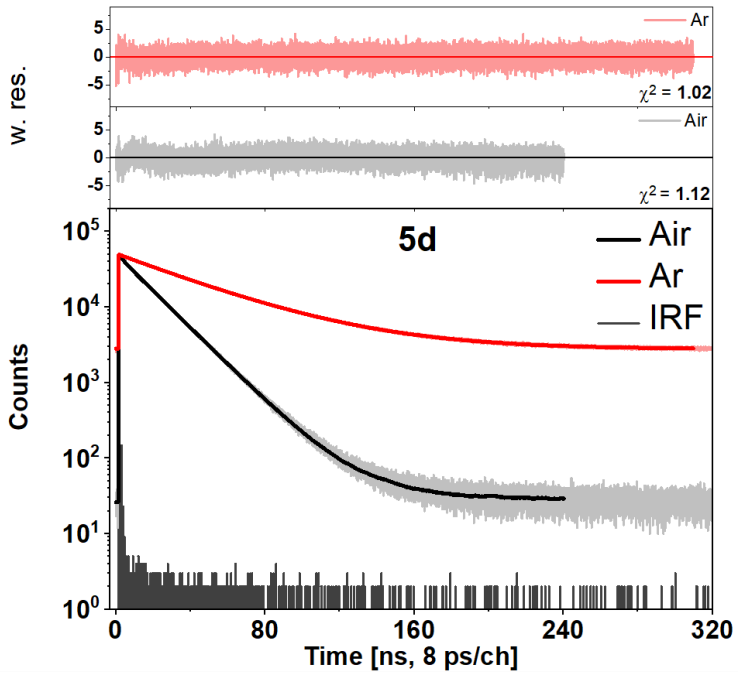

Figure S7. Prompt fluorescence of compound **5d** in air-saturated and nitrogen-purged solutions in toluene measured by TCSPC. Lifetime fit results with fixed lifetime fractions are shown in Table S6.

Table S6. Prompt fluorescence lifetime fit of compound **5d** with fixed lifetime fractions.

5d	x_1	τ_1 [ns]	x_2	τ_2 [ns]	$\langle\tau\rangle_x$ [ns]	$\langle\tau\rangle_F$ [ns]	χ_r^2
Air	0.90	17.74	0.10	2.22	16.20	17.53	1.12
Ar	0.90	47.64	0.10	30.74	45.96	46.52	1.02

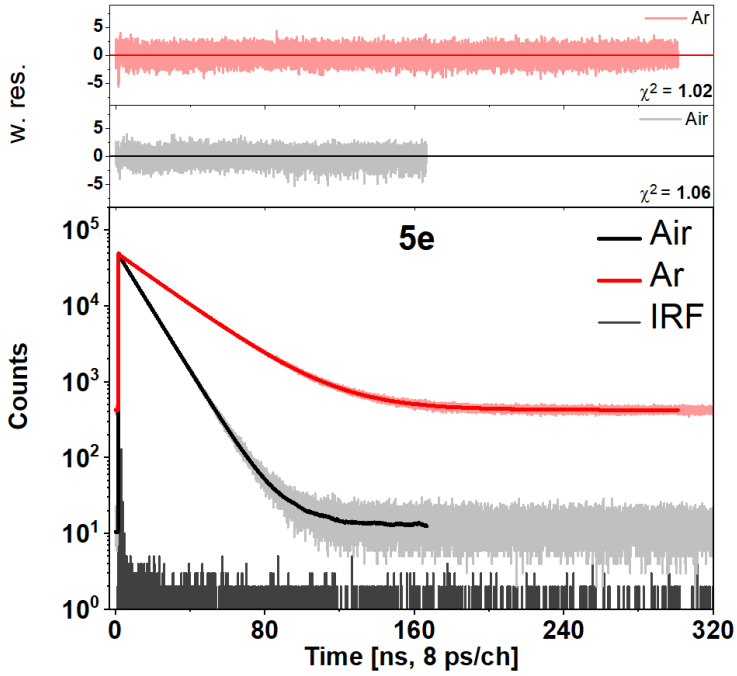

Figure S8. Prompt fluorescence of compound **5e** in air-saturated and nitrogen-purged solutions in toluene measured by TCSPC. Lifetime fit results with fixed lifetime fractions are shown in Table S7.

Table S7. Prompt fluorescence lifetime fit of compound **5e** with fixed lifetime fractions.

5e	x_1	τ_1 [ns]	x_2	τ_2 [ns]	$\langle\tau\rangle_x$ [ns]	$\langle\tau\rangle_F$ [ns]	χ_r^2
Air	0.91	10.87	0.09	0.95	9.94	10.78	1.06
Ar	0.91	24.60	0.09	0.39	22.34	24.56	1.02

1.6 Oxygen quenching

1.6.1 Singlet quenching by oxygen

By applying the Stern-Volmer equation (eq. S14), we predicted the prompt fluorescence lifetimes in air-saturated solutions [$\langle\tau\rangle^{Air}$] based on the measured prompt fluorescence lifetimes under nitrogen [$\langle\tau\rangle^{N_2}$] and a quenching constant derived from diffusion ($k_{q,diff.}$), since oxygen quenching is a diffusion-controlled process.[21] The predicted and measured air-saturated prompt fluorescence lifetimes are in excellent agreement (Table S8).

$$\langle\tau\rangle^{air} = \frac{\langle\tau\rangle^{N_2}}{1 + k_{q,diff.} \cdot \langle\tau\rangle^{N_2} \cdot [O_2]}$$ eq. S14

The oxygen concentration $[O_2]$ in toluene is 1.8 mM at 20 °C and an O_2 partial pressure of 0.213 bar.[22] The quenching constant ($k_{q,diff.}$) is calculated according to eq. S15.

$$k_{q,diff.} = 4\pi N_A (r_{dye} + r_{O_2})(D_{dye} + D_{O_2})$$ eq. S15

where N_A is the Avogadro constant, r_{dye} and r_{O2} are the radii of the fluorescent dye and oxygen, and D_{dye} and D_{O2} are the diffusivities of the fluorescent dye and oxygen, respectively. The dye radius, r_{dye}, is estimated in *PyMol* and via time-resolved anisotropy. The oxygen diffusivity in toluene is $D_{O2} = 4.38 \cdot 10^{-9}$ m^2/s.[23] The dye diffusivity, D_{dye}, is calculated using eq. S16.

$$D_{dye} = \frac{k_B T}{6\pi\eta r_{dye}}$$ eq. S16

where k_B is the Boltzmann constant, T is the temperature, η is the toluene viscosity.

Finally, the quenching constant derived from diffusion is $k_{q,diff.} = 2.1 \cdot 10^{10}$ M^{-1} s^{-1}.

Furthermore, we calculated the experimental quenching constants, $k_{q,exp}$, by using the measured lifetimes, and they are quite similar for all four compounds (around $2 \cdot 10^{10}$ M^{-1} s^{-1}, Table S8) and in good agreement with the previously determined $k_{q,diff.}$

Table S8. Predicted air-saturated prompt fluorescence lifetimes by the Stern-Volmer equation (eq. S14) and experimental quenching constants ($k_{q,exp}$) for compounds **5a-5d**. The species-averaged lifetimes, $\langle\tau\rangle_x$ are used. The ratio of predicted to the measured air-saturated prompt fluorescence lifetimes is equal to 1 for all four compounds.

Compound	Species-averaged lifetime, $\langle\tau\rangle_x$ [ns]			Ratio predicted / measured	$k_{q,exp.}$ [$\cdot 10^{10}$ M^{-1}s^{-1}]
	Air (measured)	N_2 (measured)	**Air (predicted)**		
5a	7.1	9.1	6.8	1.0	1.7
5b	11.2	20.2	11.5	1.0	2.2
5c	13.0	28.2	13.7	1.1	2.3
5d	16.2	46.0	16.9	1.0	2.2

1.6.2 Triplet quenching by oxygen

In our study, oxygen plays a crucial role as we have observed that the TADF properties of compounds **5b**-**5e** are highly dependent on the oxygen concentration in the toluene solution. It is known that oxygen efficiently quenches triplet states,[24] with longer lifetimes being more susceptible to quenching than shorter ones,[25] but the observed effect in our study was quite dramatic. This can be effectively illustrated by the Stern-Volmer plot (eq. S14, Figure S9). We calculated air-saturated lifetimes (τ^{Air}) for different oxygen concentrations with respect to specific oxygen-free lifetimes (denoted as τ^{N_2}).

The oxygen-free lifetimes include examples of (i): fast (21 ns, as prompt fluorescence of compound **5b**), (ii): slow (30 μs), and (iii): very slow (300 μs) processes. It becomes evident from Figure S9 that for fast processes such as prompt fluorescence, oxygen has limited time to act, and saturation is reached relatively quickly. Consequently, there is no difference in measured lifetimes if the concentration of oxygen in the solution is 10^{-5} M or 10^{-7} M, as both cases yield a lifetime of 21 ns. However, the scenario changes when observing slower processes, such as delayed fluorescence in the microseconds. Minor changes in oxygen concentration can lead to significant changes in measured lifetimes. In an air-saturated toluene solution, with a standard oxygen concentration of 1.8 mM,[22] we have not detected any delayed fluorescence for this particular compound series. Standard deoxygenation methods, such as bubbling or freeze-thaw procedures, can reach oxygen concentrations in the range of 10^{-6} M to 10^{-7} M.[26] However, even when reaching an oxygen concentration of 10^{-7} M in the solution, we are limited by diffusion, and only lifetimes of approximately 1 ms can be experimentally measured. At lower temperatures, this limit is exceeded since diffusion is considerably slower.

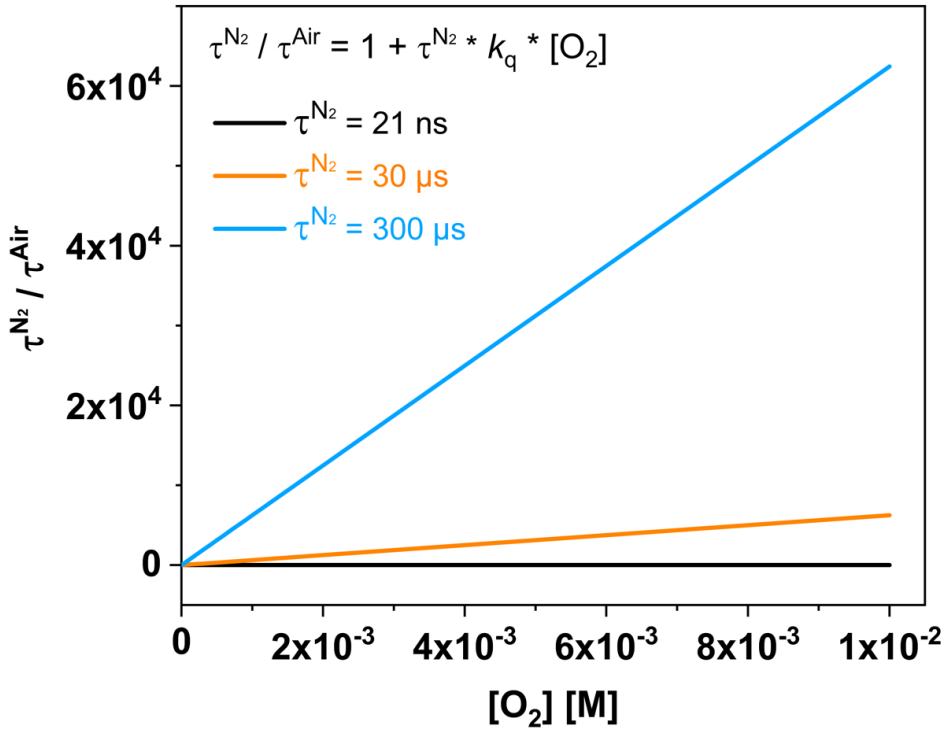

Figure S9. Oxygen quenching predicted by Stern-Volmer equation. Air-saturated lifetimes (τ^{Air}) are calculated for various oxygen concentrations in relation to specific oxygen-free lifetimes (τ^{N2}) using the Stern-Volmer equation. The selected oxygen-free lifetimes represent different process speeds: (i) fast, τ^{N2} = 21 ns; (ii) slow, τ^{N2} = 30 µs; and (iii) very slow, τ^{N2} = 300 µs.

1.7 Deoxygenation procedure

The experimental setup used for deoxygenation is shown in Figure S10. In the first step, the cryogenic UV-quartz cuvette [labelled (I)] was filled with the sample solution. One additional millilitre of solvent was added to the prepared sample to ensure that the concentration does not increase beyond the range suitable for fluorescence measurements during deoxygenation via inert gas bubbling. For this, nitrogen N5 (Air Liquide) was passed through the capillary in the sample [(II) to (III)] until the solvent level reached the initial value in the cuvette (approximately 30 min). The setup was then pressurized with nitrogen to 0.2 bar above ambient pressure and cooled to 77 K in a liquid nitrogen bath. The valve to the inert gas inlet [(II)] was closed, and the valve to the Schlenk line [(IV)] was opened. A high dynamic vacuum

($5 \cdot 10^{-6}$ bar) was applied and the cuvette was flame sealed using a propane torch at the tapered position of the attached Duran glass tube [(V)].

The exact concentration of the deoxygenated sample was then determined by UV-Vis absorption. The oxygen impermeability of the resulting ampoules was verified by an unchanged lifetime of the delayed fluorescence even over a storing period of several months.

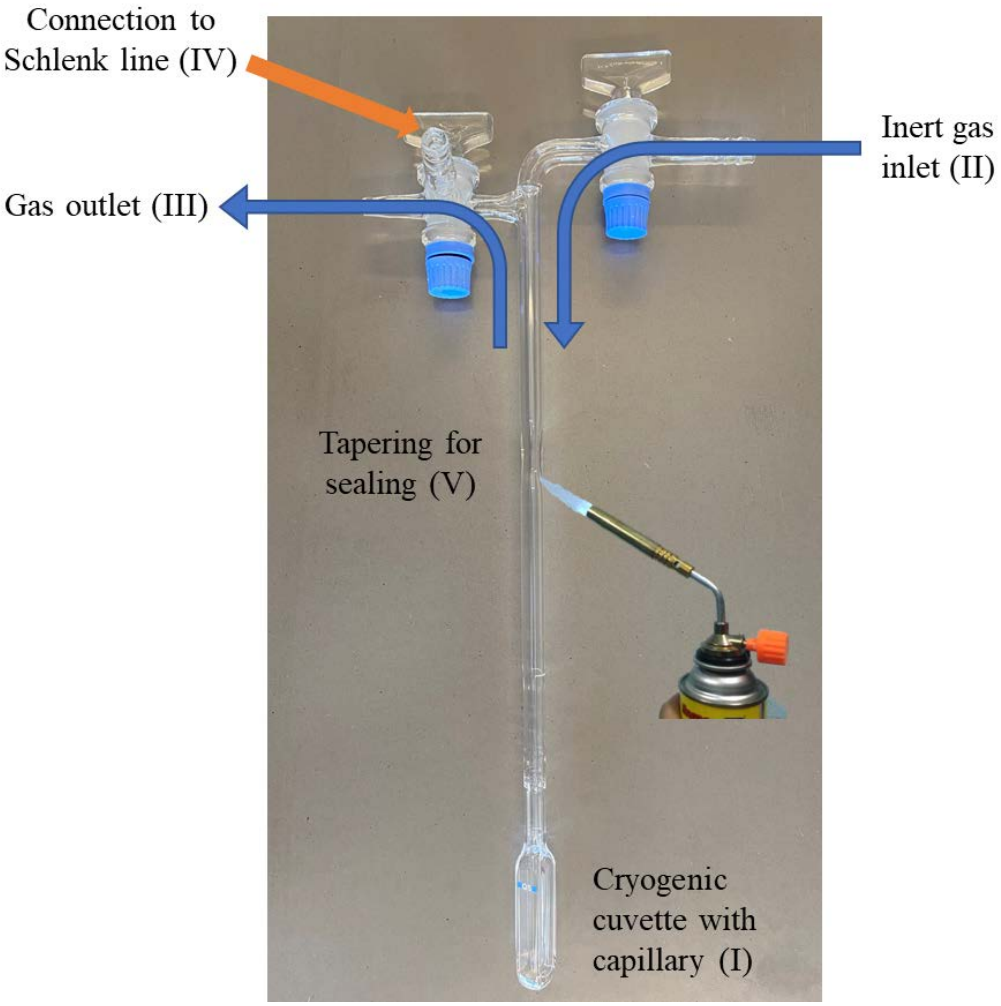

Figure S10. Setup used for degassing and sealing of the samples.

1.8 Temperature dependence of delayed fluorescence

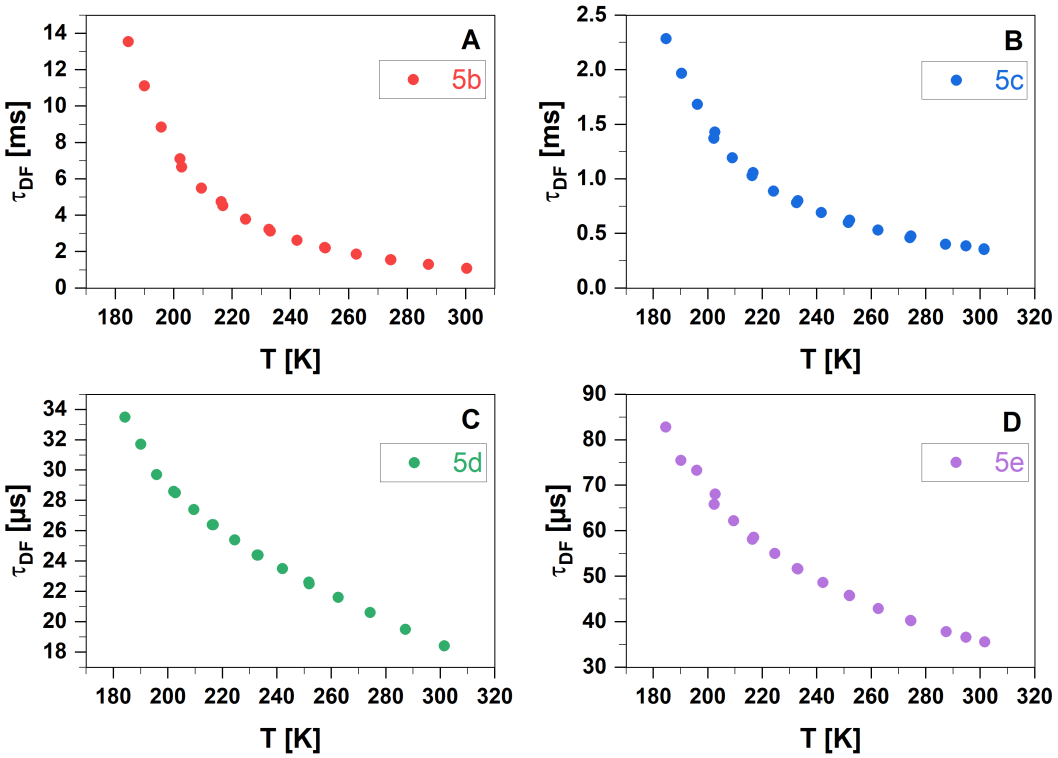

Figure S11. Temperature dependence of the delayed fluorescence lifetimes τ_{DF} of compounds **5b-5e** in liquid toluene. For all compounds, temperature series were firstly conducted from a lower to a higher temperature (i.e. from 200 K to 300 K) and then reversely (from 300 K to 182 K) to check the reproducibility of the measured data (Table S9 to Table S12).

Table S9. Temperature-dependent lifetimes of **5b**. The table contains the temperatures of the sensor and the sample (sensor T and sample T), the reciprocal sample temperature (1/Sample T), and the lifetime fit result of the measured delayed fluorescence lifetime (τ_{DF}).

Sensor T [K]	**Sample T [K]**	**1 / Sample T [$\cdot 10^{-3}$ 1/K]**	**τ_{DF} [µs]**
200.0	202.7	4.9	6661.1
206.9	209.5	4.8	5485.7
214.3	216.8	4.6	4537.1
222.2	224.6	4.5	3782.7
230.8	233.1	4.3	3124.6
240.0	242.2	4.1	2617.4
250.0	251.9	4.0	2203.2
260.9	262.6	3.8	1856.6
272.7	274.4	3.6	1562.4
285.7	287.3	3.5	1309.0
300.0	300.4	3.3	**1076.0**
272.7	274.3	3.6	1559.3
250.0	251.7	4.0	2220.2
230.8	232.6	4.3	3232.1
214.3	216.3	4.6	4741.3
200.0	202.1	4.9	7096.9
193.5	195.7	5.1	8849.0
187.5	190.0	5.3	11112.3
181.8	184.4	5.4	13552.5

Table S10. Temperature-dependent lifetimes of **5c**. The table contains the temperatures of the sensor and the sample (sensor T and sample T), the reciprocal sample temperature (1/Sample T), and the lifetime fit result of the measured delayed fluorescence lifetime (τ_{DF}).

Sensor T [K]	**Sample T [K]**	**1 / Sample T [$\cdot 10^{-3}$ 1/K]**	**τ_{DF} [µs]**
200.0	202.2	4.9	1370.9
206.9	209	4.8	1193.1
214.3	216.3	4.6	1029.1
222.2	224.1	4.5	888.0
230.8	232.6	4.3	782.5
240.0	241.7	4.1	690.6
250.0	251.6	4.0	601.5
260.9	262.5	3.8	530.6
272.7	274.2	3.6	462.0
285.7	287.2	3.5	402.0
300.0	301.4	3.3	**354.0**
300.0	301.4	3.3	**357.7**
293.0	294.7	3.4	386.8
272.7	274.5	3.6	477.3
250.0	252	4.0	622.7
230.8	233.1	4.3	800.7
214.3	216.6	4.6	1057.4
200.0	202.6	4.9	1430.5
193.5	196.1	5.1	1681.6
187.5	190.3	5.3	1967.7
181.8	184.7	5.4	2285.1

Table S11. Temperature-dependent lifetimes of **5d**. The table contains the temperatures of the sensor and the sample (sensor T and sample T), the reciprocal sample temperature (1/Sample T), and the lifetime fit result of the measured delayed fluorescence lifetime (τ_{DF}).

Sensor T [K]	**Sample T [K]**	**1 / Sample T [$\cdot 10^{-3}$ 1/K]**	**τ_{DF} [µs]**
200.0	202.7	4.9	28.5
206.9	209.5	4.8	27.4
214.3	216.7	4.6	26.4
222.2	224.5	4.5	25.4
230.8	233.1	4.3	24.4
240.0	242.1	4.1	23.5
250.0	251.9	4.0	22.5
260.9	262.5	3.8	21.6
272.7	274.3	3.6	20.6
285.7	287.2	3.5	19.5
300.0	301.5	3.3	**18.4**
272.7	274.3	3.6	20.6
250.0	251.7	4.0	22.6
230.8	232.7	4.3	24.4
214.3	216.3	4.6	26.4
200.0	202.2	4.9	28.6
193.5	195.8	5.1	29.7
187.5	190.0	5.3	31.7
181.8	184.3	5.4	33.5

Table S12. Temperature-dependent lifetimes of **5e**. The table contains the temperatures of the sensor and the sample (sensor T and sample T), the reciprocal sample temperature (1/Sample T), and the lifetime fit result of the measured delayed fluorescence lifetime (τ_{DF}).

Sensor T [K]	**Sample T [K]**	**1 / Sample T [$\cdot 10^{-3}$ 1/K]**	**τ_{DF} [µs]**
200.0	202.7	4.9	68.1
206.9	209.5	4.8	62.2
214.3	216.8	4.6	58.6
222.2	224.6	4.5	55.0
230.8	233.1	4.3	51.6
240.0	242.2	4.1	48.6
250.0	252	4.0	45.7
260.9	262.6	3.8	42.9
272.7	274.4	3.6	40.3
285.7	287.5	3.5	37.8
293.0	294.7	3.4	36.6
300.0	301.7	3.3	**35.6**
272.7	274.5	3.6	40.2
250.0	251.9	4.0	45.8
230.8	232.8	4.3	51.7
214.3	216.4	4.6	58.1
200.0	202.3	4.9	65.8
193.5	195.9	5.1	73.3
187.5	190.1	5.3	75.5
181.8	184.6	5.4	82.8

1.9 An additional proof for TADF: TRES measurements

To further investigate the spectral properties of delayed fluorescence, we conducted time-resolved emission spectroscopy (TRES) measurements. A spectral overlap between prompt and delayed fluorescence confirms that both types of emission originate from the same excited state (S_1). We integrated the specific areas under the time-resolved decay curves in microseconds to obtain the spectra of both prompt and delayed fluorescence (Figure S12). These spectra overlap for all four compounds (Figure S13 A-D), giving an additional verification to TADF.

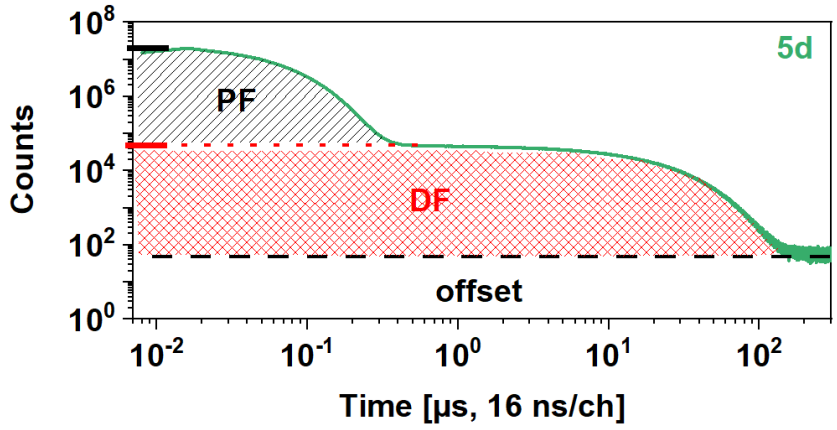

Figure S12. Integrated areas of prompt and delayed fluorescence under the time-resolved decay curves in microseconds for compound **5d**.

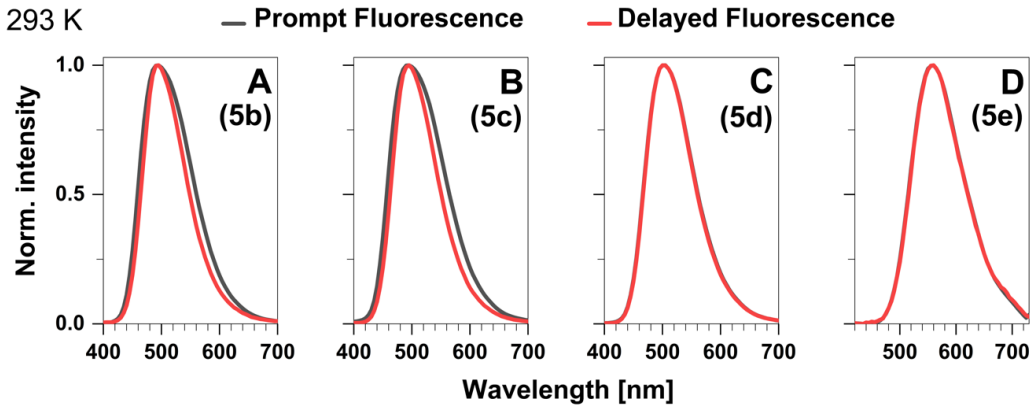

Figure S13. Time-resolved emission spectra of compounds **5b-5e** (**A-D**) in toluene at 293 K. Spectral overlap between prompt and delayed fluorescence is observed for all four compounds, indicating that both emissions originate from the same excited state.

1.10 Rate matrix and solution

The rate matrix for the excited 3-state kinetic system:

$$\begin{pmatrix} -(k_S + k_{ISC}) & k_{rISC} & 0 \\ k_{ISC} & -k_{rISC} & 0 \\ k_S & k_T & 0 \end{pmatrix} \quad \text{eq. S17}$$

has two relaxation times, the prompt and the delayed signal, as general solution:

$$k_p = -\lambda_2 = \frac{1}{2}\Big(k_S + k_{ISC} + k_{rISC} + k_T + \sqrt{(k_S + k_{ISC} - k_{rISC} - k_T)^2 + 4k_{ISC}k_{rISC}}\Big) \quad \text{eq. S18}$$

$$k_d = -\lambda_1 = \frac{1}{2}\Big(k_S + k_{ISC} + k_{rISC} + k_T - \sqrt{(k_S + k_{ISC} - k_{rISC} - k_T)^2 + 4k_{ISC}k_{rISC}}\Big) \quad \text{eq. S19}$$

with $k_S = k_{rad\_S} + k_{IC\_S}$ and $k_T = k_{rad\_T} + k_{nr\_T}$.

1.11 Discussion of previously published data on 5b

To simulate the effect of triplet quenching by O_2 the solution of the rate matrix for the delayed signal was used. Here the temperature-dependent rate constants as obtained from our kinetic analysis were inserted:

$$(k_{rad} + k_{IC}) = (k_{rad} + k_{IC})_0 e^{-Ea(1)/kT} \quad \text{eq. S20}$$

$$k_{ISC} = \frac{k_{ISC}(1)}{\sqrt{T}} + \frac{k_{0\_ISC}(2)}{\sqrt{T}} e^{-Ea(2)/kT} \quad \text{eq. S21}$$

$$k_{rISC} = \frac{k_{0\_rISC}}{\sqrt{T}} e^{-Ea(3)/kT} \quad \text{eq. S22}$$

Quenching by O_2 was introduced as the only process that depopulates T_1 to S_0:

$$k_T \equiv k_q \cdot \frac{[O_2]}{9} = \frac{2RT}{3\eta}\left(\frac{r_{dye}}{r_{O2}} + \frac{r_{O2}}{r_{dye}} + 2\right) \cdot \frac{[O_2]}{9} \approx 5.0043 \cdot \frac{RT}{\eta} \cdot \frac{[O_2]}{9} \quad \text{eq. S23}$$

The quenching rate was approximated by using the Stokes-Einstein equation, the radii of $r(O_2)$ = 84 pm and r(**5b**) = 445 pm, and assuming a quenching efficiency of 1/9 as upper limit given by spin statistics.[27] The viscosity of toluene in the temperature range studied was obtained from Ref. 28 and its eq. 1-5. With all parameters available now the delayed rate can be simulated for all relevant concentrations of O_2.

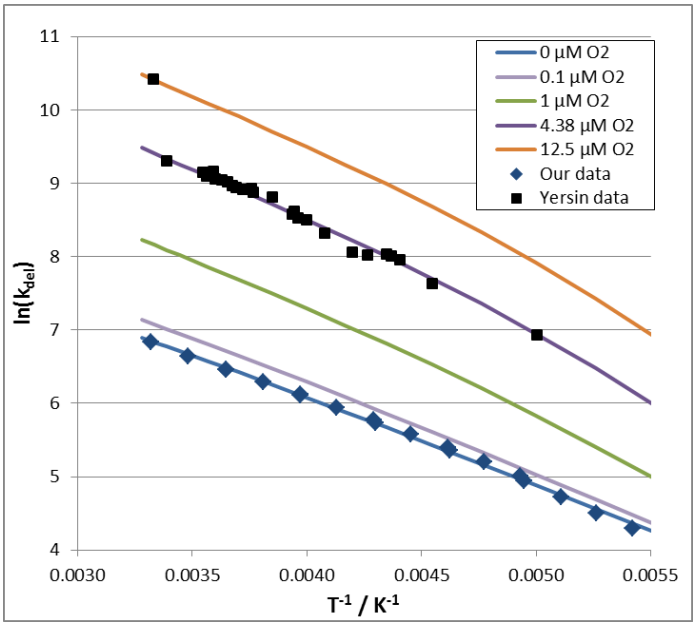

Figure S14. Temperature dependence of simulated delayed rate constant for different O_2 concentrations compared to experimental data and previously published data[29]

The experimental data points from the original publication[29] (its Figure 4) were extracted using WebPlotDigitizer Ver. 4.7[30] and are consistent with a concentration of 4.38 µM O_2. The single point on the 12.5 µM line corresponds to the reported decay time of 30 µs at 300 K (insert in Figure 4). The apparent Arrhenius-energy for the extracted data points is $E_a = 126 \pm 2$ meV. For the limiting case, i.e. negligible rISC and quenching as dominating process to depopulate T_1, an apparent Arrhenius-energy of $E_a = 129 \pm 2$ meV would be expected, just from the temperature dependence of the diffusion coefficient. It has to be noted that even in our measurements an effect of residual oxygen cannot be excluded. Thus, our reported rates for ISC and rISC as well as the activation energy for rISC would be upper limits for the system while the quantum yield for delayed fluorescence represents a lower limit.

1.12 Aggregation at lower temperatures

All samples showed signs of aggregation at lower temperatures, as indicated by a strong drop in total fluorescence intensity due to precipitation and the appearance of a highly quenched species (τ < 200 ps) in the ns decays. In addition, compound **5e** formed a very long-lifetime species (τ >> 1 ms, < 3.3% of total signal, see Figure S15) below 220 K. Upon cooling down and heating up of the sample all the species attributed to aggregation showed more or less strong hysteresis regarding their relative amount and lifetime. This behaviour prevents us from evaluating the absolute fluorescence intensities as indicator for possible changes in quantum yields. It does not significantly affect the lifetime analyses since fluorescence decay times of monomers and aggregates are well separated. In the offset evaluation of the **5e** ns-decays the fraction of aggregates with long lifetime as estimated from the µs decays was subtracted. Since the fraction of aggregates was not stable in time, and data from different measurements (ns and µs decays) needed to be combined for this purpose, the data correction was only partially successful and an increased noise level in the corrected data (**5e** below 220 K) could not be avoided.

*Aggregation in **5e***

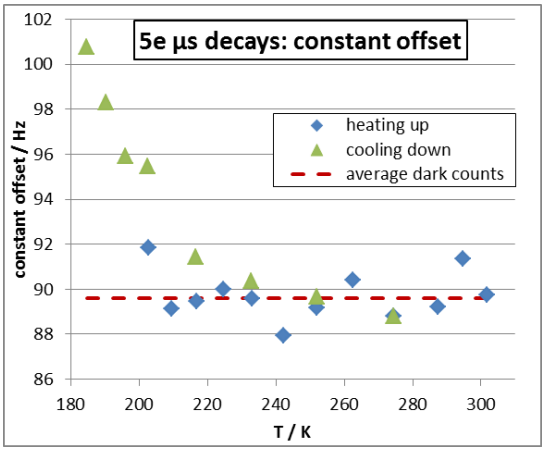

Figure S15. Aggregation in **5e**

Below 220 K the offset in the µs decays measured for 5e significantly exceeds the average dark counts of the detector, indicating the appearance of a species with lifetime much longer than the 600 µs detection time window between excitation pulses.

Chapter 2. Analytical solution of kinetics for 3-state system (S_0, S_1, T_1)

The formal solution of dynamics equation for a 3-state system:

$$\frac{d\,\boldsymbol{a}(t)}{d\,t} = \boldsymbol{K}\,\boldsymbol{a}(t);\quad \boldsymbol{a}(t) = \begin{pmatrix} a_{S0}(t) \\ a_{S1}(t) \\ a_{T1}(t) \end{pmatrix}, \qquad \text{eq. S24}$$

is:

$$\boldsymbol{a}(t) = e^{\boldsymbol{K}t}\,\boldsymbol{a}_0;\quad \boldsymbol{a}_0 = \boldsymbol{a}(t=0) \qquad \text{eq. S25}$$

The observed signal is defined by emission properties of involved states. In general, we can write:

$$a_{obs}(t) = \boldsymbol{a}_{em}\boldsymbol{a}(t) = \boldsymbol{a}_{em}e^{\boldsymbol{K}t}\,\boldsymbol{a}_0 \qquad \text{eq. S26}$$

The transition rates matrix can be eigen-values decomposed (EVD) as:

$$\boldsymbol{K} = \boldsymbol{V}\boldsymbol{\Lambda}\boldsymbol{U};$$
$$\boldsymbol{V} = \begin{pmatrix} | & | & | \\ \boldsymbol{v}_0 & \boldsymbol{v}_1 & \boldsymbol{v}_2 \\ | & | & | \end{pmatrix};\ \boldsymbol{U} = \boldsymbol{V}^{-1} = \begin{pmatrix} - & \boldsymbol{u}_0 & - \\ - & \boldsymbol{u}_1 & - \\ - & \boldsymbol{u}_2 & - \end{pmatrix};\ \boldsymbol{\Lambda} = \begin{pmatrix} \lambda_0 & 0 & 0 \\ 0 & \lambda_1 & 0 \\ 0 & 0 & \lambda_2 \end{pmatrix}, \qquad \text{eq. S27}$$

where $\boldsymbol{V}, \boldsymbol{U}$ are matrixes consisting of right (columns) and left(rows) eigen-vectors. For the following derivation, it is more convenient to rewrite EVD in eq. S27 in the equivalent form of linear combination of eigen matrixes $\boldsymbol{\Gamma}_i$:

$$\boldsymbol{K} = \sum_i \boldsymbol{\Gamma}_i\,\lambda_i;$$
$$\boldsymbol{\Gamma}_i = \boldsymbol{v}_i \otimes \boldsymbol{u}_i\,, \qquad \text{eq. S28}$$

Then the matrix exponential in eq. S25 and eq. S26 can be written as:

$$e^{\boldsymbol{K}t} = \sum_i \boldsymbol{\Gamma}_i\,e^{\lambda_i t} \qquad \text{eq. S29}$$

The transition rate matrix $\boldsymbol{K}$ for the system in absence of excitation (after excitation pulse) have the form:

$$\boldsymbol{K} = \begin{pmatrix} 0 & k_{S10} & k_{T10} \\ 0 & -(k_{S10} + k_{ISC}) & k_{RISC} \\ 0 & k_{ISC} & -(k_{RISC} + k_{T10}) \end{pmatrix}, \qquad \text{eq. S30}$$

where $k_{S10} = k_{S10,rad} + k_{IC}$. For this transition matrix in eq. S26 we can get next eigen values (negated rates):

$$\begin{cases} \lambda_0 = 0 \\ \lambda_1 = -k_p = -\frac{1}{2}(\Sigma k + \Delta k) \\ \lambda_2 = -k_d = -\frac{1}{2}(\Sigma k - \Delta k) \end{cases} \qquad \text{eq. S31}$$

$$\Sigma k = k_{S10} + k_{ISC} + k_{RISC} + k_{T10}$$

$$\Delta k = \sqrt{\begin{matrix} (k_{S10} + k_{ISC} + k_{RISC} + k_{T10})^2 - \\ 4\big((k_{S10} + k_{ISC})(k_{RISC} + k_{T10}) - k_{ISC}k_{RISC}\big) \end{matrix}}$$

Note that the two expressions for the prompt and delayed rates k_p and k_d rates above can be rewritten in the form of two simple equations:

$$\begin{cases} k_p + k_d = k_{S10} + k_{ISC} + k_{RISC} \\ k_p k_d = k_{S10} k_{RISC} \end{cases} \qquad \text{eq. S32}$$

The corresponding eigen-matrices are:

$$\boldsymbol{\Gamma}_0 = \begin{pmatrix} 1 & 1 & 1 \\ 0 & 0 & 0 \\ 0 & 0 & 0 \end{pmatrix};$$

$$\boldsymbol{\Gamma}_1 = \boldsymbol{\Gamma}_p = \frac{1}{\Delta k}\begin{pmatrix} 0 & k_d - k_{S10} & k_d - k_{T10} \\ 0 & k_p - (k_{RISC} + k_{T10}) & -k_{RISC} \\ 0 & -k_{ISC} & -k_d + (k_{RISC} + k_{T10}) \end{pmatrix}; \qquad \text{eq. S33}$$

$$\boldsymbol{\Gamma}_2 = \boldsymbol{\Gamma}_d = -\frac{1}{\Delta k}\begin{pmatrix} 0 & k_p - k_{S10} & k_p - k_{T10} \\ 0 & k_d - (k_{RISC} + k_{T10}) & -k_{RISC} \\ 0 & -k_{ISC} & -k_p + (k_{RISC} + k_{T10}) \end{pmatrix}$$

If the transitions $T_1 \rightarrow S_0$ are not emissive, the whole signal is detected as emission from the state S_1. So, the emission vector takes form: $\boldsymbol{a}_{em} = (0 \;\; \Phi_{s1} \;\; 0)$, where Φ_{s1} is the quantum yield of a $S_1 \rightarrow S_0$ transition. Next, we assume that initial population of the state T_1 is neglectable, i.e. that an excitation pulse is so short that this state is not populated. This way we get $\boldsymbol{a}_0^{\mathrm{T}} =$

($a_{S0,0}$ $a_{S1,0}$ 0). Then, substituting $\boldsymbol{a}_{em}$, $\boldsymbol{a}_0$ and $\lambda_i, \boldsymbol{\Gamma}_i$ into eq. S29 and eq. S26, we get for the observed signal:

$$
\begin{aligned}
&a_{obs}(t) = a_p e^{-k_p t} + a_d e^{-k_d t} \\
&a_p = \Phi_{s1}\, a_{S1,0} \frac{1}{\Delta k}\left(k_p - (k_{RISC} + k_{T10})\right) \\
&a_d = \Phi_{s1}\, a_{S1,0}\, \frac{1}{\Delta k}\left((k_{RISC} + k_{T10}) - k_d\right)
\end{aligned}
\qquad \text{eq. S34}
$$

In the experiment we can observe either ratio, either one of relative fractions (one of which will be dependent) of two exponential components of the decay:

$$
\begin{aligned}
&\frac{F_d^{(a)}}{F_p^{(a)}} = \frac{a_d}{a_p} = \frac{k_p - (k_{RISC} + k_{T10})}{(k_{RISC} + k_{T10}) - k_d};\ \frac{F_d^{(c)}}{F_p^{(c)}} = \frac{a_d}{a_p}\frac{k_p}{k_d} = \frac{k_p - (k_{RISC} + k_{T10})}{(k_{RISC} + k_{T10}) - k_d}\frac{k_p}{k_d} \\
&p_d^{(a)} = \frac{a_d}{a_p + a_d} = \frac{k_p - (k_{RISC} + k_{T10})}{k_p - k_d};\ p_d^{(c)} = \frac{a_d/k_d}{a_p/k_p + a_d/k_d} = \frac{1}{1 + \dfrac{F_p^{(c)}}{F_d^{(c)}}}
\end{aligned}
\qquad \text{eq. S35}
$$

Where the upper indices $(a), (c)$ stand for amplitude (intensity) and counts variants of quantities, correspondingly.

Two equations from eq. S32 and one of equations from eq. S35 gives 3 independent equations relating 3 observed quantities and 4 transition rates. Obviously, such system is incomplete and cannot give solution for all 4 rates. So, we need to make some assumptions. For example, we can assume that k_{T10} is known. Then we can solve the system of 3 equations to get k_{S10}, k_{ISC}, k_{RISC} as functions of observables (here, for example, fluorescence rates and fractions) and k_{T10}:

$$
\begin{aligned}
&\begin{cases}
k_{RISC} = k_p + k_d - \langle k \rangle^{(a)} - k_{T10} = \left(\dfrac{1}{k_d} + \dfrac{1}{k_p} - \langle \tau \rangle^{(c)}\right)^{-1} - k_{T10} \\
k_{S10} = \dfrac{k_p k_d - \langle k \rangle^{(a)} k_{T10}}{k_{RISC}} \\
k_{ISC} = \langle k \rangle^{(a)} - k_{S10}
\end{cases} \\
&\langle k \rangle^{(a)} = \left(p_p^{(a)} k_p + p_d^{(a)} k_d\right) \\
&\langle \tau \rangle^{(c)} = \left(\frac{p_d^{(c)}}{k_d} + \frac{p_p^{(c)}}{k_p}\right)
\end{aligned}
\qquad \text{eq. S36}
$$

Note: $\langle k \rangle^{(a)} = k_p + k_d - k_{RISC} - k_{T10}$.

Oleg's contribution (not only about precipitation). I will put all contribution here. It probably should be separated later and placed to different parts according to context. Thus, discussion of the model should be placed closer to diagram plots below (see also the same plot at the beginning, before main text).

1. Fitting of TCSPC data

The TCSPC data for variety of temperatures were measured in two delay times regions: with ns- and ms- time resolution. The registered fluorescence decays were fitted using a quadratic programming optimization. As expected and observed fluorescence lifetimes differs by several orders of magnitude, no regularization was applied during optimization. The example fitted spectra of fluorescence lifetimes for different temperatures are shown at the Fig. …. .

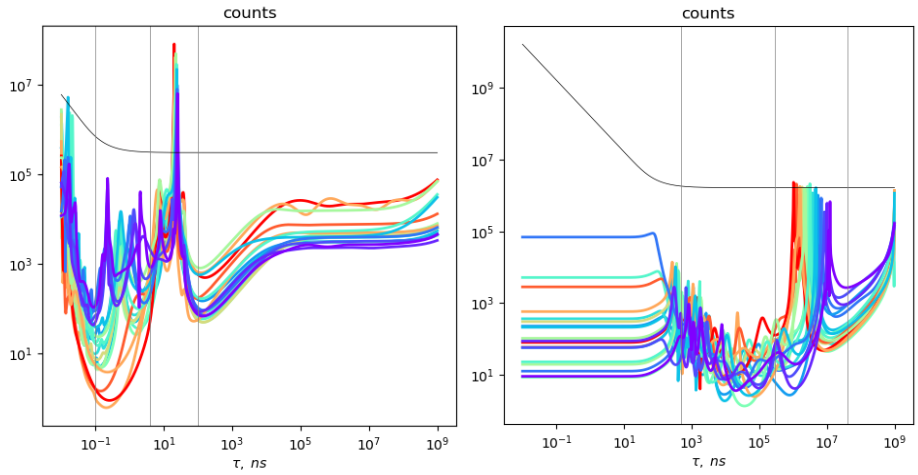

Figure S53 The fluorescence lifetime spectra for **5b** sample, obtained by the quadratic programming optimization fitting of TCSPC decays in ns- (left) and ms-ranges of delay times.

2. Precipitation

The total number of counts depend on the temperature – it drops several times with the decrease of a temperature. Also, this dependence reveal a hysteresis behaviour. See Fig… . We assume that such behaviour evidences about the precipitation of solution at low temperatures.

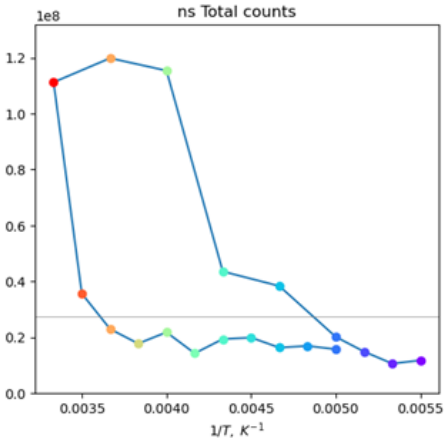

Figure S54. The temperature dependence of total number of counts for C2 sample.

3. Dominating fluorescence lifetimes

All samples reveal the presence of 2 dominating fluorescence lifetimes – one in each measurement with different delay time range. These lifetimes were calculated from the fitted spectra as average over the regions near dominating peaks (from minimum to minimum). To determine relative fraction of the prompt (shortest) lifetime only measurement in ns-region was used, as different excitation conditions of two measurements does not allow the quantitative comparison of their amplitudes. The prompt photon counts ($a_p^{(c)}$) were calculated as sum of counts around the dominating peak in the ns spectrum, and the delayed ($a_p^{(c)}$) counts are estimated as sum of all counts with lifetimes larger than last minimum of the ns-spectra, except the dark counts estimated form independent measurement. The resulting lifetimes and fractions for 5b sample are presented at the Fig. … (Upper row)

4. The analysis of lifetimes using 3-state model

The presence of two dominating fluorescence lifetimes in the fitted decays witness in favour of 3-states (ground S_0 and two excited: S_1, T_1) model of an underlying kinetics (see. Scheme 1.). To resolve the transitions times we derived analytical expressions for we have derived the analytical expressions 3 independent observables: two characteristic times (τ_{DF}, τ_{PF}) their fractions (dependent on each other as $p_D = 1 - p_F$), for a supposed 3-state (see SI, chapter 4), assuming that the signal is observed from the radiative transitions from S_1 state only. As the 3-

state system of interest is characterised by 4 transition rates ($k_{10S} = k_{rSv} + k_{ICS}$, k_{ISC}, k_{rISC}, k_{10T}) and only 3 observables are available, the exact inverted solution for all rates is impossible. So, we had to make some assumption about transition rates: here we have assumed that k_{10T} is neglectable. Our derivation of observed quantities is analogous to one given by Adachi (JPCA125p08074_Exact solution TADF kinetics_Tsuchiya+Adachi_2021). Thus, the solution is almost the same, except the expression ???, where Adachi used approximation that $p_D \ll p_F$. This approximation is really applicable for the reasonable transition rates. However, it is not necessary, as the full solution is not much more complicated. The resolved transition rates for the 5b compound are presented at the Fig. … (bottom row).

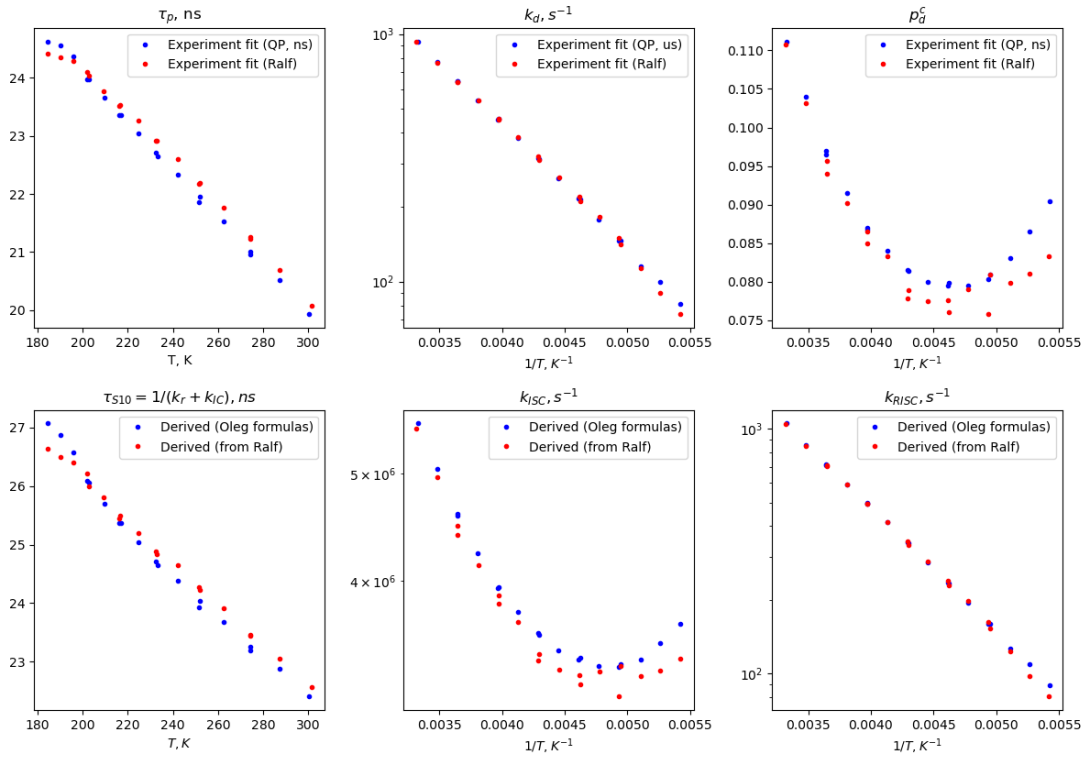

Figure S55. Fitted data analysis. **Top**: The fluorescence lifetimes (rates) and their fractions for 5b sample obtained from the data presented at Fig. … **Bottom**: The transition rates calculated from fitted data according the relations presented at SI, chapter 4.

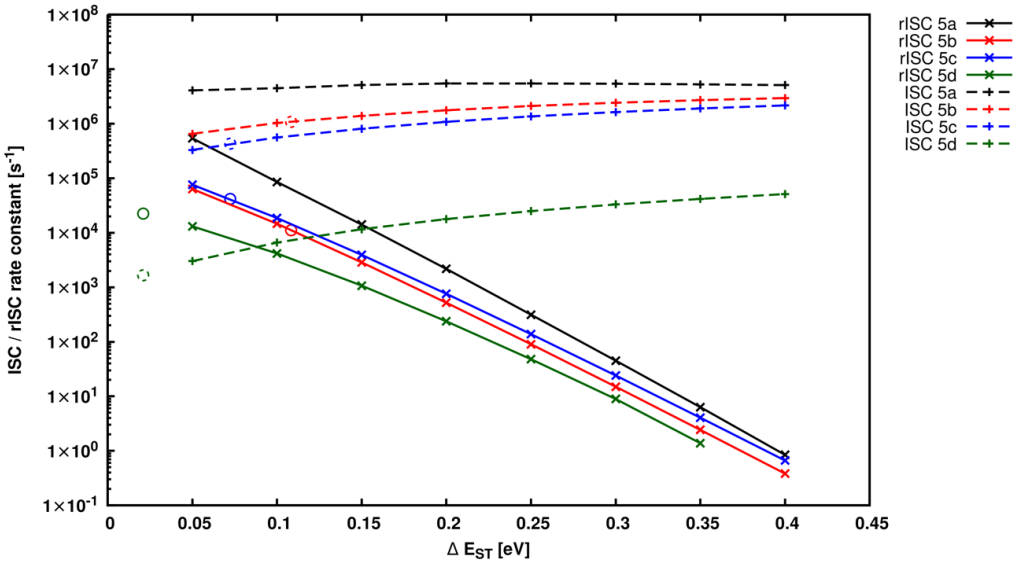

Figure S56. ISC and rISC rate constants for compound 5a to 5d. The adiabatic energy gap was successively decreased starting from 0.4 eV with an increment of 0.05 eV. Computed rate constants for the experimental energy gaps are highlighted in solid (rISC) and dashed (ISC) circles.

The potential energy surface (PES) and the according normal mode vibrations that are needed for the computation of nonradiative rate constants were computed at the optimized geometries of the lowest excited singlet and triplet state. In order to mimic the effect of a small energy gap between these states the adiabatic energy gap was decreased with an increment of 0.05 eV. The results clearly show that, unlike ISC, rISC (which is an uphill process that relies on thermal population of excited states in close energetic proximity) strongly depends on the energy gap. Rate constants were also computed for the experimental singlet-triplet gaps if given.

However, this approach leads to certain inaccuracies where the ISC rate constant is significantly lower than the rISC. Due to not recomputing the PES of the respective states at every given point a sole energetic shift leads to a crossing of two potentials and, thus, unphysical results.

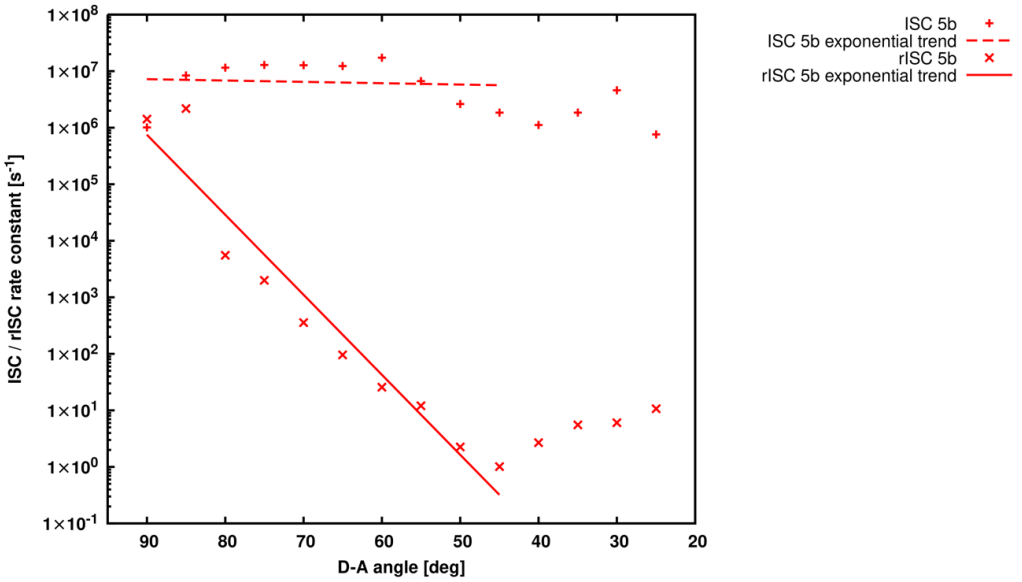

Figure S57: ISC and rISC rate constants computed for compound 5b. Results were obtained by performing a relaxed scan of the S1 and T1 geometry and using the VH-Method.

To ensure that reliable non-radiative rate constants are computed, relaxed scans were performed for the lowest excited singlet and triplet state geometries. In addition to a frequency analysis at the initial state geometry the Vertical Hessian (VH) method was used to extrapolate the PES alongside the normal mode vibrations of the respective final state. Unlike for a sole vertical shift of the PES shown in figure 1, figure 2 shows the ISC and rISC rate constants that were computed for different donor-acceptor angles and recomputed excited state potentials.

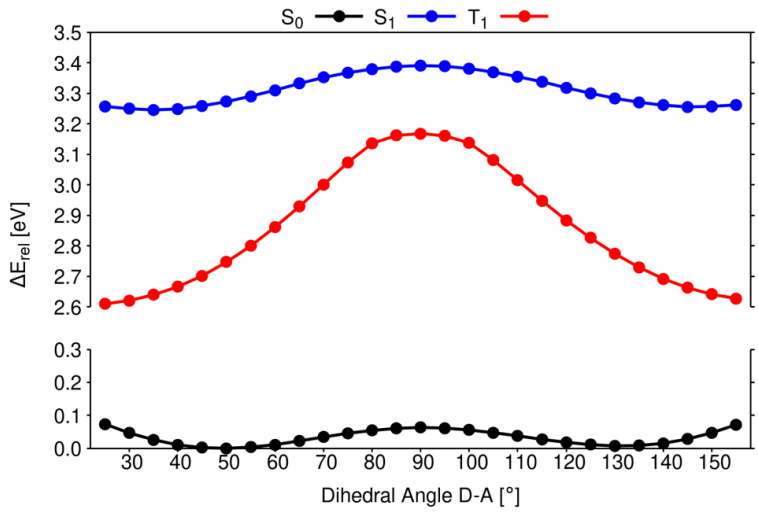

Figure S58. Relaxed interpolated pathway for compound 5a between 25 and 155 degrees for the electronic ground state and the lowest excited singlet and triplet state. Between 80 and 100 degrees the lowest optimized triplet state is of locally excited state character instead of charge-transfer character and thus in energy lower than expected.

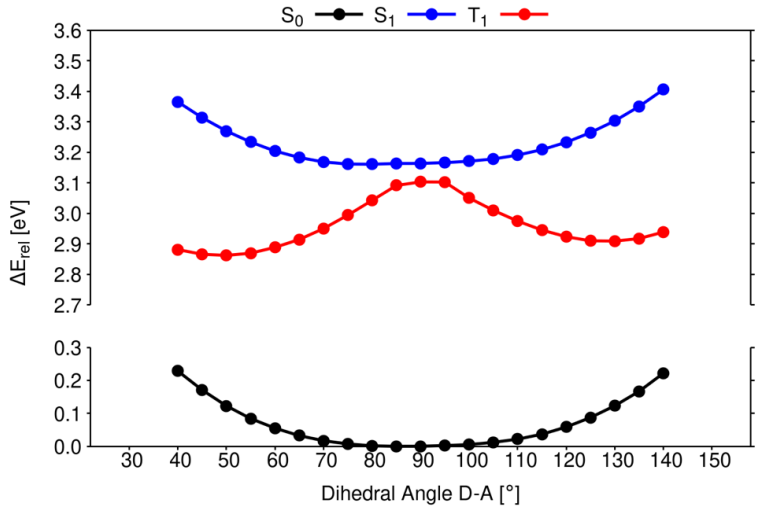

Figure S59. Relaxed interpolated pathway for compound 5d between 40 and 140 degrees for the electronic ground state and the lowest excited singlet and triplet state. Increased sterical hindrance by the methyl groups prevents a distortion beyond 40 and 140 degrees. Between 90 and 95 degrees the lowest optimized triplet state is of locally excited state character instead of charge-transfer character and thus in energy lower than expected.

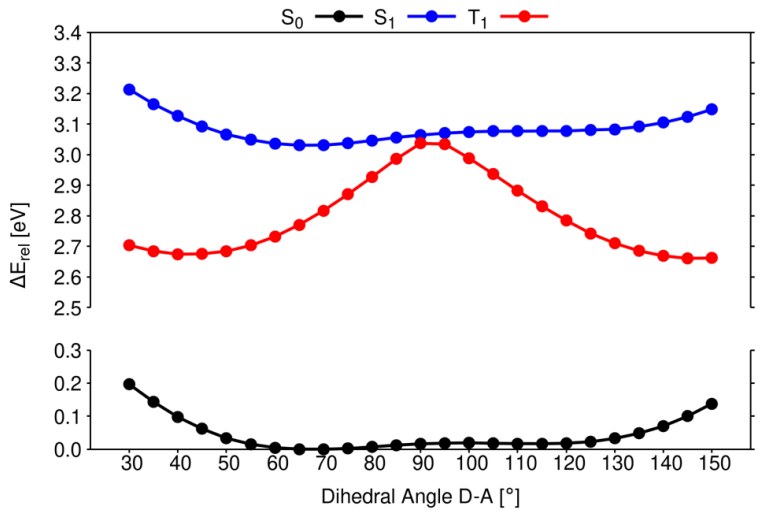

Figure S60. Relaxed interpolated pathway for compound 5e between 30 and 150 degrees for the electronic ground state and the lowest excited singlet and triplet state. For all dihedral angles shown the lowest excited triplet state is of charge-transfer character.

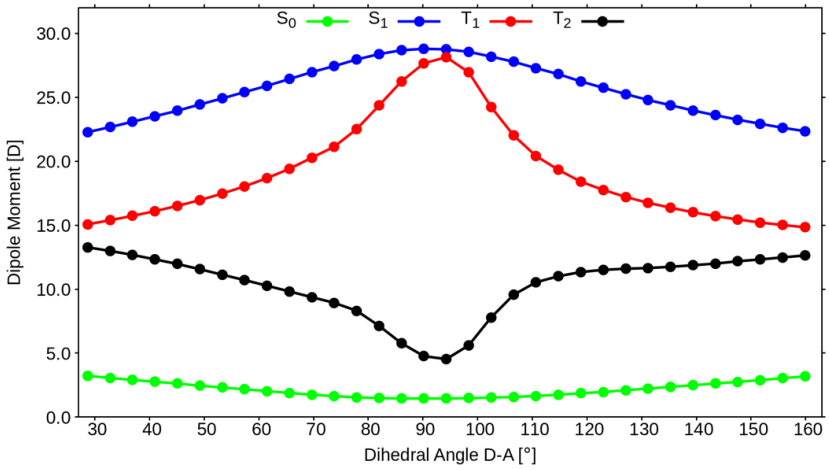

Figure S61. Dipole moment along the rotation of donor and acceptor for the electronic ground state and low-lying excited states of compound 5b. In this case In the case of a non-polar charge distribution in the electronic ground state the dipole moment can be used as a measure for the charge-transfer character.

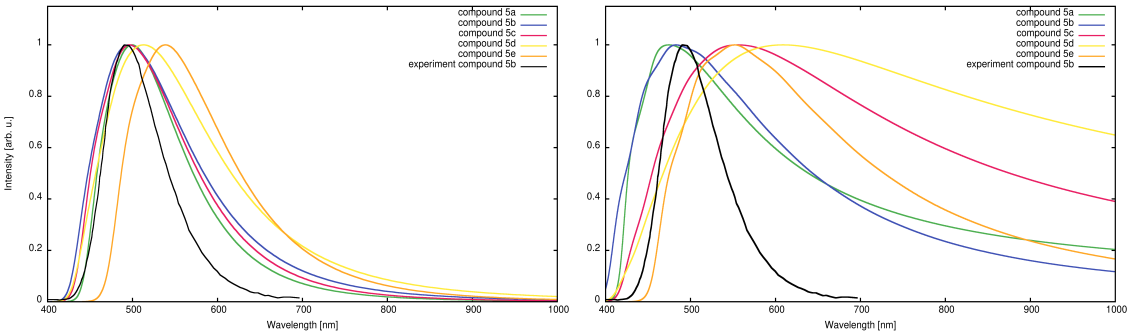

Figure S62. Emission spectra computed using the Vertical Hessian (VH, left) approach and the Adiabatic Hessian (AH, right) approach. The AH approach yields featureless broad spectra that do not allow for a meaningful comparison with the experiment. The VH method matches the spectral shape and emission maxima.

Table S21. Dihedral angle (C-C-C-C from substituent to ortho-CN) between donor and acceptor, energetic difference between the conformers and a torsional barrier estimated based on the interpolated relaxed pathway between the conformers.

	Compound				
	5a	5b	5c	5d	5e
Conf. 1, S_0 [deg]	49.6	69.7	73.5	87.1	68.0
Conf. 2, S_0 [deg]	131.2	110.7	95.8	---	112.3
$\Delta E_{DFT}(2 - 1)$ [meV]	7	15	112	---	17
$\Delta E_{DFT/MRCI}(2 - 1)$ [meV]	2	5	108	---	5
Energy Barrier1→2[meV]	ca. 60	ca. 15	ca. 38	---	ca. 20

Table S22. Supplementary information for the absorption spectra consisting of oscillator strengths f(L), band wavelengths and the percentage of charge-transfer, locally-excited character (% CT/LE) of the respective electronic states at DFT/MRCI-R2016, SVP level of theory.

	Compound				
	5a	5b	5c	5d	5e
$S_0 \rightarrow S_1$ f(l)	0.23692	0.07743	0.04683	0.00208	0.08110
$S_0 \rightarrow S_2$ f(l)	0.41659	0.28922	0.22606	0.04350	0.25488
$S_0 \rightarrow S_3$ f(l)	0.02198	0.16334	0.23080	0.43595	0.20215
$S_0 \rightarrow S_1$ [nm]	410	400	400	396	429
$S_0 \rightarrow S_2$ [nm]	331	319	315	307	331
$S_0 \rightarrow S_3$ [nm]	312	307	306	302	319
S_1 [% CT/LE]	70/20	80/10	82/9	87/3	81/9

Table S23. Dihedral angle between donor and acceptor for all compounds in the electronic ground state and the lowest excited singlet and triplet state.

	Compound				
	5a	5b	5c	5d	5e
Conf. 1, S_0 [deg]	49.6	69.7	73.5	87.1	68.0
Conf. 1, S_1 [deg]	34.3	65.9	65.2	81.8	66.6
Conf. 1, T_1 [deg]	20.9	41.7	39.5	49.3	43.0
Conf. 2, S_0 [deg]	131.2	110.7	95.8	---	112.3
Conf. 2, S_1 [deg]	147.0	122.4	---	---	117.5
Conf. 2, T_1 [deg]	161.5	147.6	145.9	128.4	146.8

Chapter 4. References

1. M. S. Sundar, G. Singh, R. S. Ampapathi and A. V. Bedekar, *Journal of Molecular Structure*, 2017, **1147**, 495-501.
2. E. Rochlin and Z. Rappoport, *The Journal of Organic Chemistry*, 1994, **59**, 3857-3870.
3. M. Hesse, H. Meier and B. Zeeh, *Spektroskopische Methoden in der organischen Chemie*, Georg Thieme Verlag, 2005.
4. C. F. Macrae, I. Sovago, S. J. Cottrell, P. T. A. Galek, P. McCabe, E. Pidcock, M. Platings, G. P. Shields, J. S. Stevens, M. Towler and P. A. Wood, *J Appl Crystallogr*, 2020, **53**, 226-235.
5. APEX2, *data collection program for the CCD area-detector system, Version 2.1-0, Bruker Analytical X-ray Systems*, Madison (WI), USA, 1997-2014.
6. *SAINT, data reduction and frame integration program for the CCD area-detector system*, *Bruker Analytical X-ray Systems*, Madison (WI), USA, 1997-2014.
7. G. M. Sheldrick, *SADABS: Area-Detector Absorption Correction*, University of Göttingen, Göttingen, Germany, 1996.
8. CrysAlis^{Pro}, Rigaku Oxford Diffraction/Agilent Technologies UK Ltd, Yarnton, England., release 1.171.40.103a, **2021**.
9. G. M. Sheldrick, *Acta Crystallogr C Struct Chem*, 2015, **71**, 3-8.
10. G. M. Sheldrick, *Acta Crystallogr A*, 2008, **64**, 112-122.
11. K. Brandenburg, *Brandenburg & H. Putz Gbr, Bonn (Germany)*, 2009-2022.
12. W. W. Parson, *Modern optical spectroscopy*, Springer, 2007.
13. E. Lippert, *Zeitschrift für Elektrochemie, Berichte der Bunsengesellschaft für physikalische Chemie*, 1957, **61**, 962-975.
14. N. Mataga, Y. Kaifu and M. Koizumi, *Bulletin of the Chemical Society of Japan*, 1956, **29**, 465-470.
15. J. Lakowicz, *Principles of Fluorescence Spectroscopy*, 3rd edition, Springer, **2006**.
16. F. B. Dias, T. J. Penfold and A. P. Monkman, *Methods Appl Fluoresc*, 2017, **5**, 012001.
17. S. J. Strickler and R. A. Berg, *The Journal of Chemical Physics*, 1962, **37**, 814-822.
18. A. Reiffers, C. Torres Ziegenbein, A. Engelhardt, R. Kühnemuth, P. Gilch and C. Czekelius, *Photochem Photobiol*, 2018, **94**, 667-676.
19. W. Haselbach, J. M. Kaminski, L. N. Kloeters, T. J. J. Müller, O. Weingart, C. M. Marian, P. Gilch and B. E. Nogueira de Faria, *Chemistry*, 2023, **29**, e202202809.

20. Y. Yoneda, H. Sotome, R. Mathew, Y. A. Lakshmanna and H. Miyasaka, *J Phys Chem A*, 2020, **124**, 265-271.
21. W. R. Ware, *The Journal of Physical Chemistry*, 1962, **66**, 455-458.
22. M. Montalti, A. Credi, L. Prodi and M. T. Gandolfi, *Handbook of photochemistry*, CRC press, 2006.
23. A. Schumpe and P. Luehring, *Journal of Chemical & Engineering Data*, 1990, **35**, 24-25.
24. P. Klán and J. Wirz, *Photochemistry of organic compounds: from concepts to practice*, John Wiley & Sons, 2009.
25. H. Kautsky, *Transactions of the Faraday Society*, 1939, **35**, 216-219.
26. N. J. Turro, *Modern molecular photochemistry*, University science books, 1991.
27. O. L. J. Gijzeman, F. Kaufman and G. Porter, *Journal of the Chemical Society, Faraday Transactions 2: Molecular and Chemical Physics*, 1973, **69**, 708-720.
28. F. J. Santos, C. A. Nieto de Castro, J. H. Dymond, N. K. Dalaouti, M. J. Assael and A. Nagashima, *Journal of physical and chemical reference data*, 2006, **35**, 1-8.
29. G. A. Sommer, L. N. Mataranga-Popa, R. Czerwieniec, T. Hofbeck, H. H. H. Homeier, T. J. J. Müller and H. Yersin, *The Journal of Physical Chemistry Letters*, 2018, **9**, 3692-3697.
30. https://automeris.io/WebPlotDigitizer.

Manuscript No.2

Boosting the Fluorescence Quantum Yield of N-Methyl-Acridone by Hydrogen Bonding in Solution and Solid State.

Matthias Jantz, David Klaverkamp, Lennart Bunnemann, Benedikt Bendel, Takin Haj Hassani Sohi, Tobias Böhmer, Christel M. Marian, Vera Vasylyeva-Shor, Markus Suta, Constantin Czekelius and Peter Gilch
Manuscript in preparation for *Journal of American Chemical Society*
Latest version from 22.01.2025

Contribution: I performed all the quantum chemical computations on the NMA derivatives and visualized the theoretical results.

Boosting the Fluorescence Quantum Yield of *N*-Methyl-Acridone by Hydrogen Bonding in Solution and Solid State

Matthias Jantz[1], David Klaverkamp[1], Lennart Bunnemann[2], Benedikt Bendel[3], Takin Haj Hassani Sohi[4], Tobias Böhmer[5], Christel M. Marian[5], Vera Vasylyeva-Shor[4], Markus Suta[3], Constantin Czekelius[2] and Peter Gilch[1]*

[1]Institut für Physikalische Chemie, Heinrich-Heine-Universität Düsseldorf, Universitätsstr. 1, 40225 Düsseldorf, Germany

[2]Institut für Organische Chemie und Makromolekulare Chemie, Heinrich-Heine-Universität Düsseldorf, Universitätsstr. 1, 40225 Düsseldorf, Germany

[3]Institut für Anorganische Chemie, Heinrich-Heine-Universität Düsseldorf, Universitätsstr. 1, 40225 Düsseldorf, Germany

[4]Institut für Anorganische Chemie und Strukturchemie, Heinrich-Heine-Universität Düsseldorf, Universitätsstr. 1, 40225 Düsseldorf, Germany

[5]Institut für Theoretische Chemie und Computerchemie, Heinrich-Heine-Universität Düsseldorf, Universitätsstr. 1, 40225 Düsseldorf, Germany

*Corresponding author e-mail: gilch@hhu.de

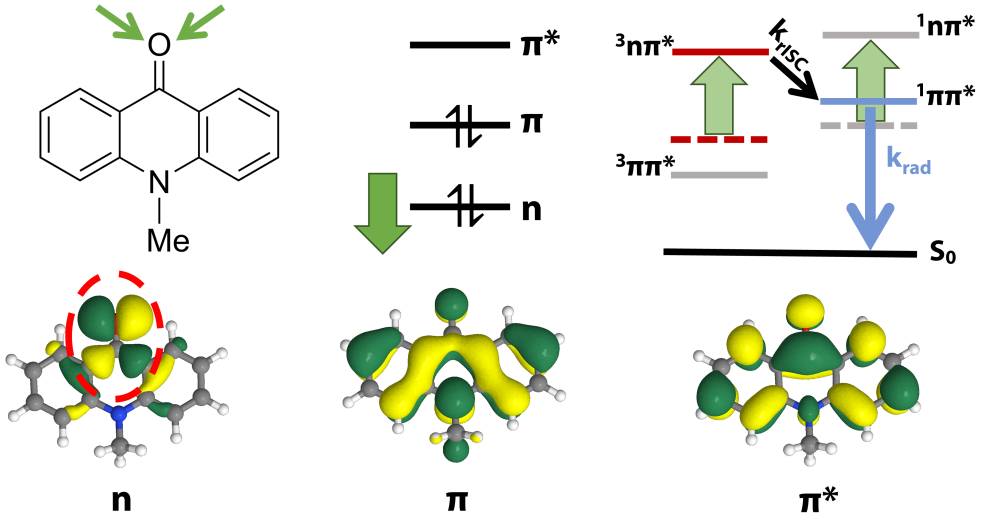

Figure X: Illustration of the impact of hydrogen bond donors at the carbonyl moiety on the NMA excitation energies. The depiction of the molecular orbitals on the bottom (adapted from ref. [DOI: 10.1021/acs.jpca.1c05098]) indicates that the n-orbital (encircled in red) is predominately affected by hydrogen bonds.

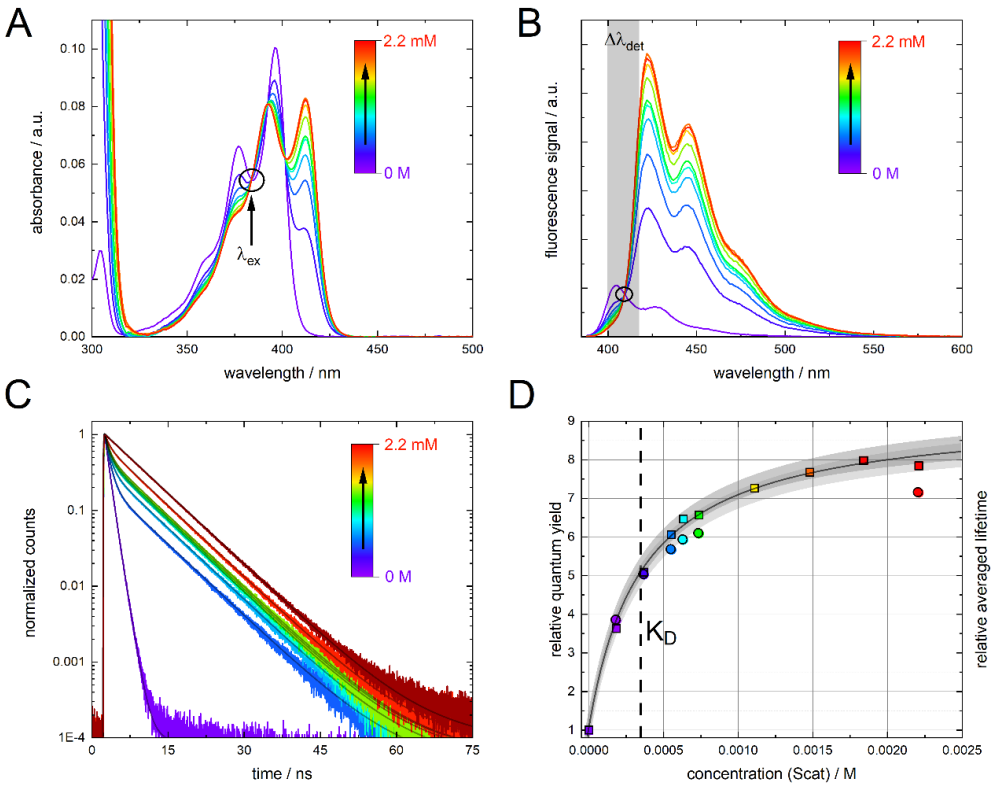

Figure X: Influence of the addition of Scat on the absorption and emission of NMA (9.3 µM) in toluene. The different Scat concentrations are color coded from purple (0 mM) to red (2.2 mM). Steady state absorption (A) and emission spectra (B) of NMA for various Scat

CXC

concentrations. The excitation wavelength (λ_{ex}) at the isosbestic point at 373 nm is highlighted. The emission spectra were recorded with an excitation and emission bandpass of 1 nm. Fluorescence decay traces (C) for excitation at 373 nm (colored) and 412 nm (2.2 mM Scat, dark red). The detection bandpass ($\Delta\lambda_{det}$) centered at 410 nm is highlighted with a grey rectangle in the emission spectra. The solid lines are representing the fits. Relative quantum yields (squares) and relative averaged lifetimes (circles) *versus* the Scat concentration (D). The increase in the relative quantum yield is fitted with a 1:1 binding model [DOI: 10.1039/C0CS00062K]. The grey areas around the fit show the 0.95 confidence (darker) and prediction band (brighter). The fitted K_D value ($3.46 \cdot 10^{-4}$ M) is marked with a black, dashed line.

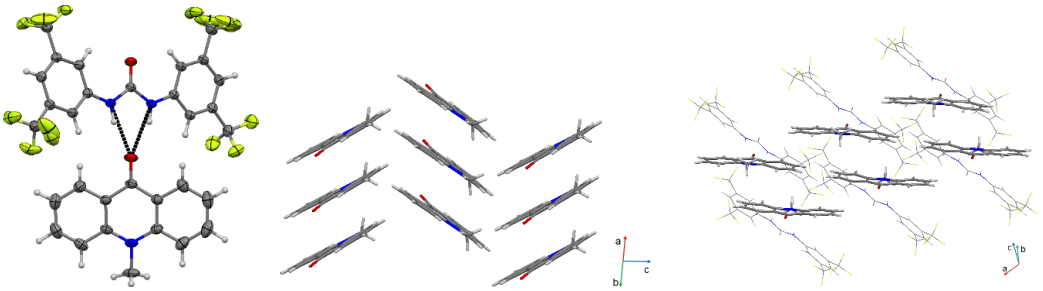

Figure X: Strong intermolecular N-H···O hydrogen bonds in NMA:SKat(1:1) co-crystal (left). Crystal packing of NMA with herringbone stacking arrangement (middle) and NMA:SKat co-crystal with parallel displaced stacks along the a axis as well as slipped stacks along the c axis (right). Interactions are shown in black dashed lines. In (right) SKat is displayed in wireframe style for clarity.

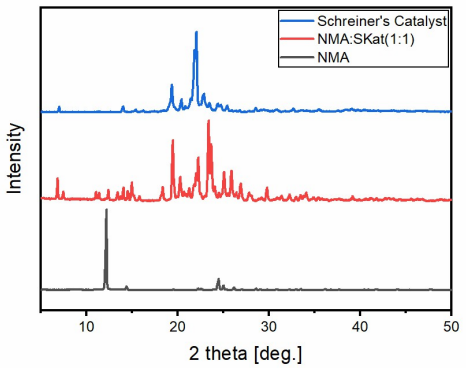

Figure X: Comparison of powder X-Ray diffraction patterns of NMA:SKat (1:1) with starting materials NMA and SKat showing a new phase formation.

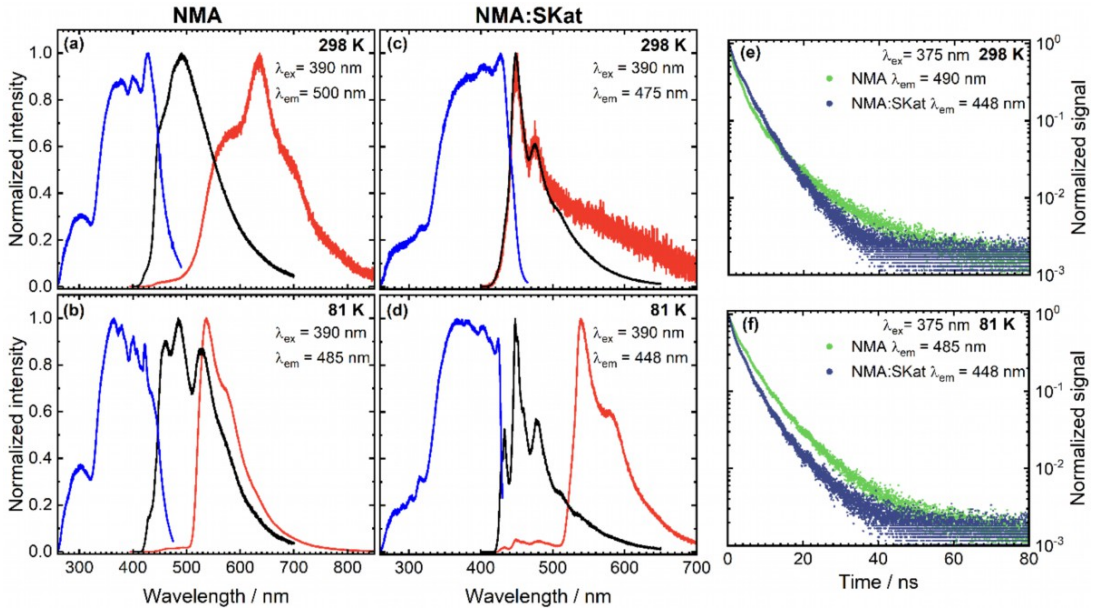

Figure X: Excitation (blue) and emission (black) spectra of NMA at 298 K (a) and 81 K (b) and NMA:SKat at 298 K (c) and 81 K (d). The emission after a 1 ms delay is depicted in red. The luminescence decay at the emission maximum for NMA and NMA:SKat at 289 K and 81 K are depicted in (e) and (f) respectively. The resulting lifetimes are depicted in Table SX. The excitation and emission wavelength are shown in the corresponding figures.

Theory

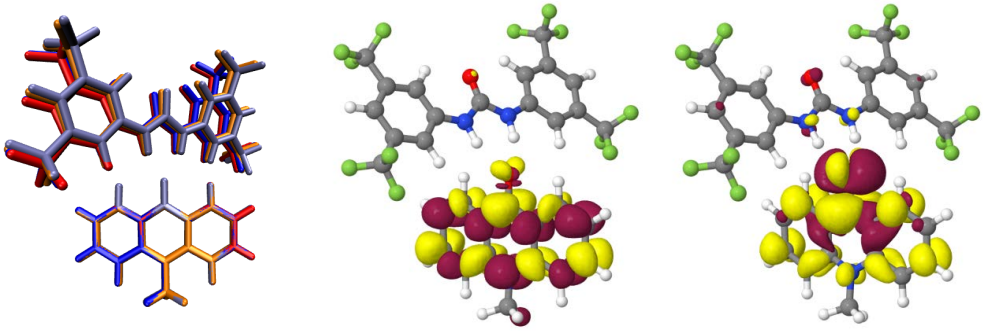

Figure X: Overlay of the optimized geometries of NMA+SKat in different environments. (left) [toluene (blue), THF (red), crystal structure with optimized hydrogen atoms (orange), optimized structure in solid state environment (cyan)] The geometries were aligned to the NMA. Difference densities (red = decrease of electronic density; yellow = increase of electronic density) for the lowest excited singlet $^1\pi\pi^*$-state (middle) and $^1n\pi^*$-state (right) for NMA+SKat. Geometries and difference densities for the corresponding triplet states differ slightly. There is no contribution of SKat to the energetically lowest electronic excitations. Computed at DFT/MRCI level of theory [def2-SV(P) / BH-LYP / PCM-Toluene]

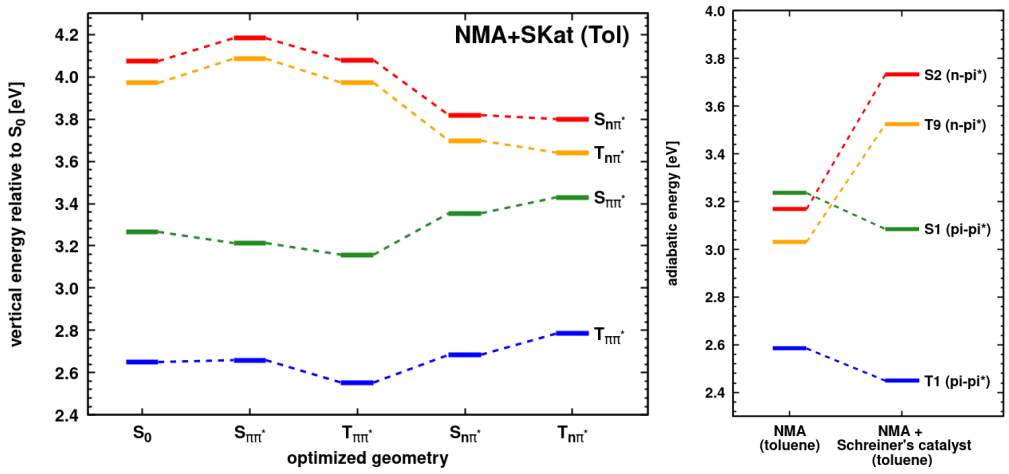

Figure X: Vertical excitation energies without ZPVE correction from the electronic ground state and the optimized geometries of the lowest excited states of NMA+SKat (left) given a rough idea about the PES of the relevant excited states. Due to no crossing of the PES, the vertical state diagram strongly advocates for an efficient radiative decay via $\pi\pi^*$-states and no nonradiative deactivation via $n\pi^*$- states. Comparison of ZPVE corrected adiabatic energies of NMA and NMA+SKat (right) computed at DFT/MRCI level of theory [def2-SV(P) / BH-LYP / PCM-Toluene]. Highlighting the effect of hydrogen bonding on the lowest excited $\pi\pi^*$- and $n\pi^*$- states in the singlet and triplet regime. A strong destabilization of the $n\pi^*$-states and slight stabilization of the $\pi\pi^*$-states is visible.

Supporting information for

Boosting the Fluorescence Quantum Yield of *N*-Methyl-Acridone by Hydrogen Bonding in Solution and Solid State

Matthias Jantz[1], David Klaverkamp[1], Lennart Bunnemann[2], Benedikt Bendel[3], Takin Haj Hassani Sohi[4], Tobias Böhmer[5], Christel M. Marian[5], Vera Vasylyeva-Shor[4], Markus Suta[3], Constantin Czekelius[2] and Peter Gilch[1]*

[1]Institut für Physikalische Chemie, Heinrich-Heine-Universität Düsseldorf, Universitätsstr. 1, 40225 Düsseldorf, Germany

[2]Institut für Organische Chemie und Makromolekulare Chemie, Heinrich-Heine-Universität Düsseldorf, Universitätsstr. 1, 40225 Düsseldorf, Germany

[3]Institut für Anorganische Chemie, Heinrich-Heine-Universität Düsseldorf, Universitätsstr. 1, 40225 Düsseldorf, Germany

[4]Institut für Anorganische Chemie und Strukturchemie, Heinrich-Heine-Universität Düsseldorf, Universitätsstr. 1, 40225 Düsseldorf, Germany

[5]Institut für Theoretische Chemie und Computerchemie, Heinrich-Heine-Universität Düsseldorf, Universitätsstr. 1, 40225 Düsseldorf, Germany

*Corresponding author e-mail: gilch@hhu.de

Table SX: Amplitudes and time constants obtained from the fits to the TCSPC data of NMA in toluene in the absence and in the presence of different Scat concentrations.

[SCat] / 10^{-4} M	A_1	τ_1	A_2	τ_2	A_3	τ_3	A_4	τ_4	$\bar{\tau}$	$\overline{\tau_{rel}}$
0	0.4040± 0.0566	1.0922± 0.0218	0.5959± 0.0358	0.7134± 0.0214			0.0001± 0.00001	18.2915 ±0.0915	0.8686± 0.0686	1.0000
1.84	0.3725± 0.1674	1.1030± 0.0993	0.4487± 0.1436	0.6917± 0.0692	0.1787± 0.0054	6.8600± 0.0343	0.0001± 0.00001	60.7553 ±0.3038	1.9550± 0.2184	2.2521
3.69	0.1541± 0.0986	1.3545± 0.2167	0.5482± 0.0384	0.7510± 0.0451	0.2975± 0.0238	6.8696± 0.0343	0.0001± 0.00002	59.8018 ±0.2990	2.6733± 0.2173	3.0794
5.53	0.1517± 0.0971	1.3473± 0.2290	0.4704± 0.0517	0.7340± 0.0514	0.3777± 0.0264	6.8682± 0.0343	0.0002± 0.00002	57.4952 ±0.2875	3.1581± 0.2311	3.6379
6.33	0.1366± 0.0984	1.3649± 0.2730	0.4516± 0.0587	0.7437± 0.0595	0.4117± 0.0288	6.8762± 0.0344	0.0002± 0.00002	62.2727 ±0.3114	3.3702± 0.2480	3.8822
7.38	0.0973± 0.0613	1.5299± 0.0321	0.4565± 0.0365	0.7591± 0.0455	0.4461± 0.0223	6.8777± 0.0344	0.0002± 0.00002	58.0402 ±0.2902	3.5746± 0.1838	4.1177
22.1	0.0449± 0.0081	2.9059± 0.6102	0.3352± 0.0101	0.7919± 0.0238	0.6196± 0.0062	6.9126± 0.0346	0.0003± 0.00002	59.7140 ±0.2986	4.6970± 0.0611	5.4106
22.1 (412 nm)	0.0130± 0.0031	1.3150± 0.4077			0.9867± 0.0049	6.9349± 0.0347	0.0003± 0.00003	60.9158 ±0.3046	6.8802± 0.0487	7.9255

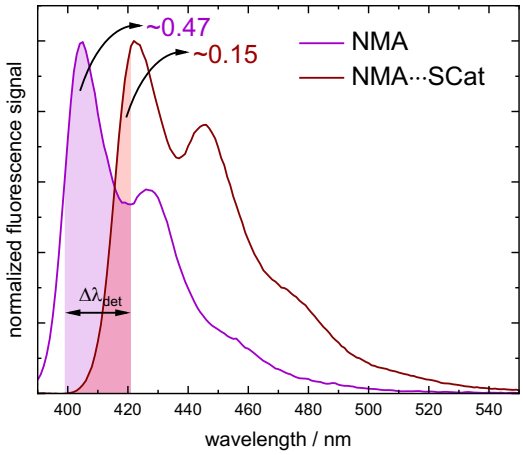

Figure SX: Normalized emission spectra of NMA (9.3 µM) in the absence (purple) and presence of Scat (2.2 mM, dark red). The residual contribution of free NMA was scaled and subtracted to obtain the NMA · · · Scat spectrum. The relative portion of the integrals which are covered by the detection bandpass ($\Delta\lambda_{det}$) centered at 410 nm are highlighted with their respective color.

CXCV

Table SX: Amplitudes and time constants obtained from the fits of the TCSPC data corrected for the different fractions which were covered by the detection bandpass.

[SCat] / 10^{-4} M	A_1^{cor}	τ_1	A_2^{cor}	τ_2	A_3^{cor}	τ_3	A_4^{cor}	τ_4	$\overline{\tau^{cor}}$	$\overline{\tau_{rel}^{cor}}$
0	0.4040	1.0922	0.5959	0.7134			0.0001	18.2915	0.8686	1.0000
1.84	0.2675	1.1030	0.3228	0.6920	0.4096	6.8600	0.00007	60.7553	3.3327	3.8390
3.69	0.0920	1.3540	0.3275	0.7510	0.5805	6.8700	0.00006	59.8018	4.3619	5.0245
5.53	0.0799	1.3470	0.2469	0.7340	0.6731	6.8700	0.00011	57.4952	4.9192	5.6665
6.33	0.0678	1.3640	0.2236	0.7440	0.7086	6.8800	0.00010	62.2727	5.1400	5.9209
7.38	0.0470	1.5300	0.2208	0.7590	0.7321	6.8800	0.00010	58.0402	5.2819	6.0844
22.1	0.0144	2.9060	0.1074	0.7919	0.8781	6.9130	0.00010	59.7150	6.2027	7.1450

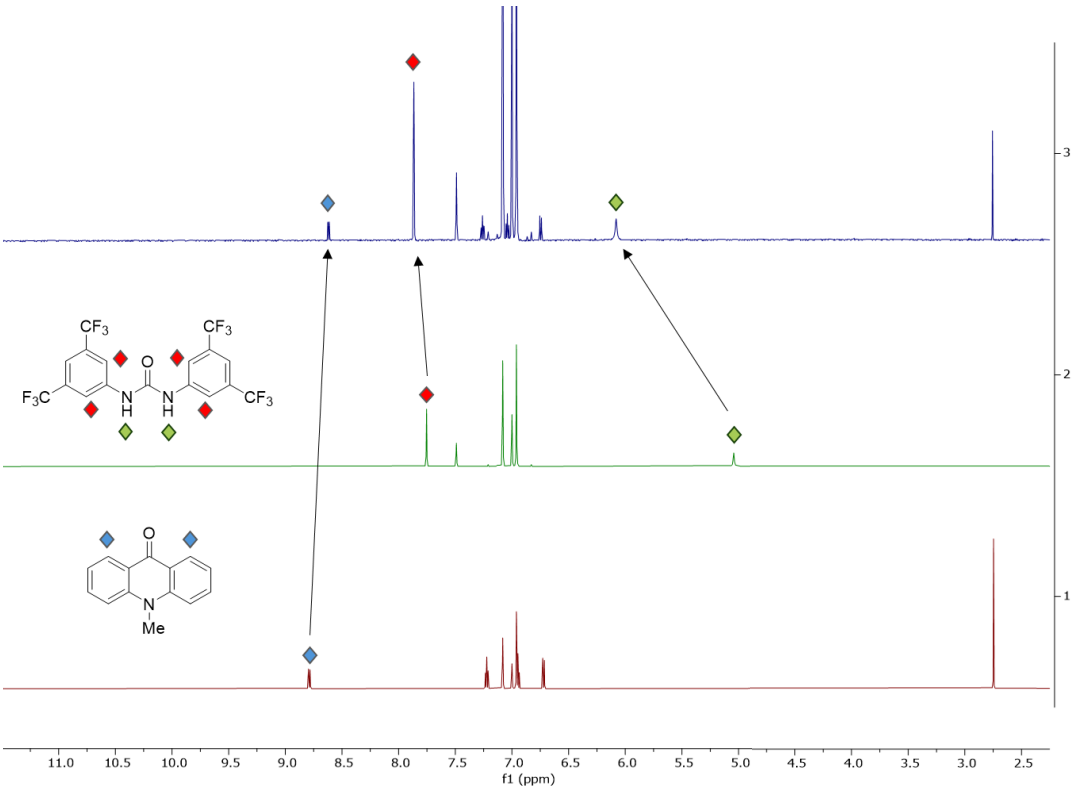

Figure 1: H-NMR-spectrums of 10-methylacridin-9(10H)-one, 1,3-bis(3,5-bis(trifluoromethyl)phenyl)urea and a mixture of both (concentrations always 0.1 M in toluene-d8); in the mixture of both a ratio of around 1 to 3 acridone to urea was present; the aromatic protons in 1,8-position of the acridone are marked with blue diamonds and the aromatic protons of the 1,3-bis(3,5-bis(trifluoromethyl)phenyl)urea are marked with red diamonds, the respective urea protons are marked with green diamonds

Computational Details

The ground state geometries of all investigated compounds were optimized using the Gaussian 16 (1) program package and DFT at PBE0 (2) / def2-SV(P) (3) level of theory. TD-DFT was used for the optimization of the excited singlet states. The Tamm-Dancoff approximation was used for the optimization of the excited triplet states. The analytic calculation of harmonic vibrational frequencies was performed using the Gaussian 16 program. Solvent effect were addressed using the PCM (4) model and the QM/MM (5) approach.

Vertical and adiabatic excitation energies and optical electronic properties were calculated using the DFT/MRCI (6; 7; 8; 9) method. 20 roots were calculated for each singlet and triplet manifold at BH-LYP (10) / def2-SV(P) (3) level of theory (grid = m4, scfconv = 8, denconv = 1d-7, esel = 1.0). The R2016 (8) Hamiltonian was used. Both vibrationally resolved absorption and emission spectra were computed using the VIBES (11; 12) program and the recently implemented VH Method (13).

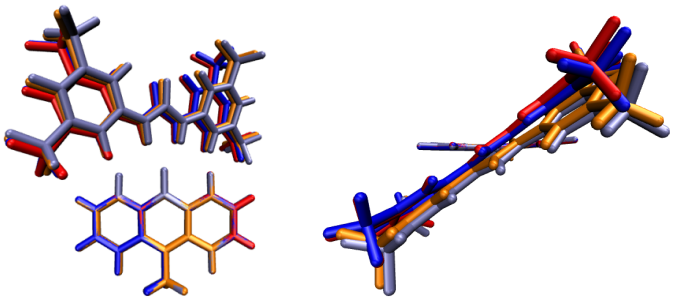

Figure X: Different perspective on the overlay of optimized geometries in different environments. This overlay is supposed to show that the solvent (PCM and QM-MM environment) has only a slight effect on the geometry and a negligible effect on the order or level of excited states that are relevant for the decay pathway mechanism. Toluene (blue), THF (red), crystal structure with optimized hydrogen atoms (orange), optimized structure in solid state environment (cyan).

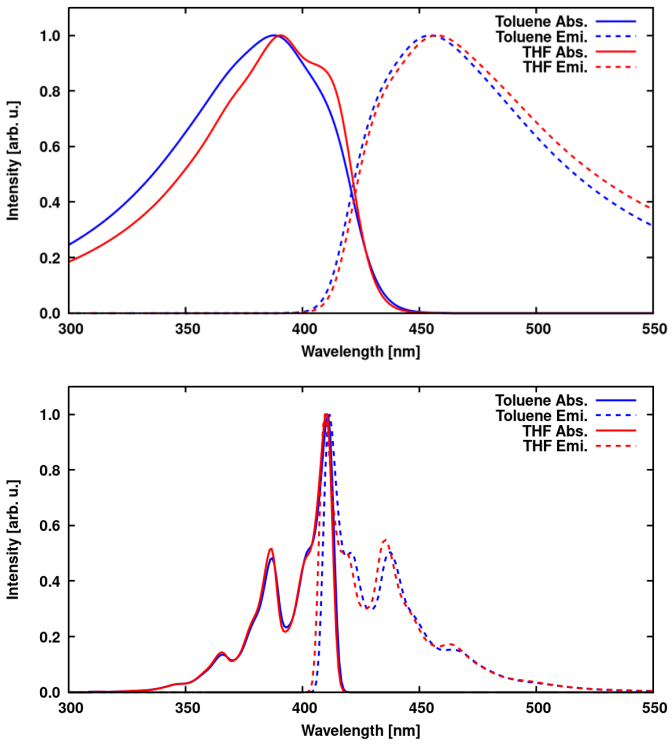

Figure X: Vibrationally resolved absorption (solid lines) and emission (dashed lines) spectra for NMA+SKat in toluene (blue) and THF (red) at 298K (top panel) and without temperature contributions (bottom panel). Strong vibrational progression is visible for NMA+SKat in toluene and THF. The absorption and emission spectra are not expected to change dramatically compared to NMA due to hydrogen bonding.

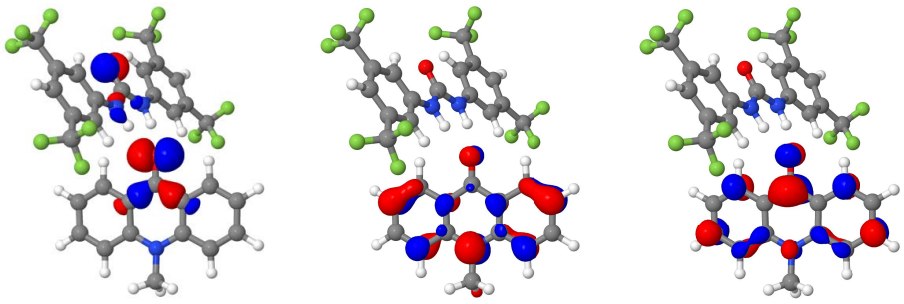

Figure X: Orbitals that are involved in the energetically lowest transitions at the optimized ground state. From left to right: HOMO-8 (n-orbital), HOMO (π-orbital), LUMO (π-orbital).

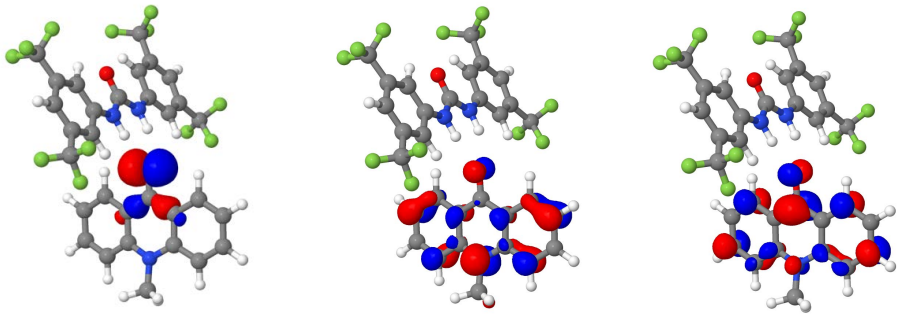

Figure X: Orbitals that are involved in the energetically lowest transitions at the optimized $n\pi^*$-triplet state to demonstrate the change of the nature of the n-orbital. From left to right: HOMO-8 (n-orbital), HOMO (π-orbital), LUMO (π-orbital).

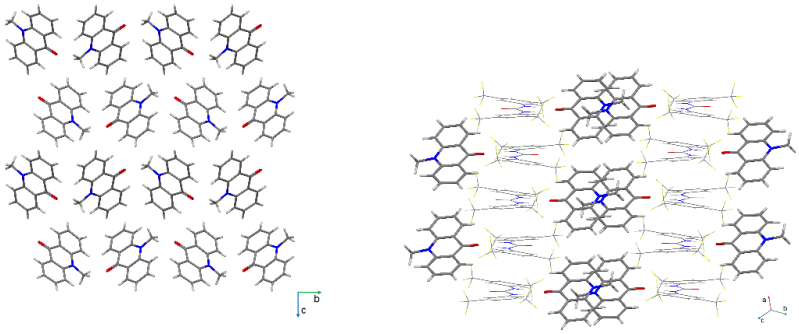

Figure SX: Packing of NMA (left) and NMA:SKat(1:1) co-crystal (right). Figure (left) displays the herringbone pattern of stacked NMA units propagating in columns along the a axis. (Right) rearranged slipped stacks of NMA are separated by SKat layers formed via strong hydrogen bonds between each NMA and SKat entity. In (right) SKat is displayed in wireframe style for clarity.

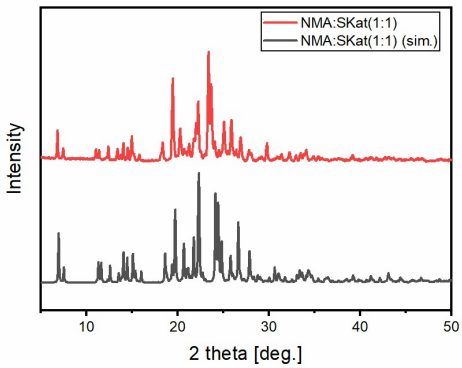

Figure SX: Experimental and simulated PXRDs of the NMA:SKat co-crystal.

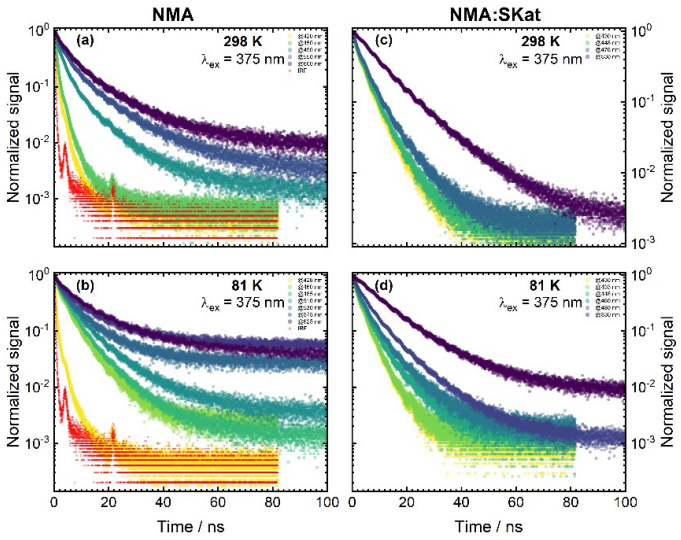

Figure SX: Luminescence decay measurements of NMA and NMA:SKat detected at different emission wavelengths under direct excitation at 298 K ((a), (c)) and 81 K ((b), (d)). The resulting lifetimes are depicted in Table SX.

Table SX: Amplitudes and lifetimes of NMA under direct excitation, detected at different emission wavelengths at 298 K. The corresponding luminescence decay measurements are depicted in figure SX (a).

λ_{em} / nm	A_1	τ_1 / ns	A_2	τ_2 / ns	A_3	τ_3 / ns
410	0.093± 0.006	2.182±0.065	0.906±0.009	0.594±0.006	0.001±0.0002	13.058±2.22
420	0.15±0.005	1.988± 0.04	0.848±0.008	0.486±0.015	0.002± 0.001	9.479±1.422
450	0.235±0.019	2.246± 0.067	0.759±0.008	0.666±0.027	0.006± 0.002	8.723±0.959
490	0.657±0.002	2.84± 0.013	0.207±0.002	0.550±0.007	0.126± 0.002	10.638±0.077
550	0.472±0.010	2.053± 0.029	0.448±0.006	6.336±0.156	0.106± 0.007	18.039±0.516
600	0.295±0.0172	2.270± 0.079	0.532±0.011	6.506±0.204	0.17± 0.01	18.759 0.465

Table SX: Amplitudes and lifetimes of NMA under direct excitation, detected at different emission wavelengths at 81 K. The corresponding luminescence decay measurements are depicted in figure SX (b).

λ_{em} / nm	A_1	τ_1 / ns	A_2	τ_2 / ns	A_3	τ_3 / ns
428	0.216±0.015	2.327±0.093	0.777±0.007	0.639±0.032	0.006±0.002	8.797±1.32
460	0.381±0.006	1.457±0.017	0.632±0.004	5.012±0.065	0.038±0.007	12.856±0.874
485	0.275±0.007	1.545±0.028	0.656±0.005	4.969±0.069	0.081±0.008	12.776±0.429
510	0.298±0.009	1.73± 0.038	0.617±0.006	5.642±0.103	0.119±0.009	15.188±0.426
530	0.274±0.013	1.638±0.064	0.583±0.009	6.093±0.188	0.128±0.014	16.97± 0.778
575	0.235±0.011	1.778±0.085	0.536±0.009	7.302±0.237	0.161±0.013	21.781±0.823
625	0.259±0.008	2.656±0.086	0.593±0.006	10.622±0.19	0.086±0.006	36.945±1.274

CC

Table SX: Amplitudes and lifetimes of NMA:SKat under direct excitation, detected at different emission wavelengths at 298 K. The corresponding luminescence decay measurements are depicted in figure SX (c).

λ_{em} / nm	A_1	τ_1 / ns	A_2	τ_2 / ns	A_3	τ_3 / ns
430	0.330±0.006	1.241±0.018	0.659±0.004	4.467±0.059	0.022±0.007	12.625±1.817
448	0.229±0.007	1.240±0.023	0.689±0.006	4.622±0.07	0.03±0.01	12.056±1.646
476	0.273±0.009	1.431±0.033	0.681±0.009	5.052±0.103	0.064±0.015	12.433±1.088
530	0.973±0.005	9.580±0.035	0.054±0.005	26.014±1.25		

Table SX: Amplitudes and lifetimes of NMA:SKat under direct excitation, detected at different emission wavelengths at 81 K. The corresponding luminescence decay measurements are depicted in figure SX (d).

λ_{em} / nm	A_1	τ_1 / ns	A_2	τ_2 / ns	A_3	τ_3 / ns
430	0.459 ±0.004	1.293 ±0.01	0.558 ±0.004	3.958 ±0.015		
433	0.427 ±0.004	1.254 ±0.009	0.580 ±0.004	4.02 ±0.014		
448	0.443 ±0.008	1.407 ±0.018	0.560 ±0.005	4.562 ±0.076	0.026 ±0.006	14.335 ±1.713
460	0.449 ±0.007	1.236 ±0.02	0.609 ±0.005	4.574 ±0.075	0.072 ±0.009	12.399 ±0.664
480	0.322 ±0.005	1.438 ±0.024	0.627 ±0.006	5.281 ±0.07	0.158 ±0.009	12.277 ±0.237
530	0.239 ±0.002	10.333 ±0.029	0.0296 ±0.003	42.131 ±3.161		

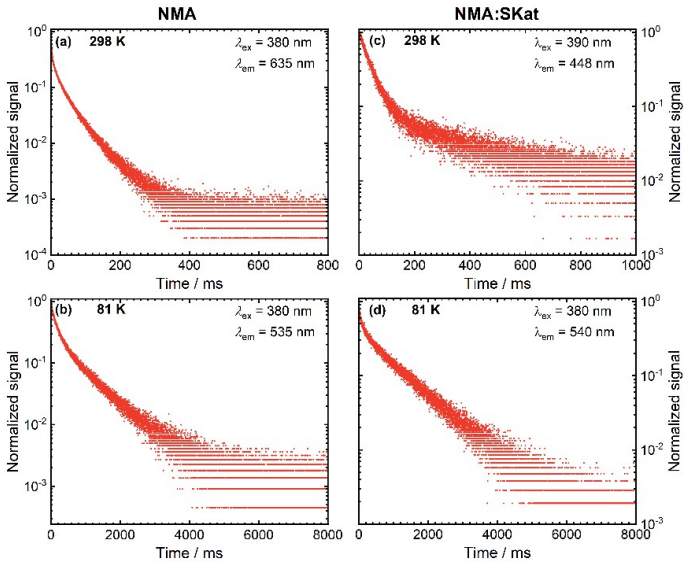

Figure SX: Luminescence decay measurements of NMA and NMA:SKat after a 1 ms delay at 298 K ((a), (c)) and 81 K ((b), (d)). The detected emission wavelength corresponds with the emission maximum after a 1 ms delay. The resulting lifetimes are depicted in Table SX.

Table SX: Table SX: Amplitudes and lifetimes of NMA and NMA:SKat after a 1 ms delay at 298 K. The corresponding luminescence decay measurements are depicted in figure SX (a) and (c).

	A_1	τ_1 / ns	A_2	τ_2 / ns	A_3	τ_3 / ns
NMA	0.537 ±0.001	1.206 ±0.005	0.259 ±0.001	8.987 ±0.059	0.188 ±0.001	46.357 ±0.127
MPK002	0.893 ±0.002	35.8403 ±0.145	0.08224 ±0.002	287.897 ±9.044		

Table SX: Amplitudes and lifetimes of NMA and NMA:SKat after a 1 ms delay at 81 K. The corresponding luminescence decay measurements are depicted in figure SX (b) and (d).

	A_1	τ_1 / ns	A_2	τ_2 / ns	A_3	τ_3 / ns
NMA	0.152 ±0.003	21.66 ±0.746	0.545 ±0.002	148.274 ±1.125	0.281 ±0.002	757.495 ±3.463
MPK002	0.427 ±0.002	75.619 ±0.701	0.417 ±0.001	948.542 ±3.023		

Literaturverzeichnis

1. **M. J. Frisch, G. W. Trucks, H. B. Schlegel, G. E. Scuseria, M. A. Robb, J. R. Cheeseman, G. Scalmani, V. Barone, G. A. Petersson, H. Nakatsuji et al.** Gaussian 16. Wallingford, Connecticut, United States of America : Gaussian, Inc., 2016.
2. **Barone, C. Adamo and V.** oward reliable density functional methods without adjustable parameters: The PBE0 model,. *J. Chem. Phys.* 1999, 110.
3. **Ahlrichs., Florian Weigend and Reinhart.** Balanced basis sets of split valence, triple zeta valence and quadruple zeta valence quality for h to rn: Design and assessment of accuracy. *Phys. Chem. Chem. Phys.,.* 2005, 7.
4. **E. Cancés, B. Mennucci, and J. Tomasi.** A new integral equation formalism for the polarizable continuum model: Theoretical background and applications to isotropic and anisotropic dielectrics. *The Journal of Chemical Physics.* 1997, 107.
5. **Weingart O, Nenov A, Altoè P, Rivalta I, Segarra-Martí J, Dokukina I, Garavelli M.** COBRAMM 2.0 - A software interface for tailoring molecular electronic structure calculations and running nanoscale (QM/MM) simulations. *J Mol Model.* 9, 2018, 24.
6. **Waletzke, Stefan Grimme and Mirko.** A combination of Kohn–Sham density functional theory and multi-reference configuration interaction methods. *J. Chem. Phys.* 1999, 111.
7. **Christel M. Marian, Adrian Heil, and Martin Kleinschmidt.** The DFT/MRCI Method. *WIREs Computational Molecular Science.* 2019, 9.
8. **Igor Lyskov, Martin Kleinschmidt, and Christel M. Marian.** Redesign of the dft/mrci hamiltonian. *The Journal of Chemical Physics.* 2016, 144.
9. **Martin Kleinschmidt, Christel M. Marian, Mirko Waletzke, and Stefan Grimme.** Parallel multireference configuration interaction calculations on mini-β-carotenes and β-carotene. *J. Chem. Phys.* 2019, 130.
10. **Becke, Axel D.** A new mixing of hartree–fock and local density-functional theories. *J. Chem. Phys.* 2, 1993, 98.
11. **Mihajlo Etinski, Vidisha Rai-Constapel, and Christel M. Marian.** Timedependent approach to spin-vibronic coupling: Implementation and assessment. *J. Chem. Phys.* 2014, 140.
12. **M. Etinski, J. Tatchen, and C. M. Marian.** Thermal and solvent effects on the triplet formation in cinnoline. *Phys. Chem. Chem. Phys.* 2014, 16.
13. **Tobias Böhmer, Martin Kleinschmidt, and Christel M. Marian. Toward the improvement of vibronic spectra and non-radiative rate constants using the vertical Hessian method.** Toward the improvement of vibronic spectra and non-radiative rate constants using the vertical Hessian method. *J. Chem. Phys.* 2024, 161.